

ADA 278 738

UNITED STATES AIR FORCE

SUMMER RESEARCH PROGRAM -- 1993

SUMMER RESEARCH PROGRAM FINAL REPORTS

VOLUME 5B

WRIGHT LABORATORY

RESEARCH & DEVELOPMENT LABORATORIES

5800 Uplander Way

Culver City, CA 90230-6608

Program Director, RDL
Gary Moore

Program Manager, AFOSR
Col. Hal Rhoades

Program Manager, RDL
Scott Licoscas

Program Administrator, RDL
Gwendolyn Smith

Program Administrator, RDL
Johnetta Thompson

Submitted to:

AIR FORCE OFFICE OF SCIENTIFIC RESEARCH

Bolling Air Force Base

Washington, D.C.

December 1993

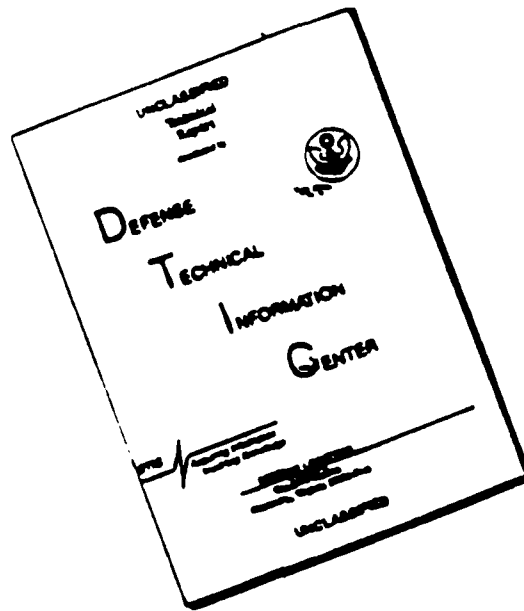
94-12243



DISC QUALITY INSPECTED 3

94 4 21 071

DISCLAIMER NOTICE



**THIS DOCUMENT IS BEST
QUALITY AVAILABLE. THE COPY
FURNISHED TO DTIC CONTAINED
A SIGNIFICANT NUMBER OF
PAGES WHICH DO NOT
REPRODUCE LEGIBLY.**

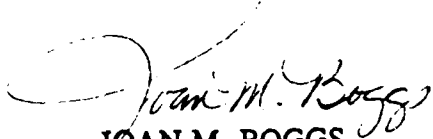
MEMORANDUM FOR DTIC (Acquisition)
(Attn: Pat Mauby)

SUBJECT: Distribution of USAF (AFOSR Summer Research Program (Air Force Laboratories) and Universal Energy Systems, Inc., and the Research Initiation Program

FROM: AFOSR/XPT

Joan M. Boggs
110 Duncan Avenue, Suite B115
Bolling AFB DC 20332-0001

1. All of the books forwarded to DTIC on the subjects above should be considered Approved for Public Release, distribution is unlimited (Distribution Statement A).
2. Thank you for processing the attached information.


JOAN M. BOGGS
Chief, Technical Information Division

*1993 SRP Vol 1, 2, 3, 4, 5A, 5B, 6, 7, 8, 9
(10 Books)*

Master Index for Faculty Members

Abbott, Ben Research, MS Box 1649 Station B Vanderbilt University Nashville, TN 37235-0000	Field: Electrical Engineering Laboratory: AEDC/ Vol-Page No: 6- 1
Abrate, Serge Assistant Professor, PhD Mechanical & Aerospace En University of Missouri - Rolla Rolla, MO 65401-0249	Field: Aeronautical Engineering Laboratory: WL/FI Vol-Page No: 5-15
Almallahi, Hussein Instructor, MS P.O. Box 308 Prairie View A&M University Prairie View, TX 77446-0000	Field: Electrical Engineering Laboratory: AL/HR Vol-Page No: 2-25
Anderson, James Associate Professor, PhD Chemistry University of Georgia Athens, GA 30602-2556	Field: Analytical Chemistry Laboratory: AL/EQ Vol-Page No: 2-18
Anderson, Richard Professor, PhD Physics University of Missouri, Rolla Rolla, MO 65401-0000	Field: Physics Laboratory: PL/LI Vol-Page No: 3- 7
Ashrafiuon, Hashem Assistant Professor, PhD Mechanical Engineering Villanova University Villanova, PA 19085-0000	Field: Mechanical Engineering Laboratory: AL/CF Vol-Page No: 2- 6
Backs, Richard Assistant Professor, PhD Dept. of Psychology Wright State University Dayton, OH 45435-0001	Field: Experimental Psychology Laboratory: AL/CF Vol-Page No: 2- 7
Baginski, Thomas Assoc Professor, PhD 200 Broun Hall Auburn University Auburn, AL 36849-5201	Field: Electrical Engineering Laboratory: WL/MN Vol-Page No: 5-40

SFRP Participant Data

Baker, Suzanne
Assistant Professor, PhD
Dept. of Psychology
James Madison University
Harrisonburg, VA 22807-0000

Field:
Laboratory: AL/OE

Vol-Page No: 2-36

Baker, Albert
Assistant Professor, PhD

Field: Electrical Engineering
Laboratory: WL/MT

Vol-Page No: 5-53

University of Cincinnati
, - 0

Balakrishnan, Sivasubramanya
Associate Professor, PhD

Field: Aerospace Engineering
Laboratory: WL/MN

Vol-Page No: 5-41

University of Missouri, Rolla
, - 0

Bannister, William
Professor, PhD

Field: Organic Chemistry
Laboratory: WL/FI

Vol-Page No: 5-16

Univ of Mass.-Lowell
Lowell, MA 1854-0000

Barnard, Kenneth
Assistant Professor, PhD

Field: Electrical Engineering
Laboratory: WL/AA

Vol-Page No: 5- 1

Memphis State University
, - 0

Bayard, Jean-Pierre
Associate Professor, PhD
6000 J Street
California State Univ-Sacramen
Sacramento, CA 95819-6019

Field: Electrical/Electronic Eng
Laboratory: RL/ER

Vol-Page No: 4- 7

Beardsley, Larry
Research Professor, MS

Field: Mathematics
Laboratory: WL/MN

Vol-Page No: 5-42

Athens State College
, - 0

Beecken, Brian
Associate Professor, PhD
3900 Bethel Dr.
Bethel College
St. Paul, MN 55112-0000

Field: Dept. of Physics
Laboratory: PL/VT

Vol-Page No: 3-23

SFRP Participant Data

Bellem, Raymond
Dept, CHM. EE cs, PhD
3200 Willow Creek Road
Embry-Riddle Aeronautical Univ
Prescott, AZ 86301-0000

Field: Dept. of Computer Science
Laboratory: PL/VT

Vol-Page No: 3-24

Bellem, Raymond
Dept, CHM. EE cs, PhD
3200 Willow Creek Road
Embry-Riddle Aeronautical Univ
Prescott, AZ 86301-0000

Field: Dept. of Computer Science
Laboratory: /

Vol-Page No: 0- 0

Bhuyan, Jay
Assistant Professor, PhD
Dept. of Computer Science
Tuskegee University
Tuskegee, AL 36088-0000

Field: Computer Science
Laboratory: PL/WS

Vol-Page No: 3-33

Biegl, Csaba
Assistant Professor, PhD
Box 1649 Station B
Vanderbilt University
Nashville, TN 37235-0000

Field: Electrical Engineering
Laboratory: AEDC/

Vol-Page No: 6- 2

Biggs, Albert
Professor, PhD
Electrical Engineering
Univ. of Alabama, Huntsville
Huntsville, AL 35899-0000

Field:
Laboratory: PL/WS

Vol-Page No: 3-34

Blystone, Robert
Professor, PhD
Trinity University
715 Stadium Drive
San Antonio, TX 78212-7200

Field: Dept of Biology
Laboratory: AL/OE

Vol-Page No: 2-37

Branting, Luther
Assistant Professor, PhD
PO Box 3682
University of Wyoming
Laramie, WY 82071-0000

Field: Dept of Computer Science
Laboratory: AL/HR

Vol-Page No: 2-26

Bryant, Barrett
Associate Professor, PhD
115A Campbell Hall
University of Alabama, Birming
Birmingham, AL 35294-1170

Field: Computer Science
Laboratory: RL/C3

Vol-Page No: 4- 1

Accession For	
NTIS CRA&I	<input checked="" type="checkbox"/>
DTIC TAB	<input type="checkbox"/>
Unannounced	<input type="checkbox"/>
Justification	
By <i>Htr</i>	
Distribution /	
Availability Codes	
Dist	Avail and/or Special
<i>A-1</i>	

SFRP Participant Data

Callens, Jr., Eugene
Association Professor, PhD
Industrial
Louisiana Technical University
Ruston, LA 71270-0000

Field: Aerospace Engineering
Laboratory: WL/MM

Vol-Page No: 5-43

Cannon, Scott
Associate Professor, PhD
Computer Science
Utah State University
Logan, UT 84322-0000

Field: Computer Science/Biophys.
Laboratory: PL/VT

Vol-Page No: 3-25

Carlisle, Gene
Professor, PhD
Dept. of Physics
West Texas State University
Canyon, TX 79016-0000

Field: Killgore Research Center
Laboratory: PL/LI

Vol-Page No: 3- 8

Catalano, George
Associate Professor, PhD
Mechanical Engineering
United States Military Academy
West Point, NY 10996-1792

Field: Department of Civil &
Laboratory: AEDC/

Vol-Page No: 6- 3

Chang, Ching
Associate Professor, PhD
Euclid Ave at E. 24th St
Cleveland State University
Cleveland, OH 44115-0000

Field: Dept. of Mathematics
Laboratory: WL/FI

Vol-Page No: 5-17

Chattopadhyay, Somnath
Assistant Professor, PhD

Field: Mechanical Engineering
Laboratory: PL/RK

University of Vermont
Burlington, VT 5405-0156

Vol-Page No: 3-14

Chen, C. L. Philip
Assistant Professor, PhD
Computer Science Engineer
Wright State University
Dayton, OH 45435-0000

Field: Electrical Engineering
Laboratory: WL/ML

Vol-Page No: 5-26

Choate, David
Assoc Professor, PhD
Dept. of Mathematics
Transylvania University
Lexington, KY 40505-0000

Field: Mathematics
Laboratory: PL/LI

Vol-Page No: 3- 9

SFRP Participant Data

Chubb, Gerald
Assistant Professor, PhD
164 W. 19th Ave.
Ohio State University
Columbus, OH 43210-0000

Field: Dept. of Aviation
Laboratory: AL/HR

Vol-Page No: 2-27

Chuong, Cheng-Jen
Associate Professor, PhD
501 W. 1st Street
University of Texas, Arlington
Arlington, TX 76019-0000

Field: Biomedical Engineering
Laboratory: AL/CF

Vol-Page No: 2- 8

Citera, Maryalice
Assistant Professor, PhD
Department of Psychology
Wright State University
Dayton, OH 4-5435

Field: Industrial Psychology
Laboratory: AL/CF

Vol-Page No: 2- 9

Collard, Jr., Sneed
Professor, PhD
Ecology & Evolutionary Bi
University of West Florida
Pensacola, FL 32514-0000

Field: Biology
Laboratory: AL/EQ

Vol-Page No: 2-19

Collier, Geoffrey
Assistant Professor, PhD
300 College St., NE
South Carolina State College
Orangeburg,, SC 29117-0000

Field: Dept of Psychology
Laboratory: AL/CF

Vol-Page No: 2-10

Cone, Milton
Assistant Professor, PhD
3200 Willow Creek Road
Embry-Riddle Aeronautical Univ
Prescott, AZ 86301-3720

Field: Electrical Engineering
Laboratory: WL/AA

Vol-Page No: 5- 2

Cundari, Thomas
Assistant Professor, PhD
Jim Smith Building
Memphis State University
Memphis, TN 38152-0000

Field: Department of Chemistry
Laboratory: PL/RK

Vol-Page No: 3-15

D'Agostino, Alfred
Assistant Professor, PhD
4202 E Fowler Ave/SCA-240
University of South Florida
Tampa, FL 33620-5250

Field: Dept of Chemistry
Laboratory: WL/ML

Vol-Page No: 5-27

SFRP Participant Data

Das, Asesh
Assistant Professor, PhD
Research Center
West Virginia University
Morgantown, WV 26505-0000

Field: Concurrent Engineering
Laboratory: AL/ER

Vol-Page No: 2-28

DeLyser, Ronald
Assistant Professor, PhD
2390 S. York Street
University of Denver
Denver, CO 80208-0177

Field: Electrical Engineering
Laboratory: PL/WS

Vol-Page No: 3-35

DeVecchio, Vito
Professor, PhD
Biology
University of Scranton
Scranton, PA 18510-4625

Field: Biochemical Genetics
Laboratory: AL/AO

Vol-Page No: 2- 1

Dey, Pradip
Associate Professor, PhD

Field: Computer Science
Laboratory: RL/IR

Hampton University
- 0

Vol-Page No: 4-16

Ding, Zhi
Assistant Professor, PhD
200 Broun Hall
Auburn University
Auburn, AL 36849-5201

Field: Electrical Engineering
Laboratory: WL/MN

Vol-Page No: 5-44

Doherty, John
Assistant Professor, PhD
201 Coover Hall
Iowa State University
Ames, IA 50011-1045

Field: Electrical Engineering
Laboratory: RL/OC

Vol-Page No: 4-21

Dolson, David
Assistant Professor, PhD

Field: Chemistry
Laboratory: WL/PO

Wright State University
- 0

Vol-Page No: 5-56

Dominic, Vincent
Assistant professor, MS
300 College Park
University of Dayton
Dayton, OH 45469-0227

Field: Electro Optics Program
Laboratory: WL/ML

Vol-Page No: 5-28

SFRP Participant Data

Donkor, Eric
Assistant Professor, PhD
Engineering
University of Connecticut
Stroes, CT 6269-1133

Field: Electrical Engineering
Laboratory: RL/OC

Vol-Page No: 4-22

Driscoll, James
Associate Professor, PhD
3004 FXB Bldg 2118
University of Michigan
Ann Arbor, MI 48109-0000

Field: Aerospace Engineering
Laboratory: WL/PO

Vol-Page No: 5-57

Duncan, Bradley
Assistant Professor, PhD
300 College Park
University of Dayton
Dayton, OH 45469-0226

Field: Electrical Engineering
Laboratory: WL/AA

Vol-Page No: 5- 3

Ehrhart, Lee
Instructor, MS
Communications & Intellig
George Mason University
Fairfax, VA 22015-1520

Field: Electrical Engineering
Laboratory: RL/C3

Vol-Page No: 4- 2

Ewert, Daniel
Assistant Professor, PhD
Electrical Engineering
North Dakota State University
Fargo, IN 58105-0000

Field: Physiology
Laboratory: AL/AO

Vol-Page No: 2- 2

Ewing, Mark
Associate Professor, PhD
2004 Learned Hall
University of Kansas
Lawrence, KS 66045-2969

Field: Engineering Mechanics
Laboratory: PL/SX

Vol-Page No: 3-22

Foo, Simon
Assistant Professor, PhD
College of Engineering
Florida State University
Tallahessee, FL 32306-0000

Field: Electrical Engineering
Laboratory: WL/MN

Vol-Page No: 5-45

Frantziskonis, George
Assistant Professor, PhD
Dept of Civil Engrng/Mech
University of Arizona
Tucson, AZ 85721-1334

Field: College of Engrng/Mines
Laboratory: WL/ML

Vol-Page No: 5-29

SFRP Participant Data

Frenzel III, James
Assistant Professor, PhD
Dept of Electrical Engr
University of Idaho
Moscow, ID 83844-1023

Field: Electrical Engineering
Laboratory: WL/AA

Vol-Page No: 5- 4

Fried, Joel
Professor, PhD
Chemical Engineering
University of Cincinnati
Cincinnati, OH 45221-0171

Field: Polymer Science
Laboratory: WL/PO

Vol-Page No: 5-58

Friedman, Jeffrey
Assistant Professor, PhD
Physics
University of Puerto Rico
Mayaguez, PR 681-0000

Field: Physics/Astrophysics
Laboratory: PL/GP

Vol-Page No: 3- 1

Fuller, Daniel
Dept. Chairman, PhD
Chemistry & Physics
Nicholls State University
Thibodaux, LA 70310-0000

Field: Chemistry
Laboratory: PL/RK

Vol-Page No: 3-16

Gao, Zhanjun
Assistant Professor, PhD
203 W. Old Main, Box 5725
Clarkson University
Potsdam, NY 13699-5725

Field: Mechanical/Aeronautical E
Laboratory: WL/ML

Vol-Page No: 5-30

Gavankar, Prasad
Asst Professor, PhD
Campus Box 191
Texas A&I University
Kingsville, TX 78363-0000

Field: Mech & Indust Engineering
Laboratory: WL/MT

Vol-Page No: 5-54

Gebert, Glenn
Assistant Professor, PhD
Mechanical
Utah State University
Logan, UT 84339-0000

Field: Aerospace Engineering
Laboratory: WL/MN

Vol-Page No: 5-46

Gedom, Larry
Professor, PhD
Natural Science
Mobile College
Mobil, AL 36663-0220

Field: Chemistry
Laboratory: AL/EQ

Vol-Page No: 2-20

SFRP Participant Data

Ghajar, Afshin
Professor, PhD
Mech. & Aerospace Engineer
Oklahoma State University
Stillwater, OK 74078-0533

Field: Mechanical Engineering
Laboratory: WL/PO

Vol-Page No: 5-59

Gopalan, Kaliappan
Associate Professor, PhD
Dept of Engineering
Purdue University, Calumet
Hammond, IN 46323-0000

Field:
Laboratory: AL/CF

Vol-Page No: 2-11

Gould, Richard
Assistant Professor, PhD
Mechanical & Aerospace En
N.Carolina State University
Raleigh, NC 27695-7910

Field: Mechanical Engineering
Laboratory: WL/PO

Vol-Page No: 5-60

Gowda, Raghava
Assistant Professor, PhD
Dept of Computer Science
University of Dayton
Dayton, OH 45469-2160

Field: Computer Information Sys.
Laboratory: WL/AA

Vol-Page No: 5- 5

Graetz, Kenneth
Assistant Professor, PhD
300 College Park
University of Dayton
Dayton, OH 45469-1430

Field: Department of Psychology
Laboratory: AL/HR

Vol-Page No: 2-29

Gray, Donald
Associate Professor, PhD
PO Box 6101
West Virginia University
Morgantown, WV 20506-6101

Field: Dept of Civil Engineering
Laboratory: AL/EQ

Vol-Page No: 2-21

Green, Bobby
Assistant Professor, MS
Box 43107
Texas Tech University
Lubbock, TX 79409-3107

Field: Electrical Engineering
Laboratory: WL/FI

Vol-Page No: 5-18

Grubbs, Elmer
Assistant Professor, MS
Engineering
New Mexico Highland University
Las Vegas, NM 87701-0000

Field: Electrical Engineering
Laboratory: WL/AA

Vol-Page No: 5- 6

SFRP Participant Data

Guest, Joyce
Associate, PhD
Department of Chemistry
University of Cincinnati
Cincinnati, OH 45221-0172

Field: Physical Chemistry
Laboratory: WL/ML

Vol-Page No: 5-31

Gumbs, Godfrey
Professor, PhD
Physics & Astronomy
University New York Hunters Co
New York, NY 10021-0000

Field: Condensed Matter Physics
Laboratory: WL/EL

Vol-Page No: 5-12

Hakkinen, Raimo
Professor, PhD
207 Jolley Hall
Washington University
St. Louis, MO 63130-0000

Field: Mechanical Engineering
Laboratory: WL/FI

Vol-Page No: 5-19

Hall, Jr., Charles
Assistant Professor, PhD
Mech & Aerospace Engr.
North Carolina Univ.
Raleigh, NC 27695-7910

Field:
Laboratory: WL/FI

Vol-Page No: 5-20

Hancock, Thomas
Assistant Professor, PhD

Field: Educational Psychology
Laboratory: AL/HR

Grand Canyon University
0

Vol-Page No: 2-30

Hannafin, Michael
Visiting Professor, PhD
305-D Stone Building, 3030
Florida State University
Tallahassee, FL 3-2306

Field: Educational Technology
Laboratory: AL/HR

Vol-Page No: 2-31

Helbig, Herbert
Professor, PhD
Physics
Clarkson University
Potsdam, NY 13699-0000

Field: Physics
Laboratory: RL/ER

Vol-Page No: 4- 8

Henry, Robert
Professor, PhD
Electrical Engineering
University of Southwestern Lou
Lafayette, LA 70504-3890

Field: Electrical Engineering
Laboratory: RL/C3

Vol-Page No: 4- 3

SFRP Participant Data

Hong, Lang
Assistant Professor, PhD
Dept of Electrical Engin
Wright State University
Dayton, OH 45435-0000

Field: Electrical Engineering
Laboratory: WL/AA

Vol-Page No: 5- 7

Hsu, Lifang
Assistant Professor, PhD

Field: Mathematical Statistics
Laboratory: RL/ER

Le Moyne College
, - 0

Vol-Page No: 4- 9

Huang, Ming
Assistant Professor, PhD
500 NW 20th Street
Florida Atlantic University
Boca Raton, FL 33431-0991

Field: Mechanical Engineering
Laboratory: AL/CF

Vol-Page No: 2-12

Humi, Mayer
Professor, PhD
Mathematics
Worcester Polytechnic Institu
Worcester, MA 1609-2280

Field: Applied Mathematics
Laboratory: PL/GP

Vol-Page No: 3- 2

Humi, Mayer
Professor, PhD
Mathematics
Worcester Polytechnic Institu
Worcester, MA 1609-2280

Field: Applied Mathematics
Laboratory: /

Vol-Page No: 0- 0

Jabbour, Kamal
Associate Professor, PhD
121 Link hall
Syracuse University
Syracuse, NY 13244-1240

Field: Electrical Engineering
Laboratory: RL/C3

Vol-Page No: 4- 4

Jaszczak, John
Assistant Professor, PhD
Dept. of Physics
Michigan Technological Univers
Houghton, MI 49931-1295

Field:
Laboratory: WL/ML

Vol-Page No: 5-32

Jeng, San-Mou
Associte, PhD
Mail Location #70
University of Cincinnati
Cincinnati, OH 45221-0070

Field: Aerospace Engineering
Laboratory: PL/RR

Vol-Page No: 3-17

SFRP Participant Data

Johnson, David
Associate Professor, PhD
Dept of Chemistry
University of Dayton
Dayton, OH 45469-2357

Field: Chemistry
Laboratory: WL/ML

Vol-Page No: 5-33

Karimi, Amir
Associate, PhD
Division Engineering
University of Texas, San Anton
San Antonio, TX 7824-9065

Field: Mechanical Engineering
Laboratory: PL/VT

Vol-Page No: 3-26

Kheyfets, Arkady
Assistant Professor, PhD
Dept. of Mathematics
North Carolina State Univ.
Raleigh, NC 27695-7003

Field:
Laboratory: PL/VT

Vol-Page No: 3-27

Koblasz, Arthur
Associate, PhD
Civil Engineering
Georgia State University
Atlanta, GA 30332-0000

Field: Engineering Science
Laboratory: AL/AO

Vol-Page No: 2- 3

Kraft, Donald
Professor, PhD
Dept. of Computer Science
Louisiana State University
Baton Rouge, LA 70803-4020

Field:
Laboratory: AL/CF

Vol-Page No: 2-13

Kumar, Rajendra
Professor, PhD
1250 Bellflower Blvd
California State University
Long Beach, CA 90840-0000

Field: Electrical Engineering
Laboratory: RL/C3

Vol-Page No: 4- 5

Kumta, Prashant
Assistant Professor, PhD
Dept of Materials Science
Carnegie-Mellon University
Pittsburgh, PA 15213-3890

Field: Materials Science
Laboratory: WL/ML

Vol-Page No: 5-34

Kuo, Spencer
Professor, PhD
Route 110
Polytechnic University
Farmingdale, NY 11735-0000

Field: Electrophysics
Laboratory: PL/GP

Vol-Page No: 3- 3

SFRP Participant Data

Lakeou, Samuel
Professor, PhD
Electrical Engineering
University of the District of
Washington, DC 20008-0000

Field: Electrical Engineering
Laboratory: PL/VT

Vol-Page No: 3-28

Langhoff, Peter
Professor, PhD

Field: Dept. of Chemistry
Laboratory: PL/RK

Vol-Page No: 3-18

Indiana University
Bloomington, IN 47405-4001

Lawless, Brother
Assoc Professor, PhD
Dept. Science /Mathematic
Fordham University
New York, NY 10021-0000

Field: Box 280
Laboratory: AL/OE

Vol-Page No: 2-38

Lee, Tzesan
Associate Professor, PhD
Dept. of Mathematics
Western Illinois University
Macomb, IL 61455-0000

Field:
Laboratory: AL/OE

Vol-Page No: 2-39

Lee, Min-Chang
Professor, PhD
167 Albany Street
Massachusetts Institute
Cambridge, MA 2139-0000

Field: Plasma Fusion Center
Laboratory: PL/GP

Vol-Page No: 3- 4

Lee, Byung-Lip
Associate Professor, PhD
Engineering Sci. & Mechan
Pennsylvania State University
University Park, PA 16802-0000

Field: Materials Engineering
Laboratory: WL/ML

Vol-Page No: 5-35

Leigh, Wallace
Assistant Professor, PhD
26 N. Main St.
Alfred University
Alfred, NY 14802-0000

Field: Electrical Engineering
Laboratory: RL/ER

Vol-Page No: 4-10

Levin, Rick
Research Engineer II, MS
EM Effects Laboratory
Georgia Institute of Technolog
Atlanta, GA 30332-0800

Field: Electrical Engineering
Laboratory: RL/ER

Vol-Page No: 4-11

SFRP Participant Data

Li, Jian Asst Professor, PhD 216 Larsen Hall University of Florida Gainesville, FL 32611-2044	Field: Electrical Engineering Laboratory: WL/AA Vol-Page No: 5- 8
Lilienfield, Lawrence Professor, PhD 3900 Reservoir Rd., NW Georgetown University Washington, DC 20007-0000	Field: Physiology & Biophysics Laboratory: WHMC/ Vol-Page No: 6-14
Lim, Tae Assistant Professor, PhD 2004 Learned Hall University of Kansas Lawrence, KA 66045-0000	Field: Mechanical/Aerospace Engr Laboratory: FJSRL/ Vol-Page No: 6- 8
Lin, Paul Associate Professor, PhD Mechanical Engineering Cleveland State University Cleveland, OH 4-4115	Field: Associate Professor Laboratory: WL/FI Vol-Page No: 5-21
Liou, Juin Associate Professor, PhD Electrical & Computer Eng University of Central Florida Orlando, FL 32816-2450	Field: Electrical Engineering Laboratory: WL/EL Vol-Page No: 5-13
Liu, David Assistant Professor, PhD 100 Institute Rd. Worcester Polytechnic Inst. Worcester, MA 1609-0000	Field: Department of Physics Laboratory: RL/ER Vol-Page No: 4-12
Losiewicz, Beth Assistant Professor, PhD Experimental Psychology Colorado State University Fort Collins, CO 80523-0000	Field: Psycholinguistics Laboratory: RL/IR Vol-Page No: 4-17
Loth, Eric Assistant Professor, PhD 104 S. Wright St, 321C University of Illinois-Urbana Urbana, IL 61801-0000	Field: Aeronaut/Astronaut Engr Laboratory: AEDC/ Vol-Page No: 6- 4

SFRP Participant Data

Lu, Christopher
Associate Professor, PhD
300 College Park
University of Dayton
Dayton, OH 45469-0246

Field: Dept Chemical Engineering
Laboratory: WL/PO

Vol-Page No: 5-61

Manoranjan, Valipuram
Associate Professor, PhD
Neill Hall
Washington State University
Pullman, WA 99164-3113

Field: Pure & Applied Mathematics
Laboratory: AL/EQ

Vol-Page No: 2-22

Marsh, James
Professor, PhD
Physics
University of West Florida
Pensacola, FL 32514-0000

Field: Physics
Laboratory: WL/MN

Vol-Page No: 5-47

Massopust, Peter
Assistant Professor, PhD

Field: Dept. of Mathematics
Laboratory: AEDC/

Sam Houston State University
Huntsville, TX 77341-0000

Vol-Page No: 6- 5

Miller, Arnold
Senior Instructor, PhD
Chemistry & Geochemistry
Colorado School of Mines
Golden, CO 80401-0000

Field:
Laboratory: FJSRL/

Vol-Page No: 6- 9

Misra, Pradeep
Associate Professor, PhD

Field: Electrical Engineering
Laboratory: WL/AA

University of St. Thomas
, - 0

Vol-Page No: 5- 9

Monsay, Evelyn
Associate Professor, PhD
1419 Salt Springs Rd
Le Moyne College
Syracuse, NY 13214-1399

Field: Physics
Laboratory: RL/OC

Vol-Page No: 4-23

Morris, Augustus
Assistant Professor, PhD

Field: Biomedical Science
Laboratory: AL/CF

Central State University
, - 0

Vol-Page No: 2-14

SFRP Participant Data

Mueller, Charles
Professor, PhD
W140 Seashore Hall
University of Iowa
Iowa City, IA 52242-0000

Field: Dept of Sociology
Laboratory: AL/HR

Vol-Page No: 2-32

Murty, Vedula
Associate Professor, MS

Field: Physics
Laboratory: PL/VT

Vol-Page No: 3-29

Texas Southern University
, - 0

Musavi, Mohamad
Assoc Professor, PhD
5708 Barrows Hall
University of Maine
Orono, ME 4469-5708

Field: Elect/Comp. Engineering
Laboratory: RL/IR

Vol-Page No: 4-18

Naishadham, Krishna
Assistant Professor, PhD
Dept. of Electrical Eng.
Wright State University
Dayton, OH 45435-0000

Field: Electrical Engineering
Laboratory: WL/EL

Vol-Page No: 5-14

Noel, Charles
Associate Professor, PhD
151A Campbell Hall
Ohio State University
Columbus, OH 43210-1295

Field: Dept of Textiles & Cloth
Laboratory: PL/RK

Vol-Page No: 3-19

Norton, Grant
Asst Professor, PhD
Mechanical & Materials En
Washington State University
Pullman, WA 99164-2920

Field: Materials Science
Laboratory: WL/ML

Vol-Page No: 5-36

Noyes, James
Professor, PhD
Mathematics & Computer Sc
Wittenberg University
Springfield, OH 45501-0720

Field: Computer Science
Laboratory: WL/FI

Vol-Page No: 5-22

Nurre, Joseph
Assistant Professor, PhD
Elec. & Computer Engineer
Ohio University
Athens, OH 45701-0000

Field: Mechanical Engineering
Laboratory: AL/CF

Vol-Page No: 2-15

SFRP Participant Data

Nygren, Thomas
Associate Professor, PhD
1885 Neil Ave. Mail
Ohio State University
Columbus, OH 43210-1222

Field: Department of Psychology
Laboratory: AL/CF

Vol-Page No: 2-16

Osterberg, Ulf
Assistant Professor, PhD
Thayer School of Engrg.
Dartmouth College
Hanover, NH 3755-0000

Field:
Laboratory: FJSRL/

Vol-Page No: 6-10

Pan, Ching-Yan
Associate Professor, PhD
Physics
Utah State University
Logan, UT 84322-4415

Field: Condensed Matter Physics
Laboratory: PL/WS

Vol-Page No: 3-36

Pandey, Ravindra
Assistant Professor, PhD
1400 Townsend Dr
Michigan Technological Univers
Houghton, MI 49931-1295

Field: Physics
Laboratory: FJSRL/

Vol-Page No: 6-11

Patton, Richard
Assistant Professor, PhD
Mechanical&Nuclear Engine
Mississippi State University
Mississippi State, MS 39762-0000

Field: Mechanical Engineering
Laboratory: PL/VT

Vol-Page No: 3-30

Peretti, Steven
Assistant Professor, PhD
Chemical Engineering
North Carolina State Univ.
Raleigh, NC 27695-7905

Field:
Laboratory: AL/EQ

Vol-Page No: 2-23

Petschek, Rolfe
Associate Professor, PhD
Department of Physics
Case Western Reserve Universit
Cleveland, OH 44106-7970

Field: Physics
Laboratory: WL/ML

Vol-Page No: 5-37

Pezeshki, Charles
Assistant Professor, PhD

Field: Mechanical Engineering
Laboratory: FJSRL/

Washington State University
Pullman, WA 99164-2920

Vol-Page No: 6-12

SFRP Participant Data

Piepmeyer, Edward
Assistant Professor, PhD
College of Pharmacy
University of South Carolina
Columbia, SC 29208-0000

Field:
Laboratory: AL/AO

Vol-Page No: 2- 4

Pittarelli, Michael
Associate Professor, PhD
PO Box 3050, Marcy Campus
SUNY, Institute of Technology
Utica, NY 13504-3050

Field: Information Sys & Engr.
Laboratory: RL/C3

Vol-Page No: 4- 6

Potasek, Mary
Research Professor, PhD

Field: Physics
Laboratory: WL/ML

Columbia University
, - 0

Vol-Page No: 5-38

Prasad, Vishwanath
Professor, PhD

Field: Mechanical Engineering
Laboratory: RL/ER

SUNY, Stony Brook
Stony Brook, NY 11794-2300

Vol-Page No: 4-13

Priestley, Keith
Research Scientist, PhD

Field: Geophysics
Laboratory: PL/GP

University of Nevada, Reno
, - 0

Vol-Page No: 3- 5

Purasinghe, Rupasiri
Professor, PhD
5151 State Univ. Dr.
California State Univ.-LA
Los Angeles, CA 90032-0000

Field: Dept of Civil Engineering
Laboratory: PL/RK

Vol-Page No: 3-20

Raghu, Surya
Assistant Professor, PhD
Mechanical Engineering
SUNY, Stony Brook
Stony Brook, NY 11794-2300

Field: Mechanical Engineering
Laboratory: WL/PO

Vol-Page No: 5-62

Ramesh, Ramaswamy
Associate Professor, PhD
School of Management
SUNY, Buffalo
Buffalo, NY 14260-0000

Field: Magement Science/Systems
Laboratory: AL/ER

Vol-Page No: 2-33

SFRP Participant Data

Ramm, Alexander
Professor, PhD
Mathematics
Kansas State University
Manhattan, KS 66506-2602

Field:
Laboratory: AL/CF

Vol-Page No: 2-17

Ray, Paul
Assistant Professor, PhD
Box 870288
University of Alabama
Tuscaloosa, AL 35487-0288

Field: Industrial Engineering
Laboratory: AL/OE

Vol-Page No: 2-40

Reimann, Michael
Assistant Instructor, MS
Information Systems
The University of Texas-Arling
Arlington, TX 76019-0437

Field: Computer Science
Laboratory: WL/MT

Vol-Page No: 5-55

Rodriguez, Armando
Assistant Professor, PhD

Field: Electrical Engineering
Laboratory: WL/MN

Arizona State University
Tempe, AZ 85287-7606

Vol-Page No: 5-48

Rohrbaugh, John
Research Engineer, PhD
347 Ferst St
Georgia Institute of Technolog
Atlanta, GA 30332-0800

Field: Sensors & Applied Electro
Laboratory: RL/ER

Vol-Page No: 4-14

Roppel, Thaddeus
Associate Professor, PhD
200 Broun Hall
Auburn University
Auburn, AL 36849-5201

Field: Electrical Engineering
Laboratory: WL/MN

Vol-Page No: 5-49

Rosenthal, Paul
Professor, PhD
Mathematics
Los Angeles City College
Los Angeles, CA 90027-0000

Field: Mathematics
Laboratory: PL/RK

Vol-Page No: 3-21

Rotz, Christopher
Associate Professor, PhD

Field: Mechanical Engineering
Laboratory: PL/VT

Brigham Young University
Provo, UT 84602-0000

Vol-Page No: 3-31

SFRP Participant Data

Rudolph, Wolfgang
Associate Professor, PhD
Dept of Physics and Astro
University of New Mexico
Albuquerque, NM 84131-0000

Field: Physics
Laboratory: PL/LI

Vol-Page No: 3- 0

Rudzinski, Walter
Professor, PhD
Dept. of Chemistry
Southwest Texas State Universi
San Marcos, TX 78610-0000

Field: Professor
Laboratory: AL/OE

Vol-Page No: 2-41

Rule, William
Asst Professor, PhD
Mechanical Engineering
University of Alabama
Tuscaloosa, AL 35487-0278

Field: Engineering Mechanics
Laboratory: WL/MN

Vol-Page No: 5-50

Ryan, Patricia
Research Associate, MS
Georgia Tech Research Ins
Georgia Institute of Tech
Atlanta, GA 30332-0000

Field: Electrical Engineering
Laboratory: WL/AA

Vol-Page No: 5-10

Saiduddin, Syed
Professor, PhD
1900 Coffey Rd
Ohio State University
Columbus, OH 43210-1092

Field: Physiology/Pharmacology
Laboratory: AL/OE

Vol-Page No: 2-42

Schonberg, William
Assoc Professor, PhD
Engineering Dept.
University of Alabama, Huntsvi
Huntsville, AL 35899-0000

Field: Civil & Environmental
Laboratory: WL/MN

Vol-Page No: 5-51

Schulz, Timothy
Assistant Professor, PhD
1400 Townsend Dr
Michigan Technological Univers
Houghton, MI 49931-1295

Field: Electrical Engineering
Laboratory: PL/LI

Vol-Page No: 3-11

Shen, Mo-How
Assistant Professor, PhD
2036 Neil Ave.
Ohio State University
Columbus,, OH 43210-1276

Field: Aerospace Engineering
Laboratory: WL/PI

Vol-Page No: 5-23

SFRP Participant Data

Sherman, Larry
Professor, PhD
Dept. of Chemistry
University of Scranton
Scranton, PA 18510-4626

Field: Analytical Chemistry
Laboratory: AL/OE

Vol-Page No: 2-43

Shively, Jon
Professor, PhD
Civil & Industrial Eng.
California State University, N
Northridge, CA 91330-0000

Field: Metallurgy
Laboratory: PL/VT

Vol-Page No: 3-32

Snapp, Robert
Assistant Professor, PhD
Dept of Computer Science
University of Vermont
Burlington, VT 5405-0000

Field: Physics
Laboratory: RL/IR

Vol-Page No: 4-19

Soumekh, Mehrdad
Associate Professor, PhD
201 Bell Hall
SUNY, Buffalo
Amherst, NY 14260-0000

Field: Elec/Computer Engineering
Laboratory: PL/LI

Vol-Page No: 3-12

Spetka, Scott
Assistant Professor, PhD
PO Box 3050, Marcy Campus
SUNY, Institute of Technology
Utica, NY 13504-3050

Field: Information Sys & Engrg
Laboratory: RL/XP

Vol-Page No: 4-26

Springer, John
Associate Professor, PhD

Field: Physics
Laboratory: AEDC/

Fisk University
, - 0

Vol-Page No: 6- 6

Stevenson, Robert
Assistant Professor, PhD
Electrical Engineering
University of Notre Dame
Notre Dame, IN 46556-0000

Field: Electrical Engineering
Laboratory: RL/IR

Vol-Page No: 4-20

Stone, Alexander
Professor, PhD
Mathematics & Statistics
University of New Mexico
Albuquerque, NM 87131-1141

Field:
Laboratory: PL/WS

Vol-Page No: 3-37

SFRP Participant Data

Sveum, Myron
Assistant Professor, MS
Electronic Engineering Te
Metropolitan State College
Denver, CO 80217-3362

Field: Electrical Engineering
Laboratory: RL/OC

Vol-Page No: 4-24

Swanson, Paul
Research Associate, PhD
Electrical Engineering
Cornell University
Ithaca, NY 14853-0000

Field: Electrical Engineering
Laboratory: RL/OC

Vol-Page No: 4-25

Swope, Richard
Professor, PhD
Engineering Science
Trinity University
San Antonio, TX 78212-0000

Field: Mechanical Engineering
Laboratory: AL/AO

Vol-Page No: 2- 5

Tan, Arjun
Professor, PhD
Physics
Alabama A&M University
Normal, AL 35762-0000

Field: Physics
Laboratory: PL/WS

Vol-Page No: 3-38

Tarvin, John
Associate Professor, PhD
800 Lakeshore Drive
Samford University
Birmingham, AL 35229-0000

Field: Department of Physics
Laboratory: AEDC/

Vol-Page No: 6- 7

Taylor, Barney
Visiting Assist Professor, PhD
1601 Peck Rd.
Miami Univ. - Hamilton
Hamilton, OH 4-5011

Field: Dept. of Physics
Laboratory: WL/ML

Vol-Page No: 5-39

Thio, Y.
Associate Professor, PhD

Field: Physics Dept.
Laboratory: PL/WS

University of Miami
Coral Gables, FL 33124-0530

Vol-Page No: 3-39

Tong, Carol
Assistant Professor, PhD
Electrical Engineering
Colorado State University
Fort Collins, CO 80523-0000

Field:
Laboratory: WL/AA

Vol-Page No: 5-11

SFRP Participant Data

Truhon, Stephen
Associate Professor, PhD
Social Sciences
Winston-Salem State University
Winston-Salem, NC 27110-0000

Field: Psychology
Laboratory: AL/HR

Vol-Page No: 2-34

Tzou, Horn-Sen
Associate Professor, PhD
Mechanical Engineering
University of Kentucky
Lexington, KY 40506-0046

Field: Mechanical Engineering
Laboratory: WL/FI

Vol-Page No: 5-24

Vogt, Brian
Professor, PhD

Field: Pharmaceutical Sciences
Laboratory: AL/EQ

Bob Jones University
- 0

Vol-Page No: 2-24

Wang, Xingwu
Asst Professor, PhD
Dept. of Electrical Eng.
Alfred University
Alfred, NY 14802-0000

Field: Physics
Laboratory: WL/FI

Vol-Page No: 5-25

Whitefield, Philip
Research Assoc Professor, PhD
Cloud & Aerosol Sciences
University of Missouri-Rolla
Rolla, MO 65401-0000

Field: Chemistry
Laboratory: PL/LI

Vol-Page No: 3-13

Willson, Robert
Research Assoc Professor, PhD
Robinson Hall
Tufts University
Medford, MA 2155-0000

Field: Physics and Astronomy
Laboratory: PL/GP

Vol-Page No: 3- 6

Witanachchi, Sarath
Assistant Professor, PhD
4202 East Fowler Avenue
University of South Florida
Tampa, FL 33620-7900

Field: Department of Physics
Laboratory: FJSRL/

Vol-Page No: 6-13

Woehr, David
Assistant Professor, PhD
Psychology
Texas A&M University
College Station, TX 77845-0000

Field: Psychology
Laboratory: AL/HR

Vol-Page No: 2-35

SFRP Participant Data

Xu, Longya
Assistant Professor, PhD
Electrical Engineering
The Ohio State University
Columbus, OH 43210-0000

Field: Electrical Engineering
Laboratory: WL/PO

Vol-Page No: 5-63

Yavuzkurt, Savas
Associate Professor, PhD

Field: Mechanical Engineering
Laboratory: WL/PO

Vol-Page No: 5-64

Pennsylvania State University
University Park, PA 16802-0000

Zhang, Xi-Cheng
Associate Professor, PhD
Physics Department
Rensselaer Polytechnic Institute
Troy, NY 12180-3590

Field: Physics
Laboratory: RL/ER

Vol-Page No: 4-15

Zhou, Kemin
Assistant Professor, PhD
Dept. of Elec & Comp. Eng
Louisiana State University
Baton Rouge, LA 70803-0000

Field:
Laboratory: WL/MN

Vol-Page No: 5-52

Zimmermann, Wayne
Associate Professor, PhD
P.O. Box 22865
Texas Woman's University
Denton, TX 76205-0865

Field: Dept Mathematics/Computer
Laboratory: PL/WS

Vol-Page No: 3-40

**ANALYTICAL METHODS FOR THE DETERMINATION
OF WEAR METALS IN PERFLUOROPOLYALKYLETHER LUBRICATING OILS**

**David W. Johnson
Associate Professor
Department of Chemistry**

**University of Dayton
300 College Park
Dayton, OH 45469-2357**

**Final Report for:
Summer Faculty Research Program
Wright Laboratory**

**Sponsored by:
Air Force Office of Scientific Research
Bolling Air Force Base, Washington, D.C.**

December, 1993

**ANALYTICAL METHODS FOR THE DETERMINATION
OF WEAR METALS IN PERFLUOROPOLYALKYLETHER LUBRICATING OILS**

**David W. Johnson
Associate Professor
Department of Chemistry
University of Dayton**

Abstract

Analytical methods for the determination of wear metals in perfluoropolyalkylether lubricants have been developed. Inductively coupled plasma atomic emission spectroscopy (ICP-AES) has been chosen as the analytical technique due to its sensitivity and lack of serious interferences. The method developed allows for the rapid determination of 20 metals along with phosphorus and sulfur. Analytical standards have been prepared using metal complexes of the β diketone 2,2-dimethyl-6,6,7,7,8,8,8-heptafluoro-3,5-octanedione. These complexes were prepared and characterized prior to use. The PFPAE lubricants studied include Krytox 143ac and Fomblin Z. Detection limits for the various metals have been determined to be in the range of 10-100 parts per billion for the various wear metals. Detection limits for phosphorus and sulfur are 10 parts per million.

ANALYTICAL METHODS FOR THE DETERMINATION OF WEAR METALS IN PERFLUOROPOLYALKYLETHER LUBRICATING OILS

David W. Johnson

INTRODUCTION

Perfluoropolyalkylethers (PFPAE) are being developed by the Air Force as high temperature lubricants for the next generation of jet engines. While several PFPAE based lubricants are commercially available, there are no good analytical methods for the analysis of metals, due to wear of bearing surfaces in these fluids. Analytical methods based on techniques such as inductively coupled plasma-atomic emission spectroscopy (ICP-AES) which are commonly used for conventional lubricants¹ fail due to the insolubility of the metal standards in PFPAE fluids. The goal of this study was to develop metal standards which are both soluble and stable in PFPAE lubricants and to develop ICP-AES methods for the determination of wear metals in the commercial PFPAE lubricants.

Metal complexes for use as standards in wear metal analysis must be both soluble in PFPAE's to at least 100 ppm metal and stable over a long period of time (months) in the presence of air. The presence of a long fluorinated chain as part of the ligand was expected to provide solubility in the fluorinated oil while the steric shielding improves the hydrolytic stability of the complex². The ligand of choice was 2,2-dimethyl-6,6,7,7,8,8,8-heptafluoro-3,5-octanedione (HFOD). These complexes were considered

because of the known hydrolytic and thermal stability and solubility in organic solvents of the complexes of rare earth metals³. Transition metal complexes containing the FOD ligand and several metals have been previously prepared and have been shown to thermally stable suggesting that these complexes would make suitable standards.

In this report the synthesis and characterization of 15 metal complexes containing the ligand 2,2-dimethyl-6,6,7,7,8,8,8-heptafluoro-3,5-octanedione is described. These standards have been used to determine dissolved metal content in fluorinated oils such as Krytox 143AC and Fomblin Z exposed to metals and high temperatures.

Experimental Methods

Synthesis

tris(2,2-dimethyl-6,6,7,7,8,8,8-heptafluoro-3,5-octanedionato) Aluminum $\text{Al}(\text{FOD})_3$: $\text{Al}(\text{FOD})_3$ was prepared by adding 8.85g (30 mmol) of HFOD dissolved in 50 mL CCl_4 to a slurry of 1.34g (9.95 mmol) of AlCl_3 in 75 mL CCl_4 . The mixture was refluxed in a hood until HCl gas was no longer being evolved. After cooling, the volume of the resulting solution was reduced to 25 mL under vacuum and the solution placed in the refrigerator overnight. The resulting crystalline solid was filtered and recrystallized from methylene chloride.

tris(2,2-dimethyl-6,6,7,7,8,8,8-heptafluoro-3,5-octanedionato) iron(III) ($\text{Fe}(\text{FOD})_3$), tris(2,2-dimethyl-6,6,7,7,8,8,8-heptafluoro-3,5-octanedionato) chromium(III) ($\text{Cr}(\text{FOD})_3$) and tris(2,2-dimethyl-6,6,7,7,8,8,8-heptafluoro-3,5-octanedionato)manganese(III) ($\text{Mn}(\text{FOD})_3$): These complexes were prepared by the method described in the literature⁴.

2,2-dimethyl-6,6,7,7,8,8,8-heptafluoro-3,5-octanedionato Complexes of Sodium, Magnesium, Calcium, Barium, Nickel(II), Copper(II), Zinc, Cadmium, Lead(II) and Mercury(II): These complexes were prepared by adding 5.92g (20.0 mmol) of 2,2-dimethyl-6,6,7,7,8,8,8-heptafluoro-3,5-octanedione dissolved in 15 mL methanol to a solution of the appropriate metal nitrate or chloride (10.0 mmol) dissolved in 25 mL of methanol. An aqueous solution of sodium hydroxide (5.05 mL of 3.97 M) was slowly added. During the addition a precipitate formed but on further addition, redissolved. The resulting solution was poured into 500 mL of deionized water. The resulting precipitate was filtered and recrystallized from methylene chloride. The crystalline solid was dried at 60 C under vacuum for 1 hour and stored in a desiccator. Yield data and metal analysis is shown in Table 1.

Phosphorus and Sulfur: The commercially available compounds pentafluorophenylsulfide and tris(pentafluorophenyl)phosphine were used as the standards for sulfur and phosphorus.

Table I. Metal and Thermogravimetric Analysis Data for Metal FOD Complexes.

Complex	%Yield	% Metal actual (Calc.)	%H ₂ O actual (Calc.)	% Residue	T _{1/2}
Na(FOD)	56	7.12 (7.23)			
Mg(FOD) ₂	80	3.91 (3.96)	N.O.	2.16	170
Ca(FOD) ₂	74	6.08 (6.18)	2.76 (2.78)	0.9	220
Ni(FOD) ₂	32	8.76 (8.80)	2.97 (2.70)	1.3	185
Cu(FOD) ₂	38	9.68 (9.72)	N.O.	0.7	160
Zn(FOD) ₂	82	9.88 (9.97)	N.O.	0.8	205
Ba(FOD) ₂	76	18.36 (18.42)	2.44 (2.42)	0.1	230
Cd(FOD) ₂	69	15.48 (15.60)	3.90 (2.50)	1.6	215
Hg(FOD) ₂	37	25.08 (25.37)	(2.28)		
Pb(FOD) ₂	39	26.02 (25.98)	N.O.	0.9	185
Al(FOD) ₃	65	2.94 (2.96)	N.O.	0.1	160
V(FOD) ₃	40	5.38 (5.44)	N.O.	1.7	195
Cr(FOD) ₃	43	5.51 (5.55)	N.O.	1.0	155
Fe(FOD) ₃	51	5.95 (5.93)	N.O.	0.9	165
Mn(FOD) ₃	47	5.77 (5.84)	N.O.		
Co(FOD) ₃	45	6.19 (6.24)	N.O.	0.8	175

Degradation Studies

Lubricant degradation in the presence of metals was examined by sealing weighed samples of various powders or iron wire (0.5 g) and PFPAE based lubricant (5.0 g) inside pyrex test tubes. The sealed tubes were weighed, heated at the desired temperature for the listed time and reweighed. Tubes showing significant weight loss were discarded. The tubes were opened, 20g of Freon E6 was added and the samples were filtered through a 0.5 micron filter. The samples were then ready for analysis by ICP-AES.

Caution: Several of the test tubes developed a substantial pressure or ruptured during the course of the experiment. Safety glasses should be used at all times when handling the test tubes.

Physical Methods

The metal content of the complexes was determined by ICP-AES. A known mass of complex was dissolved in 1.00g methyl-isobutyl ketone (MIBK). The resulting solution was mixed with 19.00g of kerosene for ICP analysis. Standards were prepared from appropriate Conostan standards in the same solvent as was used for the samples. Thermogravimetric analysis data was obtained on a Dupont model 2100 thermal analysis system. A heating rate of 10 C/min under an atmosphere of nitrogen, flowing at 50cc/min was used for all

samples. Infrared spectra for all of the metal complexes were measured as nujol mulls using a Perkin-Elmer model 283 infrared spectrophotometer. Fluorine 19 NMR spectra were measured at 56 MHz using a Varian EM-360L NMR spectrometer. Proton NMR spectra at 270 MHz and carbon 13 NMR spectra at 68.7 MHz were measured using a JEOL FX270 NMR spectrometer.

Inductively Coupled Plasma-Atomic Emission Spectroscopy

Metal concentrations in PFPAE fluids were measured using a Jarrell Ash Polyscan 61-E spectrometer. Standards were prepared by dissolving known masses of each metal FOD complex in Freon E6. Samples of the PFPAE fluid were mixed with appropriate amount of the standard solution and Freon E6 in a 1:4 ratio of oil to freon in order to obtain the various concentrations of standard solutions. All oil samples were diluted 1:4 with Freon E6 before analysis. For analysis an RF power of 1750 watts, a nebulizer pressure of 22 PSI and a pump rate of 80 RPM was used. The samples were aspirated for a minimum of 45 seconds to insure equilibration within the plasma.

Results

Synthesis: The synthetic approach to these complexes relies on the rapid reaction of the FOD⁻ ion with the metal cation and the insolubility of the resulting complex in aqueous solution. All of

the complexes were isolated in moderate to good yields as soft crystalline solids. The complexes prepared in this manner often precipitate as hydrates, however upon heating at 60 C under vacuum, most of the complexes dehydrate and give either the anhydrous complex or a stable monohydrate.

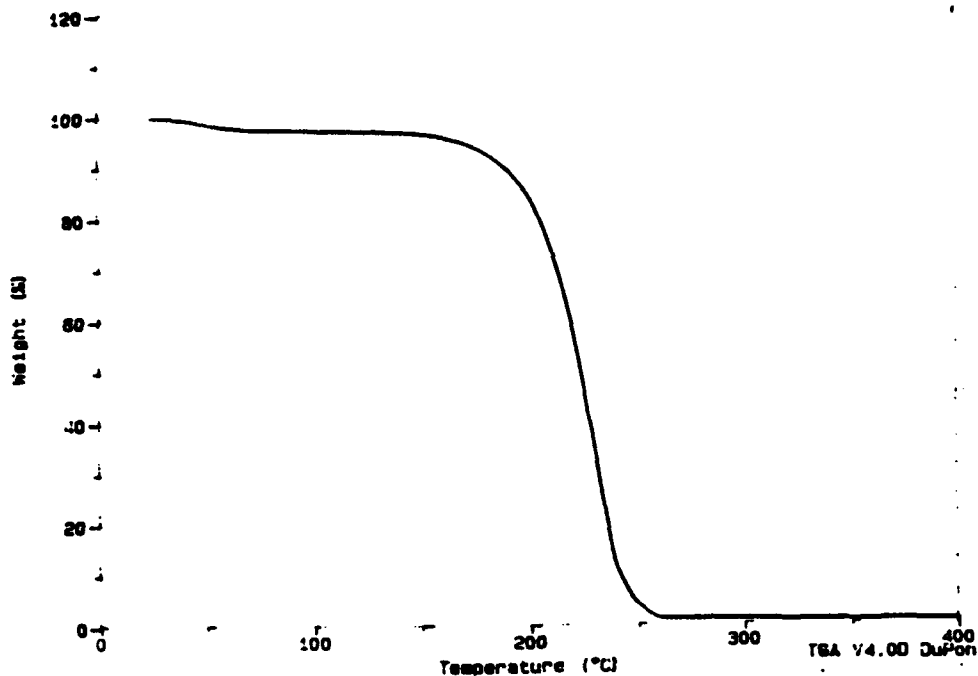
The presence of a single water of hydration in these complexes is shown by thermogravimetric analysis. Thermogravimetric analysis curves for $\text{Ca}(\text{FOD})_2 \cdot \text{H}_2\text{O}$ and $\text{Cu}(\text{FOD})_2$ are shown in Figure 1. The curves indicate that these complexes sublime at temperatures of about 200 C leaving very little residue (<1%). The water of hydration in the calcium complex is lost first in a well defined step at about 65 C. The thermogravimetric analysis data for all of the complexes is given in Table 1. The thermogravimetric analysis indicates that the calcium, copper and barium complexes described here are different than the oligomeric complexes reported by Sievers et.al.⁵ The 50 C lowering of the sublimation is consistent with the lower molecular weight of the monomeric complexes.

The proton NMR spectra of these complexes also serve as an indicator of the hydration of the complex. The anhydrous complexes have peaks at 1.1 ppm representing the protons of the t-butyl group and at 6.1 ppm representing the C-H of the chelate ring⁶. The proton NMR spectrum of the cobalt complex shows splitting of both peaks due to the two possible isomers for this complex. The proton NMR spectra of the hydrated spectra show an additional peak between

Sample: CA(FOD)2
 Size: 10.3830 mg
 Method: TGA ANALYSIS
 Comment: 10C/MIN TO 600C, 50CC/MIN, NITROGEN

TGA

File: C:\TGA\F002.DWK
 Operator: DMJ
 Run Date: 3-Jun-93 15:33



Sample: CU(FOD)2
 Size: 13.1470 mg
 Method: TGA ANALYSIS
 Comment: 10C/MIN TO 600C, 50CC/MIN, NITROGEN

TGA

File: C:\TGA\F0022.DWK
 Operator: DMJ
 Run Date: 4-Jun-93 11:04

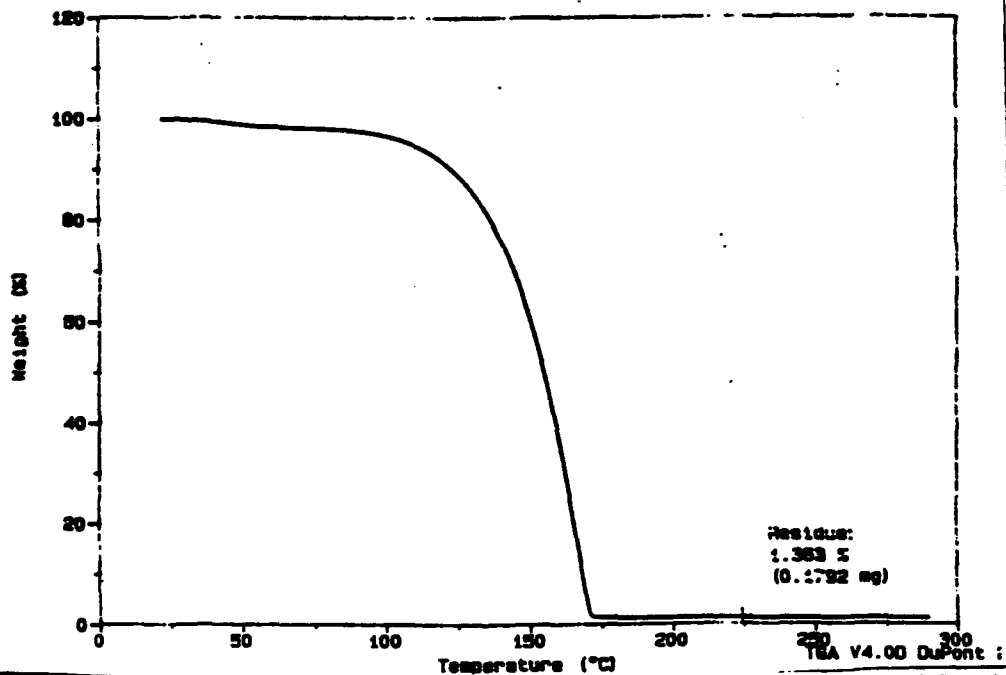


Figure 1. Thermogravimetric Analysis Curves for a) $\text{Ca}(\text{FOD})_2$ and b) $\text{Cu}(\text{FOD})_2$

2 and 4 ppm due to the water of hydration. Fluorine 19 NMR spectra show the expected splitting patterns for the $\text{CF}_3\text{CF}_2\text{CF}_2$ group of the ligand⁷. Infrared spectra for all of the complexes show the expected FOD ligand bands shifted slightly due to the presence of the metal ion⁸. The infrared spectra are consistent with the level of hydration for the complexes found by TGA.

Analytical Standards: The suitability of the various metal complexes of 2,2-dimethyl-6,6,7,7,8,3,8-heptafluoro-3,5-octanedione as analytical standards for ICP-AES analysis was studied in several manners. The complexes were all found to be soluble in Krytox 143AC, Fomblin Z and Freon E6 to a minimum of 100 ppm. Solutions of each metal FOD complex were examined using ICP to determine if the wavelengths available on the polychrometer would suffer from any serious interferences. Only the aluminum complex showed any interference. The observed interference is similar to the interference observed when oil samples are analyzed.

While metal standards for 15 metals have been prepared, the standards for aluminum, iron, chromium, cobalt, nickel, and zinc were selected for more thorough study. A calibration curve for each of these metals, using concentrations from 1 ppm to 100 ppm has been measured with the results shown in Table II. Also contained in Table II is the estimate of the detection limit based on three times the standard deviation of the readings of the blank solution. Detection limits for the various metals in solution are in the

Table II. Calibration Data and Detection Limits for Various Metals in Krytox 143AC Diluted 1:4 with Freon E6.5.

Element	λ	Correlation Coefficient	Detection Limit (ppb)	Oil Detection Limit (ppb)
Al	308.2	0.999	44	220
Ba	493.4	1.000	1	5
Cd	228.8	1.000	8	38
Co	228.6	0.994	18	90
Cr	267.7	0.999	32	160
Cu	324.7	1.000	14	71
Fe	259.9	1.000	8	40
Mg	279.5	0.999	2	10
Na	588.9	0.999	20	100
Ni	231.6	0.999	24	120
Zn	213.8	0.999	28	140

range of 1-50 ppb under the conditions of this analysis, corresponding to concentrations between 5 and 250 ppb in the original oil sample.

In order for routine analysis of oil samples by ICP-AES to be practical, several of the analytical standards should be mixed in a single solution. Table III shows the results of an experiment where weighed amounts of all six of the complexes were mixed. The instrument was standardized using the individual solutions of the six metal ions and then the mixed solution was analyzed. The metal analysis of the resulting solution shows deviations between 0.5 and

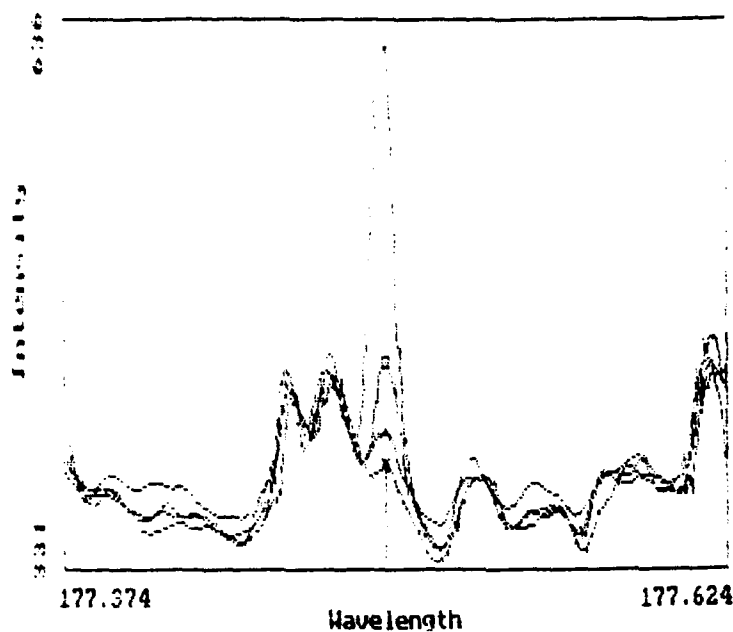
Table III. Analysis of a Mixed Metal Standard.

Metal	Actual ppm	0 Days Found ppm (%RSD)	% Dev	7 Days Found ppm (%RSD)	% Dev
Al	16.8	16.6 (0.5)	-1.2	16.4 (1.0)	-2.4
Co	16.6	16.5 (0.6)	-0.6	16.7 (0.8)	+0.6
Cr	17.7	17.6 (0.2)	-0.6	17.5 (1.1)	-1.2
Fe	17.5	17.3 (0.2)	-1.1	17.3 (0.9)	-1.1
Ni	16.4	16.1 (0.4)	-1.8	16.2 (1.0)	-1.2
Zn	21.7	21.5 (0.4)	-0.9	21.4 (0.8)	-1.4

1.5 %, well within the expected experimental error. The same solution was analyzed after one week had passed, giving essentially the same results. The results indicate no reason why several metal complexes cannot be combined into a single standard solution. The standard deviation of these determinations is relatively small. The standard deviation of the analysis of the week old solution is substantially large, in part due to only a small number (3) of determinations being made.

Phosphorus and sulfur were determined using the sequential portion of the ICP. Based on background scans, the wavelength of choice for sulfur was determined to be 182 nm and the wavelength of choice for phosphorus was determined to be 213 nm. Wavelength scans

Element: P Wavelength: 177.499 Interval: 1 Window: 0.3 nm



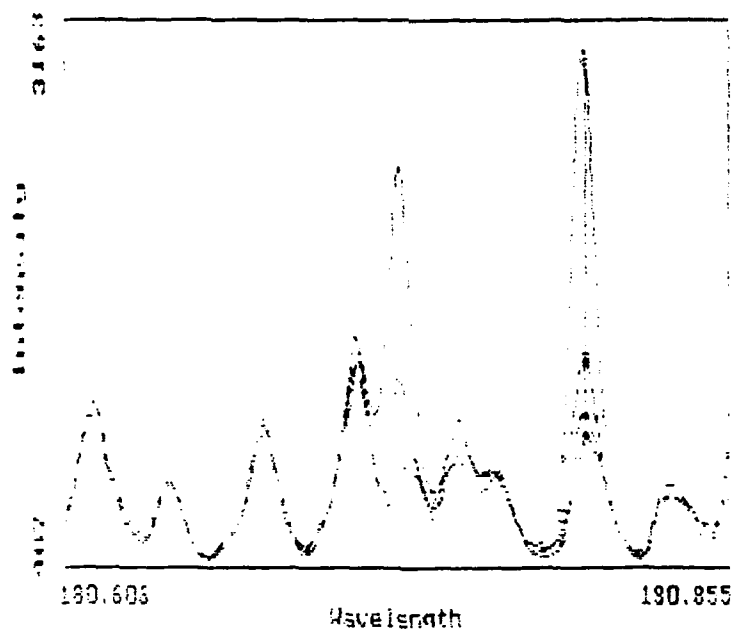
SAMPLE INFO

Scan Name

- 1 scan1
- 2 25ppm
- 3 10 ppm
- 4 blank

Cursor Wavelength: 177.495

Element: S Wavelength: 189.731 Interval: 1 Window: 0.2 nm



SAMPLE INFO

Scan Name

- 1 100 ppm
- 2 25 ppm
- 3 10 ppm
- 4 blank

Cursor Wavelength: 189.832

Figure 2. Wavelength Scans for the Determination of Phosphorus and Sulfur in Perfluoropolyalkylether Lubricants.

for several concentrations of phosphorus and sulfur are shown in Figure 2. The detection limit based on three times the standard deviation in the baseline was determined to be 10 ppm for both phosphorus and sulfur.

Lubricant Degradation Studies

The initial experiments using these metal FOD complexes as analytical standards was in the analysis of lubricant samples exposed to high temperatures in the presence of metals. The initial fluids chosen were Krytox 143AC and Fomblin Z exposed to iron, chromium and nickel powders at 235 and 290 C for 24 hours. The liquid contents of the tubes were then analyzed by ICP-AES. The results of this experiment are shown in Table IV. The results for any tube which showed a significant change in mass (>0.05 g) are denoted in Table IV with a *.

In general, Fomblin Z is found to be much more reactive than Krytox 143AC. Both Krytox 143AC and Fomblin Z were found to react with chromium to give large chromium concentrations. The samples where Fomblin Z was in contact with chromium at 290 C were not analyzed because the decomposition of the fluid generated enough gas to break the glass tube. The results in Table IV show that iron and nickel react with the fluids to give small amounts of metal dissolved in the fluid. Examination of the tubes before opening gives a visual indication of reaction. The iron samples had a layer

Table IV. Metal Concentrations in Krytox 143AC and Fomblin Z Exposed to Metals at 235 and 290 C.

Metal	Fluid	Temp. C	ppm Fe	ppm Cr	ppm Ni
Fe	Fomblin Z	235	0.01		
Fe	Fomblin Z	235	0.36*		
Fe	Fomblin Z	290	0.14		
Fe	Fomblin Z	290	0.13		
Fe	Krytox 143AC	235	0.01		
Fe	Krytox 143AC	235	0.01		
Fe	Krytox 143AC	290	0.42		
Fe	Krytox 143AC	290	0.37		
Ni	Fomblin Z	235			0.47
Ni	Fomblin Z	235			1.495
Ni	Fomblin Z	290			32.97*
Ni	Fomblin Z	290			0.23
Ni	Krytox 143AC	235			0.70
Ni	Krytox 143AC	235			0.01
Ni	Krytox 143AC	290			0.03
Ni	Krytox 143AC	290			0.04
Cr	Fomblin Z	235		8.1	
Cr	Fomblin Z	235		6.8	
Cr	Fomblin Z	290	no liquid for analysis		
Cr	Fomblin Z	290	' ' ' '		
Cr	Krytox 143AC	235		0.23	
Cr	Krytox 143AC	290		0.35	
Cr	Krytox 143AC	290		0.34	

* A loss of weight greater than 0.05g was seen in this sample.

of black powder on top of the light gray powder. The composition of the black solid will be the subject of further investigations.

A second series of experiments where lubricant degradation in static tests were investigated used various forms of oxidized iron (Fe_2O_3 , Fe_3O_4 or FeF_3) and iron wire in contact with Krytox 143AC. Separate samples were heated at 246 and 274 C for 48 hours cooled and analyzed by ICP. The results of this experiment are shown in Table V. The iron wire was found to show very little reaction. The data indicate that iron oxide (Fe_2O_3 or Fe_3O_4) are much more reactive than iron metal under the conditions of the test.

Iron(III) fluoride (FeF_3) is also observed to be quite reactive towards Krytox 143AC. The test tubes containing FeF_3 developed a substantial pressure during the test. When the tubes were opened the pressure was sufficient to blow the top of the tube to the ceiling. The FeF_3 powder used in these tubes was observed to change from a pale green characteristic of FeF_3 to an orange solid indicating some chemical reaction. The characterization of these products has not been attempted. The formation of FeF_3 is thought to be an important step in the degradation mechanism of PFPAE lubricants⁹.

Table V. The Effect of Oxidized Iron Compounds on Lubricant Reaction.

Sample	Fluid	Temp	Mass of Sample	ppm Fe (a)	ppm Fe (b)
Fe wire	Krytox 143AC	246	0.5042	2.29*	6.26*
Fe wire	Krytox 143AC	274	0.5041	0.06	0.10
Fe wire	Krytox 143AC	274	0.5076	0.02	0.05
Fe wire	Krytox 143AC	274	0.5039	0.72	3.50
Fe ₃ O ₄	Krytox 143AC	274	0.5026	4.40	1.48
Fe ₃ O ₄	Krytox 143AC	274	0.5002	0.83	0.43
Fe ₃ O ₄	Krytox 143AC	246	0.5073	0.88	8.19
Fe ₃ O ₄	Krytox 143AC	246	0.5022	4.95	10.09
Fe ₃ O ₄	Krytox 143AC	274	0.5057	19.08	52.23
Fe ₂ O ₃	Krytox 143AC	246	0.5044	7.15	11.33
Fe ₂ O ₃	Krytox 143AC	274	0.5018	3.54	6.67
Fe ₂ O ₃	Krytox 143AC	246	0.5088	26.89	44.97
Fe ₂ O ₃	Krytox 143AC	274	0.5065	1.69	1.12
Fe 10% FeF ₃	Krytox 143AC	274	0.5022	2.16	11.76
Fe 10% FeF ₃	Krytox 143AC	246	0.5063	2.86	1.47
Fe 10% FeF ₃	Krytox 143AC	246	0.5044	0.77	4.06
FeF ₃	Krytox 143AC	246	0.5041	12.17	39.05
FeF ₃	Krytox 143AC	246	0.5018	1.71	17.73
FeF ₃	Krytox 143AC	274	0.5057	3.72	6.91
FeF ₃	Krytox 143AC	274	0.5084	2.25	

(a) The contents of the samples were allowed to settle after exposure to the high temperature to give analysis results;

(b) The contents of the sample were shaken for 15 minutes to give results.

Conclusions

Several conclusions can be drawn from the data acquired as part of the AFOSR SFRP program. These conclusions are summarized below.

1. Metal complexes of β diketone 2,2-dimethyl-6,6,7,7,8,8,8-heptafluoro-3,5-octanedione can be used as metal standards for the analysis of fluorinated lubricants by ICP-AES. The metal complexes dissolve in the fluorinated fluids and are sufficiently stable for their use as standards.
2. Analysis of Krytox 143AC and Fomblin Z indicate that Fomblin Z is more reactive with iron, chromium and nickel than Krytox 143AC; although both of the fluids react with the three metals studied.
3. Oxidized iron compounds such as Fe_2O_3 or FeF_3 are much more reactive than pure iron. It is possible that the observed reactivity of iron is due to the iron oxide which coats the surface of the metal.

References Cited

1. Eisentraut, K.J.; Newman, R.W.; Saba, C.S.; Kauffman, R.E. and Rhine, W.E.; Anal. Chem.; 56, 1086A, (1984).
2. Eisentraut, K.J. and Sievers, R.E.; J. Am. Chem. Soc., 87, 5254, (1965).
3. Springer, C.S. Jr., Meek, D.W. and Sievers, R.E. Inorg. Chem. 6, 1105, (1967).
4. Sweet, T. R. and Brengartner, D. Anal. Chim. Acta, 56, 39, (1974); Kowalski, B.R.; Isenhour, T.L. and Sievers, R.E.; Anal. Chem., 41, 998, (1969).
5. Turnipseed, S.B.; Barkley, R.M. and Sievers, R.E. Inorg. Chem.; 30; 1164 (1991).
6. Kutal, C.; in "Nuclear Magnetic Resonance Shift Reagents"; R.E. Sievers, Ed.; Accademic Press, 1973, 87.
7. Mooney, E.F. "An Introduction to 19F NMR Spectroscopy"; Heyden/Sadtler, 1970, p 9-29.
8. K. Nakamoto, "Infrared and raman Spectra of Inorganic and Coordination Compounds", Third Edition, Wiley Interscience, 1978.
9. Carre, D.J.; ASLE Trans.; 29, 121, (1986).; Carre, D.J. and Markowitz, J.A.; ASLE Trans.; 28, 40, (1985).

**PROCESSING ASPECTS OF GLASS MATRIX, FIBER AND CERAMIC
COMPOSITES FOR ELECTRONIC PACKAGING**

**Prashant N. Kumta
Assistant Professor
Department of Materials Science and Engineering**

**Carnegie Mellon University
5000 Forbes Avenue
Pittsburgh, PA 15213**

**Final Report for :
Summer Research Extension Program
Wright Patterson Laboratory**

**Sponsored by :
Air Force Office of Scientific Research
Bolling Air Force Base, Washington, D.C.**

December 1993

PROCESSING ASPECTS OF GLASS MATRIX, FIBER AND CERAMIC COMPOSITES FOR ELECTRONIC PACKAGING

Prashant N. Kumta
Assistant Professor
Department of Materials Science and Engineering
Carnegie Mellon University

Abstract

Glasses and glass-ceramics are well known for their low dielectric constants ($\epsilon \approx 3-5$) at 1MHz which makes them useful candidate materials as substrates for high speed electronic packaging. On the other hand crystalline ceramics have moderate dielectric constants ($\epsilon \approx 9-12$) at 1MHz while non-oxide ceramics such as AlN and SiC have excellent thermal conductivity values useful for high power packages. Glass matrix, fiber and glass infiltrated ceramic composites with interconnected phases therefore, have the potential of displaying optimum thermal and electric characteristics which could make them useful as substrates for electronic packaging. Borosilicate-Nicalon fiber-glass composites were fabricated using pressure and pressureless sintering techniques. At the same time preliminary experiments were conducted to fabricate composites using SCS fiber and borosilicate glass incorporating tape casting approaches. Preliminary experiments were also conducted to process porous aluminum nitride ceramics hot infiltrated with borosilicate glass. Results of optical characterization of the composites indicate that infiltration of Nicalon cloth with glass is achieved by hot pressing at 1000°C using a pressure of 1000 psi, while the tape casting and lamination approach followed by sintering is useful for fabricating Nicalon tows and glass composites. On the other hand aluminum nitride ceramics were fabricated with $\approx 28\%$ interconnected pores. Hot infiltration yielded $\approx 100 \mu\text{m}$ penetration of glass into the pores of the nitride ceramic. The paper discusses the processing aspects of these composites.

PROCESSING ASPECTS OF GLASS MATRIX, FIBER AND CERAMIC COMPOSITES FOR ELECTRONIC PACKAGING

Prashant N. Kumta

INTRODUCTION

Advancement in circuit technology and the resultant thrust towards miniaturization of devices and increasing device density has placed stringent requirements on substrate technology. These requirements are based on a large part on attaining excellent heat dissipation and fast signal propagation. The main heat dissipation mechanism is by thermal conduction, while signal propagation is based on the velocity of the electric signal given by

$$v = \frac{1}{\sqrt{\mu\epsilon}}$$

where μ is the relative magnetic permeability and ϵ is the relative dielectric permittivity of the material. The substrate materials therefore need to possess excellent thermal conductivity and minimum dielectric constant. As a result, the choice of materials satisfying these criteria is restricted mainly to ceramics and polymers. The role of ceramic materials as substrates in several packages such as dual-in-line packages, chip carriers, and pin grid arrays is well known and ceramic packaging is becoming one of the most actively pursued areas of research [1-6].

Ceramics have dielectric constants ranging from 4 to 10,000, thermal expansion coefficients matching silicon ($30 \times 10^{-7} / ^\circ\text{C}$), and display a range of thermal conductivities making them one of the best insulators and heat conductors. They even exhibit better heat conduction than aluminum metal. They are also highly refractory materials with excellent temperature stability making them good materials for hermetic applications. The main drawback of ceramic materials with respect to packaging is their moderate to high dielectric constant and the high processing temperatures. Research in the development of materials for packaging application has been focussed at achieving objectives which include lower dielectric constant, lower processing temperatures, thermal expansion match to silicon, improved thermal conductivity, improved techniques of power dissipation, multilayer processing and high mechanical strength. The materials that have been identified for these purposes have been AlN, BeO, SiC, cubic BN and diamond among the ceramic materials, while glasses and glass-ceramics have also been investigated for packaging applications because of their low dielectric constants[7-16]. Table 1 lists the crystalline ceramic materials of interest for electronic packaging. Heat dissipation in devices implementing crystalline ceramics is mainly from the bottom of the device through the substrate itself.

Glass-ceramics with their dielectric constant around 5 and their excellent thermal expansion match with silicon coupled with the ability to co-sinter with copper, or gold make them potentially one of the best candidate materials for high-performance multilayer ceramic substrates[17]. In

addition, thin film metallization and dielectric material could be easily deposited onto the surface of these substrates, therefore making them amenable for high performance application. The major disadvantage of glass-ceramics are their low thermal conductivity which make them poor materials for heat dissipation in packaging application where the chip is bonded face-in in the cavity up configuration. However, in the case of the application where the heat dissipation occurs from the back of the chip, this limitation is largely overcome by external vias and water cooling mechanism as in the thermal conduction module of IBM[18].

Much of the heat is removed from the back of the silicon chip (flip-chip) by implementing expensive external cooling modes rather than the substrate itself. From the above it can be seen that there are basically two different types of packaging technologies to cope with the substrate material limitations. One geared towards high power devices employing by and large crystalline ceramics and the other directed towards high speed devices utilizing glass-ceramics. Considerable expenses are therefore incurred for implementing different package designs and fabrication technologies to maintain high quality performance. The need for these two technologies could be obviated by a composite with suitable thermal and dielectric properties.

MATERIALS SELECTION AND METHODOLOGY

The formation of the composite is contingent on the selection of the glass as the matrix and the selection of second phase material. The choice of selection is very strongly dependent on the dielectric and thermal conductivity values of the materials. It is therefore desirable to select two materials, one with the lowest dielectric constant and the other having a high thermal conductivity. Among the materials cordierite, borosilicate glasses and glass-ceramics of these two systems have received the most attention for high speed packaging because of their low dielectric constants. Other glasses have also been developed which show potentially lower dielectric constants such as borophosphosilicate glasses researched by Macdowell and Beall[19,20]. However, since borosilicate glasses have been well studied and considerable information available in the literature in regards to the processing and electrical and thermal properties it was decided as the material of choice. From the list provided in Table 1, the choice of high thermal conducting electrically insulating materials are limited to AlN, SiC, BeO and diamond. AlN is an extremely good choice over beryllia for high performance packages. Diamond on the other hand is an excellent material but once again the difficulty in synthesizing fine particles and obtaining a continuous phase limits its choice. Silicon carbide as seen from Table 1 has a thermal conductivity of 270 W/m-K, and as a fiber (Nicalon) is commercially available and has been extensively studied for composite applications. The ceramic fiber grade however, has a thermal conductivity of 12 W/m-K along the fiber axis at room temperature and a dielectric constant of 9 at 1MHz. Nicalon was therefore selected as the second phase for these preliminary studies despite its rather poor thermal conductivity mainly because of the connectivity issue discussed later. Recently, Ramakrishnan et

al.[21] have fabricated borosilicate glass matrix-Nicalon fiber composites and have studied their tensile behavior.

As discussed above, the main goal of the study was to fabricate composites with optimum thermal conductivity and dielectric constant for applications as substrates in electronic packaging. The properties of such a composite can be predicted to some extent based on certain mathematical models. There are several models that exist, the one that is most well known is the volume fraction model[22-24]. Based on the empirical rules set by the models, it can be seen that a certain volume fraction of two different phases could result in an optimum thermal conductivity and dielectric constant. However, what is important for thermal conductivity is the interconnectivity which the models do not take into account. Thermal conductivity and dielectric constants in a particular direction are influenced more by connected rather than dispersed phases. Thus, using ceramic fibers and arranging their geometries can serve to be quite effective in achieving the desired optimal thermal and electrical properties. The weakness of poor thermal conductivity of most ceramic fibers however can be solved by coating them with the appropriate material. In such cases, the effective dielectric and thermal conductivity are more realistically predicted by the percolation theory and the effective medium theory[25].

In regard towards connectivity, one can also envisage the use of thermally conducting aluminum nitride as a composite material if it is possible to deliberately introduce continuous porosity. Thus, essentially, this would involve fabricating a two phase material having interconnected pores as one phase with thermally conducting aluminum nitride as the second phase. Initial experiments on sintering of aluminum nitride by Prochazka et al.[26] have indicated that during heat treatment of the green bodies there is essentially coarsening in absence of densification. This suggests that the geometry of the interconnected structure remains unchanged while the scale increases with temperature. They also performed surface area measurements which indicate an effective surface to surface transport process operating at relatively low temperatures.

At Wright Patterson, therefore, preliminary experiments were conducted on two aspects. One based on the fabrication of glass-fiber composite using similar concepts of Button et al.[25] except with the use of glass matrix and high thermal conductivity Nicalon fiber in order to fabricate composites which could potentially exhibit good optimal dielectric and thermal conductivity. Such substrates could be essentially used at both low (room temperature) and high temperature ($\approx 700^{\circ}\text{C}$) devices. The other aspect of the research was to fabricate porous aluminum nitride compacts and to analyze the compacts for presence of continuous pores. Glass was then infiltrated into the pores of the compacts.

EXPERIMENTAL PROCEDURE

The experimental section will be divided into two parts one related to the fabrication of glass-fiber composites and the other related to the processing of porous aluminum nitride.

A. PROCESSING OF GLASS-FIBER COMPOSITES

Since the thermally conducting phase is the fiber, good interconnectivity in three dimensions could be envisioned by using a 3-D interwoven cloth. However, considering the preliminary nature of the work, in order to test the feasibility of the concept, it was decided to use a plain weave Nicalon 2-D woven cloth from Nippon Carbon Co. Ltd., Japan. The matrix material chosen was a 7760 grade borosilicate glass commercially obtained from Corning. The properties of both these materials relevant for the present work are shown in Table 2.

Two different approaches were followed in the experiments mainly based on pressure and pressureless sintering.

I. Tape Casting and Sintering

In this case, the borosilicate glass powder was initially dispersed into solution using fish oil as the dispersant. The dispersed glass is then mixed with a binder and a plasticizer to blend the glass with the binder. The resultant colloidal dispersion is then cast into a 8 mil tape. The tape casting procedure followed was similar to that developed by Rollie Dutton at Wright Patterson. The tapes were then stripped from the bench and then laminated with the Nicalon cloth. Four different routes as shown in Figure 1 were followed using the tape casting and sintering technique.

Method 1

In this route, the tapes were laminated directly with cloth at temperatures of 300°F for 15-30 minutes. The laminated tapes were then sintered using a controlled heat treatment cycle. The first cycle consisted of heating the tapes to a temperature of 500°C in flowing oxygen at a pressure of 5psi at the rate of 2°C/min and holding the samples at the temperature for 1h. After the 1h hold, the samples were then heated in vacuum to 880°C ($\approx 50^\circ\text{C}$ above the softening point) at 5°C/min and held for 1h and 20min. to initiate and complete the sintering of the composite. The atmosphere was then switched to argon and the samples were cooled to room temperature using a cooling rate of 2°C/min. At the end of this step, the composites were sectioned and the cross sections observed using optical microscopy.

Method 2

In this route, the tape casting slurry was vacuum infiltrated into the Nicalon cloth whose sizing was earlier removed by keeping the cloths at 600°C for 5-15 minutes. The vacuum infiltrated specimens were then laminated between six 8 mils thick tapes and laminated at 300°F for 30 min. The laminated tapes were then heated at 2°C/min to 500°C in flowing oxygen to remove the organics. A graphite slab weighing 120g was used as a dead weight in order to facilitate the glass to flow into the tows of the cloth. After a hold of 80 min., the samples were then heated in vacuum to 1000°C at 10°C/min and held for 80 min. The composite specimens were held at 1000°C for 80 min. after which the samples were cooled very slowly at 2°C/min under an atmosphere of argon to 500°C and kept there for atleast 3-5hrs before cooling the samples down to room temperature at

2°C/min. In another sample, a load of 100g was placed on the laminated specimens, while placing two layers of cloth between tapes for lamination. The samples were then analyzed using optical microscopy.

Method 3

In this route instead of the 2-D woven cloth experimental trials were conducted using SCS-0 and SCS-6 fiber as the second phase. The fibers were initially rolled onto aluminum foils with a interfiber distance of 8 mils to form a pre-preg. The pre-pregs were then laminated using 1/8" tape casted tape at 200°F initially for 5 min. and then applying a very slight load for 10 min. Four pre-pregs were laminated each between two layers of tape in 0-90 orientation so that a configuration similar to the 2-D woven cloth could be attained. A final lamination was performed at 250°F for 15 min. initially and then applying a slight load for an additional 15 min. The laminates were then subjected to a similar heat treatment as described above in methods 1 and 2. Identical procedures were also followed using SCS-6 fibers.

Method 4

In this procedure commercially obtained Nicalon tows whose sizing was removed were used as the second phase. The procedure consisted of initially removing the sizing from the fiber tows at 600°C for 15 min. The tows were then dip coated into the tape casting slurry containing the borosilicate glass powders. The dip coated tows were then dried in air and then laminated between four layers of tape using similar procedures as described in 1 and 2. The tapes containing the dip coated tows were then subjected to an initial burn out at 500°C and then sintered in vacuum at 900°C similar to methods 1 and 2. Similar procedure was also followed using dip coated Nicalon tows placed in 0-90 orientation except that the sintering was conducted at a temperature of 1000°C.

II. Hot Pressing

This procedure was followed only using the 2-D woven cloth along with the borosilicate glass powder (7760 grade from Corning). The detailed experimental procedure consisted of the following steps. The 2-D woven cloth was initially treated for sizing removal at 600°C for \approx 8-12h. The cloths were then vacuum infiltrated with the tape casting slurry. Immediately following the vacuum infiltration, the wet cloth was placed between two tapes either 8mils or 16 mils thick and then dried in air. The dried tapes were then laminated between two 8mils or 16 mils thick tapes at 300°F for 10 min. initially and then with a load at 300°F for an additional 10 min. The laminated samples were then placed in an ashing furnace for removal of organics and binder. The samples were heated at the rate of 2°C/min to 500°C and kept for 80 minutes after which the temperature was brought down at 2°C/min. to room temperature. After this treatment, these samples were then loaded into a die and packed with the glass powder after placing graphoil foils at the bottom and top of the die cavity. A stacking sequence consisting of alternate layers of glass powder followed by the cloth was used. Initial experiments consisted of using just the laminated cloth without

packing any additional glass powder. The experiments were then modified with two layers of cloth alternating with glass powder. Finally, five layers of laminated cloths were stacked in the die with alternating layers of glass powder in order to minimize the distance between the cloth layers and enhance the connectivity.

After the samples were stacked into the die, the die was loaded into the hot press. The system was then pumped down to 35 μ m. The die was then heated to 1000°C in vacuum and then a pressure of 1500-2000 psi was then applied to the samples. The load was kept constant for \approx 30 minutes after which the samples were cooled down to room temperature. The samples were then recovered from the die and observed for glass penetration using optical microscopy.

B. PROCESSING OF POROUS ALUMINUM NITRIDE

The experimental procedure consisted of using commercially obtained aluminum nitride from Starck chemicals in Germany. The as-received powders were mixed with acetone and cold pressed into pellets (1/4" thick) and 0.5" in diameter by application of pressure \approx 1000 psi. The cold pressed pellets were dried overnight and then cold isostatically pressed at \approx 35000 psi. to a final dimension of 7/32" thickness and 7/16" diameter. The pellets were then placed in a closed graphite crucible covered with loose aluminum nitride powder. The pellets were then sintered in a static nitrogen atmosphere of 1 atmospheric pressure. Two sets of experiments were conducted one at 1800-1880°C for one hour. Another set of experiments were conducted on powders that were ball milled in ethanol for 24h and then cold pressed followed by cold isostatic press to form green compacts. These compacts were then sintered under identical conditions except at a temperature of 1900-1920°C for one hour. After the sintering experiments, the samples were polished and observed under an optical microscope. Meanwhile, glass infiltration experiments were conducted on both the pellets using the borosilicate glass. The infiltration was conducted by placing the pellets in a graphite die covered with the 7760 commercially obtained Corning grade glass that was used in part A. The loaded die was then heated to 1000°C and a pressure of 1500-2000 psi was then applied for 30 minutes. The sample was then recovered and the cross sections observed under an optical microscope to observe the glass infiltration.

RESULTS AND DISCUSSION

The report discusses the results of the preliminary trials conducted at Wright Patterson. These results will be presented in three sections. Section I will discuss the results of the experiments conducted primarily on tape casting, lamination and sintering of the Nicalon 2-D cloth, the SCS-0 and SCS-6 fibers and on plain Nicalon tows. On the other hand section II will discuss the results of the work conducted on hot pressing of the Nicalon cloth and the borosilicate glass. Section III will then discuss the results on the processing of porous aluminum nitride and preliminary trial conducted on infiltration of the borosilicate glass.

Section I: Tape Casting and Sintering

Method 1: Tape casting and lamination of 2-D Nicalon cloth followed by sintering

In order to fabricate the composite initial trials were conducted to observe the feasibility of direct lamination of the Nicalon cloth placed between two 8 mil cast tapes of borosilicate glass. The tapes with the cloth were laminated and then sintered following the schedule described in the experimental section. The resulting composite on removal from the furnace was extremely fragile and would peel off at several places. There was noticeable surface cracks due to thermal stresses. The samples were cut and mounted on epoxy and then polished following standard ceramic polishing procedures. The optical micrograph obtained on the cross section of the sample is shown in Figure 2. The micrograph clearly shows that the glass has only been able to wet just the surface of the tows without resulting in any penetration at all. This could be because of several reasons. First, the temperature not being high enough to cause the glass to be sufficiently fluid to penetrate the fibers. Second, the fiber spacing $\approx 10\mu\text{m}$ is too small requiring extremely high capillary pressures to cause penetration of the glass through the fiber spacing. For example making an erroneous assumption for the sake of simplicity that the glass possesses the same surface energy as water (78 dynes/cm) the capillary pressure amounts to 156000 Pa. This suggests the need to provide for additional on the top of composite during sintering to cause reasonable penetration.

Method 2: Effect of increased temperature, vacuum infiltration and pressure

Based on the above results, it was decided to initiate initial contact between the glass and the Nicalon fibers by vacuum infiltration. Hence, the Nicalon cloth was initially pretreated to remove the sizing and then vacuum infiltrated with the borosilicate slurry. After infiltration, the cloth was placed between two tapes and then laminated. The laminated tape was then heated to a higher sintering temperature of 1000°C and after the initial hold of 80 minutes was then subjected to a slow cool ($2^\circ\text{C}/\text{minute}$) to 500°C . The composite was held at this temperature for at least 3h before cooling down to room temperature. In order to induce penetration a dead weight of $\approx 120\text{g}$ was placed on top of the composite. Modification of the initial conditions appeared to cause visible changes in the composite. Figure 3 shows the cross section of the composite observed under an optical microscope after routine grinding and polishing. The micrographs clearly show an improvement over the earlier case in terms of penetration of the glass into the fiber spacing. Since the two layers of the cloth were laminated after infiltration, the micrographs show the longitudinal cross section of the fibers also. Although, penetration has improved, there still appears to be porosity in the glass matrix suggesting possibly the requirement for longer heat treatment in vacuum. Repeating the procedure once again using a dead weight of 100g however once again showed considerable porosity in the glass although, there were regions wherein the glass had penetrated into the fiber spacings.

These experiments therefore suggest that vacuum infiltration combined with a higher

temperature and use of a dead weight helped to improve the penetration of the glass melt into the fiber spacing. However, the concept of tape casting and sintering seems to be quite inadequate on its own to result in a good composite with complete wetting of the glass and the fiber. As mentioned, one of the main reasons is the high viscosity and the tremendous capillary pressures that need to be overcome to cause penetration into the fine fiber spacing. On the other hand, it should be mentioned that the glass powder is quite coarse with an average particle size of $\approx 10\mu\text{m}$. Thus, vacuum infiltration does not result in adequate penetration into the fiber spacing. However, the use of a sol-gel derived sol or a much finer glass particle size could result in improved wettability improving the quality of the composite.

Method 3: Tape casting and lamination of SCS-0 and SCS-6 fiber followed by sintering

These experiments were conducted since the tape casting and sintering approach failed to provide with an adequate quality composite on which the electrical and thermal properties could be measured. Initial experiments were conducted using the SCS-0 grade fiber which is essentially non stoichiometric SiC with excess carbon and some oxygen. The fibers were initially rolled onto a pre-preg as described in the experimental section and then laminated onto the borosilicate tapes. Similar sintering procedures were followed as with the 2-D Nicalon cloth. Four layers of the fibers were placed in 0-90 orientation and laminated following identical procedures as in the case of the 2-D Nicalon cloth. The composites were heated to 1000°C for sintering and cooled down at $2^{\circ}\text{C}/\text{minute}$ to 500°C at which it was kept for almost 4h before cooling down to room temperature. The composite however, was not at all transparent and appeared dark and unclear as though, there was unburnt binder trapped inside the composite. The cross section of the composite also revealed the presence of considerable porosity visible to the naked eye suggesting fiber degradation. This could possibly be because of the diffusion of Na^+ from the glass into the interface of the fiber and the glass causing reaction with the oxygen in the fiber. Similar observations have been cited by Mah et al.[27] at Wright Patterson using the SCS-0 fibers with sodium containing glass.

In the case of the SCS-6 fibers, once again similar sintering procedure reported for the cloth was followed. Four layers of the fibers were laminated in 0-90 orientations and then subjected to sintering after binder burn out at 500°C at 1000°C . Figure 4 shows the cross section of the composite observed under an optical microscope. The micrographs clearly indicate fiber swimming that has occurred during the sintering process. At the same time considerable porosity is seen particularly close to the fibers. The SCS-6 fibers are chemically made up of a central carbon core, an inner coating covering the core, four SiC layers deposited on the inner coating, and an outermost coating whose composition has long been a controversy[28]. However, recently Ning et al.[28] have reported the results of the microchemical analysis of the SCS-6 fiber. Their studies indicate that the outermost layers are made up of four different layers of SiC, the Si to C ratio not being exactly stoichiometric. The porosity could arise from the reaction of the outer core with the

glass. A possible reaction being that of carbon with sodium oxide to form CO. This can be seen very clearly in Figure 5.

Method 4: Tape casting and lamination of Nicalon fiber tows followed by sintering

All the above processes with the cloth as well as with pre-pregs of SCS-0 and SCS-6 seemed to indicate problems of inadequate penetration in the case of the cloth and reaction with the fiber of the glass in the case of the pre-pregs. It was therefore decided to study and apply the tape casting and sintering approach to commercially obtained Nicalon tows. The tows were stripped of the sizing by heating in air at 600°C. They were then dipped into the borosilicate glass slurry. The dip coated tows were then laminated and sintered following identical processes as those discussed earlier in method 1. Two set of experiments were conducted using the dip coated tows, one in which the composites were heated to 900°C and the other in which the composites were heated to 1000°C with the tows arranged in 0-90 orientation. Figure 6 shows the cross section of the composites observed under an optical microscope. The micrographs clearly indicate very good wetting of the fiber with the glass in contrast to that in the case of the cloth, although some random porosity is evident. In the case of the tows arranged in the 0-90 orientation also, it can be seen that there is good wetting obtained.

Section II. Hot Pressing of the glass and the Nicalon cloth

From the discussion above it can be seen that the tape casting and sintering approach shows some promise in the case of fabrication of composites using Nicalon tows. On the other hand it is extremely difficult to achieve good glass penetration into the fiber tows in the case of the Nicalon 2-D cloth. It was clear that in order to achieve penetration there is need for application of pressure in addition to increasing the temperature. Hot pressing was therefore seen as a solution to the problem. Several sets of samples were hot pressed in order to obtain the right set of processing parameters of temperature (1000°C) and pressure (\approx 1500-2000 psi). The samples were hot pressed for 30 minutes and then cut, mounted and polished to be observed under the optical microscope. Figure 7 shows the cross section of a representative composite. The micrograph clearly shows regions where the glass has completely penetrated the fiber tows in a uniform fashion. There are very few regions where the glass has not penetrated into the fiber spacing. Another noticeable effect is the densification of the glass with very minimum porosity. Thus, it was possible to fabricate uniformly penetrated glass-fiber composite using the hot pressing technique at a temperature of 1000°C and pressure of 1000 psi. Following this success, it was decided to fabricate a composite comprising of five layers of the cloth very closely spaced so that good connectivity could be achieved for the dielectric measurements.

Section III. Processing of Porous Aluminum Nitride

The as-received aluminum nitride powders were cold pressed and then isostatically pressed to form a green pellet. The resulting pellets were then sintered in nitrogen at 1900°C for one hour.

The samples were polished and observed under an optical microscope. Figure 8 shows the optical micrograph of the polished specimen. As can be seen the micrographs taken at magnifications of 100X clearly indicate presence of connected pores continuous on the surface. Densities of the samples were also measured using Pycnometry which indicated the densities to be 3.257g/cc very close to the theoretical density. At the same time the apparent density of the samples was calculated to be 2.32 g/cc. A comparison of the two therefore indicates presence \approx 28% porosity in the samples. The fact that there is porosity in the samples and that the pycnometric studies yielded theoretical density suggests the interconnected nature of pores. These results are extremely promising particularly for the application in electronic packaging due to the interconnected nature of the microstructure.

Following on these encouraging results, it was decided to infiltrate the nitride ceramic with the borosilicate glass. The hot infiltration was conducted at 1000°C and a pressure of 1500 psi. The resulting composite was mounted, sectioned, polished and observed under the optical microscope. Figure 9 shows the cross sections of the polished samples. The micrographs indicate that the glass has penetrated only to a distance of 75-100 μ m. These results therefore suggest the tremendous potential of these experiments for obtaining a porous AlN ceramic satisfying both the electrical and thermal requirements. The low penetration of the glass into the ceramic infact could provide the hermetic seal required for the reliability of the substrate against atmospheric moisture. Future work will be directed towards measuring the thermal and electrical characteristics of these composites.

CONCLUSIONS

The results of the preliminary studies conducted on processing of glass-fiber and glass-ceramic composites indicate the extreme difficulty faced in trying to apply the tape casting and sintering approach particularly, in the case of the 2-D woven fiber cloth. However, the results of the work suggest the potential of this approach for processing of composites using slurry coated Nicalon tows where successful penetration of the tows with the glass was achieved. Substantial fiber degradation was observed in the case of the SCS-0 fiber due to a possible interaction of glass with the fiber. However, hot pressing of borosilicate and Nicalon cloth at 1000°C and 1500 psi resulted in the formation of good composites with successful penetration of the fiber tows with glass. At the same time preliminary sintering studies conducted on commercially obtained AlN powders resulted in ceramic with \approx 28% connected porosity. Hot infiltration of the ceramic provided \approx 75-100 μ m penetration of the glass into the connected pores. These results particularly, those with the AlN are therefore extremely encouraging in terms of the goals of the research and will form a part of the extension research proposal to be submitted to the AFOSR.

ACKNOWLEDGEMENTS

The author would like to acknowledge the support of the Air Force Office of Scientific Research for providing support for the summer research. In addition, the author would like to

thank Drs. Tai-il Mah, Rollie Dutton and Edmund Moore for useful technical assistance. The help of Kristi Keller, Cathy Gustafson, Charlie Cook, Marlin Cooke, Mark Dodd, George Cornish and Dennis Petri of UES and all the support staff in the ceramics group at Wright Patterson Laboratories is also acknowledged. The author would also like to thank Ms. Kim Andrews and Ms. Cindy Emerick for their help in preparation of samples for characterization. Finally, the author would like to acknowledge the support of Drs. Ron Kerans, Alan Katz and Paul Jero for providing the opportunity to participate in the summer faculty program.

REFERENCES

1. 'Microelectronic Packaging Handbook', Edited by R.R. Tummala and E.J. Rymaszewski, Van Nostrand Reinhold, New York, (1989).
2. G. Geiger, Bulletin American Ceramic society, 69, (1990) 1131.
3. E.M. Rabinovich, J. Electronic Packaging, 111, (1989) 183.
4. R.R. Tummala and R.B. Shaw, High Tech Ceramics, Ed. P. Vincenzini, Elsevier Science Publishers B.V. Amsterdam, (1987) 75.
5. J.L. Sprague, IEEE Transactions on Components, Hybrids, and Manufacturing Technology, 13, (1990) 390.
6. K.R. Kinsman, J. Metals, 6, (1988) 7.
7. N. Kuramoto, H. Taniguchi and I. Aso, Ceramic Bulletin, 68, NO. 4, (1989) 883.
8. N. Kuramoto and H. Taniguchi, J. Mater. Sci. Lett., 3, (1984) 471.
9. T.B. Troczynski and P.S. Nickolson, J. Amer. Ceram. Soc., 72 [8] (1989) 1488-1491.
10. N.S. Van Damme, S.M. Richard and S.R. Wizer, J. Am. Ceram. Soc., 72 [8] (1989) 1409-1414.
11. A. Hai, T. Shi, K. Wakimura, Sennan, M. Tonaka. Shimonoseki, Mitsui Toatsu Chem. Inc. Tokyo, Japan, "Method For Preparing Aluminum Nitride And Its Sintering". U.S. Patent No. 4869925, (1989).
12. U. Klabunde, W. Chester, E.J. Newitt, C. Ford, F.N. Tebbe, H. Del. E.I. DuPont de Nemours & Co. Wilmington, Delaware, "Gas Phase Preparation of Aluminum Nitride", U.S. Patent No. 4865830, (1989).
13. S.L. Dole, R.H. Arendt, W.D. Pasco, General Electric Co., Schenectady, N.Y., "Alkaline Earth Fluoride Additive For Sintering Aluminum Nitride", U.S. Pat. No. 4843042, (1989).
14. S. Kuratani, K. Uno, S. Mizuno, H. Sakuramoto, and S. Nishiyama, Narumichina Corp., Nagoya, Japan, "Black Sintered Body of Aluminum Nitride And Process For Producing the Same", U.S. Pat. No. 4843038, (1989).
15. S. Mizuno, S. Kuratani, K. Uno, H. Sakuramoto, and S. Nishiyama, Narumochina Corp., Nagoya, Japan, "Sintered Body of Aluminum Nitride", U.S. Pat. No. 4833108, (1989).
16. A. Ikegami and T. Yasuda, "High Thermal Conductive SiC Substrate and Its Applications", 5th European Hybrid Microelectronics Conference, (1985) 465.
17. R.R. Tummala, J. Am. Ceram. Soc. 74 (1991) 895.
18. A.J. Blodgett, Jr., Scientific American, 249 (1983) 2.
19. J.F. MacDowell, G.H. Beall, Proc. of the 1st International Science and Technology conference, "Materials and Processes for Microelectronic Systems", Ceramic Transactions, Ed. K.M. Nair, R. Pohanka and R.C. Buchanan, Vol. 15 (1989) 259.
20. J.F. MacDowell and G.H. Beall, Mat. Res. Soc. Symp. Proc., "Advanced Electronic Packaging Materials", Ed. A.T. Barfknecht, J.P. Partridge, C.J. Chen and Che-Yu Li, Vol. 167 (1989).
21. V. Ramakrishnan and N. Jayaraman, J. Materials Science 27 (1992) 2423.
22. W.D. Kingery, H.K. Bowen and D.R. Uhlmann, 'Introduction to Ceramics', John

Wiley & Sons, Second Edition, (1976) 635.

23. A.J. Moulson and J.M. Herbert, 'Electroceramics, Materials, Properties and Applications', Chapman and Hall (1990) 79.

24. L.E. Cross and T.R. Gururaja, Mat. Res. Soc. Symp., "Electronic Packaging Materials Science II", Eds. K.A. Jackson, R.C. Pohanka, D.R. Uhlmann and D.R. Ulrich, Vol. 72 (1986).

25. D.P. Button, B.A. Yost, R.H. French, W.Y. Hsu, J.D. Bolt, M.A. Subramanian, H.M. Zhang, R.E. Giedd, A.J. Whitaker and D.G. Onn, Advances in Ceramics, Vol. 26, "Ceramic Substrates and Packages for Electronic Applications", Eds. M.F. Yan, K. Niwa, H.M. O'Bryan, Jr., and W.S. Young, American Ceramic Society (1989) 87-105.

26. S. Prochazka and C.F. Bobik, Materials Science Research, Vol. 13, "Sintering Processes", Ed. G.C. Kuczynski, Proc. 5th Intl. Conference on Sintering and Related Phenomena, (1979) 321.

27. T. Mah, Private Conversation, (1993).

28. X.J. Ning, P. Pirouz and S.C. Farmer, J. Amer. Ceram. Soc. 76 (1993) 2033.

Table 1. Properties of Selected Ceramic Substrate Materials.

Substrate Properties	AlN	SiC	BeO	Glass-Ceramics	90% Alumina	cubic BN	Diamond
Thermal Conductivity (W/m-K)	230	270	290	5	25	250	2000
Coefficient of Thermal expansion (20-200 C) ($\times 10^{-7}/^{\circ}\text{C}$)	43	37	68	30-42	67	48	35
Dielectric Constant at 1 MHz	8.9	42	6.8	5.0	9.4	7.1	5.6
Flexural Strength (MPa)	350	420	250	210	280	-	-

Table 2. Characteristics of materials selected for the glass-fiber composite

I Glass System

Borosilicate glass (Corning grade 7760)

Composition:

silica 70-80%

boron oxide 10-20%

sodium oxide 1-10%

alumina 1-10%

arsenic oxide < 1%

potassium oxide 1-10%

Properties

Dielectric Constant: 4.5 @ 1MHz, 20 C

II. Fiber

Nicalon (2-D) cloth (Plain weave 1 sq. m., Nippon Carbon Co. Ltd., Japan)

Properties

Dielectric Constant: 6.2 @ 1MHz

Thermal Conductivity: 12W/m-K

Figure 1. Flow sheet showing the different paths followed in the tape casting and sintering approach

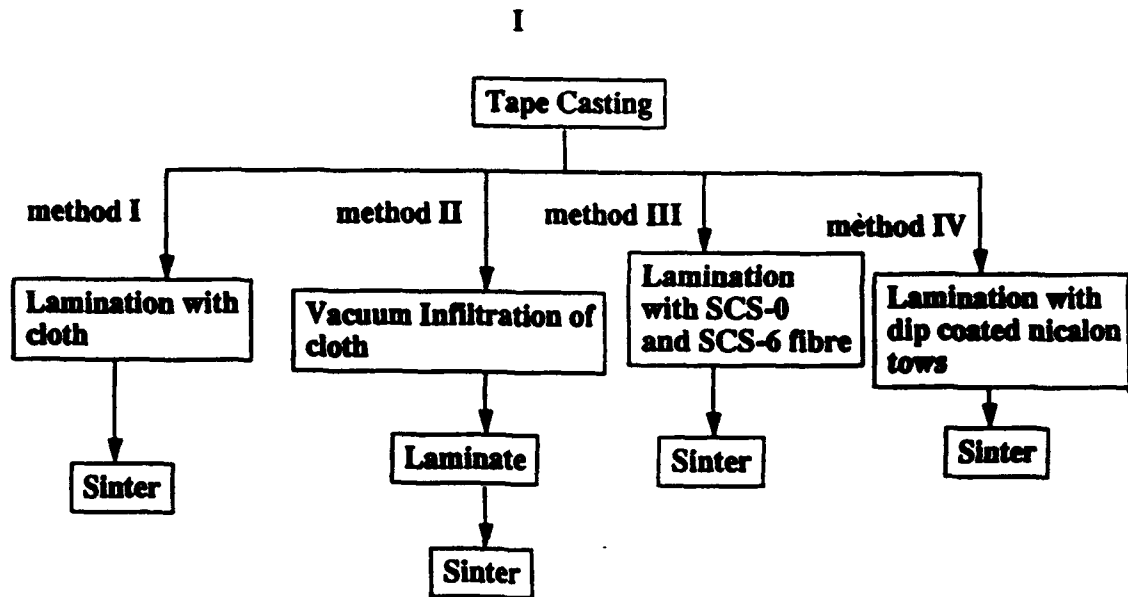


Figure 2. Optical micrograph showing the polished cross section of glass-fiber (2-D cloth) composite obtained using the tape casting and sintering approach. The micrograph is taken at a magnification of 200X.

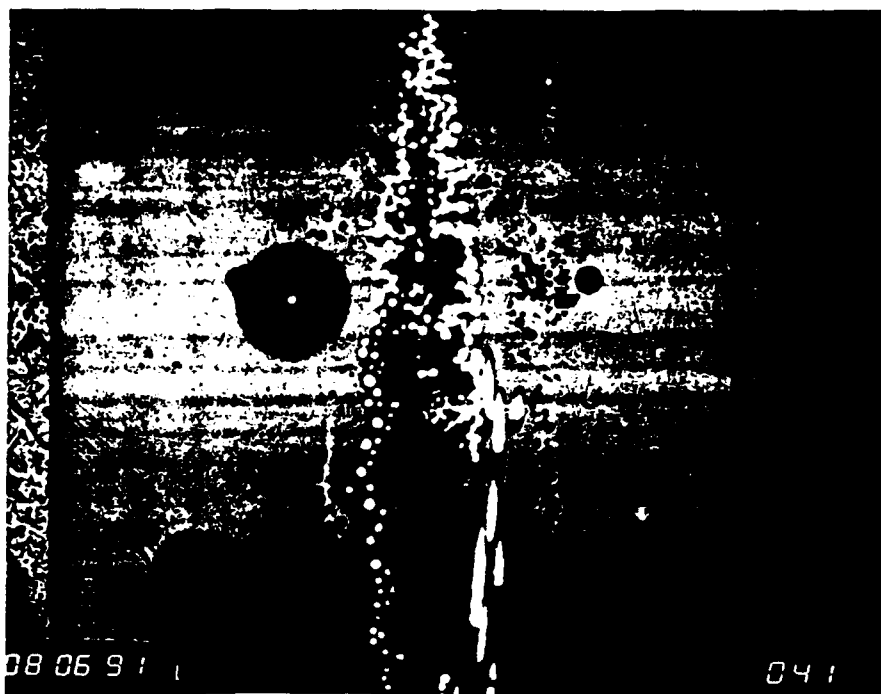


Figure 3. Optical micrograph showing the polished cross section of glass-fiber (2-D cloth) composite processed using vacuum infiltration and sintered at a higher temperature using a dead weight of 120 g. The micrograph shows improved penetration of the glass into the fiber tows. The micrograph is taken at a magnification of 100X magnification.



Figure 4. Optical micrograph showing the polished cross section of glass-SCS-6 fiber composite taken at 400X magnification. The micrographs show fiber swimming and possible degradation of the outer carbide coating.

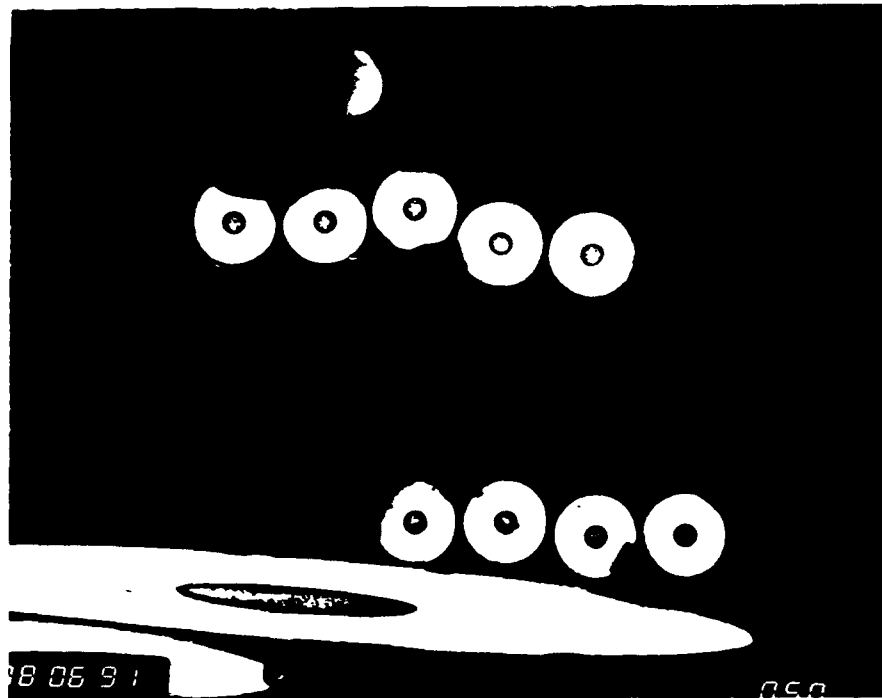


Figure 5. Optical micrograph showing the polished cross section of glass-SCS-6 fiber composite taken at 100X magnification. The micrographs show fiber swimming as well as porosity near the fiber possibly due to degradation of the outer fiber coating.

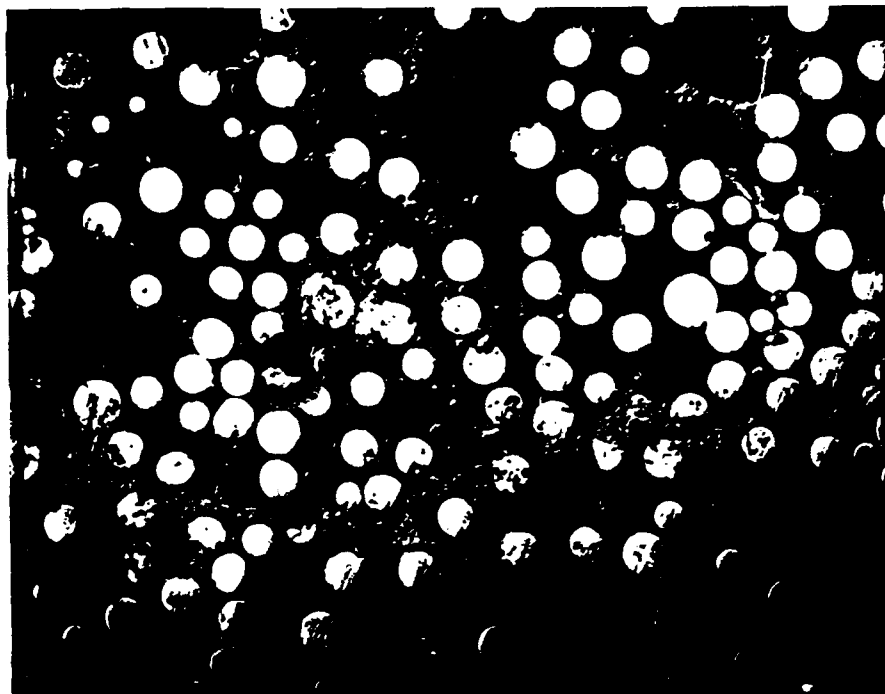


Figure 6. Optical micrograph showing the polished cross section of glass and Nicalon fiber tows dip coated in glass slurry. The micrographs taken at 400X magnification show good penetration of glass into the fiber spacing.

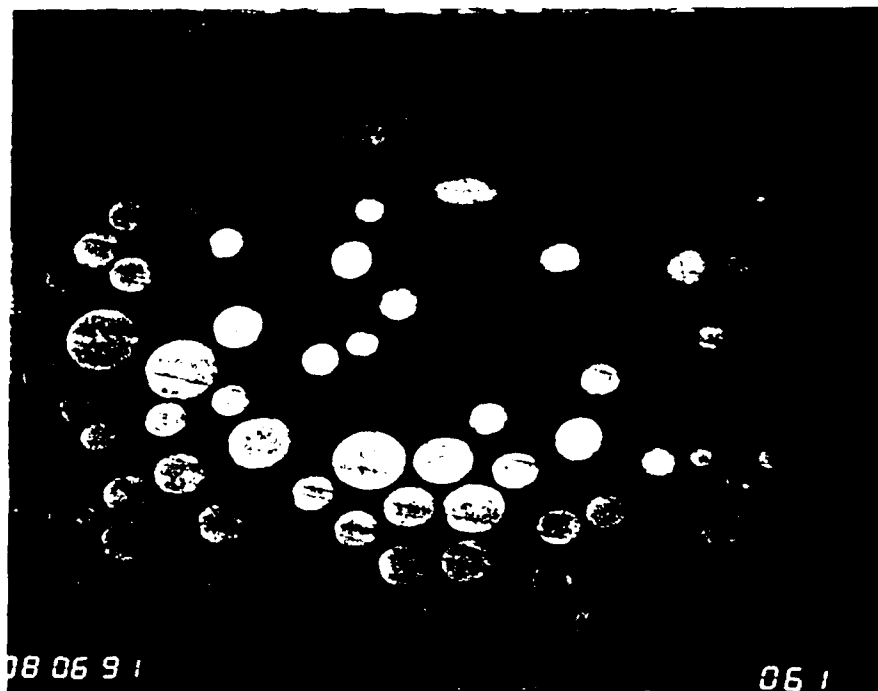


Figure 7 Optical micrograph showing the polished cross section of hot pressed glass fiber (2 D cloth) composite processed at 1000 °C and 1500 psi pressure. The micrograph taken at 400X magnification show good penetration of the glass into the fiber spacing. The glass is also visibly dense with no porosity.

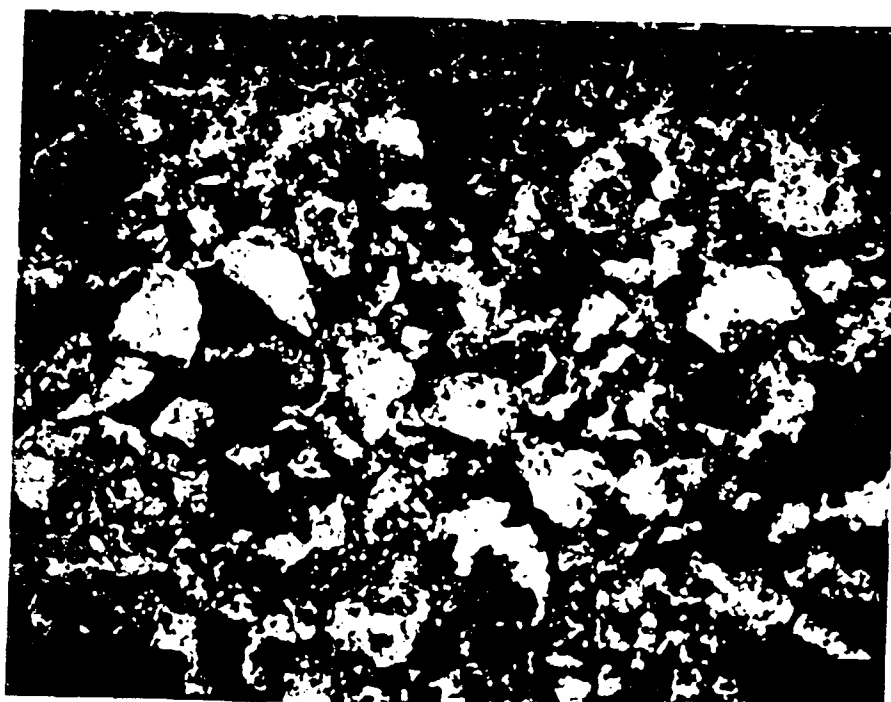


Figure 8 Optical micrograph showing the polished cross section of the sintered aluminum nitride pellet at 200X magnification. The micrographs show the presence of well-sintered porosity.



Figure 9. Optical micrograph showing the polished cross section of sintered aluminum nitride hot infiltrated with borosilicate glass. The glass has penetrated to a distance of ≈ 100 μm into the pores in the nitride ceramic. The micrographs are taken at a magnification of 200X (top) and 300X (bottom).

Hydrothermal Effects on the Structural Integrity of Graphite Fiber-Cyanate Ester Resin Composites

B. L. ("Les") Lee
Associate Professor
Department of Engineering Science and Mechanics

The Pennsylvania State University
227 Hammond Building
University Park, PA 16802

Final Report for:
Summer Faculty Research Program
Air Force Wright Laboratory
Materials Directorate, Non-Metallic Materials Division
(USAF Researcher: Capt. Michael W. Holl)

Sponsored by:
AIR FORCE OFFICE OF SCIENTIFIC RESEARCH

September, 1993

INTRODUCTION

Fiber-reinforced polymer matrix composites which form various structural components of aircraft are subjected to a complex history of temperature, moisture and other environmental conditions. Their effects, particularly the effects of moisture absorption and thermal cycling, have been extensively studied since the early 1970's [1-9]. Excellent review articles have been available on these subjects. Among them, worthwhile to note are the reviews done by Springer [4], Adams [5], Ashbee [6], and Wolff [7] on the moisture effects. Reflecting the state of technology, the past investigations were concentrated in the epoxy resin matrix composites typically reinforced by graphite, glass or aramid fibers. As a result, hydrophilic nature of epoxy resins as composite matrices has been well-documented. Since many applications cannot accept moisture-sensitive nature of epoxy resin matrix composites, intensive research works were performed to introduce new thermosetting resins with a reduced tendency of moisture absorption without penalizing the processability. One important example of the achievement in this direction was the synthesis of polycyanurate, so-called *cyanate ester*, resins for composites [7,10,11]. Neat resin casting of cyanate ester was reported to exhibit an equilibrium level of water absorption as low as 0.7% at 100°C [7].

Cyanate ester resin matrix composites reinforced by glass or aramid fibers established their presence in the application for multi-layer electric circuit board as early as the late 1970's, because of the following considerations [10]: (a) their glass transition temperatures (T_g) exceeding those of epoxy resins and matching molten solder temperature (220-270°C); (b) low dielectric loss properties; and (c) excellent processability (epoxy-like). Recently, successful efforts for toughening of the resins by the inclusion of elastomer or thermoplastic secondary-phase have led to a serious consideration of cyanate ester resin matrix composites for their use in primary structure applications [10, 12-17]. Currently available cyanate ester resins for structural composites offer a desirable combination of high resistance to moisture absorption, reasonably good fracture toughness, and acceptable processability. In addition, a relatively low cure temperature (177°C) and a large amount of free volume after gelation were reported to allow the cure shrinkage less than 1% creating more residual stress-free composite parts [10].

In the case of epoxy resin matrix composites, moisture absorption was shown to relieve the residual stresses by matrix swelling and temporarily increase the resistance to matrix/interface cracking [18,19]. The occurrence of this type of interaction is expected to

be negligible in the cyanate ester resin matrix composites which absorb a very small amount of water. However, the question of whether this small amount of water absorbed will eventually influence the fiber-matrix *interface* of cyanate ester resin matrix composites as in the case of epoxy resin composites has not been resolved [6,7]. Aside from the issue of moisture effect on the interfacial adhesion, the structural integrity of cyanate ester resin matrix composites should be assured under the condition of thermal spike or cycling. Here a systematic data base is lacking, despite the claims by the resin producers of better microcrack resistance of cyanate ester resin composites over the epoxy resin composites upon thermal cycling. One of the first questions to resolve in this area appears to be whether the effect of thermal cycling can be represented by the cumulative sum of thermal degradation effect at the peak temperature. An equally important question is what factors control a critical frequency of thermal cycling above which the deviation from cumulative effects occurs. These questions were not fully examined even in the case of conventional thermoset resin matrix composites where extensive data base exists for thermal cycling.

Our study plans to assess the long-term structural integrity of graphite fiber-reinforced cyanate ester resin matrix composites with a special attention to the issues raised and discussed so far. As a first step toward this goal, the weight change and the retention of matrix/interface dependent mechanical properties of the composite systems have been measured on the exposure to *high humidity* and *thermal cycling* respectively. In consideration of the long-term structural integrity, the study has included the evaluation of not only static strength but also *fatigue* lifetime profile of composites. A study has been initiated to resolve the question of whether the effect of thermal cycling can be represented by the cumulative sum of thermal degradation effect. Continuing study will eventually assess cumulative effects of temperature cycling or spike in conjunction with moisture exposure on the mechanical performance of composites. When completed, the efforts will to clarify the mechanisms of hydrothermal environment-induced change of the composite performance, and thereby provide a technical basis for the future work on the environmental fatigue of composite structures. Preliminary findings of our efforts are reported in this paper which will be the first one of the series.

OBJECTIVES

(a) To examine the effects of moisture absorption, temperature cycling, and their combination on the long-term structural integrity, particularly matrix/interface dependent mechanical properties, of graphite fiber-reinforced cyanate ester resin matrix composites; (b) to assess the mechanisms of hydrothermal environment-induced change of the composite performance; and (c) to provide a technical basis for the future work on the environmental fatigue of composite structures.

EXPERIMENTS

Specimen Preparation Unidirectional composite prepreg was obtained from ICI Fiberite Composite Materials Inc. (Tempe, AZ). The reinforcement was Hercules IM7 graphite fiber. The resin matrix for the prepreg was ICI 954-2 cyanate ester resin which reportedly contains thermoplastic toughener of a proprietary nature. *Off-axis angle-ply* laminates were prepared by laying up four prepreg plies with a symmetric configuration of $(+45/-45^\circ)_s$ and curing them in autoclave. The following cure conditions recommended by the materials supplier were used: heat-up rate of $3^\circ\text{C}/\text{min}$; 1 hour at 121°C (250°F) followed by 2 hours at 177°C (350°F); pressure of 0.69 MPa (100 psi). Some of the laminates were subjected to an optional postcure cycle consisting of 2 hours at 232°C (450°F) under contact pressure. The thickness and the resin content of cured composite panels was approximately 0.57 mm and ??% by weight respectively. Two types of straight strip specimens were cut with water coolant from the panels: 12.5 mm X 62.5 mm (Type I), and 18.75 mm X 125 mm (Type II). The specimens were immediately placed in a desiccator after cutting. Their weights were monitored until they reached an asymptote due to drying-out of moisture.

Environmental Exposure Both Type I and Type II specimens of graphite fiber/cyanate ester resin composite were placed for various periods of time in a humidity chamber which were maintained at 95% RH and 60°C (140°F). The weight gain of each specimen due to moisture absorption was measured in a chemical balance after the moisture was removed from the specimen surface by soft paper tissue. The results of the specimens exposed to high humidity continuously were compared with those of the specimens which were taken out of the humidity chamber for weighing, re-exposed to the humidity, and re-

weighed. Both techniques produced the same consistent results within the range of data scattering.

A separate lot of composite specimens were also exposed to dry heat at 150°C (302°F) or 204°C (400°F) in either cyclic or static mode. Static exposure of the composite specimens to dry heat was performed using an oven without air-circulation. Thermal cycling between elevated temperature and ambient temperature was accomplished by shuttling the specimen between the preheated oven and an open area with cooling fan. Shuttling action was performed using a hydraulic test machine operated at a frequency of 1.67×10^{-3} Hz (10 min/cycle) in a stroke-controlled mode. The above cyclic frequency allowed 5 minutes' exposure at elevated temperature per each cycle. After the exposure to various environments described so far, the Type I specimens were used for the measurement of weight change. The Type II specimens were used for tensile testing in static as well as dynamic mode.

Mechanical Testing After the exposure to moist heat (95% RH, 60°C), dry heat (150 or 204°C), or thermal cycling (to 150 or 204°C from ambient temperature) for various periods of time, the Type II specimens of graphite fiber/cyanate ester resin composite were subjected to static uniaxial tension until failure occurs. The rate of deflection and the initial gage length of the specimen were 1.25 mm/min and 75mm respectively. The in-plane shear strength and modulus were defined according to the procedure of ASTM D3518. Monitoring of strain along the transverse as well as axial direction, which is needed for the calculation of in-plane shear modulus, was limited to the case of dry specimens. In the case of axial strain measurement, bonded strain gage technique was used along with an extensometer. A reasonably close agreement between the two types of measurement was observed. For wet specimens, only the axial strain was measured by an extensometer.

In the case of dry specimens and the specimens exposed to moist heat (95% RH, 60°C) for 50 days, tension-tension fatigue experiments were performed at ambient condition. The number of cycles to failure were measured at various levels of stress range to define S-N (stress range vs fatigue life) relationship. Cyclic frequency and the minimum-to-maximum stress ratio were fixed at 10 Hz and 0.1 respectively. No preventive measure was taken to reduce moisture desorption of wet specimens during the fatigue experiment.

Failure Analysis Along with mechanical testing, the morphology and the extent of damage propagation of graphite fiber/cyanate ester resin composites were examined by

optical microscopy. Scanning electron microscopy (SEM) was used to observe the mode of failure before and after the exposure to moist heat, dry heat, or thermal cycling. Small pieces of composite laminates were mounted on specimen studs. The samples were coated in a sputter coater with a thin layer of gold palladium. The fracture patterns of the coated samples were examined using the secondary electron mode.

RESULTS AND DISCUSSIONS

Moisture Absorption As discussed previously, the weight change and the retention of matrix/interface dependent mechanical properties of composites are our immediate and foremost concern in assessing the long-term structural integrity of graphite fiber-reinforced cyanate ester resin matrix composites. Our test results clearly showed that IM7 graphite fiber-reinforced 954-2 cyanate ester resin composites absorb a remarkably small amount of moisture on the exposure to 95% RH condition at 60°C up to 36 days (Figure 1). The moisture content remained almost constant at a level of around 0.3% by weight after the initial pick-up within 1 day. Postcured specimens appeared to follow the same trend with a slightly higher moisture content. These values are comparable to the assumed equilibrium level of moisture content reported by the materials supplier [10-12]. However, a possible error in our estimation of moisture content cannot be ruled out, mainly because of extremely low degree of weight change involved and uncertain effectiveness of removing the moisture absorbed during cutting of the specimen.

One interesting finding was that the degree of moisture absorption undergoes a rather sudden increase to the level of 1% after the exposure for around 50 days. After this increase, the moisture content remained constant around 1% up to 100 days' exposure forming a second level of equilibrium. Even at this level, the moisture content of cyanate ester resin composite is still lower than that of epoxy resin composites which typically exhibit an equilibrium moisture content of 1.5 to 1.8% [4]. The observed pattern of moisture gain, a sudden increase of moisture content after 50 days and the existence of dual equilibrium levels, clearly indicates that moisture absorption behavior of IM7 graphite fiber-reinforced 954-2 cyanate ester resin composites cannot be described by a concentration-dependent form of Fick's law. Moisture diffusion behavior of fiber-reinforced composites can deviate from Fick's law for the following reasons [4]: (a) the development of cracks or delamination altering the structure of material, (b) moisture

propagation along the fiber-matrix interface, (c) voids in the matrix, and (d) non-Fickian behavior of matrix itself without defects.

Our microscopy study showed that the composite specimens in dry state are virtually void-free and well-compacted. However, on the exposure to moist heat (95% RH, 60°C) for 50 days, the composite underwent extensive cracking of matrix/interface region (Figure 2). The damage took the form of not only the delamination between the plies but also translaminar cracking within the ply. Some matrix cracks remained in the subsurface region but lying parallel to the plane of surface. Less cracks were observed in the matrix-rich pockets of composites. The observed damage of matrix/interface region is believed to be a primary source of a sudden moisture gain after 50 days' exposure. Other potential sources for anomalous diffusion behavior of cyanate ester resin matrix composites will be checked in our future work. The question of moisture propagation along the fiber-matrix interface will be examined by comparing the moisture absorption behavior of the composite specimens with their edges exposed and that of the specimens with the sealed edges.

Although it is almost certain that the damage of matrix/interface region is responsible for a sudden moisture gain after 50 days' exposure, the cause of damage formation in the composites still remains to be answered. As discussed, matrix swelling effect should not be a factor in the cyanate ester resin matrix composites which initially absorb a very small amount of water. At the temperature of 60°C, the possibility of having the cracks due to the volume expansion of absorbed moisture is rather slim. Therefore, the only explanation of the phenomenon is that, on a prolonged exposure to humidity, this small amount of absorbed water gradually weakens the matrix *interface* of cyanate ester resin composites as in the case of epoxy resin composites. In the case of graphite fiber/epoxy resin composites, Browning et al [20] showed that matrix/interface dependent 90° strength of unidirectional lamina decreases by almost 40% at the moisture content of around 1%. As will be discussed later, in-plane shear strength of our graphite fiber/cyanate ester resin composites decreased by 20% at the same level of moisture content. Although weakening of fiber-matrix bonding has been confirmed by subsequent failure analysis, a rather unusual occurrence of moisture-induced cracks in the absence of external loading is still difficult to explain. Moisture-induced cracks might be related to the fact that cyanate ester resins exhibit a large amount of free volume after gelation which led to very low level of cure shrinkage and residual stresses [10]. More study including chemical analyses of cured vs postcured composite systems is planned to probe the cause of matrix cracking.

Moisture Effects on the Mechanical Properties A sudden moisture gain after 50 days' humidity exposure associated with extensive matrix/interface cracking was found to have direct influences on the static strength and fatigue lifetime profile of IM7 graphite fiber-reinforced 954-2 cyanate ester resin composites. Static in-plane shear strength of composites decreased from 70 MPa in dry state to 58 MPa after the humidity exposure. As shown in Figure 3, S-N (stress range vs the number of cycles to failure) curve of wet specimens clearly shifted to the left of that of dry specimens, although the data tended to be more scattered for the wet specimens. At a given stress amplitude, the composite specimens which contained extensive cracks as a result of humidity exposure exhibited almost exponentially shorter fatigue lifetime. When the same data are plotted in log-log scale (Figure 4), the S-N relationship took the following form of $S = a N^{-b}$ where a and b are constants. The slope of S-N curve, represented by $(-b)$, were found to be lower for wet specimens with extensive matrix cracking (-0.045) than dry specimens (-0.059) .

Past research work [21,22] showed that, when the fatigue lifetime is dominated by the damage propagation phase, $(-b)$ is equal to $(-1/m)$ where m is a power-law factor of Paris' law. Fatigue crack growth data for most polymers and composites were reported to follow Paris' law which takes the following form: $da/dN = A(\Delta K)^m$ where a is crack length, N is cycles, ΔK is the range of stress intensity factor on each cycle, A and m are constants. If the above-discussed relationship is valid for our composite system at least in a qualitative sense, the rate of crack growth at a given range of stress intensity factor should be higher for the wet specimens (already with extensive matrix/interface cracks initiated) than dry specimens. This hypothetical conclusion seems to be consistent with the previous assumption of fiber-matrix interface weakened by absorbed moisture. Separate experiments involving the measurement of delamination growth under cyclic loading are planned to verify the relationship between the slope of S-N curve and m factor of Paris law.

Moisture Effects on Failure Modes Weakening of fiber-matrix interface due to moisture absorption was confirmed by extensive failure analysis of the composite specimens based on scanning electron microscopy (SEM). One difficulty in the failure analysis was the lack of any quantitative means of measuring the extent to which matrix remnants adhere to the fibers in the crack path region. However, the fracture surface of dry composite specimens displayed a clear tendency of having the remnant of matrix resin clinging to the fibers even in a highly-fibrillated region with many bare fibers, as shown in Figure 5-a. Compared with dry specimens, wet specimens showed a much more reduced

tendency of having the deposit of matrix resin on the fibers. The frequency of observing the resin deposit over the given area was found to be distinctly lower for wet specimens. When observed, the remnants of matrix resin often showed an appearance of being easily peeled (Figure 5-b).

Thermal Cycling vs Static Exposure

In addition to the study of moisture effects, our research program examined how thermal cycling influences the static strength of cyanate ester resin matrix composites. The study is intended to be a preliminary phase of the future investigation which will assess cumulative effects of temperature cycling or spike in conjunction with moisture exposure on the mechanical performance of composites. As discussed, one of the first questions to resolve was whether the effect of thermal cycling can be represented by cumulative sum of thermal degradation effect at peak temperature. Within this context, the in-plane shear strength of unpostcured laminates of graphite fiber/cyanate ester resin composites was measured after static exposure at 150°C as well as temperature cycling to 150°C for various durations up to 5 days. The in-plane shear strength of postcured laminates was measured after static exposure as well as cycling to the heat of 204°C. Both test results were plotted as a function of exposure time at 150 or 204°C. As shown in Figures 6 and 7, the in-plane shear strength of IM7 graphite fiber/954-2 cyanate ester resin composites decreased steadily on the exposure to dry heat. The rate of strength degradation on static exposure to heat (about 4% per day) was found to be close to that of thermal cycling expressed as a function of time at peak temperature. In the case of postcured specimens, a slight deviation occurred within the range of data scattering.

From the above test results, it is reasonable to conclude that, at a frequency of 10 min/cycle and for a relatively short duration, the effect of thermal cycling can be represented by the cumulative sum of thermal degradation effect at peak temperature. This conclusion was further supported by the results of ensuing morphology study. The study based on fluorescent dye-enhanced optical microscopy revealed that any of the specimens subjected to static heat or thermal cycling do not contain microcracks (Figure 8). Obviously the degradation of materials occurred at a molecular level. The same mechanisms of strength degradation can be assumed under static heat as well as thermal cycling. However, the situation may be altered under thermal cycling condition at higher frequency range and/or longer durations. Our future program will examine this possibility and, if necessary, define a critical frequency above which thermal cycling effects deviates from the cumulative sum of thermal degradation effect at peak temperature.

CONCLUDING REMARKS

Our study plans to assess the long-term structural integrity of graphite fiber-reinforced cyanate ester resin matrix composites. As a first step toward this goal, the weight change and the retention of in-plane shear strength of the composite systems have been measured on the exposure to *high humidity* and *thermal cycling* respectively. Initial test results clearly showed that cyanate ester resin matrix composites absorb a remarkably small amount of moisture on the exposure to 95% RH condition at 60°C up to 36 days. Postcured specimens appeared to follow the same trend with a slightly higher moisture content. One interesting finding was that the degree of moisture absorption undergoes a rather sudden increase to an equilibrium level of 1% after the exposure for around 50 days. The observed pattern of moisture gain clearly indicates that moisture absorption behavior of graphite fiber/cyanate ester resin composites cannot be described by a concentration-dependent form of Fick's law.

The morphology study showed that, on the exposure to moist heat for 50 days, the composite undergoes extensive cracking of matrix/interface region in the form of the delamination between the plies as well as translaminar cracking within the ply. The observed damage of matrix/interface region is believed to be responsible for a sudden moisture gain. Since matrix swelling effect is negligible in the cyanate ester resin matrix composites which initially absorb a very small amount of water, the phenomenon is presumed to be caused by weakening of the fiber-matrix *interface* as in the case of epoxy resin composites. Weakening of fiber-matrix bonding was confirmed by the failure analysis. Rather unusual occurrence of moisture-induced cracks in the absence of external loading might be related to the fact that cyanate ester resins exhibit a large amount of free volume after gelation which led to very low level of cure shrinkage and residual stresses.

A sudden moisture gain associated with extensive matrix/interface cracking was found to reduce in-plane shear strength of composites by 20%. At a given stress amplitude, the composite specimens exposed to the humidity for 50 days suffered an exponential decrease of fatigue lifetime. From the assumed relationship between the slope of S-N curve and the *m* factor of Paris law, it was hypothesized that the rate of crack growth is higher for wet specimens (already with extensive matrix/interface cracks initiated) than dry specimens. This hypothetical conclusion seems to be consistent with the results of the failure analysis which indicates weakening of fiber-matrix interface due to the absorbed moisture. The fracture surface of wet specimens showed a reduced tendency of having the deposit of

matrix resin on the fibers. When observed, the remnants of matrix resin often showed an appearance of being easily peeled in wet specimens.

In addition to the effects of moisture absorption, the study examined the question of whether the effect of thermal cycling can be represented by the cumulative result of thermal degradation effect. The retention of in-plane shear strength of graphite fiber/cyanate ester resin composites was monitored on the exposure to dry heat at 150 or 204°C. The rate of strength degradation on the static exposure to heat was found to be close to that of thermal cycling expressed as a function of time at peak temperature. At a frequency of 10 min/cycle and for a relatively short duration, the effect of thermal cycling seems to be represented by the cumulative sum of thermal degradation effect at peak temperature. None of the specimens subjected to static heat or thermal cycling exhibited microcracking, suggesting that the degradation of materials occurred at molecular level.

Acknowledgements

I wish to thank the Materials Directorate of Air Force Wright Laboratory and the Air Force Office of Scientific Research for sponsorship of this research. The Research and Laboratories, Inc. helped us in all administrative aspects of this program.

I sincerely appreciate continuing support and encouragement for this research work from Capt. Michael Holl, Mr. Kenneth Johnson, and Mr. Roger Griswold at the Non-Metallic Materials Division of the Materials Directorate. Mr. Tom Witman, a summer student from the Wright State Univ., provided a valuable help throughout the research program.

I am also very grateful to Dr. Ran Y. Kim at the Univ. of Dayton Research Institute, and Messrs. Brett Bolan and Terry Christiansen at the Materials Directorate for their advices for the research program.

Finally my sincere thanks should go to Messrs. Ron Cornwell, Ron Esterline and Ken Lindsay at the Univ. of Dayton Research Institute who played an essential role in this program by preparing the specimens and performing various physical testing.

References

- [1] Herz, J., "Moisture Effects on the High Temperature Strength of Fiber-Reinforced Resin Composites", Proc. of 4th SAMPE Nat'l Tech. Conf., 1 (1972).
- [2] Browning, C. E., "The Effects of Moisture on the Properties of High Performance Structural Resins and Composites", Proc. of 28th SPI Reinforced Plastics/Composite Inst. Annual Tech. Conf., Sect 15-A (1973).
- [3] Plueddemann, E. P., ed., Interfaces in Polymer Matrix Composites (Composite Materials, Vol.6), Academic Press, New York, NY (1974).
- [4] Springer, G. S., ed., Environmental Effects on Composite Materials, Vol. 1-3, Technomic Publishing Co., Westport, CT (1981, 1984, 1988).
- [5] Adams, D. F., Environmental Effects on Composite Materials (Seminar Notes), Technomic Publishing Co., Lancaster, PA (1993).
- [6] Ashbee, K. H. G., Fundamental Principles of Fiber-Reinforced Composites, Chapter 10, Technomic Publishing Co., Lancaster, PA (1989).
- [7] Wolff, E. G., "Moisture Effects on Polymer Matrix Composites", SAMPE J, Vol. 29, No. 3, 11 (1993).
- [8] Herakovich, C. T., J. G. Gavis, and J. S. Mills, "Thermal Microcracking of Celion 6000/PMR15 Graphite/Polyimide", in Thermal Stresses in Severe Environments edited by D. P. H. Hasselman and R. A. Heller, Plenum Press, New York, NY (1980).
- [9] S. S. Tompkins and S. L. Williams, "Effects of Thermal Cycling on Mechanical Properties of Graphite/Polyimide Composites", *J. Spacecraft*, Vol. 21, No. 3, 274 (1984).
- [10] McConnell, V. P., "Tough Promises from Cyanate Ester", *Advanced Composites*, Vol. 7, No. 3, 28 (1992).
- [11] Shimp, D. A., J. R. Christenson, and S. L. Ising, "Cyanate Esters - An Emerging Family of Versatile Composite Resins", Proc. of 34th Int'l SAMPE Symposium, 222 (1989).
- [12] Almen, G., P. Mackenzie, V. Malhotra, and R. Maskell, "Toughened Cyanates for Aerospace Applications", Proc. of 35th Int'l SAMPE Symposium (1990).
- [13] Lee, F. W., M. A. Boyle, and P. Lefebvre, "High Service Temperature, Damage Tolerant Prepreg Systems Based on Cyanate Chemistry", Proc. of 35th Int'l SAMPE Symposium (1990).
- [14] Yang, P. C., D. M. Pickelman, and E. P. Woo, "A New Cyanate Matrix Resin with Improved Toughness: Toughening Mechanism and Composite Properties", Proc. of 35th Int'l SAMPE Symposium, 1131 (1990).
- [15] Yang, P. C., E. P. Woo, S. A. Laman, J. J. Jakubowski, D. M. Pickelman, and H. J. Sue, "Rubber-Toughened Cyanate Composites: Properties and Toughening Mechanism", Proc. of 36th Int'l SAMPE Symposium, 437 (1991).

- [16] Speak, S. C., H. Sitt, and R. H. Fuse, "Novel Cyanate Ester Based Products for High Performance Radome Applications", Proc. of 36th Int'l SAMPE Symposium, 336 (1991).
- [17] Cinquin, J., and P. Abjean, "Correlation between Wet Ageing, Humidity Absorption and Properties of Composite Materials Based on Different Resins Family", Proc. of 38th Int'l SAMPE Symposium, 1539 (1993).
- [18] Hahn, H. T., "Residual Stresses in Polymer Matrix Composite Laminates", J. of Composite Materials, Vol. 10, 266 (1976).
- [19] Lee, B. L., R. W. Lewis, and R. E. Sacher, "Effects of Static Immersion in Water on the Tensile Strength of Crossply Laminates", Proc. of the 2nd Int'l Conf. on Composite Materials, 1560 (1978).
- [20] Browning, C. E., G. E. Husman, and J. M. Whitney, "Moisture Effects in Epoxy Matrix Composites", in Composite Materials: Testing and Design (4th Conf.), ASTM STP #617, 481, ASTM, Philadelphia, PA (1976).
- [21] Tetelman, A. S., and A. J. McEvily, Fracture of Structural Materials, p.371, John Wiley, New York (1967).
- [22] Mandell, J. F., J. P. F. Chevaillier, K. L. Smith, and D. D. Huang, "Fatigue of PVC and Polysulfone", M. I. T. Research Report R84-1, M. I. T., Cambridge, MA (1984).

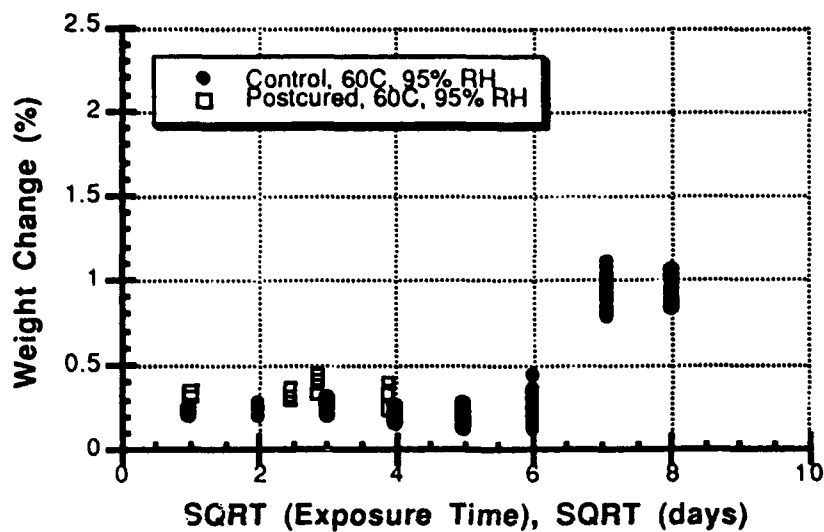


Figure 1. Moisture absorption of graphite fiber-cyanate ester resin composite on the exposure to 95% RH condition at 60°C



Figure 2. Cracking of matrix/interface region of graphite fiber-cyanate ester resin composite on the exposure to 95% RH condition at 60°C for 50 days

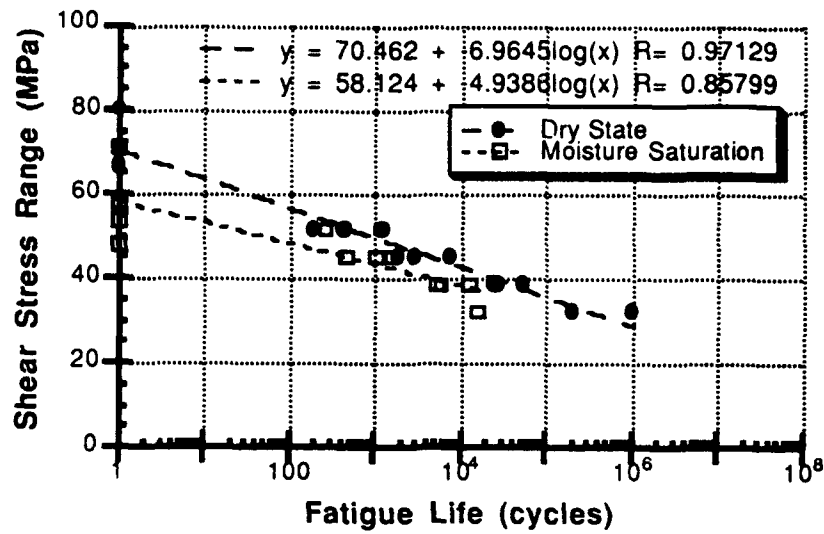


Figure 3. S-N curves of dry and wet (50 days, 95% RH, 60°C) specimens of graphite fiber-cyanate ester resin composite; Semi-log scale.

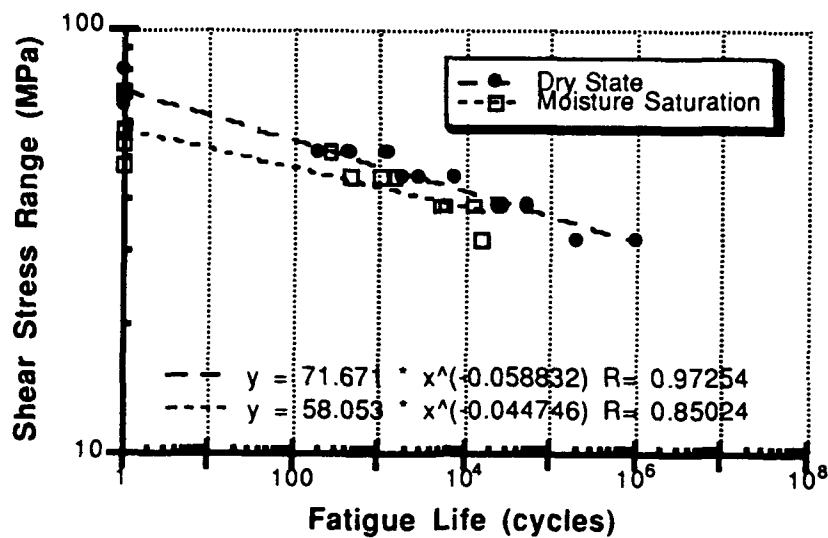


Figure 4. S-N curves of dry and wet (50 days, 95% RH, 60°C) specimens of graphite fiber-cyanate ester resin composite; Log-log scale.

(a)



(b)

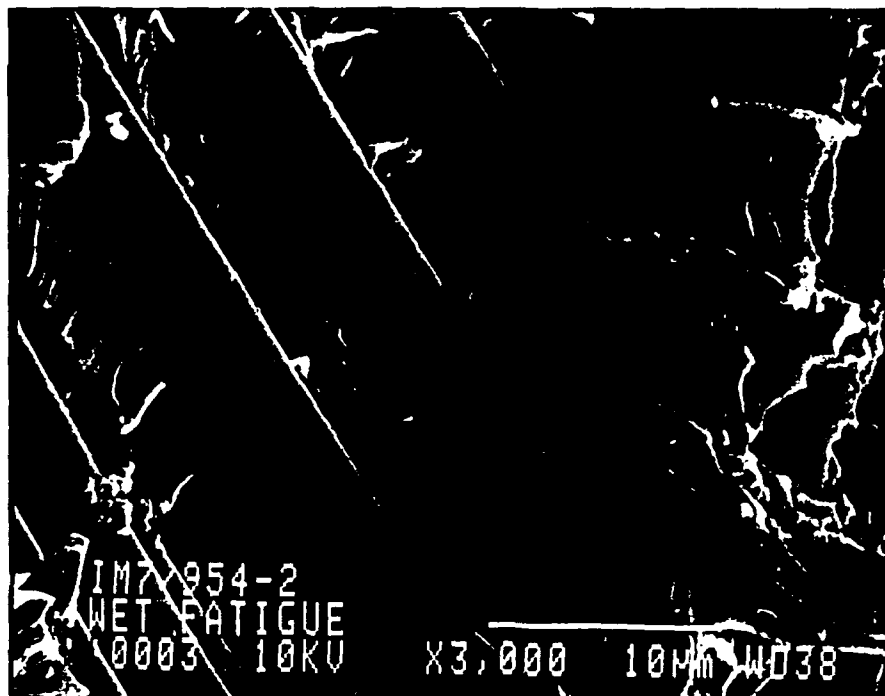


Figure 5. The fracture surfaces of graphite fiber-cyanate ester resin composite specimens: (a) the remnant of matrix resin clinging to the fibers even in a highly-fibrillated region (dry specimen); (b) the remnants of matrix resin with an appearance of being easily peeled (wet specimen).

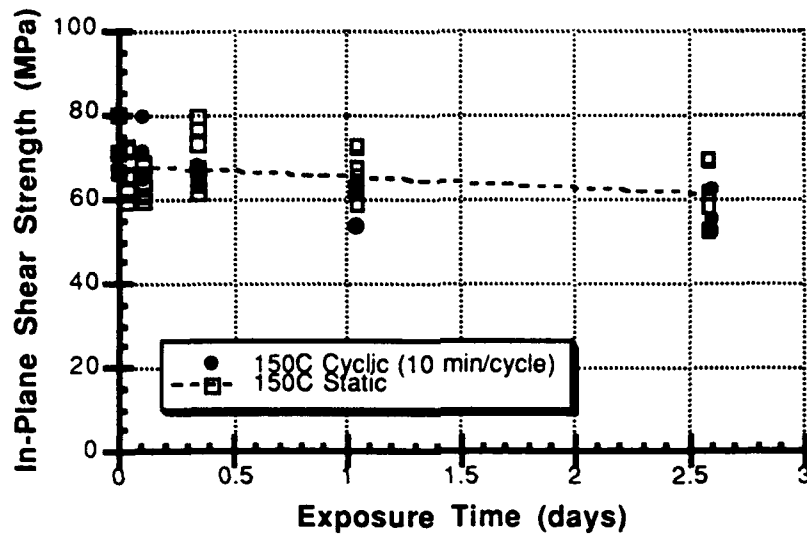


Figure 6. The changes of in-plane shear strength of graphite fiber-cyanate ester resin composites after static exposure vs cycling to 150°C (Not postcured)

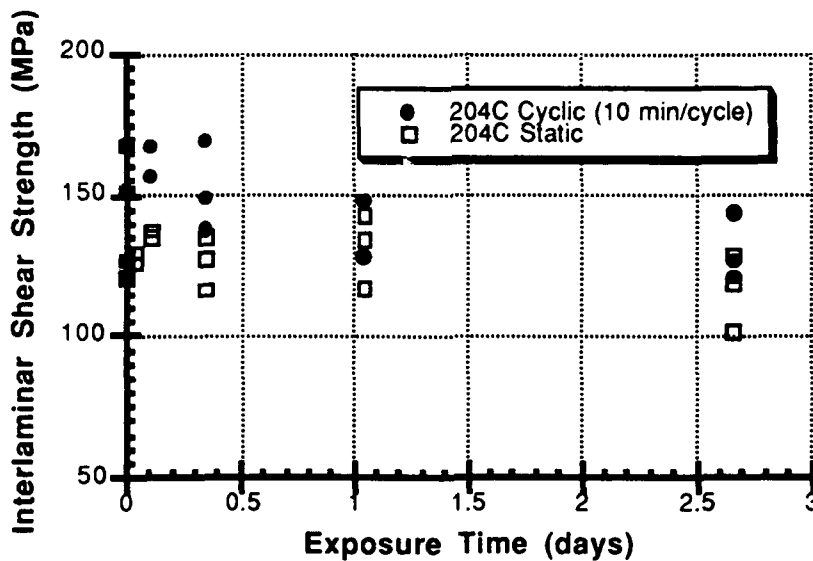


Figure 7. The changes of in-plane shear strength of graphite fiber-cyanate ester resin composites after static exposure vs cycling to 204°C (Postcured)

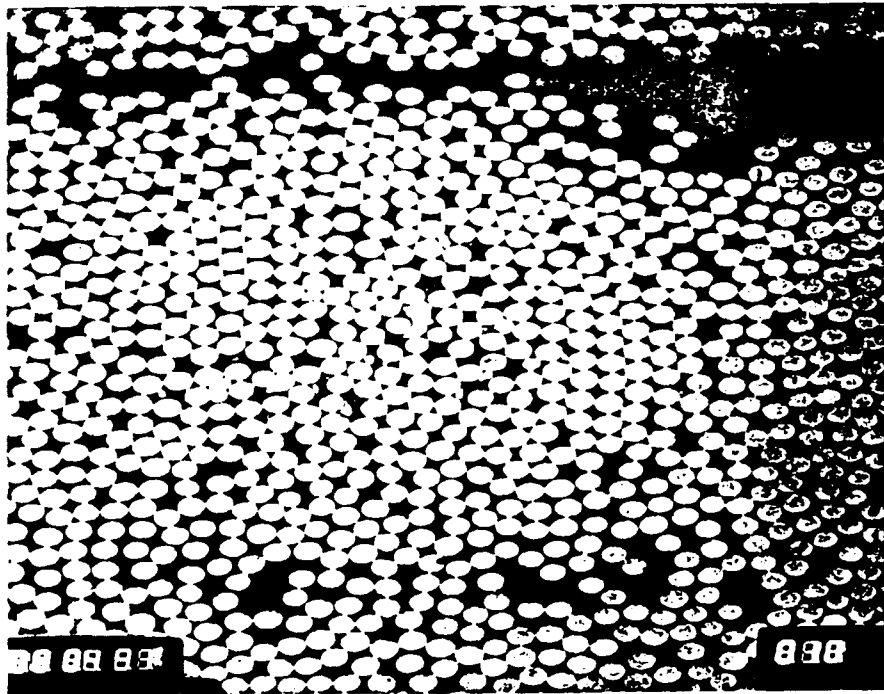


Figure 8. Fluorescent dye-enhanced optical micrograph for the graphite fiber-cyanate ester resin composite specimen subjected to thermal cycling to 150°C

A STUDY OF THE GROWTH OF $\text{YBa}_2\text{Cu}_3\text{O}_{7-\delta}$ THIN FILMS ON LaAlO_3
BY PULSED-LASER DEPOSITION

M. Grant Norton
Assistant Professor
Department of Mechanical and Materials Engineering

Washington State University
Pullman WA 99164-2920

Final Report for:
Summer Faculty Research Program
Wright Laboratory

Sponsored by:
Air Force Office of Scientific Research
Bolling Air Force Base, Washington D.C.

September 1993

A STUDY OF THE GROWTH OF $\text{YBa}_2\text{Cu}_3\text{O}_{7-\delta}$ THIN FILMS ON LaAlO_3
BY PULSED-LASER DEPOSITION

M. Grant Norton
Assistant Professor
Department of Mechanical and Materials Engineering
Washington State University

Abstract

The growth of $\text{YBa}_2\text{Cu}_3\text{O}_{7-\delta}$ thin films on LaAlO_3 substrates has been studied. The films were formed using the pulsed-laser deposition technique. This technique employs a high energy laser to ablate material from a target, the ablated material is deposited onto a substrate where film nucleation and growth can occur. The microstructure and superconducting properties of the films were determined as a function of film thickness. It was found that the films were close to the stoichiometric (123) composition, however there was evidence, both in terms of the the film's microstructure and properties, to suggest the formation of secondary phases. X-ray diffraction studies on similar films indicated that they consisted predominantly of grains oriented with their c axis perpendicular to the film-substrate interface. Examination of the surface topography of the films using atomic force microscopy also suggested the presence of grains oriented with the c axis in the film-substrate interface plane. Particles were detected on the surface of all the films and the frequency of these particles depended upon the position of the substrate during film growth. Films grown on substrates located on the left hand side of the sample holder had fewer surface particles than films grown on substrates mounted in the center and right hand side of the sample holder.

A STUDY OF THE GROWTH OF $\text{YBa}_2\text{Cu}_3\text{O}_{7-\delta}$ THIN FILMS ON LaAlO_3 BY PULSED-LASER DEPOSITION

M. Grant Norton

Introduction

Since the discovery in 1986 of high-temperature superconductivity in oxide ceramics [1] there has been extensive research in this field. This research has been directed into a number of areas—the formulation of new materials with increasing transition temperatures, fabrication of existing materials into various forms, and investigation of possible device applications. Because of the low critical-current densities in bulk superconductors and the difficulties in making high- T_c superconducting wires and single crystals, the use of thin films may represent the first major commercial application of this technology.

Many thin film deposition techniques employ high substrate temperatures to obtain oriented crystalline films. High-temperature deposition often imposes a major impediment to the use of these materials in thin film form because; (a) deleterious interactions may occur between the film and the substrate, degrading or modifying the properties of the film [2] and (b) low-temperature deposition may be required for compatibility with existing technologies. Furthermore, high-temperature deposition of a number of superconducting materials is problematic because they involve constituents with widely varying vapor pressures or high melting points. The control of composition and crystal structure in such materials is difficult at practical source and substrate temperatures.

The major obstacle to low-temperature growth is the difficulty of obtaining the high surface mobility required for the nucleation and growth of crystalline or epitaxial films at low substrate temperatures. This limitation may be overcome by delivering the material to the substrate in unique chemical forms (e.g., clusters or reactive species), in charged or highly excited states, and/or with appreciable kinetic energy. This objective may be accomplished in many ways, but among them, pulsed-laser deposition (PLD) offers significant advantages.

PLD utilizes the material ablated from a target as the source of deposited material. The rate of material removal from the target can be varied considerably, from isolated atomic and ionic species, to nanometer-sized clusters, to macroscopic ($> 1\mu\text{m}$) fragments (ejecta). In any given deposition or etching process, control of the emission rate and distribution is of considerable importance. In the case of thin film synthesis, atomic/molecular neutral and ionic species are most desirable. These vapor-phase products are transported and deposited onto a substrate

where, given sufficient kinetic energy, they find low-energy configurations. The enhanced kinetics provided by energetic particles can be exploited to cause nucleation of the growth of epitaxial films at low substrate temperatures.

PLD has proven to be a very versatile technique for growing both oxide and non-oxide films largely due to the availability of high-power excimer lasers [3]. The laser-target interaction produces a high-temperature plasma consisting of high-velocity and electronically excited neutral atoms, molecules, \pm ions, and electrons. The kinetic, electronic, and chemical energies of each of these constituents play important roles in film growth. The advantages of PLD include:

- epitaxial or crystalline growth at low substrate temperatures,
- congruent deposition of materials with complex stoichiometries,
- facile deposition of materials with high melting points, provided they strongly absorb the laser power,
- ability to form metastable microstructures, due to the low substrate temperature and the nonequilibrium nature of the ablation process.

Thin films of $\text{YBa}_2\text{Cu}_3\text{O}_{7-\delta}$ (YBCO), which has been the most widely studied of the superconducting oxides, have been deposited onto a number of different substrate materials, including single crystals of MgO [e.g., Ref. 4], SrTiO_3 [e.g., Ref. 5], and LaAlO_3 [e.g., Ref. 6], and polycrystalline substrates of MgO [e.g., Ref. 7] and yttria-stabilized zirconia [e.g., Ref. 8]. The choice of substrate is mainly determined by two criteria: (a) the deposited films should have the desired physical properties, which often means that a close lattice match between film and substrate is required, and (b) the substrate should be suitable for device or technological applications, for example, it should have a low or moderately low dielectric constant. The lattice parameters of some commonly used substrate materials and their mismatch with YBCO are shown in Table I.

Table I. Lattice parameters and mismatch between YBCO and various substrate materials [9].

Material	Lattice Parameter (nm)	Lattice Mismatch (%)
$\text{YBa}_2\text{Cu}_3\text{O}_7$	0.382	-
MgO	0.421	9.7
SrTiO_3	0.391	2.3
LaAlO_3	0.378	-1.1

From Table I it can be seen that LaAlO_3 is closely lattice matched with the basal plane of the YBCO and thus provides a suitable substrate for the growth of oriented films. In this study, (001)-oriented single crystals of LaAlO_3 , prepared by the Czochralski process [10], were used.

A number of different laser systems, operating over a range of different processing parameters, have been successfully used to produce thin films of YBCO. Changes in the processing parameters do, however, affect the microstructure and/or the morphology of the films and, in turn, their properties [e.g., Refs. 11-15]. Some of the parameters which have been considered in the PLD process are listed in Table II. These parameters have been classified as primary, secondary, and tertiary to denote their role in the deposition process. The primary parameters directly control the ablation process (e.g., to yield thermal or nonthermal equilibrium) and the nature of the ablated species. Secondary parameters influence the growth and microstructure of the film, for example, whether the resulting film is amorphous or crystalline and the orientation of epitaxial films. Tertiary parameters are other variables in the deposition process which have not been well characterized as to their effect.

Table II. Effects of processing parameters on microstructure [15].

Category	Parameters	Effect on Process	Possible Effects on Microstructure
Primary	Laser wavelength Laser power density Laser pulse repetition rate	Thermal or non-thermal evaporation Ratio of neutral to ionic species in the plasma Kinetic energy of the ejected species	Retention of target stoichiometry Formation of metastable microstructures Particulates
Secondary	Substrate temperature Partial pressure/ambient	Surface mobility of the ablated species	Establishment of epitaxy Formation of metastable microstructures Control of crystal structure
Tertiary	Substrate-target distance Irradiated spot size	Film thickness Thickness distribution across substrate	Not known

In this present study, the growth and superconducting properties of YBCO films deposited on LaAlO_3 substrates was examined as a function of film thickness. The film thickness was varied by changes in the deposition time: the following deposition times were used; 5, 15, 45, 125, and 250 seconds. All the film depositions reported here were performed using the experimental conditions described in the following section. A systematic study on the effects of variation of several of the processing parameters (e.g., pulse repetition rate and substrate temperature) on the properties and microstructure of YBCO films was also conducted. The results of this latter study will be reported elsewhere.

Experimental

The YBCO films were formed by focusing a Lambda Physik LPX 305i excimer laser operating on KrF ($\lambda = 248$ nm) on to a 1" diameter stoichiometric YBCO pellet. For film deposition, a laser energy of ~ 440 mJ/pulse was used, the pulse duration was 25 ns, and the pulse repetition rate was 20 Hz. The interaction of the laser beam with the target surface produced a plume of ablated material which emanated perpendicular to the target surface. Prior to film deposition, the YBCO target was polished using SiC paper and laser irradiated (pulse energy ~ 160 mJ) in the deposition chamber for 3 minutes in an ambient of 160 mTorr of oxygen. This conditioning process was employed prior to each deposition to ensure reproducibility in the target surface. During film growth the target was rotated at 10 rpm and the laser beam simultaneously rastered across the target surface to avoid preferential ablation.

For each film growth experiment, three single crystal LaAlO_3 substrates ($5 \times 5 \times 0.5$ mm) were mounted, side-by-side, on a stainless steel plate using silver paint. After drying the silver paint ($90 - 95^\circ\text{C}$, 15 min in air), the stainless steel plate was mounted on the sample holder in the vacuum chamber. The distance between the YBCO target and the substrates was 6.42 cm and there was an angle of 45° between the plane of the target surface and the stainless steel plate. The substrates were heated by a tungsten filament lamp located just below the stainless steel plate. The temperature of the substrates was controlled by a variable resistance power supply and monitored by a thermocouple in contact with the stainless steel plate. The substrate temperature was measured by means of a two-color infra-red pyrometer which could be focused on the surface of any of the substrates. The substrate temperature (measured by the pyrometer) during deposition was $\sim 770^\circ\text{C}$. Film deposition was performed in a flowing oxygen ambient (~ 160 mTorr). Following film deposition, the chamber was filled with oxygen, the heater was turned off and the samples allowed to cool to room temperature at a pressure of ~ 490 Torr. The experimental conditions mentioned above represent the 'standard' set of deposition parameters used in this study. The only difference between films grown in different runs was the deposition time. The following deposition times were used: 5, 15, 45, 125, and 250 seconds. The reproducibility of the experimental conditions was determined by repeating several of the runs.

It should be noted that the three substrate positions on the stainless steel plate were not equivalent; there was an asymmetry in the shape of the plume of ablated material. The plume was longer and narrower on the left hand side and shorter and wider on the right hand side. This asymmetry appeared to be due to energy differences in the profile of the incident laser beam. In the results discussed below, left, center and right correspond to the position of the substrates as viewed in the direction of the incoming laser beam.

The superconducting properties of the films were determined using ac magnetic susceptibility measurements. The background to, and the experimental details of, this nondestructive technique have been described elsewhere [e.g., Refs. 16-18]. The real part of the ac susceptibility (χ') gives a rapid determination of the

superconducting transition temperature (T_c) of the film, whereas the imaginary part, related to the ac loss (χ''), supplies information on the volume behavior of the film which is dominated by coupling effects and so represents a measure of the critical current density (J_c). The coupling effects will be influenced by the presence of homophase and heterophase boundaries in the film.

The surface topography of the films was determined using atomic force microscopy (AFM) (Digital Instruments Nanoscope II) and scanning electron microscopy (SEM) (Hitachi S-900). The AFM was operated in the contact mode, wherein a sharp tip attached to a bendable cantilever directly contacts the surface of the sample being examined. The tip is then scanned laterally over the surface. The bending of the cantilever in response to surface height variations is monitored by a detection system. AFM's can have resolution down to the atomic level however in this study, because of the roughness of the films and the tip profile used, atomic resolution was not possible. The Hitachi S-900 SEM had a field emission gun source and was operated at an accelerating voltage of 2kV. The samples examined in the SEM were heated in a vacuum oven at 95°C for 12 hours prior to loading into the microscope to avoid contamination of the specimen surface under the electron beam. Coating of the samples for SEM examination was not necessary.

The thickness of the films and their average composition was measured with Rutherford backscattering spectrometry (RBS) using 2 MeV He^+ ions. An incident angle of 35° was used with a scattering angle of 170°. The RBS data were analyzed using the RUMP simulation program [19,20].

Results

RBS data obtained for the series of YBCO films is shown in Table III. The calculated thickness of the films ranged from 17 to 455 nm. RBS measures the areal density of the film, i.e., the number of atoms per unit area, and this value is converted to thickness by considering the density of the film. The uncertainty of RBS thickness measurements depends on the accuracy of the ion stopping power tables in the simulation program (estimated to be $\pm 20\%$) and on the estimated density of the film. For the purposes of the RBS simulation program, the films were assumed to be 95% of theoretical density, or 6.06 g/cm³. For films grown on substrates mounted in the center and right hand side positions of the sample holder this estimate is probably close to the actual density of the film. However, for films grown on substrates located on the left hand side of the holder the film density is less than 95%. Examination of sample 406, in a cross-section geometry, using SEM gave a measured film thickness of 90 nm. This value is approximately 15% larger than that determined by RBS on the same film; which would be consistent with the observation that films deposited on substrates situated on the left hand side of the sample holder were less dense than films deposited on substrates in the other two positions. Thus the density of films grown on substrates

placed on the left hand side of the sample holder, based on the differences in the two thickness measurements, is ~80% of the theoretical density.

The desired film stoichiometry is $\text{YBa}_2\text{Cu}_3\text{O}_7$, which in atomic percent is Y:Ba:Cu:O = 7.7:15.3:23.1:53.9. It can be seen from Table III that, in most cases, the films had compositions close to this stoichiometry. The sensitivity of RBS to an element is proportional to the square of its atomic number. Thus, the uncertainty in the cation composition measurements is small. However, for oxygen the uncertainty is much greater, therefore precluding an absolute measurement of atomic percent. The overall uncertainty in the compositions of the thicker films is estimated to be $\pm 10\%$. In the thinnest films further uncertainty in the values of the cation ratio exists because the atomic masses of Ba (from the film) and La (from the substrate) are similar, making them difficult to distinguish.

Table III. RBS data obtained from YBCO thin films on LaAlO_3 .

Sample #	Deposition Time/Position	Atomic Density ($10^{15}/\text{cm}^2$)	Thickness (nm)	Y	Ba	Cu	O
413	5 sec /left	~ 125	~ 17.4	3.4	17.2	13.6	65.8
414	5 sec /center						
415	5 sec /right						
409	15 sec /left	200	27.8	7.0	15.1	20.1	57.8
410	15 sec /center	240	33.4	5.9	14.3	16.9	63.0
411	15 sec /right	125	17.4	5.9	14.3	16.9	63.0
406	45 sec /left	580	80.6	8.1	15.4	23.2	53.3
407	45 sec /center	450	62.6	8.5	14.2	24.5	52.8
408	45 sec /right	280	38.9	7.0	13.6	22.1	57.3
403	125 sec /left	1575	219	8.6	17.2	24.1	50.1
404	125 sec /center	1100	153	10.2	17.8	29.4	42.6
405	125 sec /right	900	125	8.1	15.3	24.3	52.3
416	250 sec /left	3050	424	8.9	16.1	21.0	54.0
417	250 sec /center	3270	455	8.0	14.6	24.1	53.3
418	250 sec /right	2150	299	8.6	17.2	29.0	45.2

Figure 1 shows a montage of AFM linescans recorded from the films deposited during 45 seconds (samples 406, 407 and 408). The surface of films deposited on substrates situated on the left hand side of the sample holder, e.g., Fig. 1a, was generally smooth with occasional large particles. The image in Fig. 1b is a small area of Fig. 1a, showing that the film consists of grains which appear to be < 200 nm in diameter. The surface roughness of

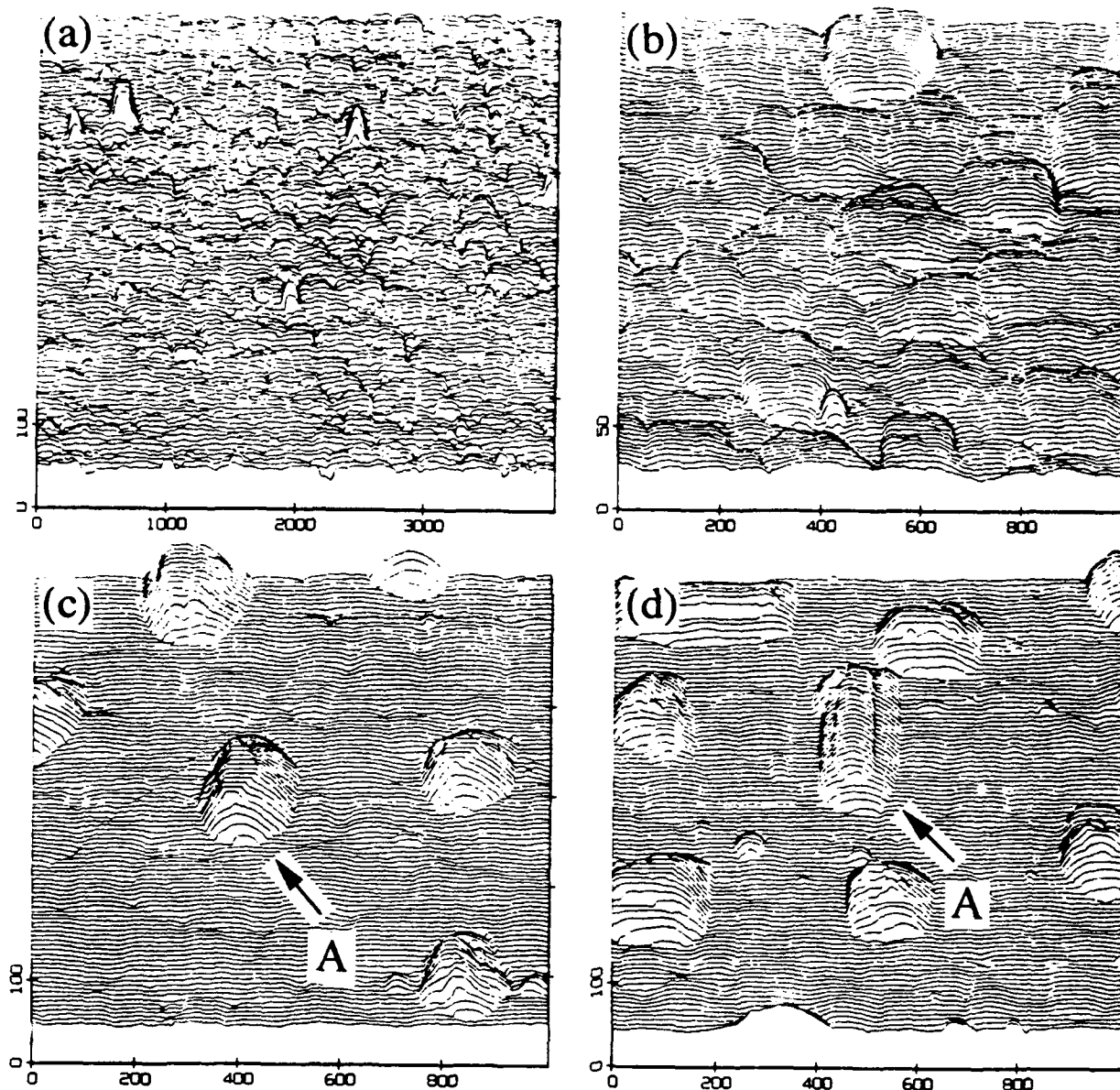


Figure 1. AFM linescans for YBCO films deposited on LaAlO_3 substrates during 45 seconds. The left hand side vertical axis is the Z axis (in nm) and gives an indication of the height of surface features. The horizontal and right hand side vertical axis measure variations in the X and Y directions (in nm), respectively. The dimensions of the X and Y axes are the same. The features indicated by arrows are explained in the text.

this area of the film was determined by AFM to be ~ 2.8 nm. Films deposited on substrates located in the center (Fig. 1c) and right hand side (Fig. 1d) positions of the holder generally exhibited more surface features. In Fig. 1c some of these features are higher than 100 nm (indicated by the flat top of grain A). The exact shape of these particles could not be determined by AFM due to the pyramidal profile of the tip. In Fig. 1d it can be seen that some of the surface features were elongated, e.g., grain A, and these grains were found to be aligned in mutually orthogonal directions. The shape of these grains is suggestive of YBCO where the c axis is lying in the plane of the film surface (a-axis oriented) [21]. The underlying granular structure in all the films was determined by X-ray diffraction to be predominantly c-axis oriented YBCO. Small peaks were observed which could be assigned to a-axis oriented material.

The observations mentioned above, for the films deposited during 45 seconds, were consistent with AFM data recorded from films grown during other deposition times. In particular, the number and shape of particles on the surface of the films appears to be a function of the position of the substrate on the sample holder during deposition. The surface of films deposited during 250 seconds on substrates located on the right hand side of the sample holder was covered with particles, many of these particles having the elongated shape shown in Fig. 1d. It is important to note that, in general, the presence of these surface features does not appear to be detrimental to the bulk superconducting properties of the films.

The AFM data were qualitatively supported by SEM images recorded from films grown during 250 seconds. Figures 2a and b, show secondary electron images (SEI) recorded from YBCO films deposited on substrates placed on the left hand side (287) and right hand side (288) positions of the sample holder, respectively. It can be seen from Fig. 2a that the film is not fully dense; large voids are clearly visible, some of which may penetrate to the film-substrate interface. This observation is consistent with the films deposited on the left hand side of the sample holder being only $\sim 80\%$ of theoretical density. Slight differences in contrast are visible within the grains, these may be due to compositional variations in the film. Film 288 shows a much denser microstructure, however small (20-30 nm diameter) voids can be seen at grain intersections. Also visible in this image are several large particles on the film surface. The size of these particles is consistent with some of the particles seen in AFM images recorded from the same film. The origin of the white speckling in Fig. 2b is not known.

All the films showed superconducting properties although significant differences were observed in these properties both as a function of film thickness and of substrate position. Figure 3 shows the temperature dependence of the complex magnetic susceptibility with varying ac field (h) for specimens 406, 407, and 408. The series of lines represents varying applied ac fields; from 1 to 7 the fields are 0.025, 0.10, 0.25, 0.50, 1.0, 1.5, and 2.2 Oe, respectively.

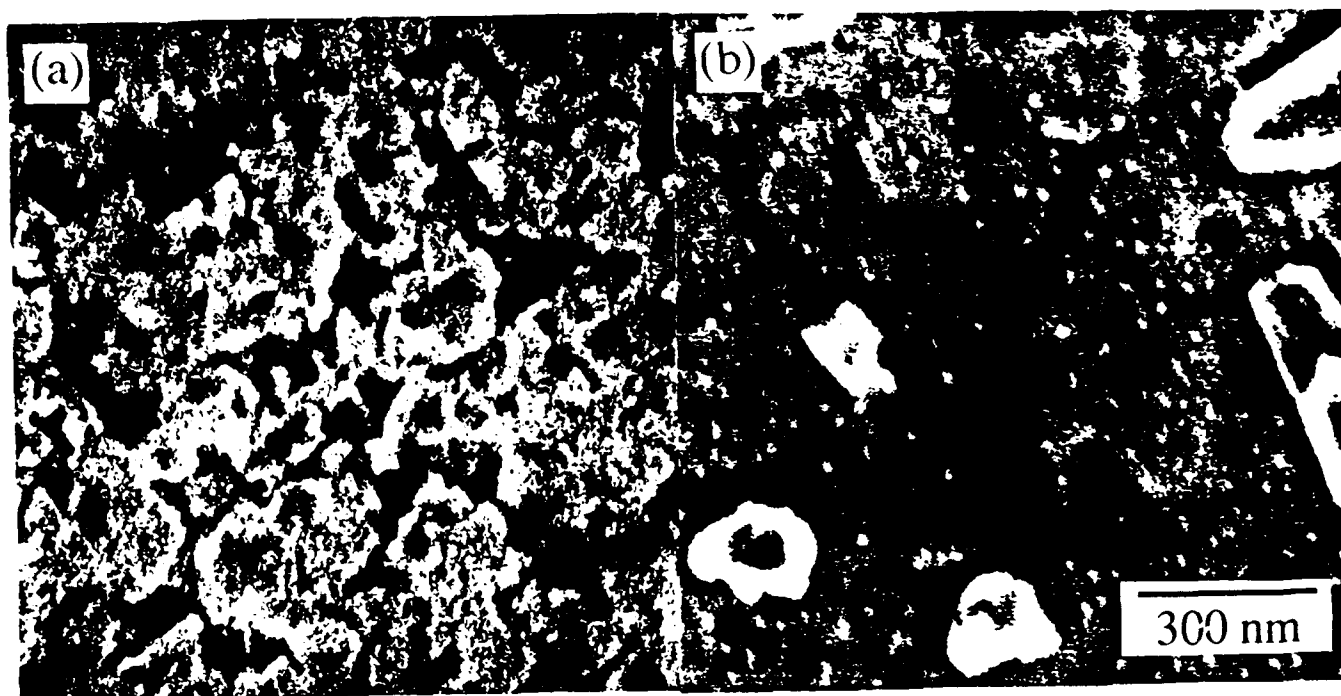


Figure 2. SEM images of laser deposited YBCO films on LaAlO_3 . The film shown in (a) was deposited on a substrate located on the left hand side of the sample holder (287), the film shown in (b) was deposited on a substrate located on the right hand side of the sample holder (288).

In film 406, two distinct superconducting transitions were detected, one at 71 K, the other at 64 K. The transition temperatures of films deposited on substrates located on the left hand side of the sample holder generally were considerably less than the maximum T_c of 92 K. Single superconducting transitions were determined for films 407 and 408, at 87 K and 84 K, respectively. The lack of a distinct secondary structure in these data implies that the films are more uniform in superconducting properties over their entire area, although the shapes of the $\chi''(T)$ curves indicate the presence of unresolved distributions in the film parameters, especially in film 408. The transition temperatures determined for all the films grown in the center and right hand side of the holder varied slightly, but in general these films were characterized by much higher T_c 's than those obtained for films grown on substrates located on the left hand side of the sample holder. The spreading of the $\chi'(T)$ curves as a function of the ac field arises out of the inability of the films to carry the current required for full shielding of the fields and is thus inversely related to J_c . In the ideal situation the spreading of the curves would be a minimum.

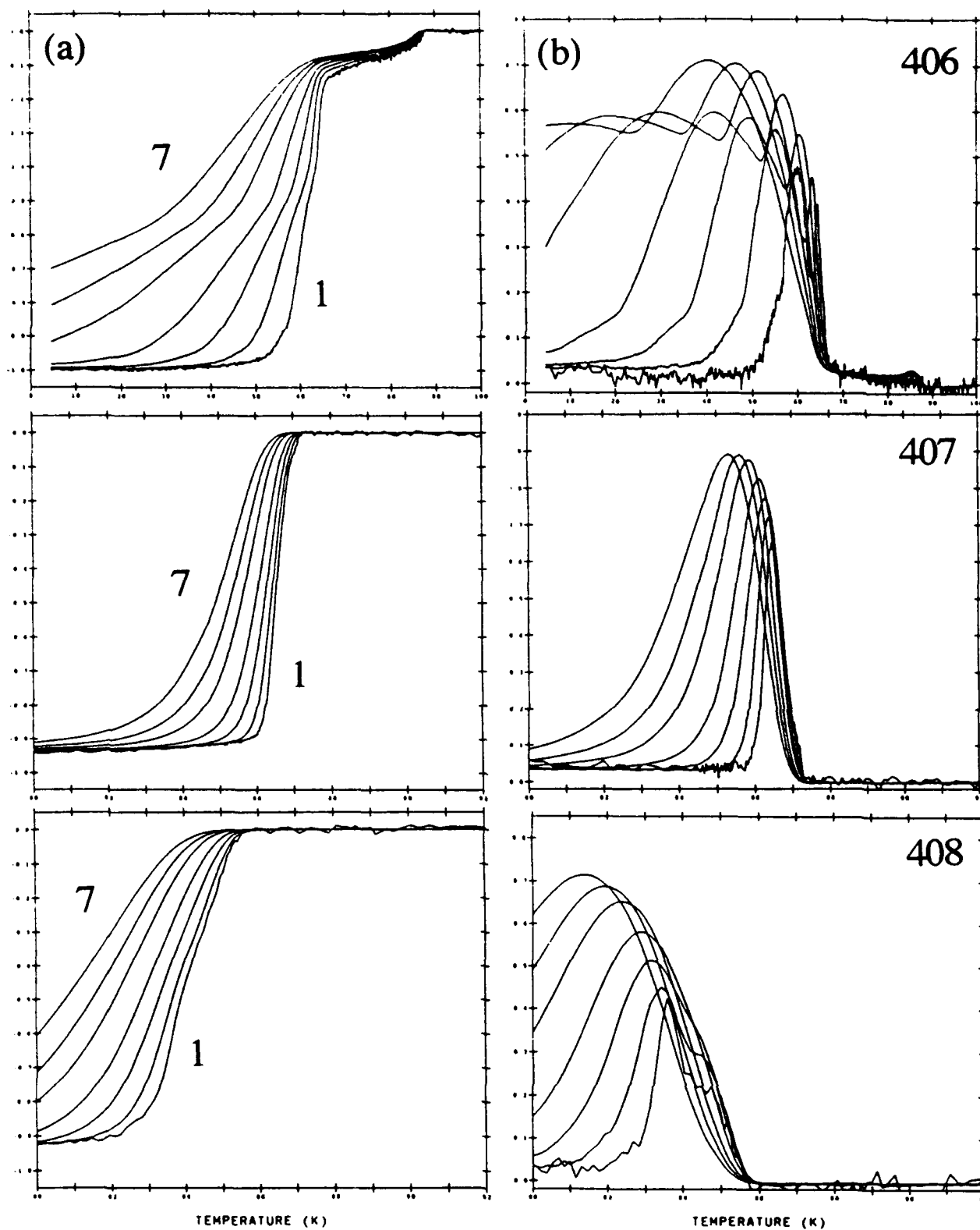


Figure 3. Temperature dependence of the complex magnetic susceptibility with varying ac field. (a) real part, χ' ; (b) imaginary part (loss), χ'' .

The variation with temperature of the ac loss parameter, χ'' , is shown in Fig. 3b for samples 406, 407, and 408. These curves portray the cyclic energy dissipation as the ac flux penetrates into the sample. The loss is proportional to the superconducting volume which is penetrated by the field, and therefore such data provide a sensitive measure of the material's overall properties and their distributions. The broadening and shift to lower temperatures of the main loss peaks, as the ac field is increased are again characteristics of the weak-link intergranular behavior which is prevalent in these ceramic superconducting materials [22]. Thus, for the data shown in Fig. 3, the critical current density of film 407 would be expected to be the highest if all the films were of the same thickness.

Discussion

Based on the RBS data, no systematic trends in the composition of the YBCO films was observed, either in terms of substrate position or film thickness. The uncertainty in the cation composition of the thinner films precludes any reasonable discussion on the apparent Y and Cu depletion in these films. One of the stated advantages of the PLD process has been that the stoichiometry of the target can be reproduced in the deposited film. This statement is true but only under certain deposition conditions. For arbitrary deposition conditions it has been shown that the stoichiometry of YBCO films may be different from the target and this difference appears to have a spatial effect [23,24]. Because the growth of YBCO thin films using PLD is typically carried out under non-equilibrium conditions most films contain a high density of defects [e.g., Ref. 25]. These defects are often stacking faults associated with the addition of extra layers in the YBCO lattice. For example, double CuO layers ($\text{YBa}_2\text{Cu}_4\text{O}_8$ structure) appear as isolated stacking defects within a matrix of a material that is predominantly found to have a single CuO layer ($\text{YBa}_2\text{Cu}_3\text{O}_7$) structure [26]. Examples of different layered defects have been observed by other groups [e.g., Refs. 27-29].

Although no evidence for compositional defects could be obtained from the RBS data, the presence of different phases in some of the YBCO films deposited in this study is suggested by the ac magnetic susceptibility data. Examination of Fig. 3a, shows clear evidence of two distinct superconducting transitions. A possible explanation for this effect may be the presence of different phases in the film, each possessing a different T_c . Small deviations in measured T_c from the maximum value of 92 K, can often be accounted for by insufficient oxygen in the crystal structure. Ex situ annealing studies at low temperature ($\sim 500^\circ\text{C}$) of similar YBCO films at Wright Laboratory has shown to result in an increase in the T_c of the film.

The contrast variations observed in the SEM images, shown in Fig. 2a, also suggest the presence of distinct phases in these films [30]. Unfortunately, the SEM used in this study was not equipped with a backscattered electron detector. Backscattered electron imaging (BEI) has a much higher sensitivity to compositional variations in a

sample. Characterization of the films using transmission electron microscopy (TEM) is in progress and it is hoped that these studies will provide further information on the microstructure of these materials.

Ex situ annealing of these films at much higher temperatures (900 - 920°C [31]), where the $\text{YBa}_2\text{Cu}_3\text{O}_7$ stoichiometry is favored, should lead to single superconducting transitions in the $\chi'(T)$ curves if the observed behavior is due to different YBCO stoichiometries. In the low temperature annealing studies it was noted that, in general, annealing resulted in the lowering of the J_c of the film, this may be due to diffusion of the excess cations toward the surface and grain boundaries of the film as was noted by Fendorf et al [25], in a study of the kinetic evolution of microstructures during 124 and 247 transformations to 123.

AFM studies revealed significant differences in the morphology of the various YBCO films. These differences were more apparent as a function of substrate position during film growth, than as a function of film thickness. Films deposited on substrates located at the left hand side of the sample holder had a granular morphology with significant intergranular porosity. The depth of these pores could not be resolved in the AFM, but from the SEM results shown in Fig. 2a they may go to the substrate surface. These films have fewer surface particles than films grown on substrates located in the other positions of the sample holder. In all films occasional large, $\sim 1 \mu\text{m}$ in diameter, particles were observed. It is proposed that these particles, which occur at random on the film surface, arise due to melting of the target. In SEM examination they appear spherical indicating melting and often have a composition close to stoichiometric YBCO [e.g., Refs. 32,33]. Particles having a similar appearance are often observed to form during the ablation of other materials, for example during rapid ablation of sodium trisilicate glass at high fluences, spark-like incandescent particles can be seen leaving the glass surface. These are small, molten glass particles created by hydrodynamic sputtering [34]. In the case of glass, repeated transient heating leads to the formation of rolling surface asperities which grow from pulse-to-pulse until the tips fly off the target surface.

Films deposited on substrates located in the center of the substrate holder show a number of different features; small (20 - 50 nm) grains, larger ($\sim 0.2 \mu\text{m}$) equiaxed grains, and elongated grains where one edge is $\sim 0.2 \mu\text{m}$ and the other $\sim 0.4 \mu\text{m}$. In some of the samples examined several of the small grains had an acicular appearance where others were equiaxed because these particles are so small it is not yet clear if they are the same or different. The large elongated grains were found to be aligned in mutually orthogonal directions. AFM provides no chemical information about the particles although similar features have been observed in other studies of YBCO films where chemical analysis has been performed [33,35]. Very small cube shaped particles, observed in YBCO films on SrTiO_3 substrates formed by dc hollow cathode magnetron sputtering by Catana et al [35], have been identified as Y_2O_3 . Chang et al [33] observed very small surface particles ($< 0.1 \mu\text{m}$) which they suggested were incipient nuclei for a-axis oriented YBCO particles. The larger elongated particles have a shape suggestive of a-axis

oriented YBCO grains [21], although, as typified by grain A in Fig. 1d, they have a terraced surface which is not so usual. Again, similar particles were observed by Catana et al [35] and identified as either Y_2O_3 or $CuYO_2$ precipitates. Further characterization of these features is obviously necessary.

Films deposited on the right hand side of the sample holder show the highest frequency of surface particles. These surface particles are mainly the large elongated grains and the larger equiaxed grains, although the smaller features are also seen. If these elongated grains are due to a-axis oriented YBCO then this type of surface morphology would be consistent with that seen in TEM studies of YBCO films grown on (001) oriented $LaAlO_3$ substrates [e.g., Refs. 36,37]. Examination of specimens prepared in a cross-section geometry by TEM show that the YBCO layer next to the substrate surface is completely c-axis oriented but above a film thickness of about 400 nm, nucleation of a-axis oriented grains occurs. Hence the film close to the substrate surface is c-axis oriented and at larger thicknesses a-axis oriented.

Another feature of interest seen in both the SEM and AFM images of films deposited on substrates located on the right hand side of the sample holder is the spherical voids. These voids are 20 - 30 nm in diameter and appear similar to voids observed in YBCO films grown on MgO [38]. TEM investigations have revealed incipient dislocations to be associated with these voids [38,39]. If the void was to be filled a dislocation would have to be formed and this may be energetically unfavorable [40].

The morphology of laser ablated YBCO films on $SrTiO_3$ has been examined as a function of substrate temperature (T_s) and oxygen pressure (pO_2) by Borck et al [41]. They found that the morphology of the films could be distinguished into distinct zones, associated with specific deposition parameters. The results of their study agreed with the model proposed by Thornton [42], where the appearance of the zones are described below:

Zone I: The low adatom diffusion leads to a film consisting of tapered crystallites which are poorly bonded and have a rough surface. Surface recrystallization may cause the grains to be single crystals which diameter increases with pO_2 and T_s .

Zone T: The films consist of densely packed columnar grains separated by dense grain boundaries. The adatom diffusion is sufficient to overcome substrate and nucleation roughness and leads to smooth surfaces.

Zone II: Surface faceting causes 'open' boundaries between the grains because of the great adatom diffusion. The grain size increases with T_s .

Zone III: Large substrate temperatures lead to large grains produced due to volume crystallization.

Thornton's model [42] deals only with pressure and temperature changes. Brock et al [41] showed that variations in the laser energy density (E) could produce changes in the film morphology. In the region where $E \sim 1 - 3 \text{ J/cm}^2$ the films exhibited outgrowths which became larger and more numerous as E was decreased. Smooth films were obtained at $E \sim 3 - 5 \text{ J/cm}^2$ and films ablated at $E > 5 \text{ J/cm}^2$ were of significant roughness. This cited study is interesting and may provide a correlation to our studies where variation of several of the deposition parameters has been performed.

Many recent studies of the growth of YBCO films using scanning probe microscopy have shown the presence of a high density of screw dislocations [e.g., Refs. 43-46]. The screw dislocation mediated growth mechanism involves the addition of adatoms to the surface step which is always present along the edge of each spiral shaped growth terrace emanating from a screw dislocation [e.g., Refs. 47,48]. In the AFM images recorded in this study there was strong evidence to suggest that this growth mechanism was occurring in these laser ablated YBCO films on LaAlO_3 substrates, however, we did not observe the individual steps. Thomson et al [49] showed that in samples imaged by STM where the individual unit cell high steps associated with the screw dislocation mediated growth could be easily seen they were not resolved in the AFM images, which showed only the broad outlines of the gross surface structure.

MGN acknowledges numerous interactions with colleagues at Wright Laboratory, especially Dr. Rand Biggers, Dr. Iman Maartense, Dr. Patrick Hemenger, and Timothy Peterson. Technical support and assistance from David Dempsey, Jeff Brown, and John Woodhouse is greatly appreciated. The RBS analysis was performed at the Army Research Laboratory in Watertown MA by Dr. J. Derek Demaree.

REFERENCES

1. J.G. Bednorz and K.A. Müller, Z. Phys. B **64**, 189 (1986)
2. X.D. Wu, A. Inam, T. Venkatesan, C.C. Chang, E.W. Chase, P. Barboux, J.M. Tarascon, and B. Wilkens, Appl. Phys. Lett. **52**, 754 (1988)
3. See, for example, papers in: Laser Ablation for Materials Synthesis, edited by D.C. Paine and J.C. Bravman, Mater. Res. Soc. Symp. Proc. **191** (1990)
4. S.E. Russek, B.H. Moeckly, R.A. Buhrman, J.T. McWhirter, A.J. Sievers, M.G. Norton, L.A. Tietz, C.B. Carter, in: High Temperature Superconductors: Fundamental Properties and Novel Materials Processing, edited by J. Narayan, C.W. Chu, L.F. Schneemeyer, D.K. Christen, Mater. Res. Soc. Symp. Proc. **169**, 455 (1990)
5. G. Koren, A. Gupta, E.A. Giess, A. Sergmuller, and R.B. Laibowitz, Appl. Phys. Lett. **54**, 1054 (1989)

6. R.W. Simon, C.E. Platt, A.E. Lee, G.S. Lee, K.P. Daly, M.S. Wire, J.A. Luine, and M. Urbanik, Appl. Phys. Lett. **53**, 2677 (1988)
7. B.H. Moeckly, S.E. Russek, D.K. Lathrop, R.A. Buhrman, M.G. Norton, and C.B. Carter, Appl. Phys. Lett. **57**, 2951 (1990)
8. D.P. Norton, D.H. Lowndes, J.D. Budai, D.K. Christen, E.C. Jones, K.W. Lay, J.E. Tkaczyk, Appl. Phys. Lett. **57**, 1164 (1990)
9. M.G. Norton and C.B. Carter, in: Laser Ablation for Materials Synthesis, edited by D.C. Paine and J.C. Bravman, Mater. Res. Soc. Symp. Proc. **191**, 165 (1990)
10. G.W. Berkstresser, A.J. Valentino, and C.D. Brandle, J. Cryst. Growth **109**, 467 (1991)
11. M.G. Norton and C.B. Carter, Physica C **172**, 47 (1990)
12. G. Koren, A. Gupta, R.J. Baseman, M.I. Lutwyche, and R.B. Laibowitz, Appl. Phys. Lett. **55**, 2450 (1989)
13. M. Balooch, D.R. Olander, and R.E. Russo, Appl. Phys. Lett. **55**, 197 (1989)
14. R.E. Muenchausen, K.M. Hubbard, S. Foltyn, R.C. Estler, and N.S. Nogar, Appl. Phys. Lett. **56**, 578 (1990)
15. M.G. Norton and C.B. Carter, Physica C **182**, 30 (1991)
16. I. Maartense, J. Appl. Phys. **53**, 2466 (1982)
17. D.W. Chung, I. Maartense, T.L. Peterson, and P.M. Hemenger, J. Appl. Phys. **68**, 3772 (1990)
18. A.K. Sarkar, B. Kumar, I. Maartense, and T.L. Peterson, J. Appl. Phys. **65**, 2392 (1989)
19. L.R. Doolittle, Nucl. Instrum. Meth. B **9**, 334 (1985)
20. L.R. Doolittle, *ibid*, **15**, 227 (1986)
21. M.G. Norton, S. McKernan, and C.B. Carter, Philos. Mag. Lett. **62**, 77 (1990)
22. I. Maartense, A.K. Sarkar, and G. Kozlowski, Physica C **181**, 25 (1991)
23. T. Venkatesan, X.D. Wu, A. Inam, and J.B. Wachtman, Appl. Phys. Lett. **52**, 1193 (1988)
24. M.C. Foote, B.B. Jones, B.D. Hunt, J.B. Barner, R.P. Vasquez, and L.J. Bajuk, Physica C **201**, 176 (1992)
25. M. Fendorf, M.E. Tidjani, C.P. Burmester, L.T. Wille, and R. Gronsky, in: High Tc Superconductor Thin Films, edited by L. Corraera, Elsevier Science Publishers, Amsterdam (1992) p. 771
26. H.W. Zandbergen, R. Gronsky, and G. Thomas, Phys. Stat. Sol. A **105**, 207 (1988)
27. R. Ramesh, D.M. Hwang, T. Venkatesan, T.S. Ravi, L. Nazar, A. Inam, X.D. Wu, B. Dutta, G. Thomas, A.F. Marshall, and T.H. Geballe, Science **247**, 57 (1989)
28. T. Krekels, G. Van Tendeloo, S. Amelinckx, J. Karpinski, S. Rusiecki, E. Kaldis, and E. Jilek, Physica C **178**, 383 (1991)
29. Y.X. Guo, R. Høier, T. Graf, and Ø. Fischer, Physica C **199**, 435 (1992)

30. D.K. Bowen and C.R. Hall, Microscopy of Materials, The MacMillan Press, London (1975)
31. N.-L. Wu, H.-D. Yu, Y.D. Yao, and E. Ruckenstein, Appl. Phys. Lett. **63**, 687 (1993)
32. M.G. Norton, L.A. Tietz, S.R. Summerfelt, and C.B. Carter, Appl. Phys. Lett. **55**, 2348 (1989)
33. C.C. Chang, X.D. Wu, R. Ramesh, X.X. Xi, T.S. Ravi, T. Venkatesan, D.M. Hwang, R.E. Muenchausen, S. Foltyn, and N.S. Nogar, Appl. Phys. Lett. **57**, 1814 (1990)
34. P.A. Eschbach, J.T. Dickinson, S.C. Langford, and L.R. Pederson, J. Vac. Sci. Technol. A **7**, 2943 (1989)
35. A. Catana, J.G. Bednorz, Ch. Gerber, J. Mannhart, and D.G. Schlom, Appl. Phys. Lett. **63**, 553 (1993)
36. C.W. Nieh, L. Anthony, J.Y. Josefowicz, and F.G. Krajenbrink, Appl. Phys. Lett. **56**, 2138 (1990)
37. S.N. Basu, A.H. Carim, and T.E. Mitchell, J. Mater. Res. **6**, 1823 (1991)
38. M.G. Norton and C.B. Carter, J. Cryst. Growth **110**, 641 (1991)
39. M.G. Norton and C.B. Carter, J. Mater. Sci. (1993 submitted for publication)
40. F.R.N. Nabarro, Theory of Crystal Dislocations, Dover, New York (1987)
41. J. Borck, S. Linzen, K. Zach, and P. Seidel, Physica C **213**, 145 (1993)
42. J.A. Thornton, J. Vac. Sci. Technol. **12**, 830 (1975)
43. Ch. Gerber, D. Anselmetti, J.G. Bednorz, J. Mannhart, and D.G. Schlom, Nature **350**, 279 (1991)
44. M. Hawley, I.D. Raistrick, J.G. Beery, and R.J. Houlton, Science **251**, 1587 (1991)
45. D.G. Schlom, D. Anselmetti, J.G. Bednorz, R.F. Broom, A. Catana, T. Frey, Ch. Gerber, H.-J. Güntherodt, H.P. Lang, and J. Mannhart, Z. Phys. B **86**, 163 (1992)
46. S.J. Pennycook, M.F. Chisholm, D.E. Jesson, R. Feenstra, S. Zhu, X.Y. Zheng, and D.J. Lowndes, Physica C **202**, 1 (1992)
47. F.C. Frank, Disc. Farad. Soc. **5**, 48 (1949)
48. W.K. Burton, N. Cabrera, F.C. Frank, Philos. Trans. R. Soc. London Ser. A **243**, 299 (1951)
49. R.E. Thomson, J. Moreland, N. Missert, D.A. Rudman, S.C. Sanders, and B.F. Cole, Appl. Phys. Lett. **63**, 614 (1993)

GROUND AND EXCITED STATE PROPERTIES OF LINEAR POLY(PHENYL) DI-METHYLENE

R.G. Petschek

Department of Physics, Case Western Reserve University, Cleveland, OH 44106-7079

Final report for the summer faculty research program

Polymer Branch, Materials Laboratory, Wright Laboratories, Wright- Patterson AFB

Sponsored by the Air Force Office of Scientific Research Bolling AFB

Wright Patterson Air Force Base ML/BP

September 30, 1993

GROUND AND EXCITED STATE PROPERTIES OF LINEAR POLY(PHENYL) DI-METHYLENE

R.G. Petschek

Department of Physics, Case Western Reserve University, Cleveland, OH 44106-7079

Abstract

This paper presents *ab initio* (631G*) calculations for the properties of α,ω n (para)phenyl-dimethylenes with $n = 1, 2, 3$. These molecules have two potential radical centers separated by aromatic spacers and potentially have a variety of forms, including the paired electron quinoidal form, a singlet or triplet biradical form and a pseudo-Jahn-Teller distorted form in with a spontaneous symmetry breaking and opposite charges on the potential radical centers. The former quinoidal structure is favored by electron pairing and charge separation rules, the others by resonance in the aromatic rings. I find that for $n = 1$ this molecule is quinoidal and for $n = 2, 3$ the molecule constrained to a D_{2h} geometry is a singlet biradical and that the radical wavefunctions are largely confined to the potential radical centers. More extensive calculations in non- D_{2h} geometries have been done for the $n = 2$. The likely consequences for polymers which consist of such potential radical centers connected by aromatic segments and of polymers containing such radical centers are discussed.

GROUND AND EXCITED STATE PROPERTIES OF LINEAR POLY(PHENYL) DI-METHYLENE

Rolfe G. Petschek

I. INTRODUCTION

The determination of the quinoidal, aromatic or other nature of molecules containing two or more potential radical centers is of interest for a variety of reasons. Small molecules with this property have been of interest for many years and have properties distinctly different from those of molecules not containing such radical centers [1]. Polymers have been proposed to have better conductivity properties when in the quinoidal form. However the quinoidal form generally has a higher energy than the aromatic form. Thus the extent to which potential radical centers can induce or facilitate the adoption of a quinoidal structure in such polymers is of interest. As the aromatic structure generally has lower energy long enough potentially aromatic segments separating potential radical centers are expected to result in one of the aromatic forms considered below. If the repulsive interactions between the electrons dominate then I expect a singlet or triplet biradical in which two electrons are not paired but are (one each) on the potential radical centers[1]. If there is an effective attractive interaction or electron pairing dominates a charge separated state is expected.

Additionally molecules of this nature are also of interest as it should be possible to make polymers - "polyradicals" - whose electronic states consist to large extent of unpaired, radical electrons separated by aromatic or other portions. Such polymers are likely have interesting new electronic and optical behaviors. Poly-radicals may have a variety of states. These include the "dimerized" state, alternating quinodial and aromatic rings, as in the pernigranuline form of poly(aniline), a charge density wave form in which the potential radicals have different charges; a conducting form in which the radicals are mobile, various forms related to ground states of the Hubbard model, including conducting, insulating, Neél antiferromagnetic, and other states.

These electronic states, particularly those for the Hubbard model, involve states with appreciable dynamic electronic correlation which are still a matter of research even in simple model systems. Rather than attempting to address this problem I have done calculations on small monomers and polymer segments to understand what part of the potentially large parameter space a particular molecular structure is in. In order to do so I have calculated both the ground and excited state properties as the excited state properties as the excited state properties give indications of the nature of the the motion of electrons from one radical center to the next.

I find that the phenyl ($n = 1$) is quinoidal and that the biphenyl ($n=2$) and triphenyl ($n = 3$) are singlet biradicals, with rather low lying triplet excitations and rather higher lying singlet excited states. On this basis I expect that the polymers consisting of such molecules connected through the methylenes will be dimerized for the phenyl and semiconducting probably antiferromagnets for the bi and tri phenyls. All calculations were done using the GAMESS quantum chemistry package[5].

This paper is organized as follows. In the next section I discuss the various potential states of the molecules under consideration, and in the third section the give simple mathematical models and discuss their generalization to related polymers. I also discuss generally the calculational techniques used for the computation. The fourth section gives computational details. Finally our results and their potential importance to various polymeric systems are discussed.

II. POTENTIAL MOLECULAR STATES

I discuss at a simple heuristic level the possible ground and excited states of the molecules under consideration and give a simple hamiltonian in terms of which one might expect to understand the behavior of small molecules and to extrapolate their behavior to polymers. The generalization of such a hamiltonian to the electronic properties of polymers is presented.

An $\alpha, \omega n$ -para-phenyl-dimethylene can have a number of possible ground states. The simplest is the quinoidal Lewis structure in which all electrons are paired and

is naively expected to give a reasonable approximation to the structure of such molecules. However it is important to note that in this structure we have eliminated the resonance stabilization associated with (each of) the aromatic rings. It is therefore expected that for sufficiently large n another class of Lewis structures should predominate, in which there can be resonance stabilization of the aromatic rings. There are three simple possibilities. First there can be unpaired electrons on (or near) the potential radical center. As these radicals can be either in a singlet or a triplet state this is two separate possibilities. Secondly there can be a pair of electrons on (or near) a single potential radical center and a missing electron on (or near) the other potential radical center, resulting in the broken symmetry charge separated state. As the phenyl rings are aromatic these structures are resonance stabilized.

In our initial calculations all these molecules were constrained to have D_{2h} symmetry in the symmetric state and correspondingly would have C_{2v} symmetry in the charge separated state. This is an approximation to the actual situation for the biphenyl which is expected to have a twist between the two phenyl rings and D_2 symmetry. The symmetry expected from a complete minimization of $n = 3$ is not clear - if the two rings twist equally and in the same direction the symmetry would be D_2 , if the rings twist in opposite directions the symmetry would be C_2 . Such twists can be suppressed in actual molecules without seriously altering the electronic properties by connecting the two phenyl rings to each other e.g. as in fluorene. Thus these D_{2h} results are interesting in the abstract. However it is important to remark that in the triplet and excited states of these molecules there may be rather large twists so that the excited electrons can avoid each other, making our D_{2h} approximation a more serious approximation. I confirmed this possibility for the biphenyl but have not done so for the triphenyl.

In the non-quinoidal states the inter-phenyl bonds have more single bond character and in consequence are expected to be more easily twisted and, by Le Châtelier's principle, favored by the twisted structure which results from the hydrogen-hydrogen

repulsion. Thus constraining $n = 2, 3$ to the D_{2h} geometry if anything decreases the biradical character. However it is likely to increase the triplet energy relative to the biradical energy. I have verified this for the biphenyl by doing the singlet biradical calculation in the general D_2 geometry and also the D_{2d} (perpendicular rings) and neighboring triplet biradicals.

In order to understand and explore the possible aromatic states we have considered the simplest calculational techniques which will incorporate their major features. The likely effects of additional terms in the calculation are discussed and to some extent calculated. The quinoidal structure and charge separated structures consist entirely of paired electrons and in consequence can be studied to first approximation using a restricted Hartree Fock (RHF) calculational technique. These states can (potentially) be found separately by first calculating the state of the system insisting that the system have the full D_{2h} symmetry and then relaxing this symmetry constraint. In practice this was done by doing a full geometry relaxation with an RHF calculation of the wavefunction. The symmetry of the wavefunction was then reduced to C_1 (no symmetry) which allows for the distortion of the wave-function into the suggested charge separated state (and others as well). An identical calculation was done in the TCSCF geometry and approximation discussed below. No attempt was made to explore the possibility that such states can exist only in non-symmetric geometries. In practise I found neither such states found nor any indication thereof such as slow convergence reflecting large susceptibilities or low lying excited states with the same multiplicity as the ground states, which also indicate large susceptibilities and this possibility was not pursued further. Results from the singlet excited state calculations (and chemical intuition) suggest that the electronic repulsion is sufficiently large in any case that such a state is unlikely to form.

The triplet biradical configuration has two unpaired electrons in a triplet configuration. These were studied also in the simplest possible calculation, a multiplicity 3 restricted open shell Hartree Fock (ROHF) calculation. The singlet biradicals were

studied using a one pair generalized valence bond (GVB) calculation. This is sometimes called the two configuration self consistent field (TCSCF) calculation. It is a multi-configurational-self-consistent field calculation with the two configurations consisting of the RHF configuration and the configuration with a pair of electrons taken from the RHF highest occupied molecular orbital (HOMO) and placed in the RHF lowest unoccupied molecular orbital (LUMO). As is known and also as discussed below, this is the simplest calculation which allows for a singlet biradical. Note that such a calculation includes as a variational possibility the RHF or quinoidal calculation and so taken literally this will always imply that the singlet biradical has a lower energy than the quinoid. In practise this is not a serious difficulty as calculationally the phenyl is essentially quinoidal and the biphenyl and triphenyl are essentially biradical. The lowest lying singlet excited state (SES) of the system was calculated using a no-pair GVB calculation. The SES calculation has not been completed successfully for the triphenyl. Calculations were done of the equilibrium geometries of each of these states and "vertical transitions", that is calculations of the energies and wavefunctions for all states in the equilibrium geometries of all other states were also calculated.

III. MATHEMATICAL MODELS

In order to understand the importance of these states and also their importance to potential poly-radicals consider the following simple two site - two electron (biradical) model hamiltonian:

$$H_d = \frac{1}{2}bx^2 + (t + ax) \sum_{s=\pm} c_{1s}^\dagger c_{2s} - J\vec{\sigma}_1 \cdot \vec{\sigma}_2 + u \sum_i n_i(n_i - 1) \quad (1)$$

where c_{is} is the annihilation operator for electrons with spin $s = \pm$ on site $i = 1, 2$, $n_i = \sum_s c_{is}^\dagger c_{is}$, $\vec{\sigma}_i$ is the total electron spin on site i given by the appropriate products of a Pauli matrices with creation and annihilation operators, x is a molecular displacement with respect to which the energy states should be minimized. In principle there are a number of such molecular displacements - one for each normal mode. In this study I were interested only in the approximate magnitude of these displacements

terms and have considered together all displacements which retain the D_{2h} geometry. For the biphenyl we separately considered the effects of non- D_{2h} displacements. The parameters in this hamiltonian are a molecular stiffness b , a hopping matrix element t , the dependence of the molecular energy on the molecular displacement a , a site-site repulsion term u , which models Coulomb repulsion and is expected to be positive, and the spin-spin interaction energy J , which is used to model the effect of exchange interactions with other electrons in the system. This effective hamiltonian is the simplest hamiltonian which contains the salient features of actual and potential molecular biradicals.

Before discussing this hamiltonian note that this model can easily be generalized to a polymer with N potential radical sites connected together resulting in

$$H_p = \sum_{i=1}^{N-1} \frac{1}{2} b x_i^2 + (t + a x_i) \sum_{s=\pm} c_{i,s}^\dagger c_{i+1,s} - J \vec{\sigma}_i \cdot \vec{\sigma}_{i+1} + u \sum_i n_i (n_i - 1) \quad (2)$$

where x_i is now a molecular displacement between the i^{th} and $i + 1^{th}$ site and the remaining variables have an identical interpretation to that which they have in the two site model. This polymer model is quite difficult to solve and I will not attempt to do so here. Note that it contains a variety of well-known models as special cases. Thus the $J = 0, u = 0$ limit of the model is the Su-Schrieffer-Heeger (SSH) model [2], which is commonly used as a model of poly(acetylene) and other poly(enes) and is known to show the dimerized state which is characteristic of known conducting polymers. The degree of dimerization is given, approximately by $a^2 t^{-2} b^{-1}$. This part of the model would be well described by e.g. simple mean-field or RHF techniques. The $a = J = 0$ limit is the well-known Hubbard model, which was one of the first models of the conductor-insulator transition and is still intensively studied [4]. For large u interactions are important and simple mean-field or RHF techniques are expected to fail. This is the "biradical" limit and has been treated by a variety of techniques in this simple model. For an actual quantum chemistry calculation multi-configurational self-consistent field techniques are potentially required. The $a = 0, u \rightarrow \infty$ limit is a model of one dimensional ferro- or anti-ferro- magnets. As the model has these

rather different behaviors in various different limits it is expected that it should be possible to design and synthesize polymers which have behavior other than either the "typical" SSH behavior or recently synthesized organic magnets. The computational determination of biradical parameters given below is a step in this design process and towards a deeper understanding of poly-radicals.

While the polymeric model is quite difficult to solve with precision (various limits have been a topic of research for many years) the simple dimer model is easily solved with the use of group theory. There are six micro-states for two electrons on two sites. They decompose into one triplet (three micro-states) which is odd under exchange of the sites, a singlet which is odd under the exchange of the sites and two singlets which are even under this exchange. As the model is symmetric under spin rotations and site exchange these subspaces are eigenspaces of the hamiltonian and only a 2×2 hamiltonian needs to be diagonalized to find all the relevant states. In molecular orbital language the triplet state is two electrons with the same spin, one in the highest occupied RHF ground state molecular orbital (HOMO) and one in the lowest unoccupied such molecular orbital (LUMO). The anti-symmetric singlet is a symmetric pair of electrons with opposite spins with one in the HOMO and one in the LUMO. Finally the two symmetric singlets are paired electrons with the two basis states are ψ_l , a pair of electrons in the LUMO, and ψ_h , a pair of electrons in the HOMO. In the non-interacting $u = 0$ limit the energy eigenstates are precisely the states given above. In the strongly repulsive $u \rightarrow \infty$ limit the relevant symmetric singlet states are $\psi_l \pm \psi_h$, exhibiting post single determinant Hartree Fock correlations. In this limit the low lying energy states consist essentially of one unpaired (radical) electron on each site. When $J = a = 0$ these states, a symmetric singlet and a triplet are degenerate to order $1/u$ so it is expected that the exchange interactions will make the triplet the lowest energy state. The other two states, a antisymmetric singlet and an excited symmetric singlet are, in the large u limit essentially the symmetric and antisymmetric combinations of the state with two electrons on one of the sites and

no electrons on the other.

IV. COMPUTATIONAL DETAILS AND RESULTS

The molecules shown were initially assumed to be planar and to have D_{2h} symmetry. Starting from an initial geometry these molecules were first geometry optimized using the RHF wave functions. Starting from the RHF geometry the geometry was optimized using three other calculational techniques, one pair GVB or TCSCF, the ROHF triplet and the GVB singlet first excited state. In all the calculations reported herein the frontier orbitals, that is the highest occupied and lowest unoccupied molecular orbitals (HOMO and LUMO) in the RHF, the singly occupied orbitals in the triplet and excited state singlet, and the partially occupied orbitals in the one pair GVB calculations were π orbitals and in all cases had the same symmetries.

The basis set used for this work was[5] 631G*. That this was adequate for ground state properties was tested by comparing the electronic states at the 631G* configuration with the electronic states for 321G*. These were quite similar. It is not expected that 631G* will give adequate results for the energy difference between the ground state and the singlet excited state, however.

The RHF HOMO was a B_{2u} state, that is odd under reflection about the molecular plane and even under all other reflections. The RHF LUMO was a B_{1g} state, that is odd under reflection about the molecular plane and odd under the reflection which interchanges the two potential radical centers and even under the remaining reflection. This symmetry property is "expected" and is consistent with the simple model given above which has two molecular orbitals which differ in symmetry only in that one is even and the other odd under interchange of the potential radical centers. The geometries of these states is given in table 1. The MCSCF parameters are given in table 2. Note that the monophenyl seems to be rather well described as a quinoidal structure and in particular the bonds which are expected to be double bonds in the quinoidal structure have bond lengths typical of carbon-carbon double bonds. In addition the modifications on doing the TCSCF calculation are rather

small, with the number of electrons in the HOMO small. Finally the geometries and energies of the singlet and triplet are quite different. I conclude that this system is well described by the quinoidal structure. In the two systems with longer intervening potentially aromatic sections, however, none of these conditions hold. In particular the equilibrium geometries are very different (particularly for the triphenyl) from the RHF, dimerized geometry, the bond lengths in the phenyl rings are typical of those in aromatic rings in both the TCSCF and triplet states and the TCSCF and triplet states have very similar energies and geometries. I conclude that the ground state of the biphenyl is not quinoidal but essentially a singlet biradical and that the ground state of the triphenyl is either a singlet or triplet biradical (we do not consider the very small energy difference between these two states in the triphenyl definitive.) However we note that the geometries of the ground and excited singlet states are in all instances rather different. Also note that the frontier orbitals which are relevant to the biradical calculation are strongly centered on the potential radical centers. This strong centering on the biradical centers is consistent with the energy of the singlet being lower. If two electrons (or other particles which repel each other) are in spatially overlapping states then the correlation hole, resulting from the fact that two like spin electrons can not be in the same location will result in a lower energy for the triplet because the repulsive interactions are not as strong. However if the electrons are in well separated states then the fact that in the singlet state the tails of the wave-function can overlap for the singlet (but not the triplet) will lower somewhat the kinetic energy in the singlet. I find the latter case. In consequence of this localization it is expected that the addition of other phenyl rings (e.g. as in the Chichibudin hydrocarbon (bi-triphenylmethylene)[1]) will not greatly alter the ground state and low lying triplet properties of the molecule.

The energies of the electronic states which I have considered in the equilibrium geometries of the electronic states considered are given in table 3. Examination of the Mulliken population data shows an appreciable change in the HOMO and LUMO

wavefunctions between the ground and triplet and singlet excited states. Thus the biphenyl is not expected that the simple model of section III will adequately describe the results for this system. In consequence detailed calculation of the biradical parameters was not pursued.

For the biphenyl I have also examined geometries which are not D_{2h} . The minimum energy for the triplet is expected where there is small overlap between the two states in which the unpaired electrons reside. When the phenyl rings are perpendicular to each other the molecule has a D_{2d} geometry; the HOMO and LUMO are degenerate; and, in an appropriate representation, reside largely on the two different rings. I have verified that if the molecule is displaced slightly from this D_{2d} geometry to a D_2 geometry then the energy of the triplet increases. I have also optimized the TCSCF singlet relaxing the geometry constraints to D_2 . However the final run for the D_2 geometry is still incomplete, although the energy is clearly very close to final.

I note from the table that, in fact, the triplet and TCSCF singlet for this molecule are very close, with consideration of non-planar configurations essential to computing which of the states has the lower energy. The current calculation predicts that this molecule will have a slightly lower energy in the singlet state, consistent with observations of the Chichibudin hydrocarbon which seems to have a lower energy in the singlet by to have an appreciable (2%) population of the triplet at room temperature. As the triplet has three times as many electronic states and twice as many symmetry elements as the singlet biradical and the entropy is not expected to be appreciably different. This suggests an energy difference of $T \ln(3/(2 \times .02)) \approx 0.1eV$, compared with our result (for a somewhat different molecule in vacua) of $0.10eV$. Considering the smallness of the difference and the differences in environment and molecular structure this agreement is remarkable. It should be noted that the actual electronic structure, charges etc. are very similar: however the geometric structure is somewhat different. This geometric difference makes the likely changes from solvent effects not inappreciable on this scale.

V. DISCUSSION OF POLYMERIC BEHAVIOR

Now consider the likely nature of polymers made from such molecules. I have in mind polymers in which there are potential radical centers along the polymer backbone consisting of a carbon atom bonded to a hydrogen and to two aromatic segments which form the polymeric backbone. Such carbon radicals are known to be quite stable. It is important to note that if the aromatic segments are phenyl then steric considerations require that there be a significant twist between the rings attached to each potential radical. As above this will tend to increase the tendency for the formation of radicals as it will favor single bonds which are a larger fraction of the wavefunction in the radical than the quinodal system.

I found that the phenyl was quinodal. As it is also known that the pernigraniline form of polyaniline is an alternating sequence of quinodal and aromatic rings it is reasonable to expect that the carbon analog should be similar, despite the differences in electro-negativity of carbon and nitrogen I expect that the carbon analog of pernigraniline polyaniline is also an alternating quinoidal-aromatic polymer. On the other hand the biphenyl and triphenyl are essentially aromatic and I expect in consequence that the corresponding polymers are also essentially aromatic. The effects of polymerization on such a system is that the potential double bonds which imply quinoidal structure can have a number of positions in the structure - most simply that in a typical quinoidal Lewis structure only one of the two linkage groups connected to a radical is expected to be quinoidal. As there are also allowed Lewis structures in which the double bonds are on the other linkage group the double bond character is expected to be reduced in the polymer relative to that in the monomer. Thus polymerization will tend to promote the aromatic configuration over the pernigraniline configuration. This is easily confirmed by a simple band structure calculation.

In the simplest view of this aromatic state there is one unpaired electron on each potential radical site. The actual situation, of course, is considerably more complex. First of all the unpaired electrons are actually not completely localized on the

potential radical sites. Thus there will be some changes in relative energies on polymerization. Secondly and more importantly the quantum states which correspond to the monomer excited states in which there is more than one electron on the potential radical sites or the frontier electrons are in the aromatic bridge have to be considered in extrapolating the monomer results to a polymer. However there is a large difference in the energy I have calculated for the differences between the TCSCF and triplet states and the singlet excited state. I do not expect that our basis set, which did not contain diffuse functions, is adequate to calculating this difference accurately (and, in fact, the observed transition energy for the monomer is too high). Nevertheless given the very large difference in energy differences it seems reasonable to hypothesize that the states in which there is essentially an unpaired electron on each potential radical site predominate at low temperatures for ground state like properties. In other words to good approximation the polymer can be viewed as a Hubbard model in the insulating (more properly semiconducting) strong repulsion ($u \rightarrow \infty$) state. This is well approximated by isolated, unpaired electrons with a barrier to conductivity comparable to the singlet-ground-state to singlet excited state energy difference (approximately 6eV in my likely inaccurate calculation). As discussed above this is likely an over-estimate. Nevertheless these polymers are expected on this basis to be poor conductors at ordinary temperatures.

As the energy maximum for the low energy triplet spin state is only 0.10eV above the energy of the "best" TCSCF singlet state it is expected that at ordinary temperatures the phenyl rings will rotate freely - primarily in the triplet state as the barrier to rotation in the singlet state is much larger than that in the triplet state. However as it is also the case that energy difference between the singlet and triplet state is much lower when the rings are allowed to rotate relative to each other it is expected that at temperatures less than .1eV $\approx 1000K$ there will be appreciable correlation between the spins that there will also be correlation between the spin state and the relative angle of the rings so that e.g. the rotation of the rings should be

apparent in the EPR spectra.

The energy difference between the singlet and triplet is rather small and it is not immediate from this calculation whether parallel or anti-parallel aligned spins will dominate in the polymer. The D_{2d} triplet, which I hypothesize is the lowest energy triplet, has energy higher than the twisted D_2 singlet. As this is consistent with expectations from the physical reasoning presented for the biphenyl in section III, we hypothesize that the singlet is the lowest energy state. However it is important to remark that the energy differences are rather small and are also (as is apparent from table 2) strongly related to the conformation of the polymer. I expect significant changes when this monomer is polymerized and possibly more subtle differences for a calculation in which more dynamic electronic dynamic electronic correlation or a superior basis set is used. Moreover the argument in section III applies in the D_{2h} geometry and does not apply in the D_{2d} geometry in which the two radical wavefunctions have completely different (π and σ) character where they overlap and, in fact, the triplet has the lower energy in this configuration. On balance however it seems more likely that the anti-aligned or singlet configuration has a lower energy. If this is the case the polymer would be well approximated by a semi-conducting antiferromagnetic state. Such states have been extensively studied and will not be discussed here. If, on the contrary, the aligned state is preferred (which seems on balance less likely) the low temperature state will be a semi-conducting ferromagnetic state.

The optical properties of this state are also of interest. I do *not* expect that they will be those of a extreme electron-electron repulsion Hubbard model. In particular the excited states of the dimer are not well approximated by two electrons on one of the radical centers and no electrons on the other radical center - rather the excited electronic state is spread out over the entire (oligo)phenyl spacer between the two radical centers. For the the poly-radical model (Eq 2) to apply to biphenyl and longer spacers it seems, from the calculations above that it must use the $t/u \rightarrow 0$ limit. This

model supposes that energy of a state depends to lowest order only on the total number of potential radical sites containing zero, one and two electrons. The excited state of the monomer which is, at least qualitatively expected to describe the excited states of the polymer does not have this character, rather one of the orbitals involved is concentrated in the (oligo)phenyl spacer. This relaxation of the electronic state in the biphenyl portion separating the two radical centers will require additional terms reflecting this relaxation when unoccupied and doubly occupied states are adjacent. In principle this can be studied, at least in part by also studying various excited and charged states of this monomer, and by studying the excited states of larger molecules (e.g. the three radical dimer). The Hubbard model would then have to be extended to include (at least) two states on each site (or one in on the spacer), one of which has low energy but large electron-electron repulsion and the other of which has a higher energy but allows for excited states with energies less than that of the singlet excited state in which the electronic energy is appreciably raised by electron-electron repulsion. As this second state seems not to reside largely on the potential radical center it is likely also to be significantly effected by the groups attached to this center so that appreciable difference are expected between the biphenyl dimethylene I have studied and more stable molecules such as the Chichibudin hydrocarbon or the potential polymers. Similar comments apply to the high temperature states of the polymer, in which there is expected to be appreciable occupation of the singlet excited state. A study of these issues is beyond the scope of this paper.

Acknowledgements: Work supported by the AFSOR though Bolling AFB and the polymer branch of Wright Laboratories, Wright Patterson AFB. Detailed conversations with and the technical assistance of Douglas Dudis (who suggested the problem to me), A. Todd Yeates and Steve Trohalaki are gratefully acknowledged.

REFERENCES

- [1] See e.g. A.W. Wheland "Advanced Organic Chemistry" John Wiley and Sons, New York (1960) p 813ff.
- [2] M.W.Schmidt, K.K.Baldrige, J.A.Boatz, J.H.Jensen, S.Koseki, M.S.Gordon, K.A.Nguyen, T.L.Windus, S.T.Elbert QCPE Bulletin 10 52-54 (1990).
- [3] See e.g. A.J. Heeger, S. Kivelson, J.R. Schrieffer and W.-P. Su, Rev. Mod. Phys. 60 781 (1988).
- [4] J.T. Gammel, R.J. Donohue, A.R. Bishop, and R.I. Swanson Phys. Rev. B42 10566 (1990) and references therein.

TABLES

Table 1: gives the equilibrium energies and geometries of α, ω *n*-(phenyl)dimethylenes in various electronic states. The symbols RHF denote the (theoretically interesting) Restricted Hartree Fock state, TCSCF is the two configuration self consistent field (HOMO - LUMO multiconfigurational self consistent field) calculation, Trip is the lowest lying triplet state and SES is the lowest lying singlet excited state. I was unable to find the equilibrium geometry for the triphenyl. Only the distances between carbons directly bonded to each other are given. All distinct such distances are given, with the numbering scheme shown in figure 1. Energies are given in Hartrees, distances in angstroms.

n	State	Energy	R_{M1}	R_{12}	R_{23}	R_{34}	$R_{41'}$	$R_{1'2'}$	$R_{2'3'}$
1	RHF D_{2h}	-307.23557	1.3301	1.4702	1.3277				
1	TCSCF D_{2h}	-307.56556	1.3462	1.4532	1.3366				
1	Trip D_{2h}	-307.53311	1.4588	1.395	1.3822				
1	SES D_{2h}	-307.34700	1.4363	1.3904	1.3602				
2	RHF D_{2h}	-537.06502	1.3319	1.4637	1.3310	1.4682	1.3622		
2	TCSCF D_{2h}	-537.07477	1.4362	1.3986	1.3768	1.4000	1.4874		
2	Trip D_{2h}	-537.07226	1.4473	1.3953	1.3799	1.3969	1.4967		
2	SES D_{2h}	-536.92095	1.3676	1.4422	1.3541	1.4310	1.4358		
2	TCSCF D_2	-537.07833							
2	Trip D_{2d}	-537.07428	1.4484	1.3970	1.3821	1.4970	1.3912		
3	RHF D_{2h}	-766.58084	1.3325	1.4632	1.3319	1.4655	1.3663	1.4594	1.3355
3	TCSCF D_{2h}	-766.61942	1.4450	1.3962	1.3794	1.3973	1.4943	1.3946	1.3807
3	Trip D_{2h}	-766.61920	1.4457	1.3958	1.3795	1.3970	1.4948	1.3943	1.3808

Table 2: Gives the MCSCF coefficients and energy lowering for the TCSCF calculations of the D_{2h} molecules considered in this paper.

Molecule	Orbital 1	Orbital 2	Energy Lowering
phenyl	0.9756	-0.2192	-0.0198
biphenyl	0.7763	-0.6304	-0.1534
triphenyl	0.7256	-0.6881	-0.1977

Table 3: Transition energy (eV) from the of equilibrium geometries of a number of electronic states to other electronic states. Labeling of states as in Table 2. The equilibrium geometry for the SES triphenyl is unavailable.

3a: Phenyl:

Equilibrium Geometry	TCSCF	Trip	SES
TCSCF	0.0	2.072	6.109
Trip	-0.622	0.0	5.131
SES	-5.830	-4.423	0.0

3b: biphenyl:

Equilibrium Geometry	TCSCF	Trip	SES
TCSCF	0.0	0.075	4.676
Trip	-.062	0.0	4.737
SES	-3.531	-3.531	0.0

3c: triphenyl:

Equilibrium Geometry	TCSCF	Trip	SES
TCSCF	0.0	0.009	—
Trip	-.009	0.0	—
SES	-4.920	-4.911	0.0

**SEMICONDUCTOR COUPLED AMPLIFIERS FOR
ELECTRO-OPTIC APPLICATIONS**

**M. J. Potasek
Research Professor
Department of Applied Physics**

**Columbia University
New York, New York 10027**

**Final Report For:
Summer Research Program
Wright-Patterson**

**Sponsored by:
Air Force Office of Scientific Research
Bolling Air Force Base, Washington, D.C.**

1993

SEMICONDUCTOR COUPLED AMPLIFIERS FOR ELECTRO-OPTIC APPLICATIONS

M. J. Potasek
Research Professor
Columbia University

Abstract

Nonlinear optical phenomena are of interest because of their wide ranging applications. In particular I have investigated coupled semiconductor waveguides of interest in electro-optic applications. Because of the available semiconductor growth facilities in the area and their growing importance in research, particular attention was paid to the III-V semiconductor multiple quantum well materials.

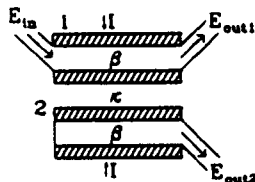
SEMICONDUCTOR COUPLED AMPLIFIERS FOR ELECTRO-OPTIC APPLICATIONS

M. J. Potasek

Introduction

Because of the prospects of integration of several components such as lasers, detectors and modulators, semiconductors are advantageous for electro-optic applications. Semiconductor waveguides are of interest for applications ranging from communications to computing. Considerable research has focussed on the quantum confined Stark effect. However because of the electron hole recombination dynamics, devices based on this concept have been slow. An alternative is the use of coupled semiconductor traveling-wave amplifiers. A single semiconductor amplifier is fabricated like a semiconductor laser with the exception of reflecting cleaved ends on the waveguide. While a simple semiconductor amplifier is useful for amplification in integrated circuits, other complex features require more complicated structures. For information processing, a nonlinear directional coupler (NLDC) is often used. The NLDC was devised for optically activated switching between two output ports (1). The switching is achieved by

using in a linear directional coupler an intensity-dependent factor for the refractive index. This locally alters the wave vector mismatch between the guides, so that the effective energy transfer and coupling length can be adjusted by varying the input power. Directional coupler switches with optical gain have previously been investigated in the linear regime (2). Recently, electrically and optically controlled partial switching of continuous wave light was observed in a twin-ridge Fabry-Perot amplifier (3). Here I consider a coupled system with distributed gain arising from carrier injection by pumping current into twin stripe contacts. The active device is composed of two coupled traveling wave semiconductor laser amplifiers. In this system self-switching arises from self-phase modulation (SPM) associated with optically induced saturation of the gain. A schematic is shown below.



In addition to the optical gain I also include nonlinear absorption (two-photon absorption TPA) and waveguide dispersion.

MATERIALS

Materials of interest are the III-V semiconductors. In particular, materials such as InGaAs are of value because their bandgap lies in the .8 to .9 μm spectral

region. These materials can form the basis of strained layer heterostructures which offer band gap engineering often not obtainable in lattice matched materials. Important parameters such as the well/barrier combination, the level of strain and the material concentration in the layers can be varied to modify the physical parameters such as the band gap, electro-optic and optical properties.

In the InGaAs/GaAs materials the InGaAs material is the well material and the GaAs is the barrier material (4,5). In thin layers the lattice mismatch induces internal strain rather than dislocations (6,7). This strain affects the structural aspects of the materials and influences their electronic properties through strain induced changes of the band structure (8,9). The smaller band gap InGaAs well material is under compression and the GaAs barriers are unstrained. However for small amounts of Indium in the material, the barrier heights are relatively low, thus making the superlattice effects more prominent (10). Furthermore, these are ternary compounds without the additional complication of added phosphorous as in the common compound InGaAsP.

The gain of the semiconductor is a significant parameter. The subband-to-subband optical gain is given by (11)

$$g_{nm}(\hbar\omega) = \frac{4\pi^2 e^2 \hbar}{n_0 c m_0^2 W \hbar\omega (2\pi)^2} \int d\mathbf{k} \sum_{\sigma} |\hat{\epsilon} \cdot \mathbf{P}_{nm}^{\sigma}(\mathbf{k})|^2 \\ \times \delta(E_n^e(\mathbf{k}) - E_m^h(\mathbf{k}) - \hbar\omega) [f^e(E_n^e(\mathbf{k})) - f^h(E_m^h(\mathbf{k}))]$$

where n_0 is the index of refraction, c is the speed of light, W is the quantum well width, $\hbar\omega$ is the photon energy and the f 's are the distribution functions for electrons in the conduction and valence bands. The total material gain is obtained by summing over all subbands n,m and integrating against a Lorentzian function (12),

$$g(E) = \int dE' \sum_{nm} g_{nm}(E') \Delta(E - E').$$

The radiative current density is evaluated from the dipole transition rate (13) for the quantum-confined carrier states,

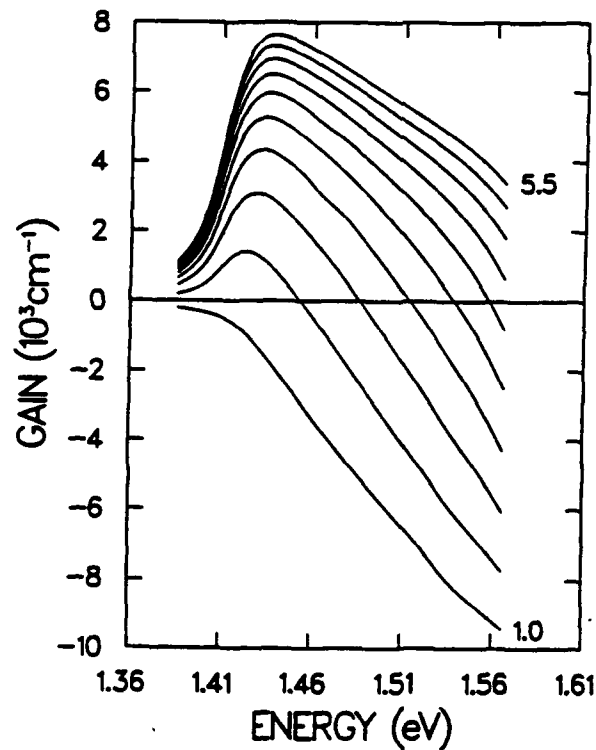
$$R_{sp} = \int d(\hbar\omega) \frac{4e^2 n_0 \hbar\omega}{3m_0^2 c^3 \hbar^2} \frac{1}{(2\pi)^2} \sum_{nm} \int dk \sum_{\sigma} |P_{nm}^{\sigma}(k)|^2 \\ \times \delta(E_n^e(k) - E_m^h(k) - \hbar\omega) [f^e(E_n^e(k))][1 - f^h(E_m^h(k))] ..$$

At low concentrations the carriers obey Boltzmann statistics with the current being proportional to the square of the injected carrier density n . But at higher carrier densities the emission rate falls off from the n^2 curve (11).

However the light only experiences optical gain in the well region, as a result it is convenient to characterize the gain by a confinement factor given by

$$\Gamma = N\gamma W.$$

where N is the number of quantum wells used in the multiquantum well structure, W is the width of each well and γ is the optical confinement per unit width of quantum well. A gain curve for InGaAs materials is shown below for 50 Å wells for various carrier injections (11).



MODE EQUATIONS

I consider an active system composed of two parallel travelling-wave semiconductor amplifiers with distributed gain arising from carrier injection by pumping current into twin stripe contacts. The input beam is injected into channel 1 and the gain of each amplifier is adjusted by varying the pumping current I (assumed the same for both waveguides). The electromagnetic field is a superposition of the modes of the isolated single-mode waveguides given as

$$E(x, y, z, t) = \frac{1}{2} \sum_{j=1}^2 [f_j(x, y) A_j(z, t) \cdot \exp \{i(\beta z - \omega_0 t)\} + \text{c.c.}]$$

where A is the slowly varying envelope of the electromagnetic field. The linear coupling between the two modal amplitudes is provided by the evanescent overlap of the two waveguide modes. The coupled equations are given by

$$\left[\frac{\partial}{\partial z} + \frac{1}{V_g} \frac{\partial}{\partial t} \right] A_1 = i\kappa A_2 + \frac{1}{2}(1 - i\alpha)g_1(N_1)A_1$$

and

$$\left[\frac{\partial}{\partial z} + \frac{1}{V_g} \frac{\partial}{\partial t} \right] A_2 = i\kappa A_1 + \frac{1}{2}(1 - i\alpha)g_2(N_2)A_2.$$

where k is the linear coupling coefficient, α is the linewidth enhancement factor, and the g 's are the intensity gains (dependent on the carrier densities, N). The linewidth enhancement factor is a constant independent of density. When $k=0$ the expressions reduce to an uncoupled semiconductor amplifier (14,15,16). For a one coupling length device light will transfer from guide 1 to guide 2 without distortion in the linear limit. When the optical pulse duration exceeds the intraband relaxation time, the induced polarization can be eliminated and the field matter interaction is given by a set of coupled field carrier rate equations. The carrier densities for the semiconductors obeys the rate equations (14,16) given by

$$\frac{\partial N_j}{\partial t} = \frac{I_j}{qV} - \frac{N_j}{\tau_c} - \frac{g_j(N_j)}{\hbar\omega_0} |A_j|^2$$

where I is the injection current, q is the electron charge, and V is the cavity volume. A linear dependence of the gain on the carrier density is used (17)

$$g_j(N_j) = \Gamma a(N_j - N_0) \quad j = 1,2$$

where N_0 is the transparency carrier density.

A cross section averaged gain relaxation equation is used since the waveguide dimensions are smaller than the carrier diffusion length(19)

$$\frac{\partial g_j}{\partial t} = -\frac{(g_j - g_0)}{\tau_c} - \frac{g_j}{E_{\text{sat}}} |A_j|^2 \quad j = 1, 2$$

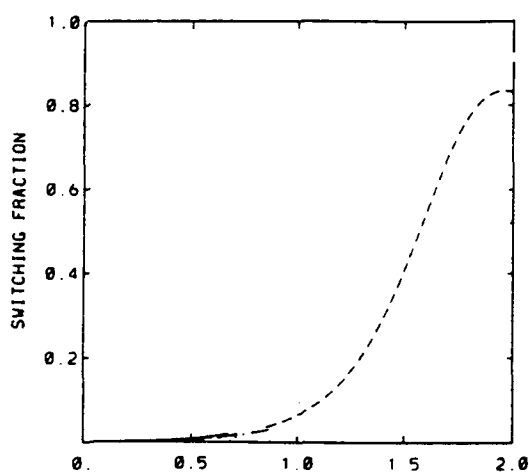
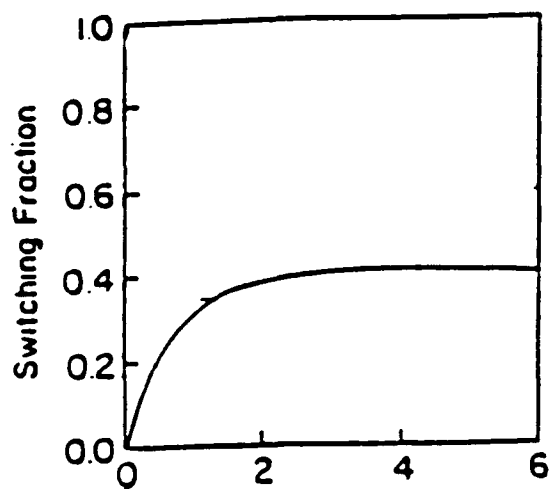
where E_{sat} is the saturation energy, I_0 is the transparency current and g_0 is the small signal gain. A one coupling length device is considered so that at low input intensities the light exits through the opposite waveguide. It is assumed that the width of the pulse is much less than the carrier lifetime. As a result the amplifiers are determined by the small signal gain and the linewidth enhancement factor. Experimental values of the linewidth enhancement factor is about 6 (18). If the nonlinear absorption and dispersion are neglected, the optical switching performance is limited to 50% of the output energy (19).

NUMERICAL RESULTS

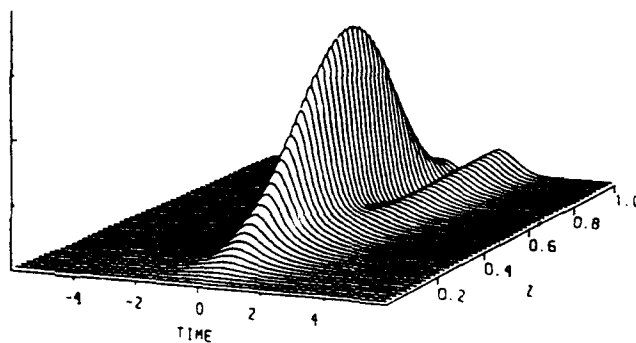
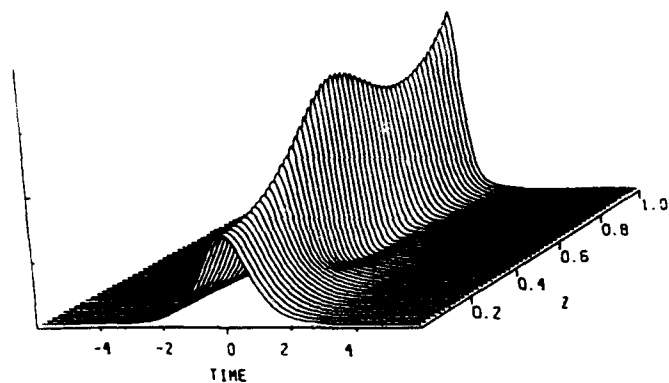
However dispersive and absorptive factors are important in semiconductor devices. Therefore I incorporate these features and study their behavior using the numerical beam propagation method (NBP). This numerical procedure uses the fast Fourier transform to calculate the propagating field for a distance $d/2$ with dispersion only and then one

multiplies the result by a nonlinear term representing the effect of the nonlinearity over the whole segment d and again propagates the field for the remaining distance with dispersion only.

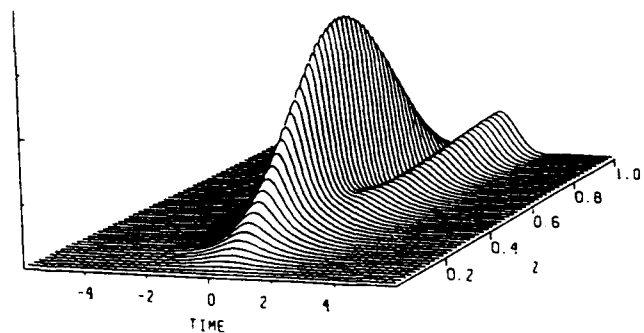
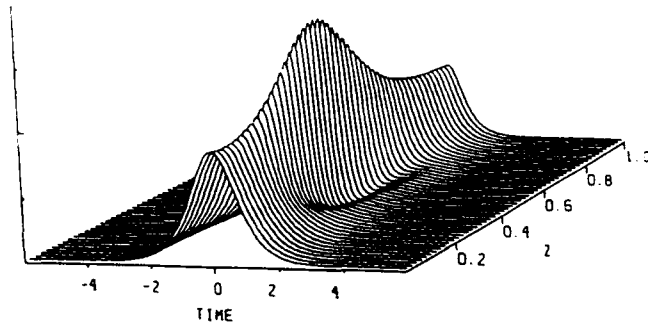
Using the NBP method, I have investigated the behavior of the semiconductors. The figure below shows the switching fraction as a function of input. The portion on the left side corresponds to no dispersion (with less than 50% of the light switching) whereas the right side includes the effects of dispersion (with about 80% of the light switching). The dispersion balances the pulse distortion caused by the self phase modulation. This results in significant improvement in waveguide performance and is an important consideration for future applications.



In semiconductors the effects of nonlinear absorption can cause distortion and loss. Therefore I have also investigated this effect. The figure below shows the effects of high power without the presence of the nonlinear absorption effects. On the left side the light input to one waveguide is amplified and remains largely in that guide. On the right side I show the opposite waveguide where little light has been transferred. This figure shows good behavior for the semiconductor devices and represents a significant result in this study.



Next I investigate the effects of the nonlinear absorption on the semiconductor. The figure below shows the new behavior. On the left side the light is amplified and then decays as the absorption takes place. On the right side the light is more of the light is transmitted and the pulse shape is deteriorated. As a result one realizes that wavelengths where the nonlinear absorption is minimized must be used.



SUMMARY

I have investigated the behavior of semiconductor amplifiers for electrooptic devices. Including more realistic physical parameters enables better device characteristics. Future investigations involve the effects of the gain saturation, the variation of the semiconductor alloy concentration, the number of quantum wells and the well and barrier width. Waveguide fabrication can be performed at WPAFB and semiconductor waveguides measured optically for waveguide loss and performance.

References

1. S. M. Jensen, IEEE J. Quantum Electron. QE-18, 1580 (1982).
2. C. J. Setterlind and L. Thylen, IEEE J. Quantum Electron. QE-22, 595 (1986).
3. D.A. H. Mace, M. J. Adams, J. Sing, M.A. Fisher, I.D. Henning and W. J. Duncan, Electron. Lett. 25, 987 (1989).
4. G. C. Osbourn, J. Vac. Sci. Tech. 21, 459 (1982).
5. S. T. Picraux, L.R. Dawson, G.C. Osbourne and W.K. Chu, Appl. Phys. Lett. 43, 930 (1983).
6. J. W. Matthews and A.E. Blakeslee, J. Cry. Growth, 27, 118 (1974).
7. G. Bastard, C. Delalande, Y. Guldner and P. Voisin, Advances in Electronics and Electron Physics, P. W. Hawkes, ed, (Academic Press, NY, 1988).
8. F. H. Pollak and M. Cardona, Phy. Rev. 172, 816 91968).
9. J. Y. Marzin and J. M. Gerard, Superlattices and Microstructures, 5, 51 (1989).
10. K. J. Moore, G. Duggan, K. Woodbridge, and C. Roberts, Phys. Rev. B 41, 1090 (1990).
11. J. Loehr, Theoretical Studies of Pseudomorphic Quantum Well Optoelectronic Devices, Technical Report N. SSEL-202, 1991.
12. G. D. Sanders and Y. C. Chang, Phys. Rev. B 35, 1300 (1987).
13. J. J. Sakurai, Advanced Quantum Mechanics (Addison-Wesley, New York, 1967).
14. N.A. Olsson and G.P. Agrawal, Appl. Phys. Lett. 55, 13 (1989).
15. G.P. Agrawal and N.A. Olsson, Opt. Lett. 14, 500 (1989).
16. G.P. Agrawal and N.A. Olsson, IEEE J. Quantum Electron., 25, 2297 (1989).

17. G.P. Agrawal and N.K. Dutta, Long Wavelength Semiconductor Lasers
(Van Nostrand, New York, 1986).
18. M. Osinski and J. Buus, IEEE J. Quant. Electron. QE-23, 9 (1988).
19. S. Trillo, S. Wabnitz, J. M. Soto-Crespo and E. M. Wright, IEEE J. Quantum Electron,
27, 410 (1991).

**PHOTOCONDUCTIVITY AND RELATED STUDIES OF THE LADDER POLYMER
POLYBENZIMIDAZOBENZOPHENANTHROLINE (BBL)**

**Barney E. Taylor
Visiting Assistant Professor
Department of Physics**

**Miami University - Hamilton
1601 Peck Blvd.
Hamilton, OH 45011**

**Final Report for:
Summer Faculty Research Program
Wright Laboratory
WL/MLBP**

**Sponsored by:
Air Force Office of Scientific Research
Bolling Air Force Base, Washington, D.C.**

September 1993

**PHOTOCONDUCTIVITY AND RELATED STUDIES OF THE LADDER POLYMER
POLYBENZIMIDAZOBENZOPHENANTHROLINE (BBL)**

**Barney E. Taylor
Visiting Assistant Professor
Department of Physics
Miami University - Hamilton**

Abstract

Polybenzimidazobenzophenanthroline (BBL) is a ladder polymer that offers hope of electronically conducting polymers for future applications. Some of the electro-optical properties of BBL have been investigated by photoconductivity and related measurements. BBL exhibits a characteristic spectrum, with a low-energy peak near 1.8 eV, and other structure. The dependence of the BBL spectra upon chopping frequency of the pump beam and applied electric field has been investigated. The PC response of BBL was found to be dependent upon both; however, the chopping frequency dependence is the more interesting. At low chopping frequencies (~ 10 Hz), a single exponential behavior was observed, while at higher chopping frequencies an inverse power law response was noted.

Attempts were made to measure the carrier lifetime and mobility of BBL by pulsed laser, time of flight experiments. Instrumental limitations caused limited success, however, a photo-induced transient signal was observed that is believed to be characteristic of BBL.

PHOTOCONDUCTIVITY AND RELATED STUDIES OF THE LADDER POLYMER

POLYBENZIMIDAZOBENZOPHENANTHROLINE (BBL)

Barney E. Taylor

Introduction

Electrically conductive polymers offer great hope for the technology of the future. Some of the improvements would be reduced aircraft weight and greater latitude in manufacturing technology - such as vacuum forming of conducting assemblies. The polymers of the future are under development today. Ladder polymers have much greater thermal stability and mechanical strength compared to conventional doped conducting polymers.¹ This document reports on the research performed on the electro-optical characterization of the conducting ladder polymer BBL (polybenzimidazobenzophenanthroline) by means of photo-conductivity (PC) and related techniques. The research had three major components: a study of trap lifetime in BBL by means of photoconductivity measurements; a study of the effect of various electric fields on the BBL PC spectrum; and a beginning investigation of the mobility of the majority charge carriers in BBL by a time of flight technique. Each of these components will be addressed separately. The experimental apparatus had to be upgraded to allow the studies to be performed. A summary of the enhancement to the experimental capability is in the Appendix.

EXPERIMENTAL AND DATA

The experiments were performed on cast BBL samples. Two different types of samples were used: 10 micron thick, free standing films, and a 1 micron film that was cast upon a glass substrate. Samples were masked with a shadow mask of approximately 1mm width and sputtered with gold/palladium electrodes to form contacts. The thinner sample was originally cast to allow the absorption coefficient of BBL to be determined from UV-VIS spectrometer measurements. Since much was already known about the sample, it seemed ideal for photoconductivity studies. The thicker free standing films were used for

some of the initial PC measurements and for the lifetime measurements that used the pulsed dye laser. Wires were attached to the sample with conducting silver paint, and the free standing samples were taped to clean glass substrates to provide support for the wires and prevent tearing of the film.

Dependence of BBL PC on Chopping Frequency

A study of the feasibility of performing PC measurements on BBL and similar prototype polymers indicated that the best PC spectra were obtained with the longest period chopping frequency of the probe light beam ². Once the experimental apparatus had been upgraded to be under computer control, a series of experiments aimed at investigating this behavior were performed on BBL samples. The chopper's speed can be externally controlled by applying a dc voltage to its control input. The experimental technique was to have the lock-in amplifier control the chopping frequency by means of the digital to analog output of the lock-in. The lock-in's reference frequency and filter frequency were tuned to the new chopping frequency (which was applied to the lock-in's external reference) under computer control. The actual chopping frequency was determined by having the lock-in report its reference frequency. The earlier conclusion that lower chopping frequencies leads to larger PC signals held true. In order to have a good signal to noise ratio for tuning the lock-in amplifier, the reference frequency was set at about one fourth of the maximum chopping rate, and an auto-tune was performed. Typically 256 measurements of both the in-phase and quadrature components of the lock-in output were acquired at each chopping frequency. The mean and standard deviation of each component of the PC was stored in a data file. The chopping frequency was altered in a predetermined manner and another set of data was obtained. A delay of two minutes was allowed for settling after an auto-tune or sensitivity change of the lock-in, and a 15 second delay occurred after the chopper speed was changed before tuning the reference channel and filters of the lock-in to the new chopping rate. Normally, the program delayed for a factor of fifteen times the time constant of the lock-in after re-tuning the reference channel before the data acquisition process was begun. A broader range of chopping frequencies can be obtained by slowing the rotational rate of the chopping blade. The inertia of the blade keeps the chopper spinning at

rates that are below the onset of rotation for an increasing control voltage. Hence, most of the chopping speed experiments were performed with decreasing chopper frequency throughout the scan to obtain data over a wider range of chopping frequencies.

The available ranges of the chopper were from 4 to 40 Hz and 40 to 400 Hz in switch selectable ranges. Studies were performed at several wavelengths. Figure 1 shows a typical result of a chopping speed run over the frequency range of 4 to 40 Hz at a wavelength of 581 nm of a free standing BBL film. Symbols indicate the magnitude, in-phase and quadrature components, and the solid line is the best fit line to the magnitude of the PC response assuming a single exponential decay. The agreement between the line and the magnitude implies a single decay time is the dominant factor for this chopping frequency range. Figure 2 shows the corresponding graph for the 40 to 400 Hz chopping rate range. Here the magnitude did not fit an exponential decay, but yields an inverse power law dependence, indicating that there are numerous mechanisms affecting the lifetime of the photoinduced carriers. Possible mechanisms will be addressed in the discussion. It is evident that combining the two orthogonal components of the lock-in output reduced the scatter in the chopping rate profile.

Figure 3 shows the effect of wavelength on the low frequency chopping study for the thin sample on the glass substrate. The data is presented on a semi-logarithmic graph, and has been normalized to account for the difference in the photon flux at the various wavelengths. The wavelengths used are given in the legend. It is interesting to note that the lines are reasonably parallel for wavelengths whose energy lie above the band gap energy of BBL.

The dc conductivity in BBL has been observed to change significantly when a sample is studied over an extended period of time³ or with temperature changes⁴. Hence it was decided to perform a repeated scan of the chopping frequency dependence experiment in the 40 to 400 Hz range at a single wavelength that is just inside the bandgap of BBL. The results of that study are shown in Figure 4. As in Figure 2 the scans yield reasonable fits to a power law equation. The photoconductivity increased with each successive scan through the various chopping frequencies, and the power law dependence changed from essentially a chopping period (inverse frequency) dependence to a

frequency to the negative two-thirds dependence. Each of the scans required approximately two hours to complete and the experiment lasted overnight with the sample being exposed both to light above the band gap energy and a continual electrical bias. Another, essentially identical, experiment was started the following morning, yielding the results shown in Figure 5. Several items are quite striking when compared to Figure 4: The PC drops during subsequent scans of the sample, while it increased in Figure 4. The feature at approximately 350 Hz is more pronounced and quite reproducible. Finally, the behavior is no longer fit by a single power law. The frequency range 40 to 120 Hz is fit by one power exponent, and the 120 to 240 Hz region is fit by another. The break in the segments was chosen by visual inspection of the data. Frequencies above 240 Hz were excluded from the fitting due to the "feature" centered at approximately 350 Hz. Possible causes of this behavior will be discussed later.

Electric Field Effects Upon the PC of BBL

This component investigated the dependence of PC spectra obtained from BBL on the value of the applied electric field. The usual bias battery was replaced with a Keithley 237 Source Measurement Unit, so that a range of different bias voltages could be investigated. The results are summarized in Figure 6 which is a plot of photoconductance versus photon energy. Several features of the graph are quite noticeable: the spectra with the lower levels of noise were obtained at bias voltages of 5 and 10 volts. The feature at about 1.8 eV exhibits strange behavior in that 37.5 and 90 V scans have almost identical amplitudes. However the higher energy portions of the two spectra differ greatly in amplitude (but with a similar shape). The 50 and 67.5 volt bias scans yielded the same response at 1.8 eV, but the 67.5 volt scan had the largest feature of any studied in the 3 eV region. This behavior will be discussed later.

Time of Flight Mobility Measurements

These experiments were performed using the Laser Photonics nitrogen pumped dye laser with Rhodamine 610 dye operating at its peak wavelength of 610 nm. In the classic time of flight experiment, the light is flashed upon an

extended sample and the delay between the flash and the observation of the photoinduced current at a different position allows one to calculate the mobility. Due to the relatively small conductivity of the BBL samples, this investigation was not as straight forward. The quiescent current through the BBL sample was typically 2 nA with reasonable bias levels. The photoinduced peak was typically on the order of 2 to 20 pA, at laser levels that did not damage the sample. The signal was detected by a Lecroy digital oscilloscope with a minimum non-averaged sensitivity of 5 mV/division and a maximum input impedance of 1 megohm. A current of 20 pA dropped across a 1 megohm resistor yields a voltage of only 20 μ V at the scope input so typically 1000 pulses were averaged to enhance the signal above the noise level. A signal was observed only when the laser spot was near the junction of the two sides of the "cross" shaped BBL sample. The initial intent was to use a "cross" shaped BBL sample with separate bias supplies for each arm of the cross. The longer arm would be illuminated with a laser pulse at various locations, and the resulting photoinduced current would be detected after traveling to the shorter arm. Unfortunately the signal in these preliminary experiments was not sufficient to perform the experiment as planned. Hence a simple two electrode sample was illuminated by the laser pulse and an attempt was made to measure the induced photocurrent. This technique met with success; a decaying waveform was observed when many scans were averaged.

Initially there was some doubt that the observed signal was indeed characteristic of BBL as opposed to the R-C time constant of the scope input. The instrumental component was deduced by adding coaxial cable with a capacitance of about 100 pF/m to the experiment and comparing oscilloscope traces. It was found that the cable did indeed effect the rise time of the peak, especially at longer cable lengths such as 3 m. However the decay was independent of the cable length, and is therefore characteristic of BBL. A typical trace is shown in Figure 7. The trace is the result of averaging the trace obtained from 2000 laser pulses hitting the sample. The vertical scales have been adjusted to cause the tails to be superposed. Clearly both curves share the same decay mechanism. Unfortunately, the decay is not a simple exponential which would give the lifetime of the majority carrier in BBL.

Discussion

Trap Lifetime

The shift in level of the orthogonal components of the PC versus chopping frequency indicated in Figure 1 is not overly surprising. If one assumes that a single process is dominant for the PC observed in the 4 to 40 Hz range, the process of PC can be simplistically thought of as a driven, damped harmonic oscillator. At some frequencies, the PC response will be enhanced - which corresponds to driving the oscillator in phase, and at other frequencies, it will be driving the oscillator out of phase - yielding a significant quadrature component.

The preceding result is not unexpected. In the field of photorefectance, a method of determining the presence of slow traps in semiconductor samples is to acquire a photorefectance spectrum at two widely different chopping frequencies and to compare the quadrature signal.⁵ A large quadrature component at the higher frequency indicates that traps are being filled during the in-phase period and emptying during the quadrature period. If, due to the much more complicated structure of BBL, there are a wide variety of trap levels with different lifetimes available, the results are consistent with both the power law behavior observed at high frequencies and the quadrature component indicating the emptying of previously filled traps. The fastest traps empty almost immediately, while slower traps take longer to empty. At high chopping rates, the slower traps do not have a chance to empty before the probe beam is again allowed to fall upon the sample replenishing traps. Hence, only the charge from the fastest traps is monitored for a high chopping rate. For a lower chopping rate, there is sufficient time for more traps to empty, thus causing a larger current. The question to be answered is whether the behavior observed at the lower chopping range (the single exponential decay) is indeed intrinsic of BBL or is just the lower limit of the experimental measurement capability. The low frequency study was repeated at a variety of wavelengths to see if the characteristic time of the response was dependent upon the wavelength of the probe beam. One would expect some variation - especially for wavelengths whose photon energies are above and below the band gap of the material. Figure 3 shows a family of curves obtained at a wide range of wavelengths. The decay time does indeed vary with

the energy of the probe beam's photons. At this time no quantitative explanation for the variation can be provided. One may speculate that there are a very large number of traps at various energy levels that can be filled by carriers created by the absorption of a photon of appropriate energy. It is not reasonable to a priori expect that all of the traps will have comparable lifetimes.

Field Effect Results

The experimental results shown in Figure 6 are consistent with earlier studies on BBL. Each BBL sample has a threshold bias level for generating a clean PC spectra. Bias levels significantly above the threshold cause a very large increase in the noise of the spectrum. Once the spectrum is noisy, only by removing the bias for a substantial time will the sample return to the previously low noise levels. The chronological order of obtaining the data in Figure 6 is as follows: day one -- 25, 15, 10, 5, 1.5, and 50 V scans; day two -- 2.5, 37.5, 67.5 and 90V. As Figures 4 and 5 show, the photoconductivity of BBL varies with successive scans. This fact coupled with the increase in noise of the entire spectrum once too high a bias has been applied allows one to understand the behavior of the spectra in Figure 6. The first scan at 25 V is relatively noisy compared to the 15 V scan which yielded the same peak at 1.8 eV with a lower noise level. The 10 V scan is near optimum for the very thin sample used in this experiment. The noise level is still lower and the peak intensity is greater than the ratio of the bias levels. On the second day, the 2.5 V bias scan is larger in amplitude than the previous day's 5 V scan, however, it is much more noisy. The 37.5 and 67.5 volt scans yielded significantly more intense peaks at the 1.8 eV feature, and they exhibited greatly differing tails at higher photon energy. The sample subsequently failed so that the measurements could not be repeated with increasing bias, or better yet, with one measurement per day and the remainder of the day to relax from the stress caused by the bias.

The noise increase on all scans above 2.8 eV is primarily due to the throughput of the experimental system. Photons in this energy range are above the peak intensity of the lamp and are much shorter in wavelength than the blaze of the grating in the monochromator. Hence, fewer photons hit the

sample each second, and the unnormalized PC signal is small in comparison to the signal at approximately 2 eV where the photon flux is much greater. The normalization process effectively shifts the higher photon energy portions of the spectrum much more than the lower energy points, leading to a significant increase in the noise level at high photon energies.

The implication from Figure 5 is that the nature of the kinetics changes with repeated measurement at 1.8 eV due to the two segments in the power law and the shift between the curves. It is possible that very long lifetime traps are being affected by the presence of the electric field as the experiment progresses. Certainly more work on this phenomena is needed.

Lifetime Studies

The decay of the photocurrent indicated in Figure 7 is surprisingly long, especially if viewed from a semiconductor background. The curve shows gradual curvature when viewed on a semi-logarithmic plot, indicating that a single mechanism is not responsible. This is consistent with the earlier observations from the chopping frequency studies. At the moment, the experiment is instrumentally limited due to the lack of an appropriate high speed current to voltage amplifier. While possible sources have been explored, such amplifiers are not readily available. Using several cascaded high gain MMIC (monolithic microwave integrated circuit) amplifiers as a preamp for the oscilloscope has been tried. However, the 50 ohm input impedance of the amplifiers more than offset their gain, yielding a less usable signal than without the amplifier.

SUMMARY AND SUGGESTIONS FOR FURTHER STUDY

BBL is a very interesting material. Slowly it is revealing its nature to probing by electrical and electro-optical means. It is clear that for whatever reason, the observed photoconductivity signal increases with an increase in the period (decrease in the frequency) of the probe beam. Although there is no a priori reason to assume that a single exponential behavior should work for a material as complex as BBL, it does fit quite well for frequencies below 40 Hz. That the kinetics are sufficiently complicated to cause the magnitude of the PC to fit a power law at higher frequencies is

not too surprising. At this time little is known about the significance of the power law exponents determined by the nonlinear least squares fitting. That polymers have long term responses to optical excitation has been recently documented in the "persistent photoconductivity" effect.⁶ Other members of the processing and properties group have been involved in the careful characterization of the dc conductivity of BBL. Routinely, large variations occur during extended measurements of BBL conductivity samples without and direct cause. In the predecessor to this study, it was observed that the dark current of a BBL sample could change by a factor of two in a very short time.⁶ Eventually it would relax toward its previous level. One possible explanation could be a change in the humidity in the laboratory due to a shift in the climate control. Some other preliminary experiments were performed before choosing the topics for the present study: A drop by a factor of 50 in the magnitude of the PC at 1.8 eV was observed over about 40 seconds when the cryostat containing the sample was evacuated to a fore pump vacuum. The recovery was even more impressive. Unfortunately, experimental limitations prevented the project from being further pursued. Certainly something in the ambient environment of BBL has a great effect on its electrical and photoconductivity.

Relatively crude measurements on the temperature dependence of BBL have been performed. It is well known that "heat treating" (annealing for a short time at about 600 K) will cause a short term increase of many orders of magnitude in the dc conductivity of BBL with a residual increase of about one order of magnitude.⁴ The photoconductivity also shows the same trends.^{2,7} Switching noise from the temperature controller for the cryostat prevented a systematic investigation of the photoconductivity of BBL, as the induced noise was much greater than the ac photocurrent in the temperature range of room temperature to about 125 °C.

These preliminary results should be followed up by detailed studies on the temperature and ambient environment's affect on the photoconductivity of BBL. A suitably fast current to voltage amplifier is needed to make good progress on the mobility/lifetime study. One possibility is to try the mobility experiment on a BBL sample at a high temperature such as 300 °C.

REFERENCES

1. F. E. Arnold and R. L. Van Deusen, *Macromolecules* 2, 497, (1969).
2. K. S. Narayan, et al., *Bull. Am. Phys. Socl*, 38, 110 (1993).
3. S. J. Bai, Private Communication.
4. C. S. Wang, C. Y. C. Lee, F. E. Arnold, *Mat. Res. Soc. Symp. Proc.*, 247, 747 (1992).
5. O. J. Glembocki, Private Communication.
6. C. H. Lee, G. Yu, A. J. Heeger, *Phys. Rev. B*, 47, 15543, (1993).
7. B. E. Taylor, "Investigation of Photo-conductivity in Ladder Polymers", *Contributive Research & Development*, 66, (1992).

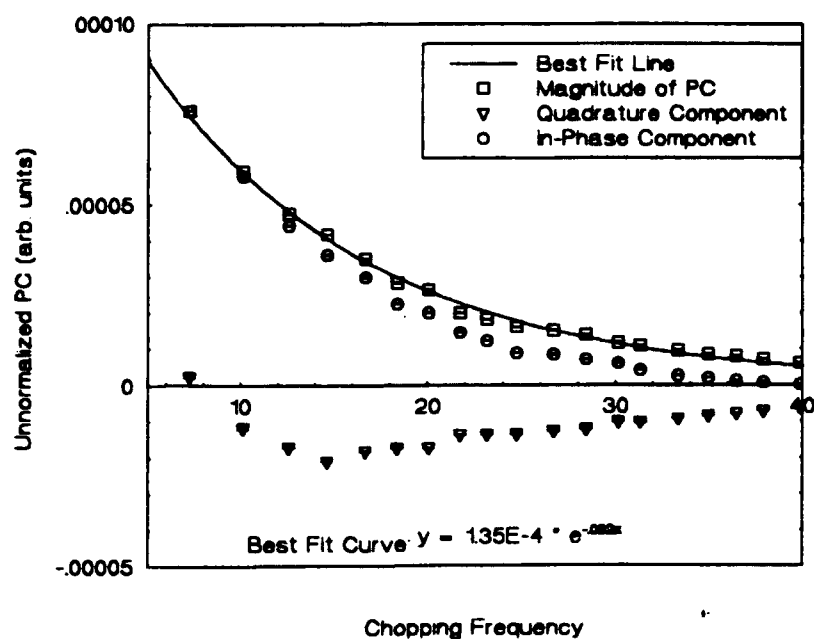


Figure 1. Photoconductive spectrum of a free standing BBL film as a function of chopping frequency at 581 nm. The magnitude was obtained from the two orthogonal components of the PC. The solid line is a best-fit single exponential decay that yielded a mean decay time of 82 ms.

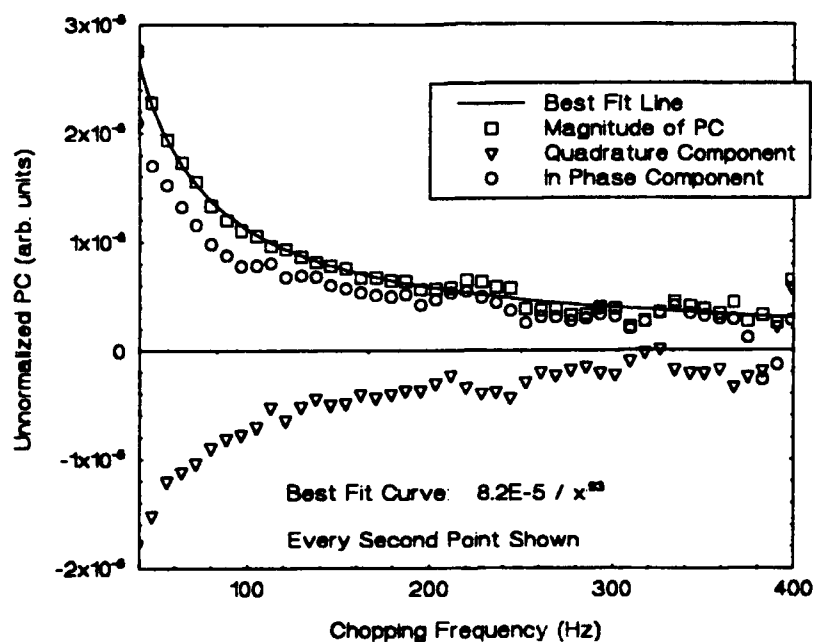


Figure 2. PC of free standing BBL at 581 nm as a function of chop frequency in the 40 to 400 Hz range. The signal to noise ratio is degraded due to the smaller signal observed at these frequencies. The solid line is a power law fit to the magnitude with a best-fit exponent of -0.93.

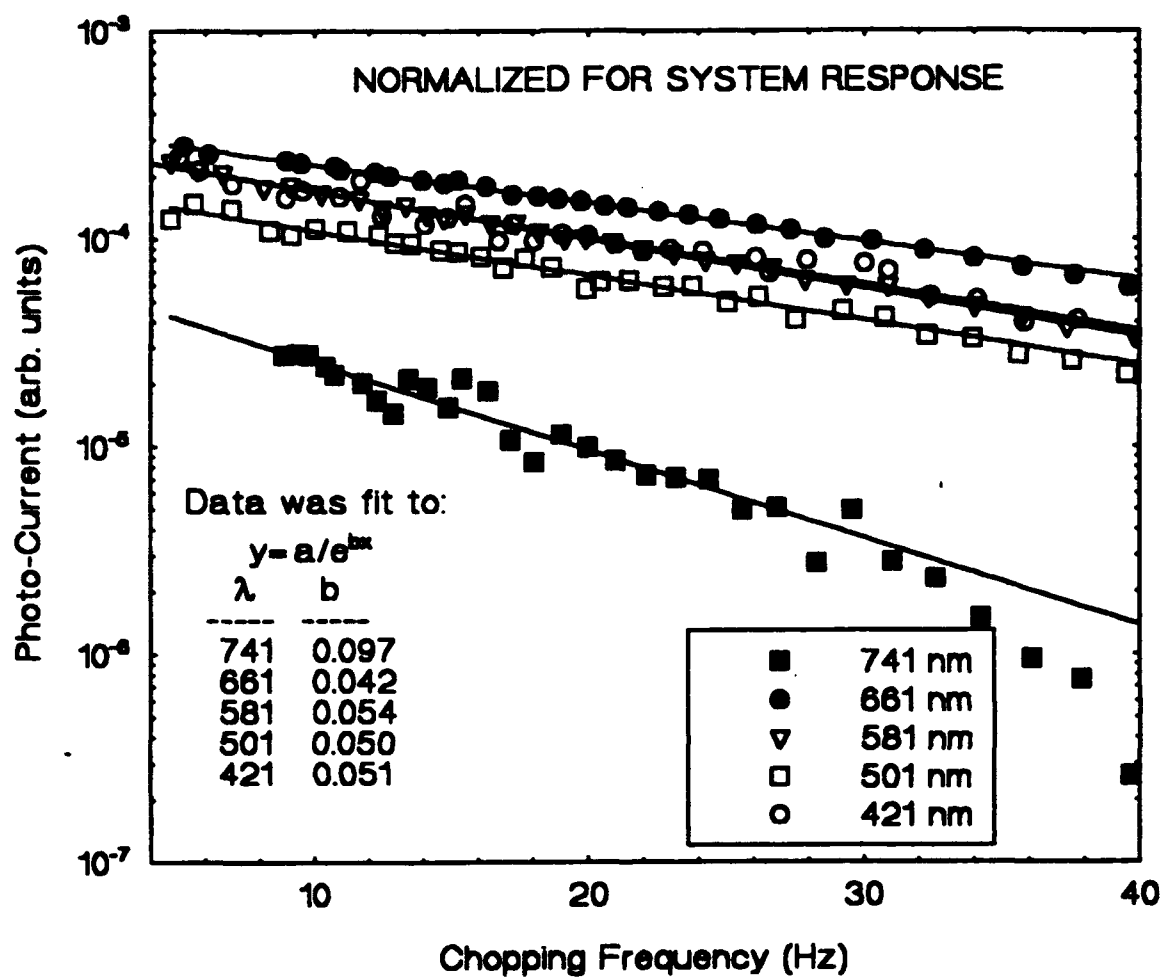


Figure 3. Photoconductivity as a function of chopping frequency for various wavelengths of the thin BBL sample cast on glass. The data was obtained with a bias of 9 V. The data has been fit to a single decaying exponential, and the resulting best-fit decay time is given in the inset table.

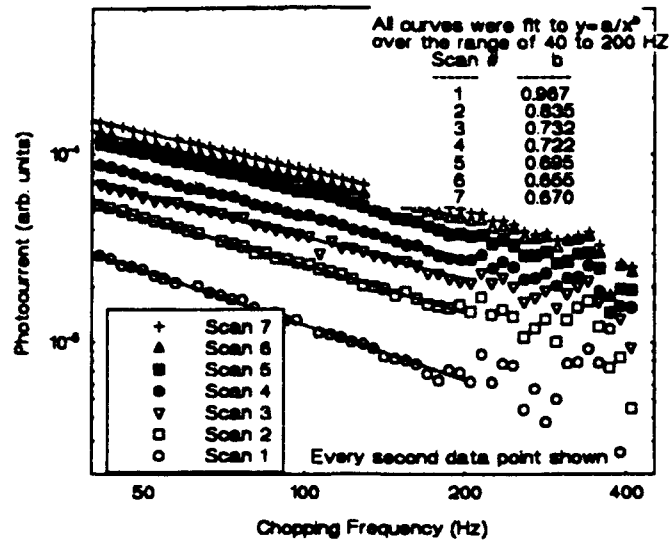


Figure 4. Repeated scans PC of the thin BBL sample that was cast on glass at 672.5 nm. The data covers the 40 to 400 Hz chopping frequency range and shows an increase in the PC with successive scans. The solid lines are the best fit curves for an inverse power law. The exponents are given in the inset table.

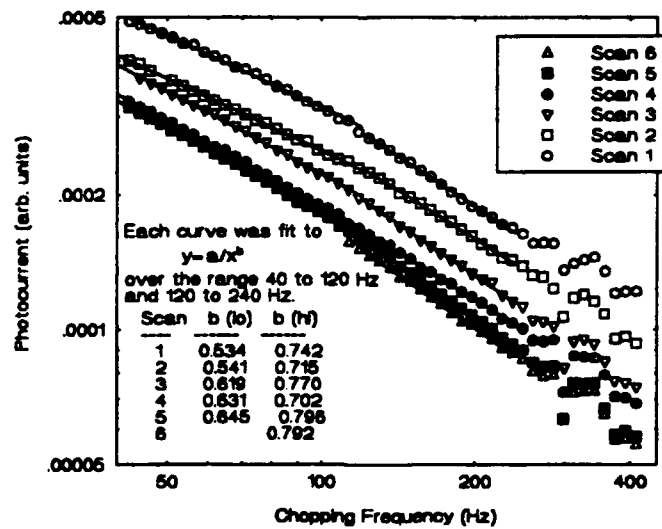


Figure 5. The same experiment of Figure 4 repeated on the next day. The sample had been exposed to light of energy higher than the band gap and an electrical bias of 9 V for approximately 24 hours. The inverse power law is seen to be two segmented. The PC dropped with each successive scan. The best-fit exponents are given in the inset table. The feature at about 350 Hz is quite prominent and reproducible.

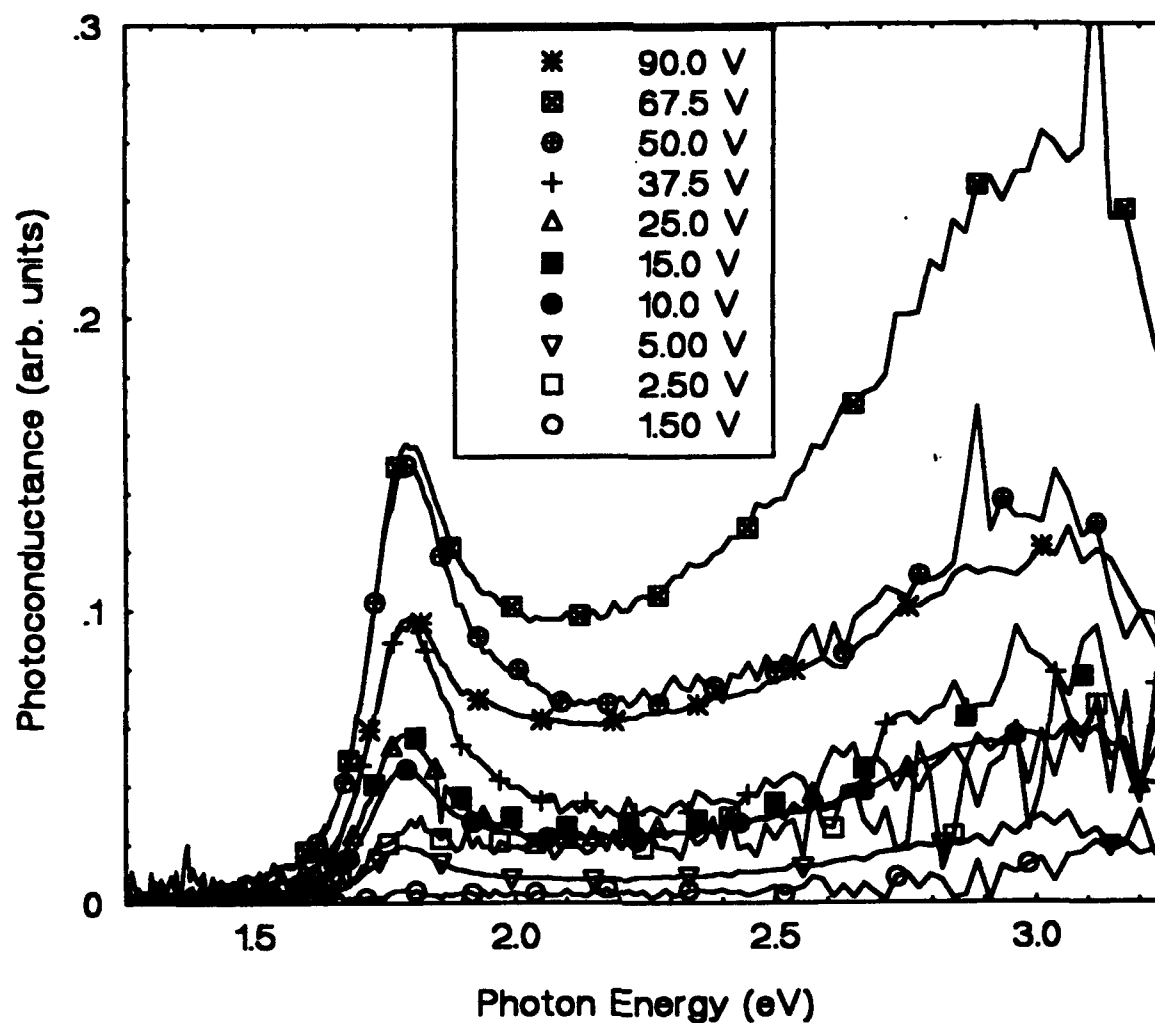


Figure 6. Field effect for the BBL on glass sample. The data has been normalized for incident photon flux, and for the applied bias, yielding photoconductance per incident photon. There are significant differences between successive spectra in both amplitude of the 1.8 eV feature and the relative intensity of the 3 eV shoulder compared to the 1.8 eV peak.

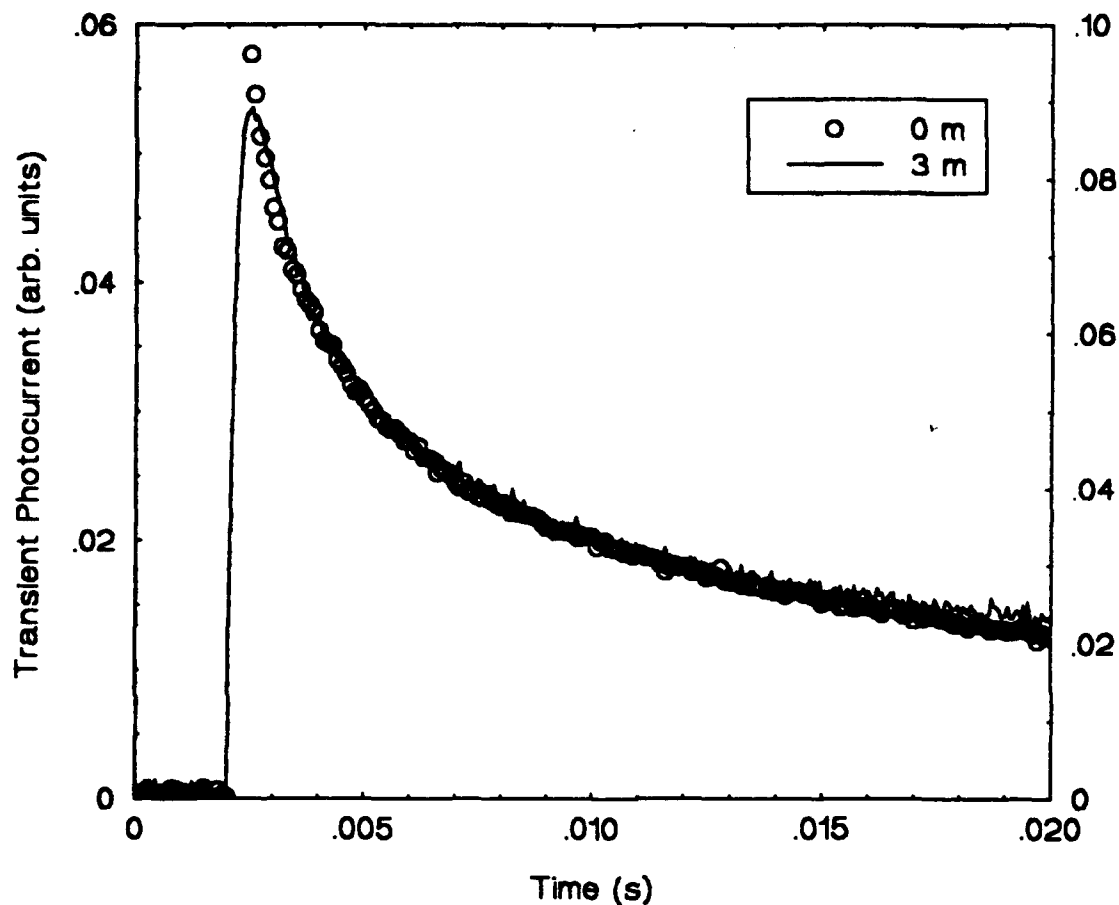


Figure 7. Transient photoconductivity in a BBL sample. The sample was irradiated with 200 microJoule pulses from a nitrogen pumped dye laser operating at 610 nm while the sample was biased by a 300 V battery. Two experiments are presented. One has the sample mounted on the input of the digital oscilloscope, and the other has 3 m of coaxial cable inserted (with a capacitance of about 300 pF). Each set of data is the result of averaging the signal obtain during each of 2000 laser pulses. The vertical scales of the two traces have been adjusted so that the curves overlap. It is obvious that the two decay regions are from the same phenomena and have been attributed to BBL. The rising regions are believed to be instrumental due to the much lower rise time when the coaxial cable was inserted.

APPENDIX

EXPERIMENTAL CAPABILITY ENHANCEMENT

Photoconductivity

Previously, a "building block" photoconductivity (PC) system had been assembled to demonstrate the viability of PC measurements on prototype conducting polymers such as BBL⁷. The previous apparatus was serviceable, but required much user interaction, and lacked the capability of automated data acquisition. Based on the success of the earlier study, newer building blocks were procured that offered the possibility of automated data acquisition. The existing one meter monochromator was replaced by a 0.5 meter monochromator with double the optical throughput of the larger unit. The new Spex 500M monochromator came with a "smart" controller and data logger unit. The smart controller was used to communicate with the data logging and control computer via a RS-232 interface. The computer is capable of setting the monochromator to any wavelength and controlling the scan.

The lock-in amplifier was upgraded to an IEEE-488 compatible, dual phase unit with a matching current to voltage preamplifier. The new system greatly reduced the electrical noise in the observed PC data. The PC signal is sent to the computer via the IEEE-488 bus. This lock-in also offers control of its settings via computer, and most importantly, verification of the current settings at the time of data acquisition. The digital to analog output (DAC) has been used to control the rotational rate of the SRS model 540 chopper, allowing a new level of experimental flexibility.

The existing tungsten-halogen lamp was supplemented with a xenon short arc lamp and power supply to provide greater light output in the blue to near ultraviolet wavelength ranges where the signal to noise ratio rapidly decreases. The data analysis programs must take into account the intensity profile of each light source before normalized conductivity spectra can be generated from the raw data.

The new system has been set up to average a number of data values at given wavelength increments. The new program offers two distinct improvements: the user is certain of the wavelength, and the averaging

increases the signal to noise ratio of the PC spectrum, allowing finer details to be ascertained from the spectrum.

At present, only the bias voltage, preamp gain, lamp settings, and slit widths must be recorded manually with each run. The user chooses the wavelength range, and increment when queried by the computer. All other information is sent to the data acquisition computer as the scan is begun. Once a lamp has been characterized at given current-voltage settings, a normalization program for those settings is compiled. The normalization program then takes the raw current versus wavelength data and generates a photoconductance per photon versus photon energy output file that is already formatted for display using a commercial graphics package.

Mobility Determination

The time of flight technique for determining the mobility of charge carriers in semiconductors is a standard technique. An experimental system to perform those measurements is in a developmental stage. Laser Photonics nitrogen pumped dye laser provides 200 μ Joule pulses at selectable wavelengths with very narrow pulse widths. A Lecroy 4 GHz digital oscilloscope is used to capture the transient photoinduced waveform when the laser pulse is allowed to fall upon a biased polymer sample. Due to the relatively small values of the photoinduced current (typically 2 pA or less), a high speed current to voltage amplifier is needed to have sufficient signal for the oscilloscope to have an adequate signal to record and average. Several attempts at building or adapting an existing amplifier to serve the purpose have failed. A much faster amplifier is presently being procured, which should enable the experiment to be performed successfully. Much useful information has been gained by the trials already performed. Unexpected the 200 μ J dye laser pulse ablated and burned the surface of the polymers - especially when focused to a line or point. When focused to a point, a 10 mm BBL film was perforated in fewer than 100 pulses. Without a suitable amplifier, 1000 pulses are typically required for a minimal transient signal to be averaged out of the noise.

**A High Voltage One-Shot Switch Implemented With a FET Current Source and
Avalanche Diode**

**Thomas A. Baginski
Associate Professor
Department of Electrical Engineering**

**Auburn University
200 Broun Hall
Auburn University, Alabama 36849-5201**

**Final Report for:
Summer Research Extension Program
Wright Laboratory**

**Sponsored by:
Air Force Office of Scientific Research
Boiling Air Force Base, Washington, D.C.**

and

**Auburn University
September 1993**

ABSTRACT

The description of a novel circuit which utilizes a FET current source and high voltage diode to realize a simple, inexpensive, one shot high voltage switch is presented. The switch was specifically designed for slapper detonators or other applications where speed, low cost and small size are important. The circuit readily lends itself to implementation in either a discrete component, hybrid or monolithic integrated circuit.

1. Introduction

High voltage switches capable of operating at high speeds are used in a variety of applications. Typically, these switches are triggered spark gap tubes which have a useful lifetime of several hundred to several thousand firings. These configurations are expensive and bulky when compared to a hybrid or monolithic integrated circuit. Also, in some applications the ability of the switch to operate repetitively is not required. The initiation of an explosive is one such example since the switch is destroyed in the blast.

Slapper detonators are one application which require a fast (i.e. low impedance) high voltage switch. This report discusses a low cost, low impedance, small, high voltage switch which is intended to actuate a slapper. The circuit could be manufactured in a discrete component, hybrid or monolithic integrated circuit which would make the configuration especially applicable for use in large volume miniature firing units.

2. Circuit Configuration

A schematic representation of one embodiment of the circuit is shown in *Figure 1*. The configuration consists of a high voltage diode D_1 , a series low resistance load R_L , and a current source comprised of Q_1 , Q_2 , R_{ref} and switch S .

The operation of the circuit is straight forward. The high voltage capacitor C_1 is charged through resistor R_C to a high voltage potential. The function of the switch is to allow the capacitor to discharge through R_L quickly. This requires the current path between C_1 and ground to be changed from a high impedance to a low impedance state as quickly as possible.

The initial biasing point of D_1 is described by

$$I_{RA} = MI_R \quad (1)$$

where I_{RA} is the actual current near the breakdown voltage, I_R is the normal reverse bias current of the diode with no avalanche effect, and

$$M = \frac{1}{1 - (V_R/BV)^n} \quad (2)$$

where M is the multiplication factor, V_R is the reverse bias, BV is the breakdown voltage and n has a value between 3 and 6. A plot of a typical characteristic is illustrated in *Figure 2*.

Diode D_1 is biased at a value of the breakdown voltage BV . At this point the diode will permit any level of current to flow through it. In order to insure that thermal runaway of the junction (which would damage the device) does not occur it is necessary to externally limit the current to a low level. The current source consisting of Q_1 , Q_2 and R_{ref} provides this function.

In the particular circuit that was tested the transistors were matched high voltage n-channel MOSFETs. The equation which relates the drain current (I_D) in the devices to the gate to source voltage (V_{gs}) assuming the device is in the saturation region is

$$I_D = K(V_{gs} - V_t)^2 \quad (3)$$

where K is constant and V_t is the threshold voltage of the device. Since the gate to source potential of both transistors is identical the drain currents of the devices are approximately equal. The value of I_D is

$$I_D = [(V_{supply} - V_{gs}) / R_{ref}] \quad (4)$$

Equations 1 and 3 can be solved simultaneously to yield the gate to source voltage which is required to ensure the diode is on the edge of avalanche breakdown. This V_{gs} can then be substituted into equation 4 to yield the value of R_{ref} to achieve this.

The switching of the configuration is initiated by closing switch S . The supply voltage is then directly coupled to the gates of the two transistors. The high potential on the gate induces a channel region of

very low resistance between the drain and source which essentially connects the drain of Q_1 to ground. The entire potential of the capacitor C_1 is then imposed directly across diode D_1 which drives the current through the diode to an extremely high value. The reverse biased junction absorbs energy equal to the power integrated over time. This value is approximately equal to

$$Q = \int_0^t V_{BV} \times I(t) \times dt \quad (5)$$

where Q is the approximate coupled energy ($V \times I \times \text{time}$).

The change in temperature of the affected volume of the junction of the diode can be calculated from

$$\Delta T = \frac{Q}{C_V} \quad (6)$$

and

$$C_V = \rho V C_p \quad (7)$$

where C_V is the heat capacity of the volume of silicon, ρ is the density of the silicon (2330 kg/m^3), V is the volume of the affected area of the junction and C_p is the specific heat of silicon (712 J/kgK).

Assuming the junction of the device is of typical dimensions used in a standard microelectronic process the effective power coupled to the junction can easily be several thousand watts. The calculated temperature change for such a structure is orders of magnitude greater than the evaporation temperature of silicon (2680°C). What physically occurs is the generation of a plasma arc which consumes the junction. The plasma acts electrically as a short circuit between the top metal contact of the diode and the device substrate. Thus, the diode has been altered to act as a closed switch with very low parasitic impedance.

Once the diode junction has made its transition to the plasma state it acts as a short circuit with an extremely low impedance. The voltage potential of C_1 is now coupled directly to the drain of Q_1 . The magnitude of this voltage is greater than the potential necessary to cause breakdown between the drain and source of transistor Q_1 . Once breakdown occurs, essentially a short circuit exists between D_1 and ground. Thus, a low impedance path exists for charge to flow from C_1

through R_L to ground.

3. TEST CONFIGURATION

The circuit was connected to a stripline to demonstrate proof of concept. A high voltage power supply was used to establish a potential of 2500 volts on the anode of diode D_1 . A commercially manufactured diode with a measured breakdown of 1300V was utilized. However, device parameters (i.e. junction area, interconnect metallization etc.) could easily be optimized for this particular application.

A slapper was fabricated on an alumina substrate as illustrated in *Figure 3*. Alumina is the most commonly used substrate material in hybrid microelectronics, is very inexpensive, and has the widest range of compatible manufacturing materials such as conductor and resistor pastes available. The metal bowtie was screen printed onto the surface using a palladium-silver conductor paste. Over the metal layer a glass dielectric was printed to build up the barrel. A flyer was constructed by applying polyimide into the barrel and then curing the material. Leads were then soldered to the ends of the slapper to permit electrical connection.

The high voltage transistors chosen were standard DMOS elements which are readily available commercially. The measured breakdown voltage between drain and source was 1050V. The switch S was a low impedance mechanical switch.

To demonstrate operation of the circuit switch S was closed and the current flowing through the slapper was measured as a function of time. The current reached a value of 3550A in approximately 150nsec. The bowtie was evaporated and a typical arc was observed. The relatively slow performance of the switch was probably due to the large inductance in the leads of the firing circuit.

4. Hybrid Slapper/Switch Configuration

It is to be noted that an alumina substrate could be utilized as a mounting vehicle for the entire circuit. A conventional slapper could be easily fabricated by depositing a thin metallic film (via e-beam evaporation, sputtering etc.) and patterning the film with conventional

microelectronic photolithographic techniques. A suitable dielectric flyer material would next be deposited and patterned (i.e. polyimide, printed ceramics, glass etc.) The thicknesses and dimensional tolerances of the configuration are easily met by these techniques.

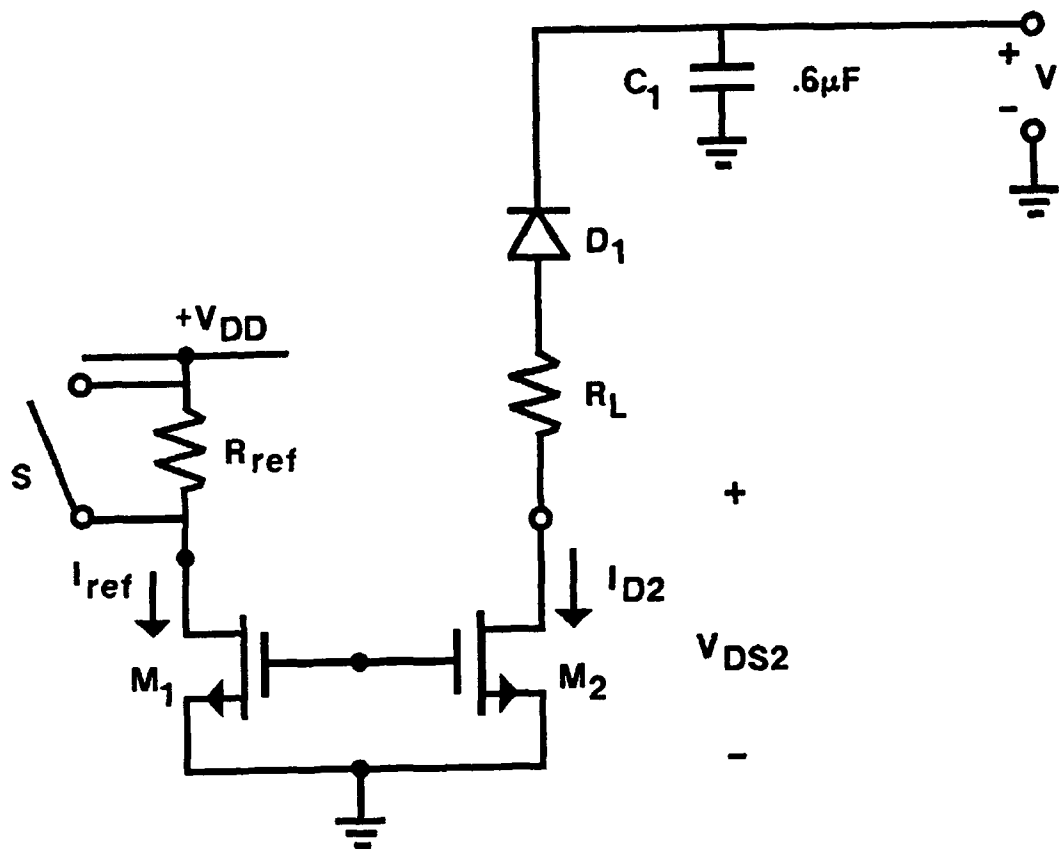
Preliminary calculations indicate that a simple planar metal-oxide-semiconductor capacitor could be fabricated by thermally growing an oxide layer on a low resistivity silicon substrate. This element could be made of a particular geometry to minimize parasitic impedance and attached to the substrate by reflow soldering.

The advantages of constructing the slapper and firing circuit on the same substrate as the switch and high voltage capacitor are numerous. This arrangement would minimize the size of the entire assembly since only one mounting vehicle is required for all components. This reduces the number of packaging steps used in the manufacturing process which reduces cost and increases reliability.

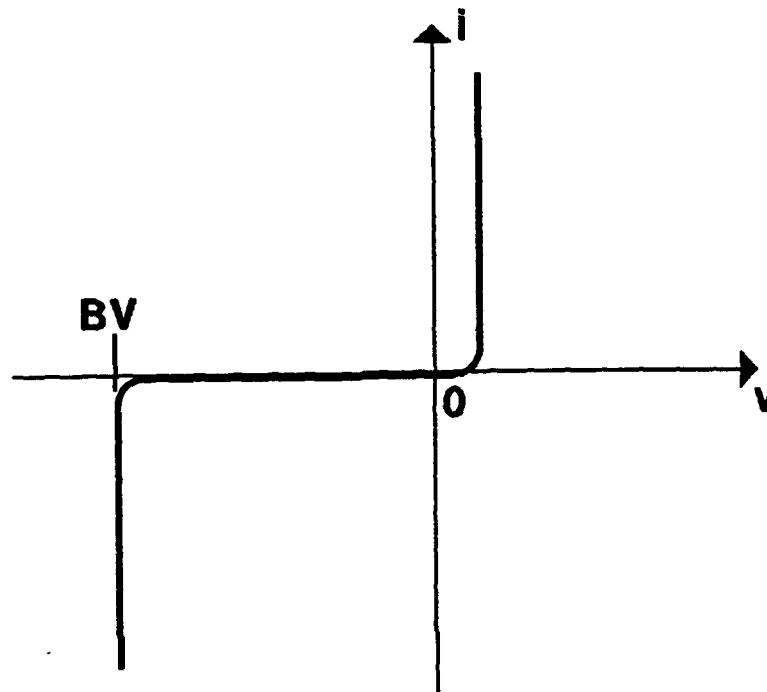
The length of the conductive paths between components is minimized since the electrical components are as close together as physically possible. The minimum lead lengths results in minimizing parasitic lead inductance and resistance which reduces the discharge time of C_1 .

Also, since many connections are printed onto the substrate and fired/sintered simultaneously, reliability of the interconnect is greatly enhanced. All solder connections can be realized by using a conventional belt solder reflow station.

Technically it would be possible to integrate the components of the switch and charging capacitor on a monolithic substrate. Microelectronic fabrication techniques are capable of producing large numbers of devices economically.



**HIGH VOLTAGE SWITCH SCHEMATIC
FIGURE 1**



THE I-V CHARACTERISTIC OF A JUNCTION DIODE
FIGURE 2

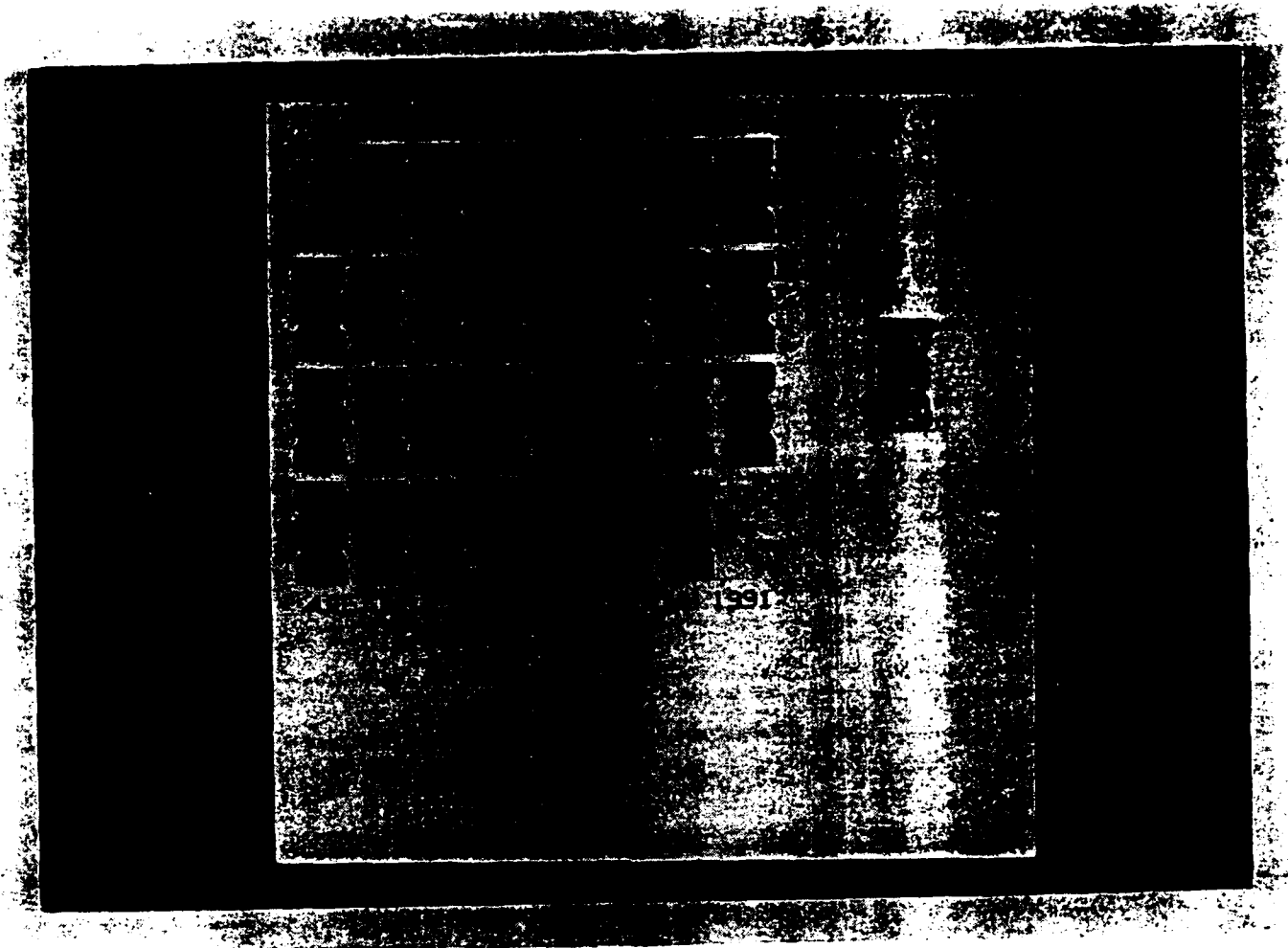


FIGURE 3

Sivasubramanya Balakrishnan's report was unavailable at time of publication .

The Integration of J-MASS With MSTARs

**Larry A. Beardsley
Assistant Professor of Mathematics
Department of Mathematics
Waters Hall
Athens State College
Athens, AL 35816**

**Final Report for
Summer Faculty Research Program
Wright Laboratories/MNGS
Eglin Air Force Base, FL 32542-5434**

**Sponsored by: Air Force Office of Scientific Research
Bolling Air Force Base, Washington, D.C.**

September, 1993

Integration of J-MASS With MSTARs

**Larry A. Beardsley
Assistant Professor
Department of Mathematics
Athens State College
Athens, Alabama**

Abstract

The J-MASS architecture is a relatively new modeling system designed to support engineers, model developers, analysts and decision makers. It implements a series of standards and provides software tools to support the development, configuration, operation and analysis of models and simulations at varying levels of complexity and detail. MSTARs (Modular Simulation Tools and Resources) is a joint project being conducted by WL/MNSH and WL/MNMF using a collection of missile simulation and analysis tools that is based on the Modular Missile Simulation (MOMS) taxonomy currently also under development by the two branches and based on the J-MASS simulation architecture. The architecture is being developed at Wright Patterson Air Force Base by ASC/RWWW and WL/AAWA-1. J-MASS is written in the object-oriented DOD-standard language, Ada, and is designed to be transportable between different hardware configurations and to operate with any workstation using a Posix-compliant Unix operation system. The initial capability of J-MASS is limited compared to the total system specification, but a Fall 1993 release will provide functionality throughout the SSE, allowing a user to log onto J-MASS and develop components, assemble them into models, configure a simulation scenario and place players within the scenario, and to execute the simulation and analyze the results through post-processing. However, at the present time the WL/MNSH and WL/MNMF branches are studying the new architecture to ascertain how the current 3DOF and 6DOF missile code can be integrated with the recommended architecture.

The Integration of J-MASS With MSTARs

Larry A. Beardsley

1 Introduction

This report is a brief description of J-MASS (Joint Modeling and Simulation System) architecture and its utility in the integration with the MOMS (modular missile system) taxonomy under the MSTARs (modular simulation tools and resources) effort.

The J-MASS architecture has been developed over a period of several years and was designed to serve as a standard modeling and simulation support system for use in the development of validated digital models of threat and friendly systems and analysis of those systems. It was targeted to support diverse simulation needs including system acquisition and development, test and evaluation, the intelligent community, and for training purposes.

A collection of missile simulation and analysis tools based on the MOMS taxonomy are currently being developed in the WL/MNSH (Wright Laboratory/ Munitions Simulation and Assessment) branch based on the J-MASS simulation architecture being developed by ASC/RWWW and WL/AWA-1. These tools can be used by all directorate organizations as well as outside organizations. The tools are being developed for both Unix and PC environments. The MOMS architecture and taxonomy will dramatically improve the capability of organizations for building and sharing missile simulations and subsystem models. It will be a reuseable, extendable set of missile subsystem model specifications in Ada, allowing diverse simulations to be built using compatible subsystem parts. However, in order for the missile code using the MOMS taxonomy to be efficient it must be based on an appropriate architecture.

The development of J-MASS began in the last quarter of 1990. The version of the tool to support the partitioning task of model development is completed. This tool supports production of object orientated design with assemblies (OODA) drawings used in all J-MASS models. These OODA drawings provide the major input to the J-MASS code generator, of which the 1.0 release was available earlier this year. The initial capability of

J-MASS is limited compared to to the total system capability, but the full 2.0 release with code generator will be available by the end of calendar year 1993.

The MNSH branch has been studying the J-MASS code to understand the architecture and to ascertain how the missile code will be designed to use the architecture most efficiently.

2 Problem Statement: J-MASS and Its Integration With MSTARS

The need for modeling and simulation becomes more important as the complexity of our technology increases and available funding for test and evaluation decreases. In the initial phases of R&D, it is important to help identify the best focus for technology minimizing expense. Once a set of concepts has been formulated, modeling and simulation (M&S) is effective in identifying the critical performance issues and selecting the best concept for accomplishing technical goals, potentially eliminating the need for multiple contracts and reducing the amount of hardware testing required to select a best approach. During exploratory and advanced development, medium to high fidelity models of a new technology should be built to help determine whether weapon performance using the technology justifies transition to Engineering Manufacturing Development (EMD). Effective demonstrations of weapon performance to a customer using quality simulations can be critical in selling the technology. During EMD, M&S is used in both all digital and hardware-in-the-loop (HIL) forms to support product improvement and augment the flight test program, markedly reducing the number of flight tests required for proof of design and as a result significantly reducing the cost of test and evaluation.

In the last few years, computer platforms have been improving greatly in performance while dropping significantly in price. Also, software engineering is being substantially improved by such techniques as object oriented programming and languages such as Ada 9X. As a result, high fidelity and high speed simulation can be theoretically accomplished today at an incredibly low cost.

However, there is a problem. For years developed laboratory projects required simulations from scratch, either by contract or in-house.

The result of this approach has been single use, non-related, non-compatible software representing models of the technology being built mated to some generic missile model or some simplified representation of a real system. Unique simulations built from scratch are expensive and time-consuming. It is difficult and near impossible to accurately predict missile system performance based on technology models without using validated simulations of the missile system being analyzed. Even if such simulations exist, they are also unique and generally are not compatible with the other simulations which have been developed. Also if other models exist, it is not possible to efficiently test another technology model which is not based on the same architecture rendering it incompatible without significant modification. Finally, when we transition our technology to be tested in facilities such as the GWEF, high speed and high fidelity models of portions of the system are required for hardware-in-the-loop (HIL) testing. Using this approach, these models must be built almost from scratch to be compatible with the unique real-time computer environment being used.

The solution to all of these problems is not a generic simulation which supposedly can simulate anything. The diversity of components to be modeled and the many ways they can be connected together makes it impossible for such a simulation to exist. The simulations which have attempted to do this were a compromise having a limited success in limited application areas. The solution is a *common software architecture* for objects in general which are designed for Ada and an extendable taxonomy of missile subsystem specifications in particular. A typical missile might have subsystems interconnected as shown in Figure 1, page 42-6.

The objects shown in Figure 1 are connected in a specific manner, but may be different for each missile being modeled. Also, some of the components may operate differently with the environment in different missile systems. For example, a radar seeker interacts with the environment differently from an infrared seeker. Also, different types of *radar* seekers may behave differently and may provide different information to other parts of the system. Obviously, what is needed is not a common missile simulation, but rather a set of reuseable components

MISSILE DATA FLOW DIAGRAM

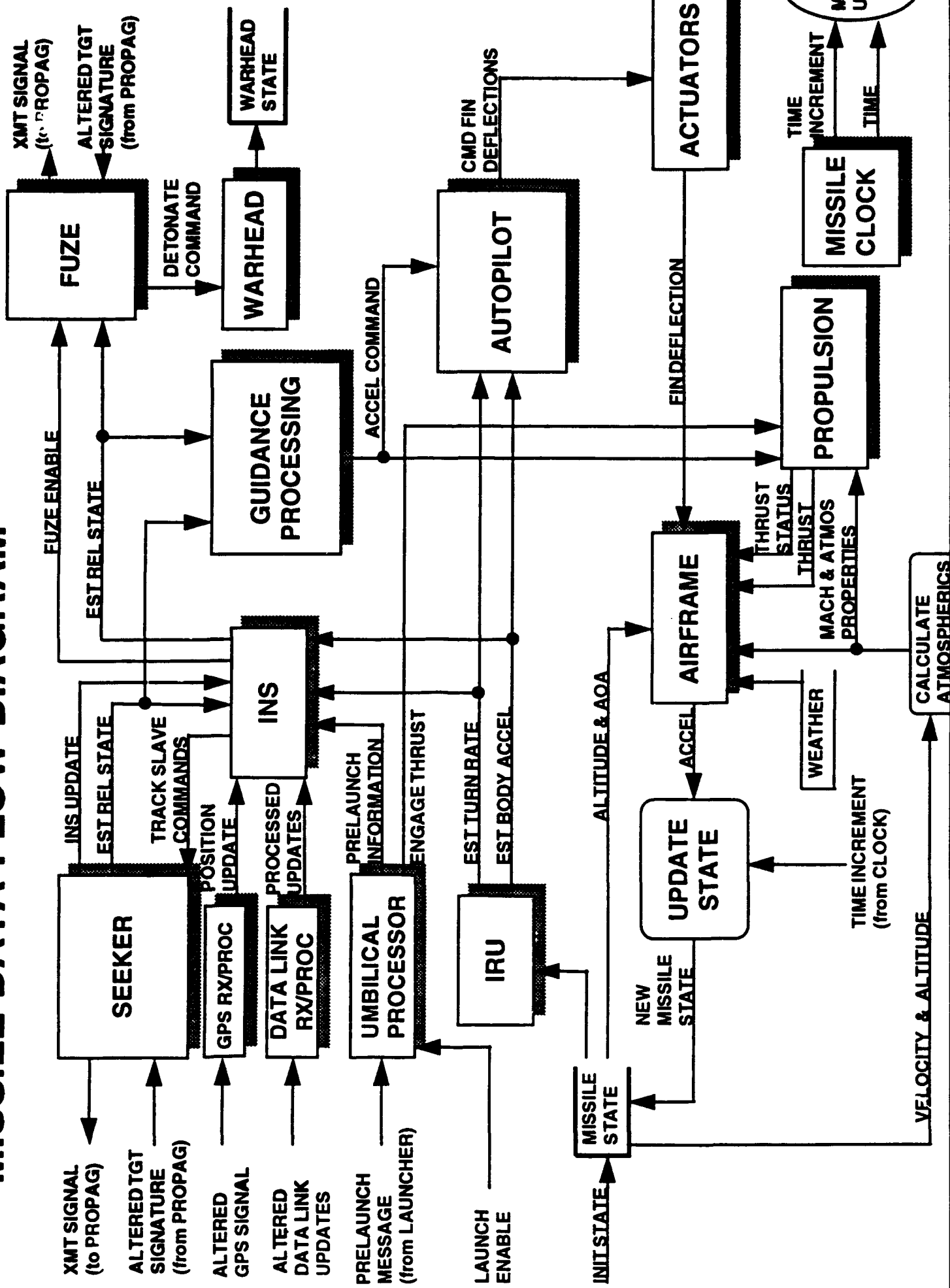


Figure 1

which can be used to build different simulations based on unique requirements.

The basic idea of an extendable taxonomy of missile subsystem components is shown in Figure 2, 42-8. The objects might be organized by mission area as shown in the figure or in some other manner. The idea is that libraries of objects can be built based on a consistent set of component specifications. The specification only requires that the object receive and provide data and function and procedure calls in a consistent (specified) manner. The code which implements this Ada specification may be anything desired and to any level of fidelity desired. For example, this means that different kinds and fidelities of autopilot models can be built using the same autopilot specification. If an autopilot model is needed for which the specification does not exist, a new class of autopilot is invented and added to the library. From the library, objects from the library can be interconnected as needed to produce a missile model defining a particular system.

The MOMS specification, being developed under the MSTARs work unit, will provide an initial taxonomy which can be used by the Armament Directorate and other agencies, and it can be extended indefinitely.

In fulfillment of the need for a new architecture, a project was undertaken by ASC/RWW to develop a Tri-Service simulation environment including a graphical user interface and a standard software architecture for components which can be developed by any organization. The project was undertaken in 1990 with the program goals of providing the Department of Defense with the structure and software necessary to reduce modeling and simulation development and operation costs, of increasing the performance and credibility of models, and of increasing responsiveness to user requirements and decreasing duplication. The J-MASS programs office coordinates the development of the standard architecture and modeling system in response to Tri-service requirements.

The problem in using J-MASS is that it is written in a relatively new language, Ada, and the architecture has been in a beginning evolutionary stage up until release 2.0 a few weeks ago. The architecture of the earliest release was not flexible enough to handle the current modeling requirements of WL/MNSH. Also, the differences between the current 2.0 release and the earlier release are great. As a result, until now learning



the structure of J-MASS was not very beneficial to the integration effort. In addition, the J-MASS code is voluminous. However, again, it is anticipated that the advantages, both in time and expense, will far outweigh the initial time spent in understanding the code and in developing it.

For reasons given later in this paper, J-MASS was chosen as the architecture upon which to integrate with MOMS. Since J-MASS was not designed in-house, the architecture needs to be studied and understood before its integration with the 6DOF missile code. My task was to aid in both the studying of the architecture and in the implementation of the 6DOF code. However, the J-MASS release which WL/MNSH wanted to study was not delivered until a few weeks before my summer tenure ended. However, the time was well spent in both learning about object-oriented programming and in studying previous releases of J-MASS. Since receiving the release, some of the data flow has been examined and discussed in this paper. However, I felt it would be instructive to first give a brief history of the J-MASS architecture and why it was chosen as a model, and why Ada was chosen as a language.

3 Why Was Ada Chosen As a Language for the Design of J-MASS

In considering Ada as a language, the J-MASS program office wanted a language that was understandable, reliable, efficient, and easily modified. The language of Ada is patterned after the engineering principles of abstraction, information hiding, modularity, localization, uniformity, completeness, and confirmability [1]. In addition it was desired that the language support object oriented programming. According to Booch, object oriented programming is a method of implementation in which programs are organized as cooperative collections of objects, each of which represents an instance of some class, and whose classes are all members of a hierarchy of classes united through inheritance relationships. An important aspect of object-orientedness is that it uses objects rather than algorithms as its fundamental logical building blocks. One of the benefits of object oriented programming is that it helps exploit the

expressive power of all object-based and object-oriented languages which is conducive to achieving significant improvements in productivity and code quality. Secondly, it encourages reuse not only of software but of entire designs. Thirdly, it produces systems that are built upon stable intermediate forms that are resilient to change. Fourthly, it reduces the risk of developing complex systems. Most importantly, it appeals to the workings of human cognition.

A comparison of FORTRAN, Ada, and C++ was made by WL/MNSH based on the software engineering principles of Booch. As a result, the choice was narrowed down to Ada or C++. Ada and C++ both have good data abstraction and information hiding capabilities, but Ada was considered to be more readable and understandable than C++.

4 Why J-MASS As a Simulation Architecture?

Now that a language had been decided on, an architecture needed to be chosen which would take advantage of Ada's assets. The architecture had to support the following:

- a. object oriented programming
- b. reuseable, reconfiguration simulation components
- c. multiple level, diverse types of simulation components
- e. automatic code generation

In addition it had to provide for loose coupling between components, produce fast executing code, and be attractive to a large base of users. Some of the simulation architectures reviewed were GENSS, TRAP, WISM, HAVE SLICK, HADAMS, TAP, AMRAAM (Litton heritage), Carnegie Mellon Software Structural Model, and JMASS. In deciding these choices, it was decided that:

(1) Litton, GENSS, AMRAAM, TRAP, and SIM all have high coupling, limited component reuseability, and do not support automatic code generation or object-oriented programming. Also, direct translation into Ada would not offer any advantages over FORTRAN since the desirable features of Ada would not be used.

- (2) Developing our own architecture would be laborious and cost intensive.
- (3) Carnegie Mellon's software architecture should lend itself to time intensive models which can be allocated to a separate processor. Current simulation architectures are difficult to modify for accomplishing this. It was desirable for the chosen architecture to be widely used. This would promote widespread sharing of parts and lower verification and validation costs for components.
- (4) J-MASS, which uses a form of Carnegie Mellon's SSM meets most requirements, and WL/MNSH will inherit products currently being developed.

With these possibilities, J-MASS was selected with Carnegie Mellon's SSM architecture decided upon as a backup architecture. The branch will make the best use of older FORTRAN simulations as a guide to effective numerical algorithms and subsystem completeness.

Two of the architectures, J-MASS and the Litton approach, are compared. The strong points of the Litton approach are:

- (1) It is organized for building simulations.
- (2) modules represent subsystems of the weapon as do modern object oriented approaches.
- (3) modules were designed to be as independent as possible except for the C-array.
- (4) use of "equivalence" statements with C-array resulted in some improvement for data visibility, modifiability, and I/O flexibility over other FORTRAN programs using only common blocks.

The weak points of the Litton approach are:

- (1) Objects are not clearly separated (e.g. missile processor processing "real world data").
- (2) Attributes are not clearly distinguishable in each subroutine (loosely defined objects).
- (3) Subsystems are not truly reuseable in other simulations without code

modifications. (that is, they are hardwired to C-array)

- (4) maintenance of C-array is a colossal task for the simulation configuration manager.

In comparison, the strong points for the J-MASS approach are:

- (1) Ada language was used and implemented to best use Ada features.
- (2) Components are reusable and reconfigurable in another system without code changes.
- (3) diverse types of simulation components are supported.
- (4) objects are loosely coupled and highly cohesive.
- (5) arbitrary levels of fidelity are possible.
- (6) allows arbitrary level of component decomposition.
- (7) all objects have the same basic structure.
- (8) outstanding data accessibility through the use of pointers exists.

The weak points of J-MASS are:

- (1) the flexible simulation design is less runtime efficient.
- (2) making model component building and configuration simple requires sophisticated simulation facilities and utilities including a data management package and a service interconnect backplane.

In addition to its strong points, J-MASS has the potential for becoming a widely used standard which in turn would promote large scale component sharing, and simulations could be understood by many. Also, we would inherit tools being developed by J-MASS such as the graphical runtime environment, graphical model building with the automatic Ada code generator, 3-D animated graphics for simulation visualization, and data plot capability.

5 What Is J-MASS?

J-MASS is a modeling system designed to support engineers, model developers, analysts and decision makers [2]. It implements a series of standards and provides software tools supporting the development, configuration, operation and analysis of models and simulations at varying levels of complexity and detail. Additionally, J-MASS provides a library of verified software components for the model designer to use, and J-MASS models are verified and validated before they are placed in this library.

Formal configuration management ensures the library retains its integrity. J-MASS is not a model; it is a system to develop and support models developed in compliance to the basic J-MASS architectural standards.

J-MASS supports models with an object-based design coded in the DOD-standard Ada software language. It is designed to be transportable between different hardware configurations and is built to operate with any workstation using a Posix-compliant Unix operating system. J-MASS uses an open systems approach. Standards are specified wherever possible, enabling J-MASS software to interface with other standard software.

One of the key parts of J-MASS design is the SSM (Software Structural Model). It identifies standard interfaces with the Simulation Support Environment (SSE) and uses information with standard formats. Rather than forcing a modeler to do more work, it tells the modeler where to place different attributes of the individual objects, encouraging standardization. With respect to the SSE, objects are processed in the same manner, and information is provided to the object when its state is updated and the object provides information back to the SSE. As a result, the designer can focus attention on designing the algorithms needed to describe what is being modeled rather than on the style of the model. When developed, the J-MASS code generator will be used to transform the algorithms into actual Ada code compliant with the J-MASS software structural model.

J-MASS includes the SSE and the modeling library as described in Figure 3, Figure 42-16. The SSE supports the modeler in accomplishing any or all of five basic functions.

- (1) develop model components
- (2) assemble model components into a model
- (3) configure simulation scenarios for execution
- (4) execute the scenario and generate data
- (5) post-processing of the data

5.1 Develop Model Components

The first step in developing a J-MASS system model is to partition the system into its components. The process continues to the level the

modeler needs to provide the detail appropriate to the task, whenever possible maintaining a one-to-one mapping from the physical world to the simulation being maintained. For example, a design engineer may partition a radar system into individual gates and amplifiers in the circuitry, while a systems analyst may decompose the radar into only the transmitter, processor and receiver. Thus, the system support environment allows model development to match the needs of the modeler without forcing detail beyond that which is required.

5.2 Assemble Model Components

After a developer partitions the system into its components, a library of already developed objects can be accessed. For example, if a design engineer needs a model of a gate, he simply accesses the library, browses through listings and descriptions of the gates in the library and retrieves the one that matches the need. The specific attributes for that object are "tailored" for the specific application. The engineer has now incorporated an object developed and validated by another modeler. The developer has saved time and money and is assured of a quality product since all of the objects in the library have been evaluated.

Usually, in a given simulation, many objects are used over and over in varying configurations but with unique data, called attributes, to produce very complex models. The model parts are easily connected using the J-MASS architecture.

5.3 Configure Simulation Scenarios

After a model is developed, it can be placed in a simulation scenario where the scenario is a "one-on-one" simulation or a "few-on-few" simulation where the focus is on system interaction.

J-MASS allows for the models in the simulations to be placed in specific physical locations. Terrain is modeled based on data from the Defense Mapping Agency. Appropriate geography, atmosphere, surface cover and other factors are added to the scenario.

J-MASS is also being developed to support simulations involving "many-on-many" player interactions. These scenarios will usually involve lower detail J-MASS models due to the scenario complexity.

5.4 Execute the Scenario

During the setup, the operator specifies the data required for subsequent analysis. Upon execution, the scenario is played out and the data is captured in files for analysis. With real-time applications, data will be available for instant viewing.

Also, modelers can execute complex scenarios using several different models, knowing that individual models will interact properly since each is designed and built to the same standards.

5.5 Post-processing

J-MASS supports an extensive analysis capability in the post-processing phase. For example, in an emulative radar model, the design engineer can actually trace signals through a circuit. Engineering graphs can be generated as well as tables, maps, traces of actual versus predicted value, position, and almost any other representation of data.

One of the benefits of J-MASS will be to allow engineers without extensive software backgrounds to construct detailed models using a concept called "visual programming". This concept will allow for the use of standard engineering notation to design a model where the code will flow from the engineering.

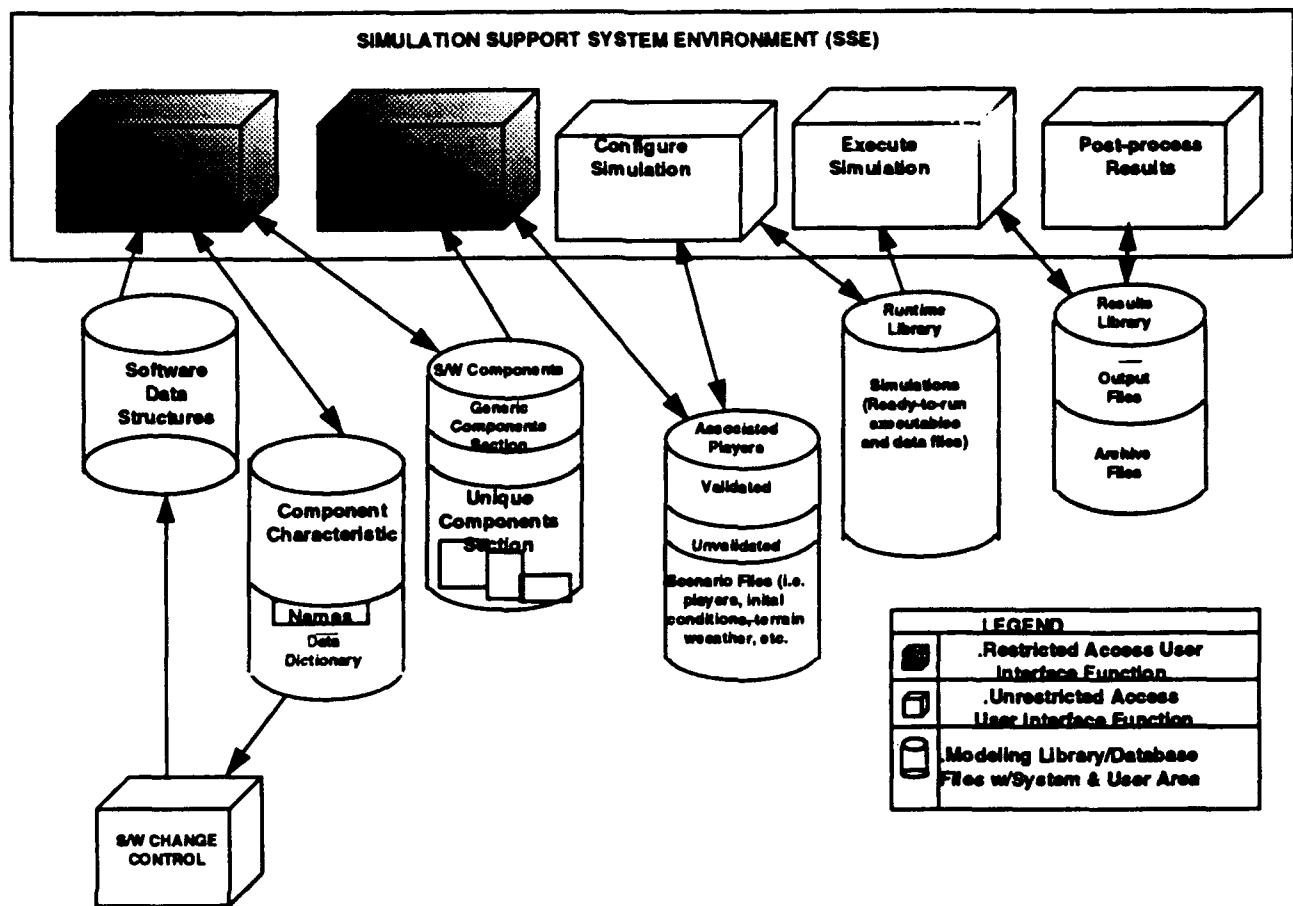


Figure 3: J-MASS Architectural Concept

6 How Does One Player Communicate With Another

To explain some of the J-MASS architecture, figure 4, page 42-17 is given to illustrate how one player communicates with another. Figure 4 depicts how the ACQ3 (ACQ3) communicates with the VAN (C3) via the communications element. Note the two terms, imports and exports. In J-MASS, an export is a construct that allows for the sending of data from one player to another, and an import is a construct allowing for the acceptance of data from another player. In comparison, inputs and outputs are data that is being manipulated within a given player. In the figure, the system directive message and backscan directive message are

being passed to the ACQ3 radar through the communication block by means of inports. Within the radar, target data and time interval is being updated. Then, the target data message is being sent to the C3 Van through an outport. Similarly, the system directive message, new system directive, and backscan are being updated within the radar and output to the C3.

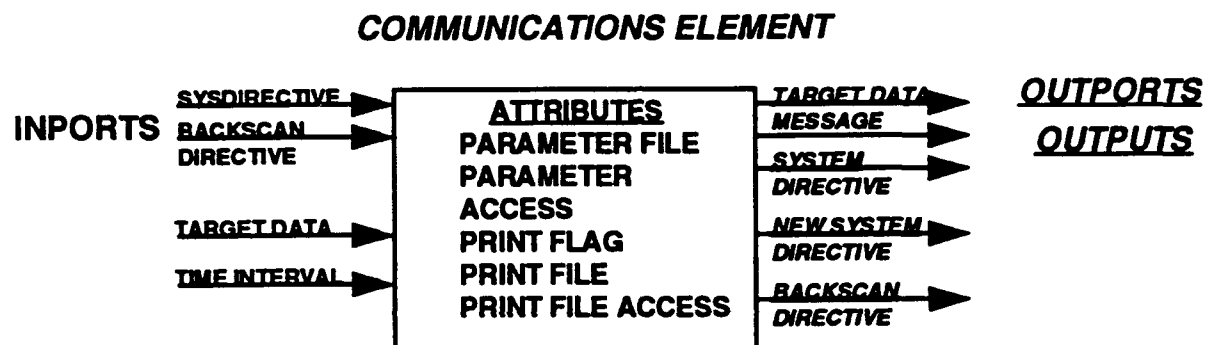


Figure 4

A more general figure of all four players is given on page 42-18, Figure 5. Note that the environment player has an in_out_port for which the signal is sent to and from the antenna element within the target acquisition player.

INTER-PLAYER COMMUNICATIONS

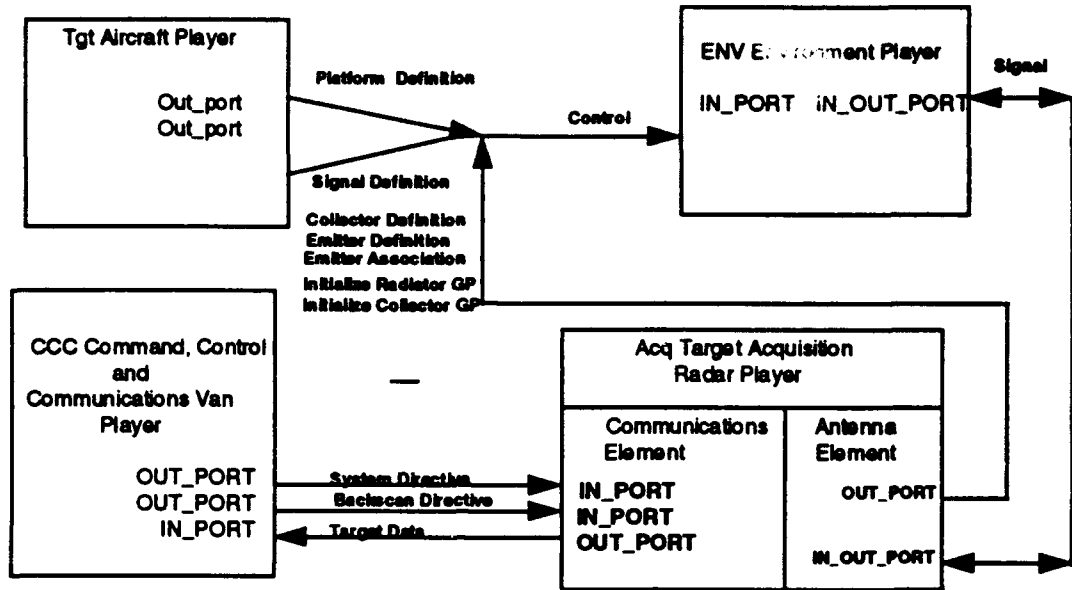


Figure 5

6 Concluding Remarks

New weapon technology is very complex, diverse, and software intensive. Previous simulations had very limited flexibility for handling these requirements. Technology design comparisons require simulation module interchangeability, and many simulation architectures are somewhat rigid. Many of them are written in FORTRAN, a language whose supersets limit transportability. Rapidly changing requirements demands that software be easily modified. The new simulation architecture, J-MASS, is a viable alternative for all of the reasons mentioned in this report. Previous simulation architectures were not sufficiently robust for optimal modeling of different weapon subsystems at multiple levels of fidelity. Also future simulation needs includes distributed components for

networked integrated technology testing. An appropriate simulation architecture should lend itself to time intensive models which can be allocated to a separate processor. J-MASS, an architecture which utilizes the object oriented approach based on Ada, offers a means to accomplish the given objectives whereas others are difficult to modify for accomplishing this. It is conjectured that the J-MASS architecture will be widely used, and this would promote the widespread sharing of parts and would lower verification and validation costs for components.

The WL/MNSH branch and myself learned a great deal of the benefits of the J-MASS architecture this summer. Although, there exist some glitches, mostly hardware related, the capabilities offered by the architecture and the time and money savings will outweigh the initial time in both fully understanding its functionality and its integration with the missile code. The development of the 6DOF code utilizing the J-MASS architecture has already begun and should be functional in the near future.

Acknowledgement

I am thankful to the Air Force Office of Scientific Research for offering me the opportunity to conduct research at Eglin AFB, Florida. In particular, I thank all of the personnel of the simulation and assessment branch of the armament directorate for both their encouragement and the affording of all the documentation and software to aid me in my study of J-MASS and the Ada language. Thanks to Capt. Patti Eggleston for the time she spent in helping me with a new word processor in typing this paper and in our study of a target model, to Capt. Eric Scarbrough for his studying of some of the J-MASS with me and in suggestions for the diagrams, to Tim Pounds for his accessibility for answering numerous questions and providing documentation and system support, and to the Branch manager, Larry Lewis for the use of some previous documentation. Many thanks to everyone already mentioned and to Dr. Martin Moorman, Ed Moorman and Yves Malette for making me feel welcome during my twelve week tenure at Eglin.

References

- [1] Grady Booch, Software Engineering With Ada, Benjamin Cummings, Second Edition (1986)**
- [2] Randy E. Brown and William K. McQuay, "The Joint Modeling and Simulation System", Journal of Electronic Defense, September, 1992.**
- [3] Gary A. Whitted, "Software Development Plan (SDP) Volume II, Software Structural Model (SSM) Design Methodly for the Modeling Library Components for the Joint Modeling & Simulation System (J-MASS) Program", Version 2.0, February 26, 1993.**

INFLUENCE OF PENETRATOR AND TARGET
PROPERTIES ON PENETRATION MECHANICS

E. Eugene Callens, Jr.
Associate Professor
J. Scott McMurtry
Graduate Student
Department of Mechanical and
Industrial Engineering

Louisiana Tech University
Ruston, LA 71272

Final Report for:
Summer Research Program
Wright Laboratory

Sponsored by:
Air Force Office of Scientific Research
Bolling Air Force Base, Washington, D.C.

September 1993

INFLUENCE OF PENETRATOR AND TARGET
PROPERTIES ON PENETRATION MECHANICS

E. Eugene Callens, Jr.
Associate Professor
J. Scott McMurtry
Graduate Student
Department of Mechanical and
Industrial Engineering
Louisiana Tech University

Abstract

A previously developed quasi-steady wave mechanics model for penetration of structural targets is modified to include an improved model for the initial and terminal transients. The improved model is then utilized in the parametric study of the influence of penetrator and target properties on penetration depth. The wave mechanics model not only predicts the trends in penetration with variation in these properties, but it also delineates the kinematic mechanisms that are responsible for these trends. It is shown that the combination of high penetrator strength and low target strength produces a local maximum in the plot of penetration depth versus impact velocity. The wave mechanics model shows that the observed decrease in penetration depth with increasing impact velocity is due to flow initiation in the high strength penetrator. For high strength targets, the strength of the penetrator is shown to have little influence on penetration depth. However, for low strength targets, increased penetration results from increased penetrator strength. The effect of penetrator L/D on the ratio of penetration depth to original penetrator length is shown to be very pronounced for L/D's less than 6 but diminishing to near insignificance for L/D's greater than 12. The wave mechanics model shows that the L/D effect is due entirely to the initial and terminal transients. The effects of target strength, penetrator strength, and penetrator density on penetration depth into concrete targets is also presented.

INFLUENCE OF PENETRATOR AND TARGET PROPERTIES ON PENETRATION MECHANICS

E. Eugene Callens, Jr.
J. Scott McMurtry

INTRODUCTION

The work reported in Ref. 1 indicates that excellent agreement with experimental data is obtained for a properly formulated one-dimensional quasi-steady wave mechanics model of the penetration processes for blunt, cylindrical penetrators. The necessity of employing a wave mechanics model is rooted in the observation that the total time for the penetration process exclusive of the terminal transient is usually less than 200 microseconds. The corresponding deceleration levels are typically more than one million times greater than the standard value of gravitational acceleration. Thus, the classical differential equations for rigid body mechanics cannot adequately describe the time resolved response of either the penetrator or target material.

A major advantage of a realistic model of the governing physical mechanisms over a straight forward correlation of experimental data is that the physically based model can delineate the processes that cause the observed and predicted data trends. For example, the interaction between the hydrodynamic flow stress and the structural stresses in the penetrator and target dictate at what penetrator velocities flow is initiated in the penetrator and/or target. The initiation of flow, in turn, has a dramatic effect on the penetrator and target response as is illustrated in the parametric studies reported below.

The current work employs a wave mechanics model to conduct a parametric study of the effects of target and penetrator compressive strength and density as well as the penetrator length to diameter ratio on penetration depth. The study covers the entire velocity range from those values where penetration is initiated and material strength effects are dominant to the hypervelocity values where material strength effects are insignificant and the penetration process is hydrodynamic in nature. The range of material densities and strengths includes all engineering materials, and the penetrator length to diameter ratios range from 1 to 50.

QUASI-STEADY WAVE MECHANICS MODEL

The quasi-steady wave mechanics model used in this study is presented in Ref. 1 and summarized below. The governing equations are the conservation of momentum, the conservation of mass, and a velocity component kinematic relationship.

The penetrator/target interface momentum equation is

$$S'_P + \rho'_P U_{PF}^2 = \rho'_T U_{TF}^2 + S'_T \quad (1)$$

where

S'_P = Stress in compressed penetrator
 S'_T = Stress in compressed target
 ρ'_P = Density of compressed penetrator
 ρ'_T = Density of compressed target
 U_{PF} = Penetrator flow velocity
 U_{TF} = Target flow velocity

The one-dimensional wave continuity equation in the penetrator is

$$\rho'_P = \rho_P \left(\frac{V_{WP}}{V_{WP} - U_{PP}} \right) \quad (2)$$

and for the target

$$\rho'_T = \rho_T \left(\frac{\bar{V}_{WT}}{\bar{V}_{WT} - \bar{U}_{PT}} \right) \quad (3)$$

where

ρ_P = Penetrator initial density
 ρ_T = Target initial density
 V_{WP} = Penetrator wave velocity
 \bar{V}_{WT} = Mean target wave velocity in the bow region
 U_{PP} = Penetrator particle velocity
 \bar{U}_{PT} = Mean target particle velocity

The particle velocity is the change in velocity associated with the passage of the disturbance wave. The kinematic relationship between the various velocity components is given by

$$V_P = U_{PF} + U_{PP} + U_{TF} + \bar{U}_{PT} \quad (4)$$

where V_P = Velocity of the free end of the penetrator.

The velocities in the penetrator and target before and after the disturbance waves are shown schematically in Fig. 1 relative to the interface.

The wave velocities are given by

$$\bar{V}_{WT} = C_{WP} + S_{IT} \bar{U}_{PT} \quad (5)$$

$$V_{NP} = C_{NP} + S_{IP} U_{PP} \quad (6)$$

where

- C_{WP} = Zero pressure wave velocity in the penetrator
- C_{WT} = Zero pressure wave velocity in the target
- S_{IP} = Hugoniot constant for the penetrator material
- S_{IT} = Hugoniot constant for the target material

The stress in the compressed penetrator is given by

$$S'_P = \rho_P U_{PP} V_{NP} \quad \text{for} \quad U_{PF} = 0 \quad (7)$$

$$S'_P = \rho_P U_{PPM} V_{NP} \quad \text{for} \quad U_{PF} > 0 \quad (8)$$

$$U_{PPM} = \frac{C_{SP} \sigma_{SP}}{\rho_P V_{NP}} \quad (9)$$

$$C_{SP} = v_P^{-1} \quad (10)$$

where

- U_{PPM} = Maximum penetrator particle velocity
- C_{SP} = Penetrator free surface maximum stress constant
- v_P = Poisson's ratio for the penetrator material
- σ_{SP} = Penetrator compressive stress

From these relationships it is observed that either the penetrator particle velocity or flow velocity is known for any condition. If the interface pressure is below the maximum allowable penetrator stress, the flow velocity is zero, and the particle velocity is the variable. If the interface pressure is above the maximum penetrator stress, the particle velocity is at its known maximum value and the flow velocity is the variable.

The stress in the compressed target is given by

$$S'_T = \rho_T \bar{U}_{PT} \bar{V}_{WT} \quad \text{for} \quad U_{TF} = 0 \quad (11)$$

$$S'_T = \rho_T \bar{U}_{PTM} \bar{V}_{WT} \quad \text{for} \quad U_{TF} > 0 \quad (12)$$

$$\bar{U}_{PTM} = \frac{C'_{ST} \sigma_{ST}}{\rho_T V_{NT}} \quad (13)$$

$$C'_{ST} = C^2_{ST} = v^{-2}_T \quad (14)$$

where

- U_{PTM} = Maximum mean target particle velocity
- C'_{ST} = Target confined surface maximum stress constant
- C_{ST} = Target free surface maximum stress constant
- v_T = Poisson's ratio for the target material
- σ_{ST} = Target compressive stress

As in the case of the penetrator, either the target particle velocity or flow velocity is known for any condition. The penetrator deceleration is determined by the wave mechanics. In this model the compression wave that originates at the penetrator/target interface upon impact is tracked in the penetrator as it travels back and forth between the interface and the free end. The compression wave reflects from the free end as an expansion wave and the penetrator free-end velocity decreases by twice the particle velocity with each reflection.

When the expansion wave reflects from the interface, the sum of the penetrator and target variable velocities decrease by twice the particle velocity. The new values of these velocities are determined from the interface momentum equation and the velocity component kinematic relationship. Again, the particle velocity changes sign with each wave reflection.

The penetrator traveling wave is tracked until the penetrator velocity falls below the target flow initiation velocity. When this occurs the developed penetration phase is complete and the remainder of the penetration process is a terminal transient cylindrical expansion of the target stress and a spherical expansion of the penetrator flow stress as presented below. The change in penetrator length due to the developed penetration phase is

$$\Delta L_{PD} = -\int (U_{PF} \pm U_{PP}) dt \quad (15)$$

The change is crater depth due to the developed penetration phase is

$$\Delta L_{CD} = \int (U_{TF} + \bar{U}_{PT}) dt \quad (16)$$

The final crater diameter at each penetration location is given by

$$\frac{D_C}{D_P} = \sqrt{\frac{\rho_P' \bar{U}_{PF}^2 + C_{ST} \sigma_{ST}}{C_{ST} \sigma_{ST}}} \quad (17)$$

where D_P = penetrator initial diameter.

INITIAL AND TERMINAL TRANSIENT MODELS

The initial and transient models have been modified from those presented in Ref. 1. The time for the initial transient is taken to be the time for the passage of the lateral release wave in the penetrator

$$\Delta t_{IT} = \frac{R_P}{V_{WPTS}} \quad (18)$$

where

V_{WPTS} = Penetrator transverse impact shock velocity.

The crater length due to the initial transient is given by

$$L_{CI} = (U_{PTS} - \bar{U}_{PTM}) \Delta t_{IT} \quad (19)$$

where

U_{PTS} = Target shock particle velocity

The length of penetrator loss during the initial transient expansion is obtained from a form of the velocity kinematic relationship

$$\Delta L_{PI} = -(V_{PI} \Delta t_{IT} - L_{CI}) \quad (20)$$

The terminal transient model is a combination of a spherical penetrator flow stress expansion and a cylindrical target particle momentum expansion. The crater length due to the spherical expansion of the penetrator flow stress is

$$L_{CTPF} = \sqrt{\frac{\rho_P' U_{PF}^2}{C_{ST} \sigma_{ST}}} - 1 \quad (21)$$

The crater length due to the cylindrical expansion of the target particle momentum is

$$L_{CTPM} = R_{PR} \left(\frac{\bar{U}_{PTFI}}{U_{PTFS}} - 1 \right) \quad (22)$$

where

U_{PTFI} = Mean target particle velocity when the penetrator velocity equals the target flow initiation velocity

U_{PTFS} = Free surface target particle velocity

Also the reference radius for the cylindrical expansion is

$$R_{PR} = \frac{V_{WTL}}{V_{WTT}} R_P \quad (23)$$

where

V_{WTL} = Target longitudinal wave velocity

V_{WTT} = Target transverse wave velocity

R_P = Penetrator radius

The total crater length due to the terminal transient is

$$L_{CT} = L_{CTPF} + L_{CTPM} \quad (24)$$

The time for the penetrator flow stress expansion is

$$t_{TTPF} = \frac{R_P}{2 U_{PF}} \left(\frac{L_{CTPF}}{R_P} \right)^2 \quad (25)$$

and the time for the target particle expansion is

$$t_{TTPM} = \frac{R_{PR}}{U_{PTFI}} \left[.5 \left(\frac{L_{CTPM}}{R_{PR}} \right)^2 + \left(\frac{L_{CTPM}}{R_{PR}} \right) \right] \quad (26)$$

The total time for the terminal transient expansion is

$$t_{TT} = t_{TTPF} + t_{TTPM} \quad (27)$$

COMPUTATIONAL RESULTS

The above equations constitute a comprehensive model for the complete terminal ballistics process including the initial transient, the developed penetration regime, and the final transient. The model predicts crater depth, penetrator velocity, and penetrator length as a function of time as well as the final crater diameter as a function of crater depth.

The equations have been programmed using the True BASIC language and the program is readily solved on a personal computer. Typical run times are 15 seconds on a 25-MHz 386 PC with a math coprocessor.

Fig. 2 presents data in terms of the ratio of penetration depth to original penetrator length (P/L) for tungsten alloy penetrators into rolled homogeneous armor (RHA) targets. The calculated P/L results are compared with data from Ref. 2 for length to diameter ratios (L/D) of 3, 6, and 12 and penetrator impact velocities (VPI) from 600 to 1600 m/s. The predictions show the experimentally observed L/D effects. Both the experiment and calculations show a change in slope at an impact velocity of approximately 800 m/s. This corresponds to the velocity at which the RHA target reaches the maximum confined surface stress and begins to flow.

Fig. 3 shows the same agreement within the experimental uncertainty for a mild steel penetrator into an aluminum target for $L/D = 3$. The experimental data from Ref. 3 extend from an impact velocity of approximately 900 m/s where target and penetrator strength effects are very significant to 5000 m/s where the penetration process is approximately hydrodynamic.

Figs. 4 and 5 compare the calculated results with experimental data from Ref. 4 for tungsten into ST52 steel and a penetrator L/D of 10.4. Two calculated curves are presented which correspond to the range of compressive strength quoted for ST52 steel. Fig. 4 presents the comparisons for crater depth, and Fig. 5 presents the comparisons for crater diameter. The agreement is seen to be excellent over the entire velocity range from 600 to 3600 m/s.

The effect of target strength on penetration depth for high and low strength penetrators is shown in Figs. 6 and 7, respectively. Both plots show increasing penetration with decreasing target strength as expected. However, for the combination of high penetrator strength and sufficiently low target strength, Fig. 6 shows a local maximum in penetration depth occurring at moderate impact velocities. The wave mechanics code clearly indicates that this decrease in penetration depth with increasing velocity is due to flow initiation in the high strength penetrator.

This phenomenon is further investigated in Figs. 8 and 9 where the effect of penetrator strength on penetration depth is presented for high and low strength targets, respectively. For high strength targets, the strength of the penetrator has little influence on penetration depth (Fig. 8).

However, for low strength targets, there is significantly more penetration associated with increasing penetrator strength at moderate to high impact velocities (Fig. 9). The local maxima are present for all but the two lowest strength penetrators. At impact velocities above 3,000 m/s, the curves are seen to coalesce due to the fact that even the highest strength penetrators are flowing under the influence of the high interface pressure. The penetration depth continues to increase with increasing velocity above 3,000 m/s due to terminal transient effects.

The effect of target density on penetration depth is presented in Figs. 10 and 11 for high and low strength targets, respectively. At high velocities, the penetration depth increases as target density decreases as expected. However, the curves cross at low velocities indicating that there is a regime where low density, high strength targets are more resistant to penetration than high density, high strength targets (Fig. 10). The wave mechanics model shows that this is due to the higher target flow initiation velocities associated with the lower target densities. This also suggests that the superior penetration resistance of ceramics over metals at low to moderate velocities may be due in part to the lower densities of the ceramics in addition to the obvious advantage of higher compressive strengths. Fig. 11 also shows that the penetration local maximum phenomenon is very pronounced for very low density targets.

Figs. 12 and 13 show the effect of penetrator density on penetration depth for high and low strength targets, respectively. The anticipated characteristic of increasing penetration with increasing density is observed in both figures. Fig. 13 shows that the local maxima occur for low strength targets if the penetrator density is sufficiently large.

Fig. 14 presents the effect of L/D on penetration depth for L/D of 1, 3, 6, 12, 20, and 50. The penetrator and target material properties are typical of a tungsten alloy penetrator into RHA. Low values of L/D are observed to have substantially high relative penetration compared to the higher L/D's. However, as L/D increases the difference diminishes and becomes nearly insignificant for L/D above 12. The wave mechanics model shows that the L/D effect is due entirely to the initial and terminal transients. There is no difference in the relative penetration of different L/D penetrators in the developed penetration regime.

The effect of target strength, penetrator strength, and penetrator density on penetration depth into concrete is shown in Figs. 15, 16, and 17, respectively, for a penetrator L/D of 12. Fig. 15 illustrates that the penetration depth has a local maximum for concrete strengths below 20,000 psi for a tungsten alloy penetrator. For normal structural strength concrete between 3,000 and 5,000 psi, the effect is quite pronounced. The consequence

of this phenomenon is that there is a limit on the impact velocity to achieve maximum penetration in concrete. The same effect is observed in Figs. 16 and 17 for all but the two lowest penetrator strengths and densities.

It is concluded that the wave mechanics model is very effective in the delineation of the effects of penetrator and target characteristics on penetration mechanics. Not only are the trends in penetration depth apparent but, more importantly, the physical mechanisms that drive these trends are exposed. The mechanisms are dynamic in nature and produce results that may not be anticipated from consideration of static material properties.

REFERENCES

1. Callens, E. Eugene, Jr. and J. Scott McMurtry, "One-Dimensional Wave Mechanics Model for Terminal Ballistics," Final Report for AFOSR Summer Research Program, Aug. 1992.
2. Tate, A., K. E. B. Green, P. G. Chamberlain, and R. G. Baker, "Model Scale Experiments of Long Rod Penetration," Proc. Fourth Int. Symp. Ballistics, Oct. 1978.
3. Christman, D. R., A. B. Wenzel, and J. V. Gehring, "Penetration Mechanisms of High-Velocity Rods," Proc. of the Seventh Hypervelocity Impact Symp., Tampa, FL, Vol. V and VI, Experiments, Nov. 17-19, 1964.
4. Hohler, V., and A. J. Stilp, Penetration of Steel and High Density Rods in Semi-infinite Steel Targets," Int. Symp. on Ballistics, 1977.

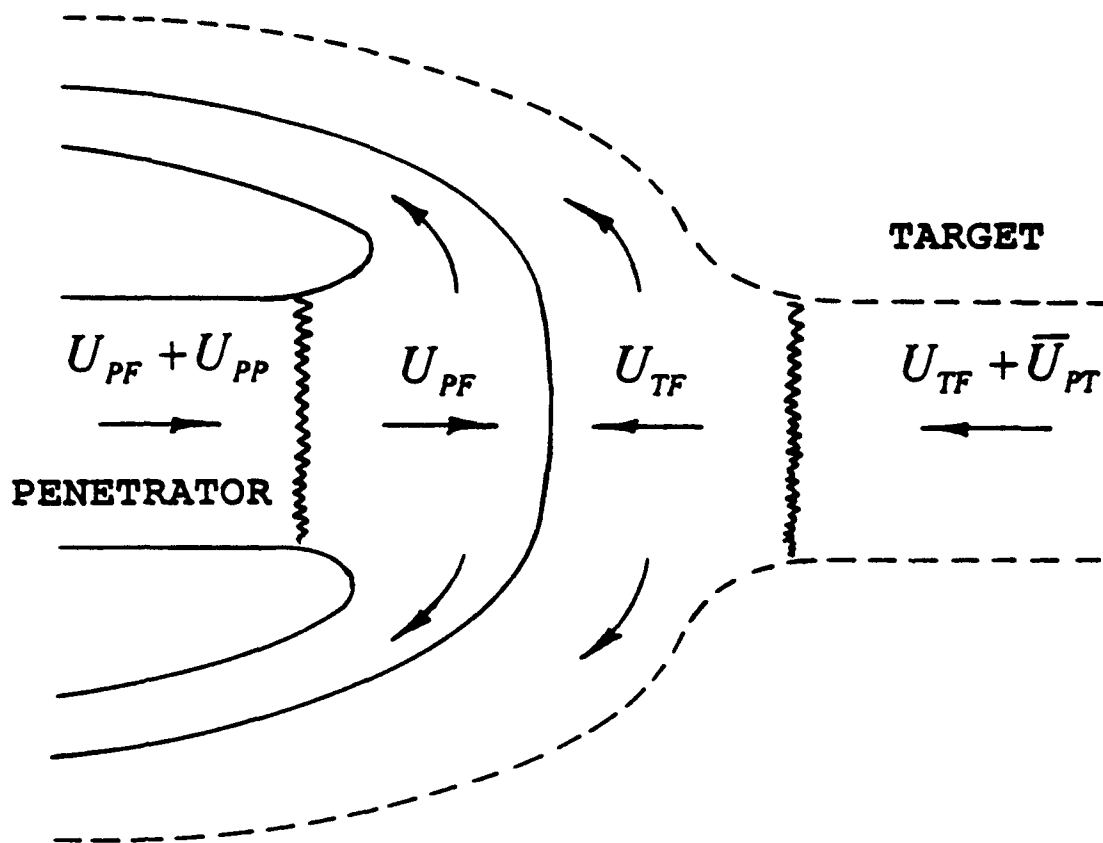


FIG. 1. FLOW AND PARTICLE VELOCITIES RELATIVE TO THE INTERFACE

FIG. 2. TUNGSTEN INTO RHA, $L/D = 3, 6, 12$

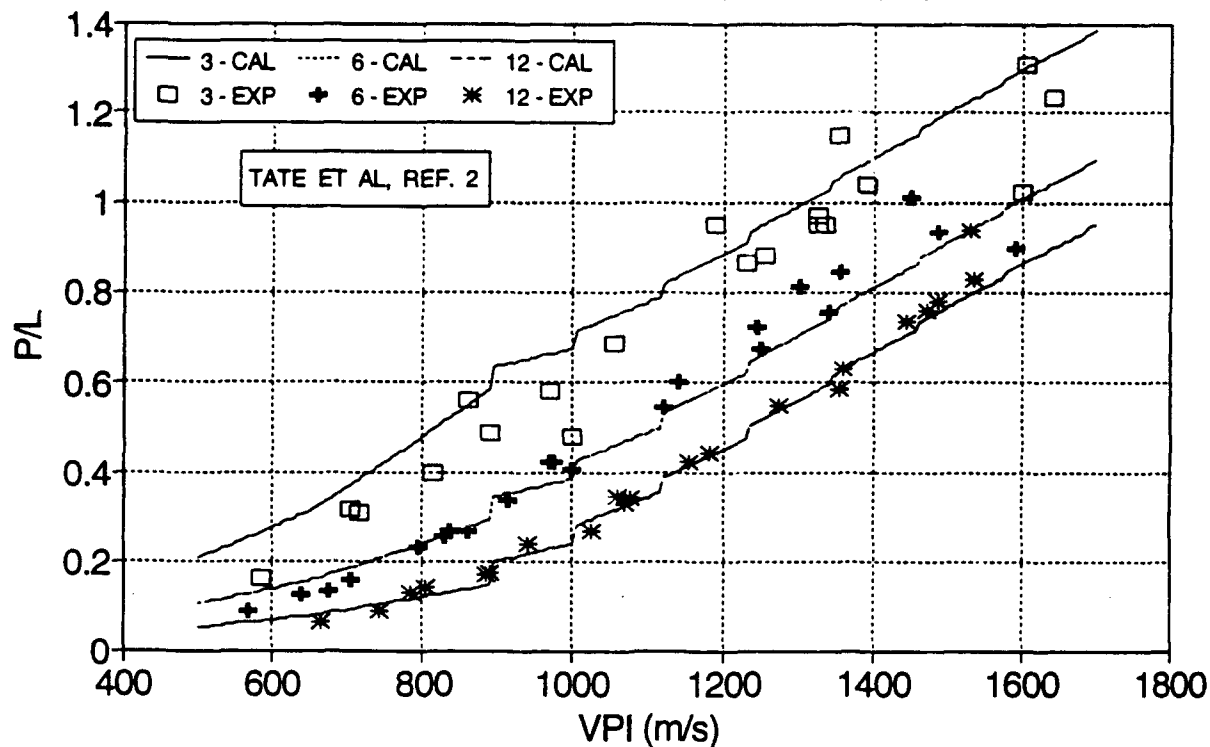


FIG. 3. MILD STEEL INTO AL, $L/D = 3$

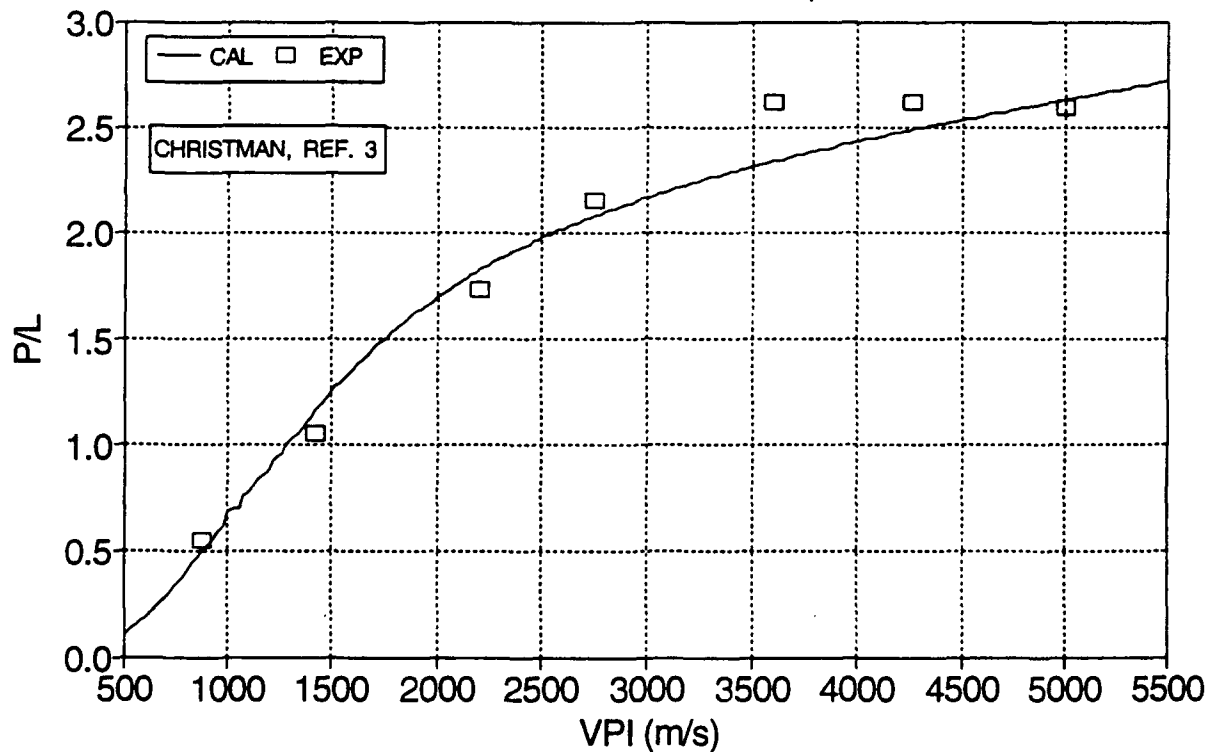


FIG. 4. TUNGSTEN INTO ST52 STEEL, $L/D = 10.4$,
CRATER DEPTH

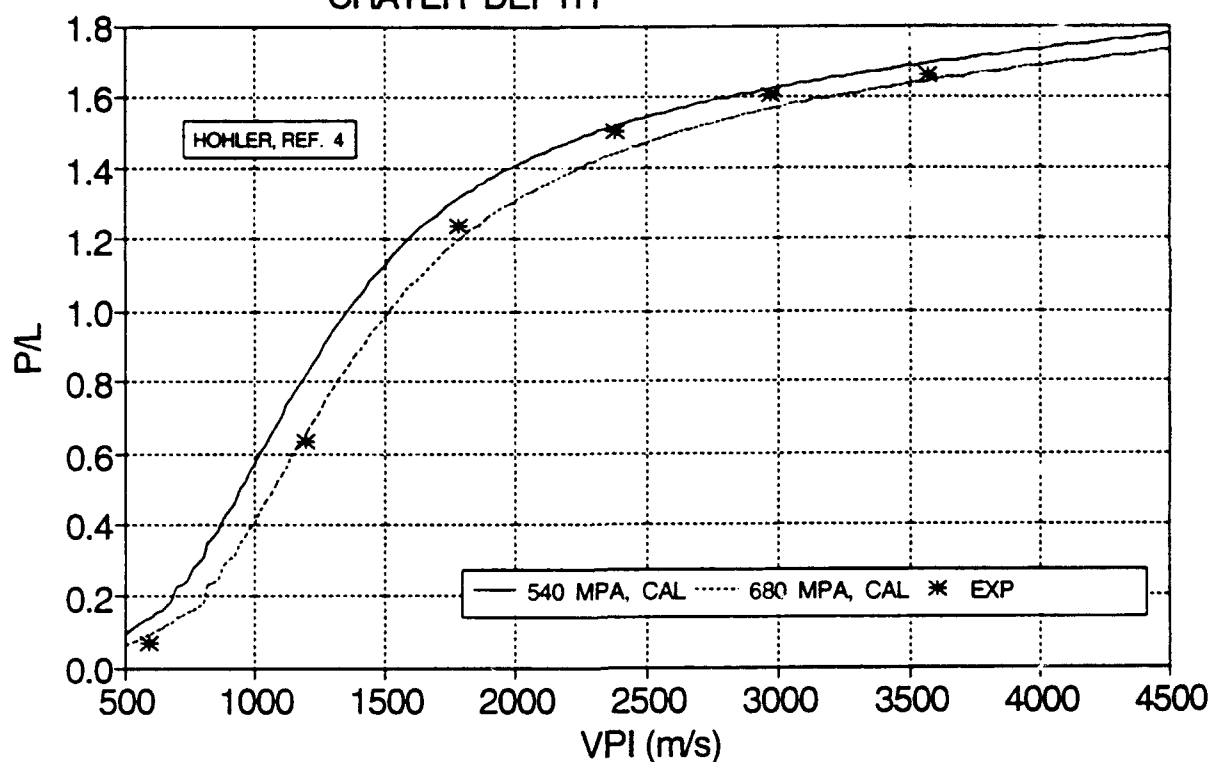


FIG. 5. TUNGSTEN INTO ST52 STEEL, $L/D = 10.4$,
CRATER DIAMETER

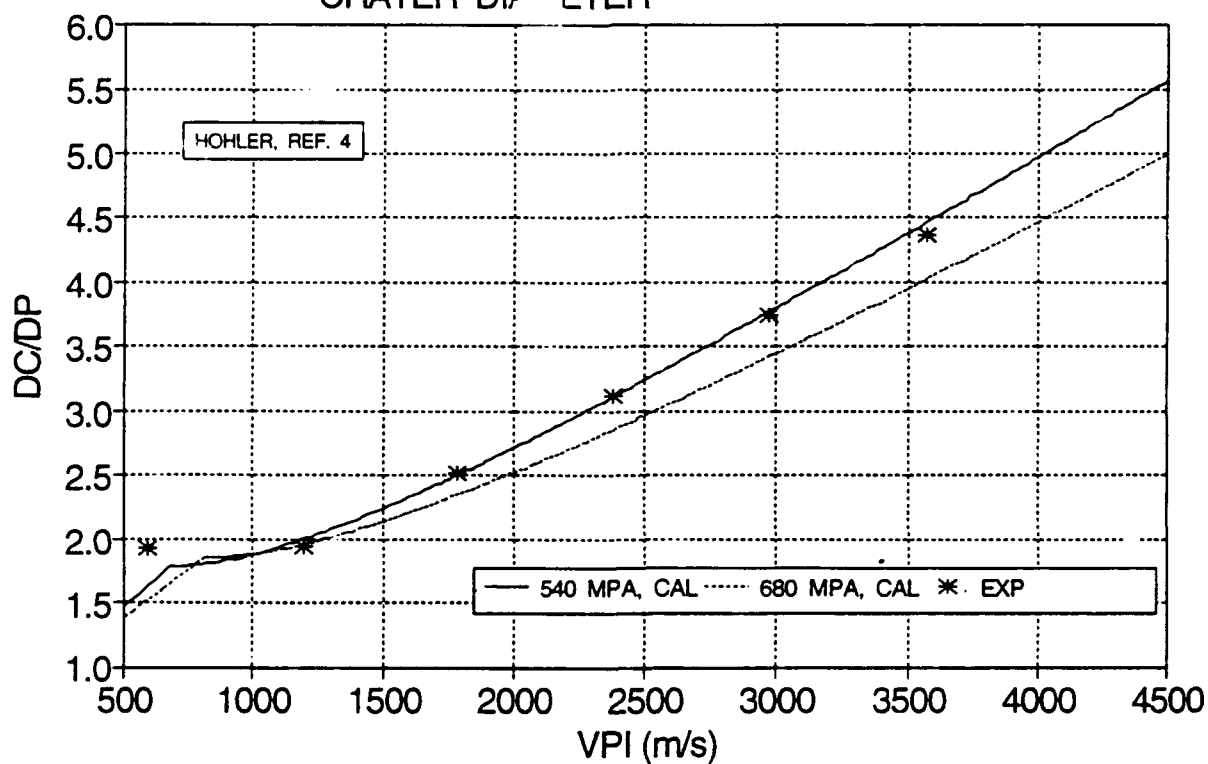


FIG. 6. EFFECT OF TARGET STRENGTH ON PENETRATION DEPTH, HIGH STRENGTH PENETRATOR

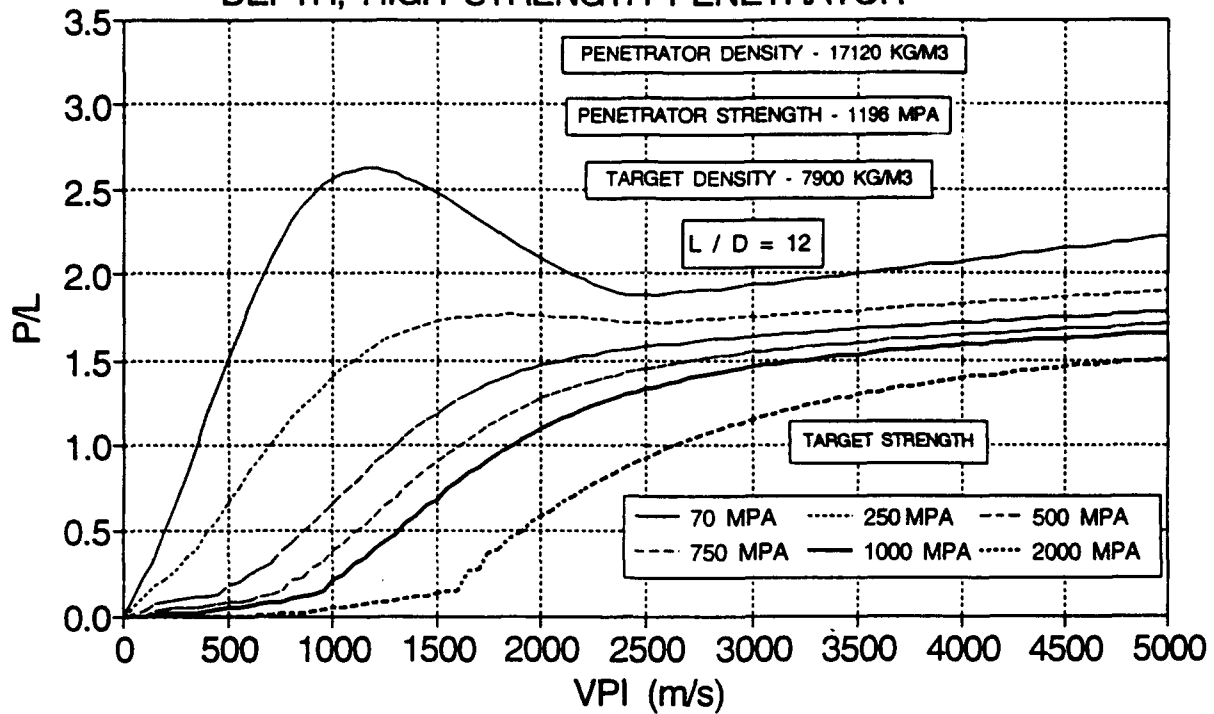


FIG. 7. EFFECT OF TARGET STRENGTH ON PENETRATION DEPTH, LOW STRENGTH PENETRATOR

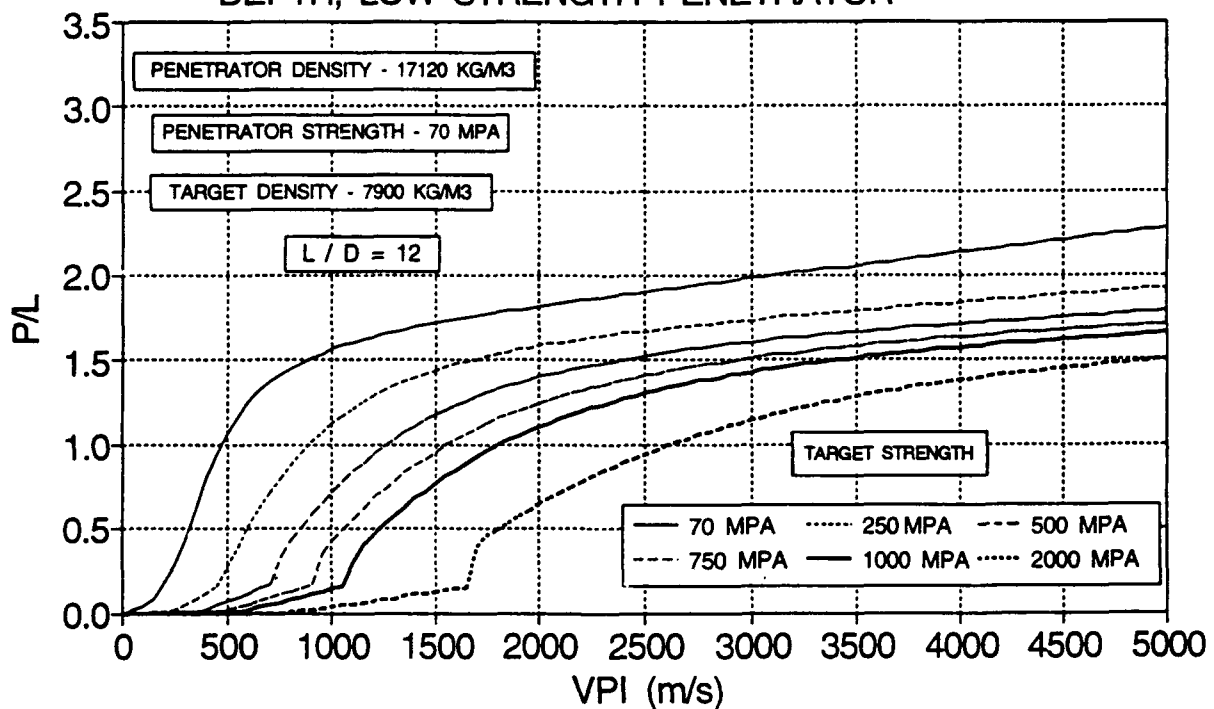


FIG. 8. EFFECT OF PENETRATOR STRENGTH ON PENETRATION DEPTH, HIGH STRENGTH TARGET

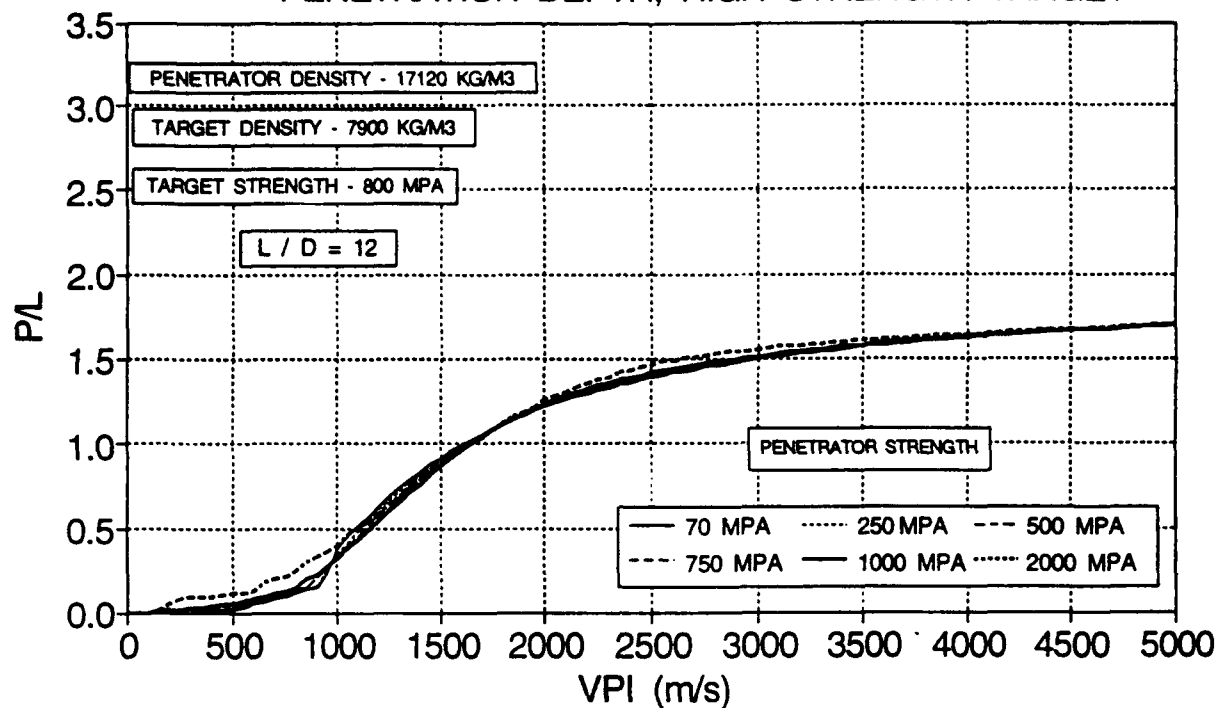


FIG. 9. EFFECT OF PENETRATOR STRENGTH ON PENETRATION DEPTH, LOW STRENGTH TARGET

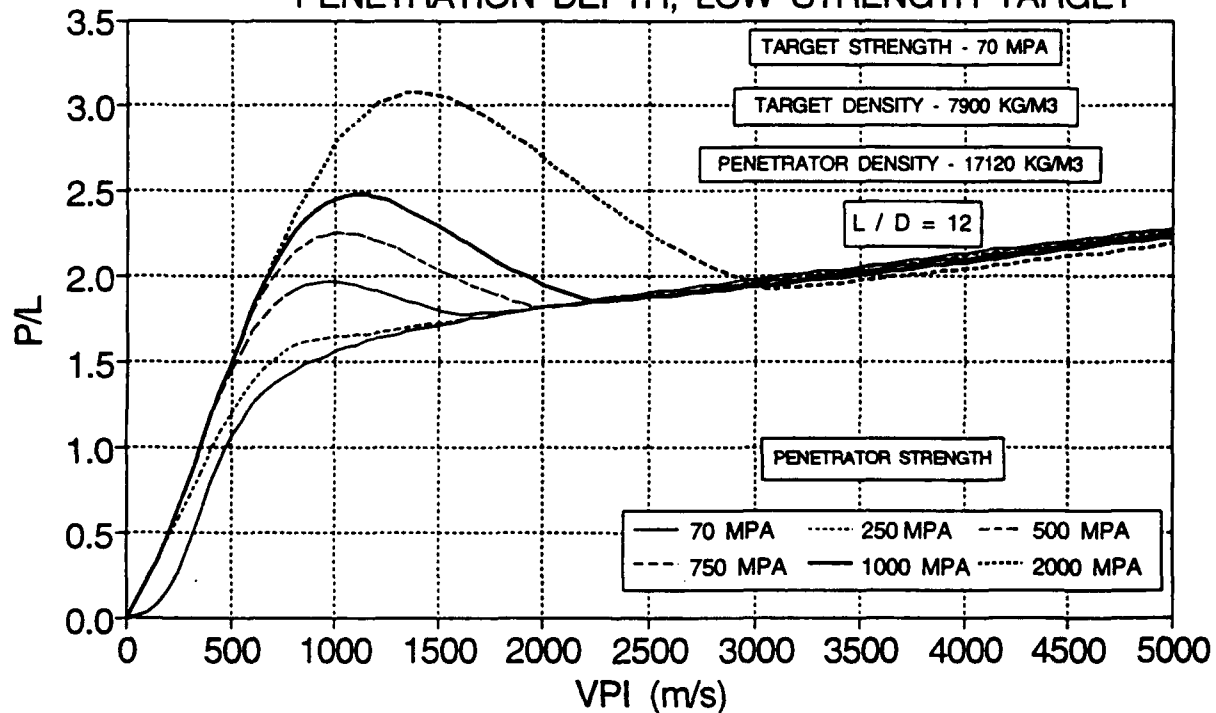


FIG. 10. EFFECT OF TARGET DENSITY ON PENETRATION DEPTH, HIGH STRENGTH TARGET

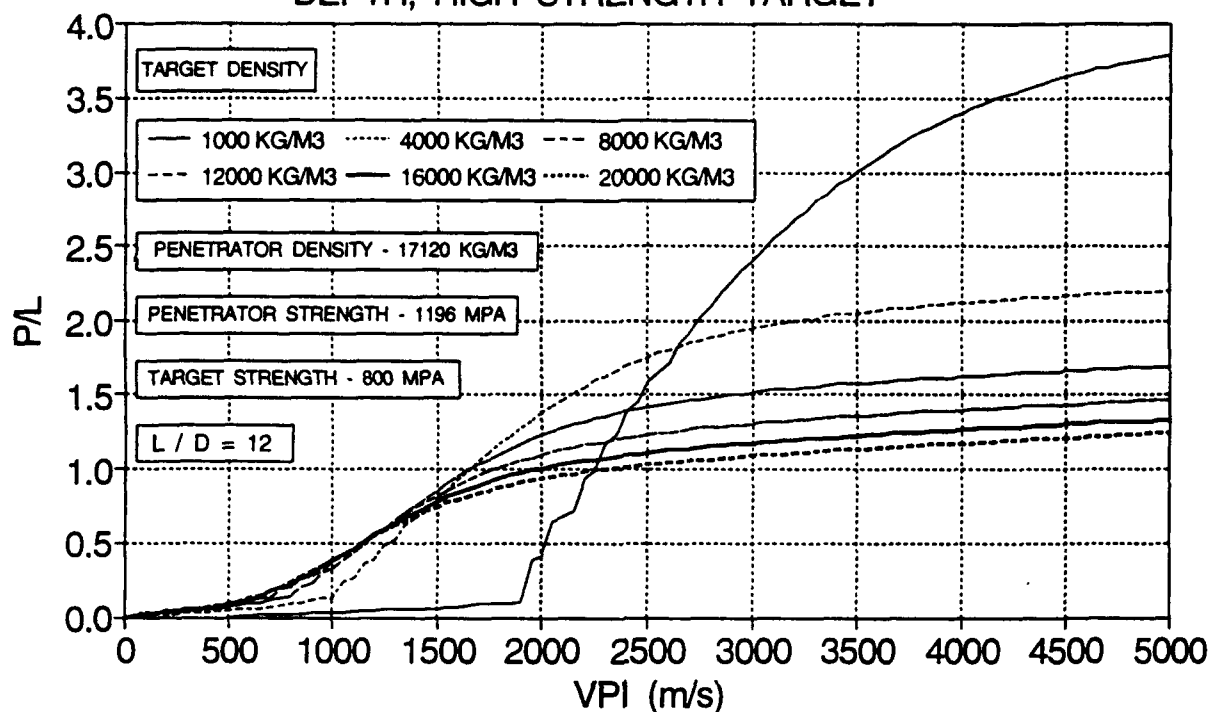


FIG. 11. EFFECT OF TARGET DENSITY ON PENETRATION DEPTH, LOW STRENGTH TARGET

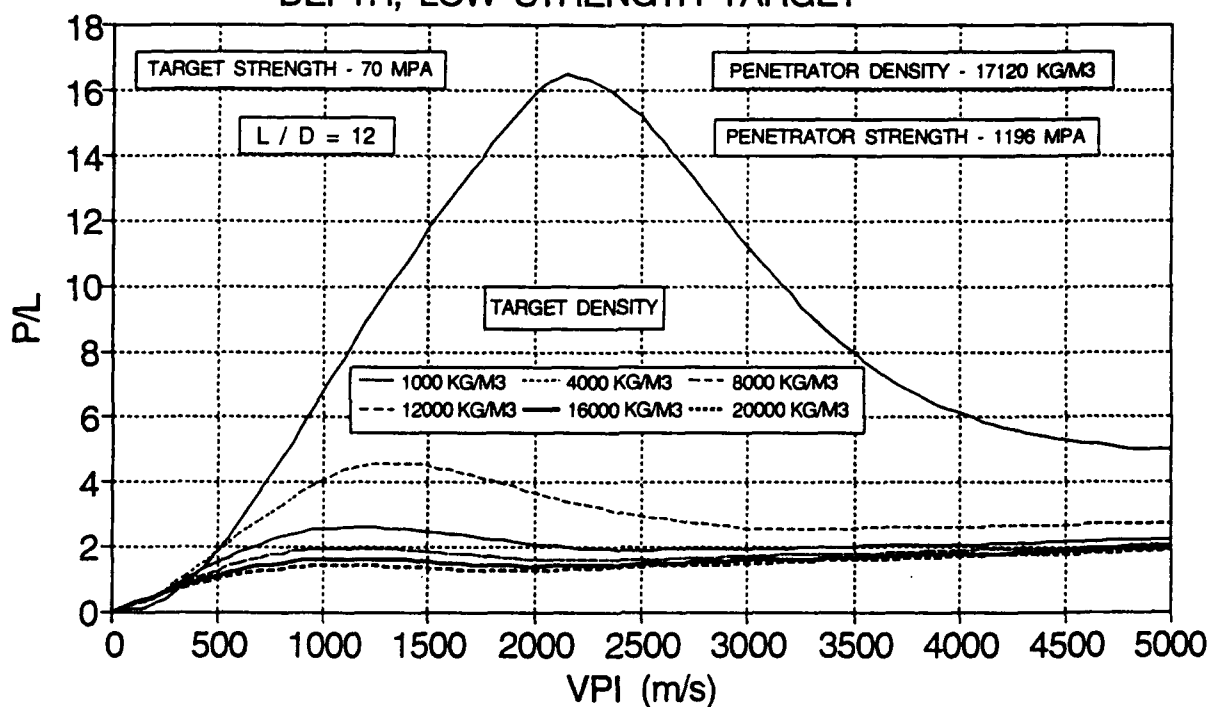


FIG. 12. EFFECT OF PENETRATOR DENSITY ON PENETRATION DEPTH, HIGH STRENGTH TARGET

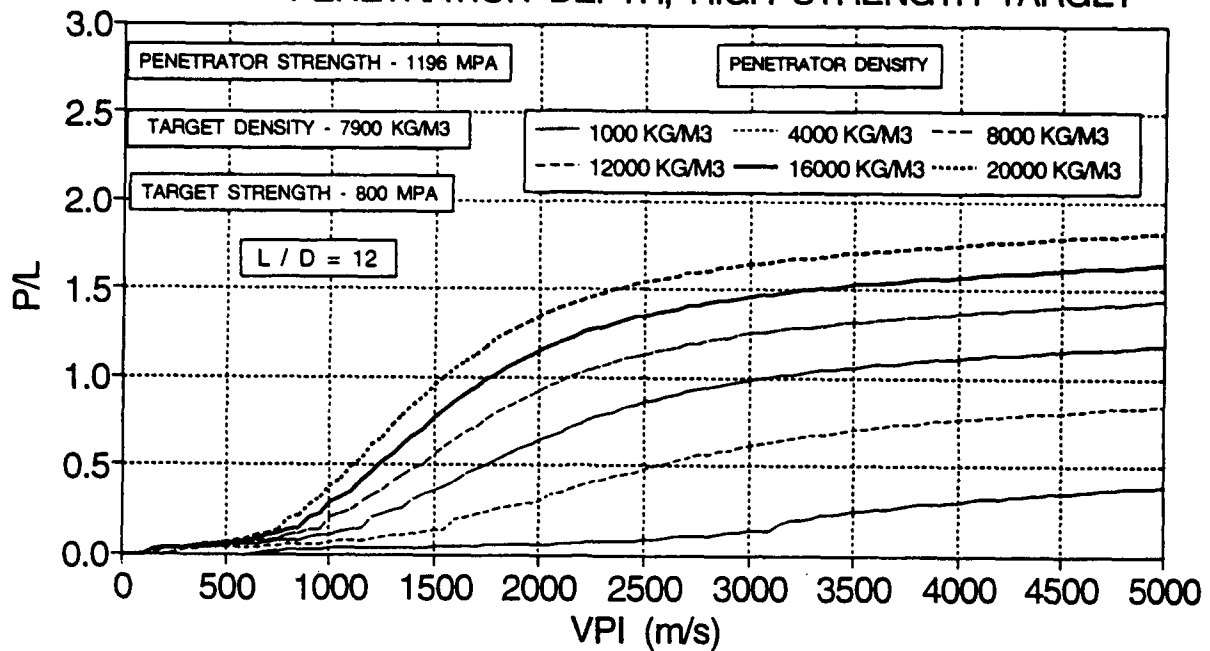


FIG. 13. EFFECT OF PENETRATOR DENSITY ON PENETRATION DEPTH, LOW STRENGTH TARGET

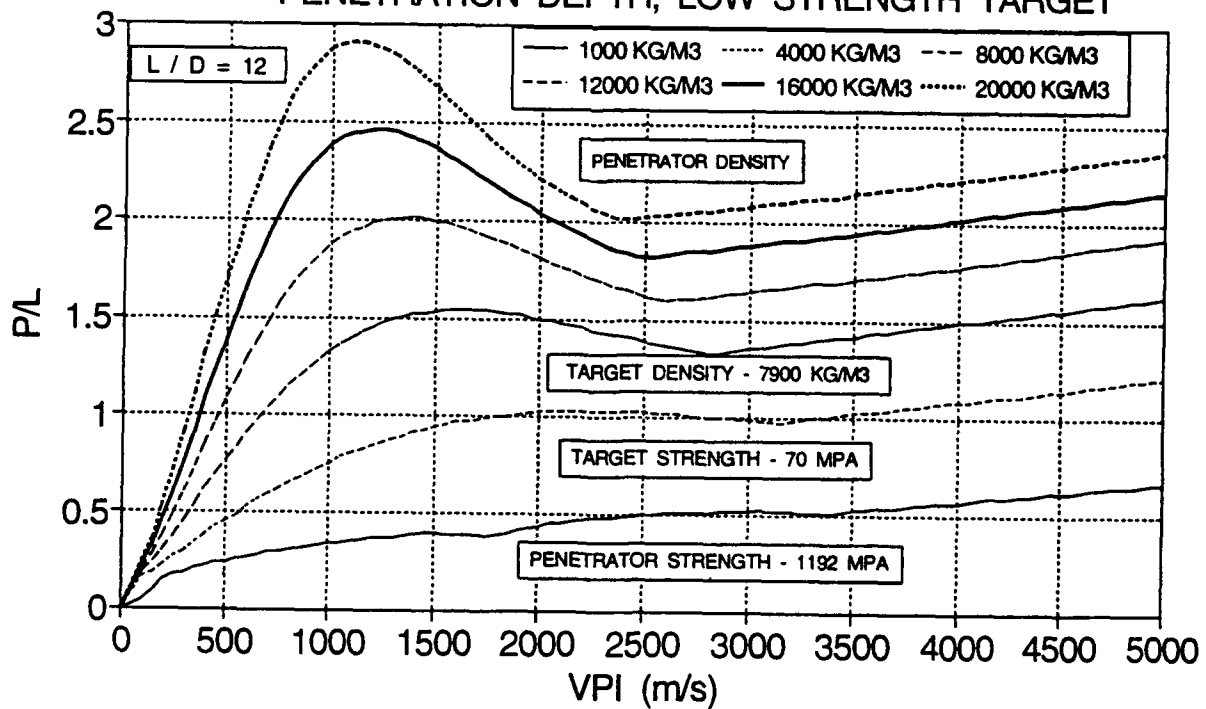


FIG. 14. EFFECT OF L/D ON PENETRATION DEPTH

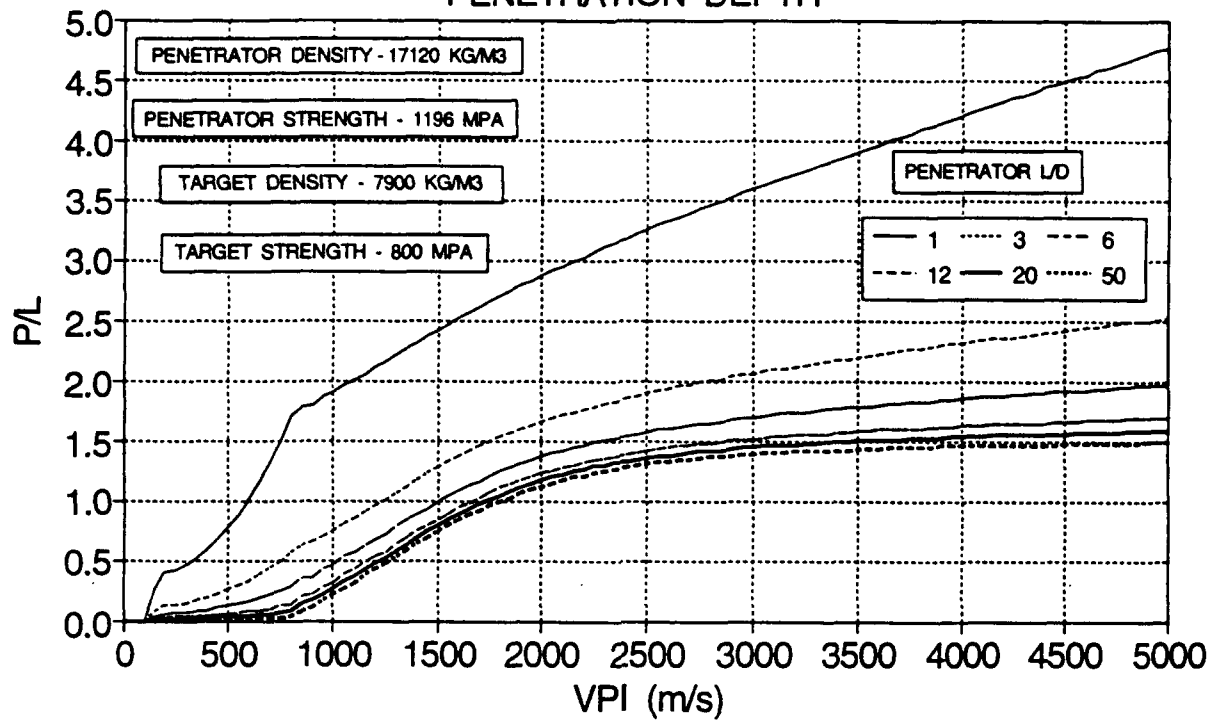


FIG. 15. EFFECT OF TARGET STRENGTH ON PENETRATION DEPTH FOR CONCRETE

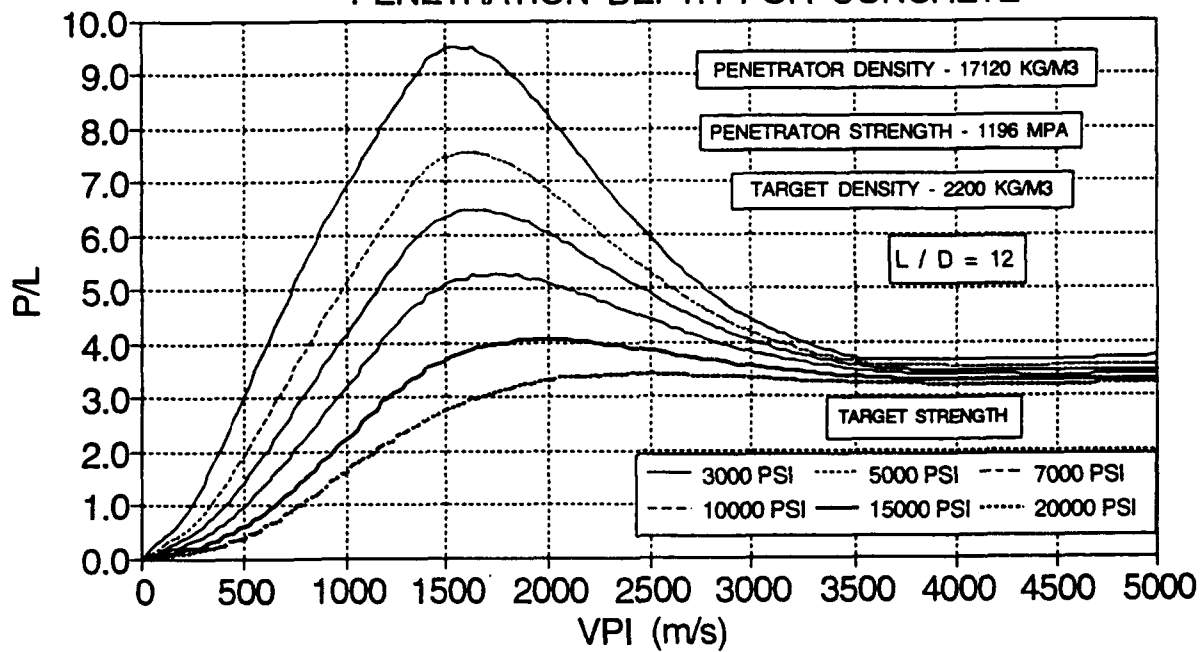


FIG. 16. EFFECT OF PENETRATOR STRENGTH ON PENETRATION DEPTH FOR CONCRETE

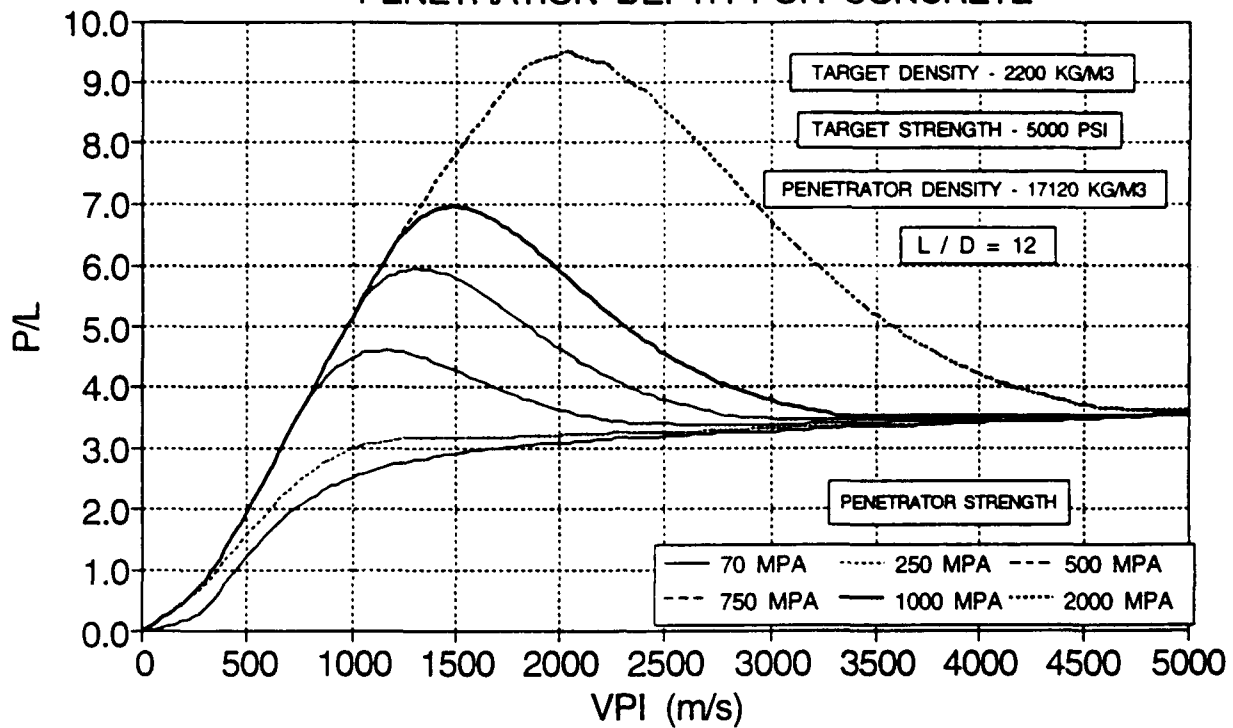
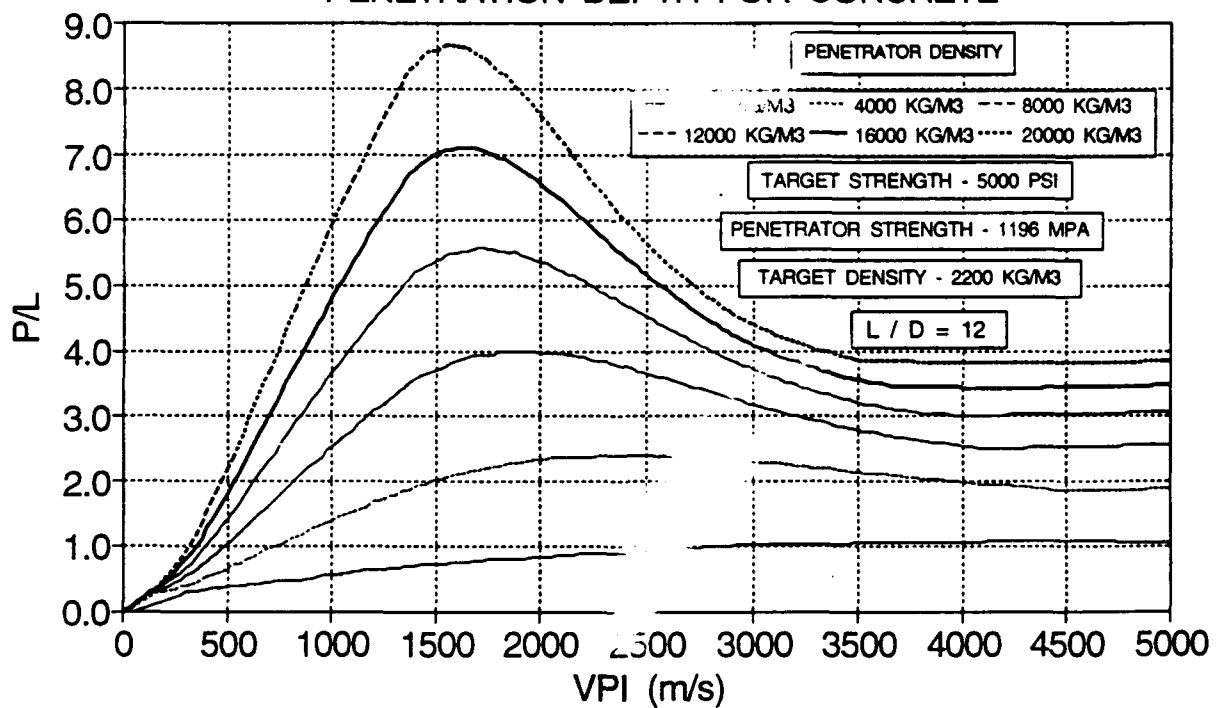


FIG. 17. EFFECT OF PENETRATOR DENSITY ON PENETRATION DEPTH FOR CONCRETE



Resolution Enhancement of Passive Millimeter-wave Imaging

Zhi Ding
Assistant Professor
Department of Electrical Engineering
Auburn University
Auburn, AL 36849
(205)-844-1817

Final Report for
Summer Faculty Research Program
Wright Laboratory/MNGS
Eglin Air Force Base, FL 32542-5434

Sponsored by: Air Force Office of Scientific Research
Bolling Air Force Base, Washington, D.C.

August 1993

Resolution Enhancement of Passive Millimeter-wave Imaging

Zhi Ding
Assistant Professor
Department of Electrical Engineering
Auburn University

Abstract

Although passive millimeter-wave imaging is capable of operating under adverse conditions and provides the advantage of stealth, its poor resolution severely limits its applicability in practice. The problem of resolution improvement for a passive millimeter-wave imaging system is investigated. The feasibility of significant image resolution improvement is studied. A new differentiation-integration deconvolution (DID) algorithm is proposed for resolution improvement on images containing extended targets and is tested through extensive simulations. A criterion for measuring super-resolution is also presented and shows that our proposed DID algorithm improves the resolution of test images by 2-3 times.

Resolution Enhancement of Passive Millimeter-wave Imaging

Zhi Ding

1 Introduction

This report describes the problem of resolution enhancement for passive millimeter-wave imaging devices and summarizes our recent results in this area supported by the AFOSR Summer Faculty Research Program.

Compared with infra-red, millimeter-wave (MMW) encounters less obstruction through fog, dust, smoke, and artificial cover. The use of passive MMW imaging in air surveillance, target seeking, and civilian applications such as vehicle guidance offers a viable alternative to infra-red (IR) imaging under such adverse conditions. Passive imaging is particularly attractive to military operations and intelligence gathering since a passive sensor emits no signal and therefore offers stealth. Unlike IR sensors that are incapable of detecting targets under cover or in foggy and dusty conditions, MMW sensors can provide adequate information in these unfavorable situations. Moreover, the use of passive millimeter-wave imaging, together with IR imaging, can improve and enhance target recognition capability and visual images. Additionally, MMW sensors are expected to be employed in many ground-based, airborne, and spaceborne applications such as autonomous aircraft landing and collision avoidance. Recent experiments by TRW [1] provide some very encouraging results.

Over the years, the wide application of MMW imaging is hindered by the hardware limitation in constructing high gain, low noise receivers. Fortunately, the technological advancement in microelectronics has drastically improve the performance of MMW receivers. Nevertheless, a more critical obstacle still exists which will require important breakthrough, namely, the improvement of poor angular resolution at MMW frequencies. This summer research project centers on the issue of resolution improvement based on the use of advanced digital signal processing of the received image signals.

In this report, the low resolution problem of passive millimeter-wave imaging is outlined in section 2. Next various existing approaches to this well-known problem are summarized with respect to their advantages and disadvantages in section 3. Our new algorithm is presented in section 4 and the issue of superresolution is discussed in detail. Simulation results of our approach compared with some existing methods are presented in section 5. Finally, a summary of this report is given in section 6.

2 Problem Statement: Diffraction Limit on Angular Resolution

Passive MMW imaging data can be collected from a single MMW sensor (antenna) by scanning a 2-dimensional scene. Alternatively, a line array or a 2-D focal-plane array can also be applied to achieve quicker and more efficient data acquisition. Nevertheless, the angular resolution of a single

sensor or an array of sensors will be dictated by the Rayleigh diffraction limit, i.e.,

$$\theta \approx \frac{\lambda}{D} \quad (2.1)$$

where λ is the millimeter wavelength and D is the aperture size of the antenna (sensor).

The diffraction severely limits the image resolution of passive MMW devices. For example, at the frequency of 94GHz, an antenna with one foot diameter has an angular resolution of approximately 0.6°. At a distance of 1 km, this translates to a target resolution of merely 10.6 meters. Such a poor resolution may be barely sufficient to identify large objects such as ships and buildings. For many practical purposes, the antenna size is limited, making it impossible to simply increase the physical aperture of the sensors to gain high image resolution. Thus, in order for passive MMW imaging to become widely applicable, its angular resolution must be significantly improved with the aid of advanced and specialized signal processing systems.

3 The Critical Issue of Image Resolution Enhancement

The low angular resolution of the passive MMW sensors due to the longer wavelength is the primary obstacle to its deployment in many military and civilian applications. Our proposed research is aimed at developing post-detection signal processing methods to significantly improve the image resolution. Our objective is to design effective solution to sharpen the received radio image based on the knowledge of the antenna beampattern.

3.1 Millimeter-wave Imaging

For the simplicity of representation, we consider the problem of resolution improvement for 1-D images. It is evident that the 2-D problem is simply a straightforward generalization of the 1-D case.

Denote the antenna beampattern as $h(\phi)$ where ϕ is the angle of signal arrival. The received passive image at the sensor after scanning a 1-D scene $x(\phi)$ can be written as

$$y(\phi) = h(\phi) \circledast x(\phi),$$

where $x(\phi)$ is the true original image, $h(\phi)$ the point spread function (PSF) of the sensor (antenna), and $y(\phi)$ is the received image. The noncoherent antenna beampattern $h(\phi)$ operates as a blurring function to the actual signal $x(\phi)$. In practice, the received signals are sampled to generate the following relationship,

$$y_k = h_k \circledast x_k. \quad (3.1)$$

Thus, recovering the source signal x_k based on y_k and h_k becomes the standard deconvolution problem. It should be noted that all signals x_k , y_k , and h_k in passive imaging are positive since the passive imaging system only forms an image of intensity irrespective of the phase. This positivity condition is in fact crucial to solving the image deconvolution problem.

The deconvolution problem has been extensively studied in the past, and image processing textbooks often contain various image restoration treatments. It has been long recognized that the

deconvolution problem is ill-posed when the bandwidth of the point spread function h_k is limited and when additive noise n_k is present in the received image:

$$y_k = h_k \otimes x_k + n_k. \quad (3.2)$$

The PSF h_k is typically lowpass in nature. As a result, all the high spatial frequency content of x_k will be attenuated by h_k and thus, high frequency (high resolution) information is either irretrievably lost in y_k or highly attenuated. In order to regain the attenuated high frequency content, an inverse filter (high-pass) needs to be used on the received image, which will have the undesirable noise amplification effect.

The ill-posed-ness of this problem arises from the conflict between the need to recover the lost high frequency information and the necessity to suppress high frequency additive noise at the same time. It is essential that the original image be recovered as precisely as possible without severely amplifying the receiver noise. Hence the optimum solution lies between the inverse filter and an ideal lowpass filter to suppress the additive noise. Wiener filtering and regularization are typical balanced solutions to accomplish such conflicting tasks.

3.2 Summary of Existing Works

Essentially, the problem of millimeter-wave image resolution enhancement is not different from the traditional image restoration problem that has been studied for years. Although many methods have been proposed and studied in the past, the image deconvolution problem is still a difficult and open problem. Achieved resolution improvement has been modest for the most part. Two basic kinds of approaches dominate the literature: linear and nonlinear deconvolutions. We now summarize their major advantages and weaknesses when applied to the millimeter-wave resolution improvement problem.

3.2.1 Linear Deconvolution

The linear deconvolution methods accomplish the task of resolution enhancement by applying a linear filter (or transformation) on the received image. The purpose of this filter is to suppress noise while recovering the attenuated high frequency content of the image. Various existing linear deconvolution methods typically belong to one of the following categories:

- Inverse Filtering [8, 14];
- Singular Value Decomposition (SVD) [7];
- Wiener Filtering (Minimum Mean Square Error) [8];
- Regularization [9, 10, 12, 15].

In inverse filtering, the objective is to recover the original image by reversing the lowpass effect of the PSF. It in effect searches for a least square solution of the convolution equation. Although very simple, the inverse filtering approach normally produces poor result due to its amplification

of receiver noises. The SVD approach is an effective alternative to inverse filtering, It attempts to approximate the inverse filter without excessive noise amplification.

Wiener filter is another way to avoid noise amplification. By minimizing the mean square error between the recovered image and the original image, Wiener filter provides a good balance between image restoration and noise suppression. Regularization was an useful tool developed by Tikhonov [9] to solve general ill-posed problems. Its objective is to deconvolve the image while maintaining certain degree of smoothness on the deconvolved image. Among numerous regularization methods, Reynold attempted to find an optimum regularization coefficient, while Gleed constructed a two-step regularization approach.

The major advantage of various linear deconvolution methods is that they are always very simple in concept and implementation. In fact, all of the linear algorithms are data independent and only require a one-step filtering or matrix operation on the received image. Thus, they are highly desirable onboard a seeker where the computational power is rather limited. Unfortunately, linear deconvolution methods can only reshape the nonzero spectrum of the received data. It cannot extrapolate or recover any lost frequency content. Hence, linear deconvolution can only achieve very modest resolution improvement. With the exception of inverse filtering that often generates noisy images, the recovered image tends to be smooth and the finer details of the image, such as sharp edges, are often suppressed.

3.2.2 Nonlinear Deconvolution

In order to recover any spectral content that has been complete filtered out by the antenna PSF, frequency domain extrapolation is necessary. Since linear methods are incapable of extrapolating in frequency domain, only nonlinear methods can more effectively increase the image bandwidth and improve the image resolution. However, this advantage can sometimes be offset by higher real time computation requirement due to their data dependency.

The basis of any nonlinear deconvolution algorithm is the use of prior knowledges with regard to the original image. In passive imaging system, the received and the original image data are all positive and bounded. In addition, the original image may only have a finite (known) spectral or spatial support. By constraining the deconvolved image to satisfy these known conditions of the original image, nonliner operations are used to assure the positivity and the finite support of the recovered image. Nonlinear operations are able to extend the image bandwidth and hence improve the image resolution.

The following nonlinear deconvolution algorithms are well known and commonly refereed to:

- Jansson-van Cittert method [6];
- Schell and Biraud method [6, 14];
- Maximum entropy deconvolution [14, 17, 18];
- Constrained iterative deconvolution (CID) method [11].

Of various constraints designed based on prior knowledges of the original image, the positivity constraint is the most important. Positivity is used in all of the above nonlinear deconvolution methods. Surprisingly, by merely imposing the positivity constraint alone, significant resolution improvement can be made.

The Schell and Biraud methods force the estimated image \hat{x}_k to be positive by letting

$$\hat{x}_k = a_k^2$$

and solving for the signal a_k . Their methods require tedious iterations and are very inefficient as a result. There are several different maximum entropy algorithms for image deconvolution. The basic idea of any maximum entropy algorithm is to view the original image as a sequence of random signal and find the deconvolved image by maximize the entropy of the random signal subject to the constraint of the convolution equation. Although maximum entropy algorithms are suitable for single frame image processing tasks, its complexity requires large amount of on-board, real time computation on passive millimeter-wave seekers. The simpler Jansson-van Cittert algorithm, however, does not generate acceptable quality images when the objects in the image are extended targets.

We concentrate on one particular algorithm that is simple and computationally suitable for implemenation onboard passive millimeter-wave seekers. Specifically, we are going to modify the CID algorithm developed by Schafer *et al.* [11]. We describe the principles of this algorithm and our modification that results in a better method for resolution enhancement of extended targets.

4 Differentiation-Integration Deconvolution Algorithm

4.1 Van Cittert, CID, and FCID algorithms

Before we introduce our deconvolution method, it is important to understand a linear inverse scheme called Van Cittert's iterative inverse. Given a frequency response $H(\omega)$,

$$H^{-1}(\omega) = \lambda \sum_{n=0}^{\infty} [1 - \lambda H(\omega)]^n. \quad (4.1)$$

From $Y(\omega) = H(\omega)X(\omega)$, the i -th step image estimate $X^{(i)}(\omega)$ can be updated through the following iteration:

$$X^{(i+1)}(\omega) = [1 - \lambda H(\omega)]X^{(i)}(\omega) + \lambda Y(\omega). \quad (4.2)$$

The constant λ should be chosen to satisfy the convergence condition

$$|\lambda H(\omega)| \leq 1.$$

If the convergence condition is satisfied, we then have

$$X^{(i)}(\omega) \longrightarrow H^{-1}(\omega)Y(\omega), \quad \text{as } i \rightarrow \infty. \quad (4.3)$$

Notice that this iterative approach is still linear and cannot accomplish any frequency extrapolation. In order to expand the image bandwidth, nonlinear operators need to be applied. By

applying the most commonly used positivity condition on x , Schafer and Richards proposed to truncate the negative portion of the signal $x_k^{(i)}$ in every iteration. This produces the so-called constrained iterative deconvolution (CID) algorithm:

$$\begin{aligned} x_k^{(i+1)} &= [1 - \lambda h_k] \odot \hat{x}_k^{(i)} + \lambda y_k \\ \hat{x}_k^{(i)} &= x_k^{(i)} \cdot U(x_k^{(i)}), \end{aligned} \quad (4.4)$$

where $U(\cdot)$ is the step function.

Richards and coworkers [2, 3, 13] improved the convergence speed of the CID method by using a quadratic Van-Cittert expansion and developed a fast constrained iterative deconvolution (FCID) algorithm. The key weakness of the FCID algorithm lies in its inability to deal with images containing large targets because of the tendency of the FCID to emphasize point targets. In fact, the original CID algorithm suffers from the same shortcoming. In air-surveillance, for example, the scene of interest may have a high value target amidst several ordinary targets. Merely separating them as point targets is insufficient to determine the fine detail of each target. Moreover, when modest additive noise is present in the image, both algorithms also tend to generate many spurious targets. Evidently, much improvement and modification are necessary in order for the constrained iterative method to be useful in passive MMW imaging.

4.2 Algorithm Development

We develop a deconvolution algorithm suitable for resolution improvement on images containing extended targets. Our method is based on the CID algorithm proposed by Schafer *et al.* [11].

We recognize that the CID algorithm performs well on images with point targets. For an image with large targets, the edges of those targets can generate derivative images with point targets. Therefore, we can apply the CID algorithm separately on the positive part and the negative part of the image derivative. Once the two parts of the image derivative are deconvolved, we can then combine them to form the deconvolved derivative for integration. Since high frequency noise tends to generate large derivatives as well, we also apply a low pass filter on the image first before taking the derivative. In applying CID, the positive part of the derivative will be constrained by positivity while the negative part will be constrained by negativity. The diagram in Figure 1 illustrates the actual procedure of this differentiation-integration deconvolution (DID) algorithm

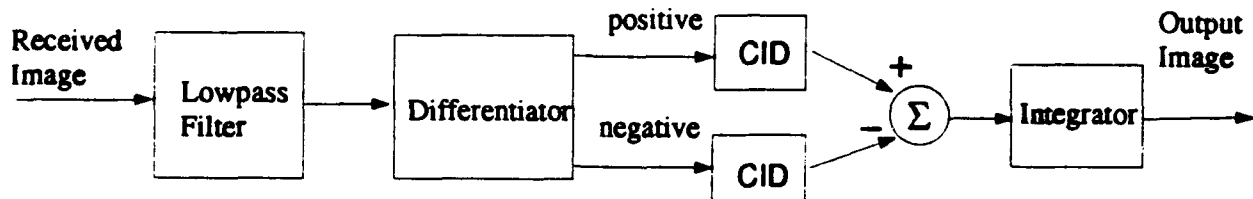


Figure 1: The differentiation-integration deconvolution (DID) algorithm.

We shall test this algorithm on two benchmark images against several existing methods. But first, we need to clarify the term "superresolution" and establish means to compare the resolution of two images.

4.3 On Superresolution

The term superresolution is an often encountered term in the literature of array signal processing as well as in image restoration. Unfortunately, this term is often misused due to its favorable connotation. The misuse of superresolution has created a lot of confusion in the area of image deconvolution. Sometimes outrageous claims of resolution improvement are made due to misunderstandings. In this section, we attempt to clarify this confusion and explain how we propose to measure the resolution improvement of any given image restoration method.

Superresolution often refers to the ability to resolve two point targets that are separated by less than the Rayleigh diffraction limit. It is typically demonstrated by showing the ability of an algorithm to locate the positions of two point targets that are so close together that they cannot be separated in the original image. In this sense, superresolution in image processing is not different from superresolution in the direction finding problem in array processing. In both cases, only point targets are of concern and the objective is merely to locate the positions of those point targets. The possible distortion on the shape or the intensity of the image is often of no concern.

In the passive millimeter-wave seeker problem, we not only need to locate the targets but also to properly identify targets in the image. Therefore, we need to improve resolution on both point targets and extended large targets. Although many "superresolution" methods claim to be capable of achieving resolution improvement by 10 times, in reality, their claims are based on separating two closeby point targets. When applied to extended targets, these algorithms typically either fail to function properly or provide very modest improvement on resolution. Clearly, the difficulty in dealing with extended targets is the key disadvantage of many existing nonlinear deconvolution methods.

Another key difficulty in dealing with extended targets lies in the very definition of superresolution. Because of the nature of the image containing extended target, Rayleigh diffraction limit can no longer be used in defining resolution. Given two images of the same scene, there is no quantitative measure to compare the resolution of the two images without visual inspection. As a result, it is difficult to determine how much resolution improvement has been made by a given deconvolution method.

In order to measure objectively the actual amount of resolution improvement, we need to return to the initial definition of angular resolution in terms of the antenna size. To improve the resolution by a factor of two, the antenna diameter needs to increase to twice its original length. The antenna needs to be four times as large to achieve four times resolution improvement, and so on.

Definition:

Let y_k^n be the image formed from x_k using antenna n times larger. The deconvolved image \hat{x}_k has resolution improvement of n times if

$$\min_i \|y_k^i - \hat{x}_k\|^2 = \|y_k^n - \hat{x}_k\|^2 < 0.1 \|x_k\|^2, \quad (4.5)$$

□

In other words, a resolution improvement of n times is accomplished if the deconvolved image

\hat{x}_k is closest to the image y_k^n formed by increasing the antenna size n times and the difference between the two images is smaller than 10% of the true image energy. While the difference between the two images is obviously a good choice for judging resolution improvement, the upper bound must be present to avoid pathological cases when \hat{x}_k bears no resemblance to the true image but is relatively closer to y_k^n .

Our definition of resolution improvement is intuitive and can easily be measured in practice. If the deconvolved image is very similar to the image received by an antenna n times larger, then certainly the angular resolution is improved by n times. Here, not only we have to separate two point targets, the fine details of the original image also need to be preserved.

5 Test Examples

5.1 Test Setups

Two benchmark images are used in testing the DID method. The objects in the images are designed to resemble extended targets. They are constructed to contain distinctly sharp edges and to span a large area in the image. Figure 2(a) and (b) show the two benchmark images used in our tests.

The antenna point spread function is chosen to be a sinc-squared function as shown in Figure 2(c) whose lowpass frequency response is shown in Figure 2(d).

For the both images, we apply the DID algorithm under different clutter and noise levels. The clutter and the additive noise are generated independently by squaring Gaussian noises. The lowpass filter in the DID algorithm was chosen to be nearly ideal and have the same passband as the PSF frequency response. In all our simulations, $\lambda = 0.1$ was also selected and 100 iterations were run for each image.

5.2 Test Results on Image A

For image A, we first apply our algorithm to the noiseless received image. No clutter was added in the original image. Figure 3 shows the received image and the deconvolved image. We then added random and independent clutters to the original image so that the signal to clutter ratio (SCR) is 10dB. 10 independent clutter patterns were simulationed and the 10 deconvolved images are shown in Figure 3 together with the received image. Satisfactory image recovery was achieved.

We then increase the noise level so that SNR=30dB and 20dB, respectively. 10 independent simulation runs were completed for the two noise levels and the recovered images are shown together with the noisy received images in Figure 4 and Figure 5, respectively. Under reasonable amount of noise level (SNR=30dB), the DID algorithm performs very well for this test image. Most of the details are recovered in the deconvolved image.

5.3 Test Results on Image B

For image B, we also apply our algorithm to the noiseless received image. Figure 6 shows the received clutterless image and the deconvolved image. We then added random and independent

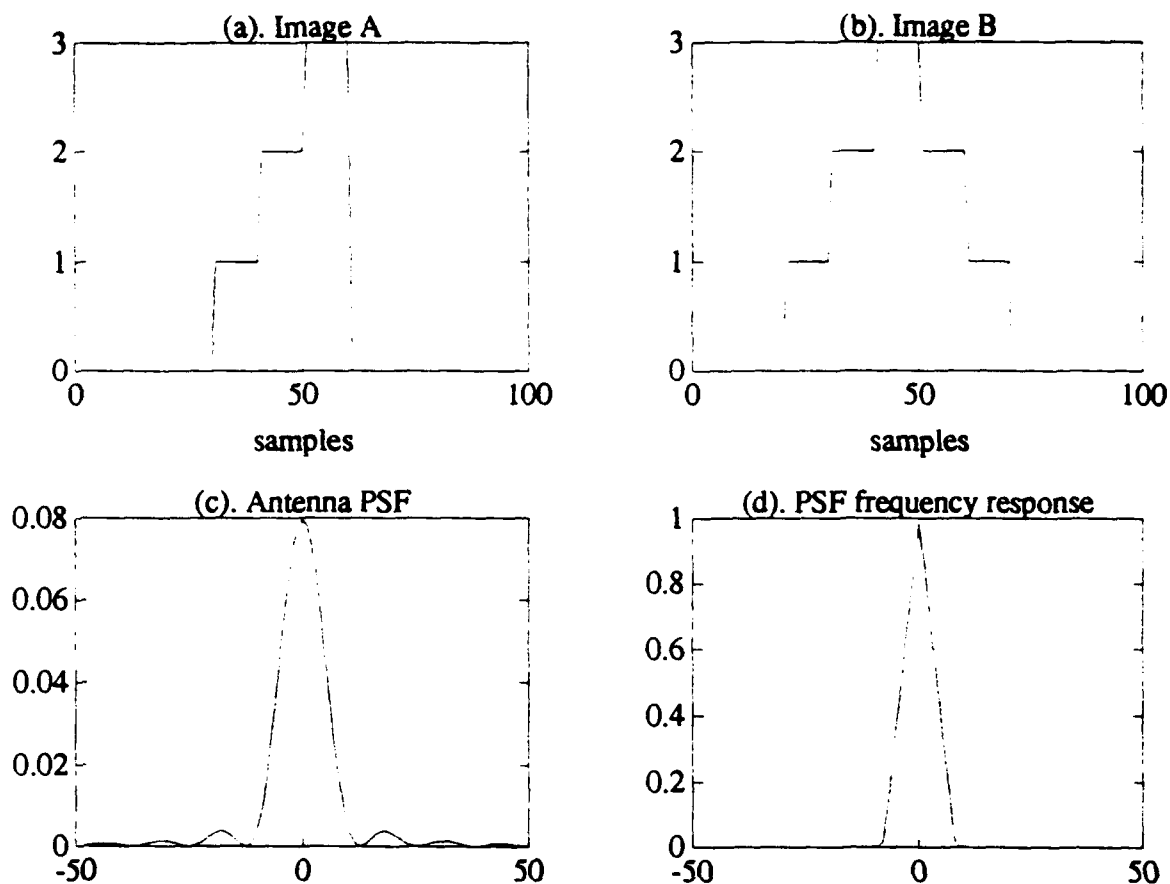


Figure 2: Two test images for resolution improvement.

clutters to the original image so that the signal to clutter ratio (SCR) is 10dB. 10 independent clutter patterns were simulated and the 10 deconvolved images are shown in Figure 6 together with the received image. Satisfactory image recovery was achieved.

We then increase the noise level so that $\text{SNR}=30\text{dB}$ and 20dB , respectively. 10 independent simulation runs were completed for the two noise levels and the recovered images are shown together with the noisy received images in Figure 7 and Figure 8, respectively. Under reasonable amount of noise level ($\text{SNR}=30\text{dB}$), the DID algorithm is also successful in deconvolving image B and recovered most of the details in the deconvolved image.

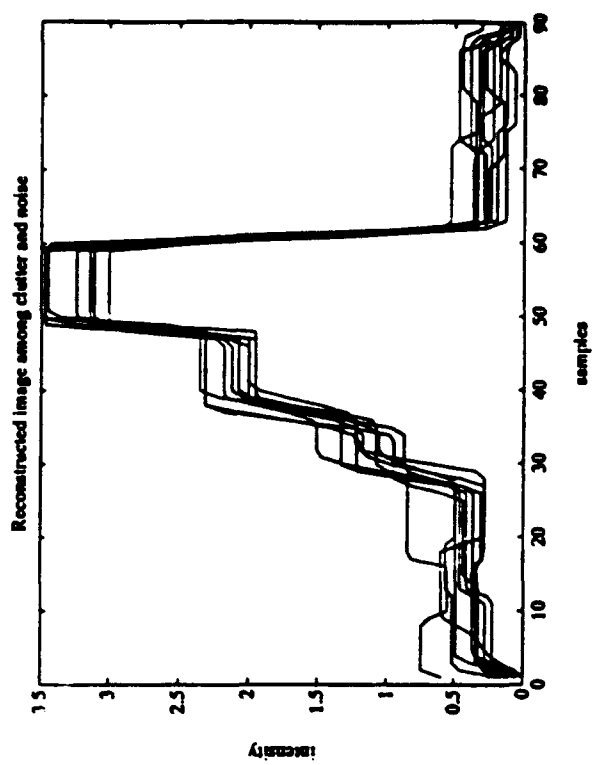
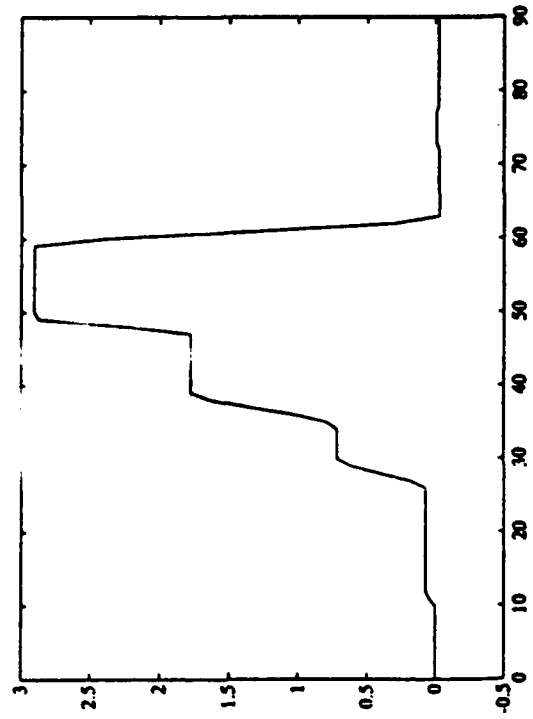
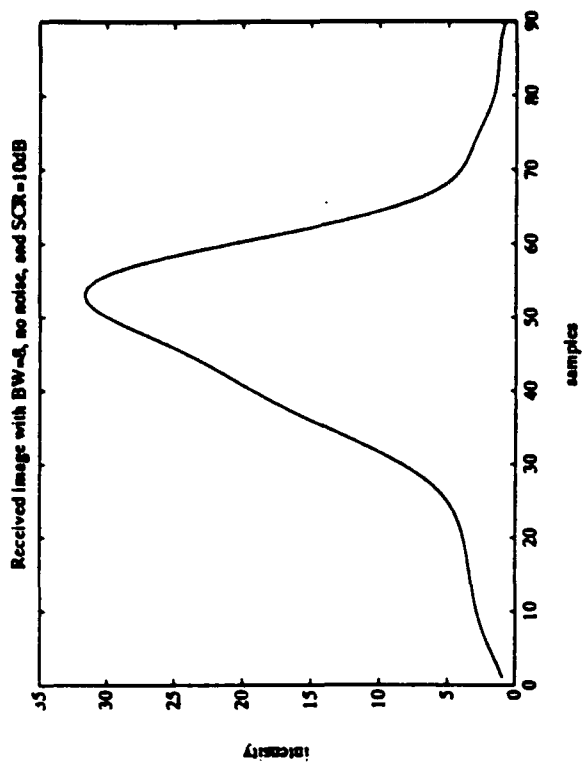
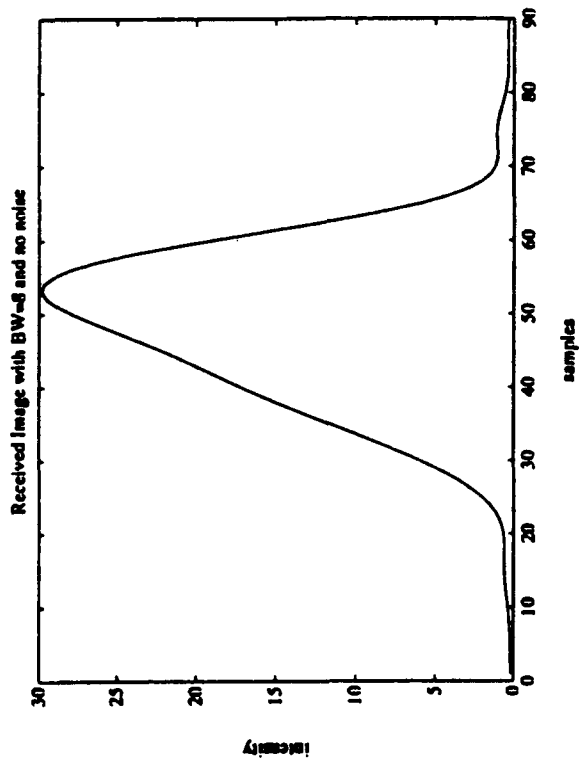


Figure 3.

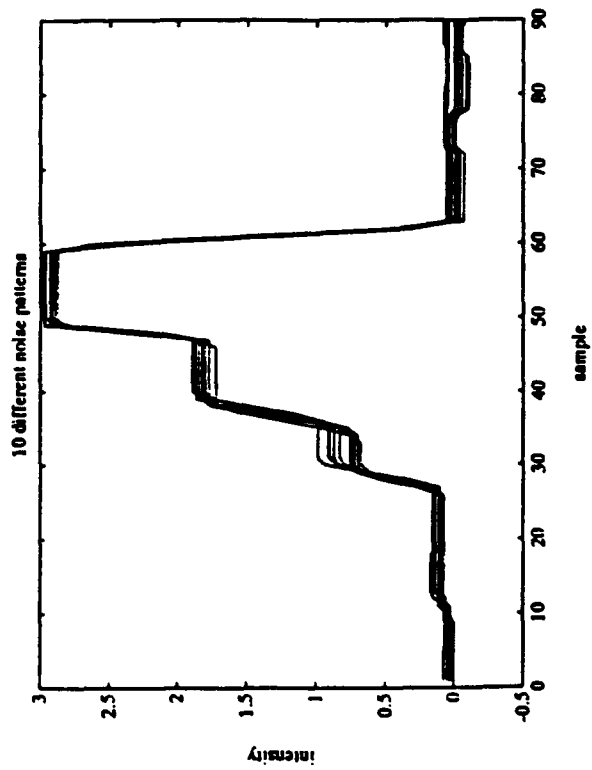
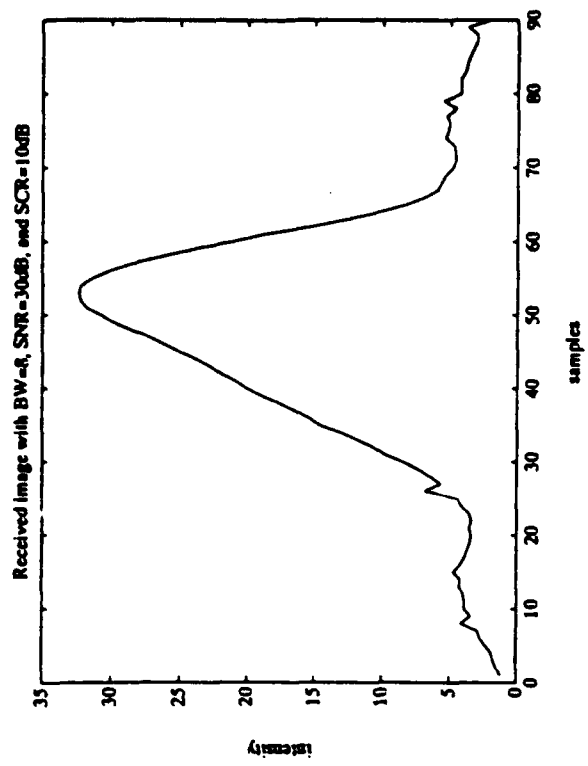
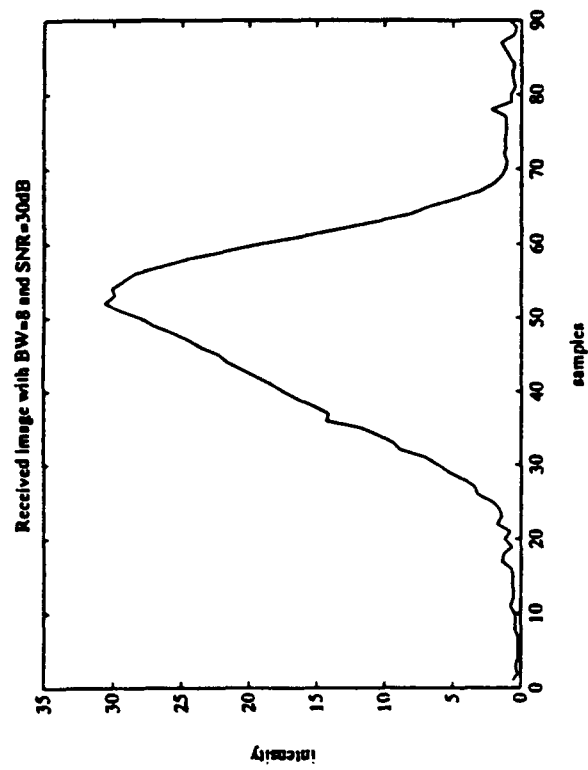


Figure 4.

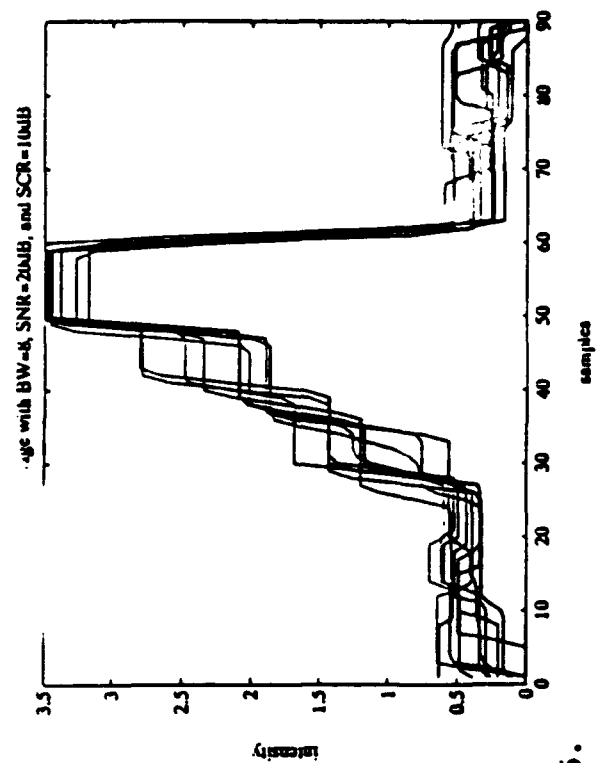
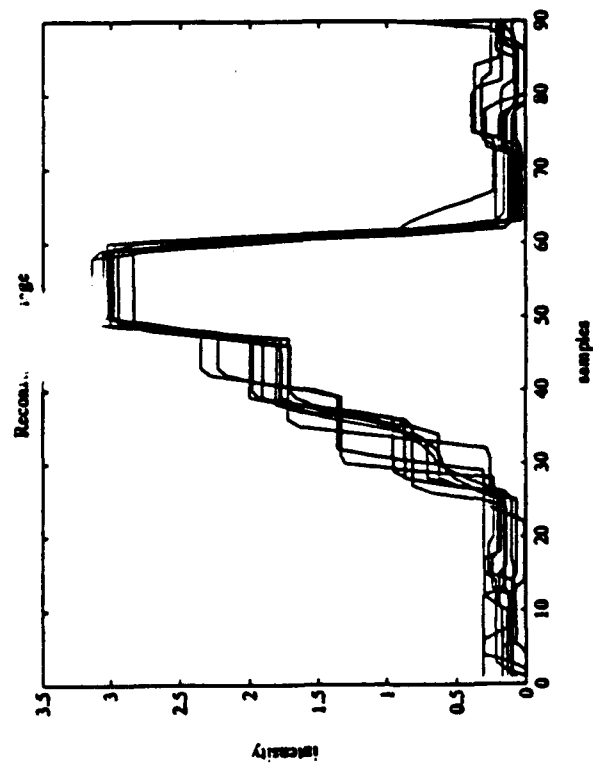
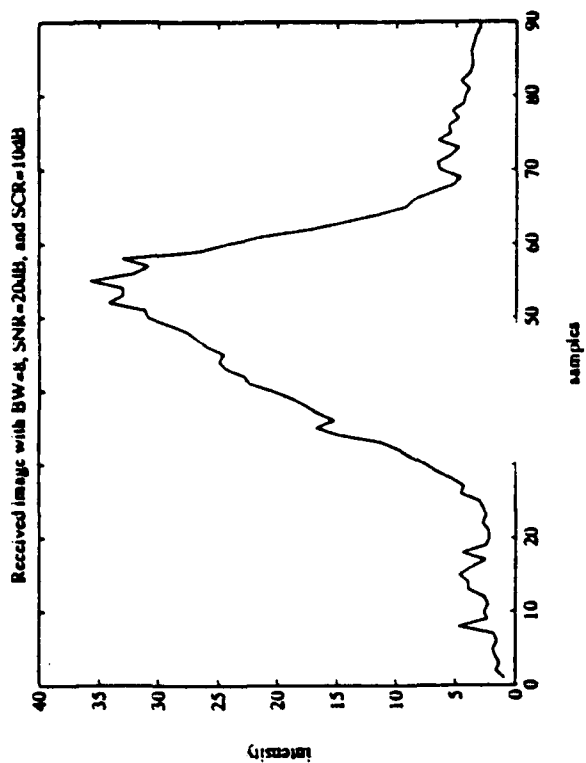
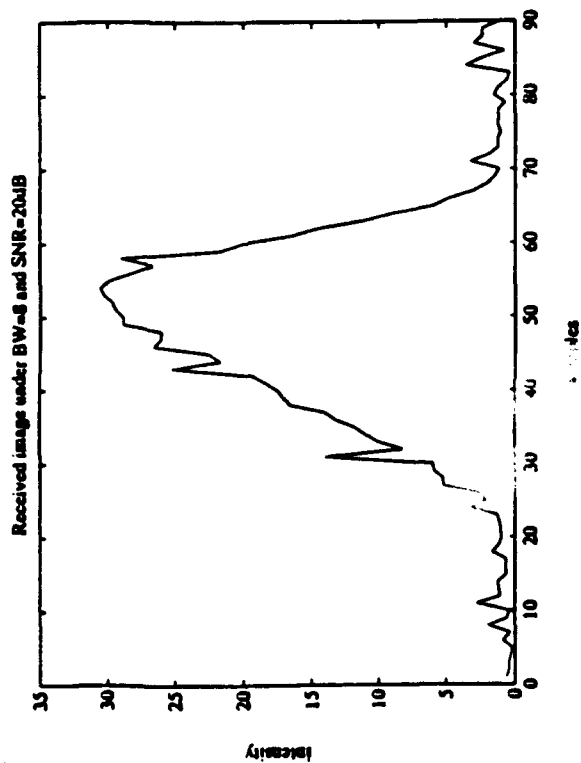


Figure 5.

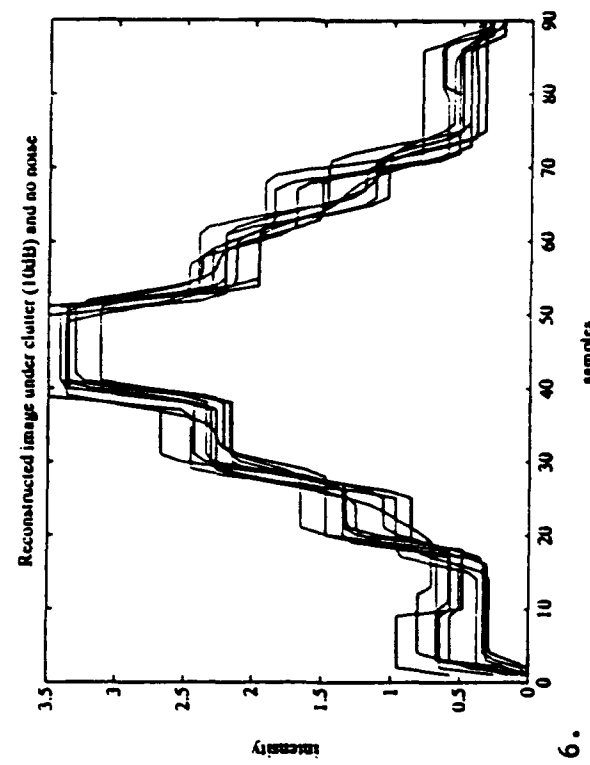
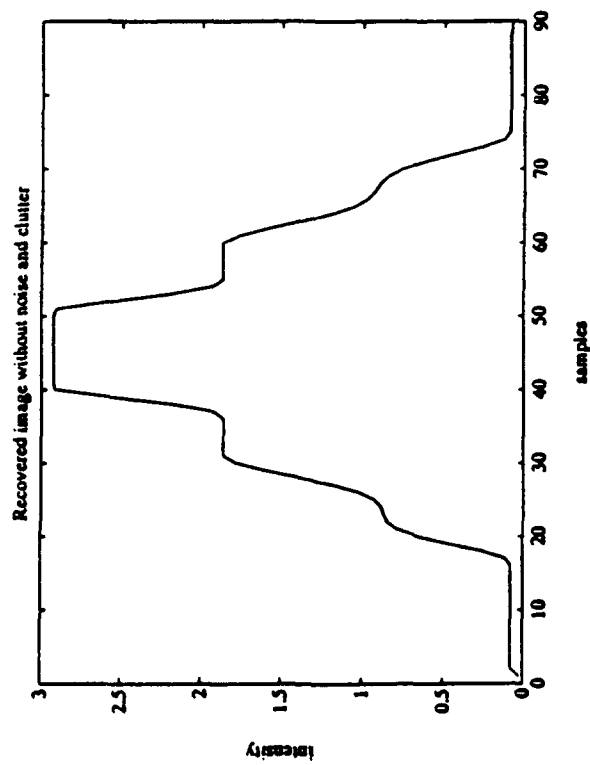
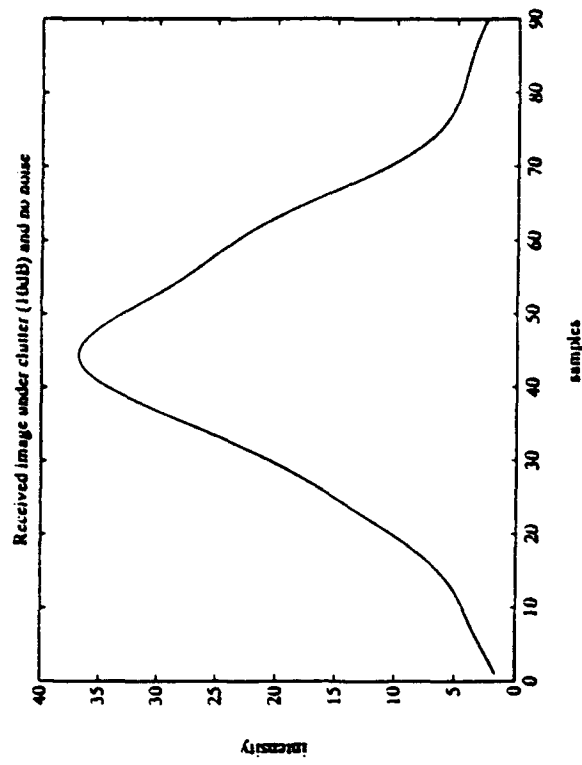
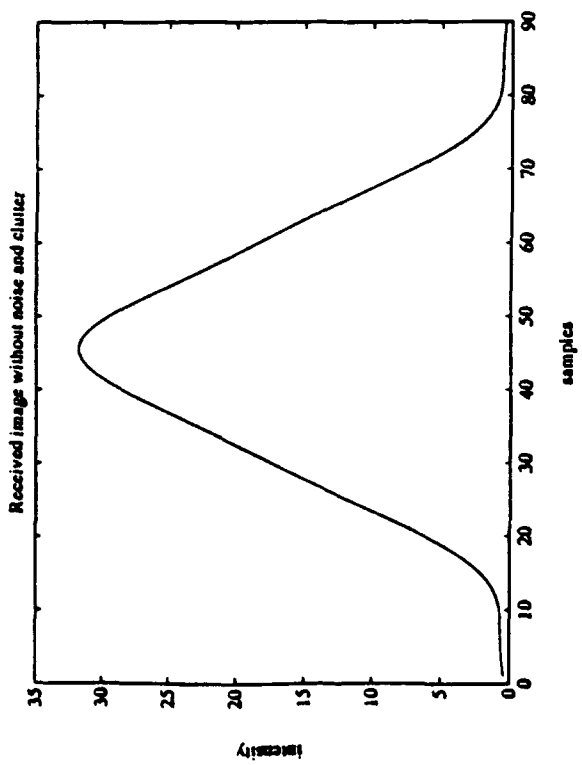


Figure 6.

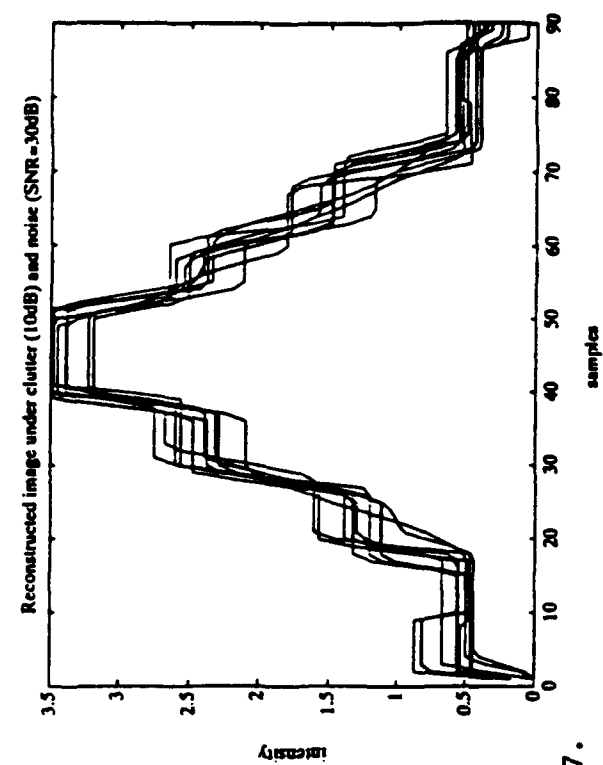
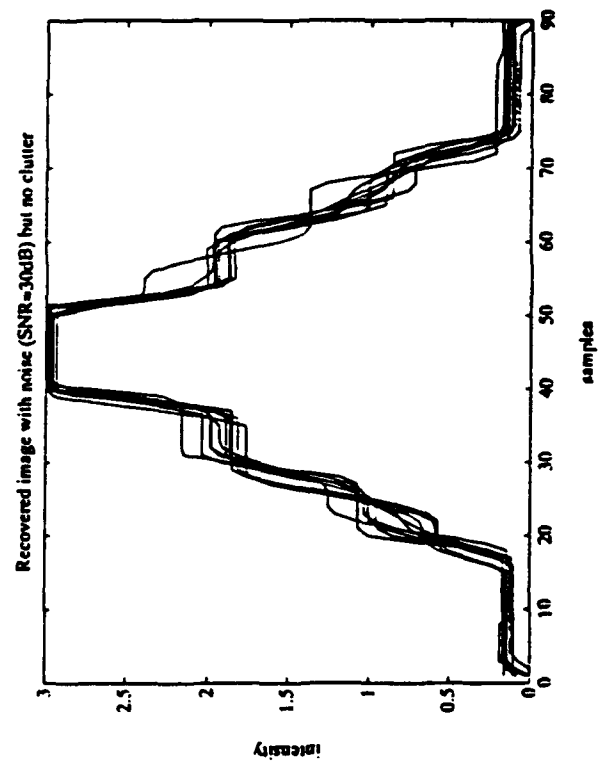
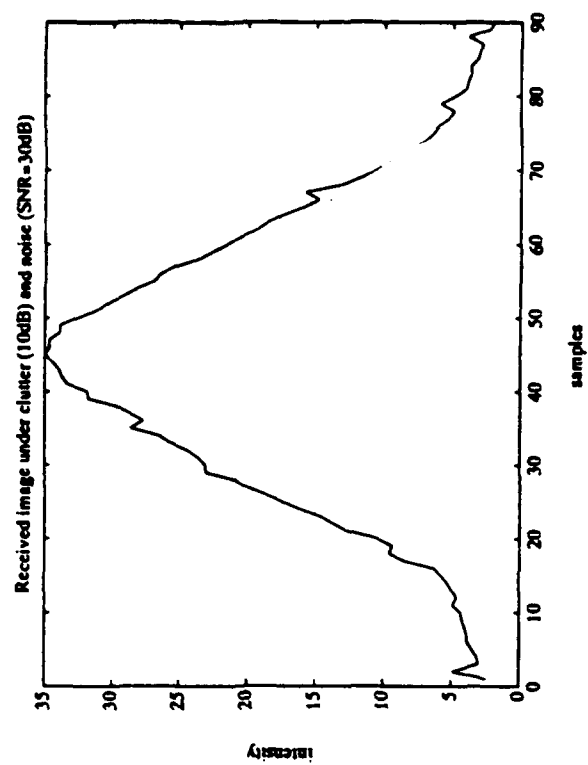
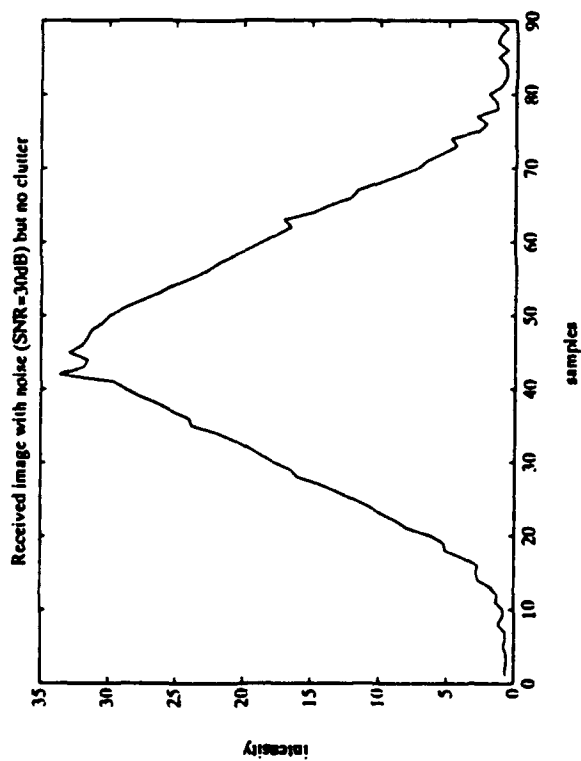


Figure 7.

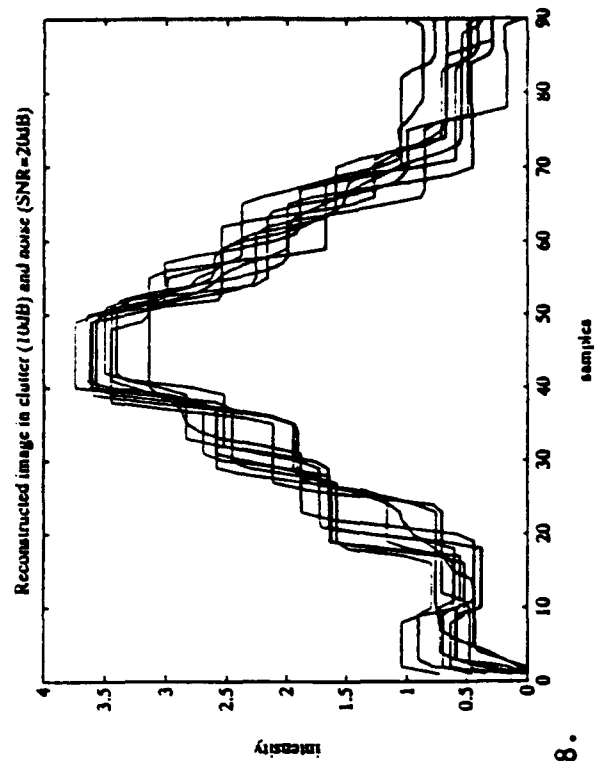
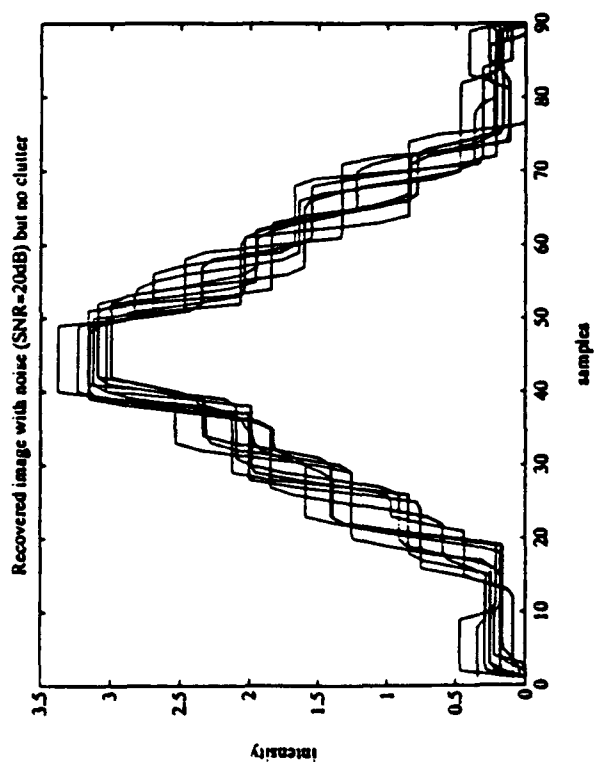
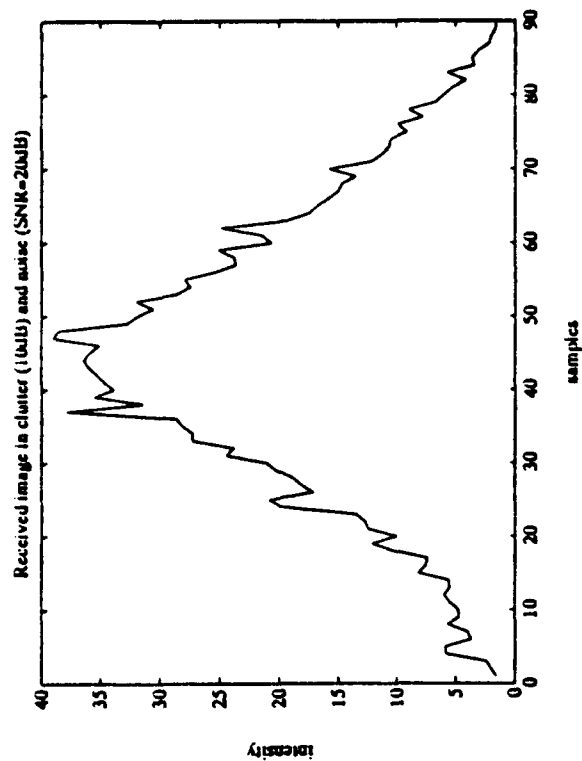
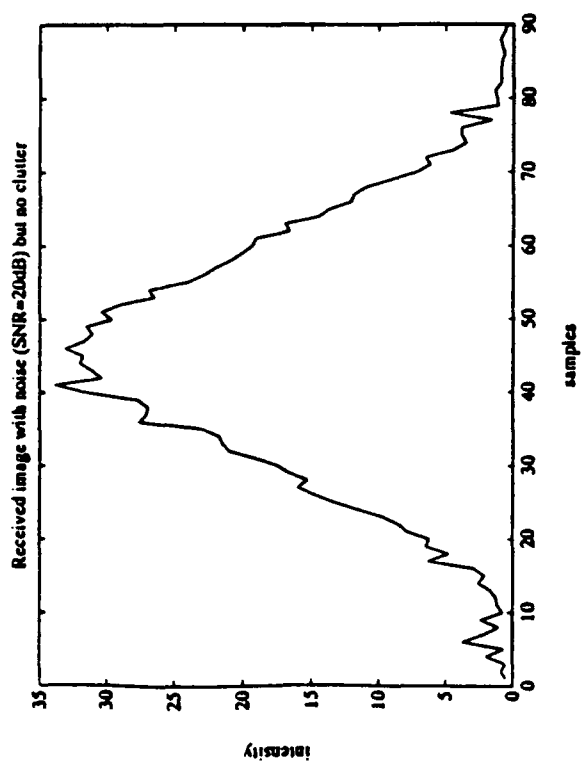


Figure 8.

5.4 Synopsis

We summarize our test results by estimating the normalized mean square errors between the true clutterless image and the deconvolved image under different noise levels. We would like to determine the amount of resolution improvement attained by the DID algorithm in our simulation. To achieve accurate measurement, we perform 100 independent simulations for each simulation setup.

Figure 9 demonstrates the effect of the noise and clutter on the deconvolution of the two test images. Clearly, as the noise increases, the NMSE tends to increase rapidly. For $\text{SNR}=10\text{dB}$, the deconvolution method fails to recover the original image as the NMSE is over 30%.

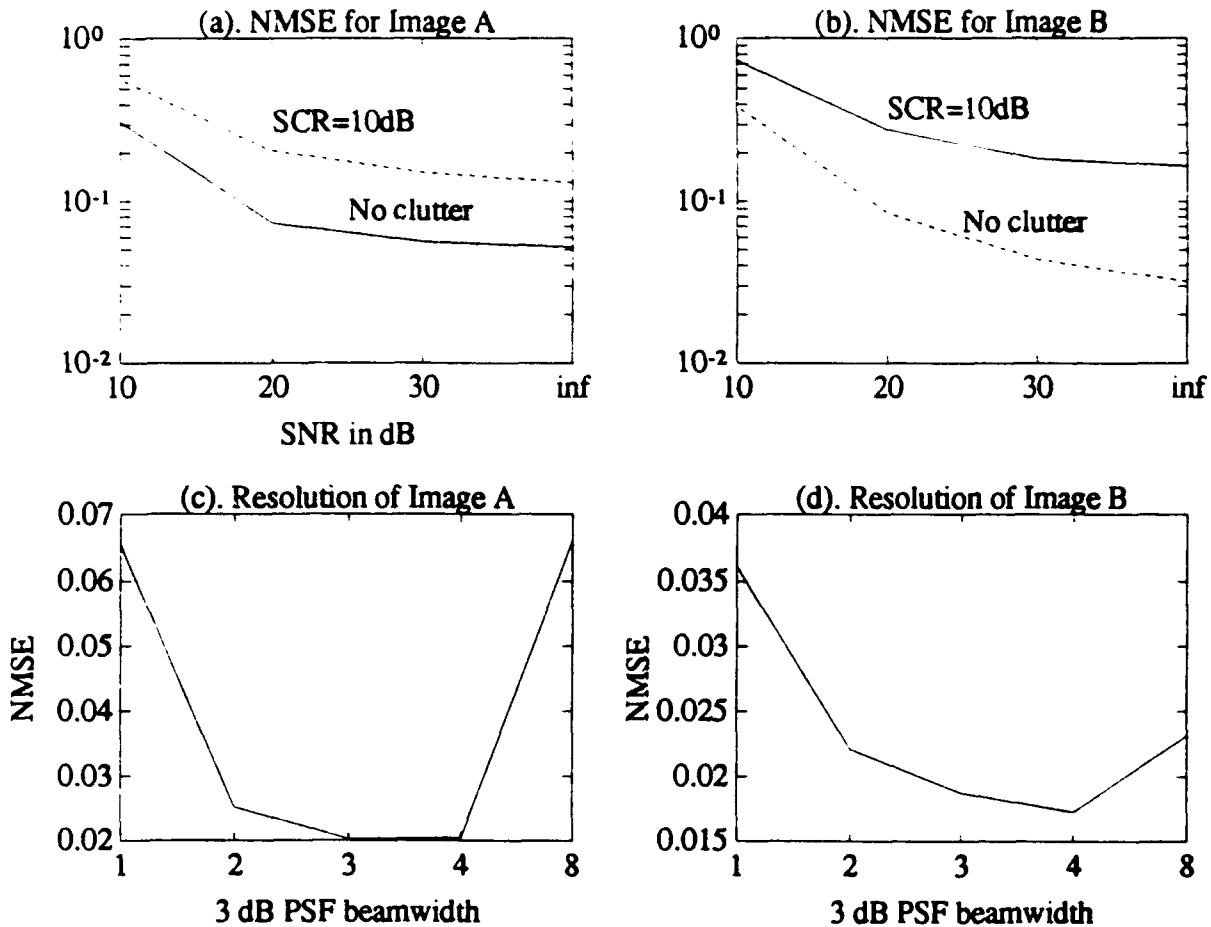


Figure 9: Resolution improvement on Images A and B using DID method.

We reduce the beamwidth of the antenna PSF to simulate the effect of antenna size increase. The original beamwidth of 8 was reduced to 4, 3, 2, and finally 1, representing the antenna size increase by factors of 2, $8/3$, 4, and 8, respectively. The images are clutterless and the receiver SNR is 30dB. Simulation results are shown in Figure 9(c) and 9(d). From Figure 9(c), we can determine that the resolution of the deconvolved Image A has been increased 3 times. From Figure 9(d), resolution of the deconvolved Image B is increased by a factor of 2. Based on these simulations, we

conclude that the DID method is capable of improving image resolution by 2 to 3 times.

6 Concluding Remarks

The research work performed during the AFOSR Summer Research program is aimed at enhancing the resolution of passive millimeter-wave imaging devices. While millimeter-wave detection offers certain advantage over IR in its easy penetration through fog, dust, smoke, and artificial cover, its poorer angular resolution poses a critical obstacle to its wide application in military and civilian environment. Our research in improving angular resolution based on the design of new image deconvolution techniques significantly improved the performance of MMW imaging. In order to make it possible for a receiver with small antenna to achieve imaging resolution comparable to the traditional IR imaging, further resolution improvement is crucial to both the military and civilian applications of passive MMW imaging systems.

Acknowledgement

The author wishes to thank his MNGS host, Mr. Bryce Sundstrom, for providing excellent technical support and for many helpful discussions throughout this project.

References

- [1] S. K. Young, R. A. Davidheiser, B. Hauss, P. S. C. Lee, M. Mussetto, M. M. Shoucri, and L. Yujiri, "Passive millimeter-wave imaging", *Quest*, TRW Space & Defense Sector, Vol-13, No. 2:3-20, Winter 1990/1991.
- [2] Mark A. Richards, "Iterative Noncoherent Angular Superresolution", In *Proc. 1988 IEEE National Radar Conf.*, pages 100-105, Ann Arbor, MI, 1988.
- [3] M. A. Richards, C. E. Morris, and M. H. Hayes, "Iterative Enhancement of Noncoherent Radar Data", In *Proc. 1986 IEEE Int. Conf. on Acoustics, Speech, and Signal Processing*, pages 1929-1932, 1986.
- [4] M. A. Richards, "Iterative Deconvolution in Noncoherent Radar Data, In *Proc. 1985 IEEE Int. Conf. on Acoustics, Speech, and Signal Processing*, pages 434-437, 1985.
- [5] E. D'Anna and M. A. Richards, "Superresolution", In *Proc. Workshop on Detection, Discrimination, and Classification of Targets in Clutter*, Huntsville, Alabama, November 1990.
- [6] Peter A. Jansson, "Modern Constrained Nonlinear Methods", In *Deconvolution with Applications in Spectroscopy*, Peter A. Jansson, ed. Academic Press, Orlando, FL.
- [7] T. S. Huang (ed.), *Picture Processing and Digital Filtering*, Springer-Verlag, 1975.
- [8] Anil K. Jain, *Fundamentals of Digital Image Processing* Prentice Hall, 1989.

- [9] A.N. Tikhonov, "Solution of Incorrectly Formulated Problems and the Regularization Method", *Soviet Math. Dokl.*, vol.4, pp. 1035-1038, 1963.
- [10] V.A. Morozov, *Methods for Solving Incorrectly Posed Problems*, Springer-Verlag, 1984.
- [11] R.W. Schafer, R.M. Mersereau, and M.A. Richards, "Constrained Iterative Restoration Algorithm", *Proceedings of the IEEE*, vol.69, no.4, pp. 432-450, April 1981.
- [12] J.W. Hilgers and W.R. Reynolds, "Instabilities in the Optimal Regularization Parameter relating to Image Recovery Problems," *Journal of Opt.Soc.Am.A*, vol.9, pp. 1273-1279, August 1992.
- [13] M.A. Richards, C.F. Barnes, C.L.Belcher, and B.M. Keel, "Super Resolution in Low Signal-to-Clutter Ratios for Millimeter Wave Seekers," *Final Report AFATL-TR-90-62*, Air Force Armament Laboratory, Eglin AFB, September 1990.
- [14] B.R. Frieden, "Image Enhancement and Restoration", In *Picture Processing and Digital Filtering*, T. S. Huang, ed., Springer-Verlag, 1975.
- [15] D.G. Gleed and A. H. Lettington, "Application of Superresolution Techniques to Passive Millimeter-wave images", *Unpublished Report*, Royal Signals and Radar Establishment, Gt Malvern, Worcs, UK, 1991.
- [16] R. Appleby and A.H. Lettington, "Passive Millimeter Wave Imaging", *Electronics and Communications Engineering Journal*, vol.3, no.1, pp.13-16, 1991.
- [17] X. Zhuang, E ,Ostevold, and R.M. Haralick, "A Differential Equation Approach to Maximum Entropy Image Reconstruction", *IEEE Transactions on Acoustics, Speech, and Signal Processing*, vol.35, no.2, pp. 208-218, February 1987.
- [18] S.F. Gull and J. Skilling, "Maximum Entropy Method in Image Processing", *IEE Proceedings*, Part F, vol.131, no.6, pp. 646-659, Oct.1984.

**Field-Induced Atomic-Scale Manipulation of Semiconductor,
Metal, and Conductive Polymer Surfaces with a STM**

**Simon Y. Foo
Assistant Professor
Department of Electrical Engineering**

**Florida State University
Tallahassee, FL 32306**

**Final Report for:
Summer Faculty Research Program
Wright Laboratory**

**Sponsored by:
Air Force Office of Scientific Research
Bolling Air Force Base, Washington, DC**

July 1993

Field-Induced Atomic-Scale Manipulation of Semiconductor,
Metal, and Conductive Polymer Surfaces with a STM

Simon Y. Foo
Assistant Professor
Department of Electrical Engineering
Florida State University

Abstract

The goal of our experiments is to demonstrate the ability to "etch" very fine grooves (a few angstroms in width and depth) on semiconductor, metal, and conductive polymer surfaces using a scanning tunneling microscope (STM). Specifically, our specimens consist of n-type and p-type <111> silicon, gallium-arsenide, gold, and polypyrrol, with air and water being the electrolytes. The motivation behind this work is the theory of field-induced evaporation of surface atoms, i.e., atoms can be removed if an appropriately voltage-biased STM tip is brought close to a conducting surface. A "C" program *drives* the STM tip to a specific location on the surface to be etched making a groove or a ditch. Grooves traced out in a fractal pattern are expected to provide high surface area electrodes necessary to achieve high capacitance. This research may eventually lead to the fabrication of ultra-high-speed quantum devices as well as high capacitance electrodes for high energy density capacitors.

Field-Induced Atomic-Scale Manipulation of Semiconductor, Metal, and Conductive Polymer Surfaces with a STM

Simon Y. Foo

Introduction

The ability to "see" beyond the capabilities of our eyes has always been fascinating and challenging. Typically our human eye has a resolution of about 100 μm , limited by rods and cones in the retina. The more powerful optical microscope has a maximum magnification of 1000X over human eye (i.e., about 0.1 to 0.2 μm resolution), limited only by the diffraction of light. In contrast, the scanning electron microscope (SEM) has a maximum resolution of 50 to 100 \AA , limited by the focus of the electron beam. The recent invention of the scanning tunneling microscope (STM) in 1982 gave us the ability to see in even more details - right down to the atoms! The STM is capable of imaging the atomic structure of conductive surfaces with an incredible resolution of 1 to 3 \AA , limited only by the sharpness of the tip (ideally one atom at the end of tip!). The drawback of the STM is that the sample under observation has to be conductive in order for electron tunneling to occur.

Surprisingly, the STM, which was invented by Binnig and Rohrer [1], is useful not only to "observe" atoms but also to "manipulate" atoms of semiconductor surfaces. The first demonstration of the latter was done by Becker et al. [2], where atomic-scale protrusions on Ge $\langle 111 \rangle$ surface were made by increasing the bias of a W tip under constant tunneling current. Since then, there has been considerable interest in using the scanning tunneling microscope (STM) to modify the surface topography of semiconductors at nanometer-scale (see [3] -[7]). Manipulation of semiconductor surfaces is of particular interest for the fabrication of ultra-high-speed quantum devices and high energy capacitors.

Field-Induced Evaporation of Surface Atoms

Lyo and Avouris [5] and Kobayashi et al. [7] have shown that if a STM tip, biased with either a positive or a negative voltage, is placed close to a Si $\langle 111 \rangle$ surface, Si atoms are removed from the surface, i.e., a hole is created on the surface. Grooves or ditches can be created by scanning the tip parallel to the surface. The diameter of the hole and the width of the ditch can be controlled by changing the magnitude of the tip bias and the duration of scan. Specifically, the amount of Si atoms removed from surface depends on experimental parameters such as polarity, magnitude, duration of bias voltage applied to the tip, the elec-

tron tunneling current between the tip and the surface, and the material of the tip [7].

The result can be explained in terms of field-induced emission of ions from the Si sample. If we apply an appropriate positive (/negative) voltage to the STM tip, a strong positive (/negative) field is created at the Si surface. This strong field ionizes Si atoms at the surface into negative (/positive) ions and pulls them apart from the surface, i.e., Si atoms at the surface evaporate as negative or positive ions, depending on the polarity of the tip voltage.

The Burleigh Instructional STM

The STM system used in our experiments is a low-cost Burleigh Instructional STM system, as shown in Figure 1. Basically, the system consists of the Mechanical Head, Control Electronics, data acquisition card, and a computer. The sample to be examined or etched is mounted inside the Mechanical Head cavity, as shown in Figure 1(b). The tip which is typically made of either tungsten (W) or Platinum Iridium (PtIr) is held magnetically by a piezoelectric (PZT) ceramic. The bending and elongation of the PZT under appropriate high voltage are responsible for the scanning and terrain-following actions of the STM. A general idea of how the STM works is shown in Figure 2. In a constant-current mode, a constant tunneling current is maintained through the Negative Feedback Control Electronics as the PZT tip scans across a surface. The negative feedback can be adjusted by the Servo Loop Response controls (Figure 2(b)), which are used to optimize the PZT-Z motion when scanning a particular sample terrain. Basically the Time Constant and Gain controls determines how fast and how much to adjust the Z position, respectively, while the Filter acts as a low-pass filter. That is, if the Time Constant is set to minimum, the servo loop will respond to any variations in the terrain very quickly. If the Gain is set high, the servo loop response to any tunneling current variation will be very large. If the Filter is set high, all high-frequency signals in the tunneling current will be filtered out. In all our imaging experiments, Time Constant is set to maximum (compensated by slower scanning rate of 0.5 ms/sample), Gain set to minimum (to avoid oscillations), and Filter set to maximum. A tip bias voltage of 0.05V and reference current of 2 nA are used. For more accurate results, the STM should be placed in a ultra-high-vacuum (UHV) chamber to avoid electron scattering and adsorption by reactive gases in the air. Otherwise dust particles or gases present in the air between the tip and the sample may form an undesired conducting path thereby distorting the true image. Typically a chamber pressure of $1\text{E}-8$ to $1\text{E}-10$ Torr is considered UHV.

Experiments

The initial experiment to demonstrate the theory of field-induced evaporation of surface atoms is to simply position the STM tip at the center of scanning area, apply a constant -10V bias to the tip for about 60 seconds, and then observe the groove made (if any) by imaging the whole area using a small +0.05V tip bias. The specimens for our experiments consist of n-type <111> and p-type <111> silicon, gallium-arsenide, gold, and polypyrrol, a conductive polymer with a high surface area, as shown in Figure 3.

The major variables which influence the quality of STM work are tip preparation and vibration isolation. Tip preparation is very important in getting good atomic-scale images of surfaces. In order to achieve the atomic resolution capabilities of the STM, the probe must be sharpened to a tip such that it has only one atom at the tip end (ideally!). This atom is primarily responsible for the current tunneling between the tip and the conductive sample. There are two preferred tip materials for STM work, namely W and PtIr wires. PtIr wires are quite expensive but soft enough to be cut diagonally into a sharp tip using a metal cutter. In contrast, W wires are cheaper, alot harder, and will ruin most cutters. The preferred method is to electrochemically etched the W wire into a very sharp tip. Both PtIr and W tips are can electrochemically etched using an adjustable AC autotransformer (also called Variac or Powerstat), as shown in Figure 4(a)-(b). It is also possible to etch W wire using a constant DC power supply, as shown in Figure 4(c)-(d). In both cases, the anode is the W or PtIr wire while the cathode can be a simple copper wire. The etching solution used is a 5 molar potassium hydroxide (KOH) solution. Figure 5 shows the SEM pictures of a not-so-sharp PtIr tip (cut using a pair of cutters) and a very sharp electrochemically etched W tip. Note that tips with long "wiskers" are very susceptible to acoustic vibrations, and therefore they are unsuitable for STM work.

When the STM is used in a constant tunneling current mode, it is required that the tip and the sample surface be only 10 Å apart at all times without crashing the tip onto the surface and distorting the true image of the surface profile. Therefore, it is extremely important that any vibrations due to walking around the room, air conditioning fan blowing, etc., be eliminated as much as possible. There are basically three methods for isolating the STM from these vibrations, as shown in Figure 6. Historically, the first method of vibration isolation used was the superconducting levitation or the Meissner Effect. The STM is placed on an array of magnets levitated above a superconductor chilled by liquid nitrogen. Alternatively, a simple vibration isolation method is to hang the STM by elastic springs from a fixed point. Any small vibrations to the plate holding the STM head is absorbed by the springs. Yet another way is to place the STM on top of a series of metal plates, stacked on top of each other and separated by "O" rings (elastomer spacers). These

spacers act as springs and dampers.

The initial experiments were first performed under normal room conditions, i.e., with air as the etching medium. The samples were first imaged using a +0.05V bias with a constant 2 nA tunneling current, before a large bias of -10V is applied to the tip. After 60 seconds elapse, the same spot is imaged again to observe the effect if any. Figure 7 shows the STM image (30Å by 30Å) of low and high-surface area polypyrrol. Dark spaces between surface atoms are due to the fact that atoms beneath the surface atoms are about 3 Å away, with an extremely small probability of electron tunneling. Other dark areas are due to atoms with less energetic electrons and non-conductive contaminants. Figure 8(a) shows the diamond-shape arrangement of the n-type Si atoms in the <111>-plane; Figure 8(b) shows gold-coated p-type <111> Si; Figure 9(a), gold-coated GaAs; and Figure 9(b), defects in polycrystalline GaAs. However, we were unable to observe any "ditches" created by the evaporation of surface atoms under normal room conditions.

We then proceed to using water as the etching medium since hydrogen atoms are highly reactive. A teflon "tub" has to be specially built to accomodate the sample and the water. This tub sits on top of the sample carriage, and is carefully inserted into the STM Head cavity. Figure 10 shows the setup of the experiment.

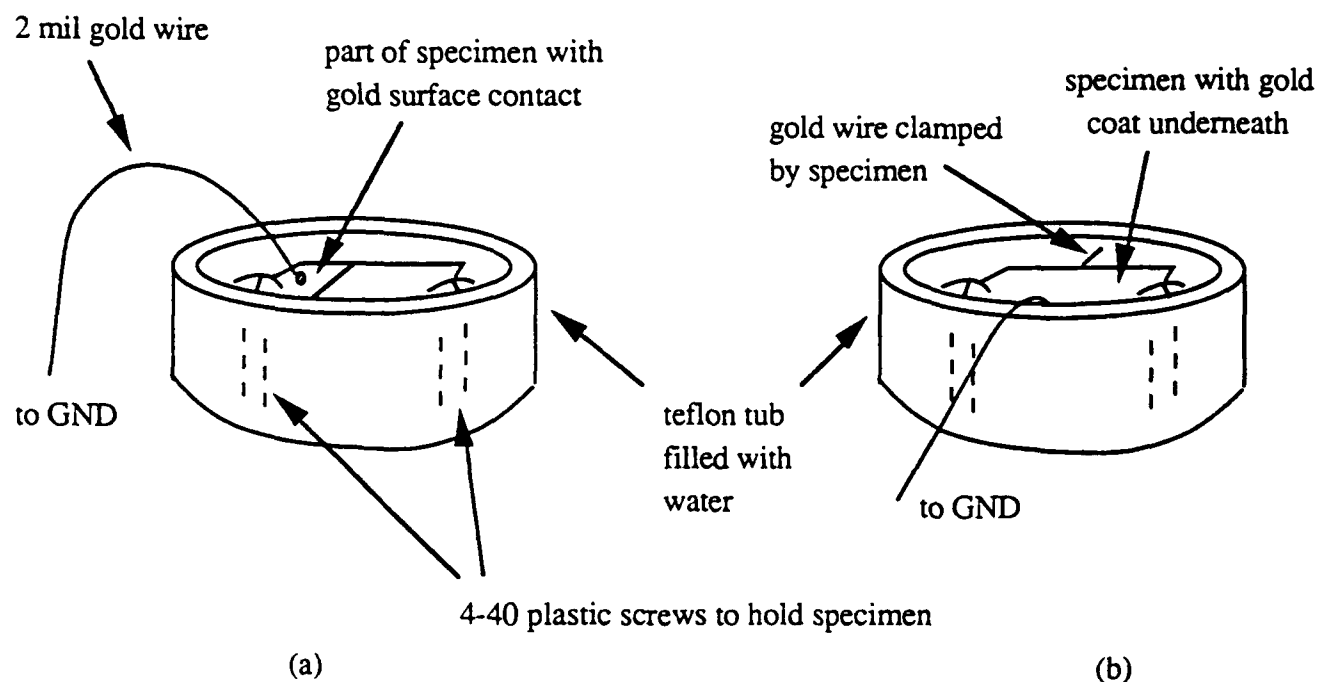


Figure 10. (a) An elegant setup to electrochemically "etch" a specimen using the STM.
(b) A crude but workable alternative.

A -10V bias is apply at the tip for 60 seconds as the tip is positioned at the center of the scanning area. Figure 11 shows the surface profile of a gold-coated GaAs sample before and after the effect is applied. Notice a distinct edge on the surface has been created as gold atoms are stripped from the surface and deposited as gold molecules in the water. The evaporated region appeared dark probably due to electrons with insufficient energies for tunneling. The "ditch" did not appear centered in the scanning area due to movements between the etching and imaging stages.

High Density Fractals

One of the potential payoffs in this research is the fabrication of high surface area electrodes for high energy capacitors. Grooves etched in a fractal pattern are expected to provide high surface area electrodes necessary to achieve high capacitance. Since capacitance $C = kA/d$ (where k is the dielectric constant of the insulating medium between the two electrodes, A is the surface area of the electrode, and d is the separation between the electrodes), very dense fractals are preferred in etching electrodes as to provide high surface area. Examples of such high density fractals are Peano curves, Peano-Gosper curves, and Hilbert curves, as shown in Figure 12. A "C" program is written to *drive* the STM tip according to a fractal curve. Figure 13 shows the output for the fractal scan for a snake-like fractal curve (not shown here). However, due to time constraints, the experiments to etch fractal curves on conductive polymers using the STM are put off until the next phase of this project.

Conclusion

Some initial success has been reported in this research although the goals are still far from being accomplished. The experiments have not been performed under suitable environment due to undesired factors such as vibrations from walking around the room and the air-conditioner, 60Hz noise from other electrical units, lack of UHV, etc. However, there is enough evidence from our initial results and recent literature to prove that it is possible to etch nanometer-scale grooves on semiconductors using a STM. We are also optimistic that it is possible to etch fractal curves on conductive polymers in our effort to make higher surface area electrodes for high-energy capacitors.

Acknowledgement

I would like to express my sincere appreciation to Dr. Duane Finello and Mr. Ron Boulet (Chief, WL/MNMF) whose support makes it possible for me to participate in this AFOSR research program. Also many thanks to Luis Santana and TSGT Russ Huffman

for their assistance in taking the SEM pictures.

References

- [1] G. Binnig and H. Rohrer, *Helv. Phys. Acta* **55**, 726 (1982).
- [2] R. S. Becker, J. A. Golovchenko, B. S. Swartzentrouber, *Nature* **325**, 419 (1987).
- [3] L. J. Whitman, J. A. Stroscio, R. A. Dragoset, and R. J. Celotta, *Science* **251**, 1206 (1991).
- [4] J. A. Stroscio and D. M. Eigler, *Science* **254**, 1319 (1991).
- [5] I. W. Lyo and P. Avouris, *Science* **253**, 173 (1991).
- [6] J. A. Stroscio and D. M. Eigler, *Science* **254**, 1319 (1991).
- [7] A. Kobayashi, F. Grey, R. S. Williams, and M. Aono, *Science* **259**, 1724 (1993).
- [8] *Burleigh Instructional STM Workbook*, Burleigh Instruments, Inc. (1992).
- [9] *AD3100/ADA3100 User's Manual*, Real Time Devices, Inc. (1991).

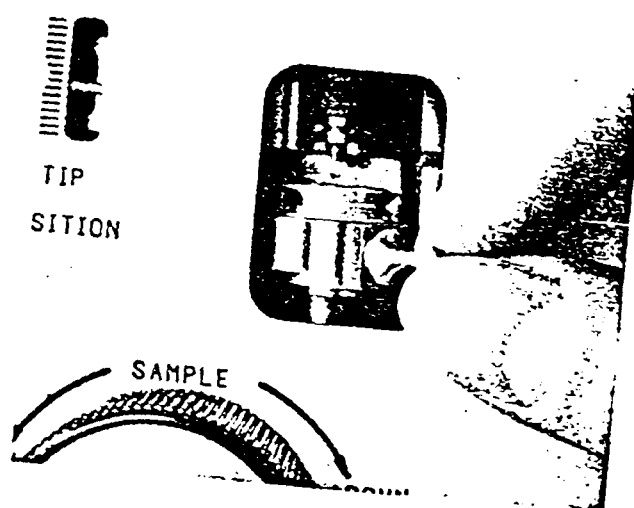
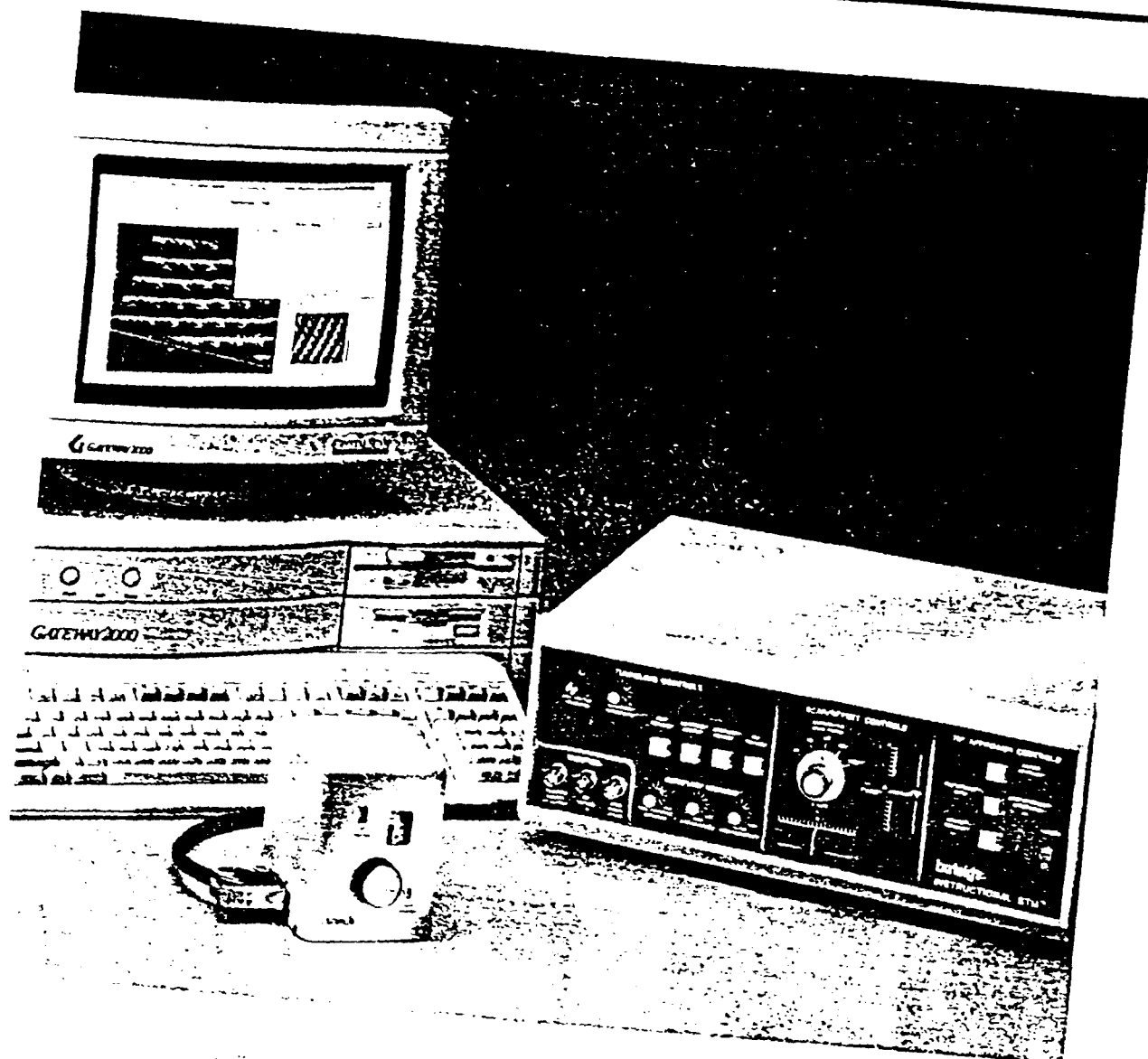


Figure 1. TOP: The Burleigh Instructional STM System;
 BOTTOM: A close-up view of the Mechanical Head cavity showing the tip and
 the sample mounted on a carriage.

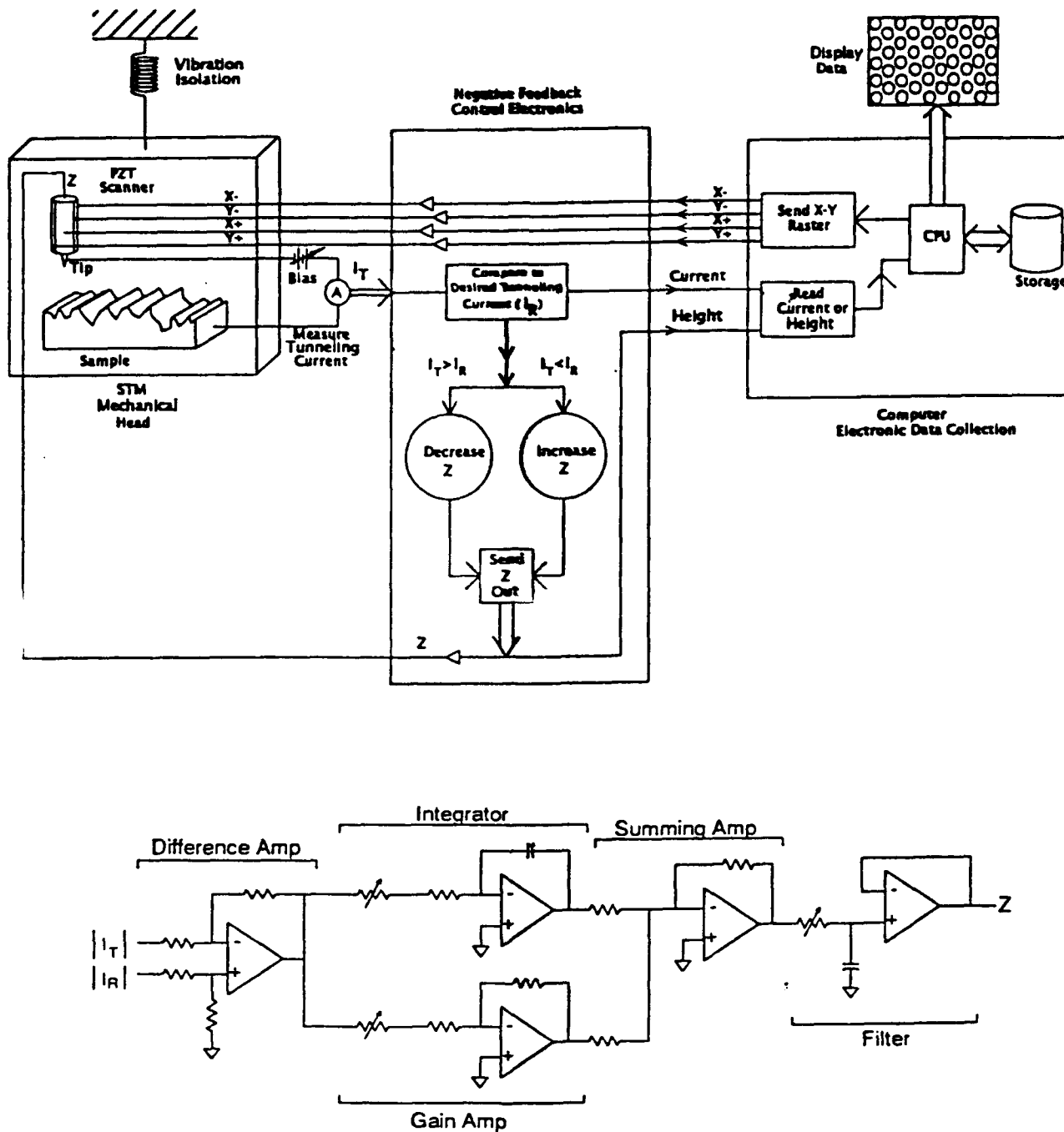


Figure 2. TOP: Block diagram of the STM system: the STM Mechanical Head, consisting of vibration-isolation mechanism, PZT, sample, and tip; Negative Feedback Control Electronics; and Computer Electronic Data Collection center; BOTTOM: The Negative Feedback/Control Electronics where the inputs are the measured tunneling current I_T and reference current I_R . The difference signal can be amplified and used as "error" to adjust the Z output of the servo loop.

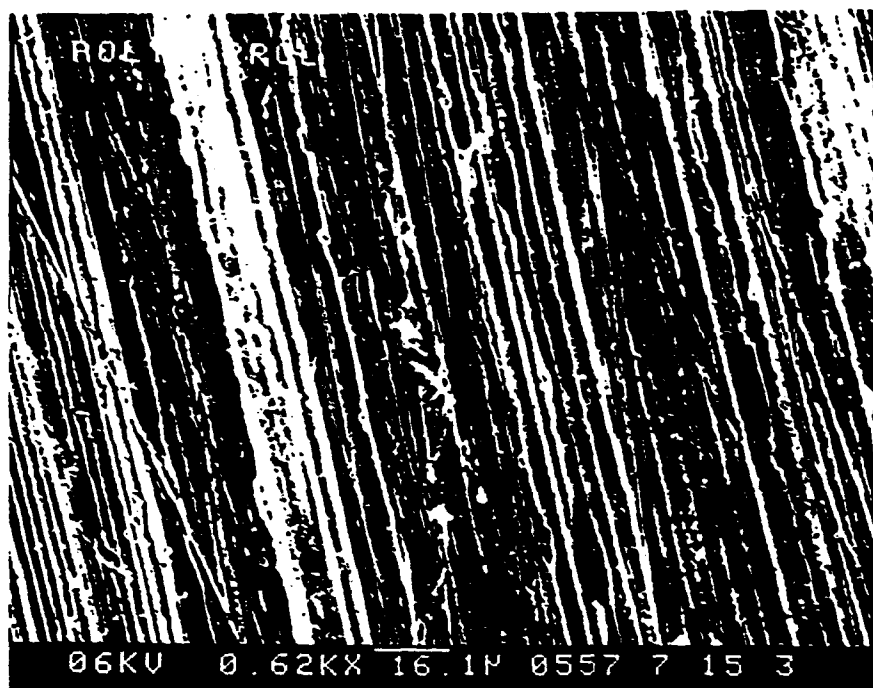


Figure 3. A SEM picture of high surface area polypyrrol.

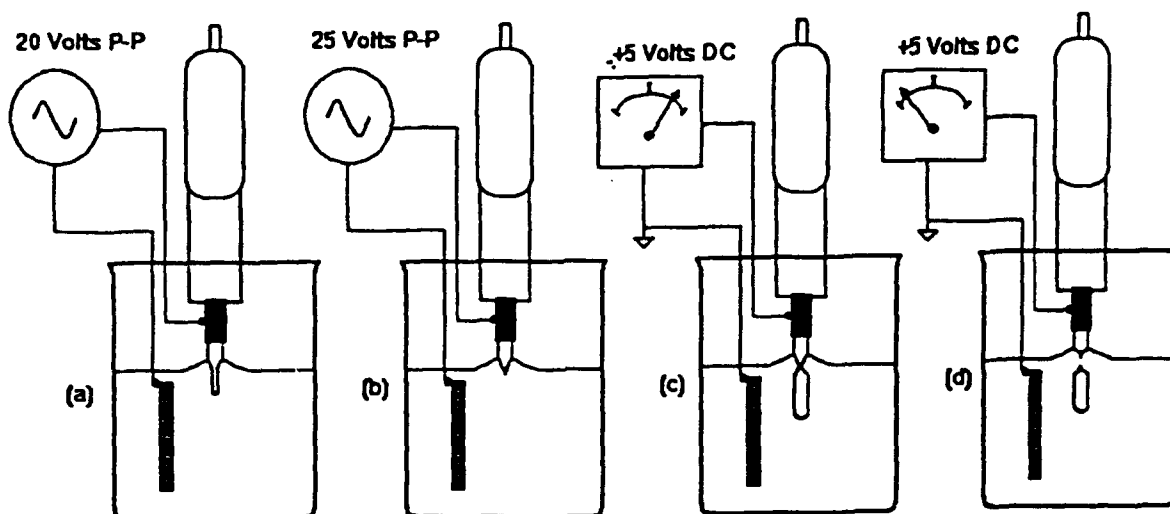


Figure 4. Electrochemical etching of tips. Fix the tip to a holder. Immerse the tip partially in beaker of etching solution (5 molar KOH in our case). Attach anode and cathode wires, and turn on power. In the AC etching of (a) - (b), tip etches away from bottom towards the surface. This method can be used for both W and PtIr tips. DC etching method (c) - (d) is used only for W wires. The tip breaks off and leaves a sharp tip.

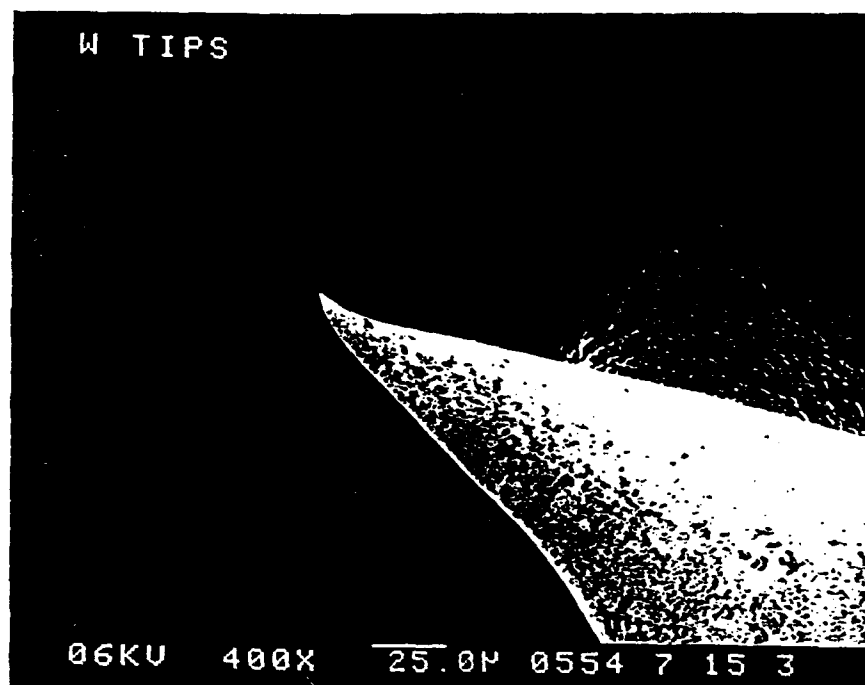
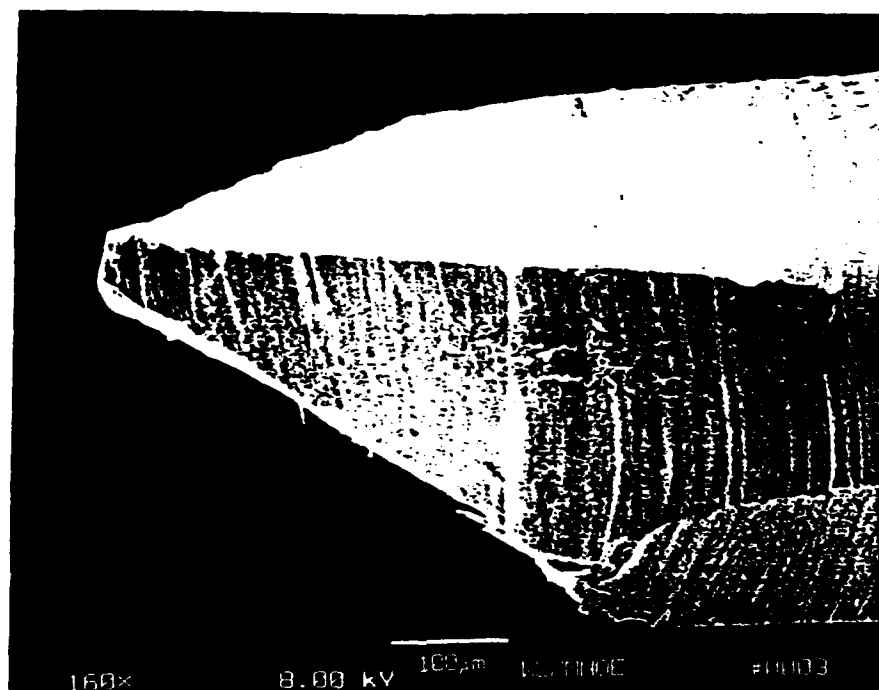


Figure 5. TOP: SEM picture of a PtIr tip cut with a pair of cutters;
 BOTTOM: SEM picture of an electrochemically etched W tip.

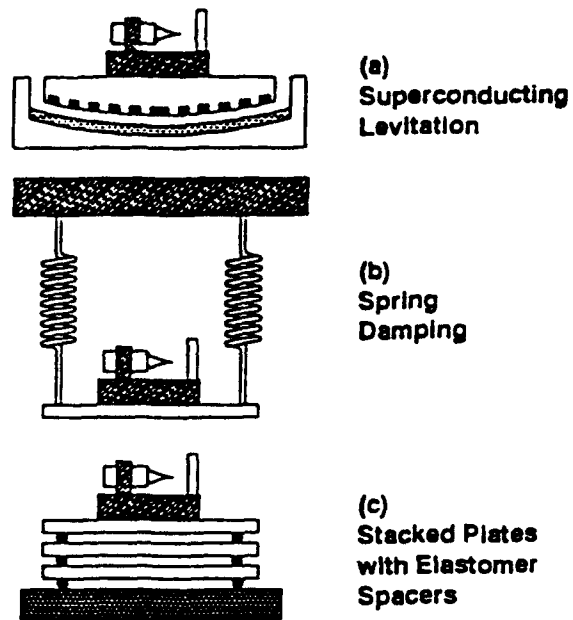


Figure 6. Three methods of vibration isolation for STM work. (a) The Meisner Effect keeps the STM head magnetically levitated; (b) the more traditional elastic springs in conjunction with magnets for Eddie Current damping; and (c) stacked plates with "O" rings as spacers.

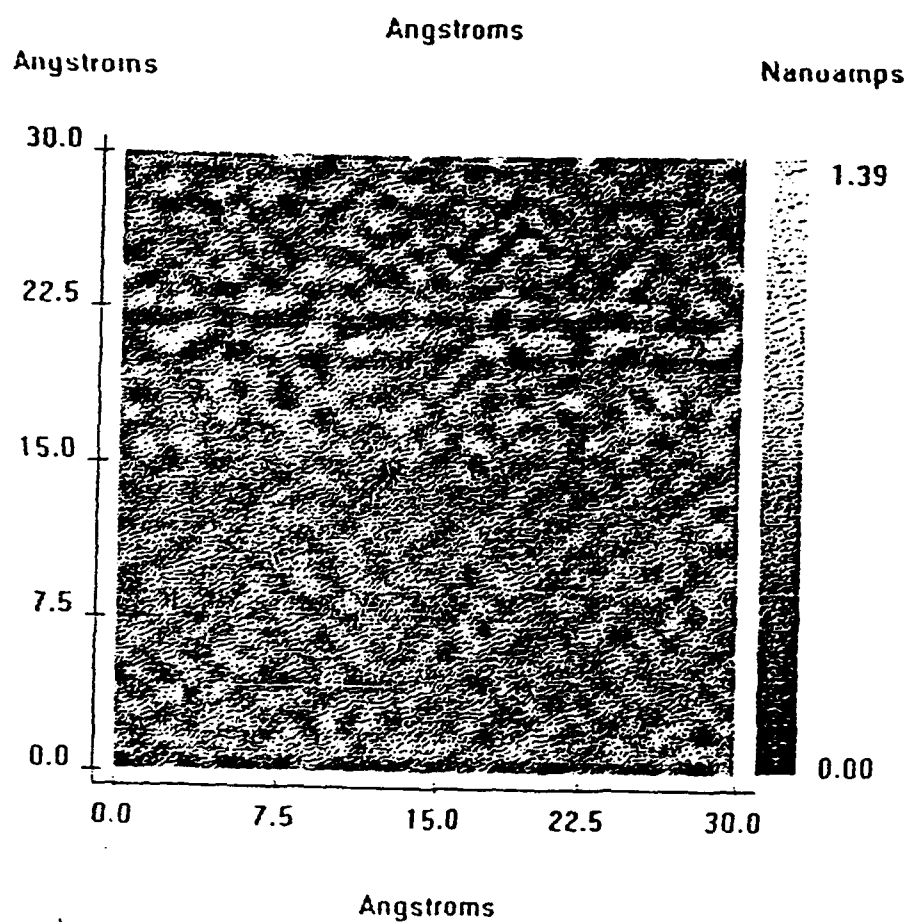
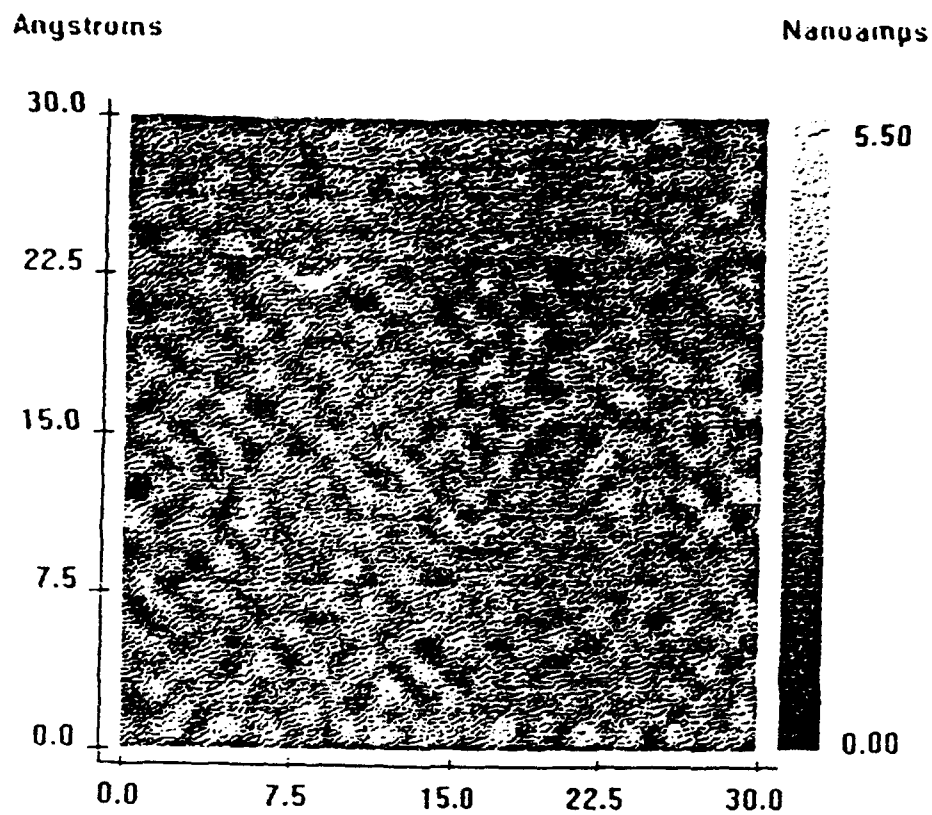


Figure 7. TOP: Low surface area doped polypyrrol; and
BOTTOM: High surface area doped polypyrrol.

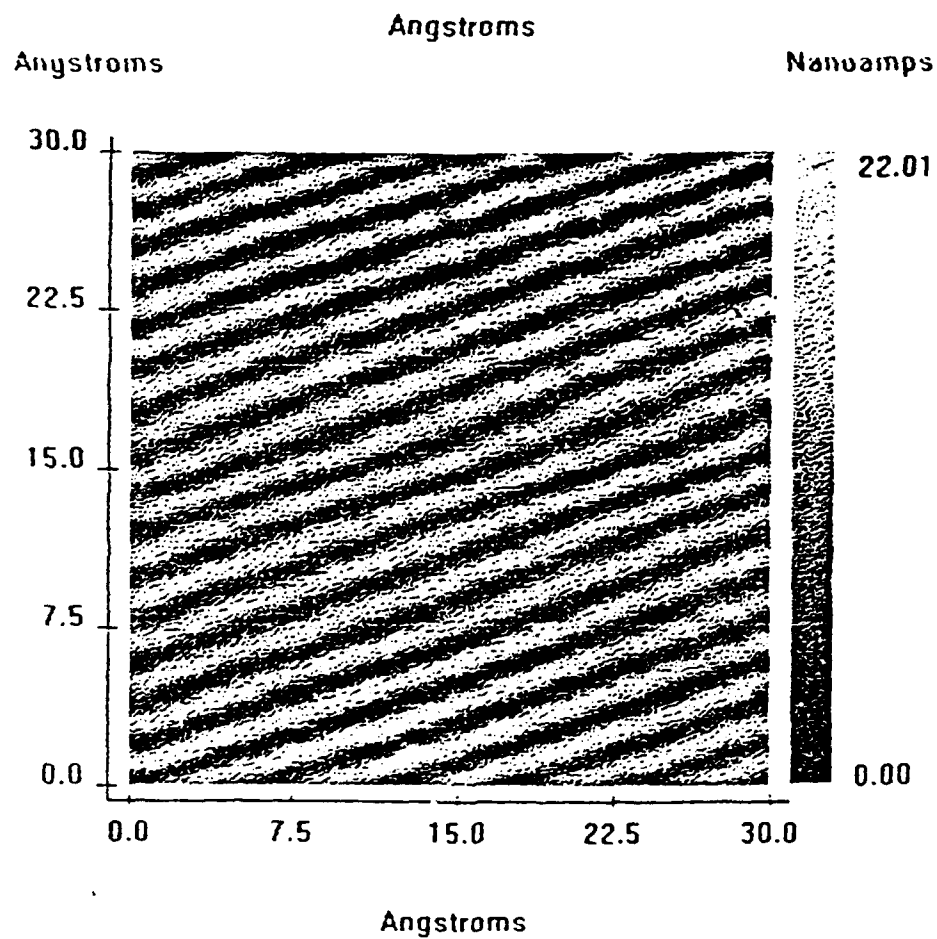
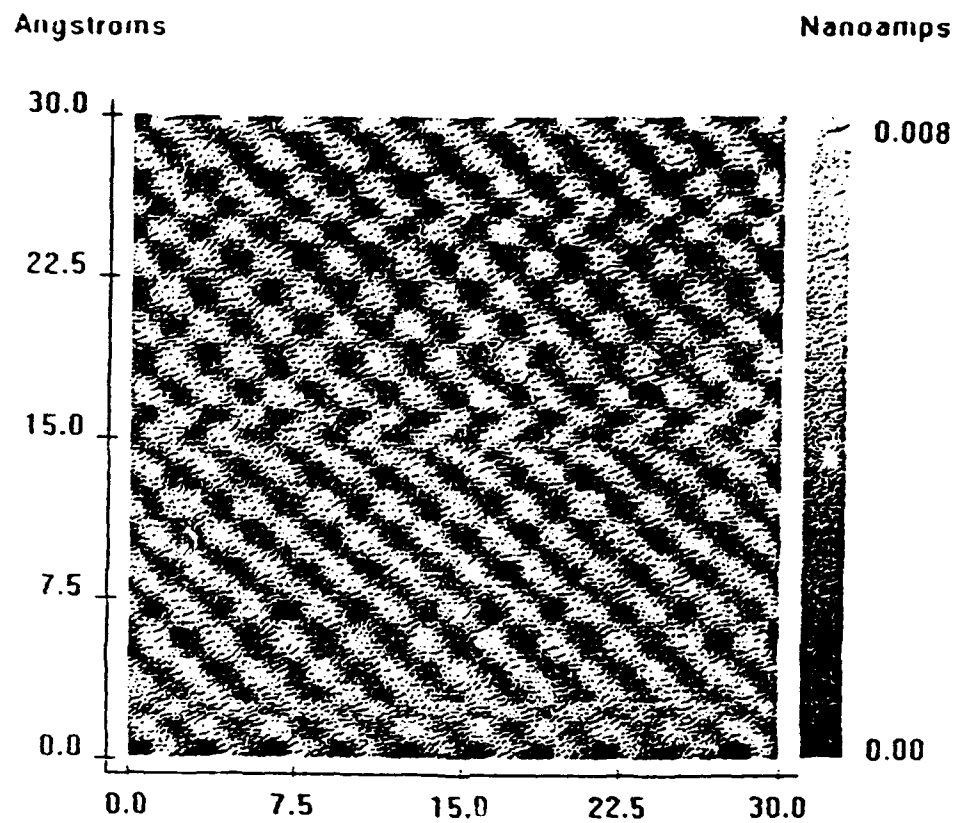


Figure 8. TOP: n-type <111> Si; and
 BOTTOM: Gold coated p-type <111> Si.

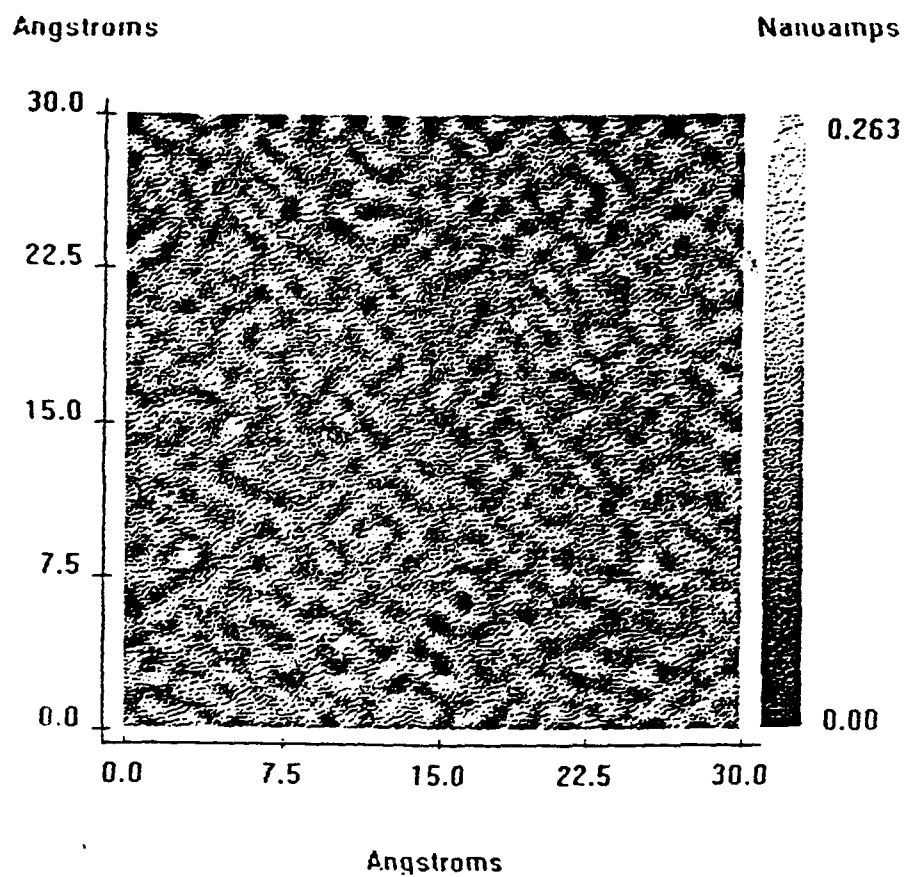
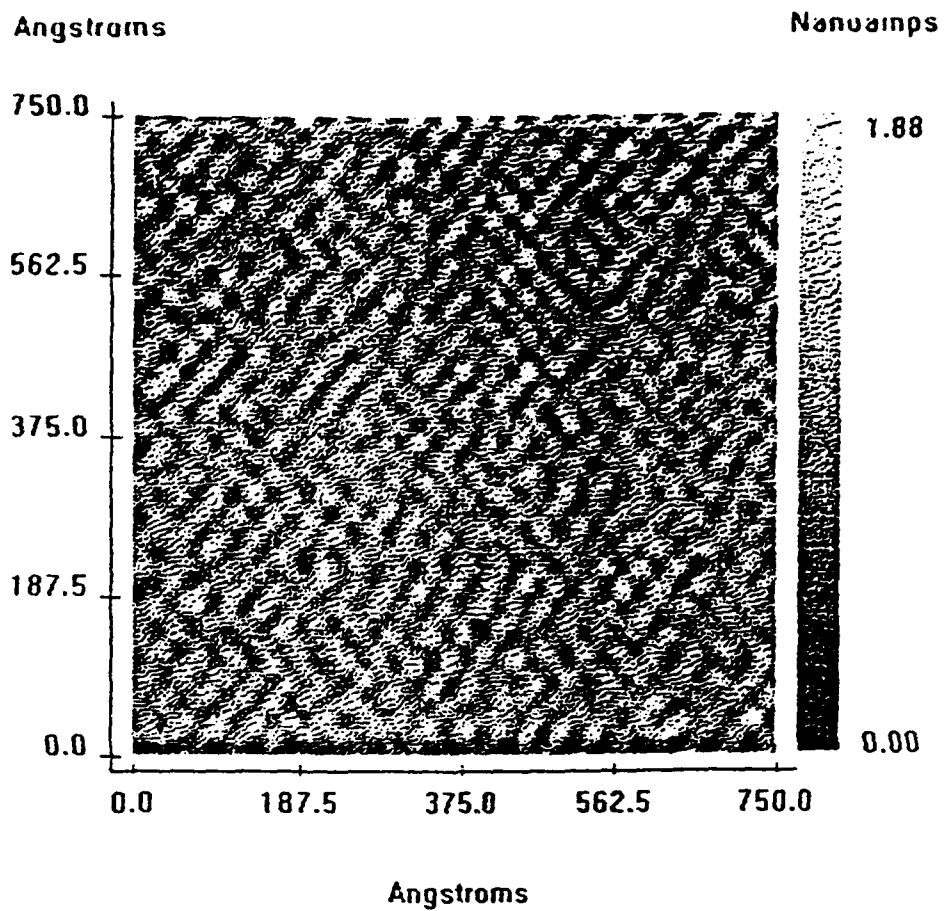


Figure 9. TOP: Gold coated GaAs; and
BOTTOM: polycrystalline GaAs.

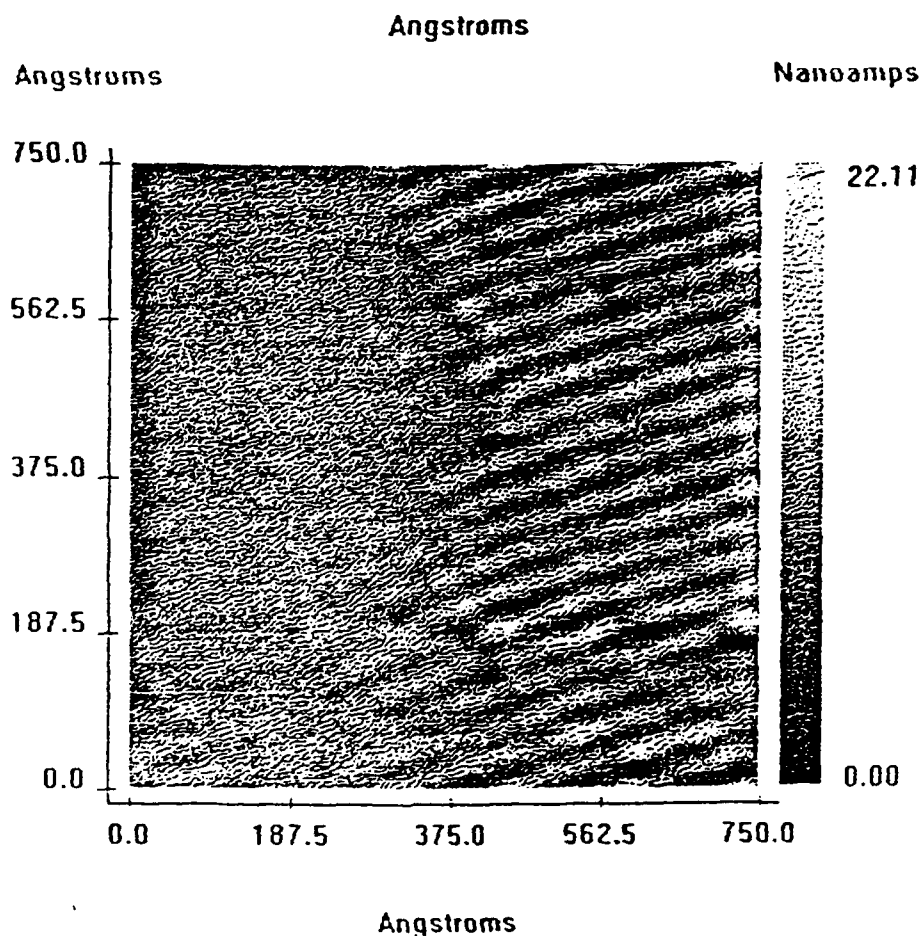
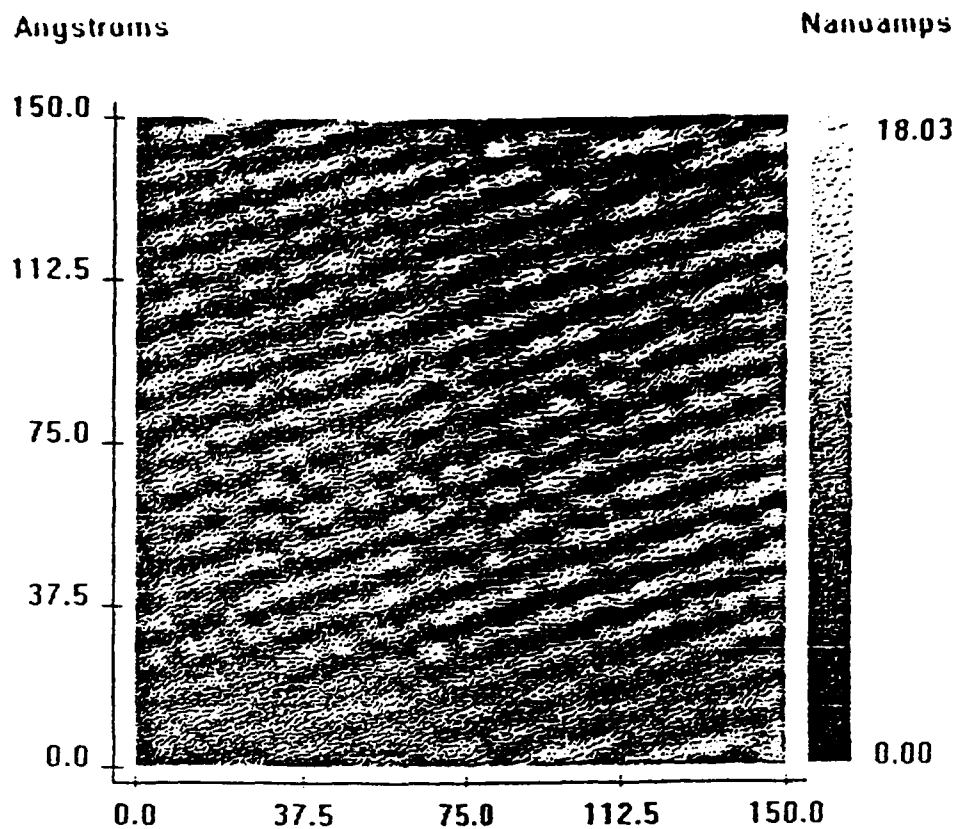


Figure 11. TOP: Gold coated GaAs (before "etching", 150Å by 150Å area);
 BOTTOM: After "etching", 750Å by 750Å image showing area of
 surface atoms evaporated by the -10V tip bias for 60 seconds.

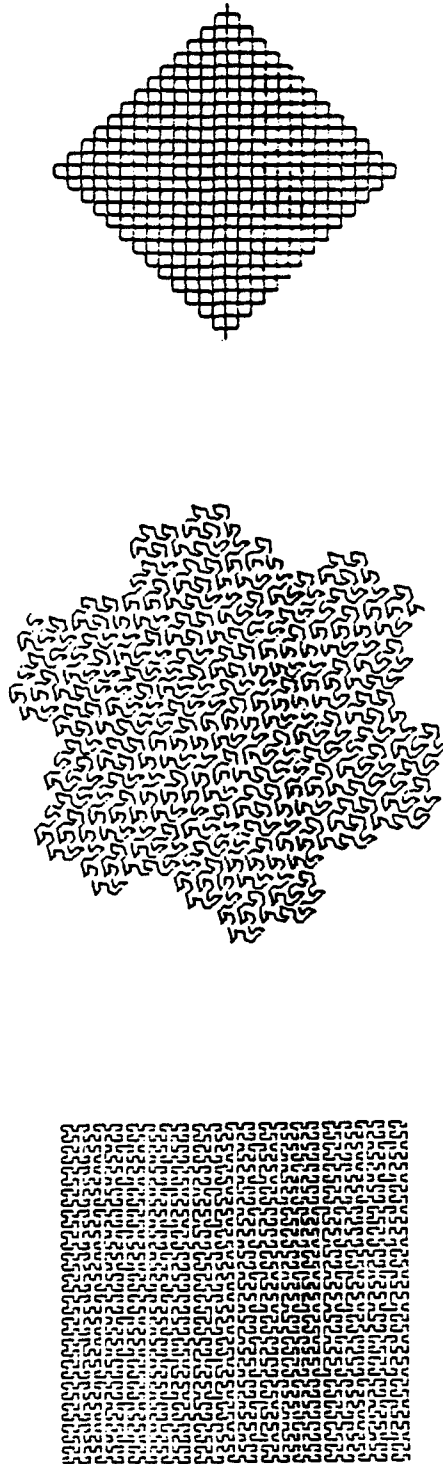
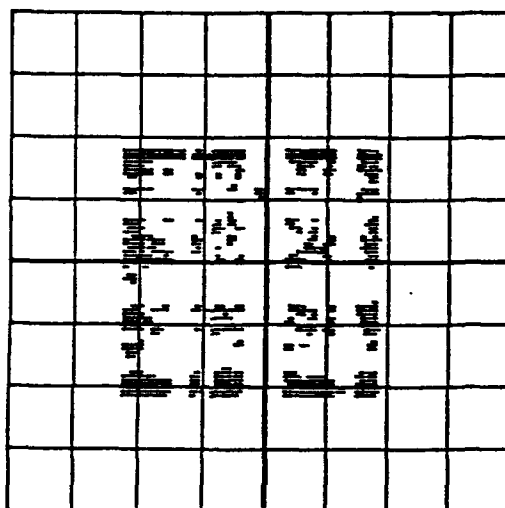


Figure 12. TOP: Peano curves (level=3);
MIDDLE: Peano-Gosper curves (level=4); and
BOTTOM: Hilbert curves (level=6).

X=T2

Y=T1



A1
5 ns 1 V

A2
5 ns 1 V

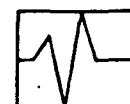
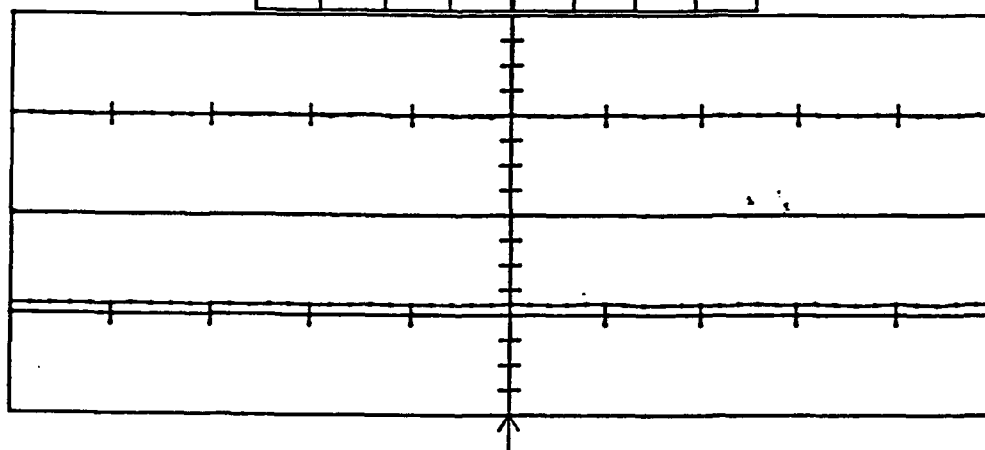


Figure 13. The output of the fractal program as captured on a digitizing oscilloscope.

**AN ANALYSIS OF THE HIGH
ANGLE OF ATTACK AERODYNAMICS OF
ARBITRARY BODIES UNDER-GOING
RAPID MANEUVERS**

**Glenn Gebert
Assistant Professor
Department of Mechanical and Aerospace Engineering**

**Utah State University
Logan, UT 84322**

**Final Report for:
Summer Faculty Research Program
Flight Vehicles Branch/Weapons Flight Mechanics Division
Armament Directorate
Eglin AFB, Florida**

**Sponsored by:
Air Force Office of Scientific Research
Bolling Air Force Base, Washington, D.C.**

and

Utah State University

September 1993

AN ANALYSIS OF THE HIGH ANGLE OF ATTACK AERODYNAMICS OF ARBITRARY BODIES UNDER-GOING RAPID MANEUVERS

**Glenn A. Gebert
Assistant Professor
Department of Mechanical and Aerospace Engineering
Utah State University**

Abstract

Little is known about the aerodynamics of finned missiles at high angles of attack. There have been several analytical approaches and only a few experimental studies. Virtually all high angle of attack research on slender bodies has been concerned with the static aerodynamics. At large angles of attack, a vortex dominated wake forms on the leeward side of the body. During rapid maneuvers (rapid pitching, yawing or rolling), the body and its fins translate through the vortical flow. As a result large, unsteady forces and moments develop. The focus of this study was to develop a quick method for estimating the aerodynamics of rapidly maneuvering bodies. A discrete vortex approach was utilized for its ability to rapidly estimate the gross high angle of attack aerodynamic loadings on finned and unfinned bodies. Significant modification of the aerodynamic loading is observed, and the stability derivatives show large fluctuations for the unsteady motion. The discrete vortex method rapidly determines the flow characteristics of the body, and calculates the total body aerodynamics.

AN ANALYSIS OF THE TOTAL HIGH ANGLE OF ATTACK AERODYNAMICS OF ARBITRARY BODIES UNDER-GOING RAPID MANEUVERS

Glenn A. Gebert

Introduction

The development of supermaneuverable fighters has renewed an interest in high angle of attack aerodynamics. Current fighter designs allow them to perform controlled maneuvers at angles of attack up to 70° . Although a considerable amount of work is being performed on the characteristics of the aircraft, little is known about the behavior of the weapons when launched in such extreme flight conditions. Typically, a launching aircraft will perform a high angle of attack maneuver (supermaneuver) only as a last resort. The maneuver is generally achieved when the airplane has lost most of its velocity, and tries one last time to successfully launch its weapons. Thus, it was the concern of this study to examine the aerodynamic characteristics of weapons at high incident angles and low Mach numbers.

Typically, the behavior of a weapons system is initially evaluated by developing and running six degree-of-freedom (6-DOF) computer simulations. For these simulations, the aerodynamics of the body must be input. It is known that at high angles of attack, the aerodynamics become highly non-linear. Thus, an aerodynamic database must be used in the simulation rather than the usual low angle of attack linearized aerodynamic equations. This means that the aerodynamics for a large number of flight conditions must be determined.

An additional complication arises due to the fact that at moderate and high angles of attack, large out-of-plane loading (side force, yawing and rolling moment) occur. Figure 1 shows a schematic of a finned body at a high angle of attack. A vortex dominated wake develops on the leeward side of the body. At moderate angles of attack, the vortices are largely symmetric. At high angles of attack the vortex structure is still steady but asymmetric. At incidence, an axisymmetric body will develop in-plane loading (normal and axial force, pitching moment). However, due to the vortical wake, the in-plane loading will be modified and large out-of-plane

loading will occur. The out-of-plane loading is extremely difficult to predict since the flow asymmetry is due to slight manufacturing imperfections at the nose tip of the body or disturbances in the upstream flow. Although the vortices are largely stable in time, conditions can change which cause them to set up differently into a new stable configuration and yield new loadings for the same flight conditions.

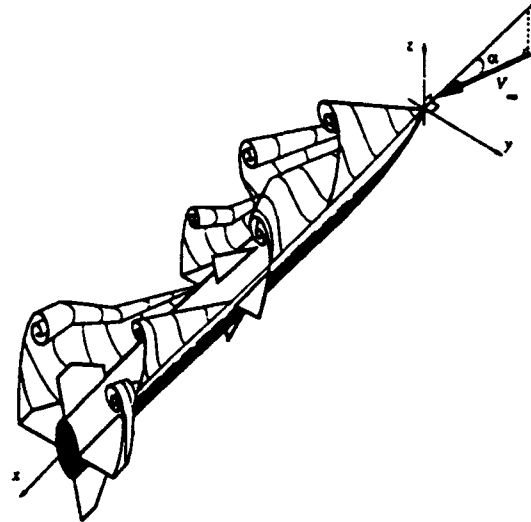


Figure 1. Schematic of an Axisymmetric, Slender, Finned Body at a High Angle of Attack

The aerodynamic databases for use in 6-DOF simulations can essentially be generated in one of the four following ways, 1) Empirical Relations, 2) Wind Tunnel Tests, 3) Navier-Stokes Solutions, or 4) Discrete Vortex Methods. Since few experiments have been done with high angle of attack bodies, no real empirical relations exist. Wind tunnel tests are too costly for design missiles, and Navier-Stokes solutions take too long to generate entire aerodynamic databases. The only present practical method for the production of entire high angle of attack aerodynamic databases are discrete vortex methods. This lower order solution attempts to capture the essential physics of the flow while rapidly calculating the gross properties.

The usefulness of discrete vortex methods has been shown by a number of researchers [Ref. 1-10]. Although the method does not give as detailed results as other CFD solutions, it has the advantages of being very fast and still determines the in-plane as well as the out-of-plane loadings. The present study has extended previous discrete vortex analysis to include the effect of unsteady motion of the body. In this analyses, the body can experience pitching, yawing or rolling motion at given angles of attack and Mach number. The stability derivatives are then calculated for the resulting data.

Theoretical Development

A discrete vortex approach marches the flow solution down from nose tip to the tail of the body. The downstream effects are negligible on the upstream flow. In subsonic flow, this is of course an approximation, but it leads to rapid solutions while still holding on to the dominant physics. The flow at each cross flow section is analyzed as a two-dimensional flow. At each section, the boundary layer separates and a small amount of vorticity is injected into the flow. The upstream flows are convected to downstream sections. The vortices of upstream sections are allowed to interact with each other and the body, and they tend to roll up in large vortical structure. At an arbitrary axial location on the body, the cross flow velocities are given in Ref. 8 as

$$w - iv = V_\infty \sin(\alpha) \bar{\omega} \quad (1)$$

where

$$\begin{aligned} \bar{\omega} = & \left(1 - \frac{a^2}{\zeta^2}\right) + \frac{1}{2\pi i} \sum_{j=1}^N \lambda_j \Gamma_j \left(\frac{2\zeta - \zeta_j}{\zeta^2 - \zeta \zeta_j} + \frac{\bar{\zeta}_j}{a^2 - \zeta \bar{\zeta}_j} \right) + a \frac{da}{dx} \frac{1}{\tan(\alpha)} \frac{1}{\zeta} \\ & + \frac{1}{2\pi} \sum_{k=1}^{2N_f} \left\{ \sum_{m=1}^M \mu_{k,m} \left[-e^{i\theta_k} \ln \left(\frac{\zeta - \zeta_k - s_{k,m+1} e^{i\theta_k}}{\zeta - \zeta_k - s_{k,m} e^{i\theta_k}} \right) + \right. \right. \\ & \left. \left. e^{-i\theta_k} \left(\frac{a}{\zeta} \right)^2 \ln \left(\frac{a^2 - \zeta(\bar{\zeta}_k - s_{k,m+1} e^{-i\theta_k})}{a^2 - \zeta(\bar{\zeta}_k - s_{k,m} e^{-i\theta_k})} \right) \right] \right\} + \frac{\Gamma_B}{2\pi i \zeta} \end{aligned} \quad (2)$$

where α is the angle of attack made by the body centerline and the upstream velocity vector. These equations give the velocity in complex variables. Referring to the coordinate system shown in Fig. 1, the u , v , and w velocities are in the x , y , and z directions, respectively. The position of the point where the velocity is being calculated is specified as $\zeta = z + iy$, where $i = \sqrt{-1}$, and the x value gives the cross section location. The upstream velocity is V_∞ , a is the radius of the axisymmetric body at the section, λ is a semi-infinite vortex weighting factor [Ref. 8], N is the number of shed nascent vortices at the sections, Γ is the strength of the vortices, and ζ_j is the complex location of each vortex. The overbar ($\bar{}$) denotes a complex conjugate. The equation is developed for the possibility of N_f fins at the section which are modeled as source/sink sheets. The strength of each given panel along the fin is μ , and the radial fins make an

angle θ with the z axis. The source panels start at the location ζ_k and have a length $s_{k,m}$. The strengths of the source/sinks are found by standard collocation techniques. The final term is due to the spinning of the body, and it will be discussed later.

The strengths of the shed vortices are found by integrating the vorticity across the boundary layer at the point where it separates. As a result the vortex strength is

$$\Gamma_j = \pm \frac{1}{2} \tan(\alpha) \bar{\omega}_e^2 \Delta x \quad (3)$$

where the value of $\bar{\omega}_e$ is given by Eq. (2) evaluated at the separation point in the previous step. Note that the calculation of the velocity field has been written at discrete axial positions. Rather than continuous shedding of vorticity, discrete vortices (nascent vortices) are introduced into the flow at given intervals. The separation locations are found using an integral boundary layer solver for both laminar and turbulent boundary layers.

For a known axisymmetric shape, angle of attack and flow velocity, Eqs. (1-3) define the potential incompressible flow field around a slender finned body. The upstream flows are assumed to convect to downstream locations at the axial velocity. Essentially the spatially developing flow is transformed into a time developing flow around a body of changing cross section. The transformation is simply

$$x = V_\infty \cos(\alpha) t \quad (4)$$

The forces on the fins are found through sectioning the fins into panels, determining the actual angle of attack seen by each panel, and then determining the force on the panel by the following formula,

$$C_{N_f} = \left[A_p \omega_f \sin(2\alpha_p) \pm 2.2 \sin^2(\alpha_p) \right] \frac{1}{S_{ref}} \quad (5)$$

where C_{N_f} is the panel incompressible normal force coefficient, A_p is the area of the panel, ω_f is a separation weighting factor which is set such that $\omega_f = \pi$ when α_p is less than the separation angle of 12° , and $\omega_f = 2.5$ when

α , is greater than 12° . For the thin plate airfoils modeled, it was assumed that the flow separates on the suction surface when the angle of attack is greater than 12° . The angle α_p is the local angle of attack experienced by the panel center, and S_{ref} is the body reference area. This formula gives adequate behavior of the lifting surface aerodynamics. Since the equation is applied to each panel of the fin, the non-uniform upstream flow is taken into account. The appropriate forces and moments are determined by the weighted sums of the equation over the panel.

All of the previous equations were developed for a uniform upstream velocity, a constant angle of attack, and roll angle. If the body is undergoing rapid maneuvers, the roll angle and angle of attack seen at each section will vary. Figure 2 shows schematically the velocity seen at each section. The cross flow velocity is due to the cross flow component of the upstream velocity and the component due to the pitching motion of the body.

From Fig. 2 it is readily seen that the angle of attack seen at each axial location x along the body is

$$\alpha_s = \tan^{-1} \left[\frac{V_\infty \sin(\alpha) + (x - x_{cg})q}{V_\infty \cos(\alpha)} \right] \quad (6)$$

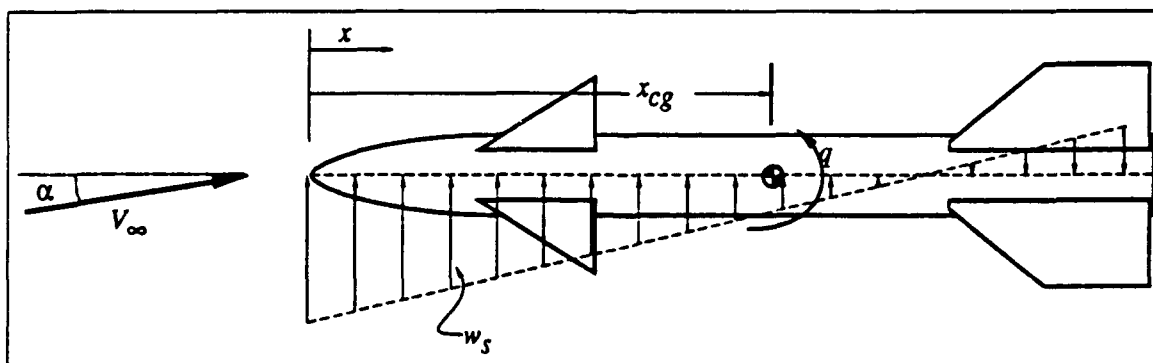


Figure 2. Schematic of the velocity distribution of a pitching body at an angle of attack.

where α_s is the angle of attack seen at the given section, x_{cg} is the axial location of the body center of gravity, and q is the pitching rate of the body. Each section sees an apparent upstream velocity V'_∞ of

$$V'_\infty = \sqrt{\left[V_\infty \sin(\alpha) + (x - x_{cg})q\right]^2 + (V_\infty \cos \alpha)^2} \quad (7)$$

Since the equations are written in terms of a total angle of attack, the same relations hold for a body with a yawing rate r as for a pitching body.

For a body experiencing roll, the final term of Eq. (2) must be introduced to account for the roll. A single vortex is located at the center of the body which induces a velocity equal to the roll rate at the body surface. Thus, in Eq. (2), the strength of the vortex Γ_B is

$$\Gamma_B = 2\pi a^2 p \quad (8)$$

where p is the roll rate. This term in the classic way accounts for the viscosity at the surface of the spinning body. This term must be included with the rest of the velocity field when utilizing the integral boundary layer solver to determine the separation locations on the body. These integral methods require that the flow is marched for the stagnation point to the separation location.

For the rolling body, the definition of the stagnation point becomes more difficult. In this analysis, the boundary layer solvers were marched forward from the point where the potential flow velocity at the body surface is equal to (in magnitude and direction) the body rotation. For the boundary layer solution, the rotation rate is subtracted from the potential flow for the driving potential flow (pressure gradient) in the boundary layer equations. Thus, in this manner at the "stagnation" point, the imposed potential velocity in the boundary layer solver is identically zero. Away from the stagnation point, the potential velocity is adjusted accordingly. This approximation of the boundary layer solver leads to rapid solutions, and is in accordance with the approximate nature of this approach.

The fins on the nose tip are modeled as source/sink sheets as was discussed. However, the fins are rolling with the body. Therefore, as the flow is marched from section to section, the fins move to different angular positions at the appropriate rate. For an analysis with fins on the missile an estimation of the boundary layer separation point is made. If a fin is within the region of the body between the stagnation location and the

projected separation location, the flow is assumed to separate at the fin tip. If no fin is there, the flow integral boundary layer solver is run to determine the separation location.

For the determination of the source/sink distribution on the fin and the strength of the vorticity shed at the fin tip, the rotation of the fin must be taken into account. The velocity that the fin sees at any radial location due to the rotation of the fin is $v_\theta = r_f \dot{\phi}$ where v_θ is the velocity in the angular direction, and r_f is the radial location to a point on the fin. This additional velocity component must be included with the rest of the velocity field when determining the strength of the sources and sinks that will make the normal component of the velocity at the fin surface equal to zero.

These changes were incorporated into a discrete vortex code named *DEVO*, which stands for *Discrete Elemental VOrtex* program. The *DEVO* code can handle a wide variety of slender body shapes, at total angles of attack from 0° to 70° , and Mach numbers from 0 to 5. For this analysis, only the low subsonic portions of the code were used. The modified code was run on the Eglin AFB Cray YMP. Each solution took approximately 15 minutes of CPU time, with the higher angles of attack requiring more time as discussed in Ref. 8.

Results

The missile tested for this study is shown in Fig. 3. The body is an Air Force AMRAAM without the wire harness. A full scale body was run so the body diameter is 7 inches. All tests were run at a Mach number of 0.15.

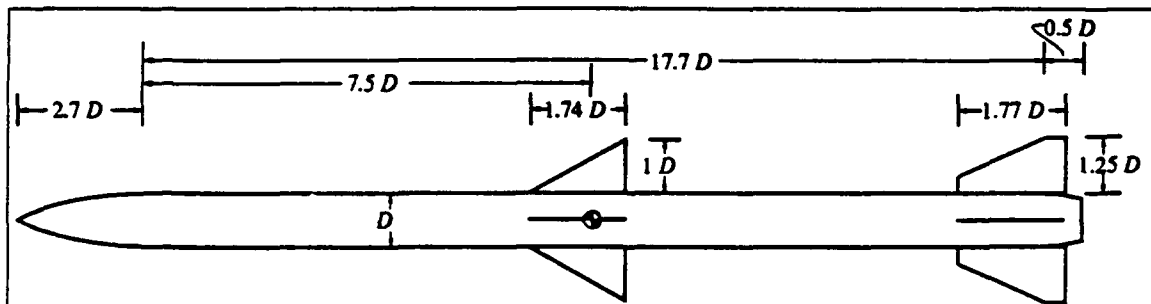


Figure 3. Specifications of the AMRAAM-like missile used for testing.

Figure 4 shows a computer image of the missile at 40° angle of attack. The image was generated using the *YAPP* program [Ref. 11] developed at Eglin AFB. In this figure, the body is not pitching. The figure shows the total pressure field calculated by the *DEVO* program at a particular cross sectional plane near the tail of the body. Additionally, the vortex formation on one side of the forward part of the body is shown. Although more difficult to see without color, the total pressure shows the position of the vortices that exist near the body. As the body experiences pitching motion, the tail fins will convect through these vortices, and radically alter the aerodynamics forces.

Figure 5 shows a similar computer image of a missile pitching at $q = 2.0$ rad/s, and at a 40° angle of attack. By comparing with Fig. 4, it can be seen that the flow field significantly changes from the static aerodynamic case. The changes in the flow field cause significant changes in the body aerodynamics.



Figure 4. Computer generated image of a missile and flow field for a static flight attitude of Mach = 0.15 and 40° angle of attack.

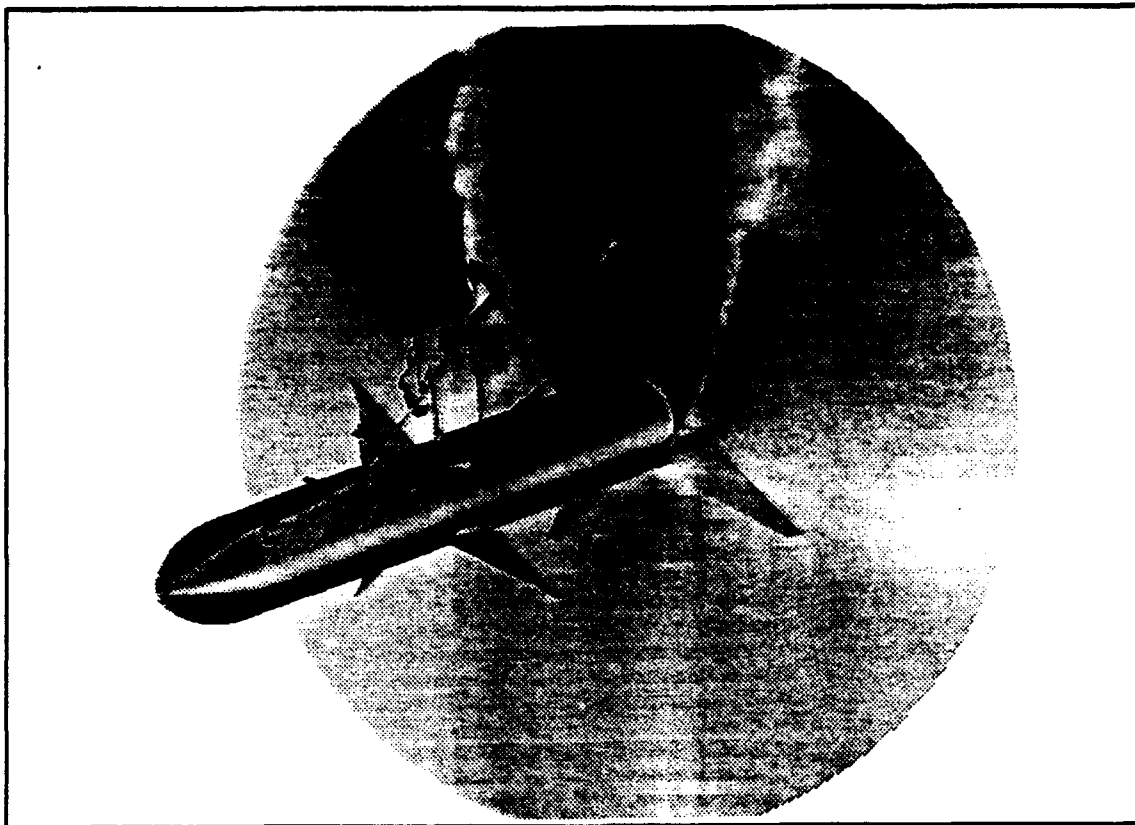


Figure 5. Computer generated image of the surrounding flow field and the missile pitching at $q = 2.0$ rad/s at a Mach = 0.15 and 40° angle of attack.

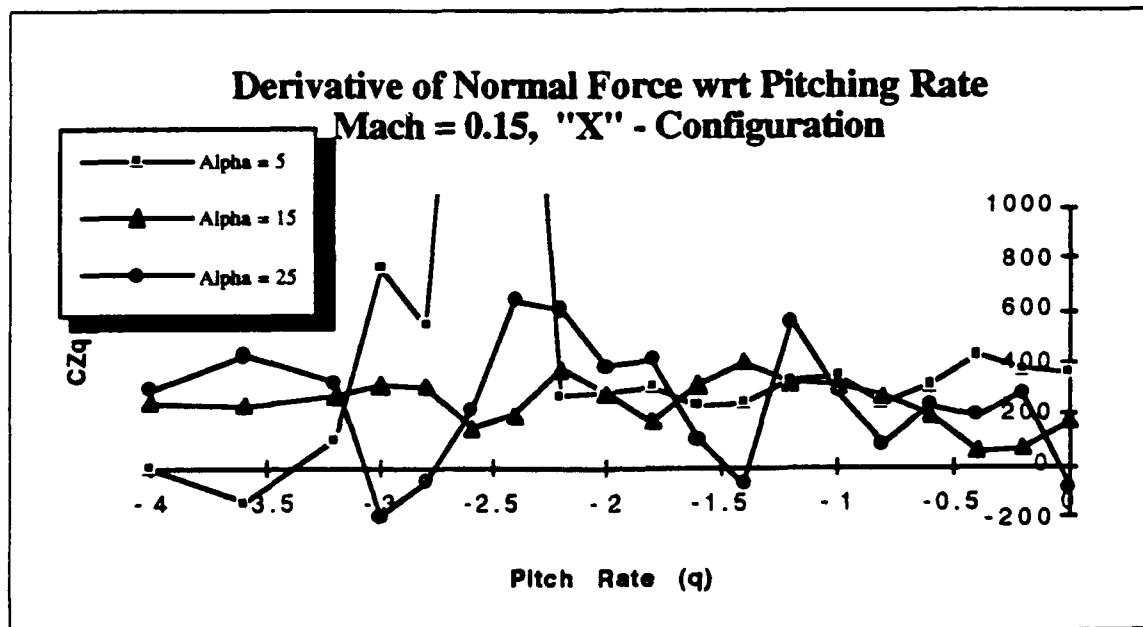


Figure 6. Stability derivative of the normal force wrt the pitching rate for various low and moderate angles of attack.

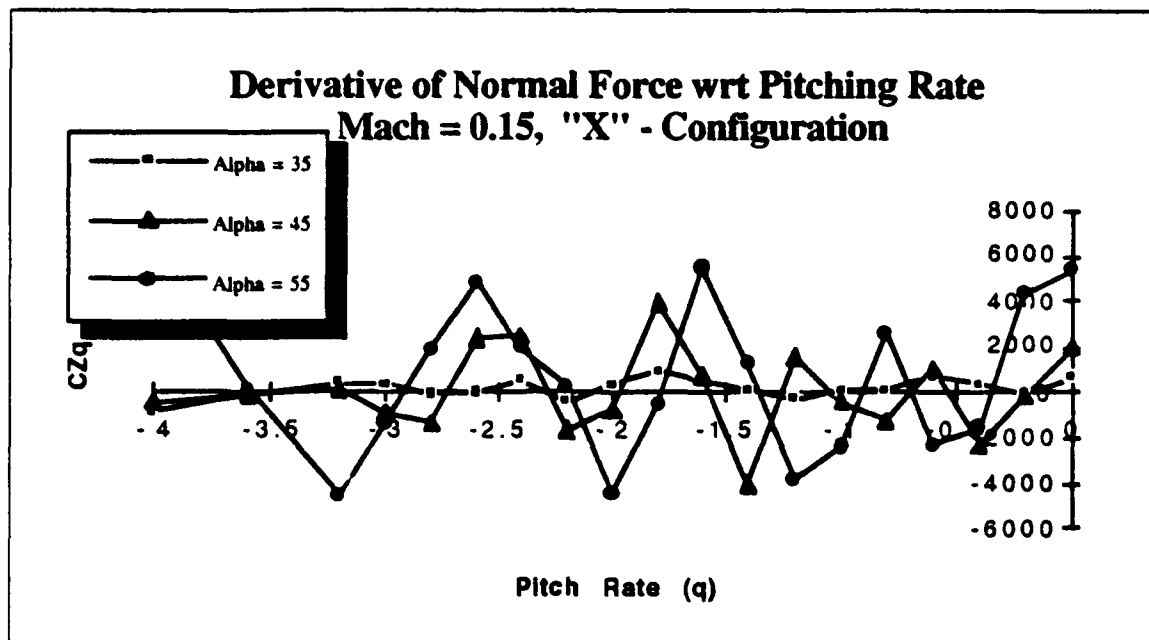


Figure 7. Stability derivative of the normal force wrt the pitching rate for various high angles of attack.

Figures 6 through 15 show the stability derivatives for a pitching missile. The body is flying in an "x"-configuration. Figures 6 and 7 show the derivative of the normal force with respect to the pitch rate. The stability derivative is defined in the usual way as $C_{Zq} = \partial C_Z / \partial (qL/2V_\infty)$. The

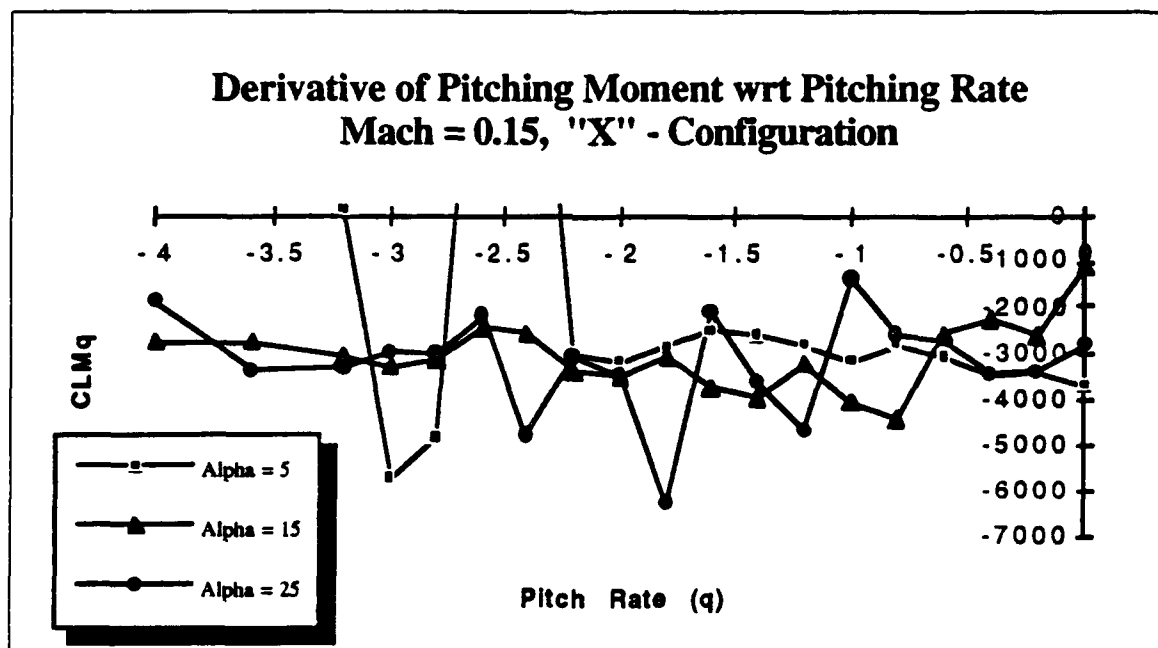


Figure 8. Stability derivative of the pitching moment wrt the pitching rate for various low and moderate angles of attack.

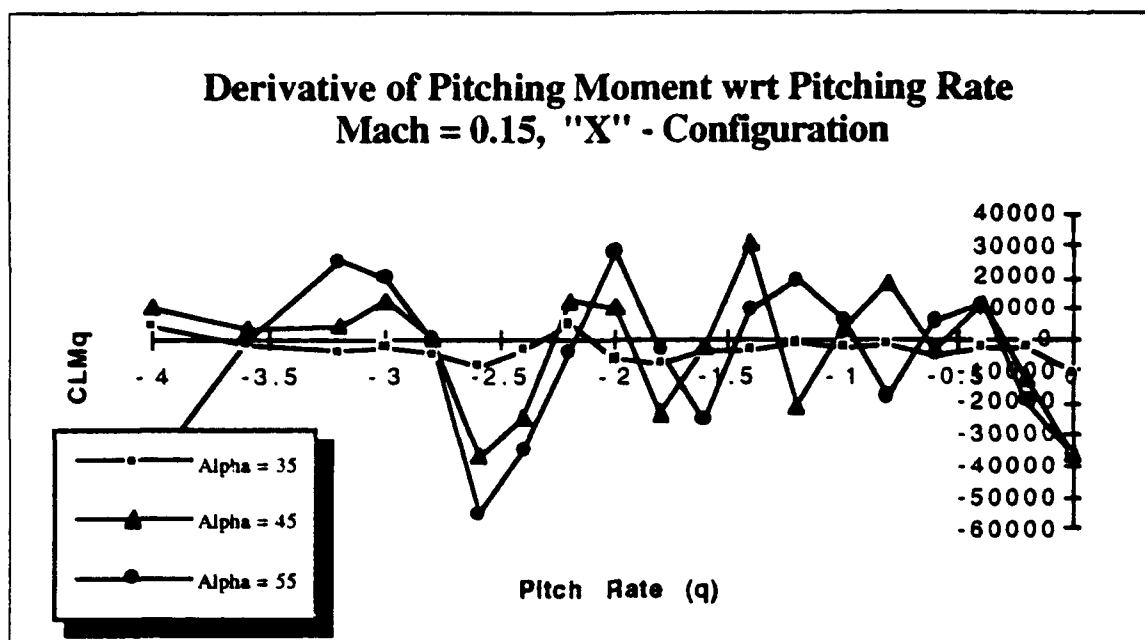


Figure 9. Stability derivative of the pitching moment wrt the pitching rate for various high angles of attack.

prediction of this derivative is rather difficult both analytically and experimentally. The figures show considerable scatter of the data. However, it is apparent from the figures that at the lower angles of attack, the stability derivative is reasonably well behaved, and at moderate and large angles of incidence, considerable scatter occurs in the data.

Figures 8 and 9 show the pitch damping derivative with respect to the pitch rate. As with the normal force, the curves are best behaved at low angles of attack. As the angle of attack increases, the derivatives become more irregular. This behavior is due to the motions of the lifting surfaces through the wake vorticity. The overall angle of attack seen by a surface can rapidly change from positive to negative, as it moves through the vortex core.

The out-of-plane stability derivatives for pitching motion are shown in Figs. 10-15. It is expected that the out-of-plane loading will be even more erratic than the in-plane since the entire loading is due to the asymmetric vortex formation. The figures do show highly non-linear behavior at moderate and high angles of attack. However, at low angles of attack as seen in figures 10, 12, 14, the out-of-plane stability derivatives are all quite small. This is probably due to the fact that the out-of-plane loading itself is quite small at low angles of incidence.

At high angles of attack, the out-of-plane stability derivatives become huge. When the incidence angles are large, the out-of-plane loading can change rapidly. As a result, the derivatives, which are calculated by means of finite differences, reflect the rapid changes in the out-of-plane loading.

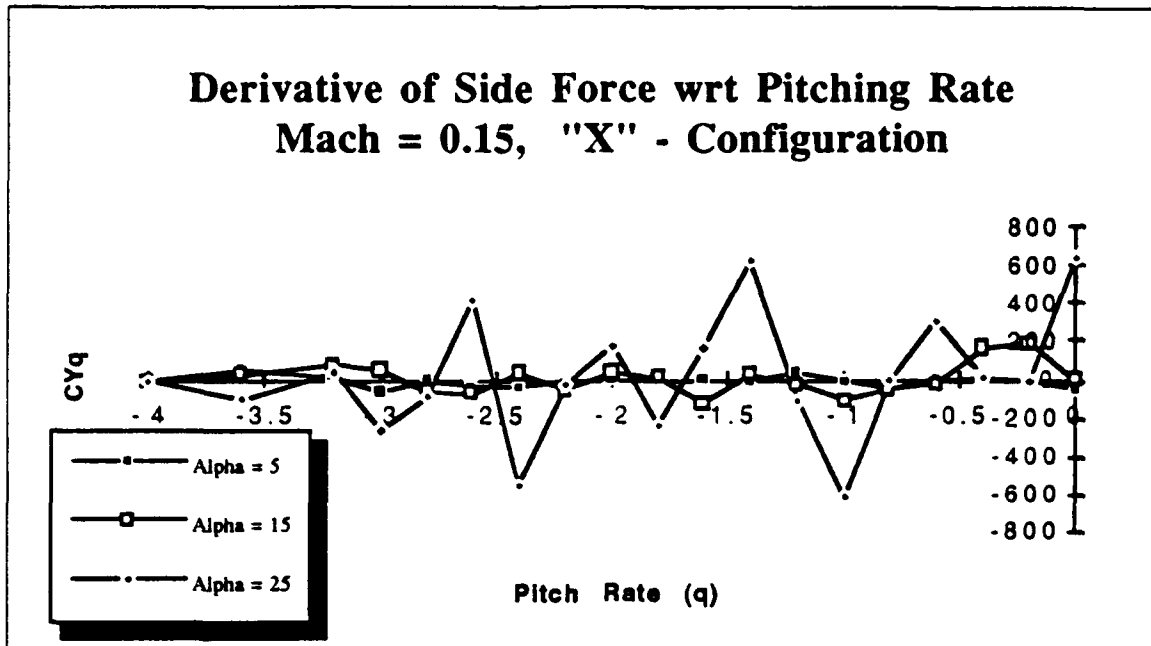


Figure 10. Stability derivative of the side force wrt the pitching rate for various low and moderate angles of attack.

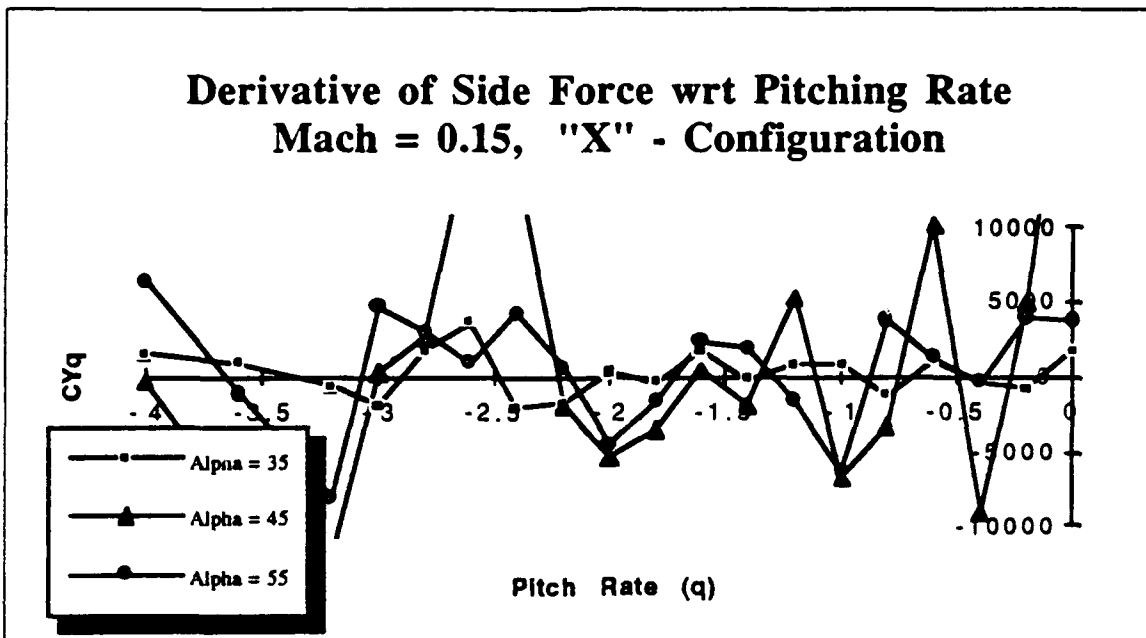


Figure 11. Stability derivative of the side force wrt the pitching rate for various high angles of attack.

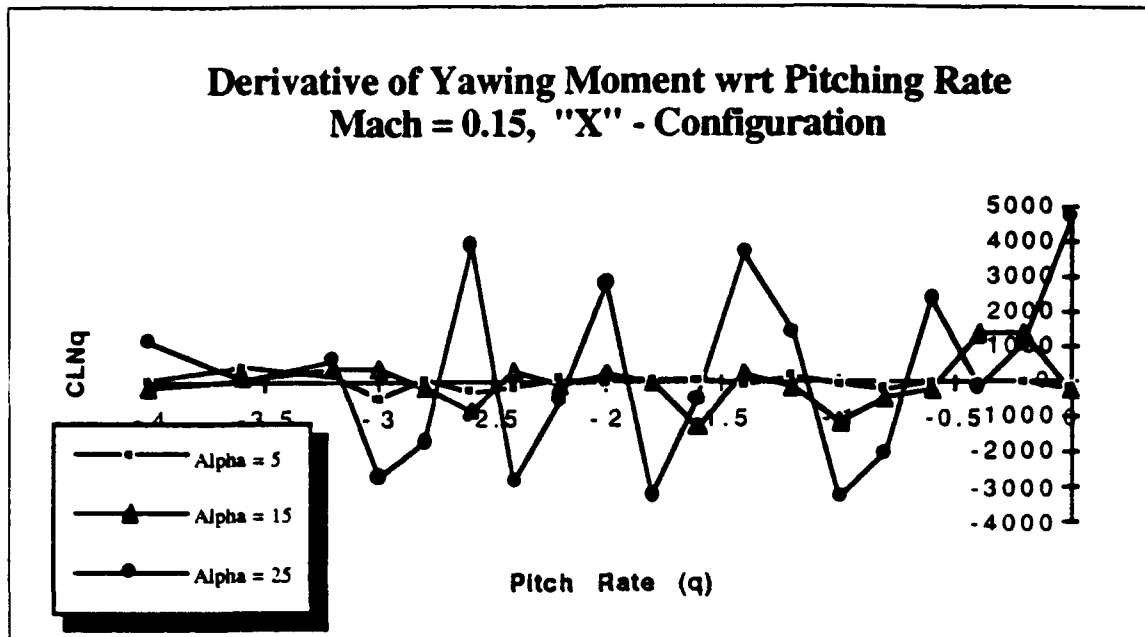


Figure 12. Stability derivative of the yawing moment wrt the pitching rate for various low and moderate angles of attack.

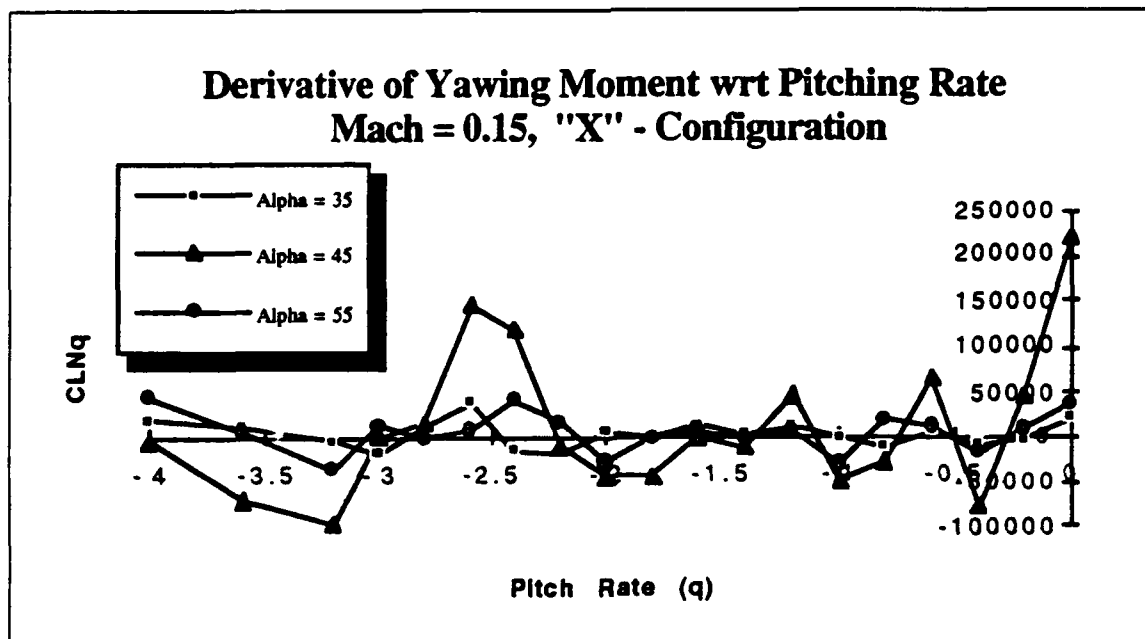


Figure 13. Stability derivative of the yawing moment wrt the pitching rate for various high angles of attack.

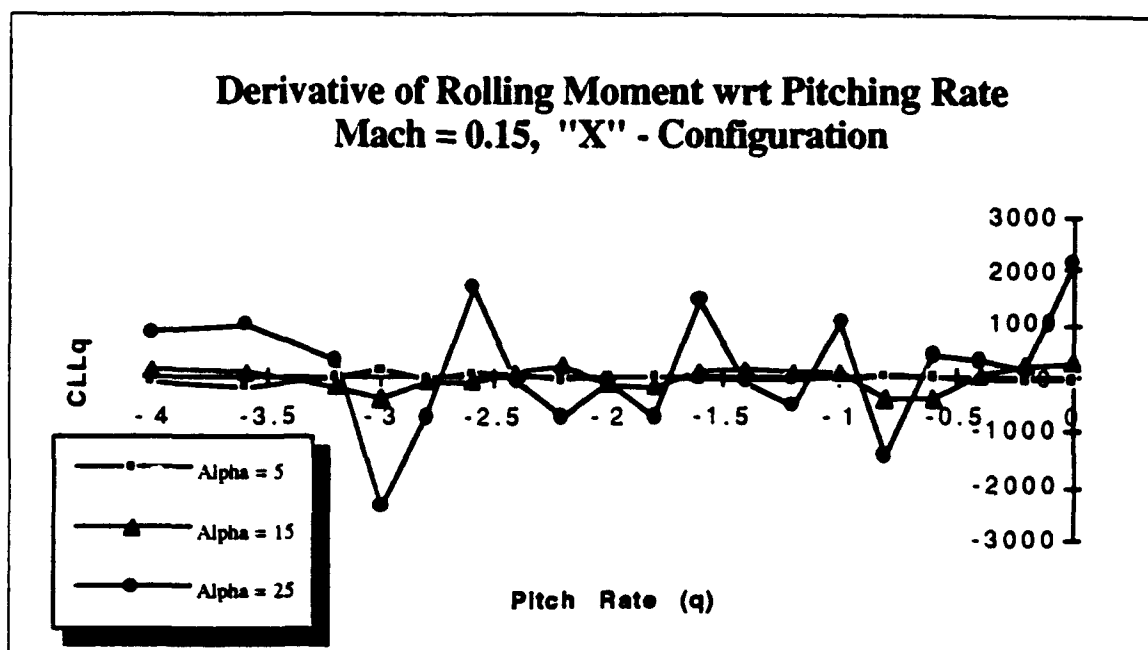


Figure 14. Stability derivative of the rolling moment wrt the pitching rate for various low and moderate angles of attack.

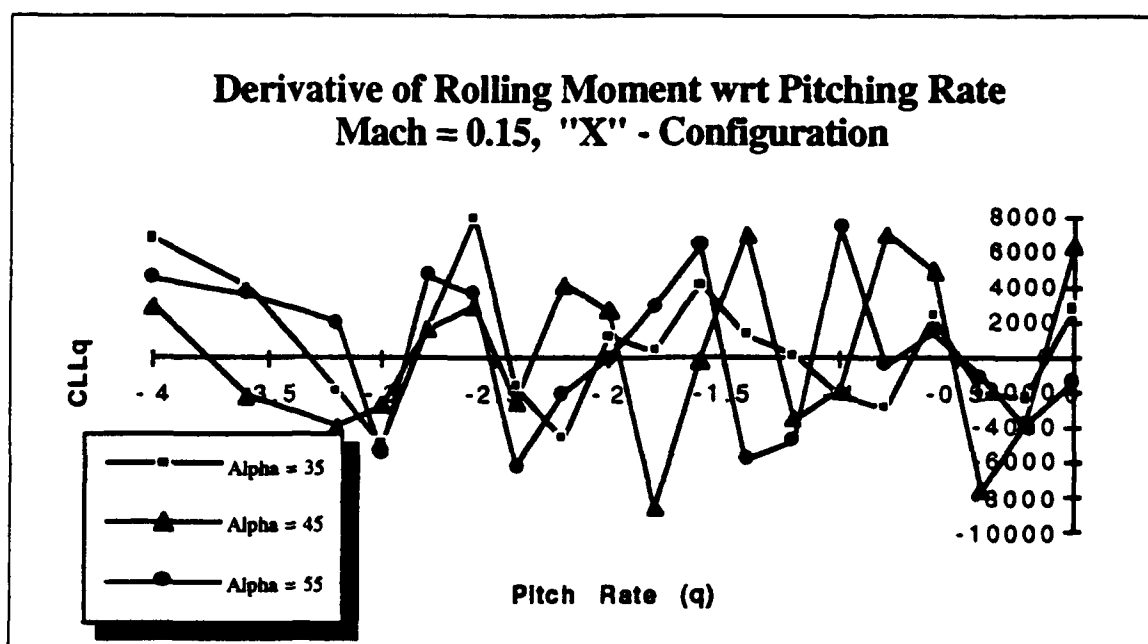


Figure 15. Stability derivative of the rolling moment wrt the pitching rate for various high angles of attack.

The side loading can rapidly change sign and magnitude for a very small change in pitching rate which results in the large derivatives.

For the out-of-plane loading, the curves should not be used to determine the actual value of the stability derivatives, but give an indication of the dependence of the out-of-plane loading on the motions of the body. The figures give a good indication that the out-of-plane loading is of negligible importance at low angles of attack. However, at high angles of attack, there is considerable effect not only in the static loading, but also the stability derivatives.

Figures 16-19 show the derivatives of the aerodynamic coefficients with respect to roll rate. As with the pitching body, the body experiencing roll has reasonably well behaved stability derivatives at low angles of attack, but extremely large and fluctuating derivatives at the high incidence angles. For brevity, only the out-of-plane loadings are given here.

The derivative of the side force with respect to roll rate is shown in Fig. 16. Only the high angle of attack results are shown here. The force shows considerable effect of roll rate roll coupling, and the results are similar for the normal force. The graph shows that the higher the angle of attack, the larger the overall magnitude of the stability derivative.

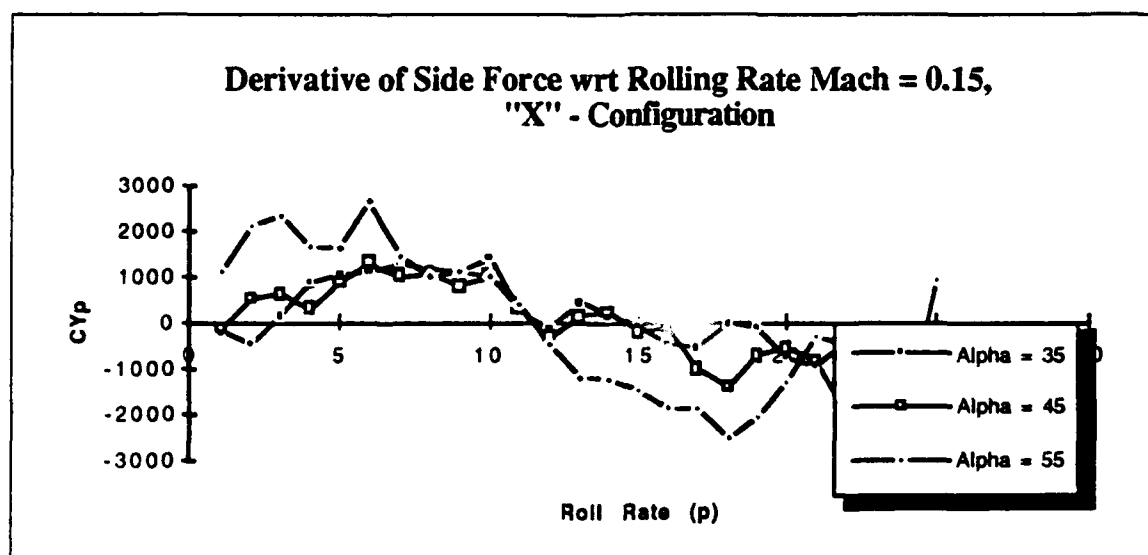


Figure 16. Stability derivative of the side force wrt the rolling rate for various high angles of attack.

Figure 17 gives the stability derivative of the yawing moment with respect to the roll rate for the body at high angles of attack. Again, considerable scatter is shown in the data. For all the values shown, the derivatives are quite large.

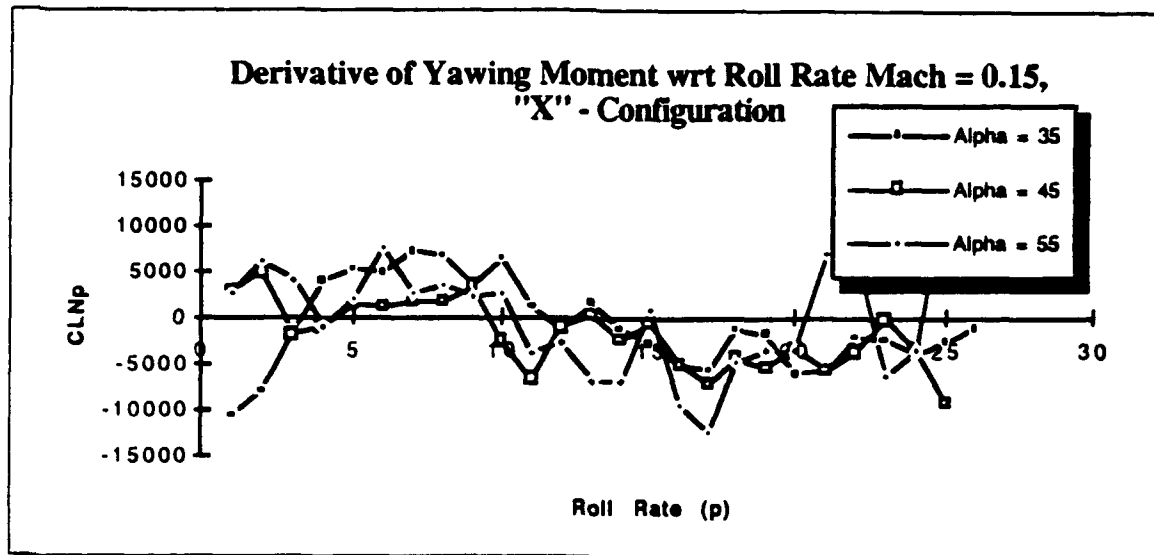


Figure 17. Stability derivative of the yawing moment wrt the rolling rate for various high angles of attack.

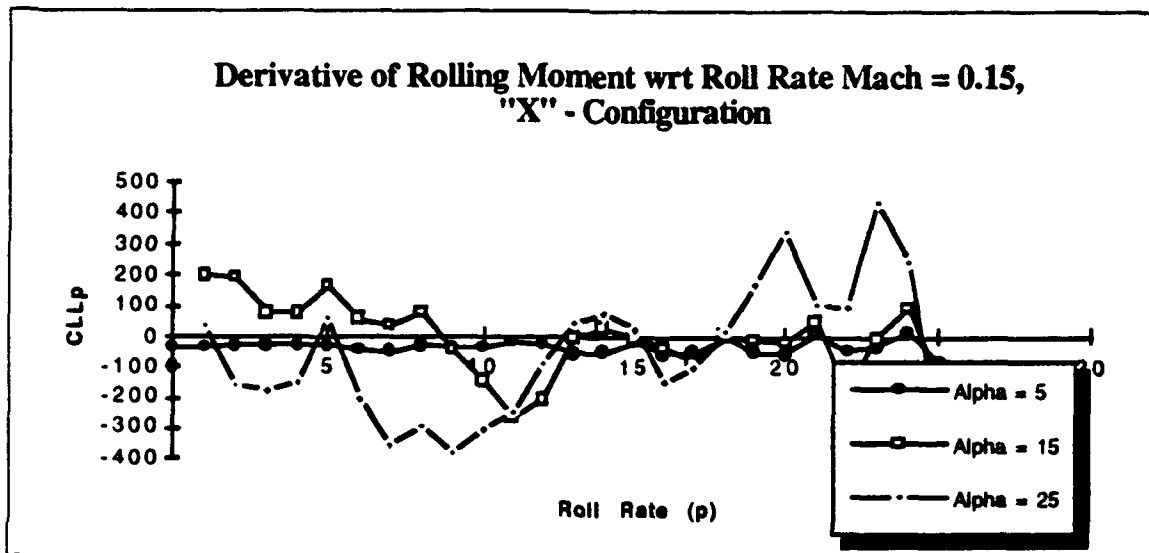


Figure 18. Stability derivative of the rolling moment wrt the rolling rate for low and moderate angles of attack.

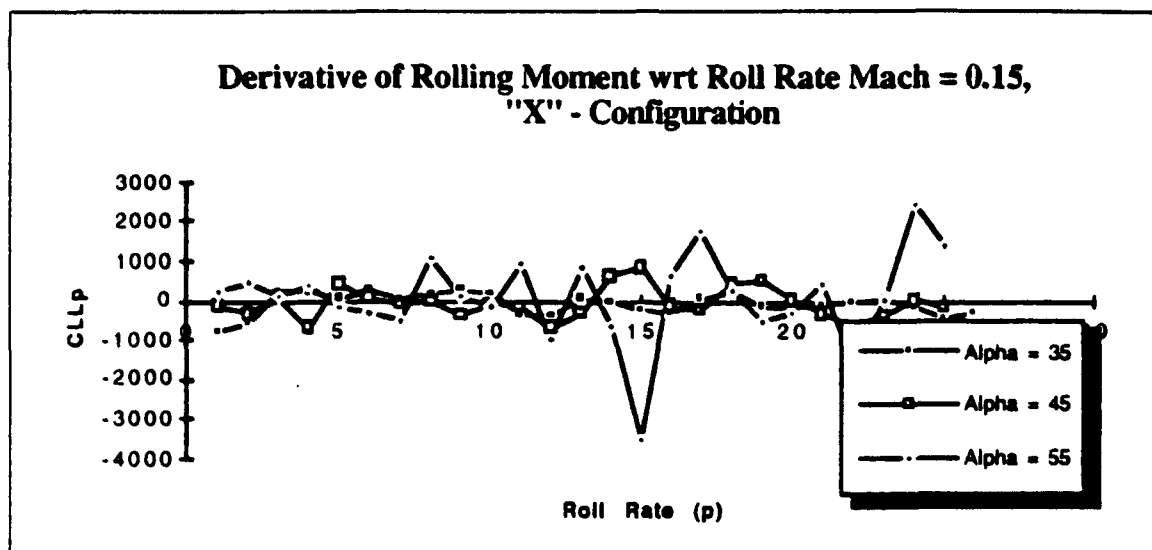


Figure 19. Stability derivative of the rolling moment wrt the rolling rate for high angles of attack.

The last two figures show the derivative of the rolling moment with respect to the rolling rate. Figure 18 shows the stability derivative at low and moderate angles of attack, and Fig. 19 gives it at high angles of attack. Note that at low angles of attack, the roll damping derivative is rather small and nearly constant. However, as the angle of attack is increased, the derivative gets increasingly large, and oscillates with the roll rate. This effect is due to the fins rolling through the core of the shed vorticity, and inducing large forces and moments on the fins in doing so.

Conclusion

In the past, little time has been spent in the study of finned slender bodies at high angles of attack. It is known that for certain geometries in a range of high angles of attack, large symmetric or asymmetric vortical structures form on the leeward side of the body. When lifting surfaces are on the body, the interaction between the vortical flow and the fins can significantly affect the overall forces and moments of the body. Previous research has employed various techniques to estimate the static aerodynamic loading on the body, but apparently no studies have ever been conducted on the aerodynamics of maneuvering finned bodies.

The present study attempted to estimate the stability derivatives of a body undergoing rapid pitching, yawing, and rolling. A discrete vortex

method was used to rapidly determine the total aerodynamic loading. An existing discrete vortex code was modified to account for the effects of a maneuvering body. The result showed significant interaction between the lifting surfaces and the vortical structures of the flow.

The estimated stability derivatives were shown to behave reasonably well and remain more or less constant at low angles of incidence. However, at moderate and high angles of attack, the stability derivatives showed extremely non-linear behavior. The motion of the lifting surfaces through the vortical flow quickly changes the loading on the body leading to extremely large stability derivatives.

This study has shown that a possibility for gross error in the estimation of the total high angle of attack body aerodynamics can exist if the effects of pitching, yawing, and rolling are neglected. Further research needs to be performed (both analytical and experimental) in this area. This initial work has pointed to a possible problem, but more detailed studies need to occur.

References

1. Wardlaw, A. B., "Prediction of Normal Force, Pitching Moment, and Yawing Force on Bodies of Revolution at Angles of Attack up to 50 Degrees Using a Concentrated Vortex Flow-Field Model," NOL TR 73-209, Oct. 1973.
2. Wardlaw, A. B., "High Angle of Attack Missile Aerodynamics," AGARD LS-98, Feb. 1979, pp. 5.1-5.53.
3. Marshall, F. J. and Deffenbaugh, F. D., "Separated Flow Over Bodies of Revolution Using Discrete Vorticity Cross Wake," NASA CR-2414, June 1974.
4. Thomsom, K. D. and Morrison, D. F., "The Spacing, Position, and Strength of Vortices in the Wake of Slender, Cylindrical Bodies at Large Incidence," *Journal of Fluid Mechanics*, Vol. 50, 1971, pp. 751-783.
5. Angelucci, S. B., "A Multivortex Method for Axisymmetric Bodies at Angle of Attack," *Journal of Aircraft*, Vol. 8, Dec. 1971, pp. 959-966.

6. Mendnehall, M. R. and Lesieutre, D. J., "Prediction of Vortex Shedding from Circular and Noncircular Bodies in Subsonic Flow," *NASA CR 4037*, Jan 1987.
7. Mendnehall, M. R. and Perkins, S. C., Jr., "Vortex Cloud Model for Body Vortex Shedding and Tracking," *Tactical Missile Aerodynamics*, edited by M. J. Hemsch and J. N. Nielson, Vol. 104, Progress in Astronautics and Aeronautics, AIAA, N.Y., 1986, pp. 519-571.
8. Gebert, G. A. "Determination of Slender Body Aerodynamics Using Discrete Vortex Methods," accepted for publication in the *AIAA Journal of Spacecraft and Rockets*, November 1992.
9. Mendnehall, M. R. and Lesieutre, D. J., "Prediction of Subsonic Vortex Shedding from Forebodies with Chines," *Journal of Aircraft*, Vol. 29, No. 3, May-June 1992, pp. 404-412.
10. Gebert, G. A. "Discrete Vortex Methods for the Determination of Finned Body Aerodynamics," submitted to the *AIAA Journal of Spacecraft and Rockets*, April 1993.
11. Belk, D. and Maple, R., "Visualization of Vortical Flows with Yet Another Post Processor," AIAA Aerospace Sciences Meeting, Reno, NV, Paper 93-0222, Jan. 1993.

HOLOGRAPHY OF EXPLODING SHELLS

James S. Marsh

Professor

Department of Physics

The University of West Florida

Pensacola, FL 32514

Final Report for:

Summer Faculty Research Program

Wright Laboratory

Armament Directorate

WL/MNSI, Eglin AFB

Sponsored by:

Air Force Office of Scientific Research

Bolling Air Force Base, Washington, D.C.

August 1993

HOLOGRAPHY OF EXPLODING SHELLS

James S. Marsh
Professor
Department of Physics
The University of West Florida

Abstract

A holography laboratory was set up and the capability to produce high quality transmission and reflection holograms was developed as the first phase of a project to make cylindrical holograms of exploding shells.

HOLOGRAPHY OF EXPLODING SHELLS

James S. Marsh

Introduction

Holograms of rapidly moving objects were produced as early as 1966 by Brooks et. al. (1966), on flat plates using a multimode ruby laser. For objects moving with supersonic speeds, and with the geometries available, a hologram of the actual object is not obtained. Rather the object is viewed against a bright background, and a kind of holographic shadowgram is produced. The shadowgram is a three dimensional object and perspective changes are observed in the hologram as the viewing angle is changed.

The Armament Directorate is interested in studying the dynamics of shell fragments produced by exploding shells. A pilot program to investigate the feasibility of making cylindrical holograms of exploding shells, using pulsed laser light from a multimode ruby laser, was assigned to LTV in 1989. The successful outcome of that program showed (Hough and Gustafson, 1989) that high quality single and double pulsed holograms could indeed be made. These holograms allow scanning of the shell fragment field through a full 180 degree arc. This is important in order to determine, in three dimensions, the positions and shapes of the fragments. The dimensional stability problems associated with film shrinkage, reconstruction with wavelengths different from that of the

radiation used to make the hologram, etc., were solved by superimposing a holographic image of a standardized cylindrical grid on the hologram. By double pulsing the ruby laser at a suitable time interval it was possible to produce a double exposure hologram that allowed the vector velocity of each of the fragments to be determined.

Methodology

With the success of the pilot program, it was decided to set up a facility at Eglin AFB for the purpose of routine holographic imagery of exploding shell fragments. A ruby laser capable of producing a 3 joule pulse in a 20 nanosecond time frame, in either single or double pulse mode, was purchased. This instrument, in addition to a 60 milliwatt Helium-Neon Laser, darkroom hardware and chemicals, and assorted optical hardware, was on the scene when I arrived in May to assist with the optical issues involved in setting up the facility and bringing it to a state in which high quality holograms could be produced as necessary in a routine manner. The facility adjoins a long tunnel in which the gun will be fired. The tunnel is connected to the facility by means of a 6 inch port drilled into the wall separating the two.

The work this summer resulted in the routine production within the facility of high quality single beam and double beam transmission and reflection holograms using the 60 milliwatt He-Ne laser. These are

produced using techniques found in the standard textbooks on the subject. These include Collier et. al. (1971), Abramson (1981), Unterseher et. al. (1987), and Trolinger (1988).

In addition the Ruby laser, operating in the region of 400 millijoule pulses in single pulse mode, was used to produce good single beam transmission and reflection holograms within the facility. Attempts to produce cylindrical holograms within the facility with the ruby laser were less successful. The reason appears to be inadequate optical components. Appropriate optical components for this purpose were ordered but had not arrived by the date of this report.

Projections

What was accomplished this summer, the routine production of standard holograms, may be regarded as phase one of the project to produce holograms of exploding shells. In phase two the ruby laser beam will be sent into the tunnel where cylindrical holograms of stationary objects will be made. This phase awaits the arrival of appropriate hardware and optical components. Phase three will be the holography of exploding shells in the tunnel. Implementation of this phase will involve detectors and timing circuits to slave the ruby pulse to the passage of the shell.

BIBLIOGRAPHY

N. Abramson, "The Making and Evaluation of Holograms," Academic Press, New York, (1981)

R. E. Brooks, L. O. Heflinger, and R. F. Wuerker, "Pulsed Laser Holograms," IEEE J. Quantum Electron. **QE-2**, 275 (1966)

R. J. Collier, C. B. Burkhardt, and L. H. Lin, "Optical Holography," Academic Press, New York (1971)

G. R. Hough and D. M. Gustafson, "Ballistic Applications of Lasers," SPIE Volume 1155, Ultrahigh Speed and High Speed Photography, Photonics, and Videography '89, pp. 181-188, (1989)

J. D. Trolinger, "Laser Applications in Flow Diagnostics," AGAR-Dograph No. 296, (1988)

F. Unterseher, J. Hansen, and B. Schlesinger, "Holography Handbook," Ross Books, Berkeley, CA (1987)

**A Methodology for Missile Autopilot Performance Enhancement
in the Presence of Multiple Hard Nonlinearities**

**Armando A. Rodriguez
Assistant Professor
Department of Electrical Engineering**

**Arizona State University
Center for System Science & Engineering
Tyler & Rural, GWC 612
Tempe, AZ 85287-7606**

**Final Report for:
Summer Research Program
Wright Laboratory**

**Sponsored by:
Air Force Office of Scientific Research
WL/MNAG, Eglin Air Force Base, FL.**

September 30, 1993

A Methodology for Missile Autopilot Performance Enhancement in the Presence of Multiple Hard Nonlinearities

Armando A. Rodriguez
Assistant Professor
Department of Electrical Engineering
Arizona State University

1 Abstract

The primary goal of this research effort has been to develop systematic design methods for enhancing the performance of missile autopilots. To focus the research, efforts have concentrated on the important problem of guaranteeing performance in the presence of multiple hard nonlinearities. Hard nonlinearities include, for example, saturating actuators, rate limiters, etc. Traditionally, engineers have accommodated such nonlinearities by "extending" single-input single-output (SISO) ideas, using "engineering judgement", and conducting extensive simulation. Because the SISO ideas do not extend well to multiple-input multiple-output (MIMO) problems, the techniques used have not been systematic and, more than often, have resulted in overly conservative designs. The methods developed in this research systematize the design process without sacrificing performance. More specifically, the methods are applied to an EMRAAT BTT missile with saturating actuators. It is shown that the introduced *performance enhancement system* significantly improves autopilot performance by maintaining desired directionality properties, eliminating wind-up effects, and above all guaranteeing stability.

Contents

1 Abstract	48-2
2 Motivation	48-3
3 Overview of Research	48-3
4 Performance Enhancement Methodology	48-4
4.1 Nominal Model for EMRAAT BTT Missile	48-4
4.2 Nominal Autopilot Design	48-4
4.3 Method for Accomodating Saturating Actuators	48-8
4.4 Computational Issues	48-11
4.5 Application of Method to EMRAAT BTT Missile	48-12
4.6 Unstable Operating Points and Other Hard Nonlinearities	48-12
4.7 More General Nominal Compensation Schemes	48-15
5 Significance of Work	48-15
6 Additional Collaborative Work	48-15
6.1 Computation of Structured Singular Value Using Genetic Algorithms	48-15
6.2 Performance Enhancement for Guidance Systems	48-16
6.3 Extension to Gain-Scheduled Controllers	48-16
7 Summary & Directions for Future Research	48-16
8 Bibliography	48-16
9 Appendix: Proposal for Invited Session to 1994 ACC	48-18

A Methodology for Missile Autopilot Performance Enhancement in the Presence of Multiple Hard Nonlinearities

Armando A. Rodriguez

2 Motivation

This research is motivated by the lack of systematic procedures for designing full envelop autopilots for missiles. This deficiency is particularly crucial in the design of autopilots for high performance missile systems. For such systems, hard nonlinearities such as saturating actuators and rate limiters become a critical concern because they degrade system performance. Such nonlinearities may alter the directionality properties of the autopilot, cause dynamic wind-up, and induce instability. These effects may significantly affect the miss distance and are of particular concern during the terminal phase of an air-to-air engagement when evasive target maneuvering may require abrupt control actions. In this section, a method for enhancing the performance of such systems is presented. The focus is on maintaining performance in the presence of saturating actuators. Other types of nonlinearities are also discussed.

Traditionally, control design for missile systems has been based on gain-scheduling [8]. Gain-scheduling is a method whereby linear controllers, based on linear models of the true nonlinear system, are "pieced" together over the operating envelope of the system. The initial designs often do not take into account the effects of hard nonlinearities. One motive for this research has been the lack of systematic methods to modify the original designs so that such nonlinearities can be accommodated.

For physical reasons, system designers often want to limit certain variables (e.g. angle of attack, sideslip angle, roll rate, etc.). Typically, adhoc modifications are employed and extensive simulations must be performed to justify the modifications. A procedure for systematizing this process over the full envelope of the system has been another motive for this research.

3 Overview of Research

Typically, initial autopilot designs are based on linear models and neglect nonlinearities such as saturating actuators [1], [2]. Traditionally, such nonlinearities have been addressed in a conservative manner; sacrificing performance to satisfy some "small-gain" design criterion [10], [20]. For single-input single-output (SISO) systems, methods have been developed which improve performance. These methods, however, do not extend well to multivariable applications [7].

In this work, it is shown how the initial autopilot design can be modified to accommodate the saturating actuators without sacrificing performance. The idea is to introduce a *saturation detection system* which maintains, to the extent possible, the multivariable properties of the original autopilot design [5], [6], [7]. In this paper, it is shown how to construct such a system for a generic EMRAAT (Extended Medium Range Air-to-Air Technology) missile operating near the terminal phase of an air-to-air intercept [1].

An autopilot with prescribed directionality specifications is used. It is shown how saturating actuators result in wind-up effects and destroy the intended directionality properties by preventing the autopilot from properly coordinating the fin commands. The original autopilot is then modified by introducing a *performance enhancement system*. The addition is shown to markedly improve the performance of the original autopilot. Moreover, the modification scheme not only comes with nominal stability guarantees, but also eliminates wind-up effects and maintains, to the extent possible, the directionality properties of the original design. Finally, insight is given into how the method presented can be extended to systematize the design of general nonlinear autopilots.

4 Performance Enhancement Methodology

In this section, a systematic control system design methodology is proposed for maintaining performance in the presence of saturating actuators. Other hard nonlinearities are also addressed.

4.1 Nominal Model for EMRAAT BTT Missile

Throughout this research, the focus has been placed on enhancing performance for highly maneuverable Bank-to-Turn (BTT) missile systems with multiple saturating actuators. BTT missiles offer higher maneuverability over conventional Skid-to-Turn (STT) missiles by the use of an asymmetrical shape and/or the addition of a wing [1], [2]. The model used for this study is for an EMRAAT BTT missile. For simplicity, focus has been placed on the yaw/roll dynamics with

$$Mach\ number = 2.5$$

$$Q_{pres} = 1720\ lb/ft^2$$

$$\alpha = 20\ degrees.$$

The model is given by the following system of ordinary differential equations [1]:

$$\dot{x}_p = A_p x_p + B_p u_p \quad (1)$$

$$y = C_p x_p \quad (2)$$

where

$$A_p = \begin{bmatrix} -0.818 & -0.999 & 0.349 \\ 80.29 & -0.579 & 0.009 \\ -2734 & 0.5621 & -2.10 \end{bmatrix} \quad B_p = \begin{bmatrix} 0.147 & 0.012 \\ -194.4 & 37.61 \\ -2176 & -1093 \end{bmatrix} \quad C_p = \begin{bmatrix} 1 & 0 & 0 \\ 0 & 1 & 0 \end{bmatrix} \quad (3)$$

$$u_p = \begin{bmatrix} \text{rudder} & \text{aileron} \end{bmatrix}^T \quad (4)$$

$$x_p = \begin{bmatrix} \text{sideslip} & \text{yawrate} & \text{rollrate} \end{bmatrix}^T \quad (5)$$

$$y = \begin{bmatrix} \text{sideslip} & \text{yawrate} \end{bmatrix}^T \quad (6)$$

and all variables are measured in degrees. This system has poles at $s = -0.6579, -1.4195 \pm j32.1542$. The singular values of the above missile (plant) transfer function matrix $P(s) = C_p(sI - A_p)^{-1}B_p$ are shown in Figure 1.

4.2 Nominal Autopilot Design

For purposes of demonstrating the performance enhancement concept, the LQG/LTR design methodology [21] was used to obtain a nominal linear autopilot design. The procedure is now described.

Step1: Form Design Plant. To guarantee zero steady state error to step commands, the plant P was augmented with integrators; one in each control channel. The resulting system is called the *design plant*. It has a state space triple $[A_{des}, B_{des}, C_{des}]$ given by

$$A_{des} = \begin{bmatrix} 0 & 0 \\ B_p & A_p \end{bmatrix} \quad B_{des} = \begin{bmatrix} I \\ 0 \end{bmatrix} \quad C_{des} = \begin{bmatrix} 0 & C_p \end{bmatrix} \quad (7)$$

The design plant singular values have been plotted in Figure 2.

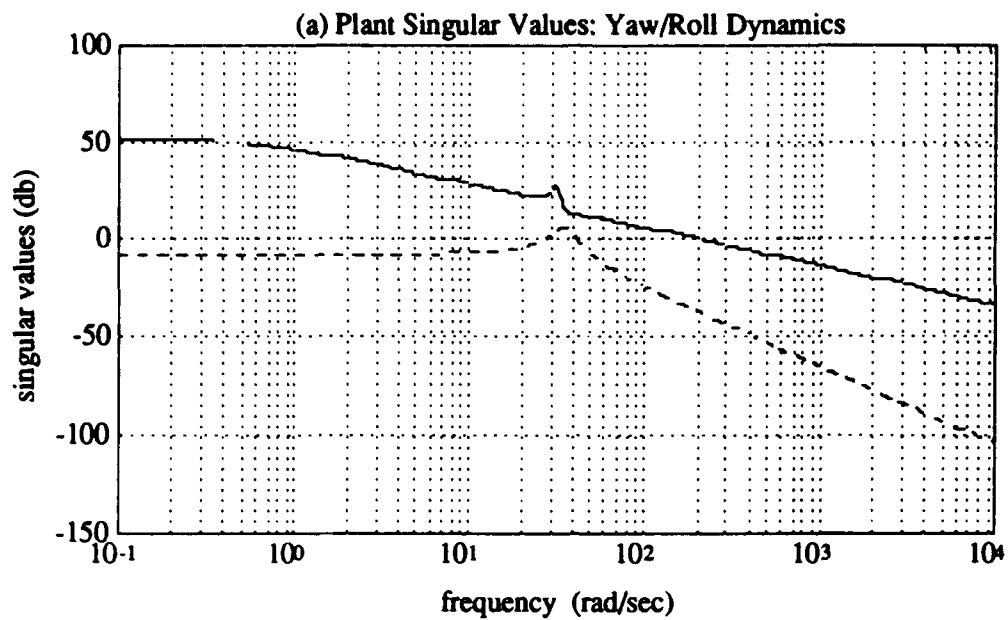


Figure 1: Plant Singular Values

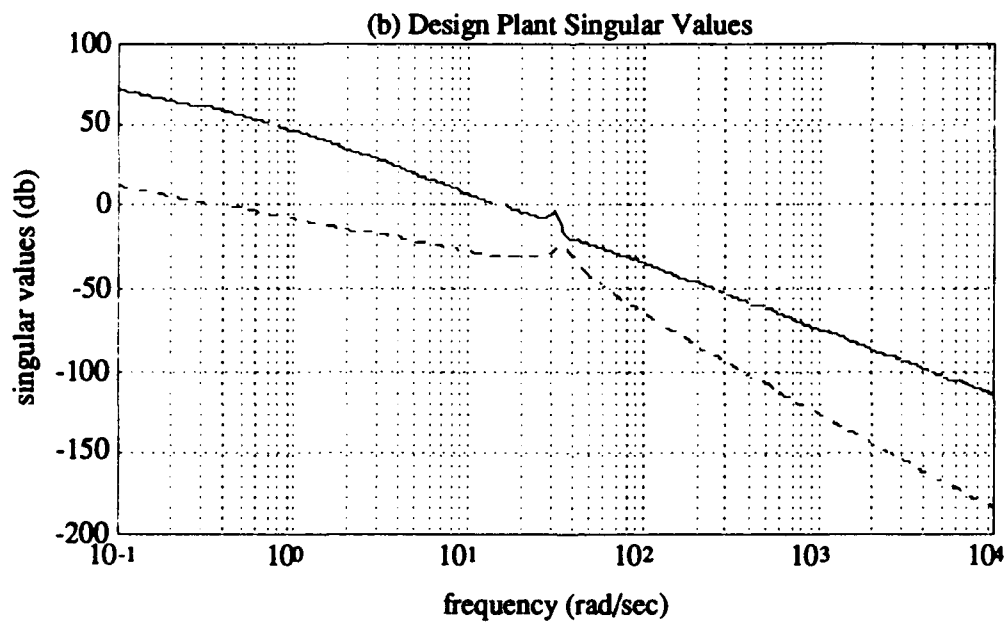


Figure 2: Design Plant Singular Values

Step2: Design Target Loop. The next step in the process is to design the target (desired) open loop transfer function matrix. The target loop was selected to have a state space triple $[A_{des}, H, C_{des}]$ where the filter gain matrix H was selected to be

$$H = 10 [v(:, 4) \quad -v(:, 5)] \begin{bmatrix} -0.0003 & 0.0912 \\ -1.6482 & -1.7159 \end{bmatrix}^{-1} = \begin{bmatrix} -0.1036 & -0.0055 \\ -4.8067 & 0.0009 \\ 2.0003 & 0.0000 \\ 0.0003 & 2.0000 \\ 4.8980 & 5.7272 \end{bmatrix} \quad (8)$$

where $v_4 = [0.0009 \quad 0 \quad -0.0001 \quad -0.3296 \quad -0.9441]^T$ and $v_5 = [0 \quad 0.0440 \quad -0.0182 \quad 0.3432 \quad 0.9381]^T$ are right eigenvectors of A_{des} corresponding to the eigenvalue $\lambda = 0$. This makes the pair (A_{des}, H) uncontrollable because the left eigenvectors of A_{des} associated with the missile modes lie in the left null space of H . By so doing, one obtains the target singular values shown in Figure 3. Here, H has been deliberately selected so that the target loop looks like an "integrator" with gain crossover frequency near 2 rad/sec.

Step 3: Recover Target Loop. The next step in the process is to recover the target loop by solving an appropriately formulated *cheap control* problem. This amounts to solving the Control Algebraic Riccati Equation (CARE)

$$0 = K_c A_{des} + A_{des}^T K_c + C_{des}^T C_{des} - K_c B_{des} \frac{1}{\rho} B_{des}^T K_c \quad (9)$$

for the unique symmetric positive definite solution K_c . This was done with a *recovery parameter* ρ of

$$\rho = 10^{-6} \quad (10)$$

Doing this yields the *control gain matrix*

$$G_\rho = \frac{1}{\rho} B_{des}^T K_c = \begin{bmatrix} 612.4440 & -88.1472 & -410.4327 & -965.3118 & -1.7612 \\ -88.1472 & 164.2489 & -564.4860 & 254.7471 & -7.1359 \end{bmatrix} \quad (11)$$

The final compensator, K (cf. Figure 5), is then given by

$$\dot{x} = Ax + Be \quad (12)$$

$$u = Cx \quad (13)$$

where $e = r - y$ and

$$A = A_{des} - B_{des} G_\rho - H C_{des} \quad (14)$$

$$B = H \quad (15)$$

$$C = G_\rho \quad (16)$$

A balanced realization for $K = [A, B, C]$ is then given by

$$A = \begin{bmatrix} -0.2903 & -107.7837 & 6.6692 & -2.5820 & -0.4031 \\ 107.6795 & -97.8098 & 63.9509 & -4.5172 & -5.3516 \\ -6.7247 & 64.8158 & -54.1931 & -40.7948 & 5.1149 \\ 3.2148 & 2.0979 & 29.5571 & -631.1537 & 429.8894 \\ 0.3648 & -3.3887 & 3.0907 & -460.0290 & -0.7433 \end{bmatrix} \quad (17)$$

$$B = \begin{bmatrix} 2.2840 & 0.4772 \\ -40.7546 & 2.1291 \\ 18.4665 & -0.2215 \\ -2.0715 & -44.6786 \\ -0.9753 & -1.1753 \end{bmatrix} \quad (18)$$

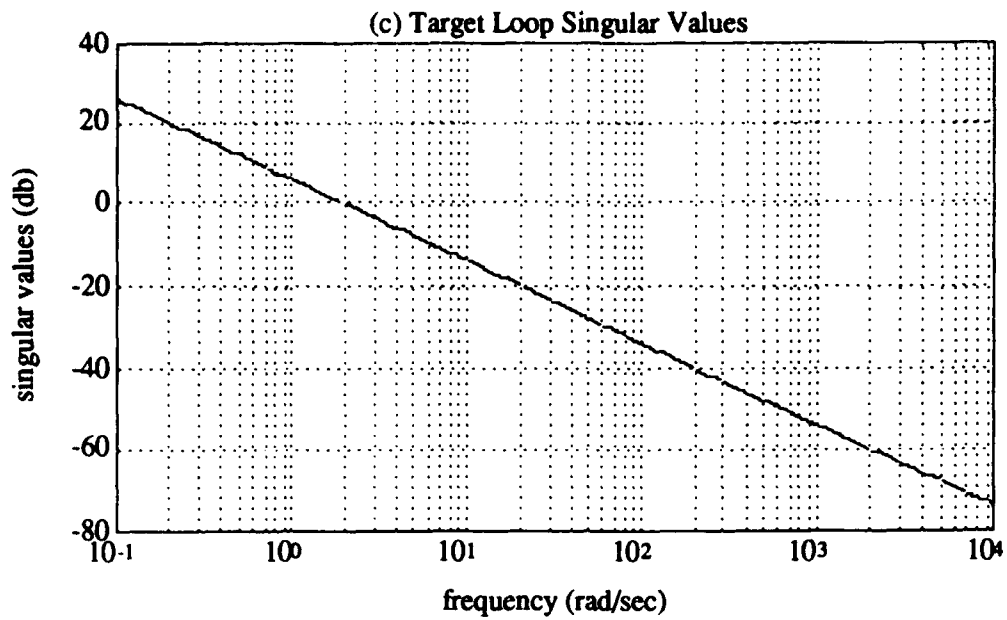


Figure 3: Target Loop Singular Values

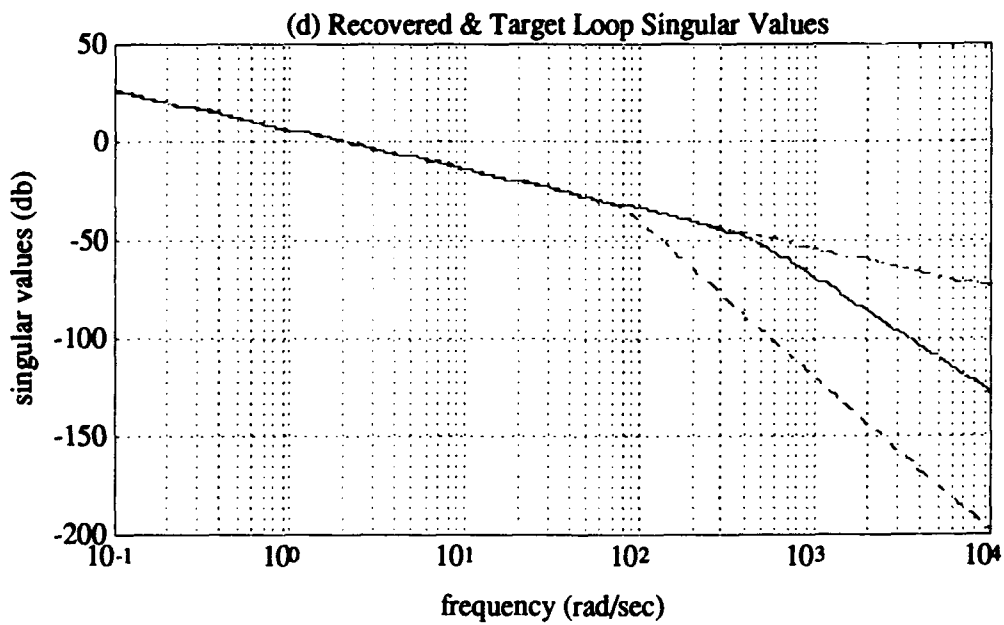


Figure 4: Recovered and Target Loop Singular Values

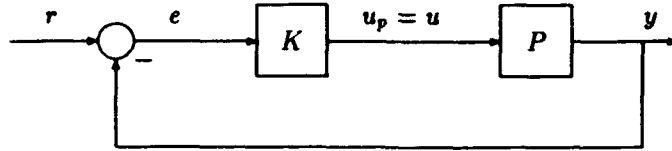


Figure 5: Visualization of Nominal Closed Loop System

$$C = \begin{bmatrix} 0.8562 & 8.5376 & -1.7085 & 43.9089 & 1.1235 \\ 2.1706 & 39.9071 & -18.3886 & -8.5133 & 1.0346 \end{bmatrix} \quad (19)$$

The recovered singular values have been plotted in Figure 4.

In what follows, the discrete-time realization

$$x_{n+1} = \tilde{A}x_n + \tilde{B}e_n \quad (20)$$

$$u_n = \tilde{C}x_n \quad (21)$$

where

$$\tilde{A} = I + T_s A \quad \tilde{B} = T_s B \quad \tilde{C} = C \quad T_s = 0.01 \text{ sec} \quad (22)$$

will also be used for K .

4.3 Method for Accomodating Saturating Actuators

While a Research Associate at Eglin Air Force Base, the principal investigator focussed on the problem of enhancing performance in the presence of multiple saturating actuators [16]-[19]. The methods developed are based on the work of [7] and the more recent work of [5].

Let P denote a linear time invariant (LTI), multiple-input multiple-output (MIMO) plant. Let K denote a LTI MIMO compensator with state space triple $[A, B, C]$. The following assumptions will be made on P and K .

Assumption 4.1 (Assumptions on P and K)

It will be assumed that

- (1) P is stable.
- (2) K has been designed so that the closed loop system in Figure 5 has desirable properties ¹.
- (3) K is neutrally stable².
- (4) The pair (A, C) is observable.

The case where P is unstable will be discussed subsequently. The compensator K may be designed using any linear design methodology (e.g. \mathcal{H}^∞ , \mathcal{H}^2 , \mathcal{L}^1 , LQG/LTR, etc.) [11]. If a complex missile model is available, the methods described in [12]-[15] may prove useful.

¹e.g. robust performance, etc.

²The matrix A may have eigenvalues on the imaginary axis so long as each has an associated eigenvector; i.e. the geometric and algebraic multiplicities coincide. Repeated roots with geometric deficiency are not permitted here. This assumption is not restrictive for missile autopilots.

Now consider the system in Figure 6. In this figure,

$$u_p(t) = \text{sat}(u(t)) \quad (23)$$

$$u(t) = k(t) * [\lambda(x, e)e(t)] \quad (24)$$

where $\text{sat}(\cdot)$ denotes a general operator modelling a saturation in each control channel, $k(t)$ is the impulse response matrix of the compensator K , $*$ denotes convolution, and $\lambda = \lambda(x, e) \in [0, 1]$ is a nonlinear scalar gain which depends on the compensator state $x(t)$ and the error signal $e(t) = y(t) - r(t)$. Without loss of generality, it will be assumed that each control saturates at ± 1 and that each saturation has a transfer characteristic with unity slope [10]. Figure 6 represents a nonlinear system. This is in contrast to Figure 5, where

$$u_p(t) = u(t) \quad (25)$$

and linearity is assured.

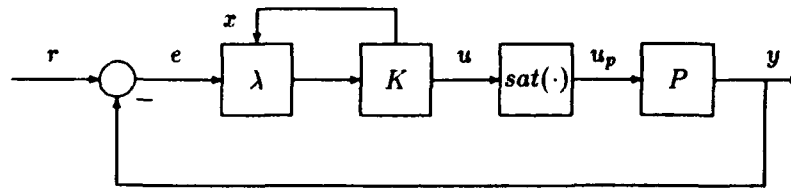


Figure 6: Visualization of Modified Compensator in System with Multiple Saturating Actuators

In [7], a procedure for computing λ is given. The idea behind the procedure is simple. If the system is not saturated, it should be allowed to operate linearly as intended with $\lambda = 1$. If the system is on the "verge of saturation" reduce the gain λ . Since λ is a scalar, such gain reduction preserves the relative coordination of the controls (i.e. the directionality properties of the original design). The procedure requires a state space representation of the compensator and guarantees \mathcal{L}^∞ finite-gain stability [10].

To present the procedure, it is necessary to define a new function.

Definition 4.1 Suppose $A \in \mathcal{R}^{n \times n}$. Given this, define the function $g : \mathcal{R}^n \rightarrow \mathcal{R}_+$ as follows:

$$g(x) \stackrel{\text{def}}{=} \|Ce^{At}x\|_{\mathcal{L}^\infty}$$

■

Notice that this function depends entirely on the homogeneous (unforced) response of the compensator, K . Given this, it is also useful to define the following set:

Definition 4.2

$$B_{AC} \stackrel{\text{def}}{=} \{x \in \mathcal{R}^n : g(x) \leq 1\}$$

■

With this definition, it follows that if the compensator state x lies within or on the boundary of B_{AC} and λ is set to zero, then the control u cannot grow in magnitude above unity.

The following proposition contains many useful properties of the function g and the set B_{AC} .

Proposition 4.1 (Properties of g and B_{AC})

- (1) g is finite-valued.
- (2) g is positive homogeneous.
- (3) g is radially non-decreasing.
- (4) g is subadditive.
- (5) g is convex.

- (6) g defines a cone.
- (7) g is continuous.
- (8) B_{AC} is closed.
- (9) B_{AC} is compact.
- (10) B_{AC} is convex.

A consequence of g being positive homogeneous is that $g(x) = \|x\|g(\frac{x}{\|x\|})$. This implies that g is completely determined from its values on the unit sphere. ■

A continuous-time algorithm for constructing λ can now be given.

Algorithm 4.1 (Construction of λ)

Let x denote the state of the (continuous-time) compensator K at time t . Let e denote the error signal at time t . The following continuous-time algorithm is proposed for constructing λ at each time t .

- (i) If x lies within B_{AC} , then $\lambda = 1$.
- (ii) If x lies on the boundary of B_{AC} , then maximize $\lambda \in [0, 1]$ such that

$$\lim_{\epsilon \rightarrow 0^+} \sup \frac{g(x + \epsilon[Ax + B\lambda e]) - g(x)}{\epsilon} \leq 0 \quad (26)$$

- (iii) If x lies outside B_{AC} , choose $\lambda \in [0, 1]$ such that above expression is minimized.

It should be noted that the expression in equation 26 is essentially the time derivative of g along the trajectories of the modified compensator: ■

$$\dot{x} = Ax + B\lambda(x, e)e \quad (27)$$

$$u = Cx \quad (28)$$

More precisely, since g in general is not differentiable, the limit in equation 26 denotes the *upper right Dini derivative* - a quantity which is well defined for g .

To implement the algorithm, one must be able to determine where the compensator state x lies with respect to the boundary of B_{AC} . To do this, one needs must be able to evaluate g on-line. Issues associated with this will be discussed in the following section. However, given that λ is computed in accordance with Algorithm 4.1, the following theorem follows.

Theorem 4.1 (Guaranteed Closed Loop Properties)

Suppose that λ is constructed in accordance with Algorithm 4.1. Let $x_0 = x(0)$. Given this, each of the following hold.

- (1) If x_0 lies within B_{AC} , then $\|u(t)\|_{\mathcal{L}^\infty} \leq 1$ for all e .
- (2) If x_0 does not lie within B_{AC} , then $\|u(t)\|_{\mathcal{L}^\infty} \leq g(x_0)$ for all e .
- (3) The closed loop system in Figure 6 will be \mathcal{L}^∞ finite-gain stable.

It should be noted that finite-gain stability can be proved because for sufficiently small exogenous signals the system in Figure 6 exhibits linear behavior. ■

4.4 Computational Issues

As pointed out in the previous section, the function g must be evaluated on-line. This issue is complicated by the fact that the definition for g given in definition 4.1 is not suitable for on-line computations. What is needed is a useful characterization, or approximation, for the function g . Also, because Algorithm 4.1 will ultimately be implemented on a digital computer, a discretized version of the algorithm is needed. These points are now addressed.

Suppose that K has a discrete-time realization $[\tilde{A}, \tilde{B}, \tilde{C}]$ as follows:

$$x_{n+1} = \tilde{A}x_n + \tilde{B}e_n \quad (29)$$

$$u_n = \tilde{C}x_n \quad (30)$$

where \tilde{A} is also at least neutrally stable. Given this, g may be approximated as follows.

Proposition 4.2 (Approximation for g .)

Given that \tilde{A} is at least neutrally stable, it follows that g may be approximated as follows:

$$g(x) \approx \tilde{g}(x) \stackrel{\text{def}}{=} \left\| \begin{bmatrix} \tilde{C} \\ \tilde{C}\tilde{A} \\ \tilde{C}\tilde{A}^2 \\ \tilde{C}\tilde{A}^3 \\ \vdots \\ \tilde{C}\tilde{A}^k \end{bmatrix} x \right\|_{\mathcal{L}^\infty}$$

where k is some sufficiently large integer which can be determined off-line.

It should be pointed out that some of the terms in the above approximation may be unnecessary. To identify these terms, the ideas in [5] may prove helpful. Given this, one can implement Algorithm 4.1 as follows.

Algorithm 4.2 (Discrete Performance Enhancement Algorithm)

Let x_n denote the state of the (discrete-time) compensator K at time n . Let e_n denote the error signal at time n . The following discrete-time algorithm is proposed for constructing λ_n at each n .

(i) If $\tilde{g}(x_n) < 1$, then $\lambda_n = 1$.

(ii) If $\tilde{g}(x_n) \approx 1$, then maximize $\lambda_n \in [0, 1]$ such that

$$\tilde{g}(\tilde{A}x_n + \tilde{B}\lambda_n e_n) - \tilde{g}(x_n) \leq 0 \quad (31)$$

(iii) If $\tilde{g}(x_n) > 1$, choose $\lambda_n \in [0, 1]$ such that above expression is minimized.

It should be noted that this algorithm requires that an on-line optimization be performed at each time-step. Consequently, efficient optimization routines must be sought.

Because λ controls the "amount" of error entering the compensator, it is referred to as an *error governor*. A simple example is now given to illustrate the ideas presented thus far.

Example 4.1 (A Simple Example)

Figure 7 shows how the above *error governor* method works for

$$P = \frac{1}{s+1}$$

$$K = 1/s$$

$r = 10$, and saturation limits of ± 9 . The linear response is very good, the saturated response causes the integrator to wind-up, and the effect of λ is to prevent this.

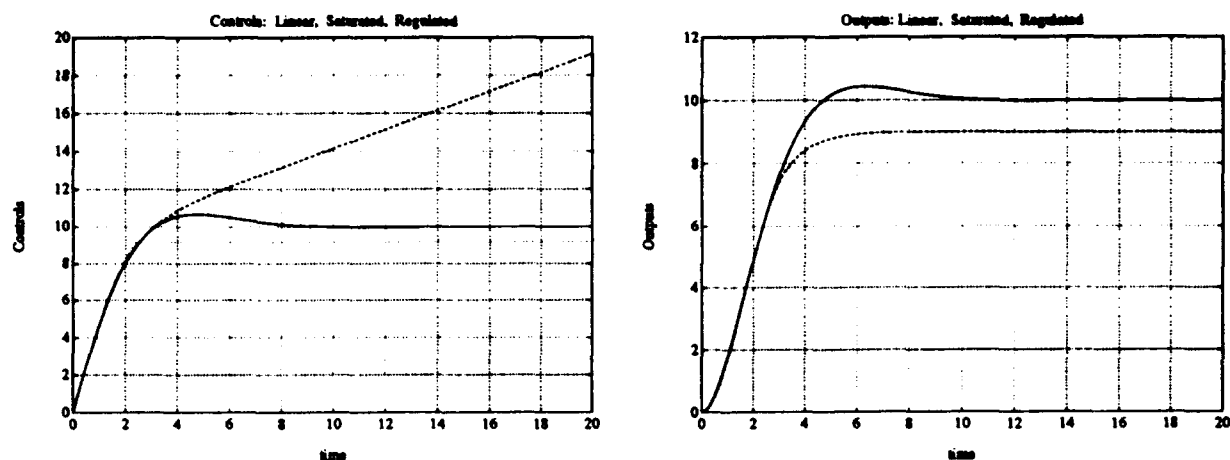


Figure 7: A Simple Example: $P = \frac{1}{s+1}$, $K = 1/s$ with $r = 10$ and $\text{satlev} = 9$

4.5 Application of Method to EMRAAT BTT Missile

The performance enhancement scheme discussed above was applied to the EMRAAT model and LQG/LTR compensator discussed earlier. A constant reference command of $r = [4.2 \ -4.2]^T$ was selected. Figure 8 contains the linear responses and the responses which occur when saturations are inserted in each control channel. The saturation limits used were ± 8 .

As expected, the linear responses are very good. The transient is well behaved and the steady state tracking error is zero. The latter follows from the *Internal Model Principle* and the fact that the compensator has an integrator in each control channel. When the saturations are introduced, however, the integrators in the compensator wind-up. This is seen in the observed aileron response generated by the compensator. The rudder response follows the linear response closely. The sideslip response is not able to achieve the commanded steady state sideslip but it also remains close. More dramatic is the observed yaw rate response which is unable to even come close to the commanded yaw rate. It is apparent that the saturations, particularly the one in the aileron control channel, destroys the directionality properties of the original LQG/LTR-based autopilot K .

To maintain the original autopilot directionality properties and prevent wind-up, the performance enhancement scheme described in the previous section was used. The resulting regulated responses are given in Figure 9. The unregulated responses are repeated in the figure for comparison sake. It is seen that the scheme maintains the directionality properties of the original autopilot to the extent possible. It permits the system to operate on the edge of saturation and completely eliminates the wind-up effects. The resulting aileron control produced by the modified compensator, for example, reaches the -8 rail and remains there.

4.6 Unstable Operating Points and Other Hard Nonlinearities

Thus far, the focus has been on missile dynamics that are locally stable. The scheme presented, however, cannot directly be used when the missile dynamics are locally unstable. Fundamentally, this is because an unstable plant has a finite downward gain margin. To address unstable operating points, the ideas in [7] were considered. In [7], the author introduces a *reference governor* which limits the rate of growth of the reference command so that saturation is avoided. It processes the reference command, the compensator state, and the plant state. Access to all of the plant states, however, is not a practical assumption. Consequently, while at Eglin Air Force Base, the principal investigator worked on the problem of designing an estimator which could generate appropriate estimates of the plant states to be used by the *reference governor*. The ideas in [3] and [4] were very helpful because they provide insight into the design of a suitable estimator. This work is still in progress [19].

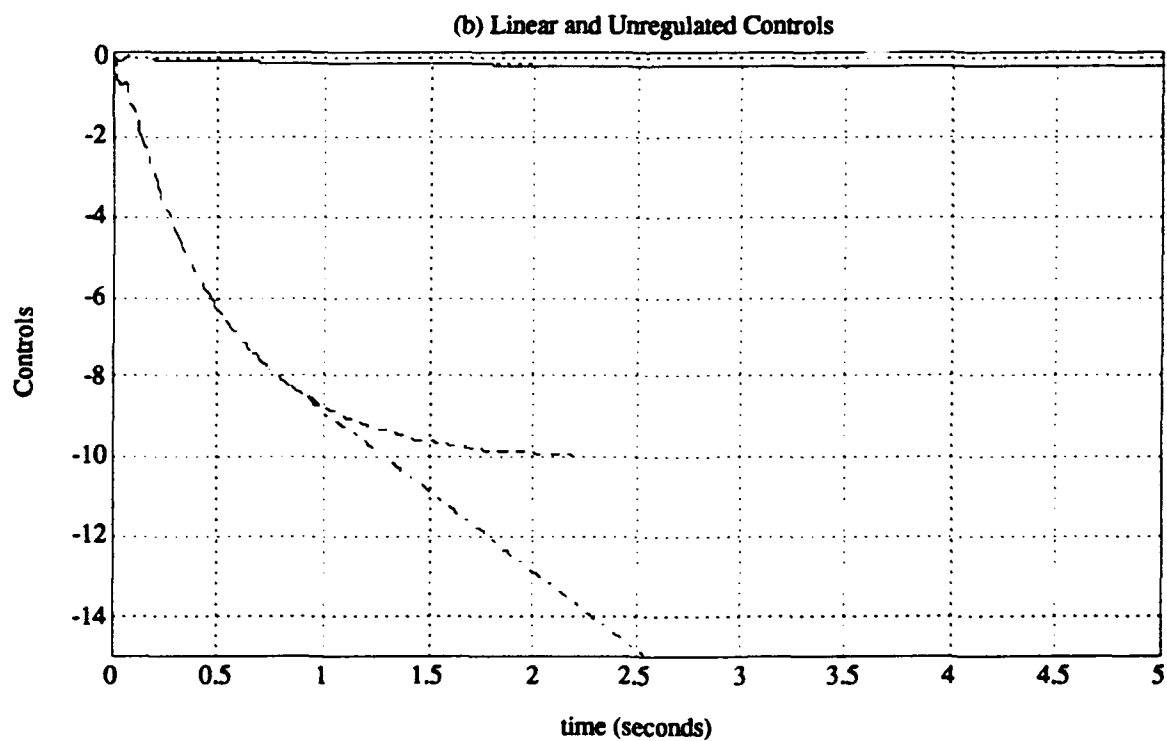
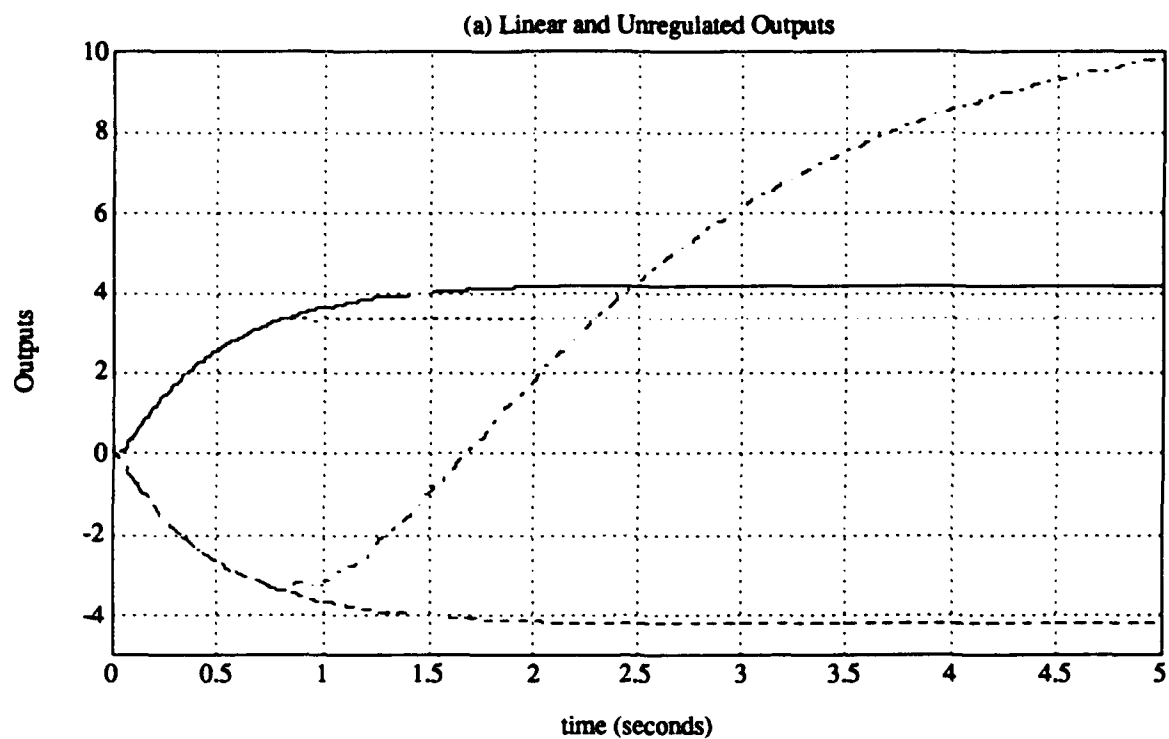


Figure 8: Linear and Unregulated Responses

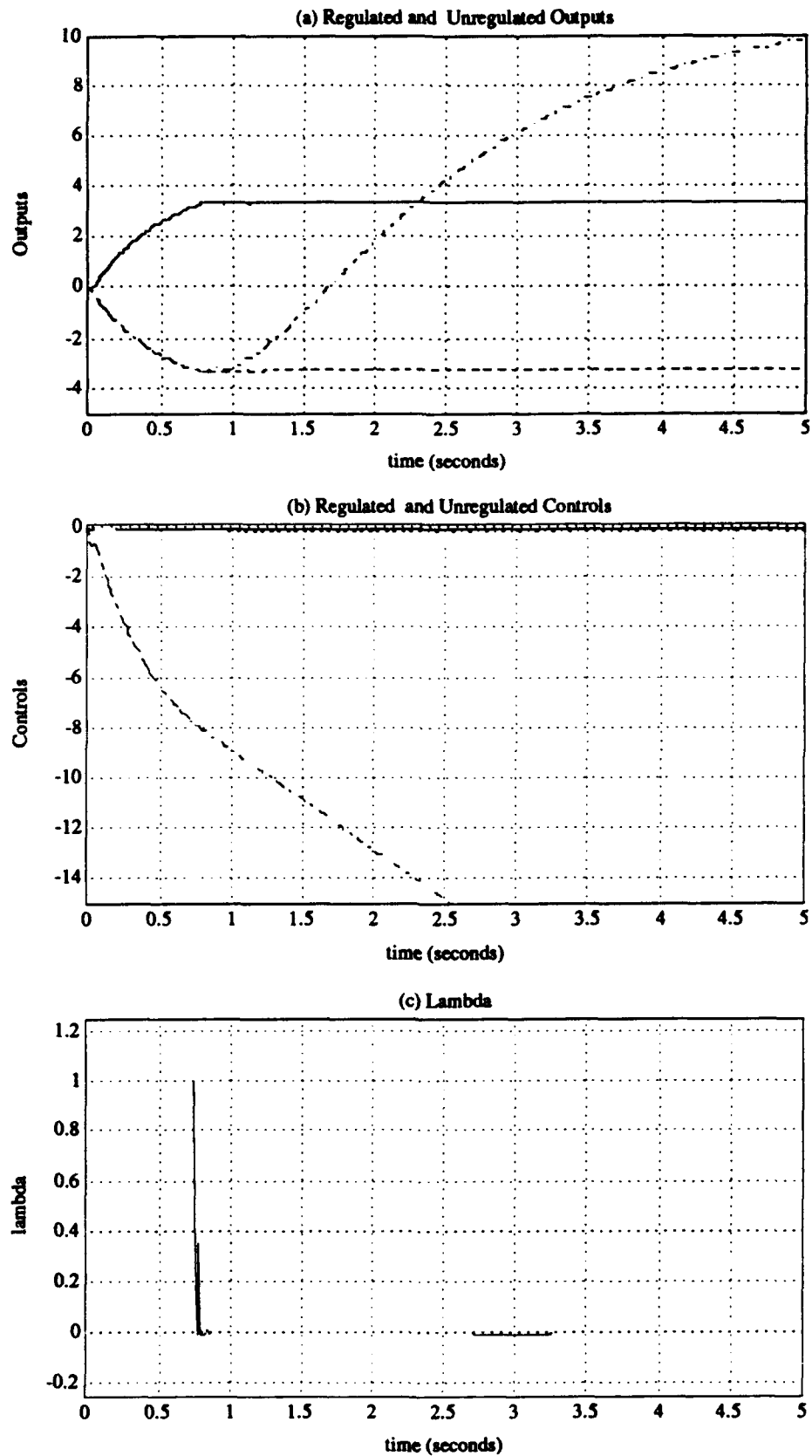


Figure 9: Regulated and Unregulated Responses

Other hard nonlinearities, such as rate limiters and α limiters, can be addressed using the methods discussed thus far.

4.7 More General Nominal Compensation Schemes

The focus, thus far, has been on linear systems and, in particular, on nominal autopilots which are linear. It is clear, however, that nonlinear autopilots can be addressed using analogous ideas. The concept of a g function, for example, can be extended to the nonlinear case. Let's see how this extension might be done.

Suppose that K is a nonlinear \mathcal{L}^∞ finite-gain stable compensator with the following discrete-time representation:

$$x_{n+1} = f(x_n, e_n) \quad (32)$$

$$u_n = h(x_n) \quad (33)$$

Now one can define the zero input map as follows.

Definition 4.3 (Nonlinear Zero Input Map)

Define the map from initial conditions $x_0 = x_{n_0}$ to u_n as follows

$$u_n = \Phi(x_{n_0}, n)$$

Given this, it becomes apparent how to define the nonlinear version g_{NL} of g .

Definition 4.4 (Nonlinear Version of g)

Suppose $x_n \in \mathcal{R}^n$. Given this, define the function $g_{NL} : \mathcal{R}^n \rightarrow \mathcal{R}_+$ as follows:

$$g_{NL}(x) \stackrel{\text{def}}{=} \|\Phi(x, n)\|_{\mathcal{L}^\infty}$$

It is clear now, how to proceed with a nonlinear extension. Note, however, that g_{NL} , unlike g , is not necessarily positive homogeneous. This implies that, in general, g_{NL} is not uniquely determined from its values on the unit sphere. These ideas are currently under development. Extending the ideas to gain-scheduled autopilots where the scheduling variable is well behaved should also be achievable.

5 Significance of Work

The methods which have been developed in this research will systematize the design of full envelope controllers for *missile systems with multiple hard nonlinearities*. Systematizing the design process should significantly reduce design time and lower system development costs. Preliminary results show clearly that the methods will increase system performance by permitting operation over the full envelope and in some cases extending this envelope. Finally, the methods developed will provide useful information to guide designers during the initial stages of system development, design, and conceptualization. Given this, the contributions of this research to missile control, and more globally to aerospace system development, should be significant.

6 Additional Collaborative Work

While at Eglin Air Force Base, the principal investigator initiated three collaborations.

6.1 Computation of Structured Singular Value Using Genetic Algorithms

The first collaboration took place with Professor Kamen Zhou of Louisiana State University and Mr. Richard Hull of the University of Central Florida. This collaboration was initiated because of the need for effective algorithms for computing the structured singular value - a constrained spectral radius problem. This problem is important for determining the stability robustness, and more importantly, the performance robustness of a missile autopilot with respect to structured uncertainty. This collaboration will result in the submittal of a paper to the AIAA Guidance and Control Conference to be held in Phoenix, Arizona in August of 1994.

6.2 Performance Enhancement for Guidance Systems

The second collaboration took place with Professor Balakrishnan of the University of Missouri-Rolla. This collaboration was initiated because of the need for systematic procedures for designing integrated guidance and control systems for missiles. Traditionally the guidance and control system have been designed separately. Our intention is to demonstrate how the performance enhancement methods discussed earlier can be used to improve missile guidance. Our efforts have resulted in the submittal of a proposal for an invited session at the American Control Conference to be held in Baltimore, Maryland in June of 1994. A summary of the proposal has been included in the Appendix. Our efforts will also result in a submittal to the AIAA Guidance and Control Conference to be held in Phoenix, Arizona in August of 1994. The submittal will be a key component in a session which Professor Balakrishnan and myself are organizing [?].

6.3 Extension to Gain-Scheduled Controllers

The third collaboration took place with Professor Jeff Shamma of the University of Texas-Austin. This collaboration took place because of Professor Shamma's expertise in gain-scheduling and my interest in extending the methods presented above to general gain-scheduled controllers.

7 Summary & Directions for Future Research

During the course of this research, methods have been developed to facilitate the design of full envelope autopilots for missiles with multiple hard nonlinearities. The focus, thus far, has been on maintaining performance near a stable operating point in the presence of saturating actuators. The methods presented maintain to the extent possible the directionality properties of the original autopilot. They also eliminate wind-up effects and come with stability guarantees.

Future directions for research include applying the methods developed to a full six (6) degree-of-freedom model for EMRAAT [1] including the guidance and target dynamics. The ideas developed will be used to address unstable operating points and other hard nonlinearities such as rate limiters and α -limiters. The ideas also need to be completely extended to the nonlinear autopilot case and to the case where the autopilot is gain-scheduled [8]-[9]. This will require the development of efficient methods for computing and analytically modelling the nonlinear version of g .

8 Bibliography

References

- [1] I.A. Hirsch, M.A. Langehough, J.A. Bossi, et al. , "Advanced Robust Autopilot," Air Force Armament Laboratory, Eglin AFB, Florida, AFATL-TR-89-64, November 1989.
- [2] J.H. Blakelock, *Automatic Control of Aircraft and Missiles*, 2nd Edition, John Wiley & Sons, Inc., 1991.
- [3] B.A. Francis and K. Glover, "Bounded Peaking in the Optimal Linear Regulator with Cheap Control," *IEEE Transactions on Automatic Control*, Vol. AC-23, No. 4, August 1978, pp. 608-617.
- [4] H.J. Sussman and P.V. Kokotovic, "The Peaking Phenomenon and the Global Stabilization of Nonlinear Systems," *IEEE Transactions on Automatic Control*, Vol. AC-36, No. 4, August 1991, pp. 424-440.
- [5] E.G. Gilbert, and K.T. Tan, "Linear Systems with State and Control Constraints: The Theory and Application of Maximal Output Admissible Sets," *IEEE Trans Automatic Control*, Vol AC-36, No. 9, September 1991, pp. 1008-1020.
- [6] K.T. Tan and E.G. Gilbert, "Constraint Governors and Reference Constraint Governors for Linear Discrete-time Systems with State and Control Constraints," submitted for publication in *IEEE Trans Automatic Control*, received October 1992.
- [7] P. Kapasouris, "Design for Performance Enhancement in Feedback Control Systems with Multiple Saturating Nonlinearities," LIDS MIT, PhD Thesis, LIDS-TH-1757, March 1988.

- [8] J.S. Shamma, "Analysis and Design of Gain Scheduled Control Systems," LIDS MIT, LIDS-TH-1770, PhD, May 1988.
- [9] J.S. Shamma and J.R. Cloutier, "A Linear Parameter Varying Approach to Gain Scheduled Missile Autopilot Design," *Proceedings of the 1992 American Control Conference*, Chicago, IL, June, 1992.
- [10] C.A. Desoer and M. Vidyasagar, *Feedback Systems: Input-Output Properties*, Academic Press, Inc, NY, 1975.
- [11] J. C. Doyle, K. Glover, P.P. Khargonekar and B.A. Francis, "State-Space Solutions to Standard \mathcal{H}^2 and \mathcal{H}^∞ Control Problems," *IEEE Trans AC*, Vol 34, No 8, August 1989.
- [12] A.A. Rodriguez and M.A. Dahleh, " \mathcal{H}^∞ Control of Stable Infinite-Dimensional Systems using Finite-Dimensional Techniques," submitted for publication in *IEEE Transactions on Automatic Control*, July, 1993.
- [13] A.A. Rodriguez and M.A. Dahleh, "Weighted \mathcal{H}^∞ Optimization for Stable Infinite-Dimensional Systems using Finite-Dimensional Techniques," *Proceedings of the 29th IEEE Conference on Decision and Control*, Honolulu, Hawaii, December 1990.
- [14] A.A. Rodriguez, "Design of \mathcal{H}^∞ Optimal Finite-Dimensional Controllers for Unstable Infinite-Dimensional Systems," submitted for publication to *AUTOMATICA*, August, 1993.
- [15] A.A. Rodriguez and M.A. Dahleh, "On the Computation of Induced Norms for Non-Compact Hankel Operators Arising From for Distributed Control Problems," *Systems & Control Letters*, December, 1992.
- [16] A.A. Rodriguez and J.R. Cloutier, "Control of a Bank-to-Turn-Missile with Saturating Actuators", submitted for publication in the *Proceedings of the 1994 American Control Conference*, Baltimore, MD.
- [17] A.A. Rodriguez and S.N. Balakrishnan, "Performance Enhancement for Missile Guidance and Control Systems", proposal submitted for invited session to *1994 American Control Conference*, Baltimore, MD.
- [18] S.N. Balakrishnan and A.A. Rodriguez, "Performance Enhancement for Integrated Missile Guidance and Control Systems", *Invited Session, 1994 AIAA Guidance and Control Conference*, Phoenix, AZ.
- [19] A.A. Rodriguez and J.R. Cloutier, "Control of an Unstable Missile with Saturating Actuators", in preparation, to be submitted to *1994 AIAA Guidance and Control Conference*, Phoenix, AZ.
- [20] M.G. Safanov, and M. Athans, "A Multiloop Generalization on the Circle Stability Criterion for Stability," *IEEE Transactions on Automatic Control*, Vol. AC-26, No. 2, April 1981, pp. 415-422.
- [21] G. Stein and M. Athans, "The LQG/LTR Procedure for Multivariable Feedback Control Design," *IEEE Transactions on Automatic Control*, Vol. AC-32, No. 2, February 1987, pp. 105-114.

9 Appendix: Proposal for Invited Session to 1994 ACC

A.A. Rodriguez	S.N. Balakrishnan
Arizona State University	University of Missouri-Rolla
Tempe, AZ 85287-7606	Rolla, MO 65401

Overview of Proposed Session

Because of the great uncertainty which an evasive target presents, the inherent nonlinear and typically unstable non-minimum phase dynamics associated with missiles, the integrated guidance and control of missile systems still represents one of the richest and most challenging control problems to the systems community. During the past decade many advances have been made in the area of robust and nonlinear control. This includes results which facilitate the design of autopilots, provide insight into gain-scheduling, and allow engineers to better address nonlinear design issues. This session is an effort to bring researchers addressing various aspects of missile guidance and control together to present new results on enhancing the performance of integrated missile guidance and control systems. The session is intended to shed light on some of the issues which researchers in the missile guidance and control community are now addressing.

Motivation and Summary

The title of the proposed session is

Performance Enhancement for Missile Guidance and Control Systems.

To properly address this subject, it is important that all aspects associated with missile guidance and control are addressed. The organizers felt, for example, that it was necessary for the session to contain methods for systematizing, optimizing, and enhancing the performance of today's autopilots and guidance systems. This includes the issue of designing the autopilot to accommodate multiple hard nonlinearities such as saturating actuators, rate limiters, etc. By so doing, autopilot performance would be enhanced and a much more flexible guidance loop could be tolerated. Such a discussion must, however, involve a discussion of various autopilot design methodologies. For this reason, papers will be presented on autopilot design using eigenstructure assignment, \mathcal{H}^∞ -based methods, and the latest optimization techniques. The organizers also felt that it was important for the session to contain new methods for improved guidance and target state tracking. This, it was felt could properly be addressed by researchers working on "approximately" analytical guidance laws and nonlinear target state estimation algorithms which exploit the structure of the engagement and the estimator coordinate system.

To accommodate the above requirements, the organizers solicited papers from researchers in academia, industry, and the military. Six (6) papers were selected to address the following topics:

1. Performance Enhancement for a Missile with Multiple Hard Nonlinearities.

A.A. Rodriguez, Arizona State University; Session Organizer.

James R. Cloutier, Armament Directorate, Eglin Air Force Base.

title: Control of a Bank-to-Turn (BTT) Missile with Saturating Actuators

2. Improved Guidance Laws for Missiles: An Analytic Approach.

S.N. Balakrishnan, University of Missouri-Rolla; Session Co-organizer.

title: Improved Guidance Laws for Missiles: An Analytic Approach

3. Autopilot Design using \mathcal{H}^∞ Design Methods.

Kevin A. Wise, McDonnell Douglas Missile Systems Co.

Eric S. Hamby, McDonnell Douglas Missile Systems Co.

title: \mathcal{H}^∞ Missile Autopilot Design With and Without Imaginary Axis Zeros

4. Methods for Improved Target State Estimation.

Chris D'Souza, Armament Directorate, Eglin Air Force Base.

James R. Cloutier, Armament Directorate, Eglin Air Force Base.

title: Spherical-based Target State Estimation

5. Autopilot Optimization using Genetic Algorithms.

Richard Hull, University of Central Florida.

Roger W. Johnson, University of Central Florida.

title: Performance Enhancement of a Missile Autopilot via Genetic Algorithm Optimization Techniques

6. Missile Eigenstructure Assignment via Dynamic Compensation.

Robert Wilson, Armament Directorate, Eglin Air Force Base.

James R. Cloutier, Armament Directorate, Eglin Air Force Base.

title: Eigenstructure Assignment via Dynamic Compensation

A STUDY OF RAW DATA FUSION USING ARTIFICIAL NEURAL NETWORKS

**Thaddeus A. Roppel
Associate Professor
Department of Electrical Engineering**

**Auburn University
Auburn, AL 36849**

**Final Report for:
Summer Faculty Research Program
Wright Laboratory**

**Sponsored by:
Air Force Office of Scientific Research
Bolling Air Force Base, Washington, D.C.**

September 1993

A STUDY OF RAW DATA FUSION USING ARTIFICIAL NEURAL NETWORKS

Thaddeus A. Roppel
Associate Professor
Department of Electrical Engineering
Auburn University

Abstract

A study of raw data fusion using neural networks was begun in Summer 1992. This is a continuation and extension of that work. It is determined that target identification (classification) can be performed by a neural network. For the particular data set that is used in these studies (the AADMS data set), identification based on IR data alone is quite good. The neural network performance degrades when MMW and IR data are used (fusion). It has been found necessary to segment out the target-related MMW data from the rest of the data file as is done with the IR data, but it is not clear that this can be done given the format of the AADMS data. Therefore, other data sets, including data from low-observable subsonic aircraft tower tests (LOSA) and some laser radar (LADAR) data have been processed for possible future use.

Details of the computer software and the data file formats are provided. This software and data had to be transported on various media from their original sources, so the re-installation process was quite time - consuming, and will be a continuing process for some time to come.

A comparison of neural network performance with classical approaches is made. Neural network operating principles include many terms that we usually ascribe to human behavior, including learning, instinct, intuition, judgement, and confidence level. Like human performance, the accuracy of neural net performance is dependent upon training. With sufficient training, highly accurate responses are obtained at high speed.

Several ideas for commercialization and technology transfer utilizing neural network -based raw data fusion are proposed, including robotics, engine diagnostics, underwater detection, chemical analysis, voice processing, and automatic facial recognition.

A STUDY OF RAW DATA FUSION USING ARTIFICIAL NEURAL NETWORKS

Thaddeus A. Roppel

1.0 Introduction

This report describes work performed from 21 June 1993 to 10 September 1993 under the Summer Faculty Research Program (SFRP) at Wright Laboratory. The laboratory focal point was Mr. Ellis Boudreaux in WL/MNG-X. This is a continuation of work begun under the 1992 SFRP and continued in the interim under the 1993 Summer Research Extension Program (SREP).

Previous work using the Westinghouse / AADMS data set demonstrated the capability to use a neural network to perform sensor fusion for enhancing ground target identification. More specifically, medium-wave infrared (MWIR) and millimeter-wave radar (MMW) data representing target scenes from AADMS were used to distinguish between T-62 tanks, LANCE missile launchers, and M-113 armored personnel carriers (APC's). The results from Summer 1992 are published in the 1992 SFRP Final Report. In summary, it was found that while IR data alone was sufficient to correctly distinguish between the tank and launcher target images, a 14% improvement in confidence was obtained by fusing the IR with the MMW data.

Further experiments on the AADMS data set subsequent to the 1992 summer program included using the leave-one-out testing method to more realistically measure performance (described later in this report), and adding the M-113 APC scenes to the testing matrix.

The new goals for the summer 1993 program were to investigate the inclusion of background non-target scenes in the testing matrix, and to prepare some new data sets for analysis. The new data sets include the Low-Observable Subsonic Aircraft (LOSA) data provided by IITRI-Huntsville, and some laser radar (LADAR) data from the ATLAS program. Also under discussion is the possibility of obtaining medium- and long-wave IR data from the AADIOS program from Integrated Sensors, Inc. (ISI). However, the AADIOS data has not been obtained as this report is written.

Section 2 of this report describes the experimental methods used in the investigations. Section 3 is a presentation of the results. Section 4 is a discussion of the results, and Section 5 describes plans for continuing work.

2.0 Experimental Methods

This section describes the basic neural network experimental approach, the leave-one-out testing method, the approach to extracting background frames for testing, and the details of pre-processing the new LOSA and LADAR data.

2.1 Neural Network Experimental Approach

The neural networks used in these experiments are simulated using the ASPIRIN package distributed as freeware and supported by MITRE. In order to conduct an experiment, it is necessary to design the neural network architecture, format the input training data for presentation to the network, initiate the neural network training, present the network with testing data, and perform analysis of the results. As an example, the AADMS data fusion experiments use a three-layer neural network with 228 inputs, 100 for IR pixels and 128 for MMW pixels. Each input is an 8-bit byte representing intensity in the original pixel data file, but this is scaled to a floating point value in the range from 0.05 to 0.95 for presentation to the network inputs. The network has 2 outputs, which also range from 0.05 to 0.95, representing the confidence in the statements "the input represents a tank," or "the input represents a missile launcher."

The hidden layer consists of 20 nodes with sigmoidal activation functions.

The neural network is trained on 9 of the 14 available target scenes. The remaining 5 scenes are reserved for testing the network. During training, the nine training scenes are presented repeatedly to the network while the back-propagation of errors method is applied to adjust the internode weights. When the output error measures are sufficiently low, training stops, and the network is considered to have learned the training data. In order to determine whether the network has actually learned the difference between a tank and a launcher (rather than just having learned about the specific tanks and launchers in the training set), we present the network with the five testing scenes held in reserve, and measure the output error. If the network correctly identifies these, then we say that the network has performed a generalization of the training data.

The design of the neural network architecture is tightly coupled to the required number of inputs and outputs. The training time and memory requirements increase with the number of connections between nodes. An experiment with a few hundred inputs is tractable with desktop computing power, but processing a 128 x 128 byte IR image combined with a large MMW image is not realistic for anything except a supercomputer. Therefore, it is necessary to reduce the amount of data presented to the network. Two techniques are combined to achieve this data reduction. First, the image is segmented so that only the pixels in the neighborhood of the target are used. Second, the pixel count is reduced by a neighborhood averaging process resulting in a 4-to-1 reduction in each dimension for an overall 16-to-1

reduction. For the AADMS data, this resulted in a 10 x 10 pixel box surrounding each target. Although the segmentation is presently being done manually, one future goal is to automate the target detection and segmentation using a neural network.

Analysis of the results of training is performed by presenting the network with the testing data and measuring output error relative to the ideal desired outputs. Several quantitative techniques are available, although the most commonly employed is to use the rms error computed over all of the outputs nodes and all of the testing inputs. This provides a single number which can be used to quantify the neural net performance. More detailed analyses, such as canonical discriminate analysis (CDA) and principal component analysis (PCA), can be used to identify specific input images that result in poor training performance and to optimize the network architecture by correlating specific hidden layer nodes with detection of unique features.

2.2 Leave-One-Out Training

The training method used on the AADMS data provided results for a single arrangement of the available target scenes into the two categories "testing" and "training." More generally, we would like to perform experiments using all possible arrangements of the available data into these categories. While this approach would be thorough and exhaustive, in practice, a sufficient amount of information for most purposes can be obtained by conducting a subset of these experiments. Namely, in leave-one-out training, all of the target scenes except one are used for training. The left-out scene is used for testing. This is repeated until each target has been left out once. By accumulating the resulting statistics, one obtains a very good picture of the overall performance of the network, as well as the effects that can be traced to specific data files. For example, it often happens that certain inputs are "outliers," that is, they do not represent the data space very well, perhaps due to excessive noise or obscuration. It is useful to identify these outliers through leave-one-out experiments.

Leave-one-out experiments were performed on the AADMS data. One tank and one launcher image were simultaneously left out for each experiment. There were 10 tank scenes and 4 launcher scenes in the data set, so the number of experiments was 10 x 4. For each of the 40 experiments, there were three possible outcomes:

- (1) The target was correctly identified.
- (2) The target was incorrectly identified.
- (3) The target was not identified, i.e., the neural network output was undecided, or not above threshold for either output.

By making a histogram of the number of times cases (1) - (3) occur during a set of 40 experiments, it is possible to assign a performance measure to the neural network. These results are presented in Section 3. In addition, similar experiments were run combining tanks and APC's, APC's and launchers, and finally all three vehicles. There were 8 APC target scenes available.

2.3 Background Scenes

All of the scenes processed to date consist of 10 x 10 pixel boxes approximately centered on targets. It is desirable to generate background scenes that do not include targets. This provides an approach to training the neural network to perform target detection by learning to distinguish between targets and non-targets. The success of this approach depends upon the ability to span the entire space of non-target scenes with a relatively few number of background training scenes. Background scenes are carefully chosen to include trees, ground, sky, buildings, and overlap regions.

2.4 Additional Data Sets

In addition to the AADMS data, the LOSA and LADAR data sets have been partially prepared for neural network training. The LOSA data is MWIR and MMW data taken using essentially the same instrumentation as was used to gather the AADMS data. The LADAR data was gathered using instrumentation implemented under the ATLAS program at the Wright Laboratory.

2.4.1 LOSA Data

The LOSA (Low-Observable Subsonic Aircraft) data set consists of tower data taken in late 1990 to early 1991 by IITRI-Huntsville at the Army Missile Command in Huntsville, Alabama. This data set and some of the ground processing software was provided by IITRI on several media. The raw data file was provided on a 90MB Bernoulli disk, the GPS was provided on 3-1/2" PC formatted diskettes, and the Mavenck video was provided on standard VHS videotape. In addition, a data catalog was provided on paper. The GPS was written in FORTRAN and Assembly Language on a VAX/VMS computer. Since IITRI had archived all the files, it was necessary for them to de-archive and extract the pertinent files before mailing them on their respective media. In this process, some of the files were contaminated and/or transferred incompletely, requiring some reconstructive work on both the data files and the program files. In addition, the GPS program files were not written to be transportable, so a number of machine-dependent modifications had to be made to the source code. The following subsections describe the LOSA data and program

files, the modifications, and the current state of usability.

2.4.1.1 Raw LOSA Data File, "RUN06.DMS"

The raw LOSA data is stored in a 28.9 MB binary file with file name RUN06.DMS. This is the data from Run 6 of Flight 6, as referenced in the data catalog entitled "DUAL MODE (MMW/IR) DATA COLLECTION ON A LOW OBSERVABLE SUBSONIC AIRCRAFT. DATA CATALOG. VOLUME I." This represents approximately three minutes of data collected against a small airplane flying toward the tower, circling around, and flying outbound. During some of the time, the dual mode seeker is locked onto the target in tracking mode. Data frames are collected at roughly 20 ms intervals and stored according to the format provided in the data catalog. The first few lines of the data file are shown in Figure 1 for illustration.

When the file was delivered from IITRI and copied to the IPL VAX at Eglin, it was found to have a two-byte CR /LF sequence inserted after every 512 byte block of the data. This was removed by using a C program entitled "s2.c" to rewrite the restored data file. This program is shown in Figure 2. The exact length of the data file is 29,941,824 bytes, or 56,527 blocks of 512 bytes each. This file is processed by the GPS package to yield radar and IR map images which are time-tagged to the Maverick video. The user can choose a time of interest by viewing the videotape, and then running the GPS software. The two major components of the GPS package are the data reduction subpackage and the map processing subpackage.

2.4.1.2 LOSA Data Reduction Software Subpackage

This subpackage consists of the following programs:

```
REDUCE_S.FOR  
FATDEF.MAR  
GETFID.MAR  
HEADER3.FOR
```

The purpose of this set of programs is to unpack the flight data and speed up the map generation processing. The call to HEADER3 in REDUCE_S has been commented out. It seems that including this call would cause the data reduction process to stop at each slot and ask the user to make corrections to the slot header. The files FATDEF and GETFID are assembly language code which perform low-level file access. A typical compile / link /execute sequence under VMS with HEADER3 commented out follows.

```
%> FORTRAN REDUCE_S  
%> MACRO FATDEF.GETFID  
%> LINK REDUCE_S.FATDEF.GETFID
```

```
cheetah@ropel13: od -v run06.dms1more
```

```
[OCTAL  
BYTE #]
```

```
0000000 0000 0000 1a00 0b00 5a00 0000 0000 0000
0000020 0000 0000 0000 0000 0000 0000 0000 0000
0000040 0000 0000 0000 0000 0000 0000 0000 0000
0000060 0000 0000 0000 0000 0000 0000 0000 0000
0000100 0000 0000 0000 0000 0000 0000 0000 0000
0000120 0000 0000 0000 0000 0000 0000 0000 0000
0000140 0000 0000 0000 0000 0000 0000 0000 0000
0000160 0000 0000 0000 0000 0000 0000 0000 0000
0000200 0000 0000 0000 0000 0000 0000 0000 0000
0000220 0000 0000 0000 0000 0000 0000 0000 0000
0000240 0000 0000 0000 0000 0000 0000 0000 0000
0000260 0000 0000 0000 0000 0000 0000 0000 0000
0000300 0000 0000 0000 0000 0000 0000 0000 0000
0000320 0000 0000 0000 0000 0000 0000 0000 0000
0000340 0000 0000 0000 0000 0000 0000 0000 0000
0000360 0000 0000 0000 0000 0000 0000 0000 0000
0000400 0000 0000 0000 0000 0000 0000 0000 0000
0000420 0000 0000 0000 0000 0000 0000 0000 0000
0000440 0000 0000 0000 0000 0000 0000 0000 0000
0000460 0000 0000 0000 0000 0000 0000 0000 0000
0000500 0000 0000 0000 0000 0000 0000 0000 0000
0000520 0000 0000 0000 0000 0000 0000 0000 0000
0000540 0000 0000 0000 0000 0000 0000 0000 0000
0000560 0000 0000 0000 0000 0000 0000 0000 0000
0000600 0000 0000 0000 0000 0000 0000 0000 0000
0000620 0000 0000 0000 0000 0000 0000 0000 0000
0000640 0000 0000 0000 0000 0000 0000 0000 0000
```

```
000660 0000 0000 0000 0000 0000 0000 0000 0000
0006700 0000 0000 0000 0000 0000 0000 0000 0000
0006720 0000 0000 0000 0000 0000 0000 0000 0000
0006740 0000 0000 0000 0000 0000 0000 0000 0000
0006760 0000 0000 0000 0000 0000 0000 0000 0000
```

```
[START BLOCK 2]
```

```
0001000 88ea 4200 0300 0000 2300 1000 0200 0000
0001020 aa00 0a00 3ce7 70e9 0a02 0d02 b0a5 1000
0001040 0001 0100 0000 0000 0000 0000 0000 0000
0001060 0000 0000 0000 0000 0000 0000 0000 0000
0001100 0000 0000 0000 0000 0000 0000 0000 0000
0001120 0000 0000 0000 0000 0000 0000 0000 0000
0001140 0000 0000 0000 0000 0000 0000 0000 0000
0001160 0000 3401 0301 d219 14e1 80e1 f81e 0060
0001200 5c53 0000 0000 0000 0000 0000 0000 0000
0001220 0000 0000 0000 0000 0000 0000 0000 0000
0001240 0000 0000 0000 0000 0000 0000 0000 0000
0001260 0000 0000 0000 0000 0000 0000 0000 0000
0001300 7200 7700 0000 0000 0000 0000 0000 6300
0001320 0000 0000 0100 0000 e000 0300 5018 0000
0001340 0000 0000 0000 0000 0000 0000 0000 0000
0001360 0000 0000 0000 0000 0000 cff2 c4ff fc18
0001400 0000 f4ff 8a16 8a16 9000 0800 0000 0000
0001420 0000 0000 0000 0000 0000 0000 0000 0000
0001440 0000 0000 0000 0000 0000 0000 0000 0000
0001460 0000 0000 0000 0000 0000 0000 0000 0000
0001500 0000 0000 0000 0000 0000 0000 0000 0000
0001520 0000 0000 0000 0000 0000 0000 0000 0000
```

Figure 1. Hex dump of the first part of the data file RUN06.DMS. The byte count is in octal, so 1000 represents 512 bytes. The first block is a header for the file. The byte order within words is low byte-high byte. For example, at the start of block 2, we have the system clock time recorded. It should be read as 0042ea88 hex. Converting to decimal yields 4.385,416 hundredths of a second. Converting this to HH:MM:SS.ss yields 12:10:54.16, the clock time seen on the Maverick video.

```

/* strips off CR/LF from run06.dms */
#include <stdio.h>
#include <stdlib.h>
FILE *fptrin, *fptrout;
char InFileName[10], OutFileName[6];
int ctr, dum, i;
main()
{
strcpy(InFileName, "run06.dms");
strcpy(OutFileName, "s.out");
fptrin=fopen(InFileName, "r");
fptrout=fopen(OutFileName, "w");
while(dum != EOF)
{
ctr = 1;
while (ctr<513)
{
dum = getc(fptrin);
putc(dum, fptrout);
ctr++;
}
dum = getc(fptrin);
dum = getc(fptrin);
}
fclose(fptrin);
fclose(fptrout);
}

```

Figure 2. The C-program "s2.c" used to strip the CR/LF sequence out of the LOSA data file "run06.dms."

%> RUN REDUCE_S

Running this program results in the creation of four output files:

0006RUN06.IR	(16,580,608 bytes)	All the IR data
0006RUN06.IQ	(9,326,592 bytes)	All the MMW data
0006RUN06.KEY	(3,294,720 bytes)	All the status words
0006RUN06.SEQ	(203,264 bytes)	Tape info and mode transitions

These output files are used by the map generating software. The last slot of the file is slot number 5964 at time 12:13:31.99.

2.4.1.3 LOSA Map Generation Software Subpackage

This subpackage consists of the following programs:

```
DBSMAP.FOR
FIND_TIM.FOR
PHASE_CO.FOR
PROMPTS.FOR
PROMPTS.INC
SETWID.FOR
TAYLOR.FOR
TRACK_FI.FOR
VAXLIB.OLB
PLOTLIB.OLB
FIND_GAI.OBJ
```

The files PLOTLIB.OLB and FIND_GAI.OBJ are contaminated and have not been restored as of this writing. The file VAXLIB.OLB was stripped of extraneous CR/LF sequences in a manner similar to RUN06.DMS. After compiling the FORTRAN programs in this list, a typical link and run sequence looks as follows:

```
%> LINK DBSMAP, FIND_TIM, PHASE_CO, PROMPTS, SETWID, TAYLOR,
        TRACK_FI, VAXLIB.OLB/LIBRARY

%> RUN DBSMAP
```

Without FIND_GAI, which computes the estimated gain imbalance between the I and Q channels of the radar data, it is necessary to comment out the call in DBSMAP.FOR and set the variable *gain_imbalance* to 1.00. It is not clear at present exactly how to handle the absence of the plotting library if plots are desired; this will be investigated further. However, map files are still generated and can be used by other user-supplied graphics routines. For example, it is possible to view the IR maps using the KBV image-processing software on a SUN workstation. Running DBSMAP with no plots requested results in the creation of the following files:

0006TIMES.06	list of dwell times processed
0006xxxx.i06	IR maps, where xxxx are requested dwell numbers
0006xxxx.m06	MMW maps

The MMW map files are generated in a call to *scale_mn* in DBSMAP.FOR, and this routine seems to be in the plotting software which is not currently working. The IR files are saved in the form of a 19-byte header followed by 128 x 128 data bytes.

2.4.2 LADAR Data

The LADAR data was provided on a 44MB Bernoulli disk. The data files are described in the data file catalog entitled "IMAGE FILE FORMAT FOR Nd:YLF DATA STORED WITH YSAVE." Each data file contains intensity and range data on scenes containing from one to six ground targets. For the purpose of viewing the intensity data using KBV, the raw data files can be converted to KBV format using the following inputs to ForImInt, the KBV foreign image conversion task: File Header = 4 bytes, Xsize = 256 bytes, Ysize = 1024 or 256 bytes (the actual file size for each file is specified in the data catalog), Row Header = 512 bytes, Record Size = 256 bytes, and Record Header = 0.

The conversion of all the available LADAR data files to intensity images in KBV image file format has been performed and the files are archived. In the future, we may extract the range data and use the range and intensity data together in some data fusion experiments for target detection and/or identification.

2.4.3 AADIOS Dual Band IR Data

On 27 July 1993, Larry Nelson and Ed McDermott of Integrated Sensors, Inc. visited the Wright Lab and presented a talk entitled "Raw Data Fusion, Status Review." ISI is under SBIR contract with the Air Force with Ellis Boudreaux as the contract monitor. ISI presented results from several studies involving dual-band IR and video / IR fusion. The dual-band IR data, which comes from the AADIOS program, will be transferred in the near future and used for neural network sensor fusion experiments.

3.0 Results

This section summarizes results from the leave-one-out training, the background frame generation, and the preparation of additional data for future experiments.

3.1 Leave-One-Out Training Results

The leave-one-out method was applied to the IR data from 14 target scenes prepared from the ADAMS data set. The cumulative results are shown in the confusion matrix below.

It is clear that certain training/testing combinations lead to incorrect classification. Further detailed analysis and explanation is presented in the report "Supervised Training in Artificial Neural Networks: Small Sample Size Methodology for Selection and Analysis of Training Sets," written by Mark Townsley at Auburn University. This report is available by making a request to Dr. Roppel. The gist of the above-referenced report is that two of the

<i>Actual Target</i>	<i>Tank</i>	<i>Classified As Launcher</i>	<i>Undecided</i>
Tank	23	11	6
Launcher	1	39	0

launchers and one of the tanks are recognized as contributing to all of the errors in classification. Visual inspection of these specific target scenes shows that differences in ground shadowing is probably the main reason. When these outliers are removed from the training data, performance improves considerably.

3.1 Leave-One-Out Fusion Results

A series of experiments was conducted to measure neural network target identification performance using fused MMW/IR data compared with using only IR data. The table which follows lists the various combinations of targets for which the leave-one-out experiments were run, and the number of times each outcome occurred (* = correctly identified, X = incorrectly identified, O = not identified). By comparing the IR-only results with the fused results in the last row of the table, it is clear that the performance is degraded by the introduction of the MMW data. The reason for this is that no attempt has yet been made to segment the MMW data as was done for the IR. Therefore, after the MMW data is averaged down from 8 x 96 x 128 pixels to just 128 pixels, the number of pixels on the target is likely to be significantly less than one. Thus, the radar data looks like noise to the neural network. The correct classification percentage drops from 45% to 38%, while the incorrect classification percentage increases from 27% to 40%. The same trend is observed for each row of the table, except for the first. Notably, this was the first combination on which experiments were performed, which accounts for the overly optimistic performance evaluation based on the Summer 1992 results.

In addition to the leave-one-out experiments discussed above, both principal component analysis (PCA) and canonical discriminant analysis (CDA) were performed on the results. A very readable discussion of these techniques is presented in "Analysis Tools for Neural Networks," by Simon Dennis and Steven Phillips. This paper is included with the ASPIRIN version 6.0 release documentation, but a copy may be obtained by requesting it from Dr. Roppel. The PCA technique analyzes the dimensions in data space along which the network tries to make maximum separation between data items (e.g., target examples). CDA performs the complementary function of analyzing the clustering of outputs performed by the network. The network after training would ideally tightly cluster all targets of each kind,

	IR only			Fused MMW/IR			TOTAL
	*	X	O	*	X	O	
Tanks & Launchers	18	11	11	19	11	10	40
Tanks & APC's	66	11	3	51	16	13	80
Launchers & APC's	17	9	6	13	12	7	32
Tanks, Launchers, & APC's	110	95	115	95	150	75	320
TOTAL	211	126	135	178	189	105	472
TOTAL %	45%	27%	29%	38%	40%	22%	100%

and maintain maximum separation between clusters. PCA and CDA were used on the fused tank / launcher AADMS data. After training, the tanks and launchers were clearly sorted into two distinct, non-overlapping clusters, indicating successful training.

3.2 Background Frames

One of the goals of this work is to investigate target detection in clutter and obscuration. For this purpose, it is necessary to train the network to distinguish between target and non-target images. Approximately 16 frames of background scenery have been generated by extraction from the AADMS scene images. These will be used in future experiments.

3.3 Results of Processing Additional Data Sets

In Section 2.4, the LOSA, LADAR, and AADIOS data sets are mentioned. Of these data sets, the most time was spent on the LOSA data. The raw data files were obtained, the ground-processing software was refurbished and the entire package was assembled and archived. The condition of the software is such that it is possible to generate IR map files, but not MMW map files at this point. A little more work (perhaps a few days) is required to get the MMW plotting capability online. The LADAR data has been transported to the SUN / Unix environment, and the IR intensity images have been converted to KBV image file format. This data will also be archived.

4.0 Discussion

The purpose of this continuing investigation is to try to determine whether neural network technology might be suitable for eventual implementation in a dual-mode seeker. Conventional data handling approaches are based on

algorithmic methods, which are in turn often based on Bayesian statistics and Gaussian noise assumptions. While these assumptions are not strictly appropriate for every problem, many years of refinement have yielded good algorithms, and so neural networks must perform very well in order to be considered advantageous.

The basic principles underlying neural network performance are these: neural networks learn from "experience," i.e., from available data; they provide fast, approximate solutions reminiscent of intuition and judgement calls in humans; and they exhibit rich, complex "behavior" characteristic of nonlinear dynamical systems. On the other hand, it is difficult to trace the "reasoning" underlying a given response, and there is inherently a very difficult validation and verification problem associated with neural networks.

Upon comparing neural network approaches with algorithmic methods we find the following distinction. Algorithmic methods try to anticipate scenarios and encode them in *rules to be followed at the time of engagement*. Neural networks, on the other hand, try to encounter scenarios in training, learn from them, and then *respond "instinctively" at the time of engagement*.

It is well worth noting that both methods depend crucially on the quality and quantity of available data. In fact, it might be appropriate to refer to the present situation in the field of target detection research as "algorithm-rich / data-starved," (ARDS).

Looking ahead to possible hardware implementation, we find that the typical neural network chip architecture is highly regular, resulting in high packing density, which in turn offers reduced parts count and weight, and increased reliability. The neural network might be thought of as a computer program which is stored in the architecture of a chip. Flexibility for modifications still exists at the layout and mask levels, however.

Distributed, redundant systems are generally highly desirable because they improve fault-tolerance and fault-avoidance capability. Neural network-based systems have been shown to lean toward graceful degradation with increasing input noise or when faced with internal failures. The details of the failure response depend on the neural net size and architecture details. A larger network will, in general, be more robust due to its increased redundancy. The combination of fast response and high reliability is the primary motivation for studying the role that neural networks might have in seeker technology.

The results thus far on the AADMS data, together with the results of other researchers, are encouraging. It is clearly possible to train a neural net to perform target identification on a small scale. It is possible that by employing hardware which is already available, a medium-scale mock-up could be developed and used for testing. It is important to pursue this approach, since the true speed advantage of the neural net approach is not realized unless the network is implemented in hardware.

It is considerably more difficult to make use of the raw MMW radar data than the IR data. Post-processing required to get an image map is tremendous, so it is probably better to avoid this if possible. It should be feasible soon to fuse the high-range resolution (HRR) profiles with the IR data, without having to perform pixel-to-pixel registration. With regard to MMW/IR fusion, the two data types should be considered to be dissimilar yet complementary, like audio and video, rather than treated like dual-band IR, which is relatively easy to pixel-register.

5.0 Plans for Continuing Work

One aspect of continuing work that will be pursued is to try to get a more usable version of the AADMS MMW data. The present version that is being used is the Doppler beam sharpened (DBS) processed data. However, there is insufficient azimuth resolution to permit registration to any degree with the IR data, and there do not seem to be any calibration markers in the data. John Watson of Nichols Research has indicated that it might be possible to de-archive the original raw MMW data.

In addition to continuing the existing work for the Air Force, we are very interested in finding commercial applications for sensor fusion technology. Technology transfer has been identified as a prime goal for DOD, and we intend to make every effort to continue this work with that in mind. Several areas of possible application include robotics, engine diagnostics, underwater detection, chemical analysis, voice processing, and automatic facial recognition. The neural network approach is quite flexible relative to the types of sensor inputs that can be accommodated. For example, a robotic application might use a combination of video, IR, and tactile inputs to identify machine parts, whereas engine diagnosis might involve a combination of audio and IR inputs.

The LOSA data from IITRI will continue to be processed. The software will be brought into as close to mint condition as possible, and all of the relevant flight data will be extracted so that it can be used for MMW/IR fusion studies. The dual-band IR AADIOS data will be obtained from ISI if at all possible, and this will be used for fusion experiments as well. Finally, we propose to study the application of neural nets to a dual-band radar problem as proposed by Larry Lewis at Wright Lab. This will require follow-up after the end of the summer research period.

It is the intent of this author and his co-workers at Auburn to apply for follow-on research support in any capacity where we can contribute to the Air Force effort in multi-mode data processing and data / sensor fusion. It is of particular interest to us to see that we maintain contact with everyone at the Wright Laboratory who has an application or an interest involving neural nets and data fusion. The author encourages communication from interested individuals, and can be reached at

(Internet) troppel@eng.auburn.edu

(Phone) (205) 844 - 1814

The End

**THE AMPLL PROGRAM FOR PREDICTING
PENETRATOR BEHAVIOR ON IMPACT**

William Keith Rule
Assistant Professor
Department of Engineering Science and Mechanics

University of Alabama
BOX 870278
Tuscaloosa, AL 35487-0278

Final Report for:
Summer Faculty Research Program
Wright Laboratory

Sponsored by:
Air Force Office of Scientific Research
Bolling Air Force Base, Washington, D.C.

August 1993

THE AMPLL PROGRAM FOR PREDICTING PENETRATOR BEHAVIOR ON IMPACT

William Keith Rule
Assistant Professor
Department of Engineering Science and Mechanics
University of Alabama

Abstract

This report describes a computer program called AMPLL (Analytical Model for Penetration with Lateral Loads). AMPLL is designed to predict the structural response of a penetrator passing through layers of air, concrete, soil, ice, and/or rock. AMPLL is based on a similar program developed by Sandia National Laboratories called SAMPLL. AMPLL differs from SAMPLL in that it has a more extensive graphical user interface and models the penetrator as a flexible body rather than a rigid body. Axial forces and lateral loads due to angle of attack and impact angle are treated. The penetrator is modeled as a series of frame finite elements, the number of which can be controlled by the user. Penetrators with arbitrary (but quasi-axisymmetric) and varying cross sections can be modeled. Plastic behavior of the penetrator is treated in an approximate fashion.

AMPLL is written in Microsoft Visual BASIC and runs on personal computers under Microsoft Windows. The structure of the program and how it can be used is described.

THE AMPLL PROGRAM FOR PREDICTING PENETRATOR BEHAVIOR ON IMPACT

William Keith Rule

Introduction

The development of a code called SAMPLL (Simplified Analytical Model of Penetration with Lateral Loading) was initiated at Sandia National Laboratories in 1982 [1, 2]. Development of this code still continues. SAMPLL was designed to approximately predict the attitude and failure of penetrators passing through layered targets of air, concrete, soil, ice, and/or rock. SAMPLL models the penetrator as a rigid body and uses a unique concept of failure called excess impulse.

This project was initiated to enhance the user interface of SAMPLL, to model the penetrator as a flexible body, and to provide a more classical, mechanics-based index of failure. The resulting program is called AMPLL (Analytical Model of Penetration with Lateral Loading), is written in Microsoft Visual BASIC, and runs under Microsoft Windows.

Instructions for running AMPLL are given in a section of this report entitled *AMPLE User Information*.

Axial and Lateral Force Model

In general, a penetrator impacting a layered target will be subjected to both axial and lateral forces. The empirical axial and lateral force models used in AMPLL are essentially identical to those of SAMPLL [1, 2]. Target layers of reinforced and unreinforced concrete, rock with horizontal bedding planes, isotropic rock, soil, ice or frozen soil, and air can be treated.

The axial forces are predicted based on the assumption that a target layer will exert a constant force, F_A , on a decelerating penetrator. Equating the work done by the target on the penetrator to the initial kinetic energy of the penetrator allows F_A to be calculated:

$$\text{WORK} = \text{KINETIC ENERGY}$$

$$F_A D = \frac{1}{2} M V^2 \quad (1)$$

$$\therefore F_A = \frac{M V^2}{2D}$$

where: D is the depth of penetration into the target, M is the mass of the penetrator, and V is the initial velocity of the penetrator. Thus, the axial force can be estimated if the depth of penetration, D , is known. Empirical equations based on extensive testing have been developed to predict D [1,3]. Such equations typically are of the form:

$$D = C_1 S N \left(\frac{W}{A} \right)^{C_2} f_1(V, W) \quad (2)$$

where: C_1 and C_2 are empirical constants, S is the penetrability of the target, N is the nose performance coefficient, W is the weight of the penetrator, A is the cross sectional area of the penetrator at the nose-body interface, and $f_1(V, W)$ is a function of V and W which depends on the target type.

The penetrability, S , is used to allow for the characteristics of a particular target type within a class of target types. For instance, nominal concrete would have an S of unity, and a high strength concrete could have an S of 1.1 or higher. The nose performance coefficient reflects the efficiency with which a particular nose type penetrates and is given by equations of the form [1]:

$$N = f_2(L_N, d) \quad (3)$$

where: L_N is the length of the nose, d is the diameter of the penetrator at the nose-body interface, and f_2 is a function of these parameters.

Axial loads are applied to the nose and to segments of the penetrator with a significant amount of flare. It is assumed that a small amount of flare will not attract significant axial forces because the nose will produce a slightly over-sized hole in the target. Axial loads on the nose and flared sections are allocated in a consistent manner to the finite elements making up these loaded segments.

Lateral loads are assumed to originate from two sources: angle of attack and penetrator angle. Lateral forces affect the attitude of the penetrator as it passes through the layers. Lateral forces can also produce large stresses in long penetrators due to bending.

Angle of attack, α , is the angle between the velocity vector and the axis of the penetrator. The angle between the velocity vector and the target surface is called the impact angle, β . The component of the velocity vector perpendicular to the penetrator axis induces the lateral force. In effect, the penetrator is impacting the target sideways. It is assumed that this type of lateral impact is similar in nature to axial impact. Accordingly, the lateral force due to angle of attack is assumed to be proportional to the axial pressure on the nose and to the angle of attack [1,2]:

$$F_\alpha = C_3 \left(\frac{F_A}{A} \right) A_s \alpha \quad (4)$$

where: C_3 is an empirical constant, and A_s is the lateral projected area of an element. Note- α should always be measured in radians.

When a penetrator enters a target a crater is formed. Similarly, as a penetrator leaves a layer, target material often spalls off the bottom. Because of these effects, angle of attack lateral forces will tend to zero

when the penetrator is near the top and bottom of a layer. It is assumed that the target layer boundary influence distance is $2.5C_4d$, where C_4 is an empirical coefficient (nominally unity) which can be adjusted for different target types [2]. Thus, the angle of attack lateral force given by Eq. 4 is adjusted to vary linearly to zero when the penetrator is within the boundary influence distance. The preceding remarks on boundary influence effects applies to the case where the target layer under consideration is bounded by softer layers or air. Adjacent layers of equal or greater hardness will not permit cratering or spalling so the boundary influence correction need not be applied for these cases [2]. The finite element model is used to calculate axial and lateral nodal velocities. Thus, an angle of attack and lateral force can be determined for each element.

Penetrator angle, ϕ , is the angle between the penetrator axis and the target surface. For normal impacts, penetrator angle lateral forces are zero. However, during an oblique impact the target material on the side of the nose closest to the surface tends to offer less resistance than the material on the bottom side of the nose. Thus, there would be a net lateral force directed towards the surface. Similar effects would occur as the penetrator approaches the bottom of the target layer. When the penetrator is relatively far from the surfaces of a target layer then the impact forces on the top and bottom surfaces of the penetrator approach each other and the penetrator angle lateral force tends to zero. This situation would occur in the central portion of a relatively thick target layer.

The distance for which these layer surface effects are assumed to be active is $5C_5d$, where C_5 is an empirical coefficient (nominally unity) which can be adjusted to account for different target types. Here surface interaction distance is defined as the perpendicular distance from the penetrator centerline to the layer surface. Penetrator angle lateral forces are only active where adjacent layers are softer than the layer under consideration. It is assumed that cylindrical portions of the penetrator will not generate penetrator angle lateral forces. However, flared sections will generate lateral forces in a manner similar to that of the nose.

Penetrator angle lateral forces are assumed to be proportional to the axial force pressure on the nose and the cosine of the penetrator angle [2]:

$$F_{\phi} = C_6 \left(\frac{F_A}{A} \right) A_s \cos(\phi) (C_7 d_{TOP} - C_8 d_{BOTTOM}) \quad (5)$$

where: C_6 , C_7 , and C_8 are empirical coefficients, and d_{TOP} and d_{BOTTOM} are the interaction distances to the top and bottom of the layer, respectively.

Finite Element Model of Penetrator

One of the major tasks of this project was to convert the rigid body model of SAMPLL to a flexible body model. This can be accomplished by modeling the penetrator as a series of plane frame finite elements which can treat both axial and bending effects. Standard frame elements with a constant cross section were adopted for this purpose [4]. Tapered elements could have been used but with no significant accuracy gain. These elements have a node at each end with three degrees of freedom: axial displacements and forces, lateral displacements and forces, and nodal rotations and moments. The stiffness matrix associated with axial deformations and forces, $[k_a]$, is:

$$[k_a] = \frac{EA_e}{L_e} \begin{bmatrix} 1 & -1 \\ -1 & 1 \end{bmatrix} \quad (6)$$

and that for flexural behavior, $[k_f]$, is:

$$[k_f] = \frac{EI_e}{L_e^3} \begin{bmatrix} 12 & 6L_e & -12 & 6L_e \\ 6L_e & 4L_e^2 & -6L_e & 2L_e^2 \\ -12 & -6L_e & 12 & -6L_e \\ 6L_e & 2L_e^2 & -6L_e & 4L_e^2 \end{bmatrix} \quad (7)$$

where: E is the modulus of the penetrator, L_e is the length of the element, A_e is the cross sectional area of the element at mid-length, and I_e is the flexural inertia of the element at mid-length. For example, a penetrator with a tubular cross section of inside radius R_i , and outside radius R_o , has a cross sectional area and an inertia given by:

$$A_e = \pi(R_o^2 - R_i^2) \quad (8)$$

$$I_e = \frac{\pi}{4}(R_o^4 - R_i^4) \quad (9)$$

Equations 6 and 7 are assembled together in an appropriate fashion to produce a 6x6 elemental stiffness matrix, $[k_e]$.

A lumped elemental mass matrix, $[m_e]$, which is diagonal, was used in the formulation [4]:

$$[m_e]_{6 \times 6} = \frac{M_e}{2} \begin{pmatrix} 1 & 1 & \frac{17.5L_e^2}{210} & 1 & 1 & \frac{17.5L_e^2}{210} \end{pmatrix} \quad (10)$$

where M_e is the mass of the element. A fully populated consistent mass matrix could also be used which might slightly improve the accuracy of the calculated results. However, lumped mass matrices have been

found to produce sufficiently accurate results and they have the advantage of being computationally cheap to invert (inverted by simply taking the reciprocal of the diagonal elements - so matrix stays diagonal).

The global mass, $[M]$, and stiffness, $[K]$, matrices are created by assembling the elemental mass and stiffness matrices in the usual fashion. The elemental mass matrices are diagonal, and so the global mass matrix will also be diagonal and thus trivial to invert. The equation of motion can then be written:

$$[M]\{\ddot{x}\} + [K]\{x\} = \{F_{\text{impact}}\} \quad (11)$$

where: $\{\ddot{x}\}$ are the nodal accelerations, $\{x\}$ are the nodal displacements, and $\{F_{\text{impact}}\}$ is a vector of external axial and lateral impact loads which were discussed in the previous section. A damping term has not been included in Eq. 11 since monolithic, high-strength metal components exhibit little damping. Equation (11) can be solved for the nodal acceleration vector:

$$\{\ddot{x}\} = [M]^{-1} \left[\{F_{\text{impact}}\} - [K]\{x\} \right] \quad (12)$$

Equation 12 shows that nodal accelerations are given by the inverse of the mass matrix multiplied into a "delta force" vector which consists of the difference between the external impact forces applied to the penetrator and the internal forces ($= [K]\{x\}$) in the penetrator. A scheme for approximately treating plastic behavior is discussed below. Up to this point it has been assumed that the penetrator is behaving elastically.

A finite difference scheme is normally used to determine the new nodal displacements, $\{x_{\text{NEW}}\}$, at the end of the next time step, ΔT , based on the acceleration vector of Eq. 12 and the current and previous displacement vectors:

$$\{\ddot{x}\} = \frac{\{x_{\text{NEW}}\} - 2\{x_{\text{CURRENT}}\} + \{x_{\text{PREVIOUS}}\}}{\Delta T^2} \quad (13)$$

Rearranging gives [4]:

$$\{x_{\text{NEW}}\} = \{\ddot{x}\}\Delta T^2 + 2\{x_{\text{CURRENT}}\} - \{x_{\text{PREVIOUS}}\} \quad (14)$$

The new velocity vector, $\{\dot{x}_{\text{NEW}}\}$, can now be calculated:

$$\{\dot{x}_{\text{NEW}}\} = \frac{\{x_{\text{NEW}}\} - \{x_{\text{PREVIOUS}}\}}{2\Delta T} \quad (15)$$

A global coordinate system is set up with the origin on the surface of the target where the nose will first impact. A global x-axis is made to run parallel to the surface of the target and in a direction parallel to the horizontal component of the penetrator velocity vector. A global z-axis runs from the surface of the target and into the target. Most oblique impacts will cause the penetrator to rotate a considerable amount. These rotations must be "factored" out of displacement, velocity, and acceleration vectors because the components of these vectors must be precisely maintained either parallel or perpendicular to the axis of the penetrator. Essentially, a local coordinate system must be made to travel with (or be in the frame of) the penetrator. This is accomplished by rotating these vectors every time step by an angle $\Delta\phi$, using the following transformation matrix:

$$\begin{Bmatrix} u'_{T+\Delta T} \\ v'_{T+\Delta T} \\ \theta'_{T+\Delta T} \end{Bmatrix} = \begin{bmatrix} \cos(\Delta\phi) & \sin(\Delta\phi) & 0 \\ -\sin(\Delta\phi) & \cos(\Delta\phi) & 0 \\ 0 & 0 & 1 \end{bmatrix} \begin{Bmatrix} u_{T+\Delta T} \\ v_{T+\Delta T} \\ \theta_{T+\Delta T} \end{Bmatrix} \quad (16)$$

where: u is the axial vector component, v is the lateral vector component, θ is the rotational vector component, and primed quantities refer to transformed quantities. $\Delta\phi$ is determined by the change in angle of a line connecting the nose to the tail that occurs over a time step ΔT . Equation 16 shows no transformation for rotational vector quantities, which is indeed the case for angular velocities and accelerations. However, for the nodal rotations themselves the transformation is:

$$\theta'_{T+\Delta T} = \theta_{T+\Delta T} - \Delta\phi \quad (17)$$

The penetrator angle is also updated each time step:

$$\phi' = \phi + \Delta\phi \quad (18)$$

The impact load vector, $\{F_{\text{impact}}\}$, need not be corrected for penetrator rotations since it is always assumed to be composed of components parallel or perpendicular to (as appropriate) the axis of the penetrator.

The penetrator is treated as a series of segments. Generally, each abrupt change in the geometry of the penetrator, such as a flared portion, is treated as a separate segment. The first segment is *always* the nose. AMPLL is formatted to handle as many as 5 segments per penetrator. The user can select the number of finite elements per segment to be used in the numerical model. Typically 4 or 5 elements are used per segment. Usually it is better to have a relatively uniform mesh density (number of elements per foot) and so in some cases it may be a good practice to partition a long segment into two or more segments to attain a more uniform mesh density.

The nose not very accurately modeled using beam finite elements because of its complex geometry. Generally, the cross section varies considerably over the length of the nose. The software linearly interpolates cross section areas, and flexural inertias based on the user input end point values for a segment. Thus, for modeling purposes it is recommended that the tip of the nose be given the following area and inertia properties:

$$A_0 = 2A_{\frac{L_N}{2}} - A_{L_N} \quad (19)$$

$$I_0 = 2I_{\frac{L_N}{2}} - I_{L_N} \quad (20)$$

where subscripts indicate where the property is evaluated ($\frac{L_N}{2}$ is half the nose length). When linear interpolation is applied to the tip values of Eqs. 19 and 20 then areas and inertias are precisely matched at $\frac{L_N}{2}$ and L_N . Alternatively, without a significant loss of accuracy, A_0 and I_0 can be simply input as $\frac{1}{3}A_{L_N}$ and $\frac{1}{3}I_{L_N}$, respectively. AMPLL does not monitor strain in the first $\frac{2}{3}$ of the nose for failure prediction purposes because of probable inaccuracies in calculated strain values and uncertainties in the loading distribution. In most cases these modeling inaccuracies are not important since the significant strains in the penetrator are at midlength where the moments are largest.

There are two important, user-controlled parameters associated with the finite element model: the number of elements used, and the size of the time step, ΔT . In general, accuracy improves as more elements are used and the time step size is reduced. However, solution times increase dramatically as the model is refined. The recommended approach is to use four elements per segment and the recommended time step size initially, and then run the problem again using one or two more elements per segment with the corresponding new recommended time step size. This approach is repeated until there is no significant change in the calculated results, which indicates that the model has converged.

The recommended time step size is based on two considerations: the time required for an axial elastic wave to pass through the shortest finite element, and the time required for the penetrator to pass through the thinnest target layer. The time step must be made shorter (AMPLL uses $\frac{1}{20}$ of these times as suggested in SAMPLL) than shortest of these two times if stable and accurate numerical results are to be obtained. The axial wave speed is approximately equal to $\sqrt{\frac{E}{\rho}}$, where E is the elastic modulus and ρ is the mass density. The axial wave transit time is defined as the length of the shortest element divided by the axial wave speed. The layer transit time is defined as the thinnest target layer divided by the initial penetrator velocity. AMPLL displays the recommended time step size and indicates which criterion governs (penetrator or target).

Currently AMPLL assumes that the penetrator material is elasto-plastic. This means that the stress versus strain plot is linear ($\sigma = E\epsilon$) until the yield stress is reached and then it is assumed that the stress

stays equal to the yield stress as strain increases further. It is assumed that behavior in tension is identical to that in compression. It is also assumed that failure occurs when strain levels reach a critical value of percent elongation, which is a material property that must be measured and depends on the particular material a penetrator is fabricated from.

Thus, the maximum axial force (either tension or compression) that can be generated by an element is equal to $\sigma_{YS}A_e$ and occurs when the cross section is fully yielded. AMPLL enforces compatibility with this upper bound by replacing A_e in Eq. 6 with an effective cross sectional area smaller than A_e when formulating the element stiffness matrix.

Similarly, an upper bound on the moment exists (called fully plastic moment, M_p) which occurs when the compression stress block and the tensile stress block of the cross section are fully yielded [5]. AMPLL ensures that M_p is not exceeded by substituting the actual moment of inertia, I_e , in Eq. 7 with an appropriately smaller effective moment of inertia when formulating the element stiffness matrix. AMPLL allows the penetrator to have arbitrary cross sections that are quasi-axisymmetric (evenly placed stringers allowed) making determination of M_p for a given cross section difficult. However, most cross sections can, to a sufficient degree of accuracy, be approximated as a tube. Accordingly, an effective tubular wall thickness, t_e , can be calculated from:

$$t_e = R_o - \sqrt{R_o^2 - \frac{A_e}{\pi}} \quad (21)$$

The compression and tension block forces are equal to $\sigma_{YS}\left(\frac{A_e}{2}\right)$ and they act at the centroids of each half of the cross section. The lines of action of these forces are separated by:

$$c = \frac{8(3R_o^2t_e - 3R_ot_e^2 + t_e^3)}{3A_e} \quad (22)$$

Finally, the fully plastic moment is:

$$M_p = \sigma_{YS}\left(\frac{A_e}{2}\right)c = \frac{4\sigma_{YS}(3R_o^2t_e - 3R_ot_e^2 + t_e^3)}{3} \quad (23)$$

This simple approach to treating yielding appears to be adequate. However, since the finite element model provides the strains in the penetrator, more sophisticated material models could be incorporated into AMPLL.

Description of Program Structure

AMPLL is written in Version 2 of Microsoft Visual BASIC (a sophisticated, object-oriented form of the BASIC computer language) which generates programs that run on Intel chip based PCs (80386, 80486, 80586) under the Microsoft windows operating system. Users *do not* need a copy of the Visual BASIC program to run AMPLL. AMPLL is composed of six fundamental types of files: code files (1_ampll.bas, 2_ampll.bas), global variable file (global.bas), form files (mainmenu.frm, selrecrd.frm, penemenu.frm, peneinfo.frm, targinfo.frm, impacond.frm, timestep.frm, seloutpt.frm, derecord.frm, viewer.frm), data files (penetrat.txt, target.txt, config.txt), output file (default name ampll.txt), and a scratch file (ampll.scr).

The code files contain the subprograms (subroutines) that perform the calculations and coordinate program flow. Two code files are required to store all the subprograms of AMPLL because code files are restricted in size to 64K. The global variable file specifies all global variables (variables that can be accessed by all parts of the code) and also provides definitions of these variables. Each form file contains information about a window that appears on the screen as AMPLL executes. Some calculations are performed in the form files.

The penetrat.txt data file stores properties of penetrators, Table 1. AMPLL allows the user to select penetrators from this file for making runs and to add newly defined penetrators to this file. Penetrators can also be deleted from this file. Similarly, the target.txt data file stores information about targets, Table 2. A complete run configuration (penetrator, target, impact and run parameters) is stored in the config.txt file to expedite reruns under similar conditions, Table 3. The results of a run, along with an echo of the input data, are optionally written to an output file with a user defined name. The data files and the output files are ASCII files which may be inspected and modified independent of AMPLL using a text editor such as Windows Notepad. While deleting records from penetrat.txt and target.txt a temporary scratch file, ampll.scr, is opened. This file is automatically deleted during the run.

AMPLL program structure is displayed in Table 4. Subprogram main_program calls a series of subprograms (set_model_parameters, set_defaults, etc.) which in turn call a series of subprograms, as indicated by the arrows and columns in Table 4. How the form, data, and scratch files are used in AMPLL is also indicated in Table 4.

AMPLL User Information

In this section the use of AMPLL will be described. First all the files on the program floppy disk should be copied into a subdirectory of a hard disk. This copying is not essential, but will greatly speed up program load time. If lack of disk space is a problem, then only files ampll.exe, grid.vbx, and vbrun200.dll (0.51 MG of disk space) need be copied. If the computer has Visual BASIC Version 2 installed in it then the

last two of these files need not be copied. To get the program started, the user double clicks (with left button of mouse) on `ampll.exe` under File Manager of Windows (or other Windows program starting techniques could be employed). A header window then appears and the user has the option of clicking on *start* to continue execution or clicking on *stop* to exit AMPLL.

Next the main menu window will appear which displays 10 options. An option may be selected by double clicking on it or by clicking on it once to select it and then clicking on the *continue* command button. Each option will now be described:

○ **Begin Impact Simulation** ~ This option is selected to start the program after the user has completed all data inputs. AMPLL then checks if all inputs are reasonable and begins the impact simulation. If some of the inputs are not reasonable (a negative cross sectional area for instance) then a warning is issued and the user is returned to the main menu window.

○ **Modify Current Penetrator or Select a New Penetrator** ~ When this option is selected a new window containing a combo box will appear. Clicking the down arrow button will display the option of modifying the current penetrator and a listing of penetrators currently stored in the data file `penetrat.txt`. Clicking on a penetrator in the list and clicking on *continue* will cause that penetrator to become the current penetrator and the main menu window will reappear. Clicking on the modify current penetrator option and then *continue* will cause two windows to appear sequentially, prompting the user for data on the penetrator. New data is entered by editing the default numbers in the white input boxes or by selecting from a combo box. The user should click on *continue* when finished with editing the data in each window. After inputting the data, the user will be given the option of storing the new penetrator in the `penetrat.txt` data file for later reference.

○ **Modify Current Target or Select a New Target** ~ This option is identical to that of the previous except here targets are dealt with instead of penetrators. Previously stored targets are contained in data file `target.txt`. Note that combo boxes are provided to select target layer types so the user will never have to type in the layer type.

○ **Modify Impact Conditions** ~ This window prompts the user for the initial penetrator velocity, the angle of attack (nose up positive), and the impact angle, β , which is the angle between the velocity vector and the surface of the target.

○ **Modify Time Step Variable** ~ Here a window pops open allowing the user to select the recommended time step size (determined as described in a previous section) or to input another time step size. The user must be sure to click on (and thus highlight) the time step to be used (recommended or user defined).

WARNING: Time step size should be reconsidered if the penetrator, the target, and/or the impact conditions are modified. If the time step is too large then the numerical model could "blow-up" (numerical values tend to $\pm\infty$). If the time step is too small then unnecessarily long execution times will result.

○ **Modify Output/Element Options** ~ This window prompts the user for a run title, the print frequency (the number of iterations that must pass before the results are printed to the screen and stored in the output file), the number of finite elements to be used per segment (same for all segments), and the point in the penetrator (as measured from the tip of the nose) to monitor velocities, accelerations and so forth.

○ **Read Previously Stored Configuration** ~ This command will cause the previously stored configuration (in file config.txt) to be read into AMPLL and become the current configuration. This includes penetrator, target, and all other parameters associated with a run. Thus, after inputting this file the impact simulation can be initiated without further input, or some aspects of the configuration can be modified before calculations begin.

○ **Save Current Configuration** ~ This choice will cause the current configuration (penetrator, target, other run parameters) to be stored in file config.txt for later reference.

○ **Delete Penetrator Definition from Data File** ~ Penetrators that are no longer of interest can be removed from the data file penetrat.txt by selecting this option. The name of the penetrator to be removed is simply selected from the combo box listing. A *cancel* button is provided to quit this command without deleting a penetrator.

○ **Delete Target Definition from Data File** ~ This menu pick is identical to the previous one except that deleting targets from the data file target.txt is the function.

○ **Exit from AMPLL Program** ~ This option will allow the user to exit from the AMPLL program without performing any calculations.

Except for the first (begin simulation) and last (exit from AMPLL) choices in the main menu described above, the user is returned to the main menu after executing an option. Thus, the usual approach

is to keep selecting menu options as required until the simulation has been defined to the user's satisfaction. Generally, the time step size should be the last model parameter selected and the recommended value should be used. It is good practice to save the configuration for future reference before beginning the simulation.

Once the simulation has begun the screen will be filled with a single, main window displaying data to help the user monitor, understand and visualize the solution. This window can be iconized by clicking the down arrow in the upper right corner of the window. This will free up the screen for other tasks as AMPLL executes in the background. Thus, productive work can continue on other applications as AMPLL runs. AMPLL can be brought back to full screen size by double clicking on AMPLL's American flag icon.

The main window displays calculated results three ways. The upper right corner of the screen contains a scrollable spread sheet displaying time, velocity, acceleration, and stress (at the point in penetrator specified by the user) as the program executes. The scroll bar can be used to scroll to any data point during the run.

Below the spread sheet is a plot area for displaying velocity, acceleration, stress, ϕ angle (angle between penetrator axis and target surface), depth, and percent elongation as a function of time. Command buttons are placed below the plot area to allow the user to select different plots as the program executes. The type on the button becomes bold when selected. The color of the plotted line changes as the penetrator passes from one layer to the next.

On the left and central portion of the screen is a to-scale (except for penetrator wall thickness) drawing of the target layers and the penetrator cross section. The current deflected shape and position of the penetrator is continuously updated on the screen as the simulation runs. Old penetrator positions are overwritten in light gray to provide a record of the trajectory. Continuously updated, color-coded, stress contours are shown on the penetrator cross section. The stress levels corresponding to the contours are shown below the drawing.

A hard copy (bit-mapped image) of the main display window can be obtained at any time by clicking on the *print* command button in the bottom right corner of the screen. Better output can be obtained if the printer is set to landscape mode (using Windows printer set-up). Also, the run can be halted at any time by clicking on the *exit* command button in the lower right corner of the screen.

It is often of interest to observe the axial and lateral forces acting on the penetrator as the simulation proceeds. A special window is available for this purpose that can be activated by pressing the *show forces* command button on the bottom right side of the screen. An adjacent *hide forces* button removes the force display window from view. The force display window is movable and resizable for the users convenience. The penetrator nose is on the left side of the window and the tail is on the right side. Vertical

dotted lines indicate element boundaries. Axial forces are shown in blue, and lateral forces in red. The largest force displayed is shown in the window title box for reference.

When the simulation is finished a message will be displayed indicating why the simulation stopped such as "Penetrator Passed Through All Target Layers". Then the user will be prompted for the name of a file in which to store the simulation output if so desired. The user will then have the opportunity to scroll through the data spread sheet, flip through the plotted data, and print out the display window. The run is terminated by the user clicking the *exit* command button. The ASCII output file can be inspected using a text editor such as Windows Notepad, can be inserted into a report in a word processing program such as Word for Windows, or can be imported to a spreadsheet such as EXCEL for plotting.

Convergence Study Results

As more elements are used and as time steps are made shorter, the accuracy of the numerical model should improve. In the limit (ignoring the effects of truncation errors), calculated results should approach and converge to exact values. Thus, convergence is a necessary characteristic of a numerical model if reliable results are to be produced. Accordingly, a convergence study was conducted using AMPLL and the results are shown in Table 5. These results are for an typical penetrator (initial velocity = 2100 ft/s, initial angle of attack $\alpha = 20^\circ$, initial penetrator angle $\phi = 78^\circ$) passing through a concrete target. Table 5 shows that AMPLL results did not change significantly as the mesh was refined for the case considered.

Test Case Results

All the details of the test cases run can not be reported here because of the classified nature of the results. However, some typical results are provided. The behavior of a small penetrator impacting a thick unreinforced concrete target was predicted using AMPLL. The results are shown in Table 6 and they appear to be reasonable. A large penetrator striking a thick unreinforced concrete target was also modeled using AMPLL, Table 7. The results follow a rational trend.

Summary and Conclusions

The well known SAMPLL code for predicting penetrator damage and trajectory on impacting hard targets was modified to produce a new code called AMPLL. The modifications consisted of:

- A new interface to make data input easier and provide for visualization of calculated results as an aid to checking the input data and understanding system behavior.
- The rigid body model of SAMPLL was replaced by a flexible body model in AMPLL, which takes the form of a finite element representation. This allows for more accurate predictions of stresses and strains in the penetrator.

- A new, more classical approach to predicting penetrator yielding was developed.

As a result of this project, the following conclusions were reached:

- The graphical user interface of AMPLL simplifies the task of data input and minimizes the chance for errors.
- Graphical display of calculated results by AMPLL helps the user understand the behavior of a penetrator during impact.
- The finite element model allows for a reasonably accurate prediction of the time history of stresses and strains (including stress wave effects) in the penetrator.
- AMPLL's limiting approach to modeling yielding appears to produce reasonable results.
- Further studies should be conducted to recalibrate the empirical coefficients derived from SAMPLL so that they will be compatible with the flexible body model of AMPLL.
- Development of a more sophisticated scheme for treating yielding in the penetrator is desirable.

Suggestions for Future Work

It is suggested that the following four tasks be conducted to enhance the reliability of AMPLL:

1. Gather together (and make readily accessible) a set (or sets) of high quality, and pertinent impact test results to serve as "official" benchmarks for computer code calibration.
2. Repeatedly run AMPLL adjusting the empirical coefficients slightly (increase a small percentage and decrease a small percentage) to determine the sensitivity of calculated results to these coefficients. Sensitivity curves could be fit through this data for each empirical coefficient to show change in calculated result (say - final velocity) versus percentage change in empirical coefficient.
3. Input the sensitivity curves and the test data set into a nonlinear optimization program to determine changes to be made to the empirical coefficients to minimize the difference (in a least squares sense) between AMPLL calculated results and the official benchmark experimental results.
4. Enhance the approach for modeling yielding in the penetrator to allow for non-elasto-plastic materials (could input stress-strain curve directly) and elastic unloading with residual plastic strain.

References

1. Young, C. W. and Young, E. R., "Simplified Analytical Model of Penetration with Lateral Loading," Sandia National Laboratories, SAND84 - 1635, May, 1985.
2. Young, C. W., "Simplified Analytical Model of Penetration with Lateral Loading (SAMPLL) - An Update," Sandia National Laboratories, SAND91 - 2175, February, 1992.
3. Young, C. W. "Depth Prediction for Earth-Penetrating Projectiles," J. of the Soil Mechanics and Foundations Division, ASCE, 95(SM3), 803 - 817, 1969.

4. Cook, R. D., Malkus, D. S., and Plesha, M. E., "Concepts and Applications of Finite Element Analysis," John Wiley and Sons, New York, 1989.
5. Cook, R. D. and Young, W. C. "Advanced Mechanics of Materials," Macmillan Publishing Company, New York, 1985.

Table 1 Contents of *penetrat.txt* Data File.

{	
pene_name\$	PENETRATOR NAME
weight#	PENETRATOR WEIGHT
numseg%	NUMBER OF SEGMENTS IN PENETRATOR
seg_length#(i%)	⇒ numseg% of these records SEGMENT LENGTH
	FORE END CROSS SECTIONAL AREA, INERTIA, OUTSIDE RADIUS
seg_area#(1, i%)	seg_inertia#(1, i%) seg_r#(1, i%) ⇒ numseg% of these records
	AFT END CROSS SECTIONAL AREA, INERTIA, OUTSIDE RADIUS
seg_area#(2, i%)	seg_inertia#(2, i%) seg_r#(2, i%) ⇒ numseg% of these records
nose_type\$	NOSE TYPE - OGIVE OR CONE
yield_stress#	YIELD STRESS
e#	ELASTIC MODULUS
per_elong#	PERCENT ELONGATION
}	

Table 2 Contents of *target.txt* Data File

{	
target_name\$	TARGET NAME
num_layers%	NUMBER OF LAYERS IN TARGET
	MATERIAL NUMBER, PENETRABILITY, THICKNESS
matl_num%(i%)	s#(i%) thick%(i%) ⇒ num_layers% of these records
}	

Table 3 Contents of *config.txt* Data File.

pene_name\$	
weight#	
numseg%	
seg_length#(i%)	⇒ numseg% of these records
seg_area#(1, i%)	seg_inertia#(1, i%) seg_r#(1, i%) ⇒ numseg% of these records
seg_area#(2, i%)	seg_inertia#(2, i%) seg_r#(2, i%) ⇒ numseg% of these records
nose_type\$	
yield_stress#	
e#	
per_elong#	
target_name\$	
num_layers%	
matl_num%(i%)	s#(i%) thick%(i%) ⇒ num_layers% of these records
v#	INITIAL IMPACT VELOCITY
alpha#	INITIAL ANGLE OF ATTACK
beta#	INITIAL IMPACT ANGLE
dt#	TIME STEP SIZE
run_title\$	RUN TITLE
prnt_freq%	ITERATION OUTPUT FREQUENCY
el_per_seg%	NUMBER OF FINITE ELEMENTS PER SEGMENT
calc_loc#	LOCATION IN PENETRATOR FOR MONITORING STRESSES, VELOCITIES, ETC.

Table 4 Subprograms, Form Files, and Data Files of AMPLL

main_program	⇒ set_model_parameters		
	set_defaults		
	get_user_inputs	⇒ mainmenu.frm	
		check_input_data	
		get_penet_targ_data	⇒ penetrat.txt
			target.txt
			selrecrd.frm
		penet_desc	⇒ penemenu.frm
			peneinfo.frm
			update_penet
		targ_desc	⇒ targinfo.frm
			update_targ
		read_penet	
		read_targ	
	targ_imp_cond	⇒ impacond.frm	
	choose_time	⇒ timestep.frm	
	select_output	⇒ seloutpt.frm	
	last_config		
	save_config	⇒ config.txt	
	delete_record	⇒ derecord.frm	
		ampll.scr	
	prepare_for_run	⇒ penet_char	
		targ_char	
		set_up_elements	⇒ mass_matrix
			areacal
		invert_mass	
		initialize	
		initialize_screen	⇒ viewer.frm
			initialize_plots
		initialize_drawing	⇒ update_drawing
	run_simulation	⇒ new_layer_entered	
		penetration_depth	
		check_layers_penetrated	
		axial_forces	
		lateral_forces	
		external_loads	
		get_global_stiff	⇒ stiffness_matrix
		matrix_mult	
		kinematics	
		update_vectors	
		calculate_stress	
		update_plots	
		update_drawing	
		update_force_plot	
		check_if_finished	
	write_to_file		

Table 5 AMPLL Convergence Study Results

Number of Elements	Time Step Size	Final Velocity (ft/s)	Final Penetrator Angle (deg)	Maximum Percent Elongation
6	DEFAULT	1853.7	72.86	1.19
12	DEFAULT	1836.5	72.19	1.14
18	DEFAULT	1839.2	72.07	1.15
24	DEFAULT	1837.2	72.02	1.15
30	DEFAULT	1831.9	72.00	1.13
12	4xDEFAULT	1836.3	72.17	1.11
12	DEFAULT	1836.5	72.19	1.14
12	DEFAULT/4	1842.9	72.19	1.15

Table 6 Small Penetrator into Thick Concrete Target

Init Velocity (ft/s)	Init Penet Angle (deg)	Init Ang of Attack (deg)	Final Vel (ft/s)	Final Penet Angle (deg)	% Elong. (yield = .67)
2150	90	0	470	90.0	0.63
2150	77	13	< 40	50.5	10.1
2650	90	0	1289	90.0	0.69
2650	87	3	1214	78.7	3.17

Table 7 Large Penetrator into Thick Concrete Target

Init Velocity (ft/s)	Init Penet Angle (deg)	Init Ang of Attack (deg)	Final Vel (ft/s)	Final Penet Angle (deg)	% Elong. (yield = .57)
1900	88	0	1487	87.97	0.32
1900	86	2	1479	81.05	1.17

**DEBRIS CLOUD MATERIAL CHARACTERIZATION FOR HYPERVELOCITY
IMPACTS OF MULTI-MATERIAL ROD PROJECTILES**

William P. Schonberg

Associate Professor

Civil & Environmental Engineering Department

University of Alabama in Huntsville

Huntsville, Alabama 35899

Final Report for:

Summer Faculty Research Program

Wright Laboratory

Sponsored by:

Air Force Office of Scientific Research

Bolling Air Force Base, Washington, D.C.

September 1993

DEBRIS CLOUD MATERIAL CHARACTERIZATION FOR HYPERVELOCITY IMPACTS OF MULTI-MATERIAL ROD PROJECTILES

**William P. Schonberg
Associate Professor
Civil & Environmental Engineering Department
University of Alabama in Huntsville
Huntsville, Alabama 35899**

Abstract

In kinetic energy weapon impacts, one or more debris clouds are created during the perforation of a target outer wall. These debris clouds expand as they move through target voids and eventually impact interior components of the target. Depending on the engagement conditions and the properties of the projectile and target materials, these debris clouds can contain solid, melted, and vaporized material. To accurately predict principle damage mechanisms and in turn the damage and break-up of targets engaged by kinetic energy weapons, the percentages of debris cloud material in each of these three states of matter must be determined. This report presents a methodology to calculate 1) the amount of debris cloud material that is solid, molten, and vaporous, 2) the debris cloud leading edge, trailing edge, center-of-mass, and expansion velocities, and 3) the angular spread of the debris cloud material. The predictions of the method are compared against empirically-based lethality assessment scheme predictions and against numerical and experimental results.

DEBRIS CLOUD MATERIAL CHARACTERIZATION FOR HYPERVELOCITY IMPACTS OF MULTI-MATERIAL PROJECTILES

William P. Schonberg, PhD

INTRODUCTION

The response of an aerospace target to a kinetic energy weapon (KEW) impact can be said to consist of two basic types: 'local response' and 'global response'. For KEW loadings, material damage associated with local response occurs very quickly (i.e. within the first 30-40 μ sec) and is limited to a volume near the impact location. Global response can refer to any one of a number of global phenomena that occur over a longer period of time, under less intense loads, and over a larger area of the target structure. In KEW impacts, one or more debris clouds are created during the initial impact on the outer wall of a target. These debris clouds expand rapidly as they propagate through target voids and eventually impact one or more interior components of the target. Depending on the impact velocity and the relative material properties of the projectile and target, these debris clouds can contain solid, melted, and vaporized material.

To accurately determine total target damage, a lethality assessment methodology (see, e.g. [1-3]) must include the effects of discrete impacts by solid debris cloud fragments as well as impulsive loadings due to molten and vaporous debris cloud material. Clearly, the amount of debris cloud material in each of the three states of matter must be known to accurately assess total target damage and break-up due to a KEW impact. This report presents a first-principles method to calculate 1) the amount of material in a debris cloud created by a perforating hypervelocity impact that is solid, molten, and vaporous, 2) the debris cloud leading edge, trailing edge, center-of-mass, and expansion velocities, and 3) the angular spread of the debris cloud material. The method presented can be used for single- and multi-material solid rod projectiles impacting an array of target plates. At this point, no adjustments have been made to account for differences in response due to projectile yaw or impact obliquity. The predictions of this methodology are compared against those of empirically-based lethality assessment schemes as well as against numerical and empirical results obtained in previous studies of hypervelocity impact debris cloud formation.

SHOCK LOADING AND RELEASE ANALYSIS

Introductory Comments

Consider the unyawed normal impact of a right circular cylindrical projectile on a thin flat target plate. In this study, the projectile is assumed to be made of one or more perfectly bonded dissimilar layers or disks. Upon impact, shock waves are set up in the projectile and target materials. As the shock waves propagate, the projectile and target materials are heated adiabatically and non-isentropically. The release of the shock pressures occurs isentropically through the action of rarefaction waves that are generated as the shock waves interact with the free surfaces of the projectile and target. This process leaves the projectile and target materials in high energy states and can cause either or both to fragment, melt, or vaporize. The residual material energy is defined as the difference between the total energy of the material in the shocked state and the energy recovered during the release process.

For the projectile and target geometries considered in this study, the shock waves are considered to be planar. This simplification allows one-dimensional relationships to be used to predict the propagation, interaction, and release of shock pressures. The pressures, energies, and densities in the projectile and target materials after the passage of a shock are calculated using the three one-dimensional shock-jump conditions, a linear relationship between the shock wave speed and particle velocity in each material, and continuity of pressure and velocity at all projectile and target interfaces. To calculate the release of the projectile and target materials from their respective shocked states, an equation-of-state (EOS) is needed.

To keep the analysis relatively simple, the Tillotson EOS [4] was used in this study.

The Tillotson Equation-of-State

In its original form, the Tillotson EOS has two parts. The first part applies when the material is in compression regardless of the internal energy (i.e. for $V < V_0$ and for all $E > 0$) and in the small region of expansion in which $V_0 < V < V_s$ provided that $E_s < E < E_s' = E_s + H_v$ where 'V' is specific volume, E_s is the total energy needed to produce incipient vaporization, and H_v is the latent heat of vaporization. The quantity V_s corresponds to the specific volume of a material that completes its release process with an internal energy $E = E_s$. The second part applies in a highly expanded state (i.e. for $V > V_s$ regardless of internal energy) or if the internal energy is high enough to cause complete vaporization even in a moderately expanded state (i.e. for $V_0 < V < V_s$ and if $E > E_s'$).

In its two-part form, the Tillotson EOS is asymptotically correct in the compression and expansion regimes and is continuous across $V = V_0$ for very high energy impacts. If we examine the two-part Tillotson EOS in more detail, we note that at $V = V_s$, there is an abrupt jump in the release isentrope for moderate impact energies, that is, when $E_s < E < E_s'$. A modification in the form of a 'mixed phase formulation' of the Tillotson EOS was proposed to eliminate this abrupt discontinuity at $V = V_s$ (see, e.g. [5,6]). This modification was motivated by the fact that if $E_s < E < E_s'$ as the isentrope crossed $V = V_0$, then sufficient energy would be present to cause only partial vaporization. Hence, the mixed phase formulation allows for some gaseous expansion in moderately high energy impacts not possible with the original Tillotson EOS.

An alternative means of eliminating the discontinuity in Tillotson EOS when $V > V_s$ and $E_s < E < E_s'$ is by uniformly subtracting the magnitude of the jump at $V = V_s$ from the pressure values calculated when $V > V_s$ [7]. The amount of the jump in the release isentrope is largest if $E = (E_s)^+$ at $V = V_s$ and decreases to zero as $E \rightarrow E_s'$. This jump correction is not intended to replace the mixed phase formulation of the Tillotson EOS, but rather to complement its use in the region $V > V_s$. In this report, the version of the Tillotson EOS in which the jump at $V = V_s$ is eliminated by the uniform subtraction approach is referred to as the Tillotson/SJC formulation while the mixed phase formulation of the Tillotson EOS is referred to as the Tillotson/MPF formulation. Unless otherwise specified, the Tillotson/SJC formulation was used in the remainder of this effort.

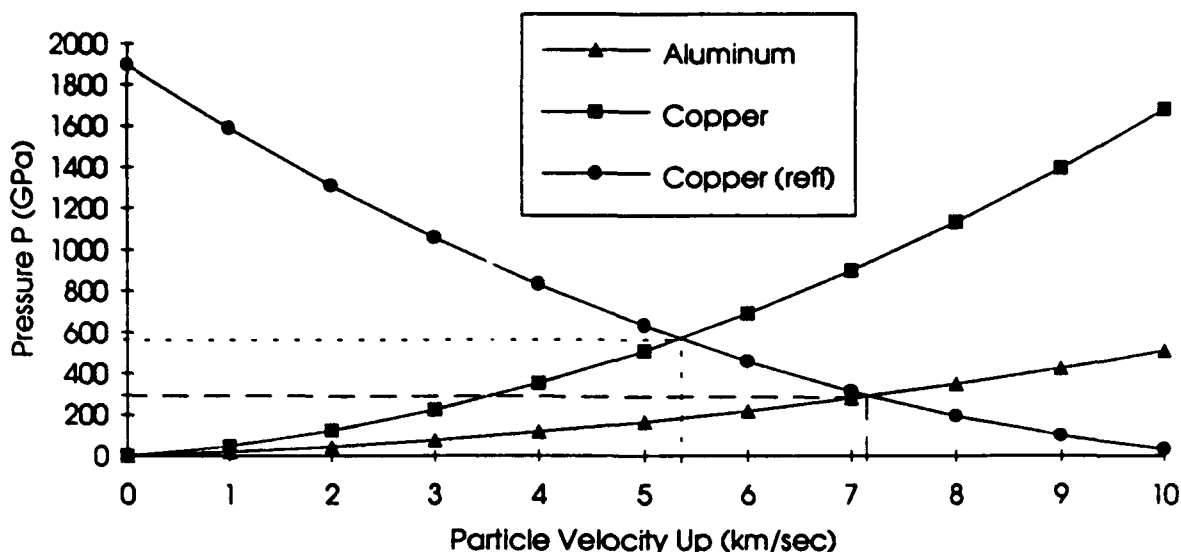
Propagation of Shock Pressures in a Multi-Material Projectile

As the shock wave generated by the impact on the target propagates through the projectile, it encounters the various interfaces between material layers. At each interface between two dissimilar materials, a transmitted shock wave and a reflected wave are generated. The properties of the reflected and transmitted waves are found using a technique based on the method of impedance matching (see, e.g., [8-11]). In this technique, continuity of pressure and particle velocity are enforced at each interface. If the reflected pressure is greater than the incident pressure, then the reflected wave is a shock wave. Conversely, if the reflected pressure is less than the incident pressure, the reflected wave is a rarefaction wave. An example of this technique is illustrated in Figure 1.

Figure 1, which consists of three Hugoniot curves drawn in pressure-particle velocity ($P-u_p$) space, shows what happens when a shock wave traveling in copper at 12 km/sec encounters an aluminum interface. Using the three one-dimensional shock jump conditions and the linear $P-u_p$ relationship for copper, it is found that a 12 km/sec shock wave in copper creates a pressure jump of 568 GPa and induces a particle velocity of 5.34 km/sec in its wake as it moves into copper at ambient conditions. To find the pressures and particle velocities of the reflected and transmitted waves, the Hugoniot for copper in $P-u_p$ space is reflected about the point defined by $u_p = 5.34$ km/sec, $P = 568$ GPa. Its point of intersection with the Hugoniot for aluminum yields the desired pressure (290 GPa) and particle velocity (7.15 km/sec) for the wave reflected back into the copper and transmitted into the aluminum.

Once the pressure and the particle velocity in a subsequent material layer are determined, the one-dimensional shock-jump conditions are used to calculate the specific volume and the energy of the shocked material. This procedure is repeated for each successive projectile material layer. Thus, while the impact conditions are used to define the shocked states in the target and first projectile layer materials, the shocked states in subsequent projectile material layers are obtained using the impedance matching technique just described and illustrated.

Figure 1. P-Up Curves for Copper and Aluminum



Release of Shock Pressures

The target shock pressures are released by the action of the rarefaction wave that is created by the reflection of the shock wave in the target from the target rear free surface. This rarefaction wave propagates through the target material and into the shocked projectile layer materials. In doing so, it also releases the projectile materials from their respective shocked states. For the purposes of the model developed herein, this process of shocking and releasing continues until the rarefaction wave overtakes the shock wave. After this point in time, it is assumed that no additional shocking and release of projectile material occurs. In this manner, the model considers only material that is "fully shocked".

As mentioned previously, in some instances the relative impedance of two adjoining projectile layer materials may result in a shock wave being reflected back into a projectile material layer that has been shocked and released. However, it is assumed for the purposes of this study that this reflected shock wave does not "re-shock" the projectile material and that the material into which it is reflected remains released. This assumption is reasonable since as the reflected shock wave moves back into the released layer material, it continuously creates rarefaction waves at the projectile edge free surfaces which release any material shocking it produces. Thus, in the model developed herein, any projectile layer material that has been shocked and released will remain released regardless of the nature of the wave reflected from its interface with an adjoining layer.

DEBRIS CLOUD MATERIAL CHARACTERIZATION

Computing the Percentages of Solid, Liquid, and Vaporous Debris Cloud Material

Once the residual internal energies in the shocked and released portions of the projectile and target

materials are obtained, the percentages of the various states of matter in the resulting debris cloud are estimated. The procedure used requires knowledge of the materials' solid and liquid specific heats (C_{ps}, C_{pl}), their melting and boiling temperatures (T_m, T_v), and their heats of fusion and vaporization (H_f, H_v) in addition to the materials' internal residual energies (E_r).

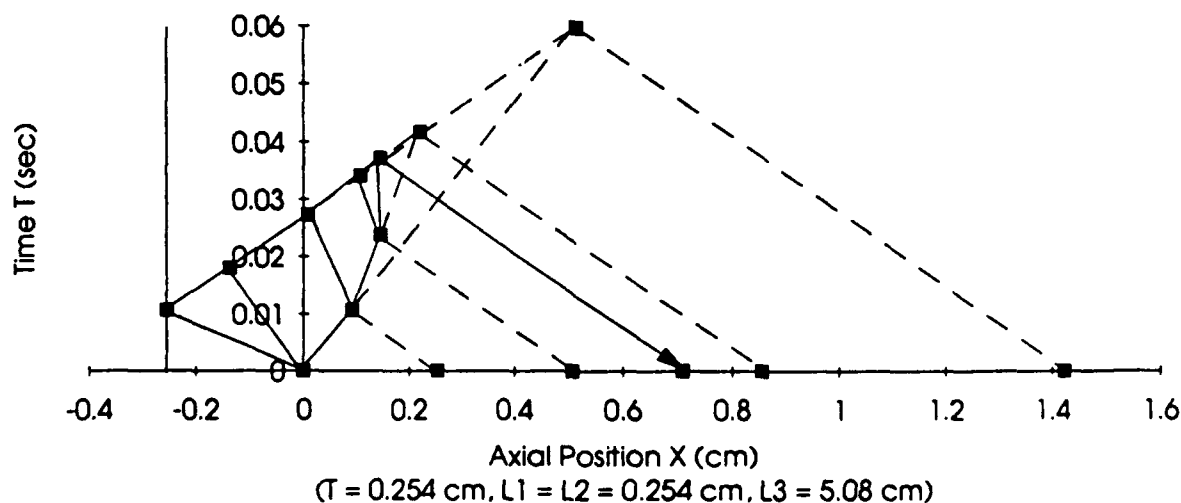
If $E_r < C_{ps}T_m$, then all of the shocked and released materials is considered to remain in a solid state. If $C_{ps}T_m < E_r < C_{ps}T_m + H_f$, then the quantity $(E_r - C_{ps}T_m)/H_f$ represents the fraction of the shocked and released material that was melted, while the remaining shocked and released material is assumed to be in solid form. If $C_{ps}T_m + H_f < E_r < C_{ps}T_m + H_f + C_{pl}(T_v - T_m)$, then all of the shocked and released material is considered to be in a liquid state. If $C_{ps}T_m + H_f + C_{pl}(T_v - T_m) < E_r < C_{ps}T_m + H_f + C_{pl}(T_v - T_m) + H_v$, then the quantity $[E_r - (C_{ps}T_m + H_f + C_{pl}(T_v - T_m))]/H_v$ represents the fraction of the shocked and released material that is vaporized, while the remaining shocked and released material is assumed to be in liquid form. If $C_{ps}T_m + H_f + C_{pl}(T_v - T_m) + H_v < E_r$, then all of the shocked and released material is considered to be vaporized.

Computing the Masses of the Solid, Liquid, and Vaporous Debris Cloud Material

To calculate the masses of the various states of the projectile and target materials in the debris cloud, the amounts of shocked and released target and projectile material need to be determined. These quantities are obtained by determining the locations in the target plate and in the projectile where the rarefaction waves overtake the corresponding shock wave. These locations are found using a technique derived from that used for single-material projectiles [12].

Figure 2 shows the results obtained when this technique is applied to a 3-layer projectile impacting an aluminum plate at 6 km/sec. The projectile materials, their stacking sequence, and the geometry of the impact are also given in Figure 2. As can be seen from Figure 2, the original rarefaction wave emanating from the target rear surface overtakes the shock wave in the projectile at a distance of approximately 0.71 cm from the leading edge of the undisturbed projectile. This implies that at the impact velocity considered, the first two projectile layers (i.e. the aluminum and the steel) are completely shocked and released as is the first 0.202 cm of the third projectile layer (i.e. the tungsten).

Figure 2. X-T Diagram for a 6 km/sec Impact
|AL| ← |AL|ST|W|



It is the material through which both the shock wave and the release wave travel that is shocked and re-

leased and which is therefore either melted or vaporized, depending on the impact velocity. Any material beyond the point at which the rarefaction wave overtakes the shock wave is assumed, for the purposes of this study, not to be shocked and to remain in a solid matter state. If the point at which the release wave overtake the shock wave is beyond the thickness of the target plate or the length of the projectile, then all of the target and/or projectile material is shocked and released. Thus, according to the assumptions and definitions presented herein, the remaining 0.306 cm of the tungsten layer in the projectile corresponding to the impact depicted in Figure 2 is unshocked and unreleased.

In calculating the amount of target material subject to shock loading and release, it is assumed that the shocked target material comes from an area of the target equal to the presented area of the projectile [13]; the remaining material ejected from the target in the creation of the target plate hole is assumed to remain in a solid, albeit undoubtedly fragmented, state. Furthermore, it is also assumed that the depth of the shocked target material extends completely through the target thickness. Were this not the case, then other target failure modes, such as plugging, for example, might come into play. This in turn would seriously compromise the validity of the assumptions made in the development of this debris cloud model. A direct consequence of this assumption is that the model developed herein is not valid for "thick" target plates, i.e. those plates in which $T/D \geq 0.75$.

Once the projectile and target mass contributions to the debris cloud and the fractions of these masses that are shocked and released are obtained, the masses of the target and projectile materials in each of the three states of matter are computed by multiplying each matter state percentage by the appropriate total shocked and released mass. The mass of the solid shocked and released material (if any) is then added to the mass of the unshocked material (if any) to obtain the total mass of the solid material component.

A limitation of this procedure is the assumption that no further projectile loading and unloading occurs beyond the point where the release waves overtake the corresponding shock wave. This is not completely correct since the shock wave does not simply cease to exist once it is overtaken by a rarefaction wave. Rather, its magnitude decreases over a finite amount of time and a finite extent of material. Some additional projectile material will be heated and possibly melted until the strength of the shock wave diminishes to a point below which melt no longer occurs.

DEBRIS CLOUD VELOCITY CHARACTERIZATION

Introductory Comments

In characterizing the velocities of the debris cloud created by a hypervelocity impact on a thin plate, there are two possibilities that need to be considered. First, all of the projectile material is shocked and released. In this case, the debris cloud consists of the projectile and target material that is shocked and released and the additional fragmented target material that is ejected from the target plate during the perforation process but, according to the assumptions made herein, is not shocked and released. In the debris cloud model developed herein, all of this material is allowed to move axially and expand radially. The quantities of interest in this case are therefore the debris cloud leading edge, center-of-mass, trailing edge, and expansion velocities, that is, v_f , v_i , v_r , and v_{exp} , respectively. Second, some of the projectile material remains, according to the assumptions employed herein, unshocked. While it would not be appropriate to call this unshocked projectile material a "residual projectile mass", it is reasonable to presume that this material is less severely stressed than that which is fully shocked and then released. Hence, it is also reasonable to presume that if there is any unshocked projectile material, then it does not significantly expand radially as it moves axially. In this case, the debris cloud consists of shocked and released target and projectile materials and the additional unshocked fragmented target material. The quantities of interest are the debris cloud leading edge, center-of-mass, and expansion velocities, that is, v_f , v_i , and v_{exp} , respectively, and the velocity of the remaining unshocked projectile material, v_{pr} . Note that due to the presence of the unshocked projectile mass, there is no debris cloud trailing edge for which to calculate a velocity.

It is noted that the equations developed in the subsequent section are presented in their most general form. They can be applied directly to a single-material projectile and adapted easily to apply to the impact of a multi-material projectile.

Debris Cloud Velocity and Spread Calculations

In both of the cases described previously, the debris cloud leading edge velocity v_f is approximated by u_{fst} , the velocity imparted to the target rear surface by the reflection of the target material shock wave. As in [14], u_{fst} is taken to be equal to the sum of the particle velocity in the target material due to the passage of the shock wave, u_{pt} , and the particle velocity due to the passage of the rarefaction wave in the target material, u_{rt} , created by the reflection of the shock wave from the target rear surface. Also common to both cases is that the half-angle measuring the spread of the debris cloud material is given by

$$\theta = \tan^{-1}(v_{exp}/v_i) \quad (1)$$

What distinguishes the two types of debris clouds mathematically is the manner in which v_i , v_{exp} , and v_r or v_{pr} are calculated. When all of the projectile material is shocked and released, then:

$$v_r = v_o - u_{fsp}; \quad (2)$$

v_i is obtained from momentum conservation before and after the impact event, that is,

$$v_i = m_p v_o / m_{dc}; \quad (3)$$

and, v_{exp} is obtained from the application of energy conservation before and after the impact event, that is,

$$m_p v_o^2 / 2 = E_{pr} + E_{tr} + m_{dc} v_i^2 / 2 + m_{dc} v_{exp}^2 / 2 \quad (4)$$

where $m_{dc} = m_p + m_t$ is the total debris cloud mass, m_p is the projectile mass, m_t is the total target hole-out mass, E_{pr} and E_{tr} are the internal projectile and target energies, respectively, that have gone into heating the projectile and target materials, and $u_{fsp} = u_{pp} + u_{rp}$ is the velocity of the rear free surface of the projectile. As in the case of u_{fst} , u_{fsp} is taken to be equal to the sum of the particle velocity in the projectile material due to the passage of the shock wave, u_{pp} , and the particle velocity due to the passage of the rarefaction wave in the projectile material, u_{rp} , created by the reflection of the shock wave from the projectile rear free surface.

In the event when not all of the projectile material is shocked and released, then v_i , v_{exp} , and v_{pr} are obtained through the solution of the following three simultaneous equations:

$$v_{exp} = v_f - v_i; \quad (5)$$

$$m_p v_o = m_{pr} v_{pr} + m_{dc} v_i; \quad (6)$$

$$m_p v_o^2 / 2 = E_{pr} + E_{tr} + m_{pr} v_{pr}^2 / 2 + m_{dc} v_i^2 / 2 + m_{dc} v_{exp}^2 / 2 \quad (7)$$

where in this case $m_{dc} = m_p + m_t - m_{pr}$ and m_{pr} is the mass of the unshocked projectile material. If the solution of the above system of equations results in a situation where there is insufficient energy available for debris cloud expansion or motion of the unshocked portion of the projectile material, then the leading edge velocity is reduced until some kinetic energy does become available.

DEBRIS CLOUD CHARACTERIZATION SCHEME VALIDATION

Single-Material Projectiles

Comparison with Experimental Results and 1-D Hydrocode Predictions

Debris cloud velocity values were calculated using DEBRIS3 (a FORTRAN77 program that implements the debris cloud characterization scheme developed herein) and compared against experimental results and one-dimensional hydrocode predictions obtained from a previous study of debris cloud formation and

growth using thin copper disks ($L/D=0.3$) impacting thin aluminum plates [14]. As can be seen in Table 1, the predictions of DEBRIS3 for v_f , v_i , and v_r were in excellent agreement with those of the 1-D hydrocode and the experimental results.

Table 1. Comparison of DEBRIS3 with Empirical Results and 1-D Hydrocode Predictions

			v_f/v_o			v_r/v_o			v_i/v_o			v_{exp}/v_o	
T	m_p	v_o	(1)	(2)	(3)	(1)	(2)	(3)	(1)	(2)	(3)	(1)	(3)
(mm)	(gms)	(km/s)											
Effect of Target Thickness													
1.0	1.0	6.39	1.44	1.41	1.40	0.91	0.89	0.89	0.36	0.34	0.34	0.24	0.27
1.5	1.0	6.36	1.44	1.41	1.40	0.88	0.83	0.84	0.36	0.34	0.34	0.24	0.32
2.0	1.0	6.38	1.42	1.41	1.40	0.83	0.79	0.79	0.35	0.34	0.33	0.27	0.36
2.5	1.0	6.53	1.46	1.41	1.40	0.79	0.76	0.75	0.35	0.34	0.33	0.27	0.38
Effect of Impact Velocity													
1.5	1.0	3.45	1.37	1.39	1.39	0.86	0.84	0.84	0.43	0.36	0.36	0.23	0.33
1.5	1.0	4.85	1.43	1.40	1.39	0.87	0.84	0.84	0.39	0.35	0.35	0.23	0.33
1.5	1.0	6.36	1.44	1.41	1.40	0.88	0.83	0.84	0.36	0.34	0.34	0.24	0.32
Effect of Projectile Mass													
2.0	1.0	6.38	1.41	1.41	1.40	0.83	0.79	0.79	0.35	0.34	0.34	0.27	0.36
2.9	3.0	5.66	1.44	1.40	1.40	0.82	0.80	0.79	—	0.34	0.34	0.23	0.36
4.4	10.0	5.12	1.40	1.40	1.39	0.83	0.80	0.79	0.36	0.35	0.35	0.22	0.37

(1) Experimental Results [14] (2) 1-D Hydrocode Predictions [14] (3) DEBRIS3 Predictions

Over all the cases considered, the average difference between the predictions of DEBRIS3 for v_f , v_i , and v_r and the corresponding experimental results was approximately 4% with a standard deviation of approximately 3%. However, the predictions of DEBRIS3 for v_{exp} exceeded the experimental results by an average of approximately 40% with a standard deviation of approximately 15%. This discrepancy may have been due to the fact that the expansion velocity measured in [14] was that of the heavier copper component of the debris cloud while the expansion velocity calculated by DEBRIS3 was based on both debris cloud materials.

Comparison with CTH and Lethality Assessment Scheme Predictions

Figure 3 presents a comparison of the predictions of DEBRIS3, the hydrocode CTH [15], and the semi-empirical code FATEPEN2 [1] for debris cloud leading edge velocity v_f for steel cylinders ($L/D=1$) normally impacting thin aluminum target plates ($T/D=0.125$). As is evident in Figure 3, the predictions of DEBRIS3 compare favorably with those of FATEPEN2 in the velocity regime for which FATEPEN2 was designed to be used (i.e. less than approximately 5 to 6 km/sec). A quick calculation reveals that the difference between the DEBRIS3 predictions of leading edge velocity and those of FATEPEN2 was approximately 26% of the DEBRIS3 values with a standard deviation of approximately 4% for the impact velocities considered. One reason for this difference could be the fact that the mass of the impacting projectile considered (approximately 1555 grains \approx 100 gms) exceeded the maximum value of projectile masses used to develop the FATEPEN2 equations.

The CTH values plotted in Figure 3 are average values of the velocities of three Lagrangian station points along the impact centerline within the aluminum target plate. These average values differed from the corresponding minimum and maximum values by approximately 0.5 km/sec at an impact speed of 2 km/sec and 3.0 km/sec at an impact speed of 14 km/sec. Inspection of Figure 3 also reveals that there is excellent agreement between the predictions of DEBRIS3 and CTH for debris cloud leading edge velocity. The average difference between the DEBRIS3 and CTH values was approximately 4% of the DEBRIS3 values

with a standard deviation of approximately 3%.

Figure 3. Debris Cloud Leading Edge Velocity Comparison
Steel Projectile ($L/D=1.0$), Aluminum Plate ($T/D=0.125$)

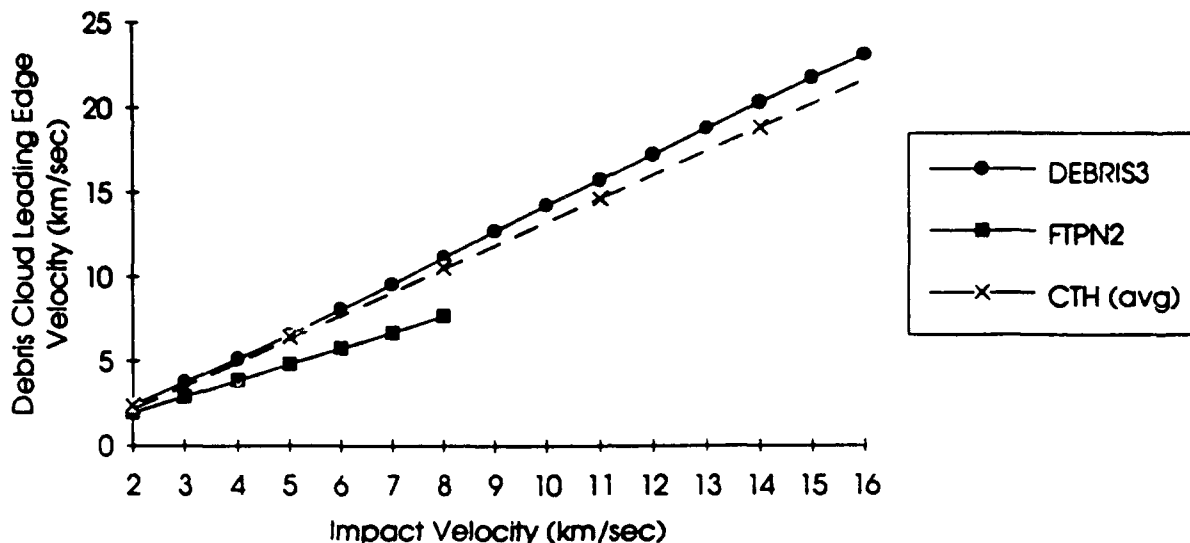
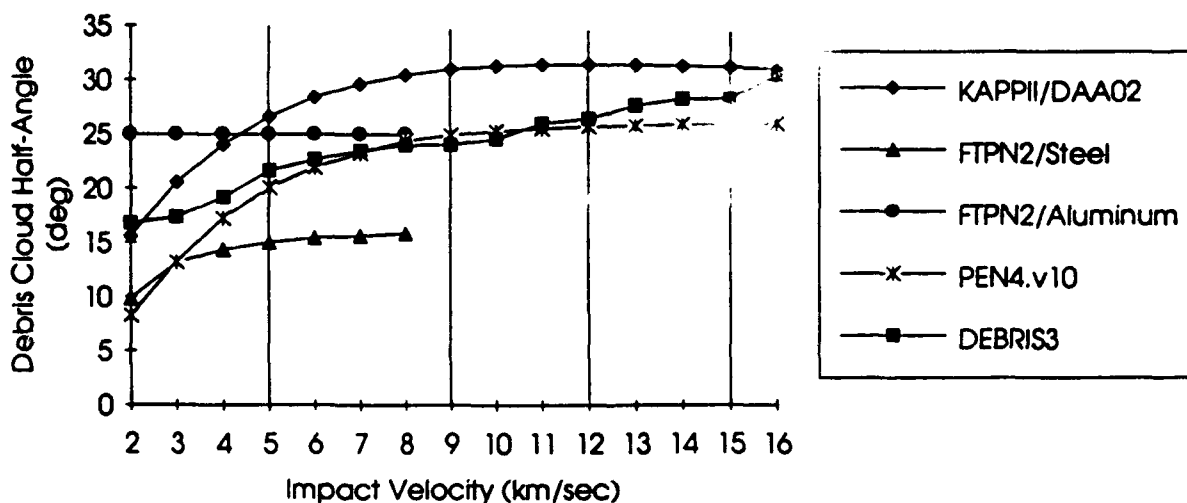


Figure 4 presents a comparison of the predictions of DEBRIS3, CTH, FATEPEN2 [1], PEN4.v10 [2], and KAPPII (version 1.1) [3] for debris cloud half-angle for steel cylinders ($L/D=1.0$) normally impacting thin aluminum target plates ($T/D=0.125$).

Figure 4. Debris Cloud Half-Angle Comparisons
Steel Projectile ($L/D=1.0$), Aluminum Plate ($T/D=0.125$)



In Figure 4, the average difference between the predictions of KAPPII and DEBRIS3 was approximately 18% of the DEBRIS3 value with a standard deviation of approximately 10%; the average difference between PEN4.v10 and DEBRIS3 was approximately 6% with a standard deviation of nearly 7%. Based

on these results, it may be argued that the predictions of DEBRIS3 agree fairly well with those of KAPP11 and PEN4. However, comparing the differences between DEBRIS3 and FATEPEN2 was somewhat more difficult because FATEPEN2 distinguishes between target debris spread and projectile debris spread while DEBRIS3 does not. In FATEPEN2, the target debris half-angle is fixed at 25° while the projectile debris half-angle is based on material properties, impact conditions, etc.

It is interesting to note that unlike the smooth curve predictions of KAPP11, FATEPEN2, and PEN4, the curve representing the growth of the debris cloud spread generated by DEBRIS3 contains numerous kinks. In particular, the impact velocities corresponding to the vertical lines in Figure 4 also correspond to impact velocities at which significant changes occur in the way the initial kinetic energy of the projectile is distributed to various competing mechanical and thermal processes during the impact event. These features of the curve predicted by DEBRIS3 are discussed in the following paragraph.

For the impact considered in Figure 4, between 2 and 5 km/sec, increasing the impact velocity resulted in a steady increase in debris cloud spread. However, at 5 km/sec, the target material began to melt. As a result, some of the additional kinetic energy of the initial impact provided as impact velocity increased beyond 5 km/sec was used up by the target material state change and was not available for debris cloud expansion. Thus, the rate of debris cloud expansion slowed, and the slope of the curve decreased as impact velocity increased beyond 5 km/sec. Between 8 and 9 km/sec, the projectile material began to melt and the target material began to vaporize. This further decreased the rate of debris cloud expansion. However, once the projectile was completely melted, the rate of debris cloud expansion increased. Near 12 km/sec, the projectile material began to experience vaporization. The rate of debris cloud expansion slowed down only slightly because by now the debris cloud consisted of a significant amount of hot vaporous material. By 15 km/sec, the debris cloud was nearly all vapor causing its rate of expansion to increase dramatically.

Multi-Material Projectiles

Introductory Comments

The validity of the multi-material modeling capability of DEBRIS3 was assessed by comparing the predictions of DEBRIS3 against experimental and numerical data. The experimental data and the results of one series of hydrocode simulations were obtained from a study that analyzed the effectiveness of layered projectiles against re-entry vehicle-type targets. The results of a second series of hydrocode runs were obtained using the CTH hydrocode specifically for the present investigation. The results of this validation exercise are presented in the next three sections.

Comparison with Experimental Results

Three high speed impact tests were performed at 4 km/sec using three different equal-weight projectiles [16]. The first was a solid 7.5 gm TA10W (i.e. a tantalum alloy with 10% tungsten) sphere, while the second and third projectiles were 7.5 gm layered spheres with a solid TA10W core surrounded by a steel shell. The outer shell of the second projectile was 1018 steel (i.e. mild strength steel) while that of the third projectile was 4340 steel (i.e. a high strength steel).

In simulating these three impact tests with DEBRIS3, the layered spheres were modeled as cylindrical projectiles with three layers. The middle layer corresponded to the spherical core while the first and third layers represented the outer shell material. The thicknesses of the first and third layer were set equal to the outer shell thickness. The thickness of the inner layer and the diameter of the cylindrical projectile were calculated by setting the inner layer thickness equal to the cylindrical projectile diameter and then solving for the diameter by equating the mass of the cylindrical projectile to the mass of the original layered sphere.

In addition to adapting the geometry of the original projectiles used in the test series to a projectile geometry that was compatible with DEBRIS3, some compromises were also made regarding the projectile and target materials. In the original test series, the target was a 2-D flat plate representation of a half-scale

re-entry vehicle, i.e. a layer of silica phenolic bonded to a thin layer of aluminum. Since the current version of DEBRIS3 does not allow for multi-material targets, the targets used in the DEBRIS3 impact simulations did not have the outer layer of silica phenolic. In addition, while a witness block was placed behind the initial multi-layer target plate in the experimental tests to record the damage of the perforating projectile and target debris, DEBRIS3 was not developed to have a predictive capability for damage to subsequent witness blocks or plates. Finally, whereas one of the original projectile materials was a tantalum alloy with 10% tungsten, the corresponding material in the DEBRIS3 impact simulations was pure tantalum.

As expected, the simplifications described in the previous two paragraphs precluded any direct comparison of the predictions of DEBRIS3 and the experimental results. However, it was possible to make qualitative comparisons of the DEBRIS3 predictions and the actual test results because the simplifications maintained some similarity between the original test materials and configurations and the materials and geometries of the DEBRIS3 impact simulations. These qualitative comparisons became possible after the DEBRIS3 predictions were analyzed to infer the relative severity of the damage levels that could have been expected on subsequent witness plates had they been placed behind the initial target plate.

First, DEBRIS3 predicted that a significant portion of the target material would be melted when impacted by the solid tantalum sphere. Alternatively, when impacted by the layered projectiles, DEBRIS3 predicted that the target material would be shocked and released but would return to a solid state of matter. This indicates that the target material would probably be fragmented but not melted. Second, DEBRIS3 predicted that the kinetic energy of the remaining unshocked projectile material would be greatest for the layered projectile with a tantalum core and a high-strength steel shell and would be least for the solid tantalum projectile. Taken together, these two features indicate that the cylindrical projectiles simulating the layered sphere projectiles would probably inflict more severe damage on a witness plate behind the target than would the cylindrical projectile simulating the solid TA10W projectile. This agrees with the actual test results, which state that among the three impact tests, the crater depth and volume in the witness block behind the target impacted by the projectile with a TA10W core and a 4340 steel shell were greatest and those in the block behind the target impacted by the solid TA10W projectile were least.

Comparison with Hydrocode Predictions -- First Series

The first series of numerical runs consisted of two sets of three high speed impacts at 11 km/sec using the SOIL hydrocode [16]. The projectiles used were similar in construction to those in the previously discussed experimental tests (i.e. one solid and two layered spheres in each test set). The major distinguishing feature between the two sets of impact simulations in this series is the mass of the projectiles: 45 gm projectiles were considered in the first set, while 5 gm projectiles were used in the second set. In both sets of simulations, the solid sphere was made out of tungsten as was the core in the layered spheres; the shells of the layered spheres were made out of different strength steels. In modeling the SOIL impact simulations with DEBRIS3, simplifications in the projectile and target geometries were made similar to those in the previous section. As a result, the following comparisons are again only qualitative in nature.

As in the DEBRIS3 simulations of the experimental tests, the DEBRIS3 simulations of the SOIL runs indicated that the solid projectiles would melt some of the target plate material whereas the layered projectiles would not. In addition, the kinetic energies of the unshocked projectile materials from the layered projectiles greatly exceeded those of the unshocked projectile materials from the solid projectiles. These two features again indicate that the layered projectiles would inflict more severe damage on a witness plate behind the target than would an equal-weight solid projectile.

Interestingly enough, while the general trends observed in the DEBRIS3 impact simulations agreed with the hypothesis that motivated the layered projectile investigation, they disagree with the actual numerical results obtained as part of that investigation. The corresponding SOIL runs predicted that the witness block damage due to the impacts of the solid projectiles would be approximately the same as the damage

caused by the layered projectiles. Apparently, either the impact and/or geometric parameters used in the SOIL runs masked subtle differences in damage levels resulting from the solid and layered projectile impacts and prevented them from being discernible, or the DEBRIS3 modeling of the projectile and target geometries over-emphasized some impact phenomenology that produced some differences in response that would otherwise have been negligible.

In any event, it is apparent that additional testing of multi-material projectile that are compatible with the modeling capabilities of DEBRIS3 are required to fully validate the predictive capabilities of DEBRIS3. As an intermediate step, several CTH runs were performed using projectile and target geometries that were ideally suited for and matched to the capabilities of DEBRIS3. The results of these runs and how they compared with the predictions of DEBRIS3 are discussed in the next section.

Comparison with Hydrocode Predictions -- Second Series

Results and General Comments

In the second series of hydrocode runs, four high speed impact simulations were performed at 10 km/sec using CTH with multi-material cylindrical projectiles. The projectile diameter and target plate thickness were kept constant at 2.54 cm and 0.3175 cm, respectively. In the first two runs, the layers were relatively "thin" (i.e. $L/D=0.1$ each), while in the second two runs, the projectile layers were relatively "thick" (i.e. $L/D=1.0$ each). In the first and third runs, an aluminum target plate was impacted by a projectile with an aluminum leading layer, a 4340 steel middle layer, and a tungsten rear layer. In the second and fourth runs, the order of the projectile materials was reversed. A detailed description of the impact and geometric parameters are given in Table 2; the results of the DEBRIS3 impact simulations and the corresponding CTH results are given in Table 3. In Tables 2 and 3, a '1' refers to the leading layer of the projectile while a '3' refers to the rear-most projectile layer.

Table 2. Geometric and Impact Parameters for DEBRIS3 and CTH Comparison Runs

Run No.				
	(1)	(2)	(3)	(4)
V (km/sec)	10.0	10.0	10.0	10.0
D (cm)	2.54	2.54	2.54	2.54
T (cm)	3.175	3.175	3.175	3.175
Target Material	Aluminum	Aluminum	Aluminum	Aluminum
Layer 1 Material	Aluminum	Tungsten	Aluminum	Tungsten
Layer 2 Material	4340 Steel	4340 Steel	4340 Steel	4340 Steel
Layer 3 Material	Tungsten	Aluminum	Tungsten	Aluminum
L ₁ (cm)	0.254	0.254	2.54	2.54
L ₂ (cm)	0.254	0.254	2.54	2.54
L ₃ (cm)	0.254	0.254	2.54	2.54
L/D	0.3	0.3	3.0	3.0
Proj. Mass (gms)	38.24	38.24	382.40	382.40

The predictions of CTH and DEBRIS3 regarding the state of the target and projectile layer materials were

compared quantitatively and qualitatively. To facilitate quantitative comparisons of material end-states, average densities were computed for each material layer using the DEBRIS3 and CTH results. The DEBRIS3 values were obtained by multiplying the mass of shocked and released material by its final density, adding to it the product of the density of the unshocked material and its mass, and then dividing by the total mass of the material layer under consideration. The CTH values are simply average values through the particular layer thickness and were obtained from density history plots along the centerline.

A feature common to all four impact simulations and evident in Table 3 is that the average target material densities predicted by DEBRIS3 were significantly higher than those predicted by CTH. However, the reason for this is that they include the solid component of target material not considered to be shocked and released by the impact (i.e. the remainder of the ejected target material not swept out by the projectile). The contributions of the solid material component to the average density of the target material are significant considering that they constitute approximately 90% of the target material in the debris cloud created by the impact. If the target hole diameter had been set equal to the projectile diameter (which is not an unreasonable assumption for the impact velocity and geometries considered), then there would not have been any unshocked target material and it is reasonable to presume that the average densities of the target material would have been much closer to the CTH values.

Table 3. Comparison of DEBRIS3 and CTH Impact Response Predictions

Run No.								
	(1)		(2)		(3)		(4)	
	DEBRIS3	CTH	DEBRIS3	CTH	DEBRIS3	CTH	DEBRIS3	CTH
V_f (km/sec)	10.65	14.27	17.36	14.20	10.65	11.08	16.26	14.28
θ (deg)	36	32	34	27	48	37	21	22
ρ_{targ} (gm/cm ³)	2.56	0.21	2.36	-0.0	2.63	1.33	2.52	-0.0
ρ_1 (gm/cm ³)	2.02	-0.0	18.52	0.67	2.22	2.25	18.98	9.20
ρ_2 (gm/cm ³)	7.04	0.17	7.25	5.50	7.83	8.53	7.83	6.94
ρ_3 (gm/cm ³)	18.42	0.97	2.48	1.41	19.17	17.19	2.71	3.39

Debris Cloud Leading Edge Velocity and Half-Angle Spread Comparisons

The differences between the DEBRIS3 predictions of debris cloud leading edge velocity and the corresponding CTH values in Runs No. 1-4 are 25.4%, 22.3%, 3.9%, and 13.9%, respectively, of the CTH values. The somewhat large differences in Runs No. 1 & 2 may be explained by the following considerations. In the characterization scheme employed by DEBRIS3, the target shock loading and release analysis used to obtain the debris cloud leading edge velocity is truly one-dimensional. That is, it is performed using only the leading projectile layer and the target material; anything behind the first projectile material layer is ignored. In the case of thick projectile layers, the use of one-dimensional equations is appropriate because the rear layers of the projectile are sufficiently far from the impact site so as not to affect the magnitude of the velocity of the target rear free surface. However, in the case of the thin

projectile layers, the second and third projectile layers are close enough to the projectile-target interface to influence the shock and release process in the target material and the resulting velocity of the target rear free surface. CTH, being a 3-D hydrocode, is apparently sensitive to these effects while DEBRIS3, being a first principles code, is not. As a result, the CTH and the DEBRIS3 predictions differ somewhat more in Runs No. 1 and 2 and are more in agreement in Runs No. 3 and 4.

The differences between the DEBRIS3 predictions of debris cloud leading edge velocity and the corresponding CTH values in Runs No. 1-4 are 11%, 26%, 23%, and 5%, respectively, of the DEBRIS3 values. The CTH predictions of debris cloud half-angle were obtained indirectly from debris cloud output plots. In some cases, the precise angles were difficult to determine from the CTH plots because not all of the debris cloud material was retained by CTH and subsequently plotted. If there is a very small fraction of a material in a cell in which more than one material is present, then it is possible for that small fraction of material to generate negative internal energies in that cell. CTH allows the user to set a flag that forces CTH to drop the cell from subsequent calculations in such cases. If this is not done, then in such cases the time-step becomes so small that the impact simulation will be forced to terminate prematurely. Apparently, in Runs No. 2 and 3, CTH dropped a fair amount of cells as the calculations proceeded which in turn produced rather sparse debris clouds. While the agreement between the DEBRIS3 predictions and the CTH values was in general fairly reasonable, this may explain in part why in Runs No. 2 and 3 the DEBRIS3 predictions of the debris cloud half-angle values were significantly higher than the CTH values.

Material Characterization Comparisons: Projectiles with Thin Layers

Although Table 3 indicates that there were significant differences between the material densities predicted by DEBRIS3 and those obtained with CTH, closer examination of the DEBRIS3 and CTH predictions of material state did in fact reveal a qualitative agreement in the results.

For example, the extremely low material densities for Run No. 1 predicted by CTH indicate that the material from the three projectile layers in both cases are in highly expanded states. However, the density of the rear-most portion of the third material layer in Run No. 1 (approximately the last 33%) was nearly 3.5 times that of the forward portion of that layer, indicating that the rear third of the final projectile layer was significantly more dense than the rest of the projectile material. Interestingly enough, for Run No. 1, DEBRIS3 predicted that the first two material layers would be in a liquid state, while the last 25% of the third layer would not be fully shocked. Thus, while the actual density values may have been different (which was not totally unexpected given the relatively simple nature of the physics employed by DEBRIS3), there was some agreement between CTH and DEBRIS3 with regard to the state of the projectile material following the initial impact.

With regard to the target material, CTH predicted that the target material would be in a highly expanded state in Run No. 1 and probably vaporized in Run No. 2; DEBRIS3 predicted that the target material would be completely melted in Run No. 1 while in Run No. 2 it would be partially vaporized as well. Thus, there was again some general agreement between CTH and DEBRIS3 regarding the state of the target material following a hypervelocity impact.

Material Characterization Comparisons: Projectiles with Thick Layers

The projectile material characterizations predicted by DEBRIS3 were again found to agree in a general sense with the post-impact material states predicted by CTH. For example, DEBRIS3 predicted that in both Run No. 3 and Run No. 4 that the second and third projectile layers would remain unshocked while part of the first layer would be shocked and released. The CTH results for Runs No. 3 & 4 clearly showed the third material layers to be relatively undisturbed and the second material layers to be only slightly deformed. These characteristics are also evident in Table 3 where the density values predicted by CTH for the second and third projectile material layers were near ambient values; the densities predicted by

DEBRIS3 for the second and third layers were naturally exactly equal to the respective ambient values due to the assumptions within the DEBRIS3 model.

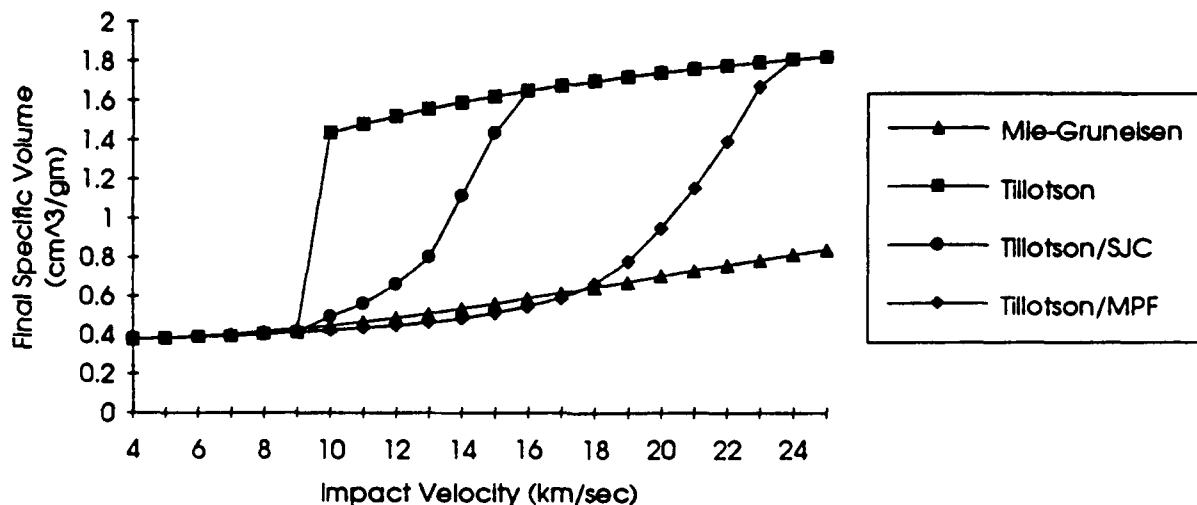
With regard to the first material layer, DEBRIS3 predicted that in Run No. 3 the entire shocked and released portion would be all liquid, whereas the shocked and released portion in Run No. 4 would be a mixture of liquid and solid material. The CTH results for both cases showed that the density of the leading edge of the first layer was approximately 30% of the ambient value, while the density of the rear portion of the leading layer approached the ambient value of the second layer material, indicating a significantly more compressed state than that of the leading edge.

Some interesting features are also evident in the CTH and DEBRIS3 predictions of the state of the target material. In Run No. 3, the average target material density as predicted by CTH is approximately 12% of ambient. This indicates a significant liquid, if not vaporous, component of the target material in the debris cloud. For Run No. 3, DEBRIS3 predicted that 100% of the shocked and released target material would be liquid and that the density of the shocked and released target material would be approximately 75% of ambient. The near-zero value of the target material density as predicted by CTH in Run No. 4 indicates a material state near complete vaporization for the ejected target material while DEBRIS3 predicted that approximately 24% of the shocked and released target material would be in a vapor state and that 76% would be liquid. The density of the shocked and released target material predicted by DEBRIS3 was 40% of the ambient value indicating a highly expanded material state.

COMPARISON OF TILLOTSON EOS FORMULATIONS

Figure 5 illustrates the differences in the final specific volumes obtained in aluminum-on-aluminum impacts using the Tillotson, Tillotson/SJC, and Tillotson/MPF EOS formulations and contrasts these with the results obtained using the Mie-Gruneisen EOS [8]. For impact velocities below approximately 9 km/sec, the results were, as expected, nearly identical. For impact velocities above approximately 24 km/sec, the final values predicted by the Tillotson EOS and the two alternative formulations of the Tillotson EOS overlap and significantly exceeded those predicted by the Mie-Gruneisen EOS due to the gaseous expansion of the released material at those impact velocities.

Figure 5. Aluminum-on-Aluminum Impact: Comparison of Final Specific Volumes



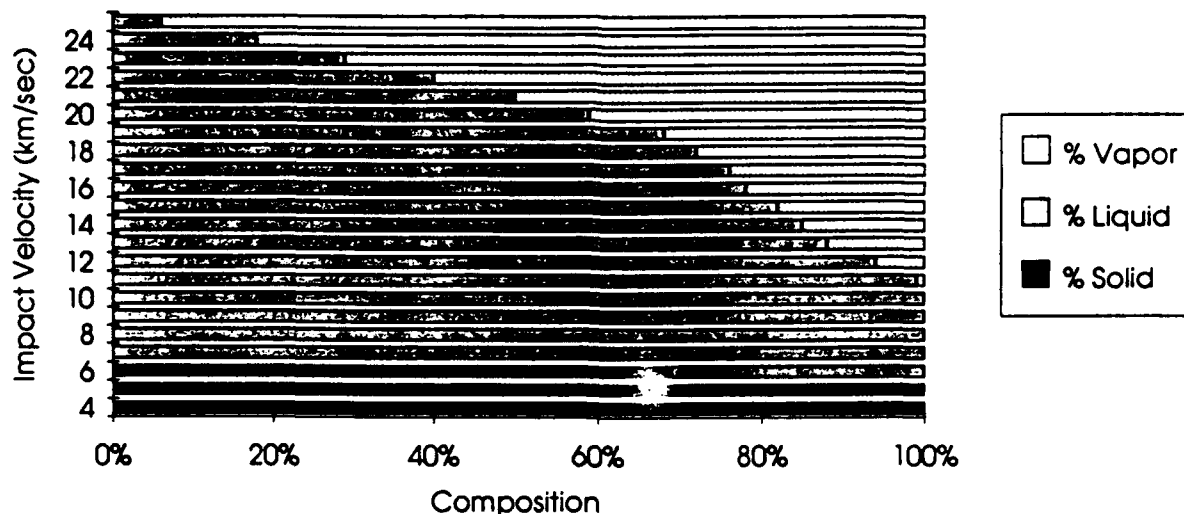
The odd behavior in the final values of specific volume due to the jump in the unmodified Tillotson EOS

began for aluminum-on-aluminum impacts at an impact velocity of approximately 9 km/sec. However, the Tillotson/SJC formulation produced a smooth transition as the material changes from a solid state (below approximately 6 km/sec) to a liquid state (between approximately 6 and 11 km/sec) to a gaseous state (above approximately 11 km/sec). The specific volumes calculated by the Tillotson/MPF formulation closely followed those of the Mie-Gruneisen EOS until an impact velocity of approximately 18 km/sec beyond which they began to diverge rapidly. Apparently, the Tillotson/SJC formulation predicted a more expanded material end-state than did the Tillotson/MPF formulation for impact velocities between 10 and 24 km/sec.

Figures 6 and 7 compare the effects of using the Tillotson/SJC and the Tillotson/MPF formulations, respectively, to calculate the percentages of the three matter states in debris clouds created by aluminum-on-aluminum impacts. While the results presented and discussed apply only to aluminum-on-aluminum impacts, the equations developed herein may be used to estimate the state of the material within a debris cloud created by the high speed impact of virtually any two materials for which the required material properties are available.

Comparing Figures 6 and 7 reveals that the Tillotson/SJC and the Tillotson/MPF formulations agreed in the percentages of the various states of matter at speeds below approx. 11 km/sec and above approximately 24 km/sec. Within the 11-24 km/sec impact velocity regime, the Tillotson/MPF formulation predicted vaporization to develop more rapidly than did the Tillotson/SJC formulation which predicted a more gradual transition to vaporized material. This appears to contradict the results shown in Figure 5 in which the Tillotson/MPF formulation initially predicted a more dense debris cloud than did the Tillotson/SJC formulation. In fact, the question is raised as to how a more expanded material state can have less vapor than a less expanded state, especially since both Tillotson EOS formulations predicted approximately the same radial expansion of the debris cloud material!

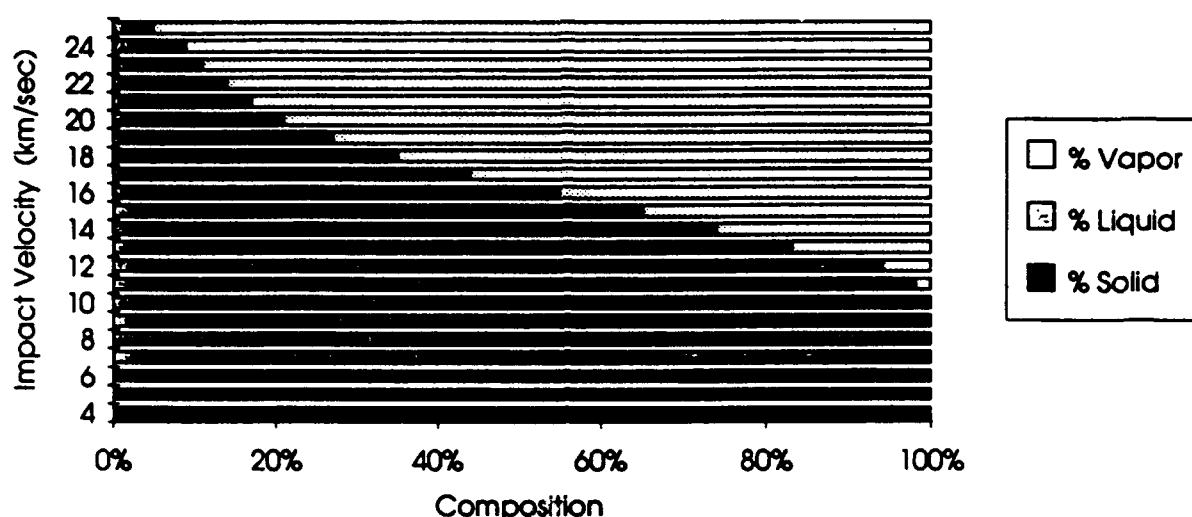
Figure 6. Debris Cloud Composition, Aluminum-on-Aluminum Impact
Tillotson/SJC Equation-of-State Formulation



The resolution of this apparent dilemma lies in the values of the leading and trailing edge velocities as predicted by the two alternative versions of the Tillotson EOS. In the 12 to 24 km/sec impact velocity regime, the Tillotson/SJC formulation predicted values of v_f and v_r that were smaller and larger, respectively, than the corresponding values predicted by the Tillotson/MPF formulation. Hence, in this

impact velocity regime, the Tillotson/SJC formulation predicted the debris cloud to have a larger axial dimension than did the Tillotson/MPF EOS while the radial dimension in both cases was approximately the same. This naturally resulted in larger debris cloud volumes with the Tillotson/SJC formulation than with the Tillotson/MPF formulation, even though the vapor content predicted by the Tillotson/SJC formulation was less than that predicted by the Tillotson/MPF formulation.

Figure 7. Debris Cloud Composition, Aluminum-on-Aluminum Impact
Tillotson/MPF Equation-of-State Formulation



SUMMARY

A methodology rooted in first-principles physics, mechanics, and thermodynamics has been developed to determine the amount of material in each of the three states of matter in a debris cloud created by the hypervelocity impact of a multi-material rod projectile on a thin target plate. The Tillotson EOS was used to calculate the residual energy in the projectile and target materials upon release from their respective shocked states. Elementary thermodynamic principles were used to determine the percentages of shocked and released projectile and target materials that were melted and vaporized during the release process. These percentages were then used to calculate the mass of the projectile and target materials in solid, liquid, and gaseous form. Debris cloud velocities were calculated using the principles of momentum and energy conservation; the spread of the debris cloud material was then readily obtained.

The predictions of the debris cloud model were compared against experimental data, the predictions of three different empirically-based codes, and against the predictions of 1-D and 3-D hydrocodes. In general, the predictions of the characterization scheme developed herein compared favorably with the experimental results, the lethality assessment schemes' predictions, and the predictions of the hydrocodes. While some of the details in the debris cloud model differed from empirical evidence, it is noted that the debris cloud model presented herein was developed solely through the application of fundamental physical principles without any empirical 'adjustment' factors. In this light, the agreement between the elementary theory predictions and the experimental results is highly encouraging.

ACKNOWLEDGMENTS

The author would like to acknowledge the support of the AFOSR Summer Faculty Research Program. In addition, the author is grateful to Mr. Danny R. Brubaker (WL/MNSA) for performing the CTH calculations during the course of this investigation. The valuable comments and suggestions of Dr. Mark

Hoffman of SAIC/Shalimar are also noted with gratitude. Finally, thanks go to Mssrs. David Jerome and Ronald Hunt (WL/MNSA) for their guidance and assistance.

REFERENCES

1. Yatteau, J.D., Zernow, R.H., and Recht, R.F., Compact Fragment Multiple Plate Perforation Model, Volumes I and II, NSWC-TR-91-399, Dahlgren, Virginia, 1991.
2. Bjorkman, M.D., Geiger, J.D., and Wilhelm, E.E., Space Station Integrated Wall Design and Penetration Damage Control, Boeing Aerospace Corporation, Final Report, Contract NAS8-36246, Seattle, Washington, 1987.
3. Greer, R. and Hatz, M., KAPPJI User's Manual, Version 1.1, Kaman Sciences Corporation, K92-17U(R), Colorado Springs, Colorado, 1992.
4. Tillotson, J.H., Metallic Eqns of State for Hypervelocity Impact, General Dynamics, General Atomic Division, Report No. GA-3216, 1962.
5. Allen, R.T., Equation of State of Rocks and Minerals, General Dynamics, General Atomic Division, Report No. GAMD-7834A, 1967.
6. Holian, K., and Burkett, M.W., "Sensitivity of Hypervelocity Impact Simulations to Eqns-of- State", Int. J. Impact Engng., Vol. 5, pp. 331-341, 1987.
7. Schonberg, W.P., Toward a Characterization of the Debris Cloud Created in a Hypervelocity Impact on a Thin Plate, WL-TR-93-7028, Eglin AFB, Florida, 1993.
8. Rice, M.H., McQueen, R.G., and Walsh, J.M., "Compression of Solids by Strong Shock Waves", Solid State Physics, Vol. 6, Seitz, F. and Turnbull, D., eds., Academic Press, New York, 1958.
9. Rinehart, J.S., Stress Transients in Solids, HyperDynamics, Santa Fe, New Mexico, 1975.
10. Goldsmith, W., Impact: The Theory and Physical Behaviour of Colliding Solids, Edward Arnold, London, 1960.
11. Zukas, J.A., et.al., High Velocity Impact Dynamics, John Wiley, New York, 1990.
12. Maiden, C.J., Gehring, J.W., and McMillan, A.R., Investigation of Fundamental Mechanism of Damage to Thin Targets by Hypervelocity Projectiles, General Motors Defense Research Laboratory, TR-63-225, Santa Barbara, California, 1963.
13. Anderson, C.E., Trucano, T.G., and Mullin, S.A., "Debris Cloud Dynamics", Int. J. Impact Engng., Vol. 9, pp. 89-113, 1990.
14. Piekutowski, A.J., "A Simple Dynamic Model for the Formation of Debris Clouds", Int. J. Impact Engng., Vol. 10, pp. 453-471, 1990.
15. Bell, R.L., et.al., CTH User's Manual Version 1.026, Sandia National Laboratories, Albuquerque, New Mexico, 1986.
16. Wilbeck, J.S., Scott, P.G., and Lew, T.M., Enhanced Fragment Lethality, AFATL-TR-88-105, Eglin Air Force Base, Florida, August, 1988.

**NEW DISCRETIZATION METHODS AND ITS APPLICATIONS IN MISSILE
AUTOPILOT CONTROL**

**Kemin Zhou
Assistant Professor
Department of Electrical and Computer Engineering
Louisiana State University
Baton Rouge, LA 70803**

**Final Report for:
AFOSR Summer Faculty Research Program
Wright Laboratory/Armament Directorate
Eglin Air Force Base, FL 32542**

**Sponsored by:
Air Force Office of Scientific Research
Bolling Air Force Base, Washington, D.C.**

August 1993

NEW DISCRETIZATION METHODS AND ITS APPLICATIONS IN MISSILE AUTOPILOT CONTROL

Kemin Zhou
Assistant Professor
Department of Electrical and Computer Engineering
Louisiana State University
Baton Rouge, LA 70803

Abstract

This paper considers the sampled-data controller design using discretization method. The work described here is motivated from the fact that the conventional textbook discretization methods do not take into consideration of the effects of the antialiasing filters and the hold devices on the system performance, which may lead to severe performance deterioration when the sampling is not very fast. In this paper, we propose several simple alternative discretization methods which compensates the performance deterioration. Our methods are inspired by the fact that the sampled-data controller (including the antialiasing filters and the hold devices) can be bounded by a conic sector with a linear time invariant optimal center. The fundamental idea of our methods is to discretize the continuous controller in such a way that the frequency response of the optimal center for the sampled-data controller approximates the frequency response of the continuous controller. This paper considers only some theoretical development of the proposed methods. The applications of these methods in the missile autopilot control will be reported in the subsequent research.

NEW DISCRETIZATION METHODS AND ITS APPLICATIONS IN MISSILE AUTOPILOT CONTROL

Kemin Zhou

1 Introduction

It has been the common practice in modern control engineering that the controllers are implemented using digital devices. This has been made possible because of the low cost and high fidelity of modern digital devices and microprocessors. The digital implementation of a controller has also the advantage that the changing of the controller design is made easy and cheap. Hence modern control design process typically involves a step of implementing a controller using digital devices. There are basically two ways to design a controller for this purpose: (a) design a discrete time controller directly; (b) design a *continuous* controller first and then find a discrete time controller by discretization. The first approach has been traditionally done by first discretizing the plant and then design a discrete time controller for the discretized plant. This method ignores the intersample behavior and, therefore, the performance of the sampled-data system is not guaranteed even if the system behaves well on the sampling instants. Recently, much research has been done on the direct sampled-data controller design, i.e., the discrete controller is designed so that the system's continuous time performance criteria are satisfied (not just on the sampling instants), see [4] and references therein.

This paper considers the more traditional approach (b), which is still widely used in practical engineering design. We shall consider a dynamical system described by a general linear fractional framework in Figure 1 with the generalized plant P which is partitioned accordingly as

$$P = \begin{bmatrix} P_{11} & P_{12} \\ P_{21} & P_{22} \end{bmatrix}.$$

Without loss of generality, we shall assume that the system performance objectives are to design an internally stabilizing controller $K(s)$ so that the transfer matrix from w to z satisfies certain

properties. Assume that the controller $K(s)$ has been obtained by some methods such as classical loop shaping, LQG, and H_∞ , then the next step is to find a discrete implementation $D(z)$.

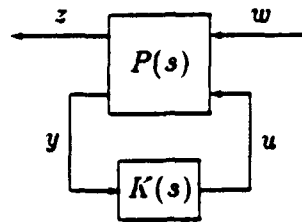


Figure 1: Continuous System

A simple method to obtain a $D(z)$ is to discretize directly the continuous time controller $K(s)$ using certain methods such as step invariance method, ramp invariance method, first order hold (FOH) equivalent, and Tustin transformation with or without prewarping, see [5], so that $D(z)$ approximates $K(s)$ in some sense. In order to reduce the aliasing due to the sampling process, an antialiasing (low pass) filter $F(s)$ is usually placed in front of the sampler. Hence a sampled-data implementation of the continuous controller can be shown in Figure 2 where $F(s)$ denotes an antialiasing filter and H denotes a hold device.

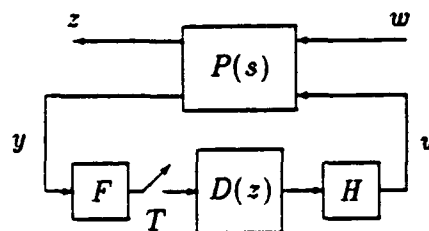


Figure 2: Sampled-Data System

Keeping in mind that the system in Figure 2 is a sampled-data implementation of Figure 1, hence a good sampled-data implementation should behave in such a way that the input/output behaviors between the controller input y and the the controller output u in Figure 2 should be as close as possible to that in Figure 1. In other words, $D(z)$ should be chosen so that the time varying operator from y to u in Figure 2 approximates $K(s)$ in some sense. However, since the above operator is time varying, finding such an approximation $D(z)$ is not easy. Fortunately, this time varying operator can be approximated by a time invariant operator. It has been shown in [12, 13] that the input/output operator from y to u in the sampled-data feedback system can be bounded

in a conic sector with the linear time invariant "optimal center"

$$C(s) = \frac{1}{T} H(s) D(e^{sT}) F(s), \quad (1)$$

i.e., the time varying operator can be approximated by $C(s)$. Therefore, as pointed out in [14], $D(z)$ should be chosen so that $C(s)$ approximates $K(s)$ in some sense.

Since the discrete controller $D(z)$ obtained from the most of the existing conventional discretization methods only approximates $K(s)$ in some sense, for example, the error of the frequency response

$$\|K(j\omega) - D(e^{j\omega T})\|$$

is small over certain frequency range, the closed-loop system performance can be significantly deteriorated due to the sampler, the hold device, and the antialiasing filter. The purpose of this paper is to propose some alternative discretization methods to (partially) overcome this difficulty. For simplicity, we shall assume that $H(s)$ is a zero-order-hold (ZOH) in this paper. The problem with higher order hold can also be treated similarly.

The paper is organized as follows. Section 2 presents several rational approximations to the ZOH transfer function. These approximations can be used to redesign a continuous time controller so that this continuous time controller takes the sampling/hold process into account in the discretization. The proposed approximations are also compared with the traditional Padé approximations. Section 3 considers another class of approximations to the ZOH where some delay factors are allowed. The proposed approximations are then combined with FOH equivalent discretization method to give better discretizations for continuous time controllers. In section 4, a convex programming discretization method is proposed. This method can be used to guarantee the closed loop performance of the sampled-data system. Some simple illustrative examples are given in Section 5.

2 Rational Approximation of $H(s)$

One way to partially overcome the difficulty due to the conventional discretization methods is to treat the antialiasing filter and the hold device as part of the plant, and then design a continuous time controller $\hat{K}(s)$ for the augmented plant as shown in Figure 3. Note that $1/T$ in $\frac{1}{T}H$ comes from the fact that the sampler has a gain of $1/T$. Then a discrete time controller $D(z)$ is obtained by applying the conventional discretization procedures on $\hat{K}(s)$. There are several drawbacks associated with this method. First of all, the controller $\hat{K}(s)$ will critically depend upon the

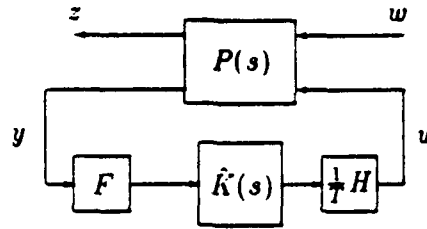


Figure 3: Continuous Controller Redesign

sampling period, therefore, the whole design process has to be repeated if the sampling period T is changed. Secondly, the design of $\hat{K}(s)$ is not easy since $H(s)$ is usually an infinite dimensional system. The second difficulty can be avoided if a finite dimensional approximation of $H(s)$ is used. For the simplicity of notation, we shall denote

$$H_T(s) := \frac{1}{T} H(s) = \frac{1 - e^{-sT}}{Ts}. \quad (2)$$

Our objective in this section is to summarize some well known approximations to $H_T(s)$ and to provide some new approximations. In addition to the applications in the above design process, these approximations are also useful in the discretization methods to be presented in the next section if the approximants are minimum phase. A simple way to find a finite dimensional approximation to $H_T(s)$ is perhaps to use the Padé approximation. Let

$$H_{\text{padé}}(s) := \frac{b_0 + b_1(sT) + \cdots + b_m(sT)^m}{a_0 + a_1(sT) + \cdots + a_n(sT)^n}.$$

We shall call $H_{\text{padé}}(s)$ the (n, m) -th order Padé approximation of $H_T(s)$ if the coefficients of the power series of $H_{\text{padé}}$ match the first $m + n + 1$ coefficients of the power series of $H_T(s)$. The results for some low order Padé approximations are shown in Table 1.

To obtain a better approximation, we shall conduct a numerical search. To fix the idea, we shall consider the approximation in the form of

$$\hat{H}_T(s) = \frac{1 + 2\xi\alpha\left(\frac{Ts}{2}\right) + \alpha^2\left(\frac{Ts}{2}\right)^2}{1 + \beta_1\left(\frac{Ts}{2}\right) + \beta_2\left(\frac{Ts}{2}\right)^2}.$$

We shall consider two cases: (a) $\hat{H}_T(s)$ is minimum phase; (b) $\hat{H}_T(s)$ is possibly nonminimum phase. The parameters are chosen to minimize the following approximation error:

$$\max_{\omega \in [0, \omega_1]} |H_T(j\omega) - \hat{H}_T(j\omega)|$$

(n, m)	Padé Approximation
$(1, 0)$	$\frac{1}{1 + (sT)/2}$
$(1, 1)$	$\frac{1 - (sT)/6}{1 + (sT)/3}$
$(2, 0)$	$\frac{1}{1 + (sT)/2 + (sT)^2/12}$
$(2, 1)$	$\frac{1}{1 + (sT)/2 + (sT)^2/12}$
$(2, 2)$	$\frac{1 - (sT)/10 + (sT)^2/60}{1 + 2(sT)/5 + (sT)^2/20}$

Table 1: Padé Approximation of $\frac{1-e^{-sT}}{Ts}$

for some $\omega_1 \leq \frac{\omega_s}{2} = \frac{\pi}{T}$. Note that the approximation accuracy beyond the frequency $\omega_s/2$ is not important since all signals beyond that frequency must be sufficiently attenuated for a good controller design by the sampling theorem. The numerical experience shows that choosing $\omega_1 = \frac{\pi}{T}$ will result in approximants with large approximation error at low frequencies. Therefore, $\omega_1 = \frac{0.8\pi}{T}$ will be used in our minimizations. To find a minimum phase approximation, we fix $\xi > 0$ and minimizing over α, β_1 , and β_2 . The minimization shows that the optimal parameters and the approximation error change very little with different choices of the damping ratio ξ . A typical set of values are

$$\xi = 1, \quad \alpha = 0.001, \quad \beta_1 = 1.0013 \approx 1, \quad \beta_2 = 0.3668$$

and the corresponding approximation error is

$$\max_{\omega \in [0, \frac{0.8\pi}{T}]} |H_T(j\omega) - \hat{H}_T(j\omega)| = 0.0085.$$

With the above parameters, an approximation is given by

$$\hat{H}_T(s) = \frac{(1 + \alpha \frac{Ts}{2})^2}{1 + \beta_1 (\frac{Ts}{2}) + \beta_2 (\frac{Ts}{2})^2} \approx \frac{1}{1 + (\frac{Ts}{2}) + \frac{1}{2.726} (\frac{Ts}{2})^2}. \quad (3)$$

It is interesting to note that this approximation is almost the same as the (2,0)-th order Padé approximation. In fact, the following transfer function is a good approximation of $H_T(s)$ for any $\gamma = 2.75 \sim 3$:

$$\hat{H}_{min}(s) = \frac{1}{1 + (\frac{Ts}{2}) + \frac{1}{\gamma} (\frac{Ts}{2})^2}.$$

If the approximation is allowed to be nonminimum phase, a second order best approximation is found to be

$$\hat{H}_{non}(s) = \frac{-0.1793 \left(\frac{T_s}{2}\right) + 0.0687 \left(\frac{T_s}{2}\right)^2}{s^2 + 0.8172 \left(\frac{T_s}{2}\right) + 0.2231 \left(\frac{T_s}{2}\right)^2}.$$

The frequency response errors for some typical Padé approximations and the best approximations are shown in Figure 4 and Figure 5. It is clear from the plots that \hat{H}_{min} with $\gamma = 2.9$ is a very good minimum phase approximation. Note that if the inverse of \hat{H}_{min} is desired to be proper or strictly proper, which is the case in the next section, then the numerator of \hat{H}_{min} may be replaced by $(1 + \alpha \frac{T}{2})^k$ for some appropriate integer k and some sufficiently small α , for example, $\alpha \leq 0.001$. The use of these approximants in the design of $\hat{K}(s)$ is standard and will not be pursued here further.

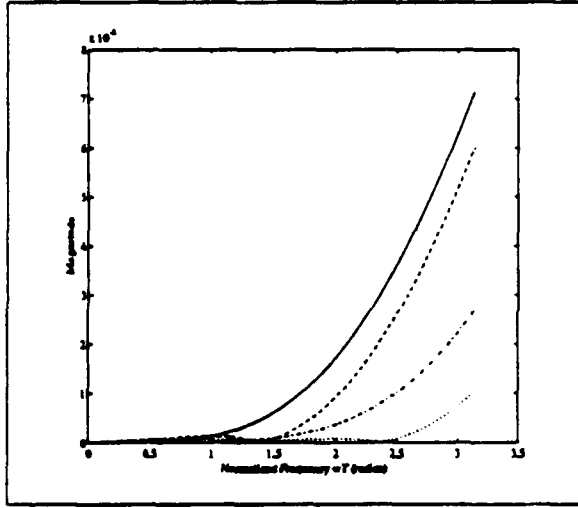


Figure 4: The magnitude approximation errors $|H_T(j\omega) - \hat{H}_T(j\omega)|$: (2,0) Padé (solid), (2,2) Padé (dashdot), \hat{H}_{min} with $\gamma = 2.9$ (dashed), \hat{H}_{non} (dotted)

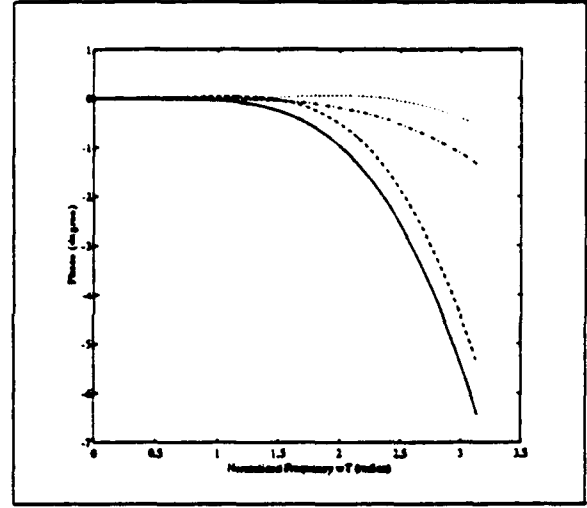


Figure 5: The phase approximation errors $\angle(H_T(j\omega) - \hat{H}_T(j\omega))$: (2,0) Padé (solid), (2,2) Padé (dashdot), \hat{H}_{min} with $\gamma = 2.9$ (dashed), \hat{H}_{non} (dotted)

3 Discretization Using FOH with Phase Lead Compensation

Another way, which has the potential to overcome both of the difficulties in the last section, is to find a $D(z)$ directly so that $C(s) = \frac{1}{T} H(s) D(e^{sT}) F(s)$ approximates $K(s)$ in some sense. For example, $D(z)$ may be chosen to minimize the frequency response between $C(s)$ and $K(s)$ over the

frequency range $[0, \omega_1]$ for some $\omega_1 \leq \frac{\omega_s}{2} = \frac{\pi}{T}$:

$$\min_{D(z)} \max_{\omega \in [0, \omega_1]} \left\| K(j\omega) - \frac{1}{T} H(j\omega) D(e^{j\omega T}) F(j\omega) \right\|. \quad (4)$$

However, this optimization is highly nontrivial. This is because $D(z)$ cannot be an arbitrary transfer matrix. It must be proper and has the same number of unstable poles as $K(s)$. We shall propose several methods in the next section to solve this optimization. In this section, we propose a simple method to approximately solve this problem. The idea is as follows:

- Let $\hat{F}(s)$ and $\hat{H}(s)$ be minimum phase (except for some time delay factors such as $e^{-\mu s}$ for $\mu < T$) approximations of $F(s)$ and $\frac{1}{T} H(s)$, respectively, so that there is no unstable pole/zero cancellation in forming the product of

$$D_c(s) := \hat{H}^{-1} K \hat{F}^{-1}$$

and, furthermore, the rational part of $D_c(s)$ is proper. Then the discrete time controller $D(z)$ is taken as the discretization of $D_c(s)$. An approximation for $F(s)$ is relatively easy to find since $F(s)$ is usually a rational stable and minimum phase transfer function. The minimum phase approximation $\hat{H}_{\min}(s)$ in the last section can also be used here for $\hat{H}_T(s)$. We shall now discuss some alternative approximations below where $\hat{H}_T(s)$ is allowed to contain a delay factor.

We shall again consider the case where H is a ZOH. In this case

$$H_T(s) := \frac{1}{T} H(s) = \frac{1 - e^{-sT}}{Ts}.$$

We shall consider several approximations of $H_T(s)$. We first note that

$$H_T(s) = \frac{e^{\frac{T}{2}s} - e^{-\frac{T}{2}s}}{Ts} e^{-\frac{T}{2}s}$$

and

$$H_T(j\omega) = \frac{\sin \frac{T}{2}\omega}{\frac{T}{2}\omega} e^{-\frac{T}{2}j\omega}.$$

Hence a simple approximation of $H_T(s)$ would be

$$\hat{H}_{\text{delay}}(s) = e^{-\frac{T}{2}s}.$$

This approximation has the advantage of having the exactly same phase as $H_T(s)$. This approximation should be considered along with the fact that the performance degradation of the digital implementation in most cases is due to the phase lag of the hold devices and the antialiasing filters.

To get a better approximation, we shall also consider the approximation in the form of

$$\hat{H}_{delay+} = e^{-\frac{T}{2}s} \frac{1 + 2\xi\alpha \left(\frac{T_2}{2}\right) + \alpha^2 \left(\frac{T_2}{2}\right)^2}{1 + \beta_1 \left(\frac{T_2}{2}\right) + \beta_2 \left(\frac{T_2}{2}\right)^2}$$

for some $\xi > 0$, $\alpha \geq 0$, $\beta_1 \geq 0$, and $\beta_2 \geq 0$. It is important to note that the zeros of $\hat{H}_{delay+}(s)$, which is part of the $D_c(s)$ poles, will be discretized to obtain the discrete time controller poles of $D(z)$. This is why the damping ratio ξ has been restricted to be positive. For the same reason, it is highly undesirable to have small damping ratio ξ . We shall choose these parameters to minimize the approximation error in frequency domain:

$$\min_{\xi, \alpha, \beta_1, \beta_2} \max_{\omega \in [0, \omega_1]} |H_T(j\omega) - \hat{H}_{delay+}(j\omega)|$$

for some $\omega_1 \leq \frac{\omega_s}{2} = \frac{\pi}{T}$. It is noted that the above optimization will result in $\xi = 0$. Table 2 and Table 3 show the optimization results with the fixed damping ratio ξ .

ξ	α	β_1	β_2	$\max_{\omega \in [0, \frac{\pi}{T}]} H_T(j\omega) - \hat{H}_{delay+}(j\omega) $
0.1	0.3854	0.1051	0	0.0160
0.2	0.3841	0.2106	0	0.0291
0.3	0.3824	0.3138	0	0.0417
0.4	0.3795	0.4140	0	0.0530
0.5	0.3717	0.5130	0	0.0629
0.6	0.3744	0.6079	0	0.0717
0.7	0.3708	0.6997	0	0.0793
0.8	0.3679	0.7904	0	0.0859
0.9	0.3627	0.8740	0	0.0918
1.0	0.3845	1.0207	0	0.0989

Table 2:

Some typical frequency responses for the approximation errors are shown in Figure 6-11. With the above approximations, $D_c(s)$ can be written in the form of

$$D_c(s) = e^{\frac{T}{2}s} G(s)$$

for some proper $G(s)$. Now $D_c(s)$ can be discretized to obtain $D(z)$. Since $D_c(s)$ has a predication factor $e^{\frac{T}{2}s}$, it is not straightforward how the existing discretization formulas can be used. In the

ξ	α	β_1	β_2	$\max_{\omega \in [0, \frac{2.8\pi}{T}]} H_T(j\omega) - \hat{H}_{delay+}(j\omega) $
0.1	0.3936	0.0957	0	0.0076
0.2	0.3928	0.1915	0	0.0142
0.3	0.3929	0.2873	0	0.0207
0.4	0.3902	0.3800	0	0.0269
0.5	0.3884	0.4721	0	0.0326
0.6	0.3872	0.5638	0	0.0378
0.7	0.3834	0.6505	0	0.0426
0.8	0.3827	0.7405	0	0.0469
0.9	0.3794	0.8246	0	0.0508
1.0	0.3763	0.9073	0	0.0543

Table 3:

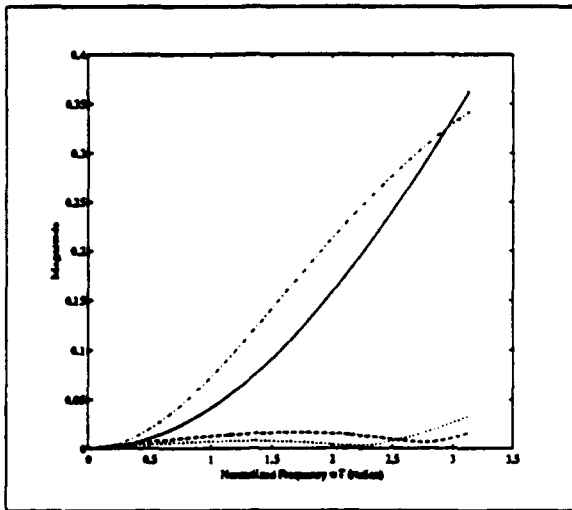


Figure 6: The magnitude approximation errors $|H_T(j\omega) - \hat{H}_T(j\omega)|$: \hat{H}_{delay} (solid), (1,0) Padé (dashdot), \hat{H}_{delay+} with $\xi = 0.1$ and $\omega_1 = \frac{\pi}{T}$ (dashed), \hat{H}_{delay+} with $\xi = 0.1$ and $\omega_1 = \frac{0.8\pi}{T}$ (dotted)

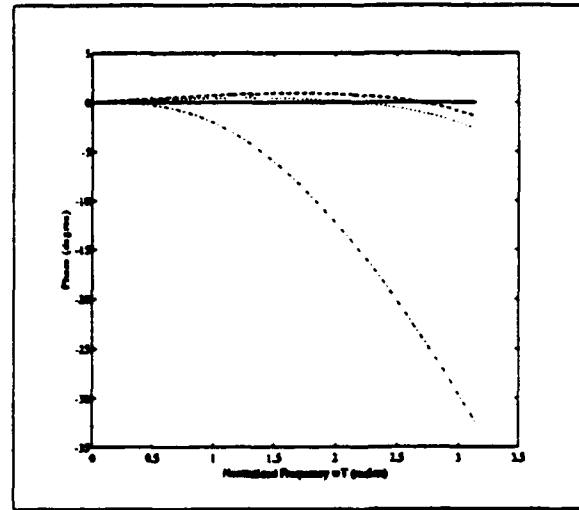


Figure 7: The phase approximation errors $\angle(H_T(j\omega) - \hat{H}_T(j\omega))$: \hat{H}_{delay} (solid), (1,0) Padé (dashdot), \hat{H}_{delay+} with $\xi = 0.1$ and $\omega_1 = \frac{\pi}{T}$ (dashed), \hat{H}_{delay+} with $\xi = 0.1$ and $\omega_1 = \frac{0.8\pi}{T}$ (dotted)

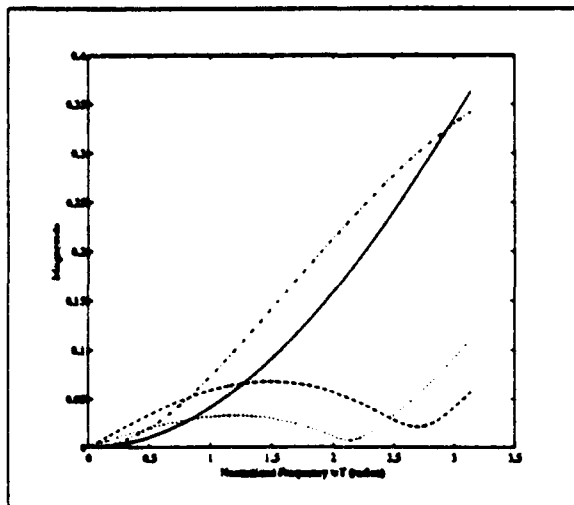


Figure 8: The magnitude approximation errors $|H_T(j\omega) - \hat{H}_T(j\omega)|$: \hat{H}_{delay} (solid), (1,0) Padé (dashdot), \hat{H}_{delay+} with $\xi = 0.5$ and $\omega_1 = \frac{\pi}{T}$ (dashed), \hat{H}_{delay+} with $\xi = 0.5$ and $\omega_1 = \frac{0.8\pi}{T}$ (dotted)

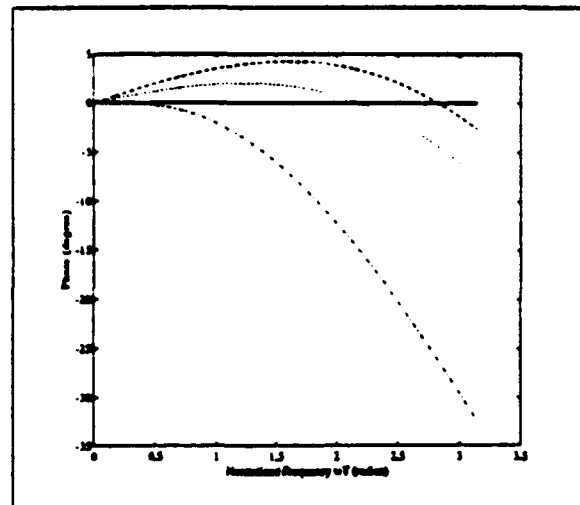


Figure 9: The phase approximation errors $\angle(H_T(j\omega) - \hat{H}_T(j\omega))$: \hat{H}_{delay} (solid), (1,0) Padé (dashdot), \hat{H}_{delay+} with $\xi = 0.5$ and $\omega_1 = \frac{\pi}{T}$ (dashed), \hat{H}_{delay+} with $\xi = 0.5$ and $\omega_1 = \frac{0.8\pi}{T}$ (dotted)

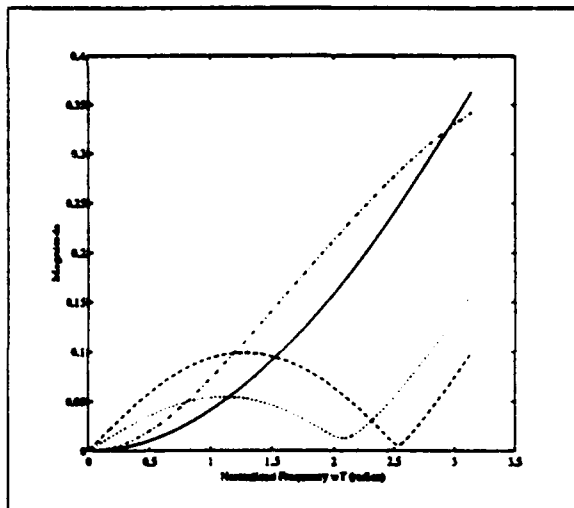


Figure 10: The magnitude approximation errors $|H_T(j\omega) - \hat{H}_T(j\omega)|$: \hat{H}_{delay} (solid), (1,0) Padé (dashdot), \hat{H}_{delay+} with $\xi = 1$ and $\omega_1 = \frac{\pi}{T}$ (dashed), \hat{H}_{delay+} with $\xi = 1$ and $\omega_1 = \frac{0.8\pi}{T}$ (dotted)

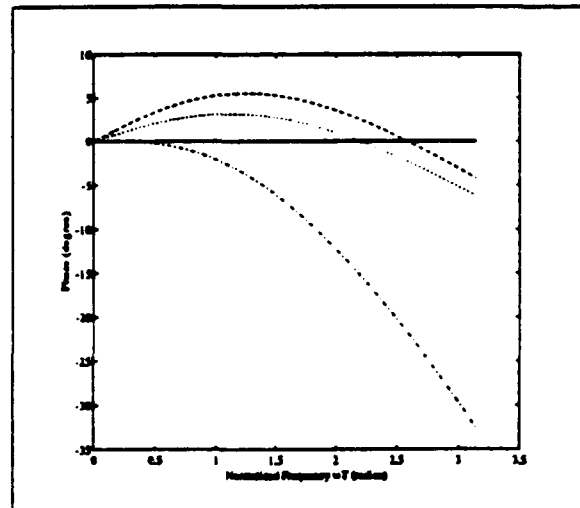
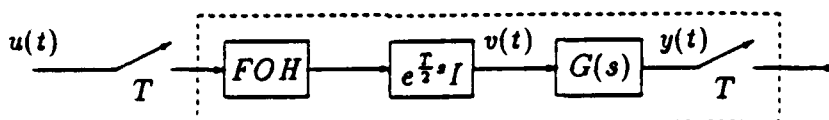


Figure 11: The phase approximation errors $\angle(H_T(j\omega) - \hat{H}_T(j\omega))$: \hat{H}_{delay} (solid), (1,0) Padé (dashdot), \hat{H}_{delay+} with $\xi = 1$ and $\omega_1 = \frac{\pi}{T}$ (dashed), \hat{H}_{delay+} with $\xi = 1$ and $\omega_1 = \frac{0.8\pi}{T}$ (dotted)

following, we shall describe a procedure for the discretization of a LTI system with predications using a First Order Hold (FOH). Let $G(s)$ be a finite dimensional LTI system with a state space realization

$$G(s) = \left[\begin{array}{c|c} A & B \\ \hline C & D \end{array} \right].$$

We want to find an equivalent discrete time system for $D_c(s) := e^{\frac{T}{2}s}G(s)$. A ZOH equivalent discrete time system can be found using the method described in Franklin et al [5]. We shall describe a method using FOH. This discretization can be illustrated by the following diagram:



Our objective is to find the discrete time state space realization for the system in the dashed box. The problem can be solved either in state space or in Z-domain. Since the FOH has the following transfer function:

$$FOH(s) = (1 - e^{-Ts})^2 \frac{Ts + 1}{Ts^2},$$

the transfer matrix for the dashed box is given by

$$\begin{aligned} G_d(z) &= \mathcal{Z} \left\{ G(s) e^{\frac{T}{2}s} FOH(s) \right\} \\ &= \frac{(1 - z^{-1})^2}{T} \mathcal{Z} \left\{ e^{\frac{T}{2}s} G(s) \frac{Ts + 1}{Ts^2} \right\}. \end{aligned}$$

Computing the above \mathcal{Z} -transform is usually complicated. In the following, we shall present a state space solution.

Lemma 1 Let $G(s) = \left[\begin{array}{c|c} A & B \\ \hline C & D \end{array} \right]$. Then a discrete time state space realization for $G_d(z)$ is given by

$$G_d(z) = \left[\begin{array}{cc|c} \Phi & -\Phi_1(\frac{1}{2}\Gamma_1 + \Gamma_2) & \Phi_1(\frac{3}{2}\Gamma_1 + \Gamma_2) - \Gamma_2 + \Phi(\Gamma_1 + \Gamma_2) \\ 0 & 0 & I \\ \hline C & -\frac{1}{2}D & C(\Gamma_1 + \Gamma_2) + \frac{3}{2}D \end{array} \right]$$

where

$$\Phi = e^{AT}, \quad \Phi_1 = e^{A\frac{T}{2}}, \quad \Gamma_1 = \int_0^{\frac{T}{2}} e^{A\eta} d\eta B, \quad \Gamma_2 = \frac{1}{T} \int_0^{\frac{T}{2}} e^{A\eta} (\frac{T}{2} - \eta) d\eta B.$$

Moreover, Φ_1 , Γ_1 , and Γ_2 satisfy the following relation:

$$\begin{bmatrix} \Phi_1 & \Gamma_1 & \Gamma_2 \\ 0 & I & I \\ 0 & 0 & I \end{bmatrix} = \exp \left\{ \begin{bmatrix} A & B & 0 \\ 0 & 0 & \frac{1}{T}I \\ 0 & 0 & 0 \end{bmatrix} T \right\}.$$

Due to space limitation, the proof is omitted. The formulas for the discretized model using higher order hold can also be derived similarly although the derivation is much more involved. It is useful to note that the poles of the discretized model has the form of $z^r \det(zI - e^{AT})$ where r = order of hold, for instance, $r = 1$ for FOH and $r = 2$ for second order hold.

4 Discretization Using Convex Optimization

The optimization problem (4) in the last section can be solved if $D(z)$ can be parameterized as a convex function of some parameters. It is easy to see that most discretization methods, such as step invariance, ramp invariance, and FOH equivalent, will result in a controller with poles at e^{AT} and 0. This motivates us the following approximation method.

Let the desired q -input and p -output discrete time controller $D(z)$ have the following form:

$$D_\alpha(z) = \frac{\alpha_0 + \alpha_1 z + \dots + \alpha_m z^m}{z^r \det(zI - e^{AT})}$$

for some $r \geq 0$ and $m \leq r + n$ where n is the dimension of A and $\alpha_i \in \mathbb{R}^{p \times q}$ for $i = 0, 1, \dots, m$ are free parameter matrices. Now $\alpha_0, \alpha_1, \dots$, and α_m are chosen so that

$$\min_{\alpha_i} \max_{\omega \in [0, \omega_1]} \left\| K(j\omega) - \frac{1}{T} H(j\omega) D_\alpha(e^{j\omega T}) F(j\omega) \right\|.$$

Note that this optimization is a convex problem and can be solved easily using standard techniques. The parameterization for D_α can also take a state space form if desired, for example, D_α may be parameterized as

$$D_\alpha(z) = \left[\begin{array}{c|c} \begin{bmatrix} e^{AT} & 0 \\ 0 & 0_{r \times r} \end{bmatrix} & \Gamma_\alpha \\ \hline C & C_r \end{array} \right] J_\alpha$$

where C_r is any matrix so that the system is observable and Γ_α and J_α are free parameters to be chosen.

Robust Stability Criterion

We should point out that finding a $D(z)$ which minimizes problem (4) may not be necessary in some applications and may require very high order controllers, i.e., large m and r , if the approximation error is required to be very small. In many cases, it is more sensible to find a lower $D(z)$ to minimize some weighted approximation error. For example, in order to make sure that the sampled-data system is closed loop stable, we should choose $D(z)$ such that a closed loop robust stability criterion is satisfied.

A reasonable robust stability criterion in this case is

$$\epsilon_{rob} := \max_{\omega} \left\| (1 + P_{22}(s)K(s))^{-1} P_{22}(s) \left(K(s) - \frac{1}{T} H(s) D_{\alpha}(e^{sT}) F(s) \right) \right\|_{s=j\omega}.$$

Note that this criterion is not exactly the robust stability criterion for the sampled-data system since $C_{\alpha}(s) = \frac{1}{T} H(s) D_{\alpha}(e^{sT}) F(s)$ is only the center of the sampled-data controller. Hence we shall choose the parameters α_i so that

$$\min_{\alpha_i} \max_{\omega} \left\| (1 + P_{22}(s)K(s))^{-1} P_{22}(s) \left(K(s) - \frac{1}{T} H(s) D_{\alpha}(e^{sT}) F(s) \right) \right\|_{s=j\omega}.$$

Closed Loop Transfer Functions

We can also formulate the problem so that the parameters in D_{α} are chosen to minimize the closed loop performance degradation due to sampling. Let

$$C_{\alpha}(s) = \frac{1}{T} H(s) D_{\alpha}(e^{sT}) F(s)$$

and denote the closed loop transfer function for the continuous system

$$T(s) = P_{11} + P_{12}K(I - P_{22}K)^{-1}P_{21}$$

and the approximate closed loop transfer function for the sampled-data system

$$T_d(s) = P_{11} + P_{12}C_{\alpha}(I - P_{22}C_{\alpha})^{-1}P_{21}.$$

Then

$$T(s) - T_d(s) = P_{12}(I - KP_{22})^{-1}(K - C_{\alpha})(I - P_{22}C_{\alpha})^{-1}P_{21}$$

and the performance degradation due to the sampled-data implementation of the continuous time controller can be measured by

$$\max_{\omega} \|T(j\omega) - T_d(j\omega)\|.$$

Thus C_α should be chosen so that the above performance degradation criterion is minimized. Since C_α appears nonlinearly in $T(s) - T_d(s)$, we shall propose the following optimization procedure, which results in a convex optimization problem in each step:

1. Let $\hat{K} = K$;
2. Find matrices $\alpha_i, i = 0, 1, \dots, m$ so that

$$\epsilon_o = \min_{\alpha_i} \max_{\omega} \|P_{12}(I - K P_{22})^{-1}(K - C_\alpha)(I - P_{22}\hat{K})^{-1}P_{21}\|_{s=j\omega}$$

3. Let $\hat{K} = C_\alpha$
4. Find matrices $\alpha_i, i = 0, 1, \dots, m$ so that

$$\epsilon = \min_{\alpha_i} \max_{\omega} \|P_{12}(I - K P_{22})^{-1}(K - C_\alpha)(I - P_{22}\hat{K})^{-1}P_{21}\|_{s=j\omega}$$

5. if $|\epsilon - \epsilon_o| < \delta$ where δ is the tolerance, then stop. Otherwise, let $\epsilon_o = \epsilon$ and go to step 3.

5 Examples

The first example is taken from the paper by Rattan and Yeh [10]. This example has also been considered in [11, 7]. The system considered in these papers is a single loop feedback system with a continuous time plant $G(s)$ and a continuous time controller $K(s)$:

$$G(s) = \frac{10}{s(s+1)}, \quad K(s) = \frac{0.416s+1}{0.139s+1}.$$

The diagrams for the original continuous time system and for the sampled-data system are shown in Figure 12 and Figure 13, respectively. The sampling period is chosen to be $T = 0.15$.

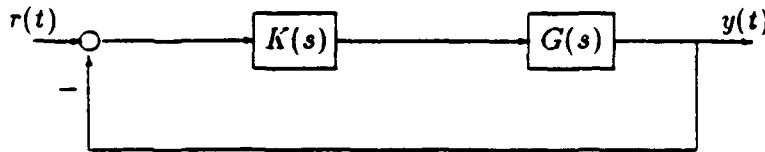


Figure 12: Single Loop Feedback System

The best controller obtained by Rattan in [11] is

$$D(z) = \frac{3.436z - 2.191}{z + 0.2390}.$$

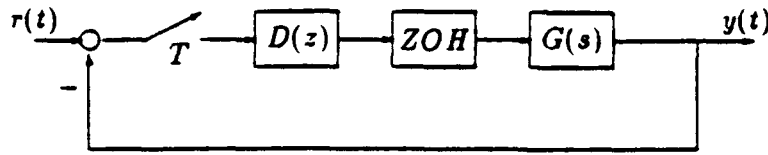


Figure 13: Sampled-Data Implementation

Using the approximation $\hat{H}_{delay} = e^{-\frac{T}{2}s}$ for the ZOH transfer function, a discrete controller is obtained using Lemma 1 as

$$D(z) = \frac{3.4319z^2 - 3.6546z + 0.8828}{z(z - 0.3399)}.$$

We have also obtained a first order discrete controller using the robust stability criterion through the convex programming method proposed in the last section. The controller is given by

$$D(z) = \frac{2.259z - 1.8133}{z - 0.3399}$$

which has the approximation error $\epsilon_{rob} = 0.3248$. The approximation error between K and C_α is shown in Figure 14. The step responses of the continuous time system and the sampled-data systems are shown in Figure 15.

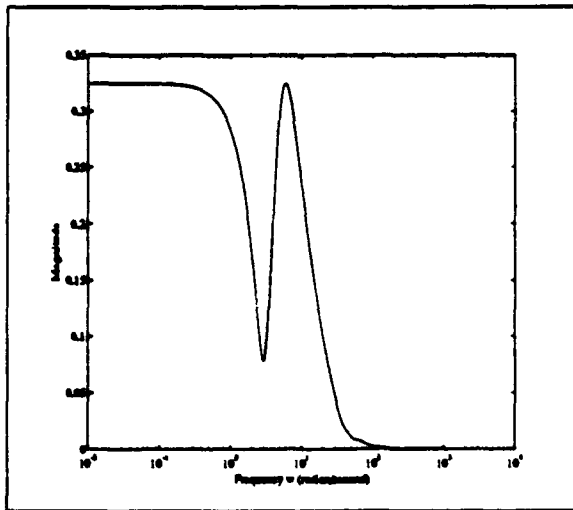


Figure 14: Approximation Error:
 $\left| \frac{G(j\omega)}{1+G(j\omega)K(j\omega)} \left(K(j\omega) - \frac{1}{T} H(j\omega) D(e^{j\omega T}) \right) \right|$

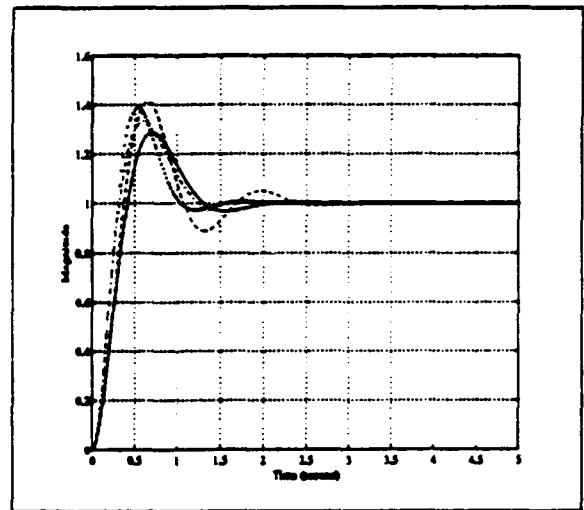


Figure 15: Step Responses: Continuous (solid), Rattan (dashdot), D_α (dashed), delay (dotted)

The step responses show that the first order approximation is not good enough, our second

order approximation using the robust stability criterion gives

$$D(z) = \frac{2.8474z^2 - 3.0456z + 0.7489}{z(z - 0.3399)}$$

which has the approximation error $\epsilon_{rob} = 0.1793$. The approximation error between K and C_α is shown in Figure 16. The step responses of the continuous time system and the sampled-data systems are shown in Figure 17.

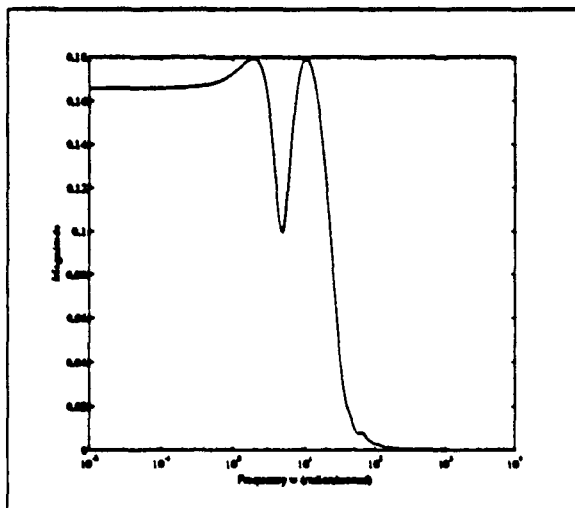


Figure 16: Approximation Error:
 $\left| \frac{G(j\omega)}{1+G(j\omega)K(j\omega)} \left(K(j\omega) - \frac{1}{T} H(j\omega) D(e^{j\omega T}) \right) \right|$

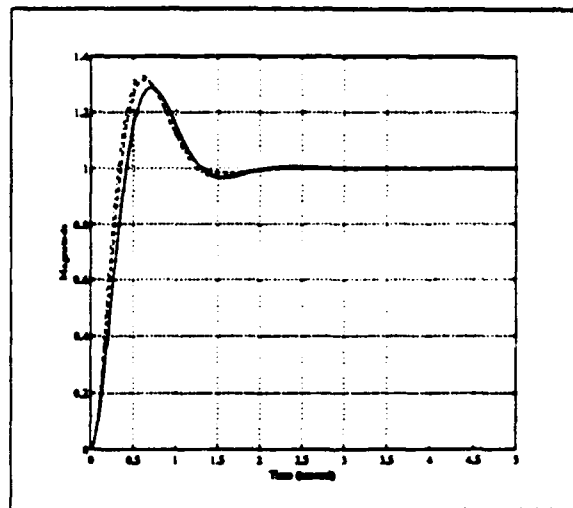


Figure 17: Step Responses: Continuous
(solid), Rattan (dashdot), D_α (dashed)

The second example is taken from Katz [6] where it is shown that most of the conventional discretization methods will result in controllers that cannot stabilize the sampled-data system. The system considered is a double integrator with

$$G(s) = \frac{863.3}{s^2}, \quad K(s) = \frac{2940s + 86436}{(s + 294)^2}$$

and $T = 1/33$. We again employ the convex programming discretization method in the last section with the robust stability criterion. Then a second order approximation gives

$$D(z) = \frac{1.5464z^2 - 1.3793z + 0.3059}{(z - 0.0003)^2}$$

which has the approximation error $\epsilon_{rob} = 0.6136$. The step response of the continuous time system and the sampled-data system are shown in Figure 19. The approximation error between K and C_α is shown in Figure 18. The performance can be further improved using a higher order approximation.

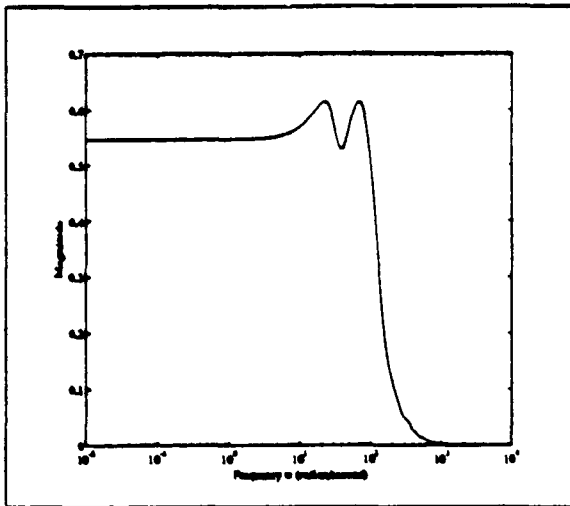


Figure 18: Approximation Error:

$$\left| \frac{G(j\omega)}{1+G(j\omega)K(j\omega)} (K(j\omega) - \frac{1}{T} H(j\omega) D(e^{j\omega T})) \right|$$

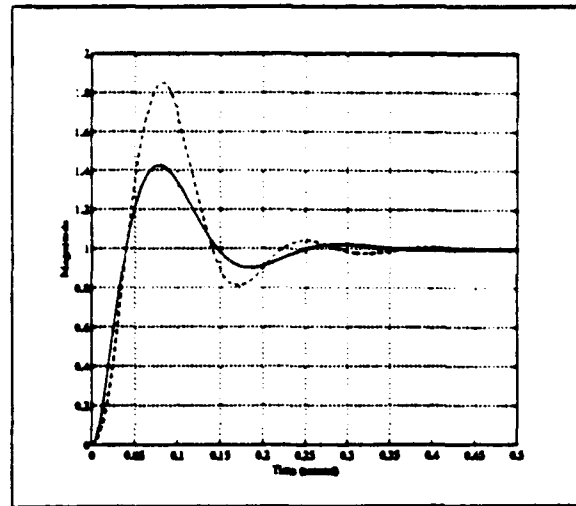


Figure 19: Step Responses: Continuous (solid), D_α (dashed)

6 Conclusions

In this research project, we have considered the sampled-data controller design using discretization method. Several new and simple discretization methods have been proposed. These new methods can be used to compensate the performance deterioration due to the discrete implementation of a continuous controller. The applications of these methods in the missile autopilot control will be reported in the subsequent research.

Acknowledgment

The author would like to thank the support by many people in WL/MNAG of Eglin AFB, in particular, the author is very grateful to Dr. James R. Cloutier and Dr. Chris D'Souza for their support which made the research in the Lab. exciting and fruitful.

References

- [1] B. D. O. Anderson, "Bode Prize Lecture (Control design: moving from theory to practice)," *IEEE Control Systems*, Vol. 13, No.4, pp. 16-25, August 1993.
- [2] K. J. Astrom and B. J. Wittenmark, *Computer Controlled Systems: Theory and Design*, 2nd Ed., 1990, Prentice Hall, Englewood Cliffs, NJ.
- [3] S. Boyd and C. H. Barratt, *Linear controller design: limits of performance*, Prentice Hall, 1991.
- [4] T. Chen and B. Francis, *Sampled-Data Control Systems*. Lecture Notes, January 1993.
- [5] G. F. Franklin, J. D. Powell, and M. L. Workman, *Digital Control of Dynamic Systems*, 2nd Ed. 1990, Addison-Wesley Publishing Company, Inc.
- [6] P. Katz, *Digital Control Using Microprocessors*, Englewood Cliffs, NJ: Prentice-Hall, 1981.
- [7] J. P. Keller and B. D. O. Anderson, "A new approach to the discretization of continuous time controllers," *IEEE Trans. Automat. Contr.*, Vol 37, No. 2., pp. 214-223, February 1992.
- [8] R. A. Kennedy and R. J. Evans, "Digital redesign of a continuous controller based on closed loop performance," *Proc. 29 IEEE Conf. Dec. Contr.*, HI, 1990, pp. 1898-1901.
- [9] H. H. Niemann, "A frequency domain design method of sampled-data compensators," *Proc. American Contr. Conf.*, San Diego, CA, May 1990, pp.1156-1158.
- [10] K. S. Rattan and H. H. Yeh, "Discretizing continuous data control systems," *Computer-Aided Design*, Vol. 10, pp. 299-306, 1978.
- [11] K. S. Rattan, "Digitalization of existing continuous control systems," *IEEE Trans. Automat. Contr.*, Vol. AC-29, pp. 282-285, 1984.
- [12] P. M. Thompson, G. Stein, and M. Athans, "Conic sectors for sampled-data feedback system," *Systems and Control Letters*, Vol. 3, pp.77-82, 1983.
- [13] P. M. Thompson, R. L. Dailey, and J. C. Doyle, "New conic sectors for sampled-data feedback system," *Systems and Control Letters*, Vol. 7, pp.395-404, 1986.
- [14] P. M. Thompson, R. Pena, and Y. Wong, "Design of sampled-data compensators based on the use of conic sectors," *Proc. American Control Conference*, pp.1462-1464, 1986.

22-KHZ VOCALIZATIONS AND STRESS IN RATS

Suzanne C. Baker
Assistant Professor
Department of Psychology

James Madison University
Harrisonburg, VA 22807

Final Report for:
Summer Research Program
Armstrong Laboratory

Sponsored by:
Air Force Office of Scientific Research
Bolling Air Force Base, Washington, DC

August 1993

22-KHZ VOCALIZATIONS AND STRESS IN RATS

Suzanne C. Baker
Assistant Professor
Department of Psychology
James Madison University

Abstract

Rats sometimes emit 22 kHz ultrasonic vocalizations in response to stressful stimuli. We examined the contexts in which this vocalization occurs as well as the physical characteristics of this vocalization in order to investigate the usefulness of 22 kHz calls in the evaluation of AF-relevant stressors. We digitally recorded and analyzed rat ultrasonic vocalizations in several contexts. In our investigations, rats vocalized in response to acoustic startle stimuli, in response to light touch by humans, and when isolated and undisturbed for long periods. The basic structure of the vocalizations appears to be similar in all these situations, although the rate of vocalizing varies widely across these situations. High-fidelity recordings were made of rat ultrasonic vocalizations in the acoustic startle testing paradigm in order to perform detailed analyses of the physical characteristics of these signals (e.g., intensity, frequency modulation, onsets and offsets), and to evaluate the relationship between these acoustic parameters and characteristics (such as intensity) of stress-inducing stimuli.

22-KHZ VOCALIZATIONS AND STRESS IN RATS

Suzanne C. Baker

Introduction

The work of the Performance Extrapolation Branch, Radiofrequency Radiation Division, Armstrong Laboratory, is directed at developing, validating, and applying animal models for predicting the effects of Air Force relevant stressors such as electromagnetic radiation and chemical and toxicological agents. Rodent and nonhuman primate models are focused on. In particular, rats have proved to be useful as subjects in a variety of previous studies in this laboratory, particularly in examining effects of electromagnetic radiation and organophosphate exposure (e.g, Murphy et al, 1990, 1991; Miller et al, 1992, 1993). A reliable, convenient, and efficient method of assessing psychological states in rodents (such as stress, emotionality, or anxiety) would therefore be of great value in this research effort.

Rats emit vocalizations in response to a variety of stimuli. While some of these vocalizations are in the range of human hearing, most rat vocalizations are ultrasonic (i.e., around 20 kHz or above). Ultrasonic vocalizations (UVs) in the range of approximately 40-70 kHz and higher occur in agonistic and sexual situations (Sales, 1972a, 1972b; Thomas and Barfield, 1985). These are brief calls (approximately 3-65 msec) which sometimes show marked frequency modulation. When given by the male during sexual behavior, these calls seem to influence female proceptive behavior (Barfield and Thomas, 1986). However, there is no conclusive evidence concerning the function of these calls in agonistic situations (Takahashi et al, 1983).

Vocalizations of around 19-24 kHz (the "22 kHz vocalization") have been noted in the following situations (see Baker et al, 1991):

- males prior to and following ejaculation (Barfield and Geyer, 1972; Brown, 1979)
- males in agonistic situations (Sales, 1972)
- exposure to a predator (Blanchard et al, 1991; 1992)
- physical restraint (Sewell, 1967; Brudzynski and Ociepa, 1992)
- home cage, isolated from colony (Francis, 1977)
- light touch by humans (Brudzynski and Ociepa, 1992)
- shock (Tonoue et al, 1987; van der Poel et al, 1989)
- avoidance learning (DeSalvia et al, 1990; Cuomo et al, 1992)
- acoustic startle (Kaltwasser, 1990, 1991; Murphy et al, 1993)

"22 kHz" ultrasonic vocalizations are typically fairly long duration (500-1200 msec) pulses of approximately 19-24 kHz with little frequency modulation. Occasional pulses are longer than 2 sec. The beginning or end of a pulse may show a brief, rapid rises or falls in frequency. Pulses are frequently emitted in bouts or series of 3 to 20 pulses or more, with pauses between the pulses. The first pulse of a bout is often of longer duration than the following pulses.

Many of the contexts in which the 22 kHz call occurs clearly might be stressful or anxiety-provoking to the rat. However, the communicative function of the call, if any, has not conclusively been demonstrated. The function of the 22 kHz call in sexual behavior is not known (Barfield and Thomas, 1986). It has been suggested that emission of the 22 kHz call by submissive rats in agonistic situations inhibits aggression by dominants; however, experiments using deafened and muted rats have not provided clear support for this hypothesis (Thomas et al, 1983; Takeuchi and Kawashima, 1986). Blanchard et al (1991) suggests that these calls might function as alarm calls in the colony situation. Administration of anxiolytic drugs such as benzodiazepines decreases 22 kHz UVs following shock (Cuomo et al, 1988; Miczek et al, 1991), strongly suggesting that in at least some contexts these vocalizations are associated with stress or anxiety states. Numerous recent studies have confirmed the usefulness of rat UV measures in behavioral teratology and in the study of pharmacologic effects (e.g., Insel & Winslow, 1991; Miczek et al, 1991; Elsner et al, 1990; Cuomo et al, 1990; Elsner et al, 1988; Bignami et al, 1992).

The use of vocalizations as an indicator of the internal state of the animal has some distinct advantages over some other methods:

- (1) Vocalization is a naturally-emitted response which has ethological validity; it occurs in response to naturally-occurring stressors.
- (2) Because vocalization is a response which is part of the rat's normal behavioral repertoire, subjects do not have to be trained in any way to emit the response. This is in contrast to escape, avoidance, or discrimination responses which require training. Vocalization can be thought of as a naturally-occurring "self-report" measure of the animal's emotional state.
- (3) Measurement of vocalizations is a non-invasive procedure, unlike, for example, the collection of blood for analysis. Therefore the measuring technique itself does not impose further stress on the animal and does not require sacrificing the animal. In addition, vocalization can be measured repeatedly in the same animal without adverse effects on the subject.
- (3) Measurement of vocalizations can be performed in many experimental situations often without extensive modification of the study protocol or apparatus.

Rat vocalizations and startle

The acoustic startle response has been extensively used in studies of pharmacologic and toxic effects. In this lab, startle responses have been studied to assess the effects of organophosphate toxicity (e.g., Miller et al, 1992). UVs are emitted by rats in the acoustic startle testing situation (Kaltwasser, 1990, 1991; Miczek & Vivian, 1993; Murphy et al 1993). The pattern of calling is influenced by the startle stimulus. A startle stimulus occurring during a bout of pulses typically causes a brief interruption of calling, followed by the beginning of a new bout.

Parameters of the startle response and UVs are sometimes correlated. For example, rats on diazepam withdrawal exhibit higher-amplitude startle responses and as well as a higher rate of UVs than controls (Miczek and Vivian, 1993). In other cases, parameters of UV and startle are not correlated (Murphy et al, 1993), suggesting that these two measures may reflect somewhat different underlying states.

During the summer research period, efforts were directed at the following tasks:

- Review of the current literature on adult rat UVs, rat pup UVs, and UVs of other rodent species. The focus was on the usefulness of vocalization measures as indicators of stress, anxiety, or emotionality.
- Broader examination of the contexts in which vocalizations are emitted by rats, in order to assess their usefulness in the measurement of stress and other emotional states.
- More detailed examination of spectral (frequency) characteristics of the vocalizations. Some earlier reports have mentioned the possibility of harmonic components of the 22 kHz call, but this possibility hasn't been closely investigated.
- Validation of measurement and recording techniques used in the lab, in particular, comparison of high-fidelity recordings with recordings made using bat detectors.

General Method

Subjects

The subject pool consisted of 24 adult male Sprague-Dawley rats. Rats were obtained from Charles River and were 43 days of age when they arrived at Brooks AFB. The rats had been subjects in other studies prior to those described here. Most had been food deprived for approximately one year, but had been on ad lib feed for several months prior to the time they were tested here. In addition, most subjects had been repeatedly handled in a Functional Observational Battery. Most of the subjects also had participated in a

previous study of acoustic startle-induced vocalization (Murphy et al, 1993), during which they had been tested in the startle apparatus 2-3 times. All rats were 19-20 months old at the time of the investigations reported here. Rats were housed in standard cages and had continuous access to food and water, except when being tested. Rats were maintained on a 12-hr /D schedule, with lights on at 0600 and off at 1800.

Apparatus

All testing equipment (except when rats were tested in their home cages) was located inside a sound-attenuated chamber. A San Diego Instruments Model SIC startle apparatus was used to present the acoustic startle stimuli. The basic design of the apparatus was a plexiglass tube mounted on a platform which detected characteristics of the startle response. The platform and tube were enclosed inside a chamber. Rats weighing over 600 g were tested in 11.3 cm diameter tubes; smaller rats were tested in 8.3 cm tubes. Acoustic startle stimuli were 108 dB broadband signals, 40 msec in duration. Presentation of the startle was controlled and startle responses were recorded using a San Diego Instruments SR-Lab Control system.

Vocalizations were detected and recorded using ultrasound detectors ("bat detectors;" Ultrasound Advice Model S-25) and/or a high-fidelity recording system consisting of a microphone (Bruel & Kjaer Type 4135) with attached cathode follower (B & K Type 2633) and amplifier (B & K Type 2610). Sensitivity of the bat detector microphone capsule is reported as better than -57 dB +/-3 dB from 20 to 120 kHz and better than -70 dB at 180 kHz (ref 1 V/microbar). The bat detector could be used in either of two settings. The "frequency divide" setting could be used to detect signals across the entire range of sensitivity of the instrument. In the "heterodyne" setting, the bat detector could be tuned to detect signals in a relatively narrow band +/- 5 kHz on either side of a selected frequency.

Frequency response of the B & K system (with microphone shield removed as for recording) extended to 200 kHz, approximately flat +/-1 dB to 100 kHz. The B & K system was calibrated relative to 20 microPa sound pressure using a pistonphone calibrator (B & K Type 4228) coupled to the B & K microphone. The calibrate signal produced by the pistonphone was 250 Hz at 123.98 dB above the reference sound pressure. Ambient pressure and corresponding correction factors were determined using a B & K UZ0004 barometer.

Output from the vocalization detection systems was monitored, digitized, and stored using Global Lab data acquisition software (ver. 2.20) and a Data Translation A/D board (#2831-G). For some studies, a custom-written computer program (M.R. Murphy, unpublished) was used to detect UVs in the data files following collection of the data. This program was designed to identify all signals above a specified amplitude which exceeded a specified duration.

I. 6-Hour Vocalization Recordings

It has been reported that rats emit unelicited, "spontaneous" UVs (both 22 kHz and higher frequency) when in their home cages and isolated from the rest of the colony for long periods (Francis, 1977; Lewis and Schriefer, 1982). We examined the occurrence of UVs in a similar testing situation in order to compare vocalizations in this context with those occurring in the startle paradigm.

Subjects. Seven rats from the subject pool were used. Subjects which had shown high levels of vocalization in earlier startle tests (Murphy et al, 1993) were selected, since rates of vocalizations are typically low in this context and the goal was to examine the general pattern of UVs in this context for comparison with UVs emitted during startle testing.

Apparatus. Subjects were tested in 24 x 45 x 20.5cm cages with wire lids. Cage bottoms were covered with shavings, and food and water were available ad lib during testing. The testing cage was placed inside a chamber, which was kept open to allow it to be illuminated. The testing cage and outer chamber were located inside the sound-attenuated chamber. Vocalizations were detected using a bat detector and were recorded using Global Lab. The bat detector microphone was suspended approximately 6cm above the cage lid. The bat detector itself was located outside the chamber, with the volume setting turned all the way down so that signals were not audible. Light was provided by a desk lamp with a 75w bulb, located so that the rat cage was illuminated. A timer was used to control the light so that it was consistent with the rat's normal L/D schedule.

Procedure. Subjects were tested individually. Each subject was removed from its home cage and placed in the testing cage and chamber. Subjects were given at least 20 min to habituate to the testing cage and chamber. The bat detector's frequency divide setting was used, so that any detectable signal within the bat detector's frequency range would be picked up. Each test lasted 6 h. Data were collected using a sampling rate of 1000 Hz, which had been shown to be suitable in previous tests using startle (Murphy et al, 1993). Some data collection periods occurred during the animals' light phase (LP) and some overlapped the light and dark phases (LDP). The amount of time in the testing session prior to the beginning of the dark phase ranged from 70-135 min, with the lights going out, on average, 107 min into testing. Due to technical difficulties, one testing session took place completely in the dark (the session began 115 min prior to the normal beginning of the dark phase for this rat). Of the 7 rats tested, 3 were tested during both time periods; the remainder were tested during only the LDP.

Results and Discussion. At least some signals were detected during each data collection session using the vocalization detection program. However, only in two cases did these signals clearly show characteristics typical of

the 22 kHz vocalization, such as bout structure. It is possible that many of these detected "signals" were not vocalizations but were due to rat movements. Scratching the cage walls and causing the metal parts of the cage to contact one another are known to cause detectable high frequency sounds.

No signals which could unequivocally be identified as vocalizations were detected during any of the 3 light phase data collection periods. Clear vocalizations were detected during 2 of the 7 (28.6%) dark phase periods. In one of these cases, a clear period of UVs began 163.85 min into the testing period, approximately 49 min into the dark phase. This bout of vocalizations continued for 10.48 min. No further UVs were detected during the session. In the other session where UVs were detected, the rat began vocalizing approximately 20 min into the habituation period, while the calls were being monitored auditorially prior to data collection. Data collection was begun, and the rat continued vocalizing for 7 min into the session. UVs began again at 271.5 min into the session, approximately 148 min into the dark phase. The bout of calling lasted approximately 3.5 min.

Francis (1977) reports calling by isolated rats during both the dark and light phases, with a peak in calling approximately in the middle of the dark phase. It should be noted that the amount of time the animals spent vocalizing in Francis' study was extremely small, and several animals showed peaks in calling during the light phase also. Small sample sizes in both Francis' study and this one make comparisons difficult.

The bout structure of the calls which were detected here appears to be similar to that of calling bouts observed during startle testing. UVs were given in series of several pulses, with longer pauses in between the series. Pulse duration was roughly the same as seen in startle tests. Although in some cases, the intensity of these spontaneous calls was as high as those observed during startle testing, in other cases the intensity was much lower. Vocalization bouts generally began with series of lower intensity pulses, working up to higher intensity and then decreasing again so that the final few series in a calling bout consisted of quite low intensity pulses.

II. Vocalization in Response to Touch

Brudzynski and Ociepa (1992) report that rats vocalize in response to gentle touch. Subjects were tested using a technique similar to that used by Brudzynski and Ociepa in order to compare parameters of UVs in this context with those given in the acoustic startle paradigm, and in order to examine more closely the spectral characteristics of the calls.

Subjects and Apparatus. Nineteen subjects were selected at random from the subject pool. Subjects were tested in their home cages, in the colony room. Vocalizations were detected using a bat detector.

Procedure. Subjects were tested during the light phase. The subject's

cage was pulled away from the cage rack, and the bat detector was held near the open end of the cage. The distance of the microphone from the rat during testing was highly variable, depending on the rat's movements, but ranged from approximately 4-30cm.

The experimenter then began touching the rat gently with a gloved hand. Rats were touched briefly (approximately .5 sec/touch) two or three times, approximately every 20-30 sec. Touches were directed to the dorsal neck and spine area, since Brudzynski and Ociepa had found touches in this region to be most likely to elicit UVs from their subjects. Latency to the first UV was noted. Until the rat began vocalizing, the frequency divide setting on the bat detector was used. Once the subject began vocalizing reliably, the bat detector was changed to the heterodyne setting, and the frequency selection dial was slowly moved through its settings. Frequencies at which calls were detected were noted. This was done up to 3 times, or until the rat stopped vocalizing. Calls were monitored on headphones throughout testing. Testing was discontinued after 15 min if the rat had not begun vocalizing at that point. No more than 4 animals were tested per day, in order to minimize disturbances in the colony room which might have influenced the animals.

Results and Discussion. Thirteen of the 19 subjects (68.4%) vocalized in response to repeated touch. This percentage is very close to that obtained by Brudzynski and Ociepa (66.7%). The average latency to vocalize for 11 of the 12 subjects which vocalized was 331.17s. Latency was not recorded for one subject.

When vocalizing, rats usually remained still, crouched down on all fours, with their heads down. One rat vocalized while rearing, exploring the cage, and grooming its face. In many cases, the rat's sides and nose could be seen to move when the calls were emitted. In a more general sense, the calls did not seem to be associated with submission or fear, since some rats which spent the entire 15-min session crouched in a corner (apparently submissive) did not vocalize at all, and some rats which did vocalize spent a great deal of time exploring the cage and investigating the area near the experimenter and the microphone.

As Brudzynski and Ociepa noted in their study, UVs did not seem to be in direct response to touch, as they rarely if ever occurred immediately following touches. There was generally an interval of several seconds between touches and UVs.

With one exception, calls detected were clearly given by the animal being tested, and no calls were detected from other colony animals. This was determined by periodically pointing the bat detector away from the animal being tested and toward other animals. In one case, UVs were detected during a test, but they were extremely faint. The subject in this case also did not show other signs of vocalization (e.g., rhythmic movement of the sides). The

calls appeared to be emitted by another nearby rat, since they increased in intensity when the bat detector was pointed towards this animal. This could not be determined with certainty since the animal did not vocalize for a long enough period.

The calls showed the typical bout structure reported for 22 kHz calls; they were emitted in series consisting of several pulses. In all cases where it the animals vocalized long enough to examine it, frequencies above the 19-24 kHz range were detected. Typically, the output generated by the bat detector sounded most intense at around 19-24 kHz; however, for individual rats, frequencies of approximately 38, 45, 50-60, and 70 kHz were commonly detected. Tuning the bat detector to frequencies falling between these would result in no signal being detected. In most cases, the signals detected were clear and intense. In some cases, the bat detector would produce faint signals signifying sound above 100 kHz. The exact frequencies which were detected varied among rats, and sometimes varied slightly within the same rat.

It is not known if these higher (>25 kHz) detected frequencies were actually part of the call and were produced by the rat, or were due to some aspect of the bat detector's functioning. The higher-frequency signals showed the same pulse/series structure typically seen with the 22 kHz call, and the signals were correlated with behavioral signs of vocalization emission. The signals were not detected by the bat detector when it was not directed toward a vocalizing rat, so the signals were not simply part of the ambient noise environment.

III. Multiple-Channel Recordings

Prior tests of UVs during startle (Murphy et al, 1993) utilized the bat detectors in the frequency divide mode. In this mode, the bat detector responds to any signals which are present across its entire sensitivity range. This type of recording therefore does not provide information concerning the frequency of these calls. In order to further investigate the spectral characteristics of acoustic startle-induced UVs, vocalizations were recorded during startle tests using several bat detectors, each tuned to detect signals in a different frequency range.

Subjects and Apparatus. Two rats from the subject pool were used in this test. They were selected because of their propensity to vocalize in the startle paradigm. Acoustic startle stimuli were presented and startle responses were measured using the San Diego Instruments startle apparatus and control system. Vocalizations were detected using several bat detectors, each of which was tuned to a different frequency using the heterodyne circuit. For the "4 mic" tests, 4 bat detectors were used, one tuned to each of the following frequencies: 24 kHz, 40 kHz, 70 kHz, and frequency divide. For the "6 mic" tests, 6 bat detectors (tuned to 22 kHz, 40 kHz, 50 kHz, 60 kHz, 70

kHz, and frequency divide setting) were used. In both tests, the bat detector microphones were located inside the startle chamber, while the bat detectors themselves were located outside the chamber. The microphones were attached in an array near openings at one end of the plexiglass startle tube. The distance from the microphones to the tube was approximately 1.5cm; the distance from the microphone to the rat varied between approximately 3 and 8cm, depending on the rat's movements. Global Lab data acquisition software was used to display the output of all channels and to record the data.

Procedure. One subject was tested twice, once using the "4 mic" procedure and once using the "6 mic" procedure. The other subject was tested using only the "6 mic" procedure. A sampling frequency of 1000 Hz was used for recording. Both rats were tested during light phase. The startle testing procedure used was identical to that used by Murphy et al (1993). Rats were tested individually. Each subject was brought into the sound-attenuated chamber and then placed in the startle apparatus. The startle chamber doors were closed, and a five minute habituation period began. Following the 5-min habituation period, 20 acoustic startle stimuli were presented at 1 minute intervals. Following the last startle, the subject spent a final 5-min period in the apparatus before being removed and placed back in its home cage. Characteristics of the startle (vmax, tmax, etc) were displayed on the monitor, but these data were not utilized in this study.

Results and Discussion. Both subjects vocalized readily in the startle paradigm. Signals were detected on all frequency settings, although there were clear differences at the different settings. In general, when they appeared, signals at each setting showed the same pattern - several pulses in series, with these series of pulses separated by longer pauses. Quite often, signals recorded on different frequency channels would begin and end simultaneously, suggesting that these were part of the same vocalization pulse. However, the intensity of the signals recorded at the different frequencies varied greatly. The 22-24 kHz signals were the strongest, and they remained fairly strong throughout the 30 min testing session. Other signals were generally of lower intensity, often dropping off or completely ceasing before the end of the session. The 60 kHz channel often registered no signal at all at the same time the others were indicating high intensity signals.

These results cannot be interpreted unequivocally. The results are consistent with those for the touch-elicited UVs discussed above. In both cases, the bat detector registered the strongest response when tuned to approximately 19-25 kHz, with other settings showing lower intensity responses and some none at all. As was stated above, it is possible that these higher frequency components are due to some aspect of the recording system and are not produced by the signalling animal. The results suggest, however, that the

"22 kHz" call have a more complex frequency structure than has been reported previously.

IV. Recordings in Startle Apparatus

We recorded each rat's vocalizations in the startle testing paradigm. The goal was to use the B & K recording system to obtain high-fidelity recordings of rat vocalizations in the testing situation.

Subjects and Apparatus. All 24 subjects from the subject pool were used. Acoustic startle stimuli were presented and startle responses were measured using the San Diego Instruments startle apparatus and control system. Vocalizations were recorded using the B & K recording system and the Global Lab data acquisition system. A bat detector was also used to monitor vocalizations.

The B & K microphone and cathode follower were suspended approximately 3.2cm above several openings in the plexiglass startle tube, at the end of the apparatus nearest the rat's head. Output from the microphone was then sent to the amplifier, and from there to the Data Translation A/D board. The converted signal was then displayed on a monitor using Global Lab.

The bat detector microphone was suspended approximately 2.4cm above a hole in the center of the startle tube. Extensive experience with the bat detector had demonstrated that it was sensitive enough to pick up vocalizations when located at this point. The bat detector itself was located outside the startle chamber.

Procedure. Prior to testing any rats, a 5-sec calibrate signal was recorded (using the pistonphone calibrator) at a sampling rate of 50 kHz. The correction factor for barometric pressure also noted. A new calibrate signal was recorded after every four rats had been tested. The microphone shield was removed during data collection.

All rats were tested during the light phase. The startle testing procedure used was identical to that used by Murphy et al (1993) and described above. Each rat was tested individually. Vocalizations were monitored during the 5-min habituation period by listening to the audible output of the bat detector on the "frequency divide" setting, and by visually monitoring the output of the B&K system using Global Lab. Volume on the bat detector was turned down prior to recording so that the bat detector output was not audible during this time.

After the startle stimuli began and when the rat was vocalizing reliably, 2 20-sec samples of vocalizations were recorded. We attempted to record 2 samples from each rat, one from the first third of the startle session and one from the final third, in order to examine whether the parameters of the calls change across the startle session. The position of the rat in the startle tube was noted prior to recording. We attempted to

record only when the rat's head was located at the same end of the tube as the B&K microphone. Once two samples had been recorded from the rat, it was removed from the startle apparatus and placed back in its home cage. Startle tubes were cleaned as necessary between trials.

Results and Discussion. Recordings were obtained from 20 of the 24 subjects (83%). Four of the subjects apparently did not vocalize at all during the test. The percentage of animals vocalizing is higher than that reported in other studies (Kaltwasser, 1990, 1991; Miczek and Vivian, 1993);

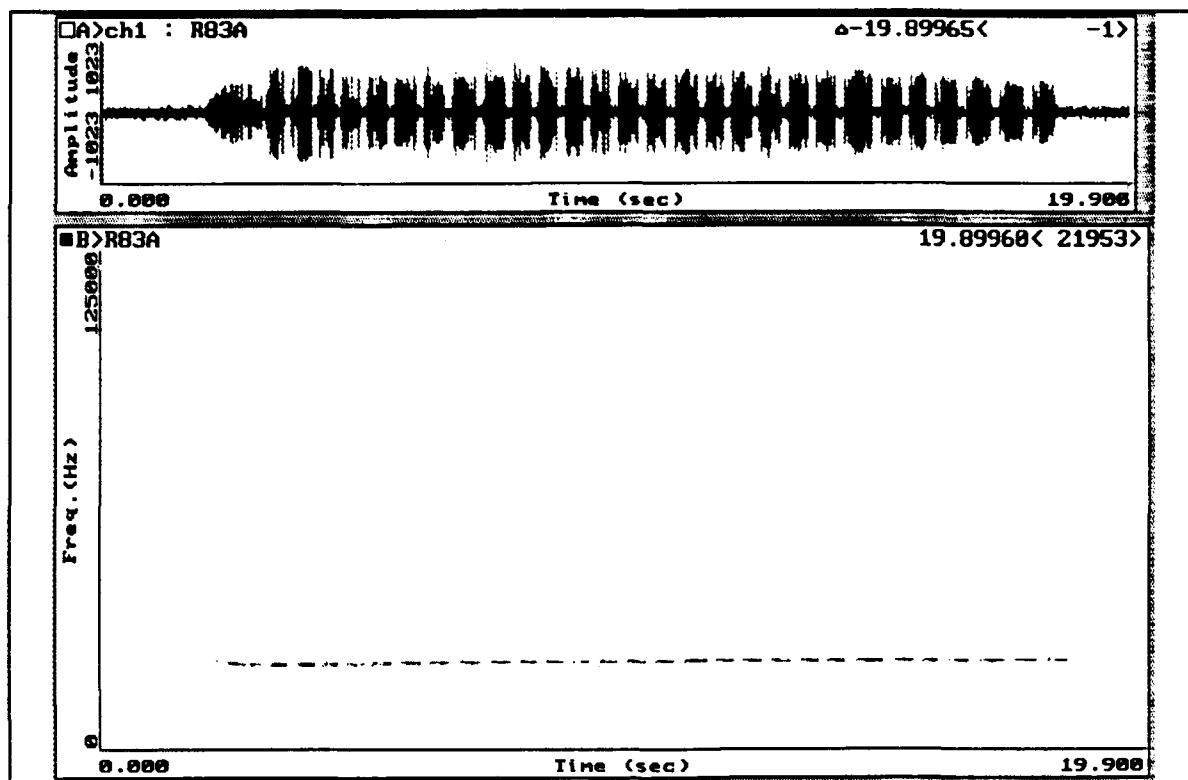


Figure 1.

however, it should be noted that the subjects tested here had previously been tested for vocalization in the startle paradigm and were selected from a larger group partly on the basis of their propensity to vocalize in this situation.

Analyses of the results are not yet complete. Parameters to be examined include duration of the pulses, spectral characteristics of the calls, and intensity measurements (rise-decay times, maximum intensity). These analyses should enable accurate characterization of the frequency of the calls, and a detailed assessment of the higher frequency (above 25 kHz) components of the calls, if they exist.

Preliminary analyses utilizing waveforms, spectrograms, power spectra, and energy distributions of ultrasonic rat vocalizations indicate that the

calls obtained in this study are acoustically similar to those reported previously by other investigators (Kaltwasser, 1990, 1991). Figure 1 shows a series of intense, narrow-band pulses emitted in rapid succession by one subject. Energy of the pulses in this series is centered around 22 kHz. An expanded view of several of these pulses is shown in Figure 2. Frequency

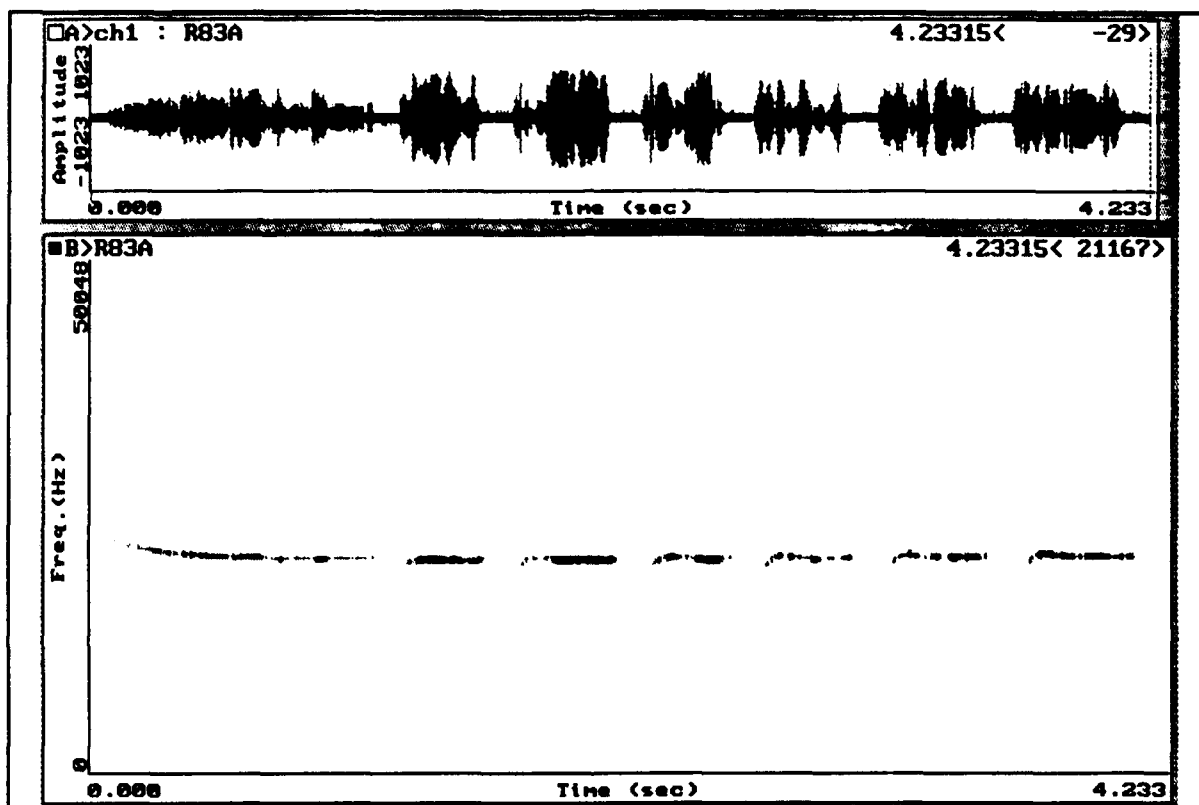


Figure 2.

modulation tends to occur over a range of about 5 kHz. Intensity of most calls exceeds 90 dB (re 20 μ Pa) sound pressure level. Call intensity, frequency modulation, onset-offset transients, rate of emission, and number of pulses per series will be examined to investigate the relationship between these parameters and characteristics of stressors.

V. B & K Microphone/Bat Detector Comparative Recordings

Simultaneous recordings using the B & K recording system and the bat detector were made in the startle paradigm. The goal was to obtain recordings for the purpose of comparing parameters of recordings obtained using these two different systems.

Subjects and Apparatus. Because the goal was to determine the comparability of recordings obtained using the B & K and bat detector recording systems, subjects were chosen on the basis of their propensity to

vocalize in the startle situation. All subjects had been previously tested in the startle paradigm. Rats were tested in the startle apparatus. Vocalizations were recorded using both the B&K system and the bat detector. Data were collected from both systems using Global Lab. Microphones were located as in the startle tests (see above).

Procedure. All recordings were made during the rats' light phase. The HF channel of the bat detector was used for recording. Data from both systems was simultaneously collected and displayed using the Global Lab system. Sampling rate was 125 kHz for both systems.

The startle procedure was the same as that used during previous startle tests (see above). A 5-min habituation period in the startle apparatus was followed by startle stimuli at 1-min intervals. Vocalizations were monitored visually using Global Lab and auditorially using the bat detector during the habituation period. When the rat began vocalizing, the gain setting on the bat detector was adjusted to make the amplitude of the signal from the bat detector approximately equivalent to the amplitude of the B & K signal.

Recordings were made after the startles began. Two 20-sec sample recordings were made from each rat. Since the goal was to record as many vocalizations as possible in order to obtain an adequate sample for comparison purposes, we attempted to record during inter-startle intervals in which the rat was vocalizing consistently and strongly. During recording, the volume setting on the bat detector was turned down so that its output was not audible. Prior to each recording, the location of the rat was checked to ensure that the rat's head was at the end of the startle tube closest to the microphone. Startle procedures were halted and the rat was removed from the startle apparatus as soon as 2 recordings had been made.

Results and Discussion. All rats vocalized during the procedure. Some rats began vocalizing during the habituation period, but recordings were not made until startle stimuli began. (One subject, for example, began vocalizing 12 sec into the habituation period.) Analyses of these data are not yet complete. Parameters similar to those listed above (startle tests) will be examined, and results for recordings made using the two different systems will be compared. If results for the two systems are comparable, this will be an indication that it may be possible to use the less expensive bat detector to obtain adequate recordings of startle-induced vocalizations.

General Discussion

In agreement with the results of studies by other investigators, we have found that rats emit 22 kHz UVs in response to acoustic startle, in response to light touch on the neck and spinal area, and "spontaneously" as a part of their normal, undisturbed behavior pattern. In all these contexts, these calls are emitted as a series of several (generally 3 to more than 20) pulses,

with each pulse lasting approximately 500 msec to over 2 sec. Although detailed analyses of the spectral characteristics of the calls are not yet complete, some of the data collected here suggest that these calls may have components at frequencies above the 19-25 kHz range in which they are usually reported. While several previous published studies have briefly mentioned the presence of harmonics in the 22 kHz call, this aspect of the call has never been fully described, and many studies do not report these components at all. It should be possible, on analyzing recordings made using the high-fidelity B&K recording system, to determine whether these high frequency components detected using the bat detector are produced by the rat or are artifacts of the recording equipment used.

It should be noted that while rats vocalized in each of the testing situations examined here, these contexts obviously were not equivalent in their ability to elicit UVs from subjects. While a high percentage of subjects vocalized in response to acoustic startle stimuli, a lower percentage vocalized in response to touch, and a still lower percentage in the isolated, undisturbed condition. Rate of vocalizing was not explicitly compared here, however, it also varied across these conditions and was consistent the results for percentage of animals vocalizing (startle > touch > isolation). These preliminary measurements of these basic aspects of rat vocalization in varying contexts strongly indicate that vocalizing may be closely related to stress-inducing properties of the context.

The usefulness of these calls in assessing the internal state of the rat has been discussed by numerous researchers. The fact that 22 kHz UVs are naturally emitted by rats in numerous situations makes them a convenient behavioral parameter to examine. Further investigations of the contexts of these calls should further establish their usefulness in toxicological assessment. More detailed examination of the physical parameters of calls given in different contexts will demonstrate whether variations in acoustic characteristics are indicative of different underlying states on the part of the animal. Further examination of the relationship between the acoustic characteristics of the call and magnitude or other characteristics of the stressor will also help establish the usefulness of this measure.

References

- Baker, S.C., Mulligan, B.E., and Murphy, M.R. Ultrasonic vocalizations by adult rats (Rattus norvegicus). AL-TR-1991-0135 (1991).
Barfield, R.J., and Geyer, L.A. Sexual behavior: Ultrasonic postejaculatory song of the male rat. Science, 176, 1349-1350 (1972).
Barfield, R.J., and Thomas, D.A. The role of ultrasonic vocalizations in the

- regulation of reproduction in rats. *Annals of the New York Academy of Sciences*, , 33-43 (1986).
- Bignami, G., Laviola, G., Alleva, E., Cagiano, R., Lacomba, C., and Cuomo, V. Developmental aspects of neurobehavioural toxicity. *Toxicology Letters*, 64/65, 231-237 (1992).
- Blanchard, R.J., Blanchard, D.C., Agullana, R., and Weiss, S.M. Twenty-two kHz alarm cries to presentation of a predator, by laboratory rats living in visible burrow systems. *Physiology & Behavior*, 50, 967-972 (1991).
- Blanchard, R.J., Agullana, R., McGee, L., Weiss, S., and Blanchard, D.C. Sex differences in the incidence and sonographic characteristics of antipredator ultrasonic cries in the laboratory rat. *Journal of Comparative Psychology*, 106, 270-277 (1992).
- Brown, R.E. The 22-kHz pre-ejaculatory vocalization of the male rat. *Physiology & Behavior*, 22, 483-489 (1979).
- Brudzynski, S.M., and Ociepa, D. Ultrasonic vocalization of laboratory rats in response to handling and touch. *Physiology & Behavior*, 52, 655-660 (1992).
- Cuomo, V., Cagiano, R., DeSalvia, M.A., Maselli, M.A., Renna, G., and Racagni, G. Ultrasonic vocalization in response to unavoidable aversive stimuli in rats: Effects of benzodiazepines. *Life Sciences*, 43, 485-491 (1988).
- Cuomo, V., Cagiano, R., DeSalvia, M.A., Mazzocchi, M., Persischella, M., and Renna, G. Ultrasonic vocalization as an indicator of emotional state during active avoidance learning in rats. *Life Sciences*, 50, 1049-1055 (1992).
- Cuomo, V., DeSalvia, M.A., Lacomba, C., Tattoli, M., and Cagiano, R. A new experimental approach for detecting emotional and motivational changes produced by neuroactive compounds in rodents. *Ann. Ist. Super. Sanita*, 26, 89-94 (1990).
- DeSalvia, M.A., Cagiano, R., Cortese, I., Lacomba, C., Renna, G., Siro Brigani, G., and Cuomo, V. Ultrasonic vocalization during the acquisition of an active avoidance schedule in rats: Effects of diazepam. *Pharmacological Research*, 22, Supp 1, 65-66 (1990).
- Elsner, J., Hodel, B., Suter, K.E., Oelke, D., Ulbrich, B., Schreiner, G., Cuomo, V., Cagiano, R., Rosengren, L.E., Karlsson, J.E., and Haglid, K.G. Detection limits of different approaches in behavioral teratology, and correlation of effects with neurochemical parameters. *Neurotoxicology and Teratology*, 10, 155-167 (1988).
- Elsner, J., Suter, D., and Alder, S. Microanalysis of ultrasound vocalizations of young rats: Assessment of the behavioral teratogenicity of methylmercury. *Neurotoxicology and Teratology*, 12, 7-14 (1990).
- Francis, R.L. 22-kHz calls by isolated rodents. *Nature*, 265, 236-238 (1977).

- Insel, T.R., and Winslow, J.T. Rat pup ultrasonic vocalizations: An ethologically relevant behaviour responsive to anxiolytics. In: *Animal Models in Psychopharmacology*, eds. B. Olivier, J. Mos, and J.L. Slangen. Basel: Birkhauser Verlag.
- Kaltwasser, M.T. Startle-inducing acoustic stimuli evoke ultrasonic vocalization in the rat. *Physiology & Behavior*, 48, 13-17. (1990).
- Kaltwasser, M.T. Acoustic startle induced ultrasonic vocalization in the rat: A novel animal model of anxiety? *Behavioural Brain Research*, 43, 133-137 (1991).
- Lewis, P.R., and Schriefer, J.A. Ultrasound production by pregnant rats. *Behavioral and Neural Biology*, 35, 422-425.
- Miczek, K.A., Tornatzky, W., and Vivian, J. Ethology and neuropharmacology: Rodent ultrasounds. In: *Animal Models in Psychopharmacology*, eds. B. Olivier, J. Mos, and J.L. Slangen. Basel: Birkhauser Verlag. (1991).
- Miczek, K.A., and Vivian, J.A. Automatic quantification of withdrawal from 5-day diazepam in rats: Ultrasonic distress vocalizations and hyperreflexia to acoustic startle stimuli. *Psychopharmacology*, 110, 379-382 (1993).
- Miller, S.A., Hartgraves, S.L., Enos, C.J., Williams, M.L., and Murphy, M.R. High dose organophosphate exposure causes permanent hyperreactivity. (Abstract) First International Behavioral Neuroscience Conference, 1992.
- Miller, S.A., Kerenyi, S.Z., Blick, D.W., and Murphy, M.R. The efficacy of physostigmine as a pretreatment for organophosphate poisoning. *Pharmacology Biochemistry and Behavior*, 44, 343-347 (1993).
- Murphy, M.R., Miller, S.A., Enos, C.J., Chambers, J.P., and Hartgraves, S.L. The use of carboxylesterase inhibitors to develop an improved rodent model of organophosphate toxicity. *Proc. Med. Def. Biosci. Rev.*, 1991.
- Murphy, M.R., Miller, S.A., Kerenyi, S.Z., Switzer, R.C., Blick, D.W., and Hartgraves, S.L. Soman toxic syndrome: Effects of soman on biochemistry, brain and behavior in rats. USAFSAM-TR-90-15 (1990).
- Murphy, M.R., Miller, S.A., Baker, S.C., Sherry, C.J., and Mulligan, B.E. System to detect and analyze rat ultrasonic vocalizations for toxicological assessment. Society for Neuroscience, 1993.
- Sales, G.D. Ultrasound and aggressive behaviour in rats and other small mammals. *Animal Behaviour*, 20, 88-100 (1972a).
- Sales, G.D. Ultrasound and mating behaviour in rodents with some observations on other behavioural situations. *Journal of Zoology, London*, 168, 149-164 (1972b).
- Sewell, G.D. Ultrasound in adult rodents. *Nature*, 215, 512 (1967).
- Takahashi, L.K., Thomas, D.A., and Barfield, R.J. Analysis of ultrasonic vocalizations emitted by residents during aggressive encounters among

- rats (Rattus norvegicus). Journal of Comparative Psychology, 97, 207-212 (1983).
- Takeuchi, H., and Kawashima, S. Ultrasonic vocalizations and aggressive behavior in male rats. Physiology and Behavior, 38, 545-550.
- Thomas, D.A., and Barfield, R.J. Ultrasonic vocalization of the female rat (Rattus norvegicus) during mating. Animal Behaviour, 33, 720-725 (1985).
- Thomas, D.A., Takahashi, L.K., and Barfield, R.J. Analysis of ultrasonic vocalizations emitted by intruders during aggressive encounters among rats (Rattus norvegicus). Journal of Comparative Psychology, 97, 201-206 (1983).
- Tonoue, T., Iwasawa, H., and Naito, H. Diazepam and endorphin independently inhibit ultrasonic distress calls in rats. European Journal of Pharmacology, 142, 133-136 (1987).
- van der Poel, A.M., Noach, E.J.K., and Miczek, K.A. Temporal patterning of ultrasonic distress calls in the adult rat: Effects of morphine and benzodiazepines. Psychopharmacology, 97, 147-148 (1989).

Acknowledgements

I would like to thank the following individuals for their assistance with various aspects of this project: Ms. Stephanie Miller, Mr. Randall Wolfe, Dr. B.E. Mulligan, Ann Jennifer Curtis, and Sgt. Max Williams. I would especially thank to thank Dr. Michael R. Murphy, the Air Force Office of Scientific Research, and Research and Development Laboratories for their sponsorship.

**A CONCEPTUAL DESIGN FRAMEWORK FOR
CONCURRENT ENGINEERING**

**Prasad S. Gavankar, Ph.D., P. E.
Assistant Professor
Department of Mechanical and Industrial Engineering**

**Texas A&M- Kingsville
Campus Box 191
Kingsville, TX 78363**

**Final Report for:
Summer Faculty Research Program
Wright Patterson Air Force Base**

**Sponsored by:
Air Force Office of Scientific Research
Bolling Air Force Base, Washington, D. C.**

August 1993

A CONCEPTUAL DESIGN FRAMEWORK FOR CONCURRENT ENGINEERING

**Prasad S. Gavankar
Assistant Professor
Department of Mechanical and Industrial Engineering
Texas A&M- Kingsville**

Abstract

This report summarizes important research in the area of conceptual design and outlines a road map for carrying out conceptual design. It studies the impact of concurrent engineering philosophy on conceptual design. A case study is given to illustrate the proposed methodology. Since more than sixty percent of product cost is determined at the conceptual level, the paper emphasizes that feed back from concurrent engineering team should be sought right at the conceptual level. The report addresses the problem of how new designs can be evaluated at the conceptual stage by taking into account manufacturing constraints and field performance data of past designs.

A CONCEPTUAL DESIGN FRAMEWORK FOR CONCURRENT ENGINEERING

Prasad S. Gavankar

1. Introduction

Design is one of the most challenging activities performed by engineers. It is also one of the leading causes of success or failure of a company in today's global market place. Until recently, designers alone were involved in design projects with little input from other departments. Modern successful organizations have changed this course by introducing experts from manufacturing, marketing, quality control and finance in design teams. This philosophy of design is popularly known as concurrent engineering.

Before exploring the impact of concurrent engineering on design, let us look at design activity more closely. There are two important characteristics associated with any design activity. First, design implies a need. Second, the existing theories of structures, machine design, ergonomics, aesthetics, etc., are interrelated theories so that design theory is a theory about these theories or a metatheory [NEWS88].

A design activity is characterized by six important states: perceived need, function, physical phenomena, embodiment, artifact type and artifact instance [DIXO88]. These six states can be explained with an example as shown below:

Need: A temperature sensitive on/off control for an electric switch.

Functions: To provide the required motion to open and close the electric switch based on temperature change.

Phenomena: Materials expand and contract with temperature change, but at different rates.

Embodiment: Thin strips of materials with different coefficients of thermal expansion affixed together. An embodiment defines the specific solution principle in the physical world.

Artifact type: Bimetallic coil. It is an instance of the embodiment type.

Instance: Coil of specified materials and dimensions.

In this report, an attempt is made to develop a procedural model to conduct conceptual design. A flow chart as well as a verbal description define the proposed steps to be followed during this important design phase. Significant past research in the area of conceptual design is summarized below.

2. Past research

The design scheme proposed in this report is primarily based on the design methodology recommended by Hubka [HUBK88]. Hubka views design process as a sequential process in which five primary steps are included. They are listed below.

1. Step-I: The customer or the potential user specifies his/her requirements.
2. Step-II: Functional requirements and constraints are drawn to express the customer needs and the corresponding constraints in concrete terms.

3. Step-III: A scheme is developed to satisfy the desired functions and constraints often decomposing the main functions into their subfunctions.
4. Step-IV: Line diagrams, popularly known as organ structures that indicate the kinematic and physical relationship of important elements in the design are drawn. The organ structures are studied to see how different functions and constraints can be satisfied.
5. Step-V: Exact component configuration, dimensions and tolerances are specified at this level.

Roth divided the design activity into four different steps [ROTH68, ROTH71]:

1. Step-I: Product requirements are analyzed for the final requirements and customer needs.
2. Step-II: Function structure diagrams are drawn to support the customer needs. The proposed designs are compared with actual customer needs and design constraints.
3. Step-III: Embodiments of the solutions to the elementary problems are synthesized in accordance with the overall function structure. Variation in these embodiments produces a host of general solutions from which the best can be chosen from the point of view of producibility constraints.
4. Step-IV: Actual production drawings are developed based on component selection carried out in Step-III.

Roth emphasizes the use of design catalogs in conceptual design.

Pahl and Beitz propose a design technique very similar to the one proposed by Hubka [PAHL84]. During the embodiment phase they propose that a designer should follow three basic rules- clarity, simplicity and safety.

Clarity of function or lack ambiguity of a design facilitates reliable prediction of the performance of the end product and in many cases saves time and costly analysis. Simplicity generally guarantees economic feasibility.

A smaller number of components and simple shapes are produced more quickly and easily. Safety imposes a consistent approach to the problem of strength, reliability, accident prevention and the protection of environment.

Pahl and Beitz provide an extensive list of design rules that will aid a designer in following DFX guidelines such as guidelines for design for design for fabrication, assembly, etc. Note that DFX guidelines are encapsulated in the three basic design rules discussed above.

Suh considers the following two design axioms as the most important criteria [SUH90]-

Axiom-1: Maintain the independence of functional requirements (FRs).

Axiom-2: Minimize the information content of the design.

Suh derives following design rules from the above axioms:

- Rule-1: Decouple of separate parts or aspects of a solution if FRs are coupled or become interdependent in the designs proposed.
- Rule-2: Minimize the number of FRs and constraints.
- Rule-3: Integrate design features in a single physical part if FRs can be independently satisfied in the proposed solution.
- Rule-4: Use standardized or interchangeable parts if the use of these parts is consistent with the FRs and constraints.

Rule-5: Use symmetrical shapes and/or arrangements if they are consistent with the FRs and constraints.

Rule-6: Specify the largest tolerance in stating FRs.

Rule-7: Seek an uncoupled design that requires less information than coupled designs in satisfying a set of FRs.

Note that rules 3 through 7 are well-known DFX guidelines.

Ullman believes in a sequential process of design with a hierarchical division of design function. This is followed by the assignment of a subassembly to each subfunction [ULLM92]. The subassemblies are then subdivided into their constituent components for detail design. Ullman emphasizes the application of quality deployment function while identifying customer needs.

Unlike the research discussed in the above sections, Taguchi's philosophy is not applicable directly to conceptual design. However, it is quite relevant to material selection, component selection and tolerance allocation and analysis. Taguchi defines quality in terms of a loss function that measures the loss the design causes to the society [TAGU90]. Taguchi shows that the loss is proportional to the square of the deviation of a design parameter from its nominal value. It is the designer's responsibility to make sure that the deviation in the manufactured part will be as small as possible. The designer, therefore, should design parts with materials that will be the least sensitive to the variation in manufacturing processes as well as to the variation caused by field noise (e.g., temperature fluctuations, vibrations). Also, the physical properties and shapes of ready-made components should be such that they are the least sensitive to in-process noise and field noise. Although the efficacy of Taguchi's design of experiments techniques has been questioned by renowned statisticians (see [BOX88] for example), Taguchi has done an excellent job of making designers aware of the importance of statistical tools in design process.

Pugh's approach to engineering design is very similar to those advocated by Hubka, Ullman and other researchers in the field of engineering design [PUGH91]. A few novelties in his method are listed below:

- (i) In concept generation, Pugh believes in recording a brilliant concept (confirmed by a formal concept selection method) even if it satisfies the design problem partially. He believes that product design specifications (consisting of FRs and constraints) are evolutionary and hence future changes in these specifications may render the current partial solution a viable future solution.
- (ii) Whereas in the past research, group effort has been emphasized in idea generation, Pugh follows McGrath's advice that "Individuals working separately generate many more, and more creative (as rated by judges) ideas than do groups, even when the redundancies among member ideas are deleted, and, of course, without the stimulation of hearing and piggy-backing on the ideas of others. The difference is large, robust, and general" [MCGR84]. In this light Pugh suggests that ideal concepts are often best generated by individuals whereas concept selection and enhancement are often best performed in groups.

Pugh's approach to design evaluation using weighted matrix has been emphasized repeatedly in the past research (see [ULLM92], for example). The weighted matrix, however, is difficult to obtain for a new generation of

products based on new technology. It is important to note that the numbers entered in the weighted matrix are judgement-based and are not absolute.

3. Classification of design:

1. Classification based on stages of development:

- a. Identification of need: Essential needs of the potential customers are explored and the market niche is identified. Also, the cost figures the customer will be willing to pay are estimated.
- b. Problem definition: Customer needs are expressed in terms of the functional requirements and constraints. This is one of the most difficult phases especially for an innovative design since the functional requirements and constraints are fuzzy in the case of innovative products.
- c. Conceptual Design: In this phase, conceptual abstract diagrams showing physical principles involved in the design are developed. Also, a decision is made on what type of components will constitute the design.
- d. Preliminary Design: In preliminary design, the general layout of different assemblies and subassemblies is determined. Material type and hardness requirements are also decided during this phase.
- e. Detail Design: Dimensions and tolerances of components and surface finish values are determined during detail design. Datums and certain manufacturing operations are also specified at this stage.
- f. Prototype Development: One or more prototype parts are fabricated according to the specifications in the detail design. The intention is to fine tune the design specification before full scale manufacture. Detail design may be revised as a result of experiences encountered during the prototype development.
- g. Manufacturing Plan Development: Detailed manufacturing sequence, tooling requirement, and a setup plan are developed at this stage while taking into account the production scheduling constraints. Manufacturing plan development is popularly known as process planning.

In this research report, steps a, b, c, as well as d are discussed. Also, conceptual design is considered as an aggregation of activities b, c, and d.

2. Classification based on type of design:

- | | |
|----------------------|-------------------------------------|
| a. Mechanical Design | d. Electronics Design |
| b. Electrical Design | e. Industrial Design |
| c. Structural Design | f. Mixed Design: most common today. |

3. Classification based on design philosophy

- | | |
|---------------------|--|
| a. Top-down design | c. Mixed design: partially top-down and partially bottom-up. |
| b. Bottom-up design | |

4. Classification based on degree of novelty [PAHL84]:

- a. Original design: involves development of an original solution principle for a system.
- b. Adaptive design: involves adapting a known system (the solution principle remaining the same) to a changed task. Here original designs of parts or assemblies are often called for.

- c. Variant design: involves varying the size and/or arrangement of certain aspects of the chosen system, the function and solution principle remaining unchanged.

The above design classifications are not mutually exclusive. In fact, any design activity may belong to one or more categories among the different classes. For example, a design of an electronic watch will fall in the categories 1a through 1g as well as in 2f.

Important characteristics of a conceptual design can be listed as follows:

1. During the initial stages of conceptual design the design problem has a high level of ambiguity.
2. At the initial stage in the designer/client relationship, not only do they both not know how the design is going to evolve, they do not understand each other completely and will have to go through a process of conflict resolution. Brain storming sessions between designer(s) and client at regular intervals during conceptual design development are highly recommended.
3. Various functional requirements (also known as functions) and constraints of the design are outlined. The designer and customer come up with a consensus when they identify four design attributes listed below.
 - (i) Primary functions: These are the most critical functions the design has to satisfy. They are largely specified by the customer and in some cases by the technology governing the design.
 - (ii) Secondary functions: The designer has some degree of flexibility in meeting these functions.
 - (iii) Primary constraints: The designer has to satisfy these constraints. They are typically specified either by the customer or the current technology.
 - (iv) Secondary constraints: These constraints are not as rigid as the primary constraints and the designer can ignore some of them if the value to cost ratio of the design is improved.

Constraints can be classified based on design considerations including performance, schedule, manufacture, transportation, maintenance, safety, ergonomics, aesthetics, costs and disposal [STAU89].

Constraints can also be categorized on the basis of their origin. Three possibilities arise- they may be inherent in the design problem, they may be introduced by the designer or they may result from the interrelationship of form and function of various modules of the design.

Constraints can be distinguished from functional requirements based on the fact that constraints are more or less rigid and often describe the environment with which the design interacts. Functional requirements, on the other hand, describe what the design is supposed to achieve.

Example:

If the design objective is to come up with a device that can be used to open cans as well as bottles for household applications, the primary functional requirements can be written as follows:

- FR1: The device should be able to open a can.
FR2: The device should be able to open a bottle.

For this example, constraints can be listed as follows:

- CR1: The customer should be able to open any can as well as any bottle using a force less than X lbf and a torque less than Y lbf-ft (primary ergonomic constraints).
- CR2: The device should be child-safe (a primary constraint).
- CR3: The device should not corrode (a primary constraint).
- CR4: The device should cost less than \$3.00 (a secondary constraint).
- CR5: The useful life of the can/bottle opener should be more than 5 years (a secondary constraint).
- CR6: The device should weigh less than 5 oz. (a secondary constraint).

If the designer(s) and customer(s) can identify the four important attributes correctly and if they are able to come up with a consensus in their classification based on the requirements and constraints, 50% of conceptual design work can be considered to be over. On the other hand, if the team does not have a clear picture of the above attributes, the design will involve too many iterations and, therefore, will be too late in producing results and so will not be successful in today's competitive market place.

5. Top-down conceptual design:

Functional modeling constitutes one of the most important activities in conceptual design. The principal steps in the mechanical embodiment of a functional requirement can be described as follows [PAHL84]:

1. Decomposition of the overall function into simple subfunctions
2. Identification of solution principles for these subfunctions
3. Combining sets of solution principles into concept variants
4. Comparative evaluation of concept variants
5. Detail design of the selected concept variant
6. Generation of manufacturing information.

In formulating the functional requirements and the constraints, it is important to specify them explicitly and to arrange them in order of their importance. The following guidelines are helpful in this task [PAHL84]:

- Step 1: Eliminate personal preferences.
- Step 2: Omit requirements that have no direct bearing on the function and the essential constraints.
- Step 3: Transform qualitative data into quantitative form and reduce them to essential statements.
- Step 4: Generalize the results of the previous step.
- Step 5: Formulate the problem in solution-neutral terms.

It is important to start with the fundamental functional need of the design rather than the functional need expressed in terms of a previously used artifact. For example, while designing a device to measure the fuel level in an automobile, the designer should concentrate not only on the use of mechanical floats as level indicators but also on all other physical phenomena that will enable accurate measurement of fuel level.

During conceptual design stage, a designer is primarily concerned with steps listed in the form of flow charts depicted in Figures 1 and 2. Note that the selection procedure for choosing the best physical principle, function structure, organ structure or component structure is described in section 8.3.

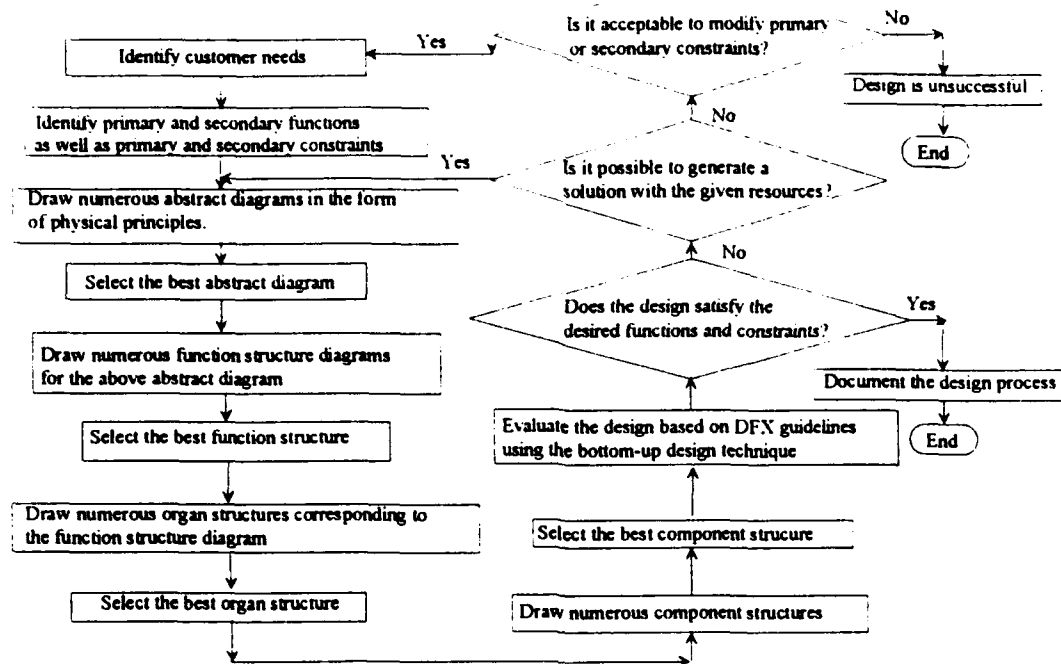


Figure 1 A schema for performing conceptual design

In mechanical designs, most functions require several components and each component may be important to several functions [ULLM92]. This means that components have to be designed for a set of functions that may or may not belong to the same functional hierarchical level. Note that the term "function" is used to denote "functional requirement" in Figure 2.

There is a strong tendency in designers to begin with their favorite idea and refine it toward a product specification. This is a very weak methodology, best expressed by the adage: if you generate one idea it will probably be a poor idea; if you generate twenty ideas then you might have one good idea [ULLM92]. In concurrent engineering environment, initial idea generation should be carried out on an individual basis and idea selection should be carried out as a group activity.

In certain design applications, functional requirements can also be expressed with the help of logical boolean operation diagrams to conceptualize and to evaluate new designs. The logical boolean operation diagrams, although more popularly used in electrical appliance designs, are also commonly used in mechanical and electro-mechanical devices.

An example functional hierarchy for lathe when viewed from top-down perspective is shown in Figure 3 [SUH84]. Top-down functional hierarchy is the easiest to come up with in the case of matching design and design synthesis. Previously established designs typically have well-documented functional hierarchies. On the other hand, the major task in novel designs, and, to a certain extent, evolutionary designs involves establishing such a functional hierarchy in the conceptual design phase.

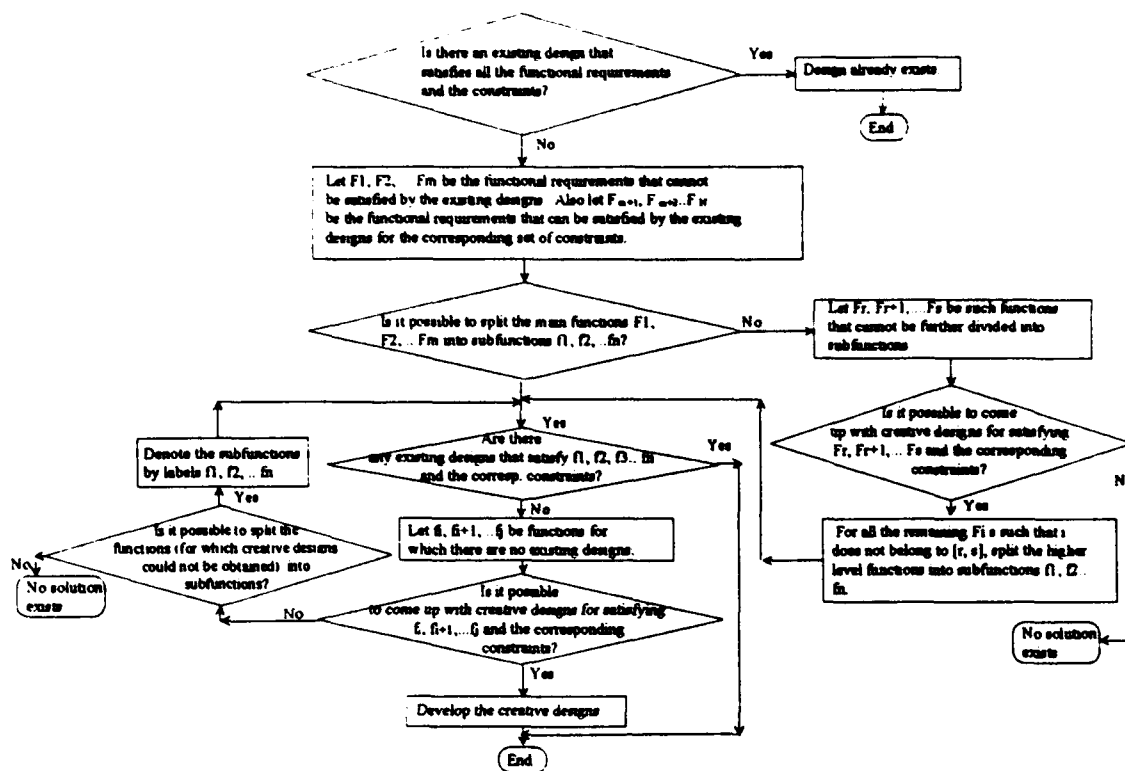


Figure 2 Functional analysis during conceptual design

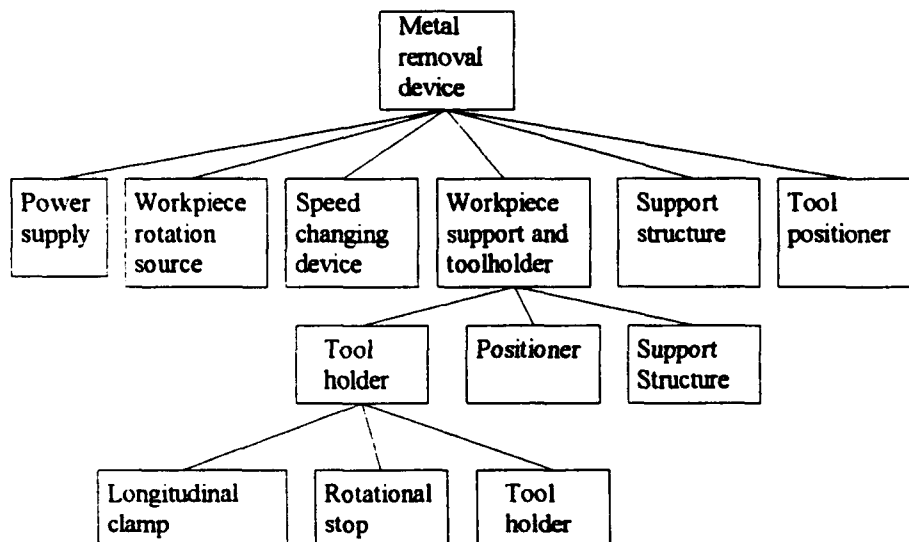


Figure 3. Top-down functional hierarchy in lathe [SUH84]

5. Development of an artifact from a subfunction using concurrent engineering

For each subfunction in the top-down function tree, the physical principle required to carry out that function has to be identified. For example, the subfunction "secure" can be achieved through a screw fit, vacuum generation (e.g., a suction cup), snap fit, magnetic force fit, etc. There are variety artifacts based on each of these physical principles. The designer may select the best artifact among the available list. The choice can be made based on the functional requirements, space constraints, etc. The selection of the best artifact can also be based on DFX

guidelines. It is important for a designer to maintain two catalogs- one containing a list of physical principles that can be used to satisfy a given function and the other containing a list of organ structures that support a physical principle. Examples of such catalogs can be found in [KOLL76] and [KRUM74]. It will be advantageous to be able to access this information with the help of a computer database. Also, the manufacturability evaluation of these organ structures will be extremely useful. This is explained more in detail in section 9.3. In the past, researchers have studied different component structures and have documented how the structures can be improved for a particular manufacturing process. A comprehensive database based on this information will be beneficial.

In a top-down design approach, feedback from different experts on manufacturing, assembly, maintainability is important in dividing the main function into subfunctions. The experts must be up-to-date on the availability of artifacts and manufacturing processes to fabricate the artifacts that will support these functions. There is no guarantee at the conceptual level if the final artifacts or the corresponding manufacturing processes will have predicted properties. However, the implementation of concurrent engineering techniques will assure that the emerging design will satisfy most DFX guidelines. For example, a modular design methodology with each design module preconceived based on DFX guidelines can be adopted as a design strategy.

At the organ structure level, producibility can be addressed as follows.

Step-I: Divide the organ structure into sub-organs.

Step-II Study the artifacts necessary to accomplish the mission denoted by the suborgans. Examples of such artifacts include motors, pulleys, electrical circuit modules, etc.

Step-III: Test the producibility of each artifact using the past manufacturing experience.

Most commercial organizations keep a record of their favorite designs to satisfy certain organ structure. In addition, they also store vendor information, manufacturing and assembly information including problems encountered as well as the field performance data. Organ structure can be modified or alternative organ structure can be selected if the current candidate is likely to develop problems from DFX considerations.

6. Bottom-up approach for conceptual design

Bottom-up design approach appears to be very effective for improving an existing design (such as the design of an automobile) as well as for improving an innovative design. Application of the concepts of house of quality (HOQ) and design of experiments (DOE) for this purpose are discussed section 9.4. Figure 4 illustrates the bottom-up approach for conceptual design. In order to develop the bottom-up hierarchy for a design, it should either be semi-finished or near-finished. It is then possible to evaluate the design for DFX guidelines. For example, two or more components in a design can be combined together and manufactured in the form of a casting rather welding the components together in the final assembly. Fewer components not only result in less manufacturing and assembly cost but also improve the quality significantly. Moreover, inventory control is easier to achieve and other administrative costs are reduced significantly.

6.1 Design evaluation using bottom-up technique

There are number of rules to assist a designer to evaluate a design for efficient manufacture [STOL86]:

1. Minimize the total number of parts.
2. Develop a modular design.
3. Use standard components.
4. Design parts to be multi-functional.
5. Design parts for multi-use.
6. Design parts for ease of fabrication.
7. Avoid separate fasteners.
8. Minimize assembly directions.
9. Maximize compliance.
10. Minimize handling.

Boothroyd and Dewhurst give similar guidelines to make a design easy to assemble [BOOT83]. The literature is full of articles providing guidelines for making a product easy to machine, easy to maintain, more reliable, etc. With increasing emphasis on making products environmentally responsible, and hence recyclable, today's designers are also forced to think in terms of making a design easy to dismantle.

It should be noted that any design, however well it may work in its current form, can usually be improved in the next pass. Feedback from the field performance, marketing personnel and customers plays a vital role in future updates.

7. Axiomatic design

Conceptual design becomes easier if one follows the two axioms proposed by Suh [SUH84]. The two design axioms are listed below:

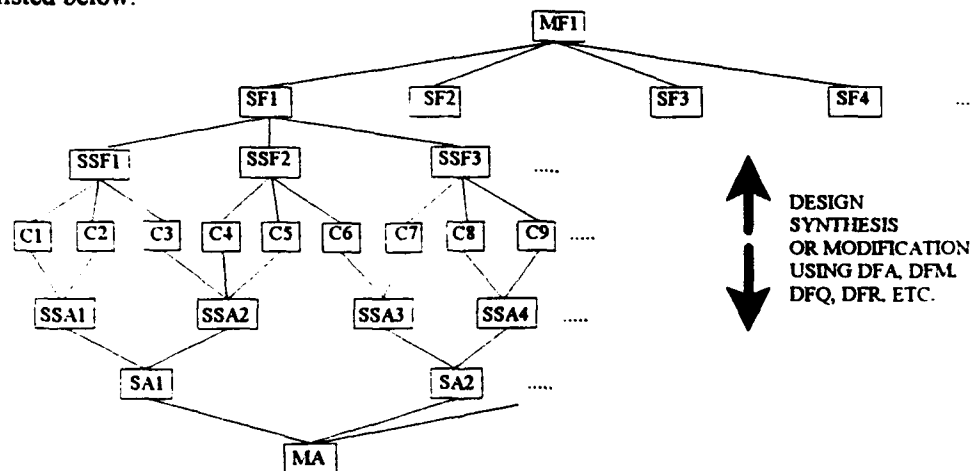


Figure 4 Bottom-up approach to conceptual design

Axiom 1 The independence axiom: Maintain the independence of the functional requirements

Axiom 2 The information axiom: Minimize the information content of the design.

It should be noted that axiom 1 emphasizes on the independence of the functional requirements of the design. This is different from physical integration of various functions within the same part of the design that frequently results in simplification of the design

Example:

Coming back to the example of can/bottle opener design, axiom 1 dictates that the device should be so designed that it performs the function of opening a can *independent* of the function of opening a bottle. Axiom 2 prompts

the designer to develop the simplest possible design, preferably using standard components, frequently used metals, etc.

8. Design aids for conceptual design

A matrix of various desired functions and various physical effects that can relate the outputs of the system to the inputs to the system can be constructed [HUBK87]. For example, the matrix can show that if the input energy in the form of electricity is to be converted to thermal energy, then the designer has the choice of using Joule heating, Peltier-effect, electric arc, and eddy current.

8.1 House Of Quality Approach to Conceptual Design

Important feedback that a designer can obtain from the House of Quality (HOQ) can be categorized into two classes [CLAU88]:

- (i) Influence of customer-perceived qualities on design attributes.
- (ii) Impact of engineering characteristics on design attributes.

Design attributes embody functional requirements as well as constraints.

Limitations of HOQ

Although HOQ approach is useful in identifying customer needs and their impact of design attributes, the approach does not take into account the following factors:

- (i) The HOQ approach highlights strong points and pitfalls of the current design against customer expectations. It advocates incremental improvements in the existing design. The HOQ technique ignores a revolutionary approach to the design.
- (ii) In many design situations, a customer attribute is a complex function of multiple design attributes. Simple algebraic weights are not sufficient to represent a design problem completely. Sensitivity analysis of design attributes and the resulting response surface will truly manifest the design problem.

In spite of the above limitations, HOQ technique furnishes a simple and useful road map for design improvement.

8.2 Sources for concept ideas

Important sources for ideas to conduct conceptual design are listed below [ULLM92]:

1. Patents

Although the patent literature is a good source of ideas, there are problems in its use. First, it is hard to find what you want in the literature. Second, it is easy to find other, interesting, distracting things not related to the problem at hand. Third, patents are difficult to read. Patent search is not an easy task. It involves three steps:

- (i) Identification of the class and/or subclass of the area of interest.
- (ii) Finding the number of the specific patents that have been filed in the class(es) identified.
- (iii) For a specific patent number, exploring the official gazette or the patents themselves.

2. Reference books and trade journals

A few abstract ideas that are useful at this stage, usually in design areas that are quite mature, can be found in reference books and trade journals.

3. Experts

Experts in other industries and universities can be consulted for new concept generation. If expertise is non-existent in a given field, it has to be developed within a company.

4. Brainstorming

Brainstorming sessions can be conducted within a company as well as outside the company to generate new ideas.

8.3 Evaluation of different concepts

Whenever there are more than one competing conceptual designs satisfying the functional requirements and constraints, a formal evaluation technique should be used for judging the best possible design that will suit a given application. Important steps in evaluating different conceptual designs can be enumerated as follows [PAHL84]:

1. Identifying evaluation criteria
2. Weighting evaluation criteria
3. Computing overall weights for each concept
4. Estimating evaluation uncertainties
5. Searching for weak spots.

Each of the above tasks are described below:

1. Identifying evaluation criteria

Criteria for evaluating conceptual designs are based primarily on customer requirements derived from market surveys, customer surveys, analyses of competitors' products, code of practice mandated by national and international standards, safety requirements and environmental concerns as well as budgetary constraints imposed by the management. Ullman classifies evaluation criteria based on the following three measures [ULLM92]:

- A. Evaluation based on feasibility judgment: Technical feasibility of a given concept is assessed here.
- B. Evaluation based on technology-readiness assessment: Designers should opt for components and processes with a proven track record.
- C. Evaluation based on go/no-go screening: Here the decision is made whether a given concept meets a given criterion or not based on the designer's judgment. If the designer fails to predict the performance, a prototype is built to check if the concept is acceptable or not.
- D. Evaluation based on the decision matrix: This is one of the most comprehensive concept evaluation technique. Numerical values are assigned to indicate how each concept performs in each evaluation category. A decision matrix very similar to quality function deployment (QFD) is built to compare the scores of different concepts against each other. The procedure of assigning weights is described below.

2. Weighting evaluation criteria

The first step in assigning weights for competing concepts in different evaluation criteria involves fixing a datum (or reference) concept. Typically, a datum concept represents the designer's favorite concept. Other concepts are

then assigned different scores depending on how they compare with the datum concept. Weights are assigned to the evaluation criteria depending on their importance to the success of the new design.

Apart from the designer(s), participants from departments such as marketing, manufacturing, quality control, etc., can help in identifying evaluation criteria for a conceptual design and in assigning appropriate weights to the individual criteria. In some cases, it is possible to evaluate a design separately using economic and technical ratings. The final rating can then be expressed as an algebraic combination of these two ratings.

3. Computing overall weights for each concept

A weighted sum of scores earned by each concept is then computed. The concept with the highest weighted score is declared winner. The process may be repeated one more time with the winner taken as the new datum concept.

4. Estimating evaluation uncertainties

There are no hard and fast rules to express the effectiveness of a design concept in precise numbers. Subjective errors in design evaluation can be minimized by active participation of the entire concurrent engineering design team. It is also important to evaluate two or more concepts thoroughly if their overall weights do not differ appreciably.

5. Searching for weak spots:

Weak spots for candidate concepts are identified and improved upon if possible. It is important to pay attention not only to the overall weighted score but also to the distribution of individual scores for the selected concepts in satisfying critical functional requirements.

The evaluation is more difficult when the conceptual design is in the form of abstract diagrams indicating the physical principles to be embodied in the design but with very little information on the artifacts. Evaluation at this stage is based on experience and reasonable assumptions about the possible set of artifacts that may be employed to support the physical principles. If the uncertainty is too large, it is recommended that a definite decision should not be made at this level [HUBK87], but that a further concretisation should be performed before coming to a decision.

8.4 Tools for conducting a conceptual design

Important tools for carrying out a conceptual design are listed in Table 1. Examples of design catalogs showing various functions and corresponding physical principles are furnished in [KOLL76] and [KRUM74]. A catalog of organ structures necessary to satisfy a given function structure is shown in [ROTH74].

8.5 Determination of functional requirements for improving an existing design

House of quality can be effectively used to evaluate the functional requirements of an existing design [HAUS88]. The house of quality shows pictorially how various design parameters impact the output performance. Critical design parameters that impact the performance of the design in the field can be quickly detected from the house of quality. Once these critical parameters are identified, design of experiments can be conducted to make the design more robust at lower costs.

9. Case study of a cloth dryer design

Let us look at the design of a cloth dryer for household applications. We will assume that the design team consists of designers, manufacturing engineers, quality control specialists, potential customers, key subcontractors, and marketing personnel. Although design ideas are developed individually predominantly by designers, a brainstorming session is conducted at regular intervals to seek the feedback from the concurrent engineering team.

Statement of the problem:

Design a cloth dryer suitable for household applications that fits in a $x \times b \times c$ cubic feet of space, weighs less than A lb., cost less than \$ B to the company and runs maintenance free for at least 5 years of common house hold use.

Solution

(i) Identification of customer needs:

Although the problem statement summarizes important customer needs in this example, the customer needs for a real life design problem are gathered from customer surveys, interviews with dealers and survey of competition. Important categories of customer include functional performance requirements, durability, reliability, space considerations, weights, cost, safety, aesthetics and environment friendliness.

Table 1. Summary of useful tools for conceptual design

Sr. No.	Design category	Design Tool
1.	Identification of customer needs	Customer survey, market survey, survey of competition, HOQ, QFD table
2.	Identification of primary and secondary functions as well as primary and secondary constraints	Customer survey, market survey, axiomatic design principles, HOQ, QFD table
3.	Development of abstract diagrams	In-house catalog listing functional requirements and corresponding physical principles
4.	Development of numerous organ structures for each abstract diagram	A catalog showing physical principles vs. physical artifacts (past company designs as well as standard industrial designs), design handbooks, patents, experts, brainstorming sessions.
5.	Selection of the best organ structure	Weighted matrix evaluation table suggested by Pugh [PUGH91], Ullman [ULLM92], etc.
6.	Development of the component structure and material specifications	A catalog showing physical principles vs. real life component <i>drawings</i> (past company designs as well as standard industrial design <i>drawings</i>), design handbooks, Taguchi's technique of robust design, design of experiments, DFX guidelines
7.	Evaluation of the design based on DFX	DFX guidelines of the company, DFX guidelines suggested by industry-wide research, commercial softwares and catalogs on DFX (e.g., Motorola 6-sigma type literature), research journals and conference proceedings

The above customer needs are elaborated in Table 2. Note that * indicates a primary requirement.

(ii) Determination of physical principle(s)

Clothes can be dried by employing centrifugal forces, heated air, solar energy, microwaves or a combination of any of these options. Note that this is not an exhaustive list of options but a representative set of options that can be used for illustrative purpose. Next, compare these physical principles with each other to see which one will best serve the customer requirements. Table 2 is constructed to match the physical principles against customer requirements. The physical principle with the largest weighted score will be chosen for further consideration provided that the principle satisfies all the "must" needs. Drying with the help of microwaves is out of consideration at this point since it cannot handle metallic pieces in clothes. Note that a combination of physical principles may also qualify for useful alternative to pursue. Let us assume that the combination of hot air and centrifugal forces emerges as the winner as a result of this analysis. Note that this analysis will change as technology evolves in areas such as textiles, micro-wave heating, etc.

(iii) Function structure diagram

At this point draw the function structure diagram to support the drying operation. Since the combination of hot air and centrifugal forces is chosen as the winning combination of the previous analysis, the design has to achieve these two functions. Figure 5 shows the functional hierarchy of a cloth dryer.

It is important to note that not all secondary functional requirements will be apparent at the outset of the design process. Only when the major components supporting the primary functions such as cloth holding, rotating and heating the air are selected, the supporting structure for the assembly will be designed.

(iv) Organ structure development

For each function structure one or more organ structures are developed next. Example organ structures are shown in Figure 6. Evaluation technique discussed in section 9.3 will be useful in selecting the winning organ structure. In addition to the customer needs listed in Table 2, the two organ structures will be evaluated against the ease of manufacture, ease of assembly, etc.

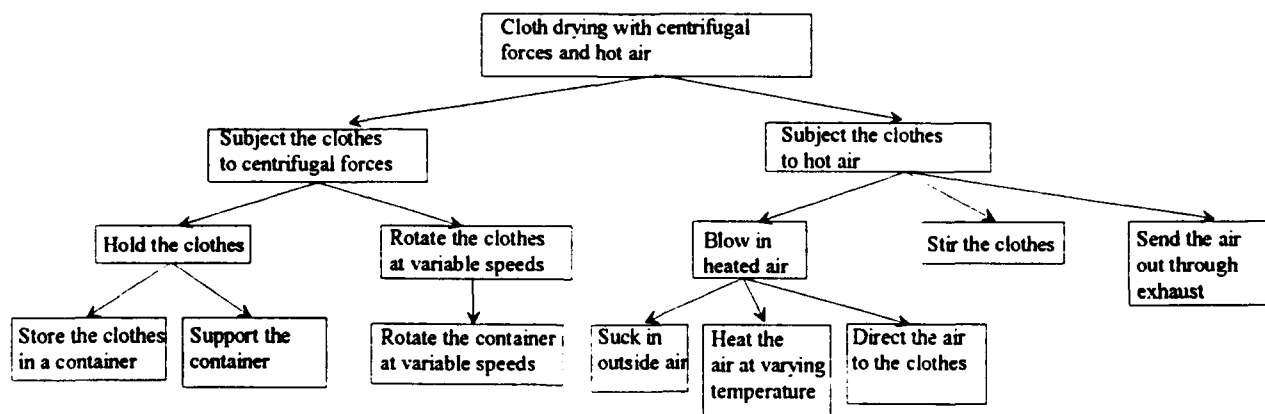


Figure 5. Function structure diagram for a dryer

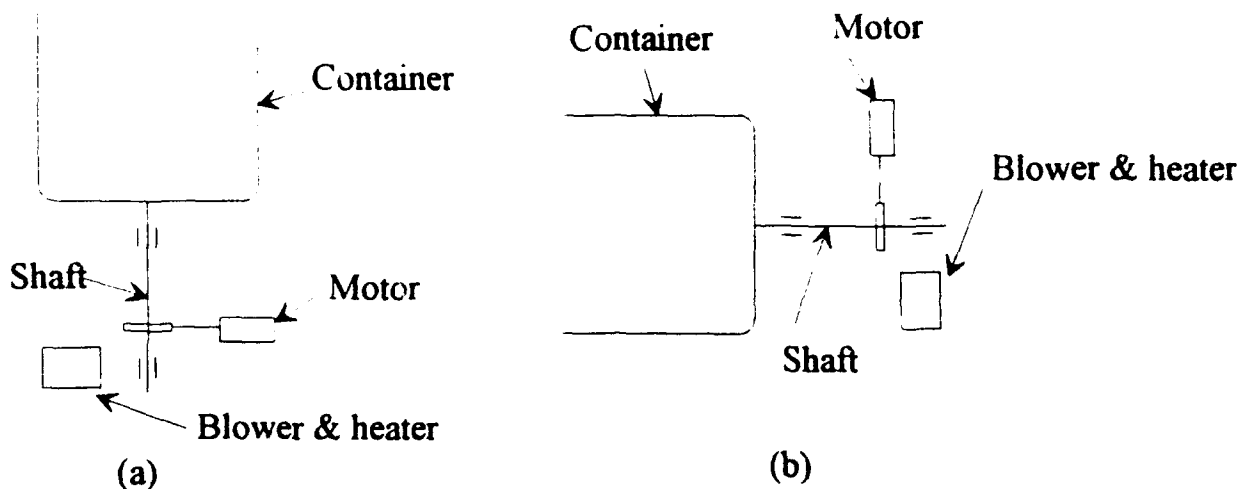


Figure 6. Two possible organ structures for a dryer

(v) *Component structure design*

Next, appropriate components have to be selected to support the functions denoted in the organ structures. Once again, more than one component structure may satisfy the functions denoted in a given organ structure. For example, the drying spindle can be driven at variable speed using either a variable speed motor or an adjustable gear box. Selection of the final component structure should be based on techniques discussed in section 9. DFX guidelines available in literature (see [BOOT83] for example) will help in finalizing the component structure.

(vi) *Bottom-up analysis*

Before finalizing the component design, it helps to conduct a bottom-up analysis of the design to see if certain parts can be combined together or replaced all together by ready-made parts or standard components. The design should also be verified for various functional requirements and constraints. Steps (i), (ii) or (iii) may have to be repeated if some of the functional requirements or constraints are not met.

Note that not all designs will involve all the above analysis phases. For instance, in the splash guard design example discussed in [ULLM92], the physical principle underlying the design is predetermined. It is certain that there will be a physical barrier between the rider and the rear wheel.

Table 2. Comparison of different physical principles of cloth drying

Customer needs	Wts.	Solar energy	Hot air	Centrifug. Forces (CF)	Micro-wave	Hot air & CF	Weighted score
Easy to start	*						
Easy to change cycle time	*						
Easy to change cloth type setting	*						
Handles more than A lb of clothes	*						
Handles more than B cub. ft. vol. of clothes	*						
Cycle time < a min. for light loads							
Cycle time < b min. for medium loads							
Cycle time < c min. for heavy loads							
Noise level < C db							
Less vibrations							
No maintenance	*						
Reliable	*						
Handles metal pieces	*						
Do not tear	*						
Do not crease	*						
Do not get entangled	*						
Do not have static							
Fits in a x b x c cu. ft.	*						
Does not rattle							
Does not wobble							
Weighs less than D lb.							
Attractive shape							
Popular color							
Cost less than \$E	*						
Requires less energy							
Fool-proof	*						
Child safe	*						
Useful life > 5 years							
Made of recyclable parts							
Disassemblable							
Recyclable							
Consumes less detergent							

References

- [BOOT83] G. Boothroyd, P. Dewhurst, "Design for assembly- a designer's handbook." Department of Engineering, University of Massachusetts, Amherst, MA, 1983.
- [BOX88] G. Box, S. Bisgaard, C. Fung, "An explanation and critique of Taguchi's contributions to quality engineering," Quality and Reliability Engineering International, vo. 4, pp. 123-131, 1988.
- [DIXO88] J. R. Dixon, M. R. Duffey, R. K. Irani, K. L. Meunier, M. F. Orelup, "A proposed taxonomy of mechanical design problems," 1988 ASME Computers in Engineering Conference, San Francisco, August 1988, pp. 41-46.

- [HAUS88] J. R. Hauser, D. Clausing, "The house of quality," *Harvard Business Review*, May-June 1988, pp. 63-73.
- [HUBK87] V. Hubka, W. E. Eder, "A scientific approach to engineering design," *Design Studies*, vol. 8, no. 3, 1987, pp. 123-137.
- [HUBK88] V. Hubka, W. E. Eder, "Theory of Technical systems. A Total Concept Theory of Engineering Design," Springer Verlag, Berlin, 1988.
- [KOLL76] R. Koller, "Konstruktionsmethode Fur den Maschinen-, Geräte- und Apparatebau," Springer, Berlin, 1976.
- [KRUM74] P. Krumhauer, "Rechnerunterstützung für die Konzeptphase der Konstruktion," Diss., TU Berlin, 1974.
- [MCGR84] J. E. McGrath, "Groups: interaction and performance," Prentice Hall, Englewood Cliffs, NJ, 1984.
- [NEWS88] W. R. Spillers, S. L. Newsome, "Design Theory: A Model for Conceptual Design," *Proceedings of the 1988 NSF Grantee Workshop on Design Theory and Methodology*, Springer-Verlag, 1988, pp. 198-215.
- [PAHL84] G. Pahl, W. Beitz, "Engineering Design," The Design Council, 1984.
- [PUGH91] S. Pugh, "Total design: integrated methods for successful product engineering," Addison-Wesley, Reading, MA, 1991.
- [ROTH68] K. Roth, "Gliederung und Rahmen einer neuen Maschinen-Geräte-Konstruktionslehre," *Feinwerktechnik* 74, pp.453-460, 1968.
- [ROTH71] K. Roth, H. J. Franke, R. Simonek, "Algorithmisches Auswahlverfahren zur Konstruktion mit Katalogen," *Feinwerktechnik* 75, pp. 337-345.
- [ROTH74] K. Roth, "Aufbau und Handhabung von Konstruktionskatalogen," VDI-Berichte 219, Dusseldorf: VDI-Verlag, 1974.
- [STAU89] L. A. Stauffer, R. A. Slughterbeck-Hyde, "The nature of constraints and their effect on quality and satisficing," *First International Conference on Design Theory and Methodology*, 1989, Montreal, pp. 1-7.
- [STOL86] H. W. Stoll, "Design for manufacture: an overview," *Applied Mechanics Review*, vol. 39, no. 9, pp. 1356-1364, 1986.
- [SUH84] N. P. Suh, "Development of the science base for the manufacturing field through axiomatic approach," *Robotics and Computer Integrated Manufacturing*, vol. 1, no. 3/4, 1984, pp. 399-455.
- [SUH90] N. P. Suh, "The principles of design," Oxford University Press, 1990.
- [TAGU90] G. Taguchi, E. A. Elsayed, T. C. Hsiang, "Quality engineering in production systems," McGraw-Hill, New York, 1990.
- [ULLM92] D. G. Ullman, "The mechanical design process," McGraw-Hill, New York, 1992.

**A METHODOLOGY FOR QUANTITATIVE ASSESSMENT OF THE EFFECT OF
INNOVATIVE BUSINESS PRACTICES ON SYSTEM LIFE CYCLE COSTS**

Michael D. Reimann, C.M.C., C.S.P.

Ph.D. Candidate

The University of Texas at Arlington - School of Business Administration

Department of Information Systems and Management Sciences

Arlington, Texas 76019-0437

Final Report for:

Summer Faculty Research Program

Wright Laboratory

Sponsored by:

Air Force Office of Scientific Research

Bolling Air Force Base, Washington, D.C.

September 1993

A METHODOLOGY FOR QUANTITATIVE ASSESSMENT OF THE EFFECT OF INNOVATIVE BUSINESS PRACTICES ON SYSTEM LIFE CYCLE COSTS

Michael D. Reimann, C.M.C., C.S.P.

Ph.D. Candidate

**Department of Information Systems and Management Sciences
The University of Texas at Arlington**

ABSTRACT

This paper presents a general approach for quantifying and assessing business practices [8,9]. The methodology is aimed at addressing high level broad scope situations a company may encounter [4,5]. Usually, mathematically or statistically based techniques have proven to be inappropriate, inadequate, or inaccurate when attempting to solve such problems [4,5,6,7]. The difficulties experienced in using these approaches have been alleviated by prescribing a logical series of general steps. These steps may be modified to fit the prevailing circumstances and data of an organization. A brief description of the steps, which form the methodology, is provided.

The majority of this paper discusses the application of the methodology to an actual business environment. The approach was used to develop a quantitative model for the acquisition of fixed wing military aircraft. A quantitative model of the business process was derived from official Department of Defense (DoD) directives [2,3]. Data used by the model came from actual cost figures for aircraft that were purchased by the Air Force, Army, and Navy over a forty year period [1]. These data represent forty-one aircraft types that were acquired at a cost of 238 billion dollars. A computer simulation program of the acquisition process, which uses the actual cost data, was developed.

A METHODOLOGY FOR QUANTITATIVE ASSESSMENT OF THE EFFECT OF INNOVATIVE BUSINESS PRACTICES ON SYSTEM LIFE CYCLE COSTS

Michael D. Reimann

INTRODUCTION

The paper presents on-going research aimed at establishing a methodology and tool for quantitatively assessing business performance [8,9]. The goal of the research is to provide decision makers with an objective technique for evaluating the potential consequences of changing business practices. Thus far, the work has progressed through three distinct phases.

The methodology was formalized during the first phase. To illustrate the approach, quantitative models for a hypothetical case were developed and analyzed [8]. A hypothesis was tested and a sensitivity analysis was conducted. This example investigated the effects that engineering approaches could have on system life cycle costs.

In the second phase, the methodology was modified to accommodate more realistic situations [9]. A statistical design of experiments was developed for gathering comprehensive and representative values for an entire state space of system life cycle costs. Simulated values were generated and analyzed. A second order equation for predicting system life cycle costs was derived from the experimental observations.

This paper describes the third phase of the research. The objective of this phase was to apply the methodology to an actual business situation and utilize empirical data in its modeling and analysis. The approach was used to develop a quantitative model for the acquisition of fixed wing military aircraft. The business process was delineated and corresponding quantitative models were developed. Appropriate data were identified and gathered. A computer program for simulating the acquisition process was designed and developed.

Eight actual acquisition cases have been identified. These cases will be described. The next phase of this research will model, simulate, and analyze these cases. Replication of these actual cases will demonstrate the efficacy of the methodology.

METHODOLOGY

The purpose of the methodology is to provide a general approach for quantitatively assessing business process performance. This approach is intended to provide decision makers with visibility into the operating envelop of a business process based on variation of influential characteristics or drivers. Three aspects are of particular importance in the development of a model which will reasonably approximate the true performance of a business process:

- An accurate functional model of the business process.
- Knowledge of the cost distributions that coincide with the subprocesses composing the business process.
- Proper identification and characterization of factors that influence process performance.

Using this information, a quantitatively based model of the business process can be derived. From this model a computer program can be developed for simulating process performance. Then a statistical experiment can be defined which systematically varies the factor levels in order to obtain a comprehensive set of experimental observations. These values must be analyzed to insure they satisfy certain statistical requirements. From the observations an equation can be developed that establishes a performance envelop for the business process. Operating characteristics of the process are determined by varying the process drivers. The methodology is composed of the steps shown in Figure 1.

An overall model of the business process is established and then it is divided into distinct phases. The phase models are further decomposed into subprocess models. The detailed models of the various phases and subprocesses are established through a collaborative effort of knowledgeable people from the host organization. Development of these models is a crucial aspect of the methodology because the functional components they define will form the basis for a quantitatively based model of the business process. Preparation of the functional business process model is indicated by Step 1 in Figure 1.

One or more metrics are established for the ensuing analysis approach. It is necessary to identify and determine potential changes to the applicable measures for each process phase and subprocess. Characteristics of these distributions are determined through appropriate and available historical information and/or estimated when necessary. In addition to the estimates of phase and subprocess central tendencies, it is necessary to specify the forms of their distributions. Determination of these characteristics is illustrated by Step 2 in Figure 1.

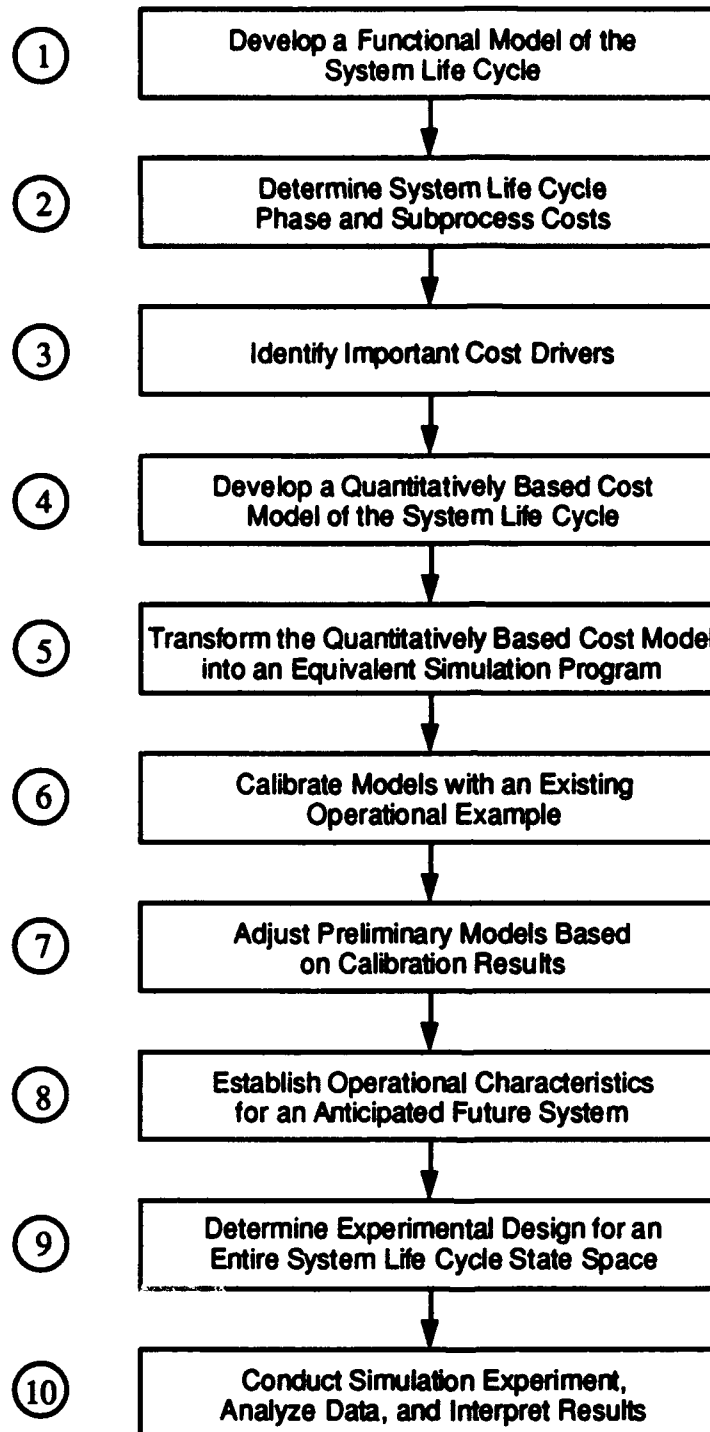


Figure 1 A Methodology for Quantitatively Assessing System Life Cycle Processes

It is also necessary to isolate drivers that influence the performance of each phase and subprocess. The characteristics of these drivers are determined from historical information, when appropriate. Otherwise, consensus of opinion by knowledgeable individuals from the host organization is needed to define and quantify the drivers. This evaluation is shown by Step 3 in Figure 1.

The functional process models developed in Step 1 serve two purposes. First they establish the basic relationships between the various phases and subprocesses of the overall business process. Second, these models identify the type of item that is being manipulated by the phases and subprocesses. Functional models typically provide minimal information concerning the metric of interest. Thus, the original functional models are inappropriate for quantification and measurement purposes. A general input/output model is used to transform the individual functionally based models into a complete quantitatively oriented model of the entire business process. This transformation is shown by Step 4 in Figure 1.

Even though the quantitatively oriented process model facilitates communication and understanding, it is not an appropriate model for implementation on a computer. Therefore it is necessary to transform the quantitative model into an equivalent representation that can be simulated by a computer program. This representation is defined as a collection of tabular values. Internal consistency checks and cross tabulation of the tabular values are used to verify the quantitative model and the simulation tool. These verifications are indicated by Step 5 in Figure 1.

The performance characteristics of a known business process, which is typical for the host organization, are simulated through the execution of a computer program. This characterization is intended to validate the functional and quantitatively based models of the process developed in Steps 1, 2, and 3. The simulation results should replicate the performance of the known process. Validation and calibration of the preliminary models are shown by Step 6 in Figure 1.

Based on the results of the calibration experiment, adjustments to the functional model, quantitative model, cost drivers, and/or computer program may be necessary. These corrections are depicted by Step 7 in Figure 1.

Expected performance characteristics for a new business process or target system are estimated by knowledgeable individuals from the host organization. As in Step 2, it is necessary to establish anticipated variation to the applicable measures and drivers for each process phase and subprocess.

The complete distribution form must be determined for each subprocess. Whenever possible, consensus of multiple opinion is used to establish these performance characteristics. Determination of these characteristics is shown by Step 8 in Figure 1.

Statistical design of experiment techniques are used to define a comprehensive set of test points for characterizing the process. These design points systematically vary the drivers of the business process in an independent fashion. An experimental design defines the appropriate procedures for assessing a complete state space of process costs. Development of this experimental design is indicated by Step 9 in Figure 1.

The experiment is conducted to generate simulated costs for the specified design points. These composite costs are tested to insure that they satisfy necessary statistical assumptions. From these cost values a mathematical function for predicting performance of the business process can be derived. The independent variables in this function are the process drivers that were identified in Step 3. Based on this function, a decision maker can vary the drivers to gain insight into overall business process performance. The simulation experiment, data analysis, and interpretation of results are indicated by Step 10 in Figure 1.

The remainder of this paper describes the development of a baseline model for the acquisition of fixed wing military aircraft. Steps 1 through 5 of the methodology guided the development of this model. Subsequent research will employ Steps 6 through 10 to model, simulate, and analyze actual business cases.

DEPARTMENT OF DEFENSE SYSTEM LIFE CYCLE

The Department of Defense (DoD) system life cycle process for major defense systems is illustrated by Figure 2 [2,3,11].

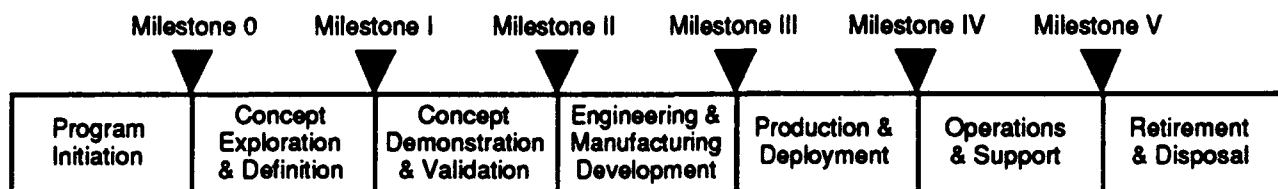


Figure 2 Department of Defense System Life Cycle Phases

As shown in Figure 2, this process consists of seven primary phases:

- Program Initiation
- Concept Exploration & Definition (C/E)
- Concept Demonstration & Validation (D/V)
- Engineering & Manufacturing Development (EMD)
- Production & Deployment (P/D)
- Operations & Support (O/S)
- Retirement & Disposal

Within the DoD, major systems are defined as systems anticipating funding levels of more than 200 million dollars in research, development, test, and evaluation or one billion dollars in procurement in constant fiscal year 1980 dollars. The process begins by conducting mission area analysis efforts in determining the user's mission need, followed by an approval for program initiation and authority to budget for a new program (Milestone 0 decision). Next, the program normally begins the C/E Phase, during which all reasonable system alternatives are explored. The program then enters the D/V Phase (Milestone I decision) during which the preferred system concepts are selected and tested to identify risk areas and to demonstrate that all experimental efforts have been completed. The results of these efforts are reviewed and the program is allowed to progress into the EMD Phase (Milestone II decision) where system detailed design and tests are performed. Once completed, the system is approved to proceed with full-rate production and initial deployment in the P/D Phase (Milestone III decision) during which the actual production or construction takes place. The initial deployment also marks the beginning of the O/S Phase. A review will be conducted one to two years after initial deployment to assure that the operational readiness and support objectives are being achieved (Milestone IV decision). Later, during the O/S Phase, modifications and product improvements are usually implemented. Another review will be conducted five to ten years after initial deployment (Milestone V decision) to determine if major upgrades are needed.

At the end of each phase the need for the program is recertified, using milestone decision reviews, by the Secretary of Defense (SECDEF) or the Service Secretary, as required, before additional resources are authorized. At each review, the decision authority can choose to continue the present phase, proceed to the next phase, or cancel the program. The SECDEF can also direct a DoD program to omit C/E or D/V phases and proceed to EMD Phase as special circumstances prevail.

A modified approach, unique to each service, is employed for non-major or non-developmental systems. Non-major systems may not follow all of the acquisition phases that major systems do. They will, however, have a development and review cycle appropriate to the nature and scope of the program. Acquisition of non-major systems is directed by the service or major command, as appropriate. Each service has its own system of reviews and approvals that achieves objectives similar to the DoD system life cycle process.

DATA

An essential factor, in this research, is the need for appropriate and accurate data. Preliminary work in the development of the methodology [8,9] indicated that reliable results are highly dependent on the cost distributions used. The data for this research were obtained from the United States Air Force Cost Estimating System (CES) [1]. The CES was developed in 1987 and contains acquisition data for Air Force, Army, and Navy aircraft purchased between the years 1948 and 1987. These data represent 238 billion dollars in expenditures for 415 aircraft lots. The CES provides a single comprehensive source of data for these aircraft systems.

Data Partitioning and Categorization

Acquisition of major weapon systems specifically addresses three of the seven DoD system life cycle phases:

- Concept Demonstration & Validation (D/V)
- Engineering & Manufacturing Development (EMD)
- Production & Deployment (P/D)

Because the CES delineates data at an acquisition lot level and not at an individual aircraft unit level, the partitioning, categorization, and classification of data used in this research were oriented at the acquisition lot level. There are fifteen basic cost categories associated with each of the three system life cycle phases in the acquisition process. Each of the basic cost categories is further subdivided into non-recurring and recurring cost categories. Non-recurring costs are those which occur on a one-time basis. Recurring costs are accumulated on a periodic basis. Since each of the fifteen basic cost categories could have both a non-recurring and a recurring component, there are potentially thirty cost categories for each of the three phases in the system acquisition process. Each acquisition lot was examined to determine the phase(s) to which it belongs. Then, all of the individual costs associated with each of the lots were assigned to appropriate acquisition process

cost categories. Table 1 summarizes the assignment of lots to the three acquisition phases and ninety cost categories in the system life cycle. The counts shown in each cell of Table 1 represent the number of systems that have non-zero acquisition costs associated with that cost category. The observed values for each cell were used to construct an individual cost profile (i.e. cumulative density function) for the cost category. In order to construct a cumulative density function it was necessary that a cell have five or more observations. Twenty-one of the ninety cells shown in Table 1 could not meet this criteria and were eliminated from further consideration.

Data Normalization

The CES utilizes the 1987 DoD inflation index to normalize the cost data for price level variations which occur over time. Using inflation indices to synchronize costs permits comparisons based on constant dollars; however, system costs can vary considerably in terms of overall acquisition cost or unit costs. These differences may be attributed to a variety of factors such as aircraft sophistication, economies of scale, or learning curve phenomena. Because of these differences, comparisons among system types, or between purchase lots within a system type, may not be reasonable or feasible.

To overcome the above noted deficiencies, it was necessary to normalize the dollar amounts into a consistent unit of measure. This unit is expressed as the proportion of a categorical cost in a lot relative to the total cost of the lot. The total lot cost is the sum of all the individual categorical costs incurred by the lot. Each of the individual costs categories within the lot is then divided by the total lot cost to establish its percentage of cost contribution to its lot.

By expressing costs as proportions, inflation no longer affects the individual lots. Therefore, it is not necessary to index the data to a specific year.

The magnitude of acquisition costs is eliminated when the costs are transformed into percentages. It is feasible to compare lots which have different acquisition quantities or where the per unit cost of the aircraft differ. Strict normalization of the data into percentages does, however, remove the ability to investigate the effects of economies of scale or learning curve phenomena.

Comparisons among different system types (i.e. F-16 versus F-18) are feasible when the costs are expressed as proportions of total lot acquisition cost. System classes (i.e. bombers versus fighters) can also be compared in this fashion. Benchmarking of aircraft manufacturers (i.e. Lockheed versus industry norm) can be conducted once the data were normalized into percentages.

System Life Cycle Phase Applicable Cost Categories	Demonstration & Validation (20 potential lots)		Engineering & Manufacturing (44 potential lots)		Production & Deployment (367 potential lots)	
	Non- Recurring	Recurring	Non- Recurring	Recurring	Non- Recurring	Recurring
Engineering	19	10	40	31	164	357
Tooling	17	10	42	32	170	349
Manufacturing	14	18	38	42	150	363
Quality Control	3*	7	26	32	101	318
Other Air Frame	9	11	30	40	102	349
System Project Management	19	0*	43	2*	128	48
System Test and Evaluation	1*	0*	17	10	99	168
Other Air Vehicle	1*	3*	19	17	60	243
Training	2*	12	20	11	58	164
Peculiar Support Equipment	7	7	27	21	109	241
Data	8	1*	33	10	135	237
Operational Site Activation	0*	0*	0*	0*	2*	4*
Industrial Facilities	0*	0*	1*	0*	2*	10
Initial Spares	4*	11	7	24	46	231
Other Air Systems	7	6	11	9	81	187

* Cost category eliminated due to an insufficient number of applicable lots.

Table 1 Applicability of Acquisition Lots to Aircraft Acquisition Phases and Cost Categories

Cumulative Density Functions

The final manipulation of the acquisition cost data was to transform the data into a computer compatible form. The data in each of the sixty-nine cost categories were converted into cumulative density functions. These conversions involved three steps:

- The observed values in each cost category were sequenced into ascending order.
- An empirical distribution function was determined for each cost category.
- A one hundred step cumulative density function (i.e. ogive) was derived from the distribution function for each cost category.

The discrete cumulative density functions were implemented as a collection of tabular data which can be interpreted by a computer simulation program. Graphs of the cumulative density functions were also generated so their characteristics could be visually examined and interpreted. Figure 3 shows one of these graphs.

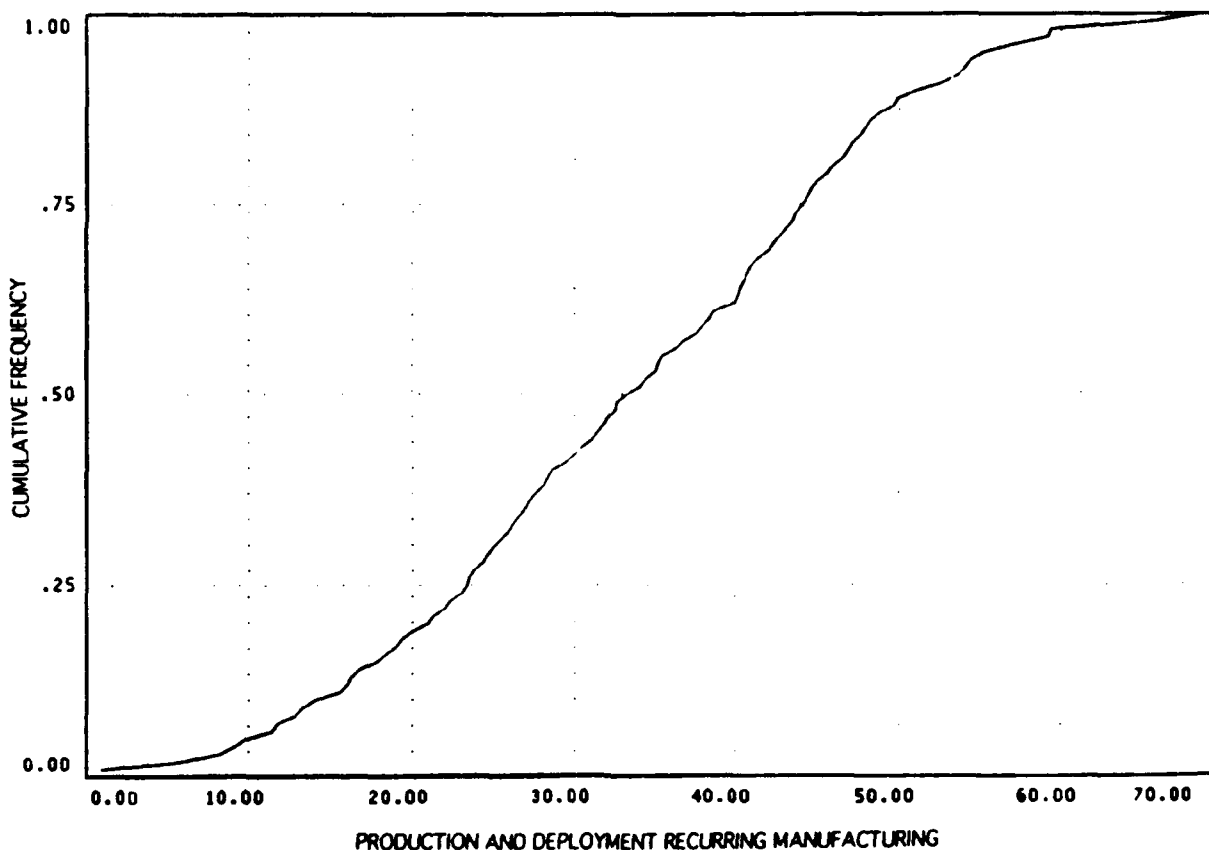


Figure 3 Cumulative Density Graph of the Percentage of Acquisition Cost Attributable to the Production and Deployment Phase Recurring Manufacturing Cost Category

DEVELOPMENT OF A QUANTITATIVELY BASED COST MODEL OF THE DEPARTMENT OF DEFENSE ACQUISITION PROCESS

Data for this research were obtained from the Cost Estimating System (CES). Since the CES provides cost data only for the acquisition segment of the DoD system life cycle, the scope of this research was limited to the three phases of this segment. Figure 4 shows the conceptual relationship among various components.

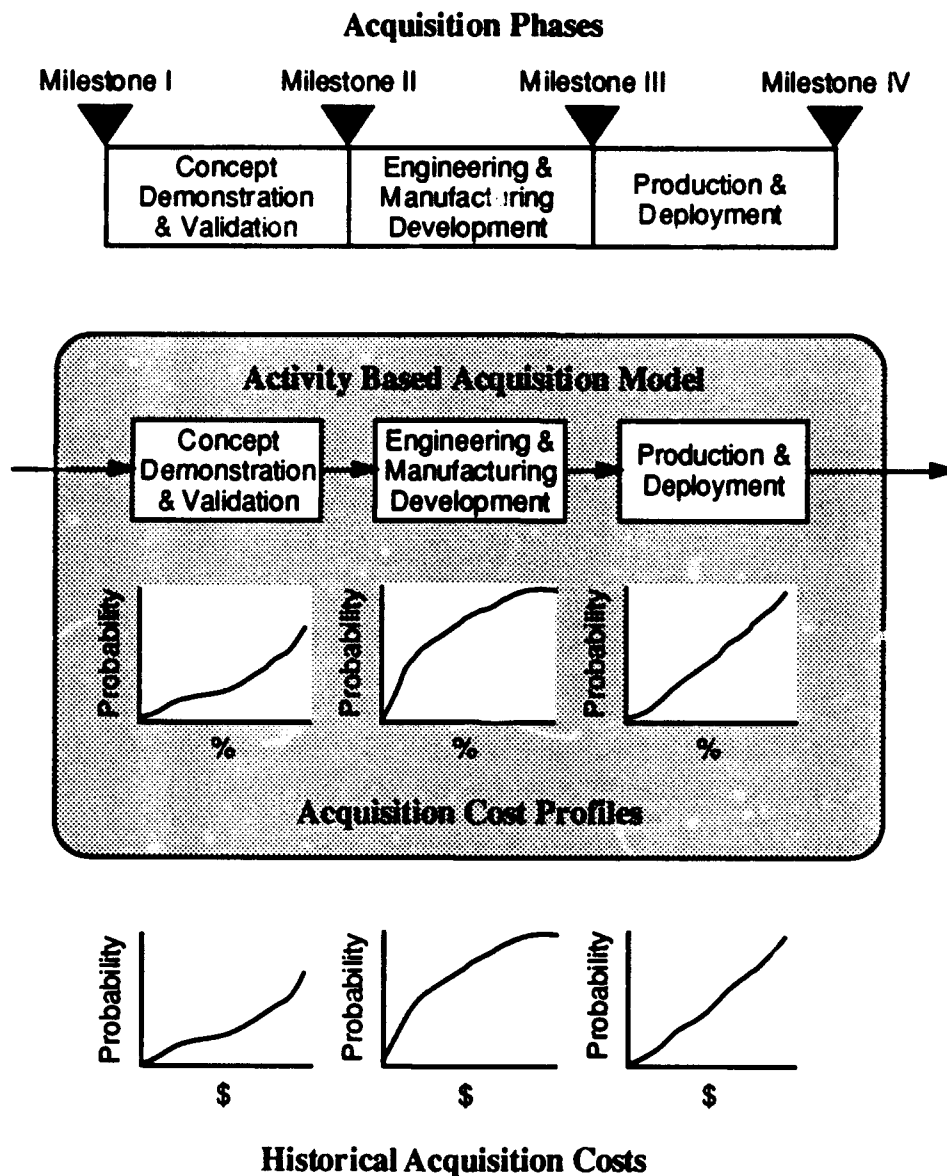


Figure 4 Integration of a Functional Model with Cost Data to Produce a Quantitatively Based Model of the DoD Acquisition Process

A narrative description of the acquisition segment was translated into equivalent activity based diagrams. The activity based models were defined so they coincide with the cost categories on a one-to-one basis. The data were transformed from a dollar basis into proportions that were consistent within and among acquisition lots. Synchronization of the activity based models with the normalized values produces a quantitatively based model of the acquisition process. This synthesis is shown as the shaded region in Figure 4.

The model illustrated in Figure 5 was used to combine the description of the acquisition process with the CES data to produce quantitatively oriented models of the subprocesses. The input to a system life cycle subprocess is indicated by the arrow entering into the outer rectangle from the left hand side. When an item is initially processed, it incurs a one-time non-recurring cost associated with that subprocess. The cost added to the item is determined from a non-recurring cost profile curve (i.e. cumulative density function) that coincides with the subprocess.

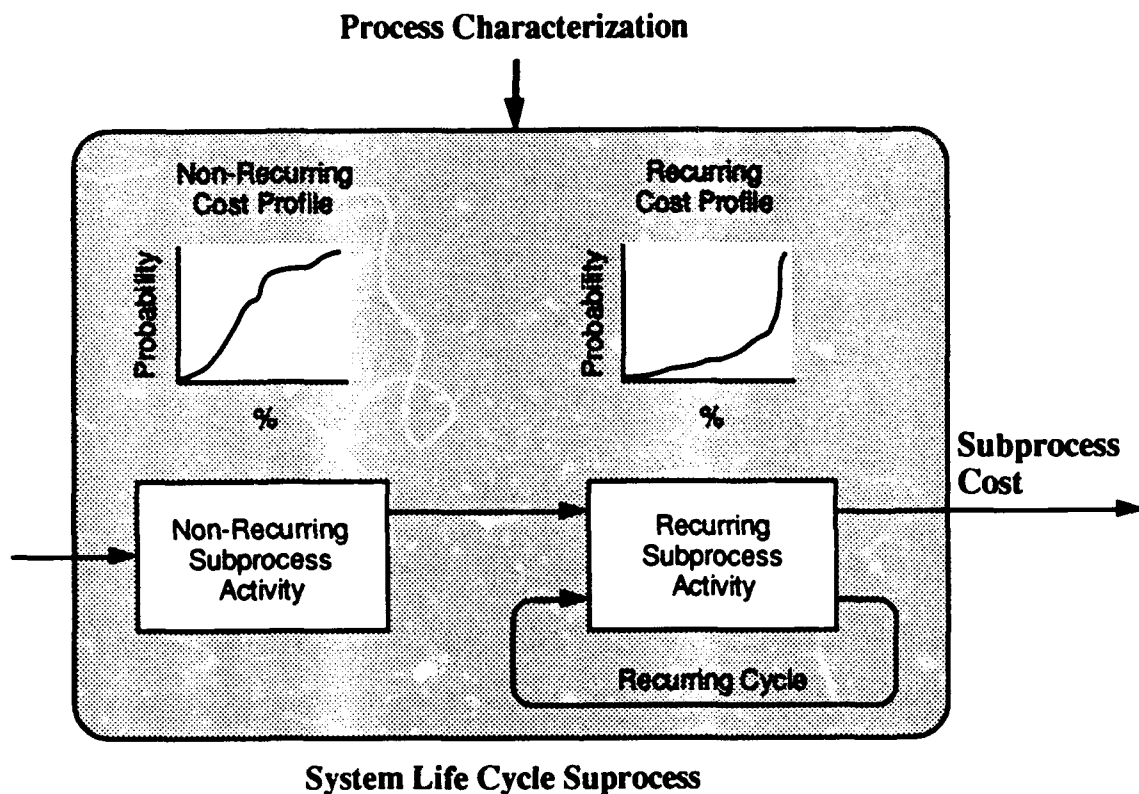


Figure 5 A General Model for Integrating Subprocess Activity Models With Cost Profile Data to Form Quantitatively Based Models

After the item has completed the non-recurring activity of the subprocess, it may then undergo a cycle of recurring subprocess activities. The cost added by each cycle is determined from a recurring cost profile curve (i.e. cumulative density function) defined for that subprocess. After a predetermined number of recurring cycles are performed, the total cost for the subprocess is established by combining its non-recurring cost with the sum of its individual recurring costs.

The arrow entering the subprocess from the top is used to alter the performance characteristics of the subprocess. Changes in process characterization correspond to variations in important business factors or drivers. Process characterization is used to alter the cost profiles or change the number of recurring cycles executed. The specific implementation of process characterization depends on the system characteristic under investigation and the influential factors that drive the business process.

The general model shown in Figure 5 was used to integrate and combine the sixty-nine cost categories which compose the acquisition portion of the DoD system life cycle. From a technical standpoint, the entire model is referred to as a network model. The visual models developed to this point were primarily used as a way to communicate concepts and ideas among individuals familiar with the business process and its data and model builders. Once the network model was finalized, it was then converted into a simulation program.

MODELING AND ANALYSIS OF EIGHT EMPIRICAL BUSINESS CASES

Based on documentation searches at the Aircraft Systems Command Cost Library and interviews of Air Force Financial Management personnel, no analyses could be identified which assess the entire Department of Defense (DoD) acquisition process or that utilize a comprehensive set of cost estimating data. Quantitatively based analyses performed by the Air Force investigate small subsets of available data which are constrained to limited portions of the acquisition process.

The current research converted acquisition cost values from the Cost Estimating System (CES) into percentages in order to obtain a uniform and consistent metric. The transformed values enable comparisons among and within lots, even though the lots may differ due to aircraft classification, aircraft type, lot size, acquisition year, or acquisition cost. With the transformed values it is possible to quantitatively investigate high level issues which were previously infeasible to assess.

Eight actual systems acquisition cases have been identified for investigation. These cases are concerned with high level issues of the acquisition process. Analyses of these cases will provide new information from which useful insights can be gained. The time available for the current research did not permit the modeling, simulation, or analysis of these cases. Subsequent research will investigate these acquisition cases. Each of the eight actual cases will be briefly described.

Cost Profiles of Fixed Wing Aircraft Acquisitions

The cumulative density functions of the sixty-nine cost categories enable comparisons of proportionate aircraft cost within cost categories. Graphs of the cumulative density functions will be examined to gain insight into the characteristics of cost distributions within individual cost categories. The categorical cost data will be analyzed using statistical techniques to determine if the data follow conventional theoretical distribution forms. These statistical tests will ascertain if theoretical distributions can be used to replace the cumulative density functions. The cost data within the categories will also be analyzed using mathematical modeling techniques. Curve fitting of the data will attempt to find reasonable mathematical approximations of the cumulative density functions. The outcomes of the statistical and mathematical analyses have important implications. If the actual cost data cannot be reasonably approximated by theoretical statistical distributions or with conventional mathematical functions, then analytical approaches which rely on these assumptions will most likely produce erroneous results. Results obtained from analytical approaches can be compared to simulated results. Because the simulation approach utilizes data which constitute an empirical population, its results can be used to validate (or invalidate) the results obtained from analytical approaches.

Comparisons Among Acquisition Costs Categories

Comparisons among acquisition cost categories are possible because the costs have been normalized into percentages. A profile of aircraft acquisition costs will be developed from the sixty-nine cost categories which comprise the acquisition process. Graphical techniques will be used to compare and contrast the various costs that contribute to total acquisition cost. Statistical comparisons of the data will be made provided the data do not violate assumptions for linearity, independence, normality, and homoscedasticity.

Comparisons of Acquisition Costs Among Fixed Wing Aircraft Classes

This analysis will investigate differences among broad classes of aircraft. The analysis will be limited to the Production and Deployment Phase of the system life cycle. There are 367 acquisition lots in this phase. The acquisition lots will be segregated into the following eight mutually exclusive aircraft classes:

- Anti-Submarine Warfare Aircraft - 24 lots
- Attack Aircraft - 81 lots
- Bombers - 17 lots
- Cargo Aircraft - 18 lots
- Electronic Warfare & Surveillance Aircraft - 31 lots
- Fighter Aircraft - 181 lots
- Tanker & Refueling Aircraft - 6 lots
- Trainers - 9 lots

Cost profiles will be developed for each of these aircraft classes. Twenty-seven acquisition cost categories compose the Production and Development Phase. These cost categories will be contrasted and compared among the eight aircraft classes.

Analysis of Fighter Aircraft Acquisition Cost Trends

The aircraft acquisitions used in this research occurred between the years 1948 and 1987. This analysis will examine changes in the proportions of acquisition costs among cost categories during this time frame. Although all three phases of the acquisition process will be considered by this analysis, it will only include 206 fighter aircraft lots. The lots will be segregated according to their year of acquisition. The forty year period will be divided into four ten year segments:

- 1948 through 1957 - 54 lots
- 1958 through 1967 - 48 lots
- 1968 through 1977 - 67 lots
- 1978 through 1987 - 37 lots

Cost profiles will be developed for each of these acquisition segments. The sixty-nine acquisition cost categories will be contrasted and compared among the four time segments.

Benchmark Analysis of a Fighter Aircraft Manufacturer

Fighter aircraft lots which were acquired for the Production and Deployment Phase will be extracted from the original 415 acquisition lots. There are 181 lots in this subset. These lots will be segregated into two groups. One group will contain all the lots that were produced by a specific aircraft manufacturer. The remaining acquisition lots will form the other group.

Cost profiles for both groups of aircraft manufacturers will be developed. There are twenty-seven cost categories in the Production and Deployment Phase of the system life cycle. These categories will be contrasted and compared between the two manufacturer groups.

Cause and Effect Analysis of B-1 Bomber Costs

The acquisition costs for the B-1 Bomber were exceptional and extraordinary. Extreme differences in cost proportions between the B-1 and other bomber types will be isolated. A root cause analysis will be conducted to ascertain why these differences exist. This analysis will be limited to Production and Deployment Phase acquisition lots. Because only five B-1 Bomber lots were ever acquired, there are insufficient data to make inferences.

Analysis of the Effect of Congressional Appropriations on Acquisition Costs of the F-16 Fighting Falcon

The system life cycle for aircraft programs typically span several decades. Funding needs for these systems are planned several years in advance of their actual expenditure. Congressional appropriations of funds are made on a yearly basis. Appropriated funds may or may not coincide with planned outlays. In cases where the actual funding level differs from the anticipated funding level, program budgets must be adjusted to accommodate the difference in funding levels.

When appropriated funds are less than the funds requested for an acquisition, the production quantity must be reduced or the acquisition schedule must be elongated. Evidence suggests that system life cycle cost will increase when the acquisition schedule is extended. The cause for this increased cost is additional recurring costs that are incurred over a longer acquisition time frame.

An actual case from the F-16 program will be modeled, simulated, and analyzed. Replication of the F-16 case will demonstrate the efficacy of the methodology.

Analysis of the Effect of Large Scale Program Reductions on the Unit Cost of the B-2 Stealth Bomber

The B-2 Stealth Bomber has been a closely guarded secret since it was originally conceived. The existence of the B-2 was only made public a few years ago. Expenditures on the B-2 for research, development, test, and evaluation have been very high when compared to other aircraft types. During the past several years, the B-2 program has experienced severe cutbacks in funding. At the present time, it is expected that the number of B-2 aircraft actually produced will only reach a fraction of the volume originally anticipated. Funds previous spent on the B-2 program must be allocated to a much smaller number of aircraft. Consequently the unit cost of the B-2 has risen dramatically.

This analysis will model and simulate the business situation experienced by the B-2 program. The B-2 case represents a radical departure from the typical fixed wing aircraft acquisition process. Replication of the B-2 acquisition case will not only demonstrate the efficacy of the methodology, it will also demonstrate its robustness to extreme changes in business practice.

SUMMARY AND CONCLUSIONS

This paper gave an overview of on-going research aimed at establishing a methodology for quantitatively assessing business performance. A brief description of the methodology was provided. The majority of this paper described the application of the methodology to an actual business environment. The methodology was used to develop a quantitative model of the Department of Defense (DoD) process for acquiring major weapon systems. An activity based model of the process was developed. A comprehensive set of data were obtained for forty-one DoD aircraft systems. These data underwent various transformations to make them consistent within and among lots. The activity based model was combined with the normalized data to form a quantitatively based model of the aircraft acquisition process. This model was converted into a computer simulation program. The work conducted during the current research was guided by the first five steps of the methodology. These steps constitute problem formulation and model development. The current research demonstrated that business processes can be modeled and simulated.

The last five steps of the methodology could not be performed in the time available for the current research. It is necessary to conduct the remainder of the methodology on one or more cases in

order to demonstrate its viability and applicability to actual problems. Eight business cases were identified and described. The first six cases do not need the entire methodology to conduct the suggested analyses. These cases only require manipulation and analysis of the normalized data. The following two business cases will utilize the remaining methodological steps to complete their modeling and analyses:

- Analysis of the Effect of Congressional Appropriations on Acquisition Costs of the F-16 Fighting Falcon
- Analysis of the Effect of Large Scale Program Reductions on the Unit Cost of the B-2 Stealth Bomber

One of these two cases will be modeled and analyzed in order to demonstrate the efficacy of the methodology.

REFERENCES

- [1] Cost Estimating System - Volume 2 - Aircraft Cost Handbook, Delta Research Corporation, Arlington, Virginia, November 1987.
- [2] Department of Defense Directive (DoDD) 5000.1, Major and Non-Major Defense Acquisition Programs, September 1, 1987.
- [3] Department of Defense Instruction (DoDI) 5000.2, Defense Acquisition Program Procedures, September 1, 1987.
- [4] Engwall, R.L., Managing Investments Strategically, Journal of Cost Management for the Manufacturing Industry, Volume 1, Number 3, Fall 1987, pp. 56-58.
- [5] Engwall, R.L., Cost/Benefit Analysis, Journal of Cost Management for the Manufacturing Industry, Volume 2, Number 3, Fall 1988, pp. 64-70.
- [6] Hayes, R.H., Garvin, D.A., Managing as if Tomorrow Mattered, Harvard Business Review, Volume 60, Number 3, May-June 1982, pp. 71-79.
- [7] Kaplan, R.S., Must CIM be Justified by Faith Alone, Harvard Business Review, Volume 64, Number 2, March-April 1986, pp. 87-95.
- [8] Reimann, M.D., Huq, F., Using Activity Based Costing to Define a Quantitative Product Life Cycle Cost Model for Concurrent Engineering, in the Proceedings of the Third International Conference on Flexible Automation and Information Management, Limerick, Ireland, June 28-30, 1993, pp. 485-496.
- [9] Reimann, M.D., Whiteside, M.M., Creating an Experiment Design for Assessing the Effects of Concurrent Engineering on Product Life Cycle Cost, in the Proceedings of the Third International Conference on Flexible Automation and Information Management, Limerick, Ireland, June 28-30, 1993, pp. 473-484.
- [10] Shumaker, G.C., Integrated Product Development Strategy, Concurrent Engineering Office, Manufacturing Technology Directorate, Wright Research and Development Center, Wright-Patterson Air Force Base, Ohio, July 1990.
- [11] Technical Management Department, The Systems Engineering Management Guide, Defense Systems Management College, Fort Belvoir, Virginia, January 1990.

**A Comparison of Biasing Options in the Laser Multiphoton Ionization Detection of
Methyl Radicals in a Filament-Assisted Chemical Vapor Deposition Reactor**

**David A. Dolson
Assistant Professor
Department of Chemistry**

**Wright State University
3640 Col. Glen Highway
Dayton, OH 45435**

Final Report for:

**Summer Faculty Research Program
Wright Laboratory
Aero-Propulsion and Power Directorate
Wright-Patterson Air Force Base**

Sponsored by:

**Air Force Office of Scientific Research
Bolling Air Force Base, Washington, D.C.**

and

**Wright Laboratory
Aero-Propulsion and Power Directorate
Wright-Patterson Air Force Base**

September, 1993

A Comparison of Biasing Options in the Laser Multiphoton Ionization Detection of
Methyl Radicals in a Filament-Assisted Chemical Vapor Deposition Reactor

David A. Dolson
Assistant Professor
Department of Chemistry
Wright State University

Abstract

An apparatus and procedures were developed for the detection of methyl radicals in a filament assisted chemical vapor deposition reactor operating with methane/hydrogen gas mixtures similar to those used in the generation of diamond-like carbon films. The apparatus was designed to detect small transient currents as the focussed output of a tunable dye laser ionizes methyl radicals between a hot filament and a deposition substrate. The current design incorporates the use of an electrode pair for ion collection, that may be translated between the filament and substrate. Results from two circuit designs with different bias geometries for ion collection are presented.

A Comparison of Biasing Options in the Laser Multiphoton Ionization Detection of Methyl Radicals in a Filament-Assisted Chemical Vapor Deposition Reactor

David A. Dolson

INTRODUCTION

There is general agreement from modeling results and from experiments that the methyl radical ($\text{CH}_3\cdot$) is one of the "growth species" linked to the transport of carbon to the substrate where diamond growth occurs in filament assisted chemical vapor deposition (CVD) of diamond-like carbon films.¹ Quantitative measurements of $[\text{CH}_3\cdot]$ using resonance enhanced multiphoton ionization (REMPI) allows for a degree of spatial resolution because ions are only created in a small focal volume. Celii and Butler² have used the REMPI³ technique to measure the relative $\text{CH}_3\cdot$ concentration in a filament-assisted diamond CVD reactor as a function of several process parameters. In their application an ion collector wire was fixed 4 mm above the substrate surface, the laser focus was approximately midway between the wire and the substrate, and the filament position was varied in order to probe the spatial $[\text{CH}_3\cdot]$ profile.

This report describes the development of a REMPI detection experiment for methyl radicals that is designed for spatial profiling of $[\text{CH}_3\cdot]$ in a fixed gap between the filament and substrate. This design avoids changing the filament-to-substrate gap as the spatial profiling is accomplished. Preliminary results are presented, and suggestions are made for continuing efforts.

APPARATUS and PROCEDURES

The filament-assisted CVD reactor was constructed from heavy-walled 4.5 inch O.D. glass pipe. The reactor was constructed in two sections, connected with an o-ring seal. Its overall length was ~18". Kovar rods, sealed through the top section of the reactor, were used to power the filament and give it support. A short section of glass rod held the tips of the kovar rods apart by ~25 mm and provided an anchor for supporting the center of the filaments. A 1" dia. port centered in this section allowed for the introduction of mixed gas flows through a 0.5" dia. pyrex tube at selected distances from the filament.

The length of the kovar rods was such that the filament was located ~5 cm inside the other section when the reactor was assembled. This section (the main body of the reactor) held the windows for passing the laser, the pressure measurement and vacuum ports, and the introduction port for a linear translator for the biasing and collection electrodes. The vacuum port was mounted to an aluminum plate for connection to a pressure control throttle valve. Flexible tubing connected this valve to the 400 m³ hr⁻¹ booster pump, which was backed by a 60 m³ hr⁻¹ two-stage rotary pump.

Typical coiled filaments were constructed using nine turns (~5 mm dia coils) of a 0.010" dia. tungsten (G.E. "218") wire which was attached to the Kovar rods by winding the free ends of the wire around the rod a few times and securing it with an alligator clip. Some filaments were more simply made from a straight length (~25 mm) of wire. The center of each filament was supported from the glass connecting rod by the use of a loop of the tungsten wire. The filament was heated by adjusting the current slowly to approximately 8 amperes, and the filament temperature was monitored with a hot filament pyrometer. A 200 sccm gas flow of 2% CH₄ in H₂ was caused to flow over the filament toward the substrate 7-14 mm away and on to the pumping port at the far end of the reactor. Gas flow rates were measured with electronic mass flow controllers, and total pressure was measured with a capacitance manometer with a 10 torr full scale rating. The substrate was a 1" dia x 0.1" thick molybdenum disc in the current work. The substrate was not connected electrically in the first circuit design (Fig. 1) to be described in this report. In the second design (Fig. 7) the substrate was electrically grounded.

In a previous circuit design using only a filament and substrate, it appeared that the collection efficiency for laser-generated ions was a function of the bias voltage used to control the discharge current. In an attempt to overcome this undesirable effect, a pair of kovar rod (0.060" dia) electrodes were mounted on a linear translator for movement between the filament and the substrate. In the first circuit design (Fig. 1), one rod was biased and the other was connected through a load resistor (1820 or 4090 ohms) to electrical ground. In the second circuit design (Fig. 7), both electrodes were tied together and connected to ground through the load resistor. Transient REMPI signals were detected as a voltage generated across the load resistor and passed through a capacitor to a digital oscilloscope (1 M Ω AC input impedance) for summed averaging over 100-1000 laser shots. Most often, peak REMPI signal levels were recorded and plotted; however, the time duration of the signals decreased at higher bias

New Circuit with Double Probes

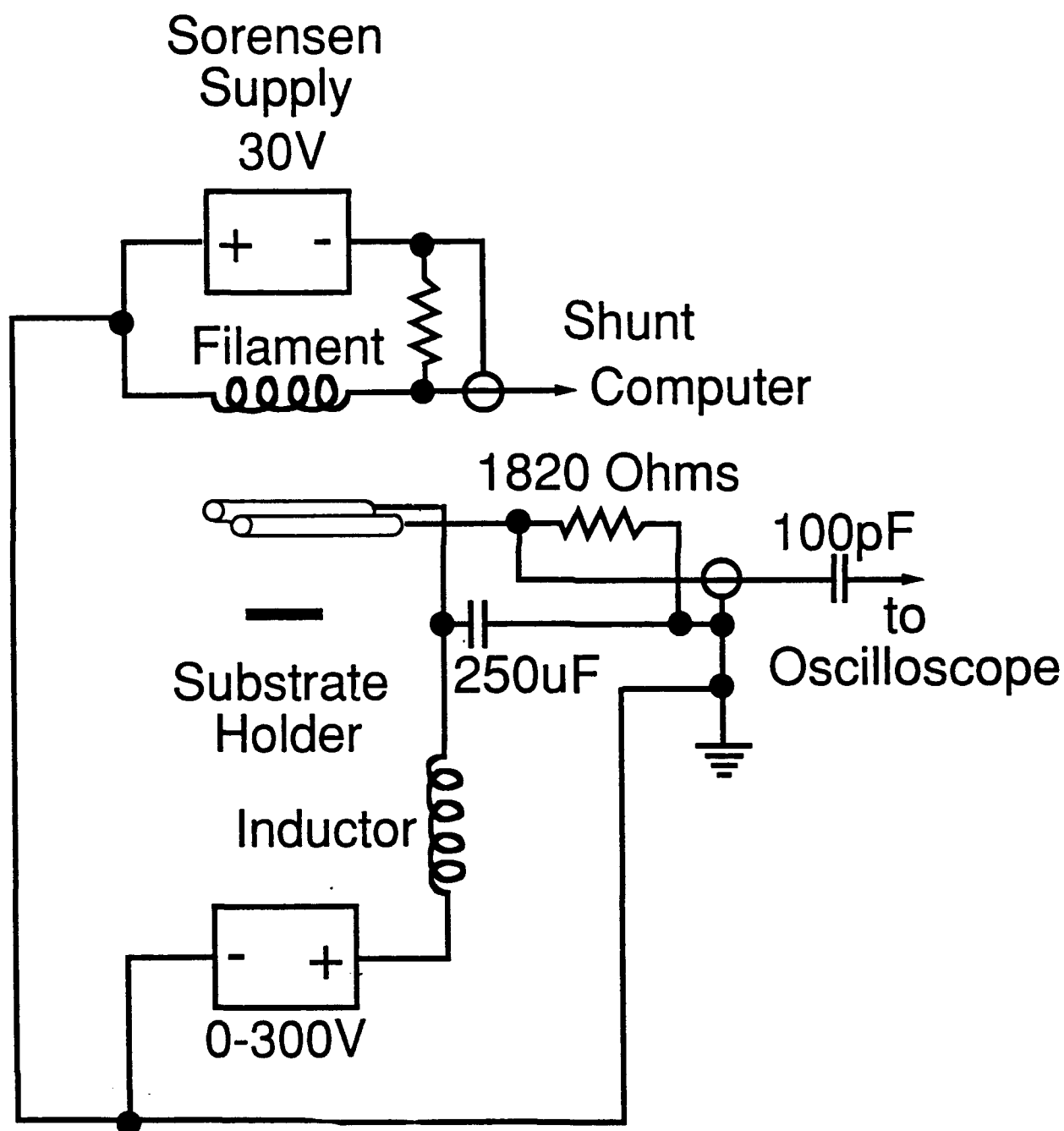


FIG. 1. Circuit design with bias and collector electrodes.

voltages and lower pressures. Consequently, a somewhat different view of the data (larger signals at lower voltages and higher pressures) is obtained by using integrated REMPI signal intensities (see Fig. 10). Unfortunately, the large amplitude electromagnetic interference generated at the time of the excimer laser firing overlapped the expected time for collection of photoelectron current. Consequently, the REMPI signals observed in this study are attributed to the movement of molecular ions.

REMPI signals were obtained by scanning the tunable output of an excimer-pumped dye laser (Lambda Physik EMG-103MSC/FL2002) near the 333.5 nm transition for methyl radicals and near 339.4 nm for methyl iodide. The dye laser delivered up to 8mJ/pulse at 333.5nm using a p-terphenyl/p-dioxane dye solution pumped at 248 nm with a KrF excimer laser. It was common for the laser power to decrease significantly by 1-2 mJ/pulse over the course of some of the longer experiments. No power correction has been made for any of the data presented here. Most of the current work was done with the laser operating at 10Hz. The laser was focussed between the electrodes with a 20 cm focal length lens. The vertical and horizontal positions of the laser could be adjusted externally with turning prisms mounted on linear translation stages. Filament, substrate, and electrode positions were determined by moving the laser beam until contact was determined visually by the spark generated.

RESULTS and DISCUSSION

The first evaluation of the circuit design with bias and collector electrodes (Fig. 1) was made using a 2% methyl iodide/hydrogen gas mixture at 10 Torr because of the ability to generate uniform concentrations with a stable species. The filament was cold for these evaluations. Fig. 2 presents a time-resolved REMPI signal observed for methyl iodide with a +150 volt bias on the one electrode and the filament biased at +27 volts to simulate the potential of a hot filament. This observation is the difference of 200 laser shots "on resonance" (at the peak near 339.4 nm) and 200 laser shots "off-resonance" (at 338.0 nm). The time-scale for observations such as this ranged from ~25 μ s at 300 volt bias to ~200 μ s with no bias.

The results for various combinations of filament and bias potentials are presented in Fig. 3. The results are qualitatively as expected. The positive potential sends positive ions to the (grounded) collector and attracts electrons (and/or negative ions, if present) to the biased electrode. The current generates a positive voltage drop across the

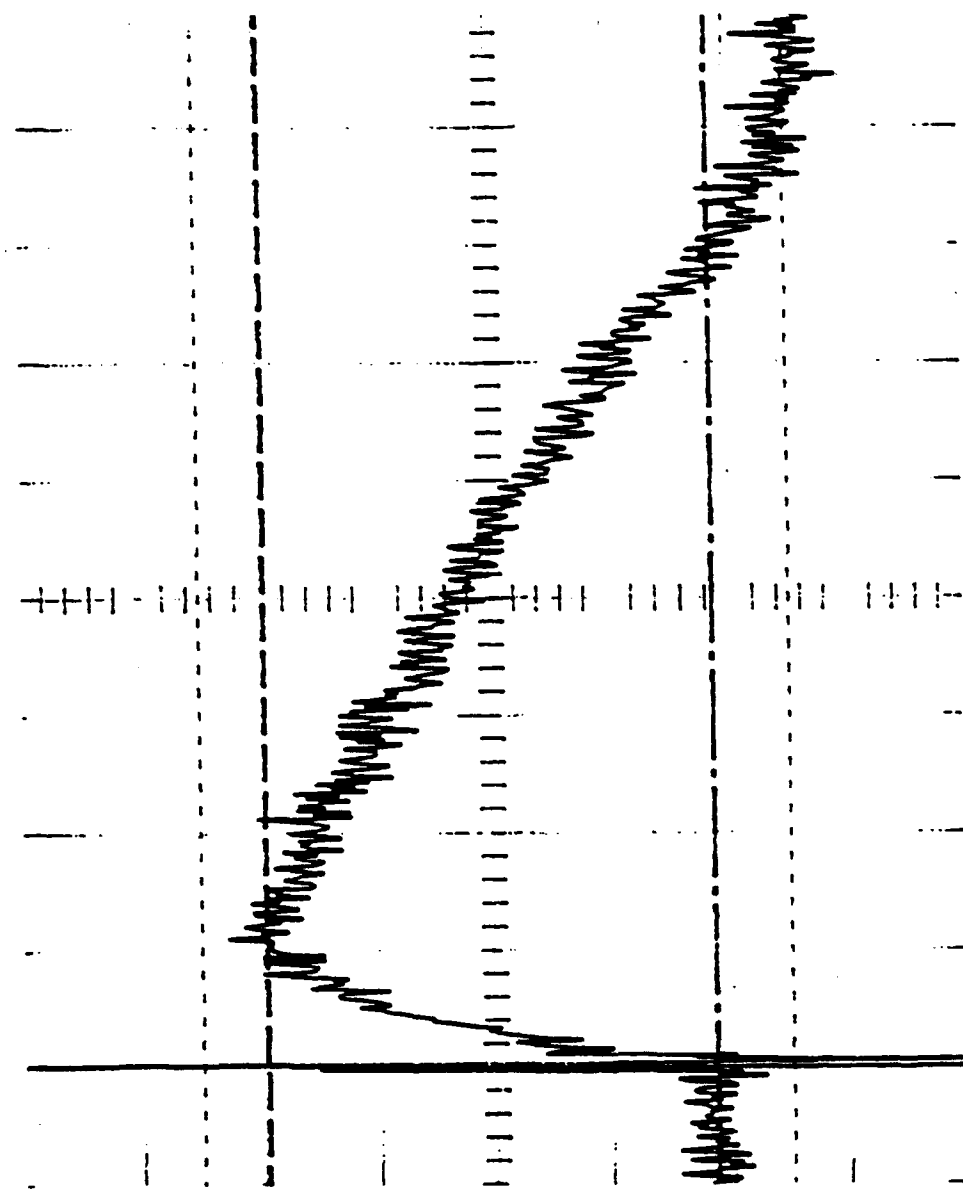


FIG. 2. Time-resolved REMPI signal from methyl iodide excited at 339.4 nm.

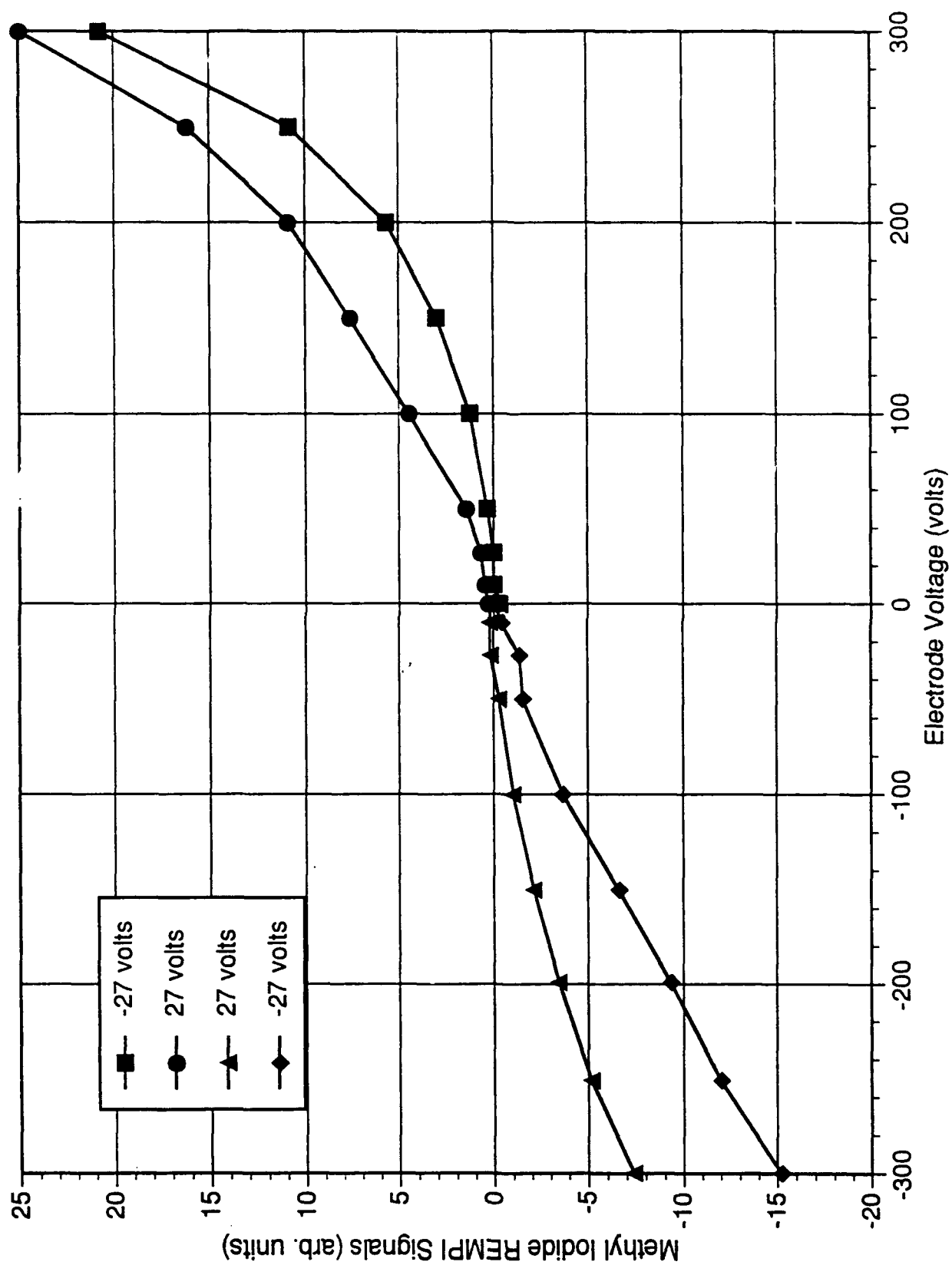


FIG. 3. Methyl Iodide REMPI signals as a function of bias voltage.

load resistor. Negative potentials generate negative polarity signals due to the reversed current direction. The increasing magnitudes of the slopes of the curves at the higher potentials is consistent with secondary ionization by accelerated photoelectrons. The actual collection of electrons is estimated to occur within 2 μ s of the laser pulse⁴, the drift time of the ions being much longer. The electron collection period is obscured by the electromagnetic interference (EMI) caused by the excimer laser pulse. Thus, most of the signals collected during this study are attributed to ion currents.

Methyl radicals were generated in a 2% methane/hydrogen gas mixture using tungsten filaments operated at typical temperatures of 1800-2000°C. The methyl radical REMPI signals are presented in Fig. 4 as a function of bias voltage and electrode micrometer readings. True distances from the filament are 2 mm greater than the stated micrometer readings. The filament potential ranges from ground at one side to -31 volts at the other side, and the filament temperature was 1970°C. The laser energy was 3 mJ/pulse, and the on- and off-resonance wavelengths were 333.5 nm and 333.0 nm, respectively.

The contrasting behavior (compared to Fig. 3) of the methyl radical REMPI signals is immediately apparent. Near the filament the peak REMPI signals are quite strong when no potential is applied to the collection electrodes, and the maximum signal occurs at -10 volts potential. The signal falls off rapidly as the potential is made increasingly negative. At +10 volt potential there is still a net negative signal, although it is of interest to note that the off-resonance signal was entirely positive. REMPI signals are more difficult to detect at more positive potentials. There is no opposite polarity similarity for the methyl radical REMPI signals as there was in Fig. 3 for methyl iodide. The same qualitative behavior with respect to potential was observed at 5mm and 9mm micrometer readings but with reduced intensity in keeping with the expected reduction in methyl radical concentration away from the filament.

Further investigation of methyl radical REMPI signals as a function of distance from the filament gave results similar to those depicted in Fig. 5. Peak signals were always greater (negative polarity) near the filament, falling off as the laser focus and collection electrodes were translated toward the substrate (14 mm filament-to-substrate gap). This behavior is in agreement with the expectation of $[\text{CH}_3\cdot]$ reduction away from the filament confirmed in other studies^{1,5}. The occurrence of larger REMPI signals at lower collection potentials is demonstrated again in this figure.

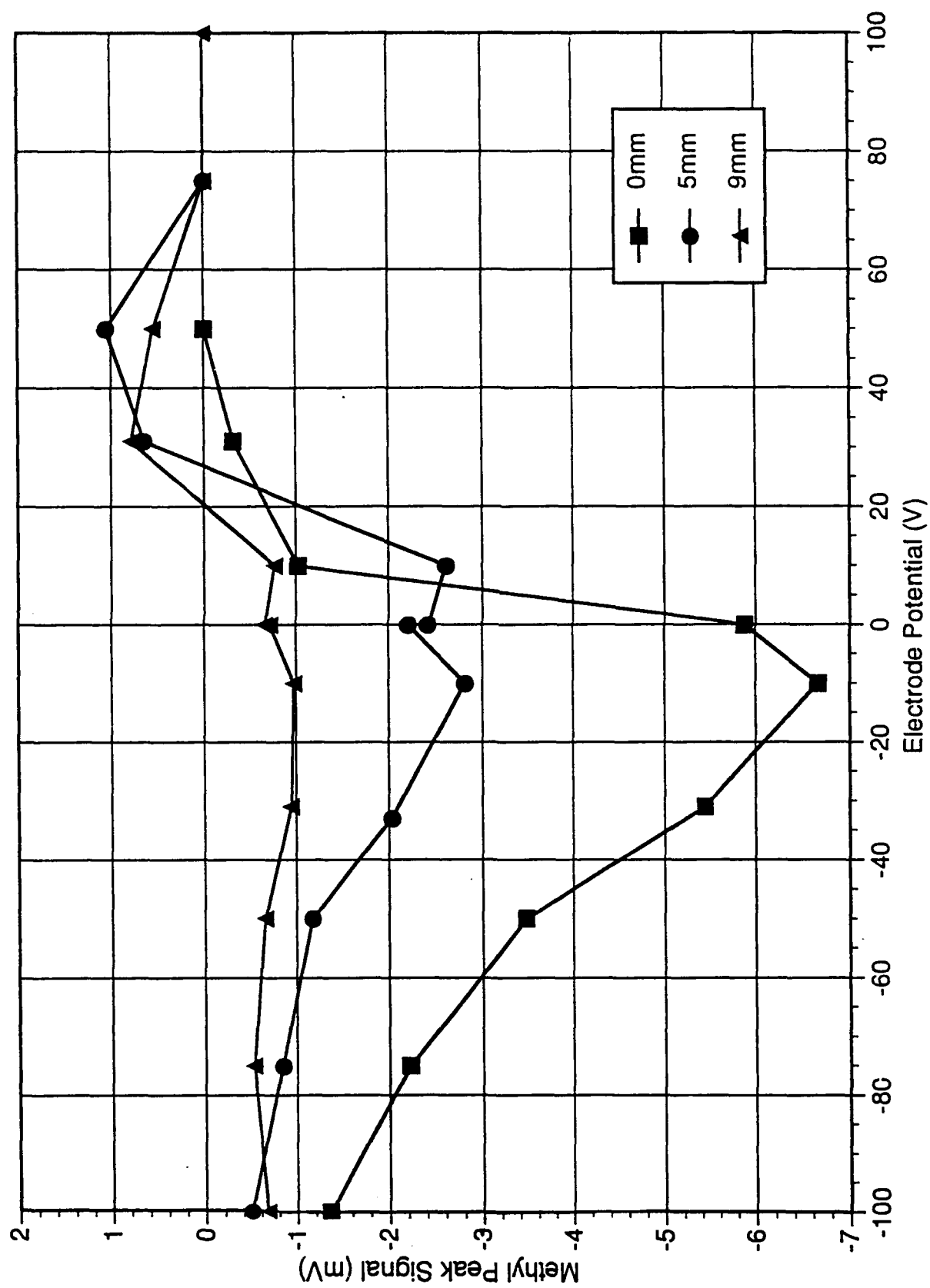


FIG. 4. Methyl radical REMPI signals as a function of bias voltage.

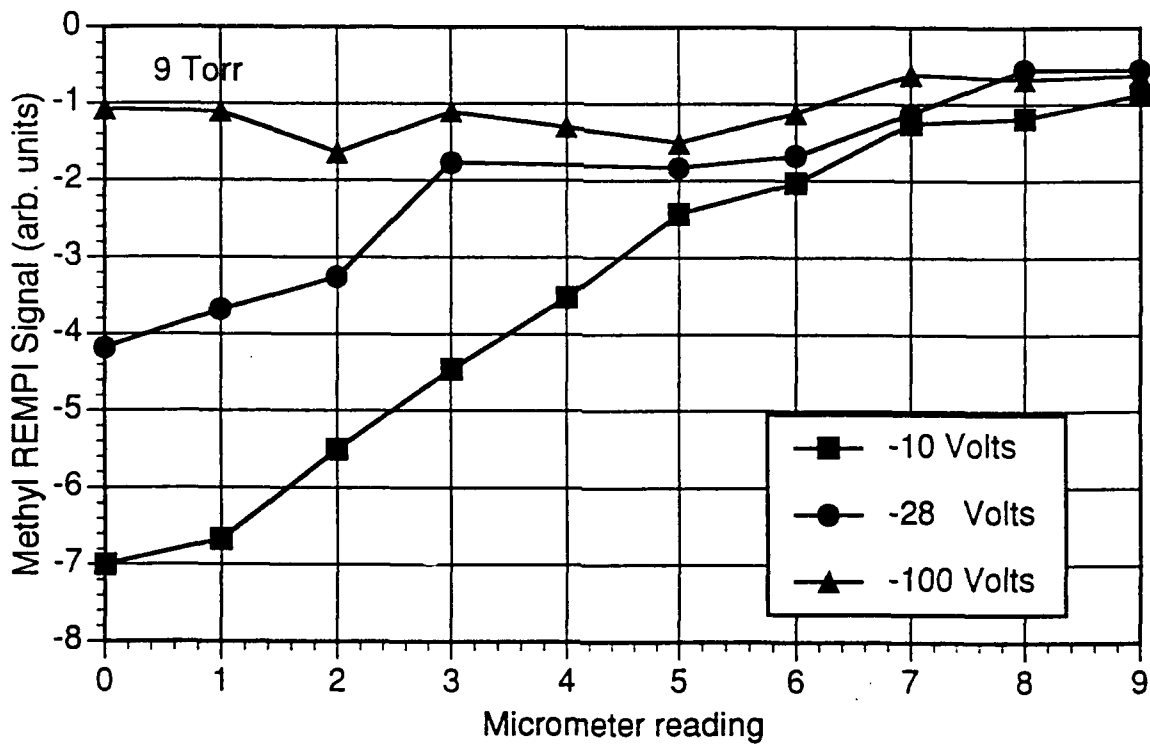
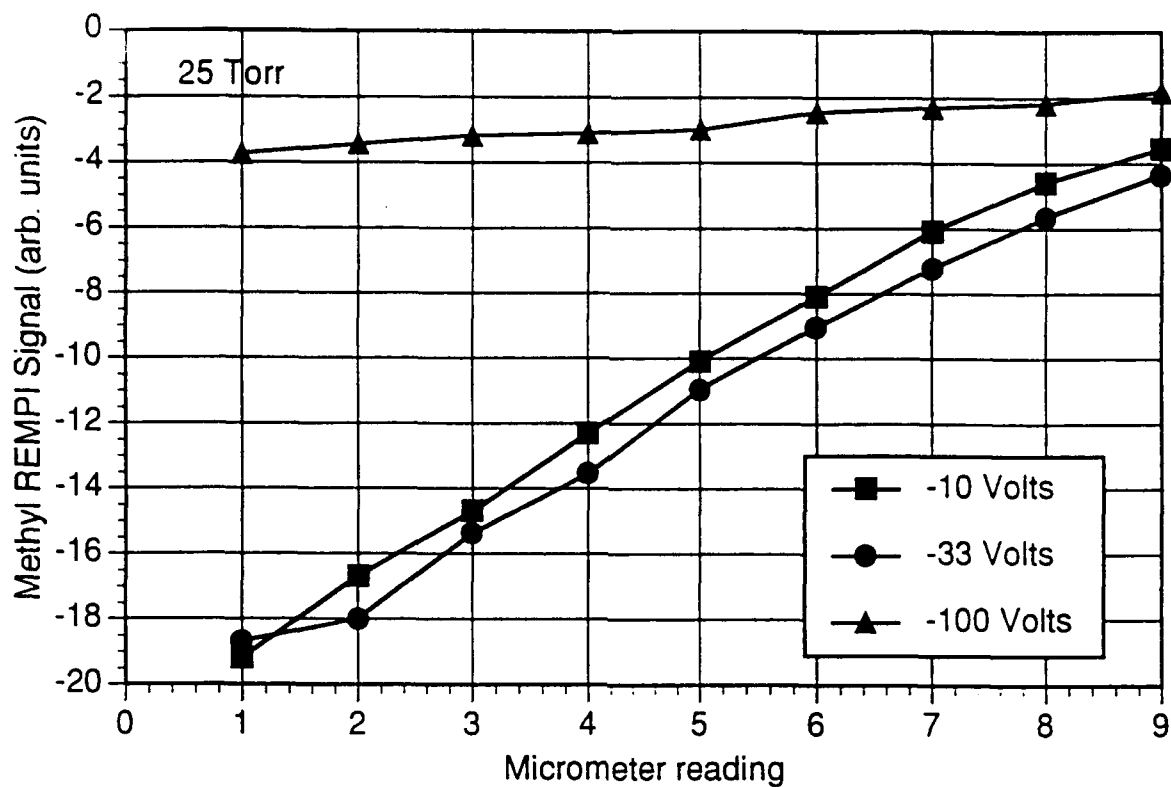


FIG. 5. Methyl radical REMPI signals as a function of distance from the filament. True distance is obtained by adding 2 mm to the micrometer reading.

During the course of this work, it was observed that the DC current through the load resistor increased, under certain biasing conditions, with increasing temperature and decreasing filament-to-electrode distance. Large DC current levels proved to suppress the REMPI signals, as shown in Fig. 6A, where peak REMPI signals and DC current are plotted versus electrode distance from filament. When the electrodes were within 4 mm of the 2020°C filament, the DC current was in excess of 0.5 mA, and the peak REMPI signals jumped to lower values. At the lower 1940°C filament temperature the DC current was not excessive, and the REMPI signal levels increase nearer to the filament (in agreement with the expectations of Fig. 5).

A further demonstration of this effect is demonstrated in Fig. 6B, where the REMPI signals (mV) and the resistor voltages (V) are plotted versus filament temperature for the 2mm electrode position. The equivalent DC current is 0.5 mA at -2 volts across the load resistor. Here, again, the peak REMPI signal suffers reduction when the filament temperature reaches a point where large currents are picked up by the collector electrode. This behavior was not noted in other studies^{1,5} where the methyl radical REMPI signals (electron current) increased with temperature up to a nearly constant value between 2200°C and 2500°C.

Near the end of this study we modified the circuit design of the apparatus to closely reproduce that reported by Corat and Goodwin⁵ in a recent publication. This design, presented in Fig. 7, grounds the substrate and incorporates an additional power supply to maintain a constant potential difference between the filament and the paired collection electrodes (20 volts more positive than the low side of the filament). The filament-to-substrate gap was 7-9 mm, depending upon the filament placement, for all of this work. Corat and Goodwin⁵ showed increasing REMPI signals from 0-50 volts electrode bias, and they were able to obtain saturated electron collection conditions over the range of 50-150 volts electrode bias (their figure 3). REMPI signals were obtained as a function of bias voltage (Fig. 8), distance from the filament (Fig. 9), and total pressure (Fig. 10) in the present study.

REMPI signals as a function of electrode bias voltage were obtained with the collection electrodes and the laser focus positioned 4 mm above the grounded substrate (~3 mm from the filament). The laser beam was parallel to the electrode rods in this study whereas the beam traveled perpendicular to the single collection electrode in the apparatus of Corat and Goodwin⁵. The squares in Fig. 8 were obtained with a (coiled) filament temperature of

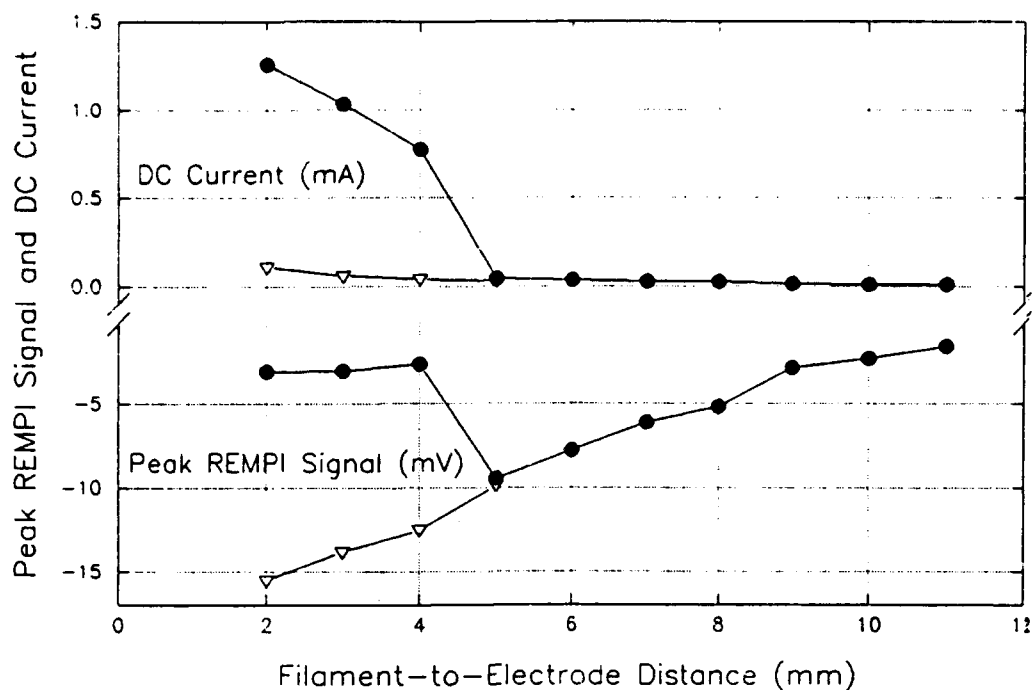


Fig. 6A Methyl radical REMPI signal and DC current as a function of electrode position.
 ● points were obtained with $T_{fil}=2020^{\circ}\text{C}$ (32.6 V @ 8.0 A) first.
 ▽ points were obtained with $T_{fil}=1940^{\circ}\text{C}$ (30.7 V @ 8.0 A) after the first set.
 Laser pulse energy was 4.8–4.9 mJ, and the collection potential was -32 V.

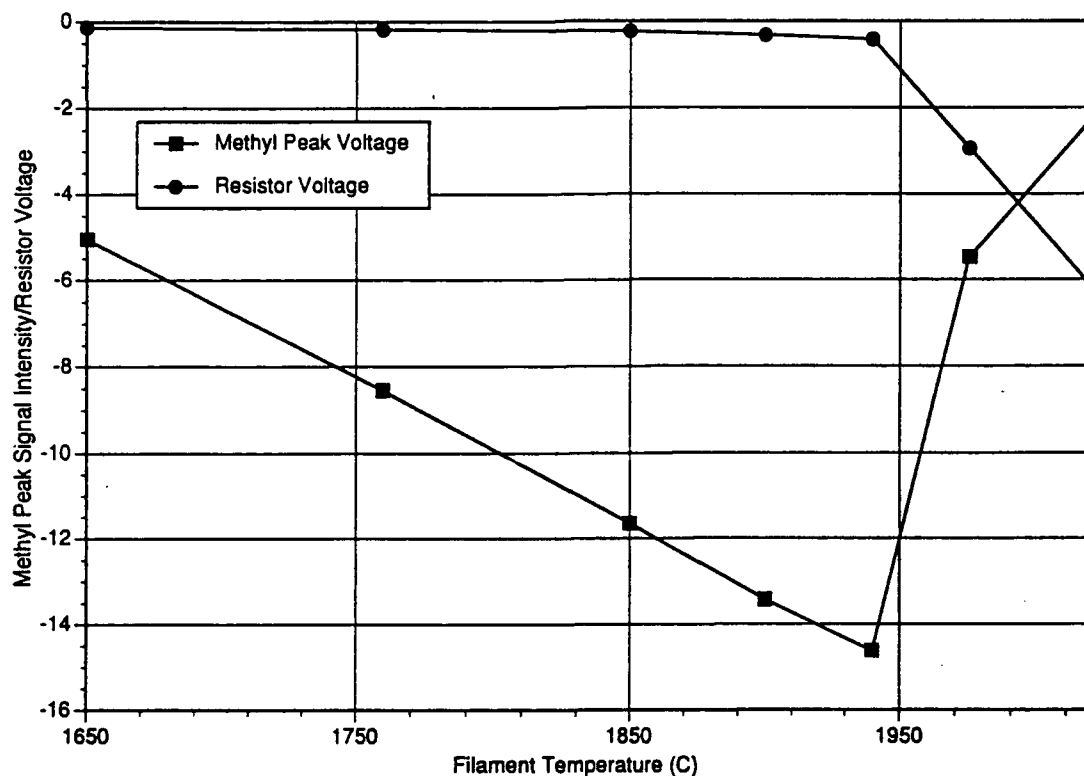
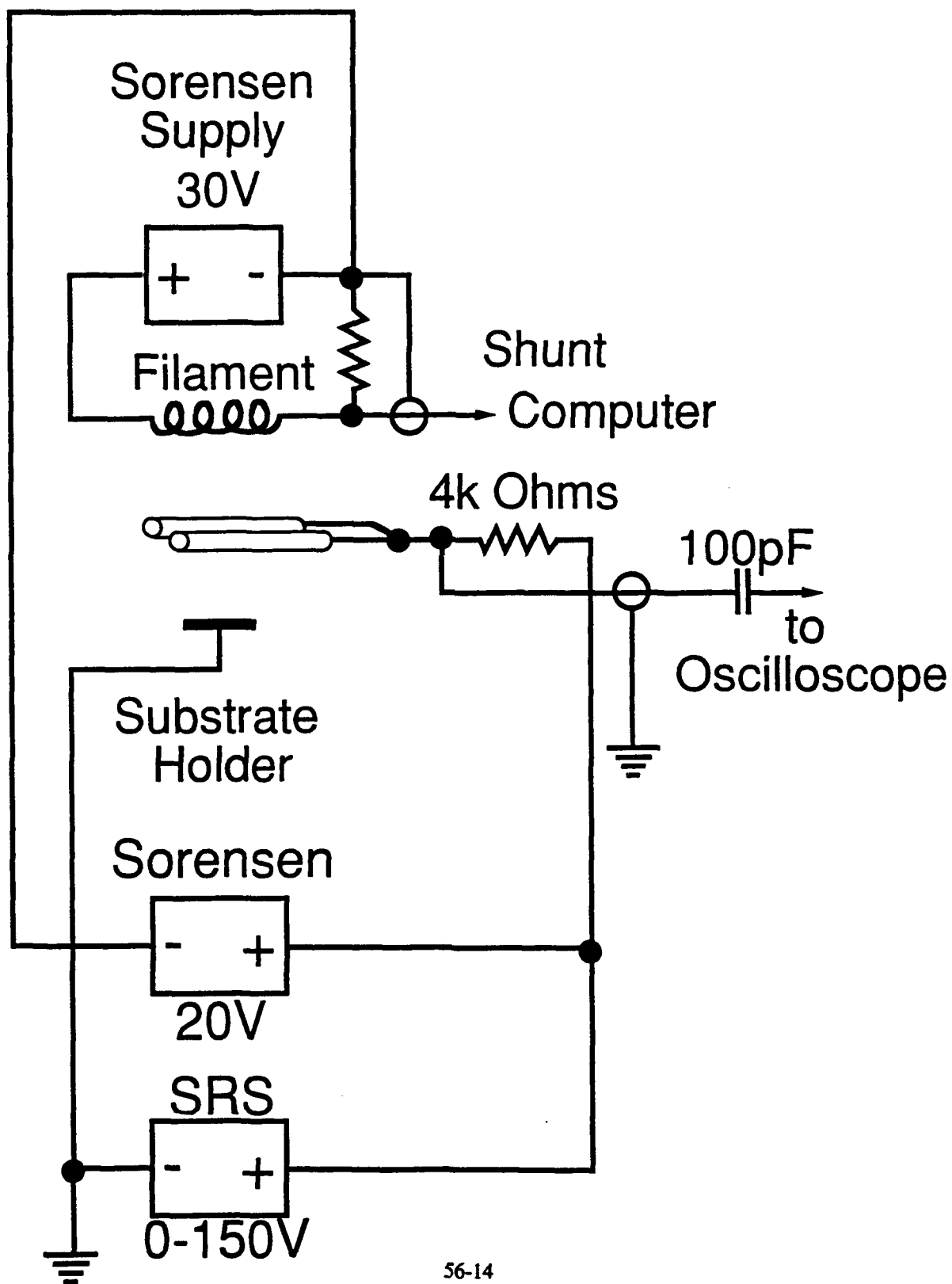


FIG. 6B Methyl radical REMPI signal and D.C. voltage across load resistor as a function of filament temperature.

Fig.7 Circuit design with constant potential between filament and collection electrodes
(similar to Goodwin's design)



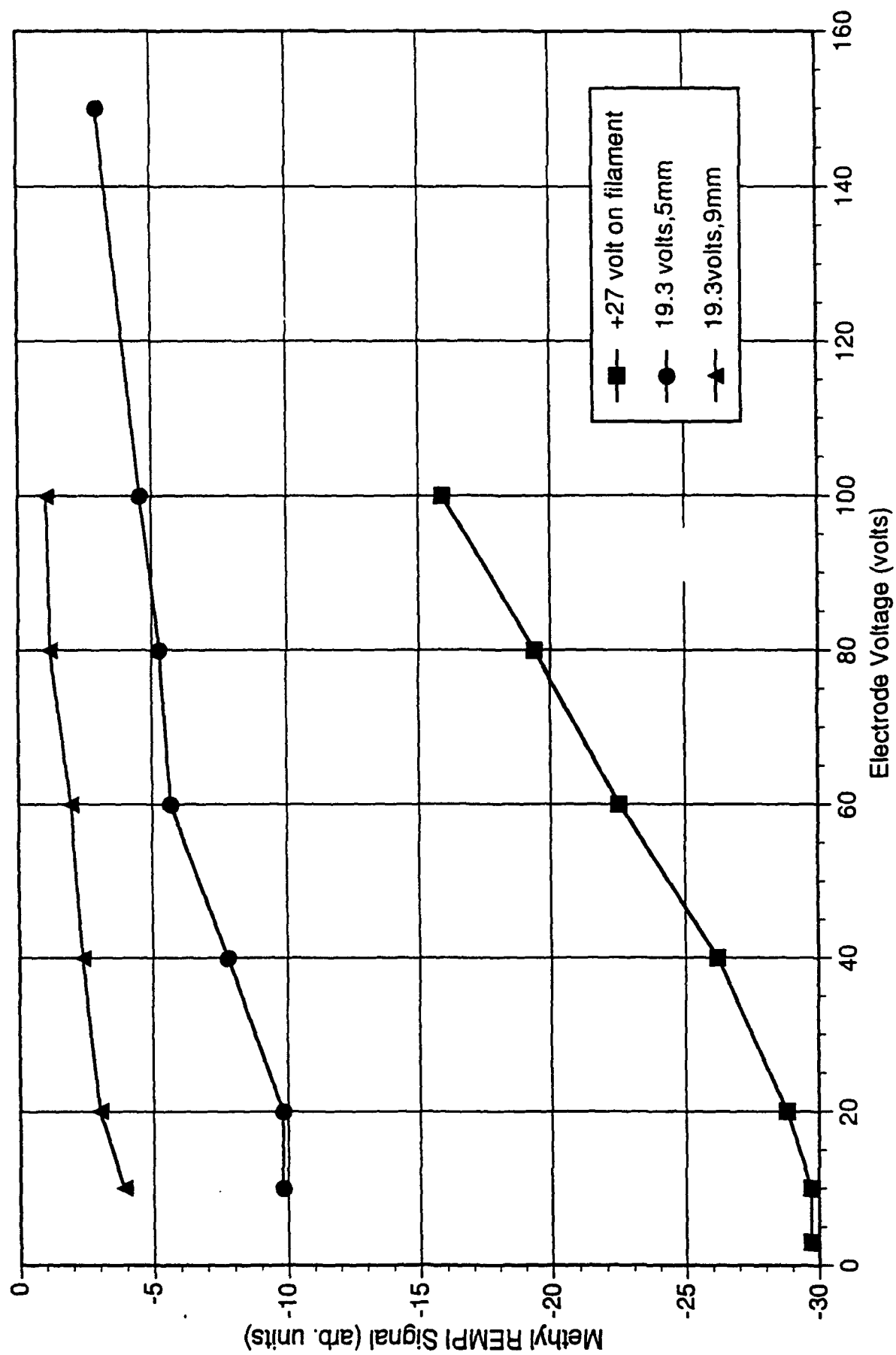


FIG. 8. Methyl REMPI Signals as a function of bias voltage.

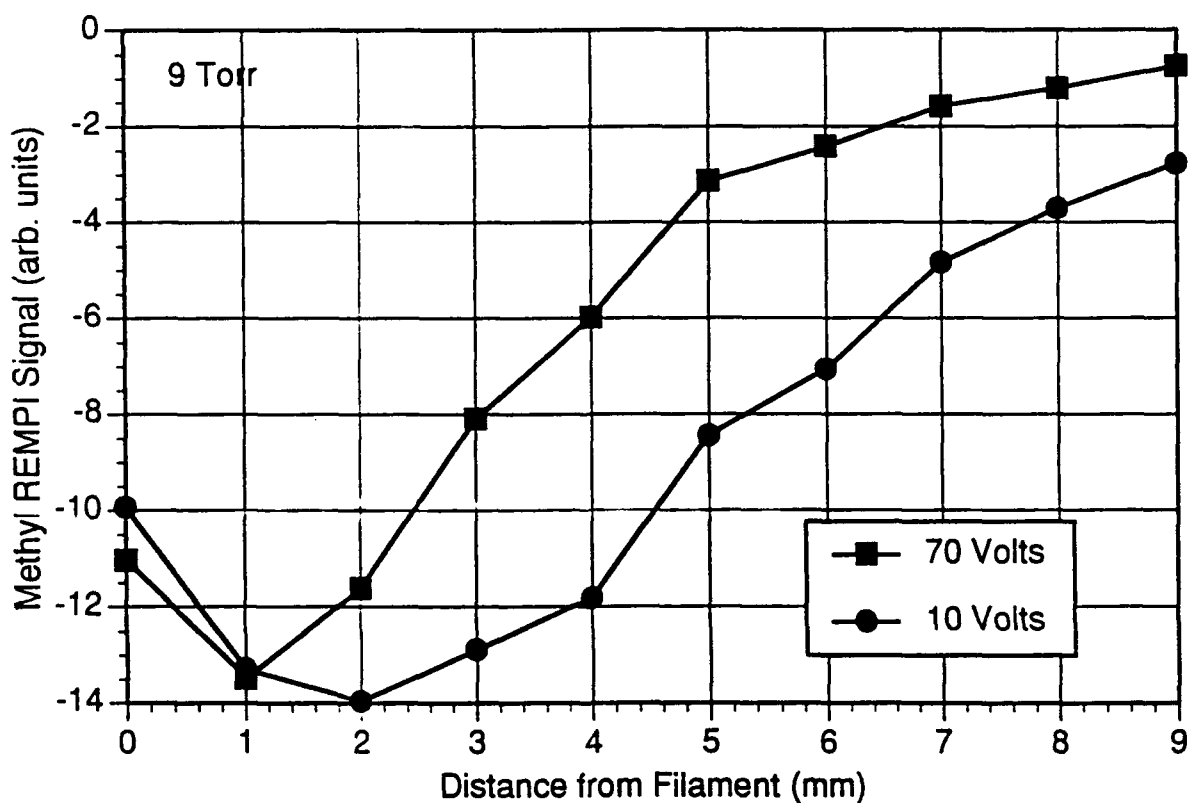
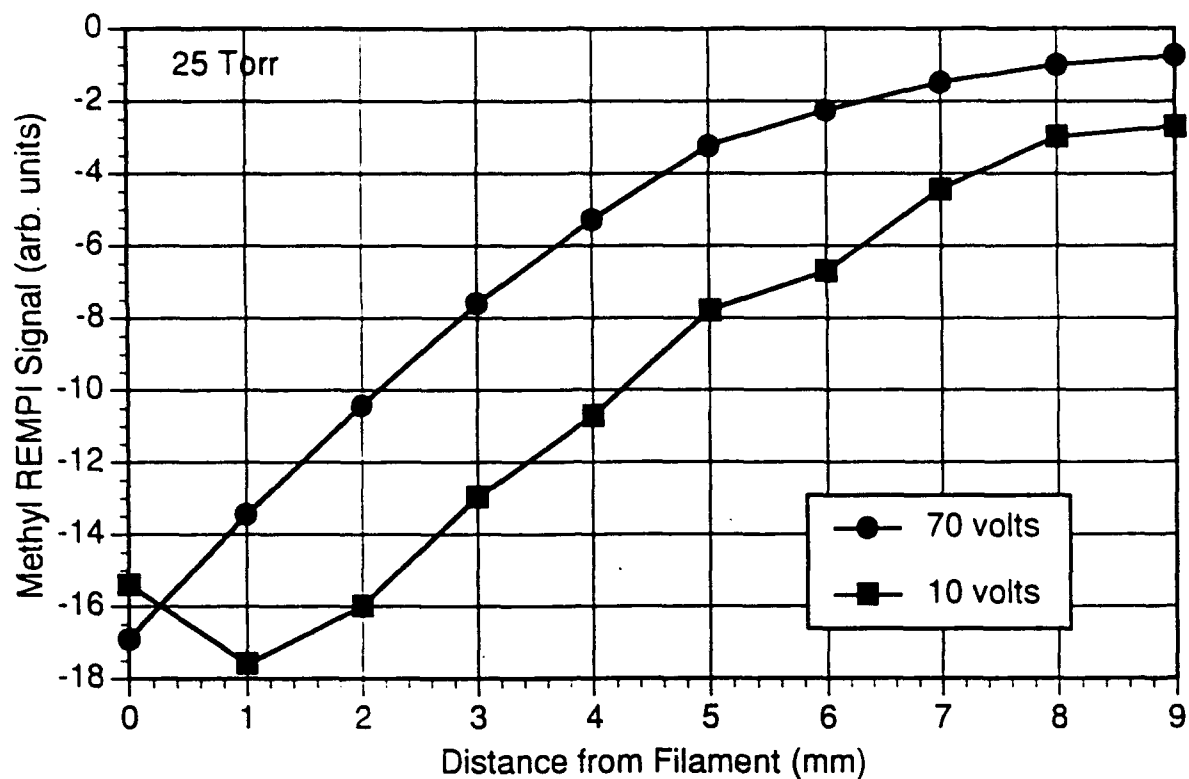


FIG. 9. Methyl radical REMPI signals as a function of distance from the filament. True distance is obtained by adding 2 mm to the micrometer reading.

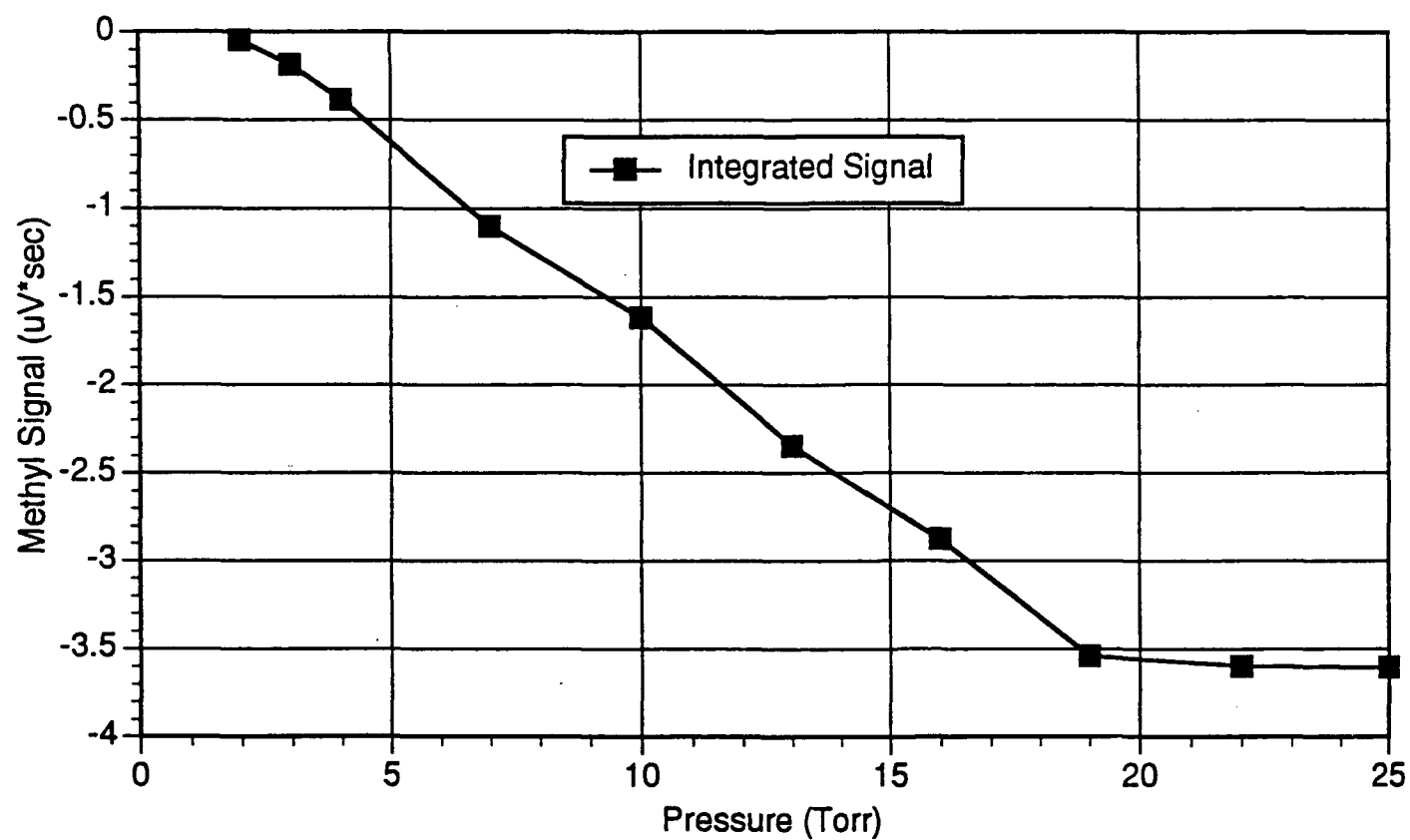
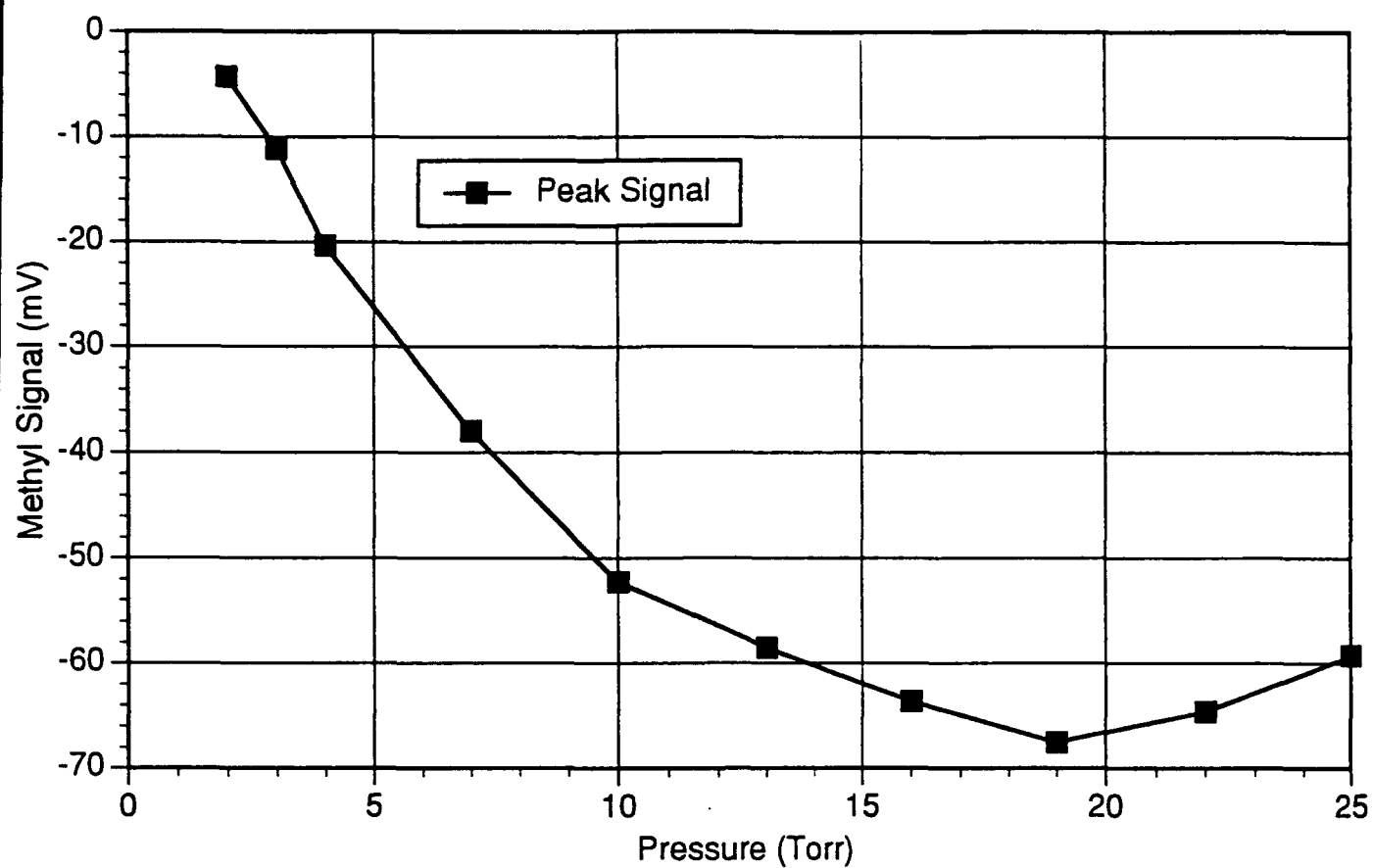


FIG. 10. Methyl radical REMPI signals as a function of total pressures.

-1900°C and 6.5 mJ/pulse laser energy. REMPI signals were reduced by a factor of two or more when the laser focus was located midway between the collection electrodes and the substrate (Corat and Goodwin's arrangement⁵). The circles and triangles in Fig. 8 were obtained on a different day with a single strand electrode, $T_{fil}=1850^{\circ}\text{C}$, and 5.2 mJ/pulse laser energy. The 5 mm and 9 mm labels of Fig. 8 are micrometer readings that correspond to 4 mm and 8 mm distances from the filament. The DC current was less than 0.1 mA for all of the data of Fig. 8. The REMPI (ion current) signals were not observed to saturate with bias voltage in the manner observed by Corat and Goodwin⁵ for electron current.

REMPI signals as a function of distance from the filament are more completely presented in Fig. 9. These data were obtained on two different days using single strand tungsten filaments at 2030°C (top) and 1880°C (bottom) and two bias voltages (10 and 70 volts) at 9 and 25 Torr total pressures. The laser pulse energies were 5.2 mJ for the 25 Torr data (top) and 4.3 mJ for the 9 Torr data (bottom). Peak REMPI signals were greater at the lower bias voltage, and they decayed as the detection point was moved away from the filament. The small decreases close to the filament are related to the larger DC currents observed at those positions (as in Fig. 6A). The observations of Figs. 8 and 9, greater REMPI signals at lower bias voltages and decreasing signal away from the filament, are qualitatively the same as those presented in Figs. 4 and 5 for the previous circuit design.

The observation of larger REMPI signals at lower collection potentials is quite puzzling. It has been suggested by one author (MDK) that the behavior is suggestive of the presence of negative ions, presumably produced by attachment of the electrons generated by the REMPI laser pulse. The electron attachment hypothesis is consistent with smaller cross-sections for the higher collection potentials that yield more energetic electrons. In fact, calculations⁶ have shown that dissociative attachment ($e^- + \text{H}_2(v) \rightarrow \text{H}^- + \text{H}^{\cdot}$) involving vibrationally excited H_2 can be efficient. Detection of H^- produced in pure hydrogen gas flowing over a hot tungsten filament suggests that the process is more efficient at lower pressures where vibrational deactivation of the $\text{H}_2(v)$ reactant is reduced⁷. In our experiments, however, higher pressures are expected to yield greater methyl concentrations, ¹¹ source of the electrons to be attached. Thus, there are competitive processes at work that make it difficult to predict the pressure dependence of the REMPI signals. Results from an investigation of REMPI signal versus total pressure of the 2% CH_4/H_2 gas mixture are presented in Fig. 10. Peak signals and integrated signals are presented. The

integration limits were from $\sim 2 \mu\text{s}$ to the point where the signal crossed zero as it underwent damped oscillation. For this experiment the filament was maintained at 1960-1990°C, the electrode bias was 15 volts, and the laser energy was 6.1 mJ/pulse. The longer time duration of the signals at lower pressure tend to increase the relative level of the integrated signals at lower pressures. The result is an approximately linear dependence of integrated REMPI signals with pressure over the range 2-20 Torr, at which point the signal seems to saturate. The DC current collected by the probe ranged from 0.27 mA at 25 Torr to 0.64 mA at 2 Torr. We do not expect that any significant reduction of signal occurred at these current levels. While the negative ion hypothesis has some support, there is one remaining observation that it still does not answer. The almost complete lack of REMPI signal with the positive collection potentials (Fig. 4) in the first circuit design is yet a mystery. The potentials modeled for the experiments indicate that ions generated between the electrodes should be detected, and the number of CH_3^+ ions should equal or exceed that of H^+ ; but little or no signal is detected.

SUMMARY and CONCLUSIONS

Methyl radical REMPI signals, with temporal and spatial resolution, were obtained from 2% methane/hydrogen gas mixtures in a filament-assisted CVD reactor using different collection geometries and biasing options. Observations were attributed to photo-generated ion currents because detection of transient electron currents was blocked by laser noise. While the observations of REMPI ion currents in 300K methyl iodide was in qualitative agreement with expectations, the REMPI signals generated from methyl radicals at 333.5 nm exhibited unconventional behavior with respect to collection potentials. A hypothesis involving the production of negative ions by dissociative attachment to vibrationally excited H_2 was considered because it was consistent with the occurrence of larger REMPI signals at lower potentials. The suggestion has been made⁸ that using a photodetachment laser pulse delayed after the REMPI laser might provide a further test of the negative ion hypothesis.

Because of the uncertainty of the source of the observed REMPI signals with the present detection methods, we cannot recommend using the present procedures even as a relative measure of methyl radical concentrations in a CVD reactor. We are confident, however, that quantitative measurements could be obtained by observing the

electron current generated in the MPI event. This would require efforts at laser EMI noise reduction so that the early time signals could be obtained with much less interference.

ACKNOWLEDGEMENTS

Ideas and assistance from Dr. Peter Bletzinger were invaluable as were conversations with Drs. Bish Ganguly and Alan Garscadden. I appreciate the calculation of electron mobilities by Rajish Nagpal and the mapping of potentials by Peter Bletzinger. The technical expertise and cheerful assistance of Mike Ray and Bob Knight made this work possible. I acknowledge the assistance of Craig Bartell and Michelle Klingshirn in collecting a significant portion of the data.

REFERENCES

1. Two reviews of the diamond CVD processes are: P. K. Bachmann; R. Messier *Chem. Eng. News*, pp 24-38, May 15, 1989. and F. G. Celii; J. E. Butler *Ann. Rev. Phys. Chem.* (1991), 42, 643-84.
2. F. G. Celii; J. E. Butler *J. Appl. Phys.* (1992), 71, 2877-83.
3. J. W. Hudgens; T. G. DiGuseppe; M. C. Lin *J. Chem. Phys.* (1983), 79, 571.
4. R. Nagpal, private communication.
5. E. J. Corat; D. G. Goodwin *J. Appl. Phys.* (1993), 74, 2021-9.
6. A. Garscadden; W. F. Bailey *Prog. Astronaut. Aeronaut.* (1981), 74(Rarefied Gas Dyn., Pt. 2), 1125-37. and W. F. Bailey; A. Garscadden *Brookhaven Natl. Lab., [Rep.] BNL* (1980), BNL-51304, Proc. Int. Symp. Prod. Neutralization Negat. Hydrogen Ion Beams, 2nd, 33-41.
7. P. Bletzinger, private communication.

**PLIF Images of Supersonic Jet Mixing in the
Wright-Patterson AFB Supersonic
Combustion Facility**

**James F. Driscoll
Associate Professor**

**Department of Aerospace Engineering
University of Michigan
312 Aerospace Engineering Building
Ann Arbor MI 48109**

**Final Report for the
1993 AFOSR Summer Faculty Research Program**

Research performed in conjunction with:

**Dr. Abdollah S. Nejad
Advanced Propulsion Division
Aero Propulsion and Power Laboratory POPT/WL
Wright-Patterson Air Force Base OH 45433**

**Sponsored by:
Air Force Office of Scientific Research
Bolling Air Force Base, Washington D.C.**

30 September 1993

PLIF Images of Supersonic Jet Mixing in the Wright-Patterson AFB Supersonic Combustion Facility

James F. Driscoll
Associate Professor

Department of Aerospace Engineering
University of Michigan
312 Aerospace Engineering Building
Ann Arbor MI 48109

Abstract

Some experimental measurements are described which resulted from an AFOSR sponsored interaction between Dr. J.F. Driscoll, Dr. A.S. Nejad of Wright-Patterson AFB, and other researchers in the Advanced Propulsion Division. The goal of the work was to study the mixing of a turbulent jet of gas that is injected coaxially into a supersonic air stream. A unique supersonic wind tunnel facility was used that was developed by, and is currently operated by Dr. Nejad. A circular, underexpanded sonic jet issues along the centerline of a Mach two wind tunnel. The injector consists of a splitter plate with a circular orifice on centerline; this design simulates a fuel injection strut in a scramjet combustor, and it was selected because the simplicity of the boundary conditions allow it to be modelled using existing numerical codes. The jet fluid is helium which is seeded with gaseous acetone. A Planar Laser-Induced Fluorescence (PLIF) imaging system was used to record images of the acetone fluorescence during the mixing process. Several methods were considered to reduce the data in order to extract images of the jet mixture fraction (f), which is the fundamental parameter of interest in mixing models.

Images of the mixing process were obtained for three different injection conditions and for several different imaging locations, including the near field and the far field of the jet. Values of the pressure ratio, defined as the jet exit static pressure to the air static pressure, were selected to be one, two and five. Results indicate that acetone fluorescence is a useful method to identify the shock wave structure and to quantify several parameters that characterize the mixing process. These parameters include the centerline decay of the mean mixture fraction, the radial profiles of mean mixture fraction, turbulent fluctuations in mixture fraction, and the eddy structure of the scalar field within the jet. The jet spreading rate is much smaller for the supersonic cases than for typical subsonic jet mixing cases. This difference occurs because several additional physical processes are introduced when the surrounding flow becomes supersonic, including the effects of velocity ratio, density ratio, and compressibility. The images obtained provide a useful set of data that are being used to develop general scaling laws for the supersonic mixing process and to improve existing numerical models of mixing.

The work also revealed that additional research is needed to quantify the pressure and temperature dependence of the fluorescence intensity from acetone at the relatively low pressures of 0.5 atm. and low static temperatures of 166 K (minus 160 degrees F) that occur in the present supersonic airflow. Calibration measurements are needed in a controlled pressure cell in order to properly reduce all to the data obtained to date. Such follow-on measurements will be proposed as a Summer Research Extension Program (SREP).

PLIF Images of Supersonic Jet Mixing in the Wright-Patterson AFB Supersonic Combustion Facility

James F. Driscoll

Introduction

The mixing between a fuel jet and a surrounding supersonic air stream is significantly different from the well-known mixing process that occurs in subsonic jets. Additional physical phenomena are introduced as the surrounding air flow velocity is increased into the supersonic range. The shear layers in some portions of the jet boundaries are driven by the higher-velocity surrounding air, rather than by the jet itself. The eddy structure is thus altered and the shape of the profiles of the turbulence levels can be changed. Shock waves occur within the underexpanded jet and other shock waves result from the expansion-recompression process associated with the injector geometry. Such shock waves tend to alter the vorticity field, due to the production of baroclinic torques and due to velocity changes induced by the shock waves. It is desired to understand these new phenomena in order to use them to improve fuel-air mixing within scramjet combustors.

In order to optimize the fuel-air mixing process, the Air Force has developed a unique, high quality supersonic wind tunnel at the Aero Propulsion and Power Laboratories that was designed by, and is now operated by, Dr. A. Nejad and his research team. Several novel fuel nozzle designs are being tested in order to achieve enhanced mixing. Concurrently, studies are in progress at the University of Michigan in which a relatively small but versatile supersonic flame tunnel is used by Dr. Driscoll and his students to obtain different, but related, experimental data, such as the blowout limits of supersonic hydrogen-air flames [2] and the lengths of supersonic flames [3]. It was decided that PLIF images of the jet mixture fraction (f) in the APL facility would be the best method to quantify the supersonic mixing process and to eventually explain the trends observed in the supersonic flame data obtained at Michigan.

Experimental Arrangement

The supersonic combustion facility at the Advanced Propulsion Division is shown schematically in Figure 1. Gruber and Nejad [1] provide a complete description of the system that is shown. The facility provides variable Mach number capability (from Mach 1.5 to 3.0) in the 5-inch by 6-inch test section. The heating and pumping capacity provides peak air flow rates of 34 lbm./sec at stagnation temperatures up to 1660 R and stagnation pressures up to 400 psig. The nominal test section static pressure and temperature for the present work were 7.35 psia and 294 R, respectively. Visible and ultraviolet optical access is provided by windows on three sides and on one end. The system is operated continuously, which is a major advantage, since it allows up to several hundred images to be obtained in a single run. Another advantage of the facility is that the air can be diverted in order to temporarily interrupt the flow to the test section (to make modifications during a

run) without shutting down the air supply system or having to cool the heated air supply lines.

The summer research described herein was a study an underexpanded sonic jet of helium that is injected along the tunnel centerline. Therefore a horizontal splitter plate was inserted along the tunnel axis and a 0.635 cm diameter circular orifice was machined at the center of the splitter plate. A static pressure tap is used to determine the static pressure at the jet exit, which is set to values that are one, two or five times that of the static pressure of the air stream.

An acetone ($\text{CH}_3\text{-CO-CH}_3$) seeder was developed by the research team in order to seed the helium jet fluid with desired concentrations of acetone vapor. Heated helium was passed upward through a enclosure containing liquid acetone. The acetone concentration is determined from the known mass flow rate of helium and the known mass of acetone that is vaporized per second.

The acetone concentrations were measured using Planar Laser-Induced Fluorescence imaging. A vertical sheet of ultraviolet laser light at 266 nm was provided by a Quanta-Ray YAG laser whose output (at 1064 nm) was frequency doubled twice. Acetone absorbs in the broadband region between 225 and 325 nm, and the resulting fluorescence is emitted in the blue region of the visible spectrum. The fluorescence intensity was recorded using a Princeton Instruments cooled, intensified CCD array camera (PI-ICCD 576) and a Vivitar F2.8 macro lens. The advantages of using acetone to mark the fuel mixture fraction is that it has a high vapor pressure (yielding a mole fraction of up to 0.30 acetone in the jet fluid), it has only mild toxicity and is non-carcinogenic, and it has a large fluorescence yield.

Data Reduction Procedure

The fluorescence signal was related to the fuel mixture fraction by utilizing the calibration results of Lozano, Yip and Hanson [4]. They state that "The dominant deexcitation path for acetone singlets is the intramolecular intersystem crossing to triplet levels: collisional quenching is negligible, and therefore the quantum yield is independent of molecular collisions, hence independent of temperature and local gas composition. For concentration measurements, acetone fluorescence signals are particularly easy to interpret." As a result of their calibration measurements, they state that "Confirming the theoretical predictions, no temperature dependence of the fluorescence emission in the temperature range of these experiments was detected. Neither were appreciable self-quenching, or quenching of the acetone fluorescence by oxygen or nitrogen observed."

The equation for the fluorescence intensity (I_f) that is used in PLIF studies is obtained by equating the rate of photon absorption to the rates of subsequent emission and collisional quenching, to yield:

$$I_f/I_{f0} = c_1 n_{\text{acet}} / [1 + c_2 Q(n_{\text{acet}}, n, T)] \quad (1)$$

where I_{f0} is the fluorescence intensity at a reference location, n_{acet} is the acetone local number density, c_1 and c_2 are constants that depend on the transition levels and the optical collection system, and Q is the quenching term that depends on total number density (n), temperature, and n_{acet} . The calibration results of Ref. 4 that are summarized in the

preceding paragraph indicates that the second term (c_2Q) in the denominator of Eq. 1 can be neglected with respect to unity.

In order to reduce the data, it is noted that Eq. 1 states that the measured intensity ratio I/I_0 is proportional to n_{acet} since Q is constant, and thus:

$$I/I_0 = n_{\text{acet}}/n_{\text{acet},0} = X_N n / n_0 \quad (2)$$

where subscript (o) refers to conditions at the nozzle exit and X_N is the mole fraction of nozzle fluid (helium and acetone) at any location in the jet. We now define the jet fluid mixture fraction (f) as the mass fraction of fluid that issued from the jet and the standard relation between mass fraction of nozzle fluid (Y_N) and mole fraction (X_N) is used:

$$f = Y_N = M_N X_N / [M_N X_N + M_A (1-X_N)]$$

The molecular weight of air is M_A and the molecular weight of the nozzle fluid is M_N . Combining the above relations, it follows that:

$$f = \{ 1 + (M_A/M_N)[(I_0/I_f)(n/n_0) - 1] \}^{-1}$$

The final step involves eliminating n/n_0 , which equals $(p/p_N)(T_N/T)$ because of the ideal gas law; p_N and T_N are the static pressure and temperatures at the fuel nozzle exit where I_0 is measured, thus the result is:

$$f = \{ 1 + (M_A/M_N)[(I_0/I_f)(p/p_N)(T_N/T) - 1] \}^{-1} \quad (3)$$

Equation (3) is the relation that provides the fuel mixture fraction (f) at each pixel location in the images. It is necessary to provide the local gas pressure and temperature (p, T) to reduce the data. This is a requirement of all PLIF studies for which the PLIF signal has a pressure and temperature dependence, which is nearly always the case. Three methods to complete the data reduction are described.

METHOD 1: Pitot probe measurements

The ratio p/T required in Eq. (3) can be determined in the first three shock cells from pitot probe measurements on centerline. Each shock cell is observed to be 3 nozzle diameters (d_N) in axial length, so three cells extend nine nozzle diameters downstream. It is known that the gas on centerline in the first three cells must be nozzle fluid only, due to observations of the shear layers in the PLIF images, and due to images obtained using Rayleigh scattering from submicron water droplets in the air stream. It also has been shown in previous work that air does not mix to centerline before nine nozzle diameters. The pressure and temperature in the first shock cell also is known from the isentropic calculations of Adamson and Nicholls [5]. Downstream of the third shock cell, the ratio of static pressure to static temperature (p/T) is approximately equal to that of the ambient airstream. It is noted that this ratio (p/T) remains approximately constant across the relatively weak compression and expansion waves downstream of the third shock cell because both p and T increase across compression waves and both p and T decrease across expansion waves so their ratio is relatively insensitive to weak waves. Therefore Eq. (3) can be used to reduce the data using the centerline pitot measurements in the first three shock cells, and it can be assumed, with no additional loss of accuracy, that the ratio p/T is constant downstream of the first three shock cells.

METHOD 2: Simultaneous PLIF/Rayleigh scattering images

The Advanced Propulsion Division research team at Wright-Patterson AFB has begun to develop a new diagnostic method which utilizes Rayleigh scattering from submicron water droplets in the air stream. The intensity of this signal is denoted I_R and the value of this signal is $I_{R,a}$ in the air stream, far from the jet. Thus:

$$I_R / I_{R,a} = n_A / n_{A,a} = X_A n / n_{A,a} = (1 - X_N) (n / n_{A,a}) \quad (4)$$

where n_A is the number density of air in the mixing region, and $n_{A,a}$ is the air number density in the unmixed air stream. Combining Eqs. (2) and (4) allows the number density of the mixture (n) to be eliminated from the two equations; thus:

$$f = [1 + (M_A/M_N)(I_{f,o}/I_f)(I_R/I_{R,a})(p_{A,a}/p_o)(T_o/T_{A,a})]^{-1} \quad (5)$$

Thus Eq. (5) allows the mixture fraction to be deduced from simultaneous images of the acetone fluorescence (I_f) and the Rayleigh images of the water droplets (I_R). Conditions are known at the fuel jet exit (subscript "o") and in the undisturbed supersonic air stream (subscript A,a). The molecular weight of the nozzle fluid (M_N) also is known. It is seen that near centerline I_R will approach zero (no water drops may reach centerline at some locations), which forces f to approach unity. Radially far away from the centerline the PLIF signal (I_f) will approach zero, causing the entire term in the square brackets to go to infinity; thus f approaches zero, which is the correct behavior.

METHOD 3: Pressure and temperature measurements using CARS

The most direct method to measure mixture fraction is to use Eq. (3) and to insert into this equation the measured values of p and T at each location. Simultaneous images of p and T would be required, which would require extensive diagnostic capabilities. Single point mean measurements of p and T may be adequate, but further research is needed to determine if the errors associated with using the mean values of p and T , rather than instantaneous values, would make this approach worthwhile.

Results

Figure 2 is a schematic of the jet fluid mixing pattern that is deduced from the acetone PLIF images, some of which are included as Figures 3-5. In addition, an image of the Rayleigh scattering from submicron water droplets appears as Fig. 6. The general features that were observed are listed on Figure 2. The first shock cell consists of a central region in which the acetone PLIF signal decreases along centerline due to the decrease in gas number density associated with the expansion waves at the exit of the underexpanded sonic jet. The PLIF signal increases across the first Mach disc due to the density increase across the shock wave. The acetone PLIF images provide an accurate indication of the location of the barrel shock and Mach disc in the first shock cell, as indicated in Figure 2. The images also provide an accurate indication of the location of the mixing layer, which exists radially outward of the barrel shock near the first shock cell.

It appears that enhanced mixing may be caused by the barrel shock at the outer edge of the first shock cell. Inspection of the PLIF images indicates that the edge of the acetone

signal is relatively smooth initially but becomes much more irregular near the end of the first shock cell, indicating that air is engulfed farther inward near the shock waves.

Figure 2 shows some filaments of jet fluid that extend radially outward into the air stream. The filaments are inclined as shown, which is opposite to the inclination of filaments of jet fluid in a jet that has no coflowing air. The inclination of the filaments is an indicator of the direction of the vorticity in the shear layer. The high velocity coflowing air is responsible for the structure that is observed in Figure 2.

A major difference between the present supersonic jet and subsonic jets is that the spreading angle of the supersonic jet is significantly smaller than the spreading angle of a subsonic jet. Schlichting [6] summarizes measurements of jet halfwidth (b), which is defined as the radial location where mean velocity is half of that on centerline. For a subsonic, axisymmetric turbulent jet, the halfwidth b is given by :

$$b = 0.08 x \quad (6)$$

The decay of the fuel mixture fraction on centerline is identical to the decay of the mean velocity (since the turbulent Schmidt number is unity) and reference 6 shows that mean mixture fraction (f) in a turbulent subsonic jet is:

$$f = f_{cl} [1 + 25(r/x)^2]^{-2} \quad (7)$$

where: $f_{cl} = 5.2 (x/d - 0.8)^{-1} \quad (8)$

The above two relations hold at all x/d locations greater than 6, which is the extent of the jet core. At x/d equal to 6, the above relation for f_{cl} equals unity. At x/d locations less than 6, f_{cl} is unity.

The present jet in a supersonic coflow has a jet spreading rate that is less than the subsonic value given by Equation (6). At least three different factors can be responsible for the reduced spreading rate, namely the ratio of the coflowing air velocity to the local jet velocity (U_A/U_J), the density ratio (ρ_A/ρ_J) and compressibility effects, as quantified by the convective Mach number (M_c).

Coflowing air causes a reduction in the spreading angle of an axisymmetric, subsonic jet; measurements of Maczynski [7] lead to the following scaling relation for the jet halfwidth (b) with coflowing air:

$$b = 0.08 x (1 + 0.144 x/\theta)^{-1/2} \quad (9)$$

where the momentum thickness (θ) is defined to be $(d_0/2)[(U_0/U_A)(U_0 - U_A)/U_A]^{1/2}$. The jet diameter is d_0 , the jet exit velocity is U_0 , and the coflowing air velocity is U_A . It is seen that as the coflowing air velocity goes to zero, θ approaches infinity and the second term in Equation 9 approaches zero, so Equation 9 becomes identical to Equation 6. For large coflow air velocity, x/θ increases with U_A , the second term dominates and jet halfwidth (b) increases as $x^{1/2}$, rather than linearly with x . The mixture fraction on centerline decays more rapidly with coflowing air than for the case of no coflowing air; Dahm and Dibble [8] have summarized previous studies and show that with coflowing air:

$$f_{cl} = 8.3 \theta/x \quad (10)$$

which is valid at x/d values greater than six. From the above definition of momentum thickness, it follows that increasing the coflow air velocity causes θ to decrease, so that at any fixed x location, the value of f_{cl} decreases. Thus coflowing air causes a more rapid decay of the centerline mixture fraction.

The density ratio also affects the jet properties. For a subsonic shear layer, Papamoschou and Roshko [9] report the following effect of density ratio on the shear layer visual width (b_{vis}):

$$b_{vis} = [1 - (U_2/U_1)] [1 + (\rho_2/\rho_1)^{1/2}] [1 + (U_2/U_1)(\rho_2/\rho_1)^{1/2}]^{-1} \quad (11)$$

where side 1 is the higher velocity side of the shear layer. Equation (11) summarizes many experiments; it shows that if U_2/U_1 goes to zero, the width of the shear layer goes to zero; it also shows that if the density of the lower velocity side (i.e., ρ_2) is increased, the second factor in square brackets in Equation 11 is increased, so the mixing layer thickness increases. This increase in layer thickness is linear with ρ_2 if the third factor in square brackets in Eq. 11 is unity (i.e., if U_2 is zero, corresponding to a jet issuing into ambient air), but will be less than linear if U_2 is not zero. It is concluded that a relation similar to Equation 11 should be valid for axisymmetric subsonic jets; thus decreasing the density of the lower velocity stream should reduce the jet spreading rate and the corresponding mass entrainment rate. In the present mixing problem, the initial jet velocities on centerline exceed the air velocity, but over most of the downstream jet mixing region the jet velocities should be less than the air stream velocity. Thus it is believed that the low density of the helium jet leads to a reduction in the jet spreading rate.

Coflowing air also decreases the mass entrainment rate into the jet. Ricou and Spalding [10] showed that the mass flowrate of air that is entrained into a subsonic, axisymmetric jet issuing into ambient air is given by:

$$m = 0.250 (\rho_A \rho_O)^{1/2} U_O d_O x \quad (12)$$

Maczynski [7] shows that coflowing air increases the mass entrainment rate; with coflowing air considered, Equation 12 must be modified to yield an entrainment rate of:

$$m = 0.250 (\rho_A \rho_O)^{1/2} U_O d_O x (1 + 0.144 x/\theta)^{1/2} \quad (13)$$

where the momentum thickness θ is defined above. Thus Equation 13 indicates that as coflow air velocity goes to zero, θ goes to infinity and the x/θ term in Equation 13 is zero. However, as coflow air is increased, the x/θ term increases, as does the mass entrainment.

A third factor that affects the jet spreading angle of the present work is the compressibility effect associated with a convective Mach number. Reference 9 indicates that the spreading angle of a compressible shear layer can decrease by a factor of five if the convective Mach number exceeds unity. Current work in the Advanced Propulsion Division is directed at the determination of the local velocity field and local Mach numbers. Such further work is needed before the effects of compressibility in the present configuration can be determined.

Values of the jet mixture fraction (f) are being obtained from the present images of the supersonic jet mixing process. Considerable data reduction is required. An AIAA paper is in preparation which will compare the supersonic jet mixing trends with the subsonic trends described above in Equations 6-13. The decay of the centerline fluorescence intensity is shown in Figure 7.

Conclusions

1. Acetone PLIF imaging has proven to be a useful method of visualize the shock structure, the vortex structure, the mixing pattern, and the jet spreading angle of an underexpanded sonic jet that undergoes mixing with a supersonic coflowing air stream. Images were obtained at three pressure ratios and several downstream locations.
2. Methods to deduce the jet mixture fraction (f) from the PLIF images have been identified and are being implemented. Results are expected to yield (a) the centerline decay of mean and rms fluctuations in mixture fraction, (b) the radial profile of such quantities, and (c) probability distribution functions for the mixture fraction.
3. The spreading angle of the supersonic jet is less than that of a subsonic jet with no coflow air; several factors can be the cause of the reduced spreading angle, including the effects of the coaxial air velocity ratio, the gas density ratio, or compressibility.
4. The work indicates a need for a follow-on calibration of the acetone PLIF technique. Follow-on measurements will be proposed to quantify the temperature and pressure dependence of the acetone PLIF signal for the particular laser wavelength used (226 nm) and for the particular temperature range (100 - 300 K) and pressure range (0.2 - 1.0 atm.) associated with this particular flowfield. The effects of the relatively slow phosphorescence process also need to be measured, since such effects could possibly introduce errors into studies of high-speed flowfields.

References

1. Gruber, M.R. and Nejad, A.S., "Supersonic Combustion Research Laboratory: Vol.1 - Design and Fabrication", Wright Laboratory Report WL-TR-93-2052.
2. Yoon, Y., Donbar, J.M., and Driscoll, J.F., "Blowout Stability Limits of a Hydrogen Jet Flame in a Supersonic, Heated, Coflowing Air Stream", to appear, Combustion Science and Technology, 1993.
3. Donbar, J.M., Yoon, Y. and Driscoll, J.F., "Flame Lengths and Heat Release Distributions Within Supersonic Hydrogen-Air Jet Flames", to be submitted to AIAA Journal of Propulsion and Power, October 1993.
4. Lozano, A., Yip, B., and Hanson, R.K., "Acetone: a Tracer for Concentration Measurements in Gaseous Flows by Planar Laser-Induced Fluorescence", Expts. in Fluids 13, 369-376, 1992.
5. Adamson, T.C., Jr. and Nicholls, J. A., J. of Aeronautical Sciences 26, 16-24, 1959.

6. Schlichting, H., Boundary Layer Theory. McGraw Hill Publishers, New York, 1968.
7. Maczynski, J.F., J. Fluid Mech. 13, 597, 1962.
8. Dahm, W.J.A. and Dibble, R.W., Twenty-Second Symposium (International) on Combustion, The Combustion Institute, Pittsburgh, 1988, pp. 801-808.
9. Papamoschou, D. and Roshko, A., J. Fluid Mech. 197, 453-477, 1988.
10. Ricou, F., and Spalding, B., J. Fluid Mech. 11, 21, 1961.

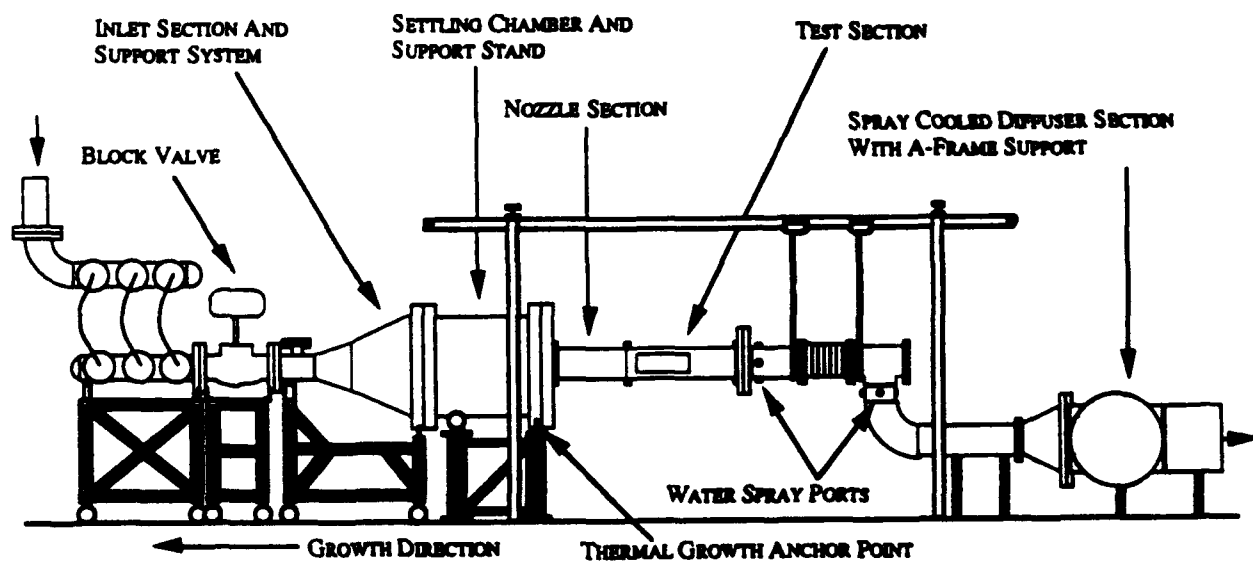


Figure 1 Schematic of Supersonic Combustion Tunnel

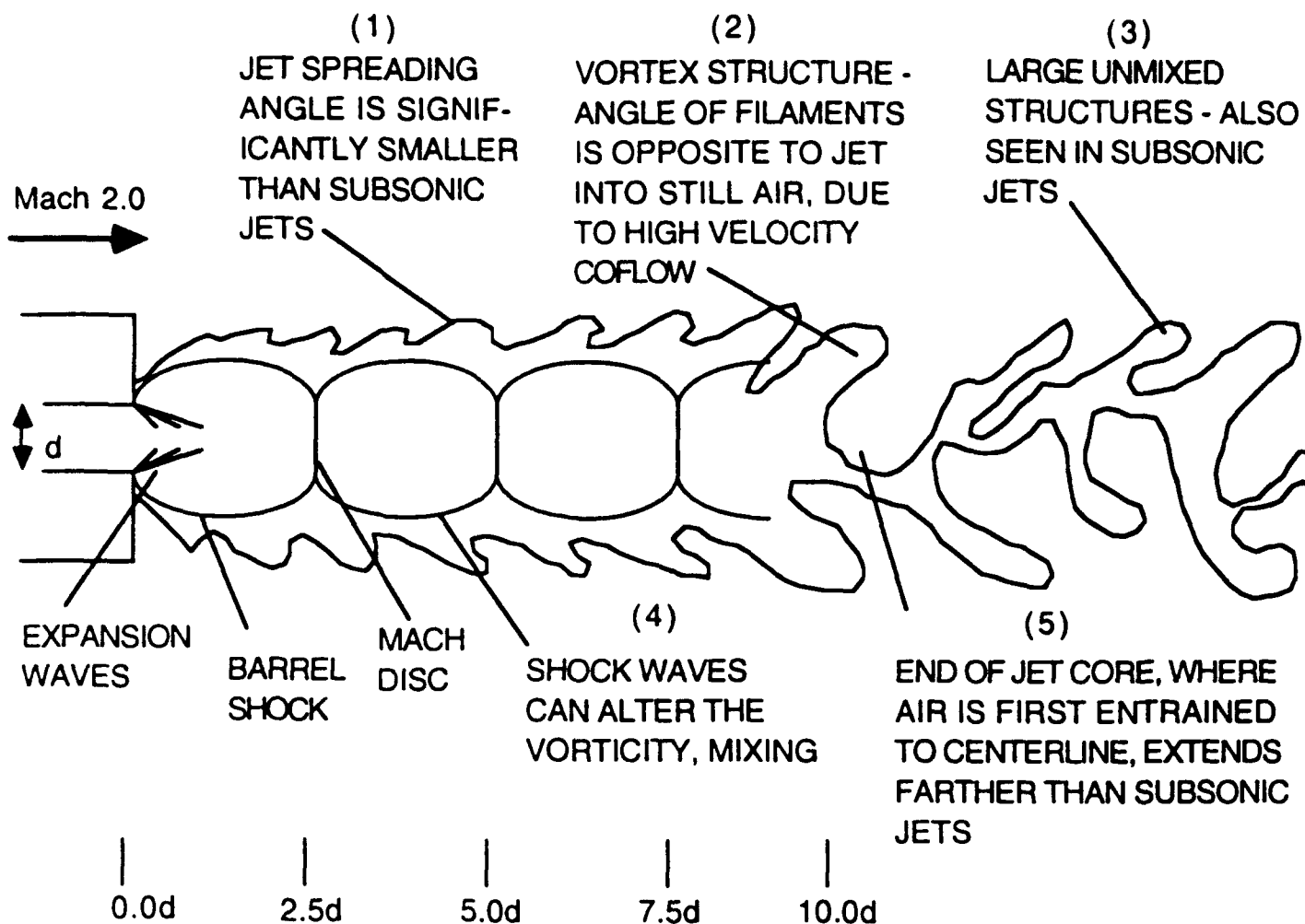


Figure 2. Schematic of the instantaneous jet mixture fraction field that is deduced from the PLIF images in the supersonic mixing study.



Figure 3. Image of the Acetone PLIF Intensity for a Pressure Ratio of Five. Outer flow Mach number is two; jet exit conditions are sonic.

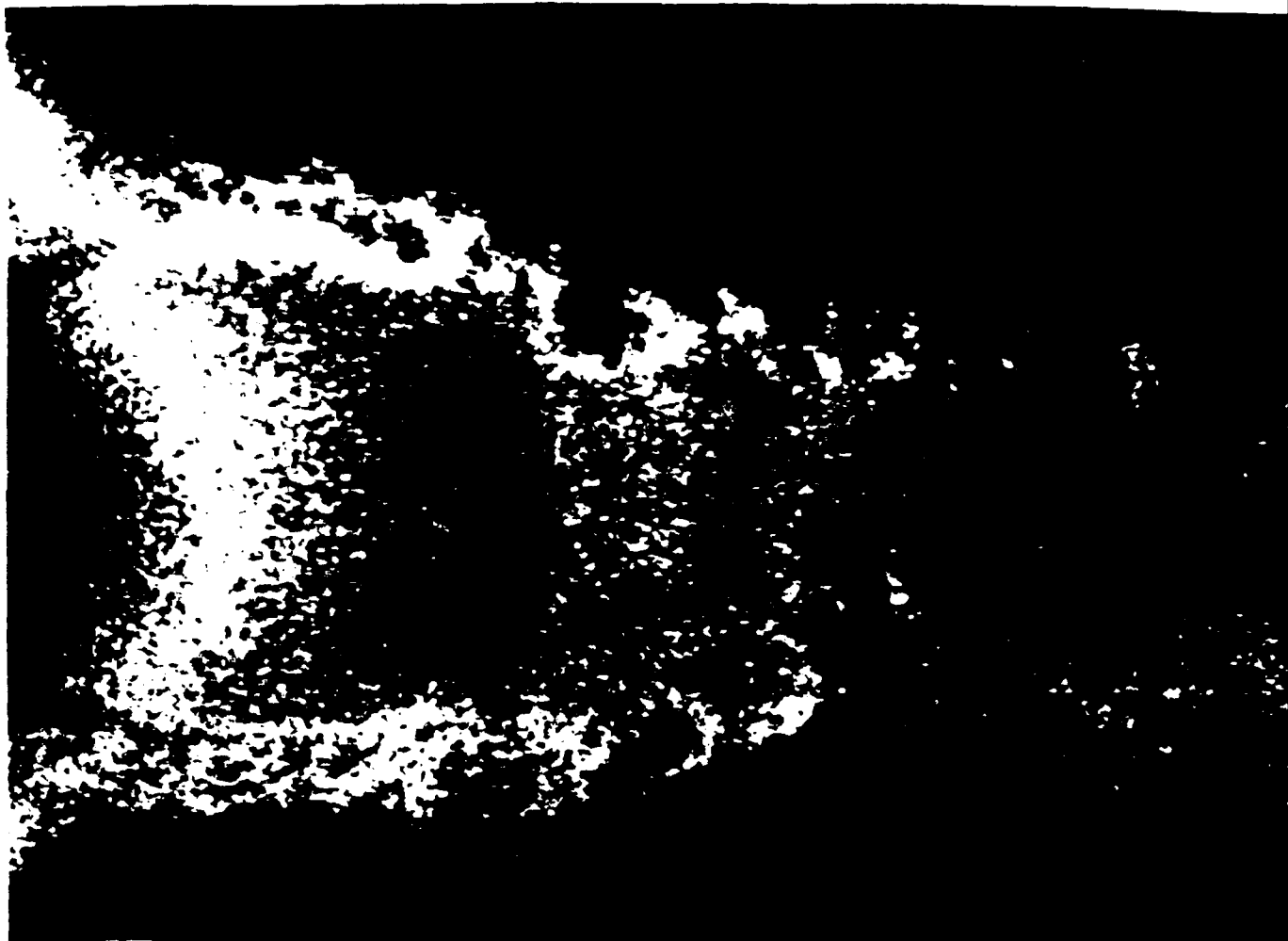


Figure 4. Magnified View of the Acetone PLIF Image for a Pressure Ratio of Five.



Figure 5. Image of the Acetone PLIF Intensity for Pressure Matched Injection. Outer flow Mach number is two.



Figure 6. Image of the Rayleigh/Mie Scattering from Submicron Water Droplets in the Supersonic Air Stream. Note recompression shock.

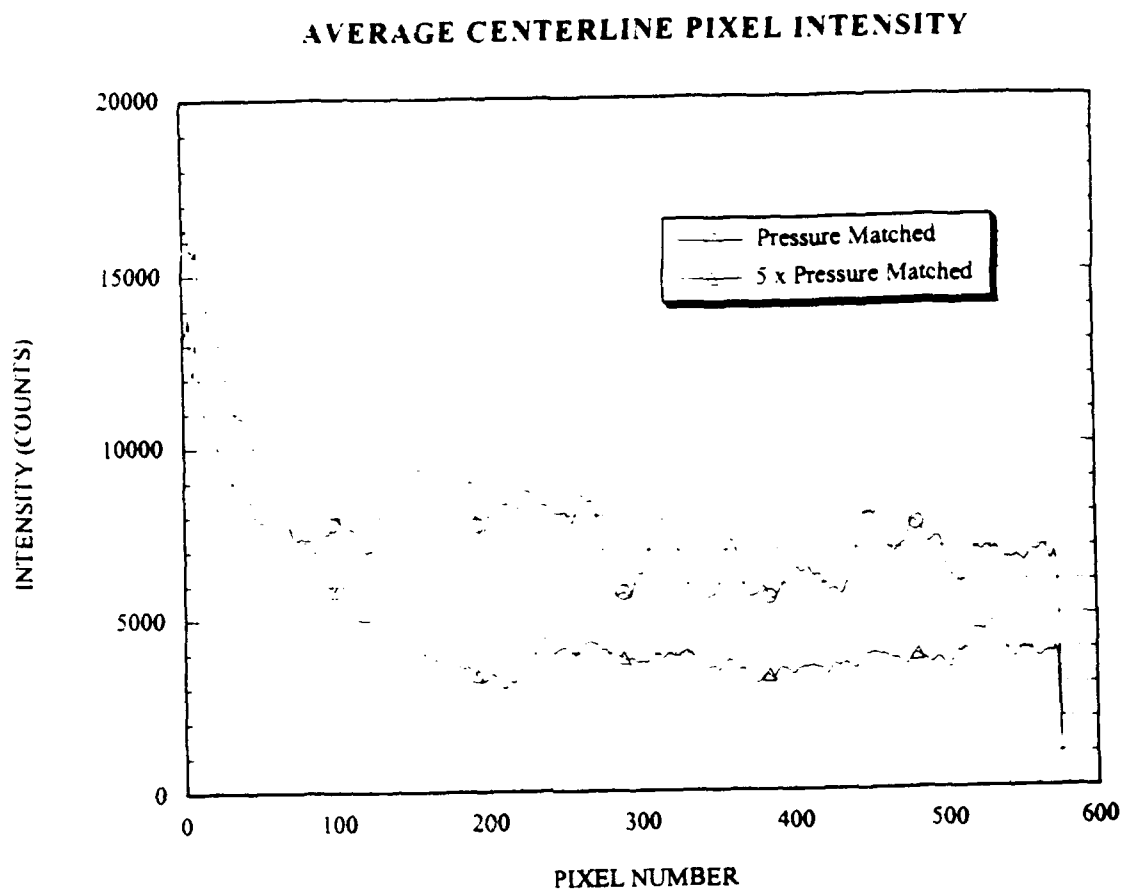


Figure 7. Decay of Acetone PLIF Signal Along Centerline

COMPUTER MODELING OF ELECTROLYTES FOR BATTERY APPLICATIONS

Joel R. Fried
Professor
Department of Chemical Engineering

University of Cincinnati
Cincinnati, OH 45221-0171

Final Report for:
Summer Faculty Research Program
Wright Laboratory-WL/PPOS-2
Battery Electrochemistry Section

Sponsored by:
Air Force Office of Scientific Research
Bolling Air Force Base, Washington, D.C.

September 1993

COMPUTER MODELING OF ELECTROLYTES FOR BATTERY APPLICATIONS

Joel R. Fried
Professor
Department of Chemical Engineering
University of Cincinnati

Abstract

Computational chemistry and computer simulation has been explored as a means of understanding electrolyte conductivity. The principal software package used in these preliminary investigations was HyperChem (Release 3, Autodesk) which provides an extensive package of semi-empirical molecular orbital methods as well as molecular mechanics and dynamics. The investigations were divided into three areas as follows:

The first involved an assessment of the ability of computational spectral analysis to provide an interpretation of the infrared spectra of salt /electrolyte mixtures. Infrared spectra were computed for six low molecular-weight solvents. Comparison of calculated and experimental spectra indicated relative agreement for principal peak assignments; however, calculated peaks were generally 200–300 cm^{-1} higher in wavenumbers. Possible approaches for further study have been suggested.

The second addressed the importance of the conformation of polymer electrolytes, especially poly(ethylene oxide) (PEO), in relation to conductivity and as a foundation for future molecular dynamics simulation of ion-electrolyte interactions. The structure of PEO containing 8 repeating units was optimized and molecular parameters were calculated for the resulting extended-chain (planar zig-zag) conformation. A 7/2 helical conformation as reported in the literature for PEO was imposed by constraining torsional angles. Energies and other parameters were evaluated by single-point AM1 calculations. It was found that the partial electric charge on the oxygen atoms in the PEO repeating unit was slightly less electronegative for the helical conformation; however, the computed dipole moment of the helical conformation was significantly higher than that of the extended chain while overall energy was approximately the same.

The final area focused on evaluating different synthesis routes for macrocyclic electrolytes. Several macrocyclic structures built by joining four furan rings were modeled and their energies and charge distributions calculated for different bridge groups and substituents. The most planar structure was obtained using an unsaturated bridge group; however, partial charge calculations showed that the central oxygen atoms on the furan rings were less electronegative than the oxygen of a single furan molecule due to resonance stabilization of the entire macrocycle.

COMPUTER MODELING OF ELECTROLYTES FOR BATTERY APPLICATIONS

Joel R. Fried

INTRODUCTION

There is significant interest to develop superior electrolyte materials for lithium battery applications with high ionic conductivity over a broad temperature range (e.g., -40 to +70°C) and with good electrode/electrolyte interfacial stability. The objective of this current research effort is to explore the applicability of computational chemistry and simulation methods to identify factors contributing to high conductivity of lithium electrolytes.

DISCUSSION OF PROBLEM

The work is focused in three areas as follows:

- 1. *Ionic conductivity in (low molecular-weight) non-aqueous solvents* — explain why the highest ionic conductivity for LiBF_4 in six non-aqueous solvents (Table I) was obtained in DMAC and DMF for which infrared spectral data indicates that solvation of the lithium cation is through the nitrogen atom compared to NMP, VL, BL, and PC for which solvation is believed to be through the carbonyl oxygen atom. It is hoped that results of these studies can clarify the role of the donor atom (i.e., oxygen or nitrogen) in the solvation process and perhaps explain why certain polymer electrolytes, such as poly(ethylene oxide) (PEO), have high conductivity.
- 2. *Simulation of Li-polymer interaction* — investigate by computer simulation how a lithium ion may be solvated by polymer electrolyte such as PEO.
- 3. *Simulation of macromolecular ion-transport tunnels* — investigate whether it may be feasible to synthesize macrocyclic complexes that can dissociate Li salts and provide a tunnel for cation transport.

METHODOLOGY

Two computer programs have been used for computation and simulation in these preliminary studies. These are ChemDraw Plus 3.1 (Cambridge Scientific Computing, Inc.) and HyperChem Release 3 (Autodesk). ChemDraw Plus (available in Macintosh version) uses molecular mechanics based on Allinger's MM2 force field for geometry optimization and dynamics simulation. HyperChem (Windows 3.1 version) provides both semi-empirical (Extended Hückel, CNDO/2, INDO, MINDO3, MNDO, AM1, PM3, ZINDO/1, and ZINDO/3) and molecular

mechanics programs (modified MM2, BIO, AMBER, and OPLS force fields) for optimization, dynamics, and computation of molecular properties. ChemDraw Plus was run on a PowerBook 180 with 10 MB RAM. Most of the calculations were performed using HyperChem running on a 486DX-33 machine (operating Windows 3.1) with 8 MB RAM.

RESULTS

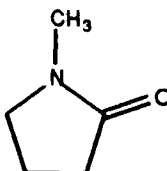
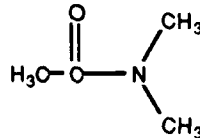
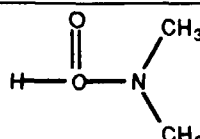
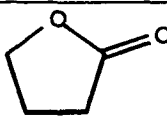
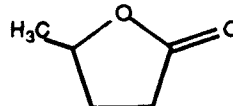
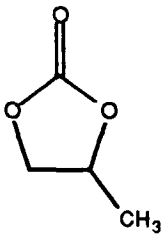
1. Ionic Conductivity in Non-Aqueous Solvents.

The reported ionic conductivity of lithium boron tetrafluoride (LiBF_4) in six solvents — NMP, DMAC, DMF, BL, VL, and PC — identified in Table I is plotted as a function of salt concentration in Figure 1. These results indicate the highest conductivities are obtained when DMAC and DMF were used as the solvent. All six solvents have carbonyl groups available for solvation. Three of the solvents (BL, VL, and PC) have oxygen atoms adjacent to the carbonyl group while three (NMP, DMAC, and DMF) have nitrogen atoms adjacent to the carbonyl group. The structures of DMAC and DMF which give the highest conductivities are similar. In each case, the lone pair of electrons from either the oxygen or nitrogen atoms can participate in a resonance structure with the carbonyl oxygen, thereby, introducing a partial negative charge on the oxygen. The greater the effect of resonance, the lower will be the wavenumber of the carbonyl bands as shown in Table I. This would suggest that the relative strength of Li–O (carbonyl) interaction should be in the order



This is roughly the order of conductivity observed (Figure 1); however, IR data suggests that **solvation of Li^+ occurs through the nitrogen atom rather than the carbonyl oxygen in DMAC and DMF.** For example, a carbonyl band at 1793 cm^{-1} is observed in addition to one at 1670 cm^{-1} for DMF containing 0.5 M LiAsF_6 . The higher wavenumber band may be explained on the basis of Li–N complexation which reduces the resonance contribution. The amine wag motion in DMF is assigned to 659 cm^{-1} . In the presence of LiAsF_6 , an additional peak (doublet) is observed at 673 cm^{-1} ; this peak increases in intensity with increasing salt concentration. Similar behavior is observed for DMAC where the corresponding peak at 590 cm^{-1} is split into two bands — one at 591 cm^{-1} and one at 602 cm^{-1} . The intensity of the higher wavenumber band increases with increasing salt concentration. In the case of NMP which also has a N atom adjacent to the carbonyl group (albeit in a ring structure), IR data indicates that solvation is through the O atom. The evidence is as follows: 1) the carbonyl band is broadened in the direction of lower wavenumbers (as it is for BL, VL, and PC) and 2) the band assigned to the amine wag motion (656 cm^{-1}) is unaffected.

Table I. Structure and Carbonyl Vibration Assignment for Non-Aqueous Solvents

Solvent	Abbrev. Formula MW	Structure	Carbonyl Str. Vibration, cm^{-1} (with electrolyte)
<i>N</i> -methyl-2-pyrrolidinone	NMP $\text{C}_5\text{H}_9\text{NO}$		1690 (1679)
dimethylacetamide	DMAC $\text{C}_4\text{H}_9\text{NO}$		1648
dimethylformamide	DMF $\text{C}_3\text{H}_7\text{NO}$		1679 (1793, 1670)
γ -butyrolactone	BL $\text{C}_4\text{H}_6\text{O}_2$		1774 (1670)
γ -valerolactone	VL $\text{C}_5\text{H}_7\text{O}_2$		1770 (1633)
propylene carbonate	PC $\text{C}_4\text{H}_5\text{O}_3$		1802 (1631)

* Unless otherwise indicated, values taken from R. C. Reid, J. M. Prausnitz, and B. E. Poling, *The Properties of Gases and Liquids*, McGraw-Hill, fourth edition, 1987.

An attempt was made to explore the nature of lithium-donor atom association by use of semi-empirical molecular-orbital programs available through HyperChem. Among available methods, only extended Hückel, CNDO, INDO, MINDO3, MNDO, AM1, and ZINDO/1 are

parameterized for Li, B, and F. Of these AM1 is recommended for spectral analysis. If As is included (i.e., LiAsF_4), only CNDO and INDO are available of which INDO (Intermediate NDO) is preferred. In these initial studies, the geometries of the six solvents were first optimized using molecular mechanics (MM+ force field). Next structures were optimized using AM1 and partial atomic charges recorded. Finally, vibrational spectra were computed using AM1.

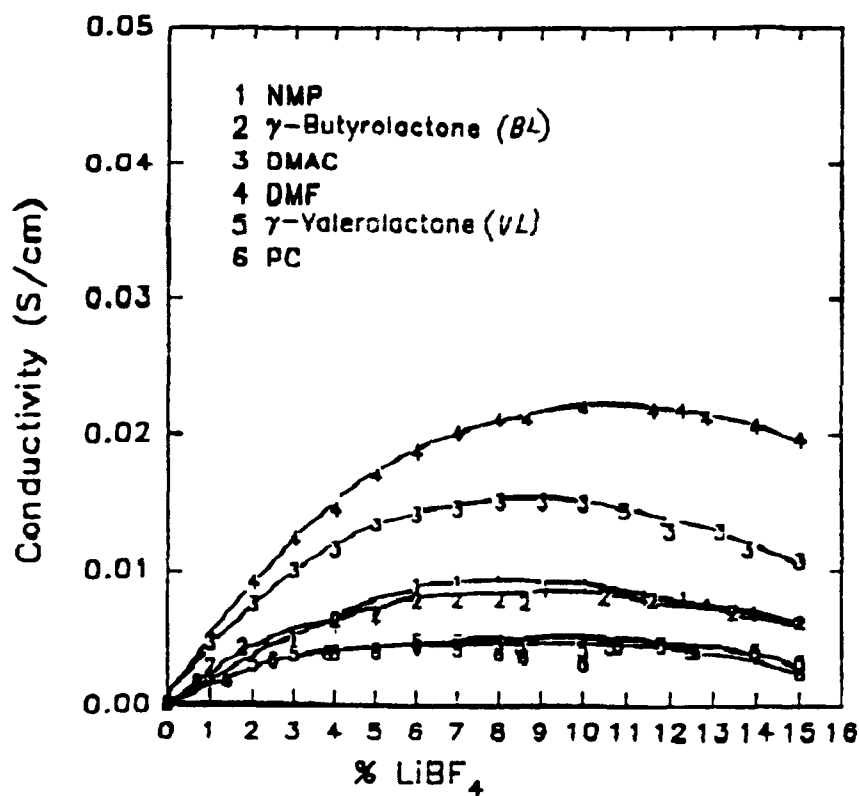


Figure 1. Conductivity of LiBF_4 versus concentration (%) in different solvents.

Results of (AM1) energy minimization, partial charge calculation, and wavenumber prediction for principal vibrations are summarized in Table II. The results of charge calculations indicated that the electrolytes with the most electronegative carbonyl oxygen atoms were those containing nitrogen atoms — NMP, DMAC, and DMF. Nitrogen atoms also were highly electronegative. In the case of VL, BL, and PC, carbonyl and ring oxygen atoms all had about the same negative charge. In the case of VL and PC, the carbon on the substituent CH_3 groups was also negative in charge (only slightly less than calculated for the oxygen atoms). These results indicating several electron-rich sites of comparable charge suggest that steric factors

must also play a significant role in determining how a cation actually interacts with an electrolyte molecule.

Table II. Results of AM1 Computations

Solvent	Optimization Energy Gradient Cycles Convergence	Partial Charges on Carbonyl Oxygen and Other Principal Atoms	Computed (AM1) Frequency (Intensity)
NMP	1536.39 0.014 155 No	carbonyl O: -0.353 N: -0.351	C=O str: 2048.17 (228.248) N: 1637.74 (101.497) 1515.70 (50.725)
DMAC	1365.0304 0.005 35 Yes	carbonyl O: -0.373 N: -0.346	C=O str: 1979.04 (179.04) C-N str: 1620.34 (135.385) N: 1574.70 (39.851)
DMF	1085.81 0.006 35 Yes	carbonyl O: -0.361 N: -0.357	C=O str: 1995.29 (244.639) 1589.17 (94.545) N: 1582.43 (36.549) 1164.07 (15.219)
BL	1206.8293 0.031 148 No	carbonyl O: -0.289 ring O: -0.251	C=O str: 2122.89 (161.483) C-O str: 1487.66 (60.699) 1346.42 (55.6150)
VL	1486.666 0.059 223 No	carbonyl O: -0.293 ring O: -0.251 methyl C: -0.226	C=O str: 2121.05 (166.520) C-O ring str: 1468.05 (80.062) 1338.32 (36.378) C-C str: 1290.61 (29.210)
PC	1307.6648 0.026 194 No	carbonyl O: -0.277 ring O: -0.244 methyl C: -0.229	C=O str: 2162.54 (276.083) ring C-O str: 1536.41 (91.737) ring C-O str: 1272.51 (68.049)

Results of vibrational analysis are also given in Table II. Principal computed vibrations are given and assignment of the molecular motion corresponding to each peak is made wherever possible (HyperChem, Release 3, provides the capability of animating vibrations). Comparison of experimental and calculated wavenumbers assigned to the carbonyl stretching vibration is given in Table III. As the data indicates, the calculated vibrational assignments are 300–400 cm^{-1} higher than the experimental values. These differences are deemed too large to be able to interpret calculated vibrational spectra for electrolyte–cation pairs in a meaningful way. Ab initio methods (e.g., Gaussian 92) should provide better predictions and will be pursued during the Summer Research Extension Program. It should be noted that spectra calculated by

Gaussian can be displayed using HyperChem. An attempt will be made to use molecular dynamics simulation of LiBF_4 -electrolyte interactions in a periodic box using HyperChem (or Quanta/CHARMm) to identify specific Li-electrolyte interactions. Representative complexes will then be isolated and spectra determined by HyperChem (AM1) and also evaluated using Gaussian. The spectra obtained in this way for the complexed spectra will then be compared with that of the pure solvent molecule obtained in the identical fashion

Table III. Comparison of Experimental and Calculated (AM1)
Carbonyl Vibration Assignments in Wavenumbers (cm^{-1})

Electrolyte	Experimental	Calculated
NMP	1690	2048
DMAC	1648	1979
DMF	1679	1995
BL	1774	2123
VL	1770	2121
PC	1802	2163

2. Simulation of Li-Polymer Interaction.

PEO is well-known to assume a $7/2$ helical conformation. In order to explore the basis of the conformational behavior of PEO, an oligomer containing 8 repeating units $\text{HO}(\text{CH}_2\text{O})_8\text{-H}$ was constructed using Hyperchem. The structure was optimized using molecular mechanics (AMBER force field) and with the use of AM1. The result was an extended zig-zag chain with oxygen atoms alternating along the chain as shown in Figure 2. Bond lengths and angles are given in Table IV. The total energy calculated by AM1 (134 orbitals) was $-1.2459 \times 10^5 \text{ kcal mol}^{-1}$ ($\text{Grad}=1.041 \text{ kcal mol}^{-1} \text{ \AA}^{-1}$). Partial charges were -0.29 for oxygen, -0.021 for carbons, and $+0.082$ for H (these were essentially unchanged when optimization was continued to 32 computational cycles for which $\text{Grad} = 0.073$).

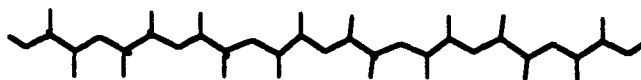


Figure 2. Extended chain structure of PEO8 obtained by AM1 geometry optimization.

The extended chain conformation obtained by geometry optimization differs from the 7/2 helix suggested from X-ray crystallographic data appearing in the literature. In order to compare the energies of the extended chain and helical chain conformations, a helix was imposed on the PEO structure by constraining the torsional angles as follows: C-C-O-C, *trans* (180°); C-O-C-C, *trans* (180°); and O-C-C-O, *gauche* (-180°). A representation of the resulting helical conformation is given in Figure 3. The total energy calculated by AM1 (134 orbitals) was -1.2456×10^5 kcal mol⁻¹ (Grad=15.824 kcal mol⁻¹ Å⁻¹) which is very close to that of the extended chain. Partial atomic charges were approximately -0.25 for oxygens (-0.33 for the terminal hydroxyl oxygens), -0.02 for carbon atoms, and +0.07 for hydrogen. The charge on oxygen in the helical conformation is slightly less negative and that on the hydrogen atoms slightly less positive than calculated for the extended chain structure (the charge on the carbon atoms were essentially unchanged). Interestingly, the dipole moment calculated for helical PEO was significantly larger (2.809 D) for the helical conformation than for the extended chain (1.719 D).

Table IV. Structural Parameters Obtained for PEO Oligomer from
AM1 Optimization of Geometry

C-O bond length	1.426 Å
C-C bond length	1.526 Å
C-H bond length	1.121 Å
C-O-C bond angle	111.9°
C-C-O bond angle	105.5°
C-C-O-C torsional angle	180
C-O-C-C torsional angle	180°
O-C-C-O torsional angle	180°

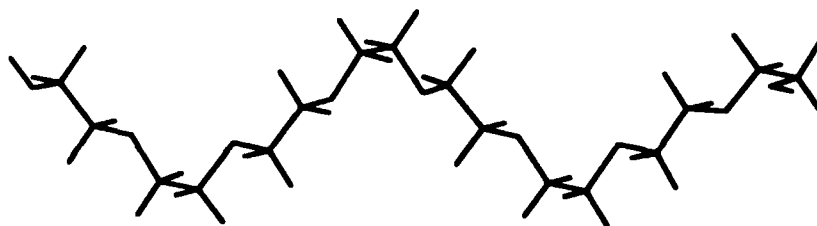


Figure 3. Helical conformation of PEO8 obtained by constraining torsional angles.

3. Simulation of Macromolecular Ion-Transport Tunnels.

An objective for the Electrochemistry Laboratory at Wright-Patterson AFB is the development of new electrolytes capable of high conductivity at low temperatures. One approach being evaluated is the development of a lithium ion-conducting polymer-electrolyte based on ionically conducting polymer tubes formed by stacking macrocyclic rings. The hope is that a suitable geometry can be defined such that the lithium ion experiences a constant solvation-coordination sphere throughout the molecular tube. In this manner, ionic conduction would occur by means of ion "hopping" that could result in substantially higher conductivity compared to ion conduction resulting from molecular motion.

Literature studies have shown that macrocyclic polyamines can form mesophases containing stacks of macrocycles forming tubes. Based upon current understanding of the importance of oxygen as an effective donor atom for the lithium cation (e.g., THF, PEO, etc.), an attempt was made to evaluate the potential for synthesizing macrocyclic structures derived from furan and acetone.

The structure of furan shown in Figure 4 with partial charges labelled, was optimized by AM1 using HyperChem. It should be noted that the oxygen has a mildly negative charge (-0.107) compared to carbons at the base of the ring (4 and 5 positions).

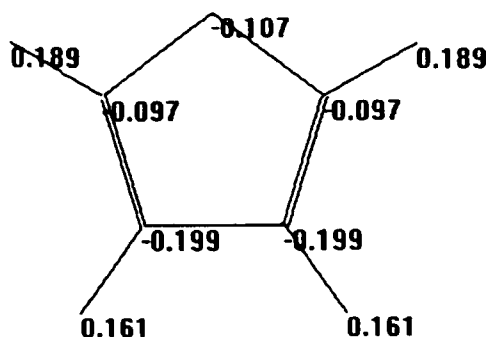


Figure 4. AM1-optimized structure of furan.

In order to construct macrocyclic structure, four furan rings first were drawn and connected by methylene bridges as shown below. The macrocyclic structure was then optimized using the molecular mechanics MM+ force field available in HyperChem. Next the structure was optimized using AM1 (calculation on 112 orbitals). After 57 cycles (ca. 5 h), the optimization was stopped before convergence ($E = -4473 \text{ kcal mol}^{-1}$; $\text{Grad} = 0.970$). The resulting structure is shown in Figure 5. The partial charge on the furan oxygens were found to be even less negative (i.e., -0.079 to -0.086) than for furan alone while the charge on the 4 and 5 carbons were in the range from -0.18 to -0.19 .

Next, the hydrogens on the methylene bridges were changed to methyl groups and the structure optimized initially using MM+ (some bend parameters substituted). The structure was then optimized using AM1 (160 orbitals). After 31 cycles (ca. 9 h), the optimization was stopped

($E = -6686.36 \text{ kcal mol}^{-1}$ and $\text{Grad} = 1.470$) and then single-point calculations were made. The structure shown in Figure 6 indicates that two opposite furan rings are pointed upward and two are pointed downward. Partial charges calculated for the furan oxygens are comparable (ca. -0.08) to the previous case; however, the partial charges of the methylene groups are reasonably electronegative (i.e., -0.2).

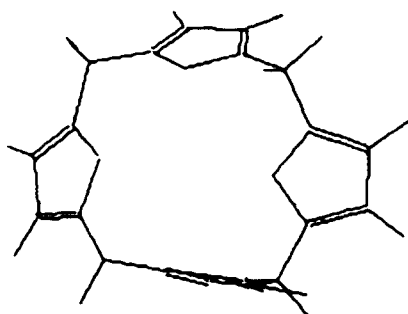


Figure 5. Macrocycle with methylene bridges (MACRO1).

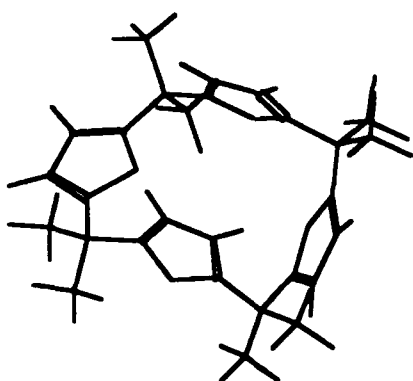


Figure 6. Macrocycle with dimethyl bridges (MACRO2).

Next, additional resonance structure is introduced through the incorporation of carbon double bonds on the bridge groups. This gave a macrocycle where the rings fell within a single plane upon initial structure building. The structure was then optimized using AM1 (128 orbitals). After 37 cycles (ca. 4 h), the optimization was terminated ($E = -5034$ and $\text{Grad} = 2.630$) and single-point calculations were made. The structure was nearly totally planar with all oxygen atoms pointing inward as shown in the Figure 7. Three-dimensional models indicate that two opposite furan rings are pointing slightly downward and two are pointing slightly upward. Values calculated for partial charges, as shown in Figure 8, indicate a more extensive resonance of the ring structure giving only very low negative charge (ca. -0.04) to the furan oxygens. Distances between opposite furan oxygens were $4.2\text{--}4.3 \text{ \AA}$.

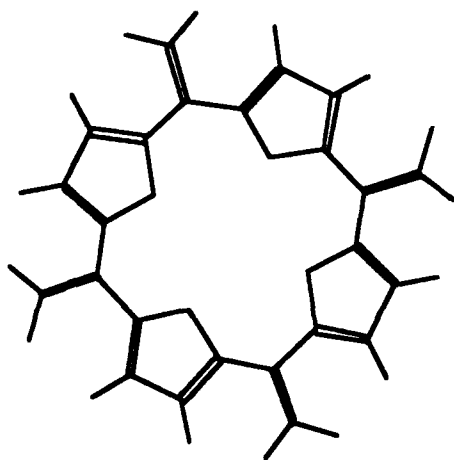


Figure 7. AM1 optimized macrocycle with unsaturated bridges.

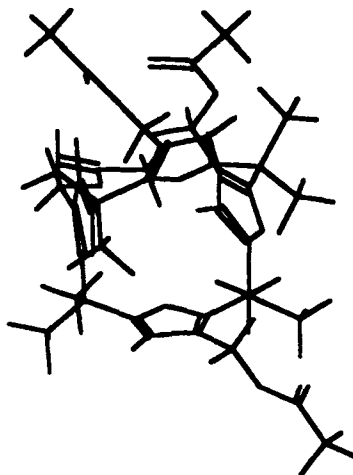
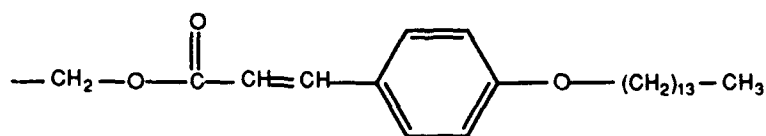


Figure 9. Macrocycle with partial reactive group substitution.

Finally, the full substituent group



was introduced and the structure optimized using MM+ (default parameters used for bends). After 1361 cycles (ca. 14 h), the optimization was terminated ($E = 102.12$; Grad = 0.0359). The final structure obtained is shown in Figure 10.

It is possible that several macrocycles of the structure given in Figure 10 could be placed in a periodic box and their interaction simulated by molecular dynamics to determine how the macrocycles interact and if a mesophase could be formed at some temperature. In addition, Li salts could be placed in the box to simulate the dissociation process and to evaluate how cations may interact with the mesophase. The computational requirements for such simulations of relatively large molecules dictates that such work be done in a high-end environment such as provided by Quanta/CHARMm operating off an IBM RS 6000 workstation available in our

laboratory. To proceed further on this relatively large project, it is necessary that the most promising macrocycle structure first be selected. Based upon the information just presented on structure and charge distribution, it was felt that first some model compounds should be synthesized and their conductivities measured to help interpret the computational results and guide a choice for the most promising macrocyclic structure.

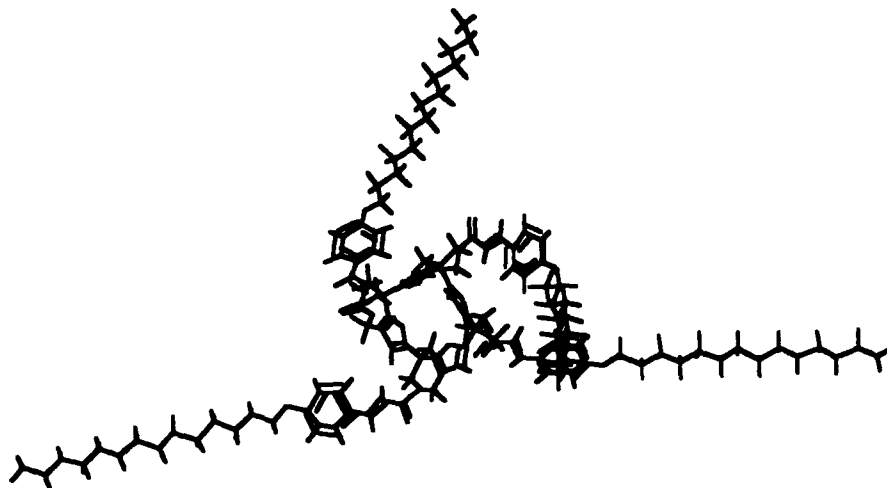


Figure 10. Structure of complete macrocycle with full reactive-group substitution.

CONCLUSIONS

Several major research groups are just beginning to use computational methods, particularly dynamic mechanical simulations, to investigate salt–electrolyte interactions. There is great potential for such approaches to quicken the development of new electrolyte materials with improved conductivities and stability for battery applications. The current effort is a first step towards these goals. For example, studies during the summer have indicated that it should be possible to identify the nature of the interaction of salts with low molecular-weight electrolytes by comparing experimental infrared data with results from simulation studies coupled with ab initio calculations of vibrational spectra. This approach will be proposed for the AFOSR Summer Research Extension Program and will serve as a starting point for the next step — a realistic

simulation of salt-*polymer* interactions. Initial studies of PEO8 indicate the importance of using the proper polymer conformational state in such work. Finally, the summer effort has shown that computer modeling can be a useful aid in evaluating different approaches for synthesizing new macrocycles for possible electrolyte applications.

ACKNOWLEDGMENT

This Research Associate wishes to express his gratitude to Dr. Lawrence G. Scalon, Jr., and Dr. Woitek Kravitz for their very helpful advice and guidance during the summer and for providing this opportunity to learn a new area of research and develop my computational skills outside the demanding distractions of everyday academic life.

COMPARISON OF HYDRAULIC AND THERMAL PERFORMANCE
OF PAO AND COOLANOL 25R LIQUID COOLANTS

Afshin J. Ghajar
Professor
School of Mechanical and Aerospace Engineering

Oklahoma State University
Stillwater, OK 74078

Final Report for:
Summer Faculty Research Program
Wright Laboratory

Sponsored by:
Air Force Office of Scientific Research
Bolling Air Force Base, Washington, D.C.

August 1993

COMPARISON OF HYDRAULIC AND THERMAL PERFORMANCE
OF PAO AND COOLANOL 25R LIQUID COOLANTS

Afshin J. Ghajar
Professor
School of Mechanical and Aerospace Engineering
Oklahoma State University

Abstract

A general method for the comparison of hydraulic and thermal performance of different liquid coolants is offered. Thermophysical property expressions for the variation of density, specific heat, thermal conductivity, and kinematic viscosity with temperature for PAO and Coolanol 25R were developed. The range of temperature for this study was from -54 to 135°C. Based on the results, the hydraulic performance of Coolanol 25R is much better than PAO at low temperatures (below 0°C) and laminar flow regime. In the turbulent region, PAO hydraulically outperforms Coolanol 25R over the entire temperature range. The thermal performance of PAO at temperatures below 61°C and in the laminar flow region, is slightly better than Coolanol 25R. In the low temperature turbulent region, Coolanol 25R thermally outperforms PAO. At other temperatures, the performance of the two liquid coolants are reasonably close and fairly independent of the flow regime.

COMPARISON OF HYDRAULIC AND THERMAL PERFORMANCE
OF PAO AND COOLANOL 25R LIQUID COOLANTS

Afshin J. Ghajar

Introduction

Silicate-ester-based fluids (e.g. Coolanol 25R) are widely used as dielectric heat transfer fluids in the Air Force and the Navy airborne radar and missile systems. These fluids have caused significant and sometimes catastrophic problems due to their hygroscopic nature and subsequent formation of flammable alcohols and silica gel. The alcohol by-product lowers the fluid flashpoint, increasing the risk of aircraft fires. The gelatinous precipitate called the "black plague", deposits on transmitter surfaces and components, causing avionics equipment to malfunction.

In order to solve the problems associated with silicate-ester-based fluids, the Naval Air Development Center and the Air Force Materials Directorate investigated the possibility of direct replacement of silicate-ester-based fluids with hydrogenated polyalphaolefin-based fluids. Their studies concluded that polyalphaolefin (PAO) fluids are chemically more stable (they do not hydrolyze to form either silica gel or alcohol by-products), less costly, offer equal or improved dielectric characteristics, and meet or exceed military requirements for a dielectric coolant [1-4].

Due to the inherent desirable properties of PAO, their ready availability, and their relatively low cost (about one-fifth of the cost of current silicate-ester-based fluids), the Air Force and the Navy have both replaced the current heat transfer fluid in the avionics system with PAO for some selected aircrafts. Other aircrafts may soon follow. Although, replacement of silicate-ester-based fluids with PAO fluid reduces the risk of aircraft fire and eliminates the coolant fluid contamination problem which results in "black plague", the overall performance of the avionics liquid cooling system with PAO in comparison to silicate ester fluids over a wide temperature range has not been fully studied. Limited unpublished studies have been conducted on the performance of specific aircraft radar transmitters with PAO [2,3].

The objective of this study was to compare the hydraulic and thermal performance of PAO and silicate ester fluids in a temperature range (-54 to

135°C) applicable to avionics equipment. Both laminar and turbulent flow regimes were considered. In order for the analysis to be general, variation of dimensionless system parameters with temperature are presented. In addition, as part of this study, equations were developed for the variation of thermophysical properties of Coolanol 25R and PAO with temperature.

THERMOPHYSICAL PROPERTIES EQUATIONS

Knowledge of thermophysical properties of the Coolanol 25R and PAO fluids as a function of fluid temperature was required for hydraulic and thermal performance analysis. Thermophysical property data for Coolanol 25R and PAO (Brayco Micronic 889) were obtained from technical data sheets provided by Chevron [5] and Castrol [6], respectively. The density (ρ), specific heat (c_p), and thermal conductivity (k) data were easily curve-fitted in the form of a polynomial in temperature using a least squares curve-fitting program. The degree of the fitted polynomial, in some cases, varied between the two fluids for the same thermophysical property. In order to avoid listing several different equations, the general form of the curve-fitted equation with the highest obtained degree of polynomial is presented in the form

$$[\text{PROPERTY}] = A + BT + CT^2 + DT^3 + ET^4 + FT^5 \quad (1)$$

In Eq. (1), the term "PROPERTY" can be either density in kg/m^3 , specific heat in kJ/kg-K or thermal conductivity in W/m-K , and the temperature (T) is in K. The curve-fitted constants A to F to be used in Eq. (1) for Coolanol 25R (C25R) and PAO are tabulated in Table 1. The curve-fitted equations for ρ , c_p , and k predict the PAO and Coolanol 25R data with a maximum deviation of less than $\pm 0.5\%$.

For variation of kinematic viscosity with temperature, the viscosity-temperature relationship suggested for petroleum oils or liquid hydrocarbons [7] was curve-fitted to the Coolanol 25R and PAO data. The equation is of the form

$$\nu = 10 (10^{A/T^B}) - C \quad (2)$$

In Eq. (2), the kinematic viscosity (ν) is in m^2/s and the temperature (T) is in K. The curve-fitted constants A, B, and C to be used in Eq. (2) for Coolanol 25R (C25R) and PAO are also tabulated in Table 1. The curve-fitted equation for ν predicts the thirteen Coolanol 25R data points with a maximum deviation of $+5.5\%$ and an average absolute deviation of 1.9% . For the

thirteen PAO data points the maximum deviation was +3.4% with an average absolute deviation of 1.3%.

Table 1. Curve-Fitted Constants for Density, Specific Heat, Thermal Conductivity, and Kinematic Viscosity Equations.

PROPERTY	FLUID	A	B	C	D	E	F
ρ	C25R	1.13×10^3	-0.784				
	PAO	1.36×10^3	-4.56	0.0157	-0.280×10^{-4}	0.174×10^{-7}	
c_p	C25R	0.492	4.49×10^{-3}				
	PAO	1.022	3.77×10^{-3}				
k	C25R	0.453	-4.64×10^{-3}	0.275×10^{-4}	-0.809×10^{-7}	0.117×10^{-9}	-0.667×10^{-13}
	PAO	0.154	-5.88×10^{-5}				
ν	C25R	8.36	3.408	0.802			
	PAO	9.67	3.923	0.700			

The variation of ρ , c_p , k , and ν with temperature for Coolanol 25R (C25R) and PAO over the temperature range from -54 to 135°C are compared in Figures 1 to 4, respectively. Another thermophysical property that plays an important role in the hydraulic and thermal performance of coolants is absolute viscosity (μ). The variation of μ with temperature for the two fluids is shown in Figure 5. The values of μ were determined from the product of density and kinematic viscosity values.

The expressions and the constants for the thermophysical properties presented in this section were also programmed. The interactive computer program produces thermophysical properties for Coolanol 25R or PAO at any temperature in the range from -54 to 135°C, in either SI or English units. Single or multi-point calculations can be performed. The tabulated results can be viewed on the screen and/or stored into a specified data file.

HEAT TRANSFER PARAMETER

From a heat transfer viewpoint, coolants are rated by first considering the applicable heat transfer correlating equation. Considering a problem of heat transfer in forced convection to a fluid in a duct or channel, the following general form of heat transfer correlation is applicable

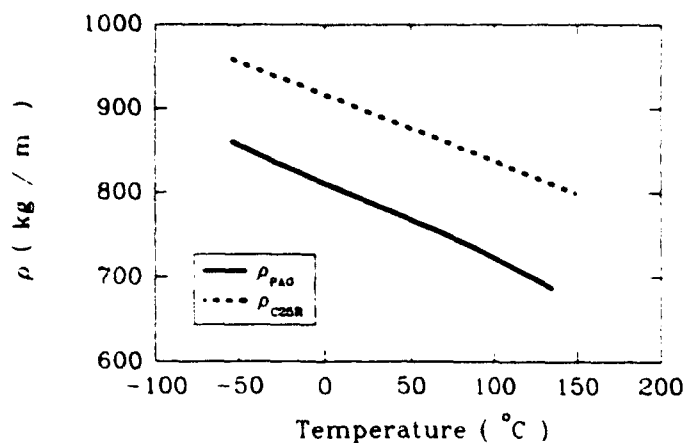


Fig. 1 Variation of density with temperature for PAO and Coolanol 25R.

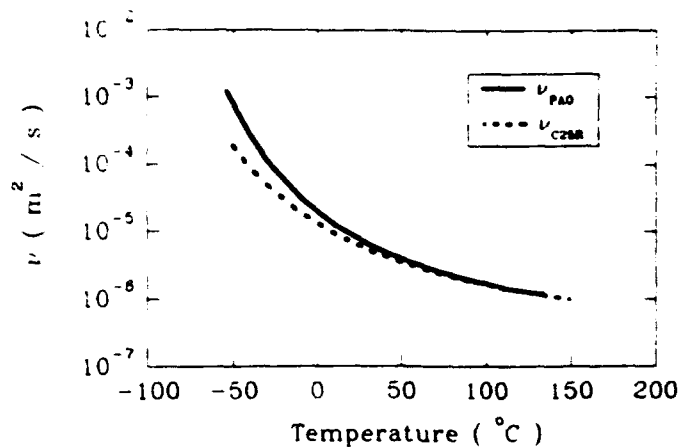


Fig. 4 Variation of kinematic viscosity with temperature for PAO and Coolanol 25R.

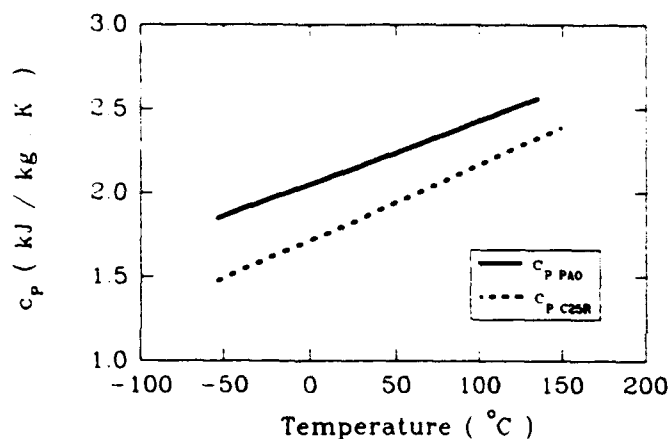


Fig. 2 Variation of specific heat with temperature for PAO and Coolanol 25R.

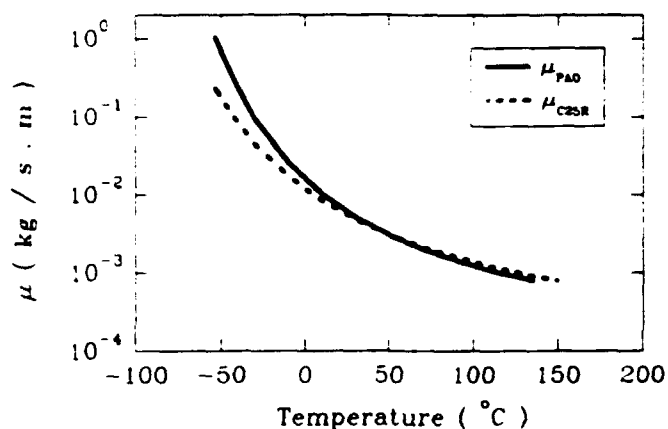


Fig. 5 Variation of absolute viscosity with temperature for PAO and Coolanol 25R.

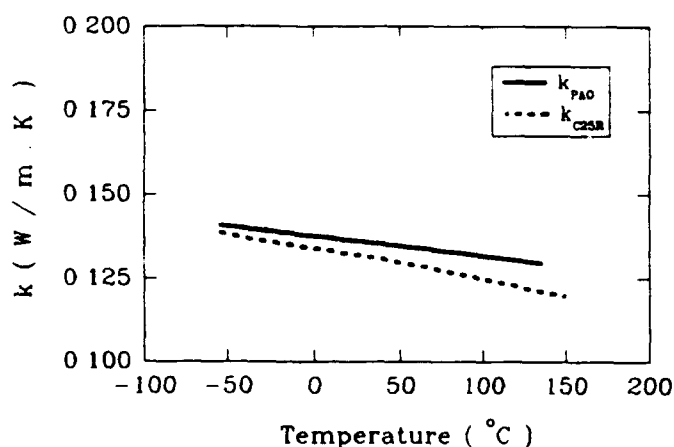


Fig. 3 Variation of thermal conductivity with temperature for PAO and Coolanol 25R.

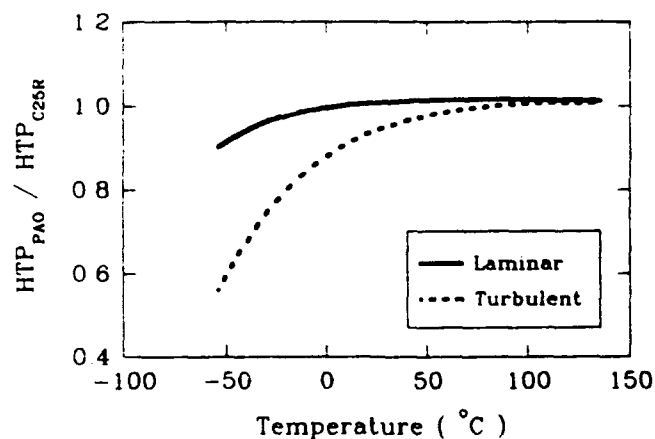


Fig. 6 Variation of PAO-to-C25R heat transfer parameter ratio with temperature (laminar and turbulent flows).

$$Nu = C Re^m Pr^n \quad (3)$$

where m is near 0.5 for laminar flow and 0.8 for turbulent flow and n is approximately 0.4 for heating in both flow regimes. The exact values of C , m , and n are flow regime and configuration dependent and should be obtained experimentally.

Substitute the definitions for Nusselt number ($Nu = hD/k$), Reynolds number ($Re = \rho V D / \mu$) and Prandtl number ($Pr = \mu c_p / k$) in Eq. (3) and solve for the heat transfer coefficient h

$$h = C \frac{k}{D} \left(\frac{\rho V D}{\mu} \right)^m \left(\frac{\mu c_p}{k} \right)^n \quad (4)$$

Apply Eq. (4) to the two fluids under consideration, PAO and Coolanol 25R, assuming that the two fluids are running through two passages of identical equivalent diameters and at identical velocities. Divide and rearrange the resulting equations to obtain

$$\frac{h_{PAO}}{h_{C25R}} = \frac{(\rho^m k^{1-n} c_p^n / \mu^{m-n})_{PAO}}{(\rho^m k^{1-n} c_p^n / \mu^{m-n})_{C25R}} \quad (5)$$

Equation (5) indicates that heat transfer coefficient can be represented in terms of a dimensional grouping of fluid heat transfer properties ρ , c_p , k , and μ . The properties contained in the grouping are definite functions of temperature.

Generalize the results of Eq. (5) by setting $a = m$, $b = 1-n$, $c = n$, and $d = m-n$ and introducing the term heat transfer parameter (HTP) defined as

$$HTP = \rho^a k^b c_p^c / \mu^d \quad (6)$$

which can be used as a rating criteria for heat transfer fluids. The heat transfer parameter is not dimensionless; therefore, its numerical value depends on the units used. The same units must be used in computing values for each coolant which is to be compared.

Equation (6) indicates that there is a way of comparing heat transfer properties of fluids on the basis of temperature (from values of ρ , c_p , k , and μ) and on the basis of configuration and flow regime (the values of exponents a , b , c , and d).

For typical values of m and n for laminar forced convection ($m = 0.5$, $n = 0.4$) and turbulent forced convection ($m = 0.8$, $n = 0.4$) in internal flows, the specific form of heat transfer parameter for each flow regime becomes

$$HTPL = \rho^{0.5} k^{0.6} c_p^{0.4} / \mu^{0.1} \quad (7)$$

$$HTPT = \rho^{0.8} k^{0.6} c_p^{0.4} / \mu^{0.4} \quad (8)$$

where HTPL and HTPT designate the laminar and turbulent heat transfer parameters, respectively.

Apply Eq. (7) or (8) to Eq. (5) to obtain an expression for the ratio of PAO-to-Coolanol 25R heat transfer coefficients in terms of the heat transfer parameter. Figure 6 shows the variation of PAO-to-C25R heat transfer parameter ratio with temperature for laminar and turbulent flow regimes. The figure indicates that there could be a substantial difference between the heat transfer properties of the two fluids. This difference strongly depends on the coolant flow regime and the coolant operating temperature. In laminar flow regime (see the solid line in Fig. 6), at the lowest coolant temperature (-54°C), the heat transfer parameter for PAO is about 11% lower than that of Coolanol 25R, and this difference quickly diminishes to about 2% at -14°C. At temperatures above -14°C, there is virtually no difference in the heat transfer properties of the two fluids. However, in turbulent flow, the differences are much larger and are sustained over a larger temperature range. Referring to the dashed line in Figure 6, at -54°C the heat transfer parameter for PAO is about 78% lower than that of Coolanol 25R. This difference slowly reduces to about 21% at -14°C and to about 2% at 56°C. Beyond this temperature, the two fluids behave the same way.

Overall, from a heat transfer view point, Coolanol 25R outperforms PAO in the low temperature region in both flow regimes. The difference is much more substantial for turbulent flow in the temperature range from -54°C to about 6°C. Therefore, at these low temperatures, in order for the heat transfer characteristics of the systems operating with PAO to be fairly comparable with the Coolanol 25R systems, operation in the laminar flow regime is recommended. The type of analysis presented here indicates how it can definitely be established which fluid has the better heat transfer properties.

HYDRAULIC PERFORMANCE

Comparison of hydraulic performance of PAO and Coolanol 25R is based on the relationship between pressure drop and flow rate. The Moody diagram [8] establishes the proper normalized dimensionless pressure drop parameter [$f = \Delta P / (L/D)(1/2\rho V^2)$] and flow parameter ($Re = \rho V D / \mu$) for a round pipe with a fixed relative roughness in the form

$$f = \phi_1 (Re) \quad (9)$$

where ϕ_1 is a function to be determined experimentally or analytically. Therefore, when the data is plotted as f versus Re , usually a log-log plot,

the data points fall on a single curve, for a constant value of a relative roughness.

The major difficulty in application of Eq. (9) to an avionics system is associated with the proper evaluation of diameter (D) and fluid velocity (V) in the definitions of f and Re. The coolant flow loop for an avionics system (e.g. radar transmitter) is very different than a long, straight, round pipe. In the coolant flow loop there are numerous bends, sudden expansions and contractions, change of flow areas, non-circular flow passages, and other local obstructions, the combined effect of which results in the overall pressure drop of the system. Therefore, the diameter (D), appearing in the definitions of f and Re must represent these effects. However, for a given system each of these local effective diameters is a constant, and consequently their combined influence can be included as a constant in the function ϕ_1 of Eq. (9). The fluid velocity (V), appearing in the definitions of f and Re must also be representative of the various local velocities within the system, due to the existence of numerous different flow areas, and hence different velocities in the system. However, the velocity at any given point in the system differs from the volume flow rate (\dot{Q}) only by the local flow area which is considered constant. Therefore, V can be replaced by \dot{Q} , and the local invariant flow areas can be included as constants in the function ϕ_1 of Eq. (9).

Based on the above discussion, the definitions of f and Re and Eq. (9) can be rearranged in the form

$$P = \phi_2 (F) \quad (10)$$

where $P = \Delta P / \rho \dot{Q}^2$ and $F = \dot{Q} / v$ are the new normalized dimensional pressure drop and flow parameters, respectively. It should be realized that these parameters are not dimensionless and Eq. (10) is a dimensional equation, and that the function ϕ_2 (which must be determined experimentally) is different for each system. This is in sharp contrast to the function ϕ_1 in Eq. (9) for a circular pipe flow, where the same function applies to all round pipes with a fixed relative roughness.

A simple form of the function ϕ_2 in Eq. (10) can be determined for low and high values of Reynolds number by inspection of Moody diagram [8]. For low Re values (laminar flow), the f versus Re is a straight line with slope of -1. For high Re values (complete turbulence), f versus Re for a given relative roughness is a straight line with a slope of zero.

The new dimensional parameters P and F differ from the Moody dimensionless parameters f and Re , by only an unknown constant at each location in the system. Therefore, the following equation should represent the functional form (ϕ_2) that exists between P and F for low and high Reynolds numbers

$$P = A + \frac{B}{F} \quad (11)$$

where A and B are experimentally determined constants for a given system.

A plot of Eq. (11) for a hypothetical situation is shown as Figure 7. This figure is a log-log plot of pressure drop parameter (P) and flow parameter (F). The plot exhibits a slope of -1 at low values of F ($P \approx B/F$) and approaches a slope of zero at high values of F ($P \approx A$). These terminal slopes are indicative of fully laminar flow at low values of F and fully turbulent flow at high values of F and are comparable with the Moody diagram. It should be realized that the constants A and B in Eq. (11) are unique for a given system but are independent of the type of fluid used in the system. This allows for generalization of the hydraulic performance of the system for the two limiting cases of Eq. (11). These limiting cases are referred to as the fully laminar and fully turbulent and will be discussed next.

Fully Laminar Case: for this case, Eq. (11) can be approximated by $P = B/F$. Using the definitions of P and F and solving for ΔP results in

$$\Delta P = B\mu\dot{Q} \quad (12)$$

Eq. (12) implies that the pressure drop and volume flow rate depend strongly on the absolute viscosity of the heat transfer fluid. Apply Eq. (12) to the two fluids under consideration, PAO and Coolanol 25R, assuming the two fluids are running through two identical systems at identical coolant flow rates. Divide the resulting equations to obtain

$$\frac{\Delta P_{PAO}}{\Delta P_{C25R}} = \frac{\mu_{PAO}}{\mu_{C25R}} \quad (13)$$

An equation similar to Eq. (13) can be developed for the volume flow rate ratio of the two fluids, assuming identical systems at identical pressure drops. The resulting equation is

$$\frac{\dot{Q}_{PAO}}{\dot{Q}_{C25R}} = \frac{\mu_{C25R}}{\mu_{PAO}} \quad (14)$$

The variations of PAO-to-C25R pressure drop and volume flow rate ratios with coolant temperature are shown in Figure 8, by the solid and broken lines, respectively. The figure indicates that the ratios vary dramatically in the

temperature range from -54 to 26°C. At these low temperatures the pressure drop ratio varies from about 1 at 26°C to about 4.4 at -54°C. This four fold increase in the pressure drop is due to the much higher absolute viscosity of PAO at these low temperatures (see Fig. 5). At temperatures warmer than 26°C, the pressure drop variation with temperature is relatively small and approaches unity at 46°C. At temperatures greater than 46°C, the pressure drop ratio drops below unity, indicating that the system with Coolanol 25R as the working fluid, experiences higher pressure drop than the system with PAO at identical operating conditions. The pressure drop difference increases with temperature, and at the highest temperature of 135°C, reaches a value of about 16%.

The variation of volume flow rate ratio with coolant temperature shown by the broken line in Figure 8, demonstrates a trend similar but opposite to the pressure drop ratio. At low temperatures, the volume flow rate of PAO is much smaller than that of Coolanol 25R for the same identical operating conditions and pressure drop. This difference decreases with increasing temperature and the ratio approaches unity around 46°C. At temperatures greater than 46°C, the volume flow rate ratio goes above unity, indicating that for the same operating conditions, the Coolanol 25R volume flow rate is lower in comparison to PAO.

The observations made about the variation of PAO-to-C25R pressure drop and volume flow rate ratios in the laminar flow region, should be put in the context of the overall system operation. The higher pressure drop associated with PAO at low temperatures (<26°C) means that when replacing Coolanol 25R with PAO, the system pump must be capable of handling the additional losses at these low temperatures. The low volume flow rate of PAO at low temperatures may not be adequate to satisfy the cooling requirements of the electronic equipments. However, replacement of Coolanol 25R with PAO, from the stand point of hydraulic performance, appears to be advantageous when operating in the laminar flow regime at temperatures above 46°C.

Fully Turbulent Case: for this case, Eq. (11) can be approximated by $P = A \cdot Q$. Using the definitions of P and F and solving for ΔP results in

$$\Delta P = A \rho Q^2 \quad (15)$$

Equation (15) implies that the pressure drop and volume flow rate depend strongly on the density of the heat transfer fluid. Apply Eq. (15) to the two fluids under consideration and follow the same identical assumptions and

procedures outlined for the previous case. The resulting equations for the pressure drop and volume flow rate ratios of PAO-to-C25R are

$$\frac{\Delta P_{PAO}}{\Delta P_{C25R}} = \frac{\rho_{PAO}}{\rho_{C25R}} \quad (16)$$

$$\frac{Q_{PAO}}{Q_{C25R}} = \left(\frac{\rho_{C25R}}{\rho_{PAO}} \right)^{1/2} \quad (17)$$

The variations of PAO-to-C25R pressure drop and volume flow rate ratios with coolant temperature are shown in Figure 9, by the solid and broken lines, respectively. The figure indicates that there is a modest variation in the ratios with respect to temperature. The PAO pressure drop at the lowest temperature of -54°C is about 11% lower than that of Coolanol 25R at comparable conditions. This pressure drop difference increases with temperature and reaches about 18% at 135°C. This behavior is due to the lower value of PAO density and the fact that the difference between densities of the two fluids increases with an increase in temperature (see Fig. 1).

The variation of volume flow rate ratio with temperature shown in Figure 9 by the broken line indicates that at the low end of the temperature range (-54°C), the volume flow rate of PAO is about 6% higher than that of Coolanol 25R at comparable conditions. As the coolant temperature increases to 135°C, this difference increases to about 9%.

From a hydraulic performance viewpoint, it appears that for the case of fully turbulent flow, replacement of Coolanol 25R with PAO would be advantageous with respect to the system pressure drop and coolant flow rate over the entire temperature range of operation.

In practice, the results of Figures 8 and 9, for fully laminar and turbulent flows, are not applicable over the entire temperature range of operation. Laminar flow (low flow rate), typically occurs when low temperature liquid (high viscosity) is used. Therefore, Figure 8 results are recommended for temperatures at or below 0°C. At these low temperatures the absolute viscosity of the coolant strongly influences the pressure drop and the volume flow rate of the system, causing the system with PAO to experience large losses in pressure and low volume flow rates. Turbulent flow (high flow rate), are typically associated with the use of warmer liquid coolant (low viscosity). In this case, Figure 9 results are recommended for temperatures at or above 100°C. At these high temperatures, the density of the coolant strongly influences the magnitude of the system pressure drop and volume flow rate. The system with PAO at these temperatures performs better than the

Coolanol 25R system. In the intermediate temperature range from 0 to 100°C, the flow might not be either fully laminar or fully turbulent and the use of Figures 8 or 9 might be questionable. In this temperature range, the pressure drop and the volume flow rate depend on both the density and the absolute viscosity of the coolant. However, the viscosity difference between PAO and Coolanol 25R is less extreme (see Fig. 5), and the lower density of PAO (see Fig. 1) has more influence on the PAO-to-C25R pressure drop and volume flow rate ratios, tending to counteract the influence of higher absolute viscosity. The end result would be ratios close to unity. Therefore these temperatures the hydraulic performance of the PAO and Coolanol systems should be very comparable.

THERMAL PERFORMANCE

One of the major objectives in the thermal analysis of an electronic box (e.g. radar transmitter), is the determination of the component hot spot surface temperature. This temperature is determined by adding all of the temperature rises along the heat flow path to the inlet temperature of the coolant. For the thermal performance analysis, assuming identical systems with the exception of the liquid coolant, only the liquid coolant contributions to the component surface temperature were considered. Temperature rises across the interface or in solids were ignored in this analysis. The liquid coolant contributes in two ways to the component surface temperature: (1) temperature rise due to the heat input from the electronics to the coolant as it flows through the electronic box, ΔTC ; and (2) temperature rise due to the thermal resistance across the liquid coolant convection-film from the surface of the component to the coolant, ΔTF . The basic forced liquid flow relationships needed for determination of these temperature rises will be presented next [9, 10].

The temperature rise in a liquid cooled system can be determined from

$$\Delta TC = \dot{q} / (\rho c_p) \dot{Q} \quad (18)$$

where ΔTC is the coolant temperature rise, \dot{q} is the power dissipation, \dot{Q} is the volume flow rate of coolant, and (ρc_p) is the heat capacity of the coolant.

In a forced liquid system, a convection-film develops and clings to the heat transfer surface and restricts the flow of heat from the electronic components to the liquid coolant. The temperature rise across the forced convection film (ΔTF) then becomes:

$$\Delta TF = \dot{q} / hA \quad (19)$$

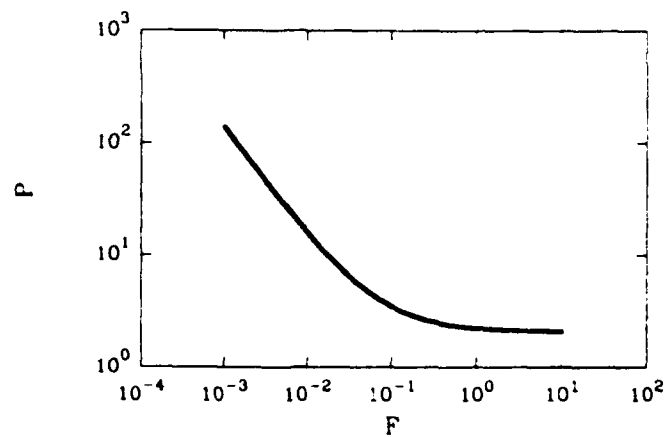


Fig. 7 Functional form between pressure drop parameter and flow parameter for a hypothetical situation.

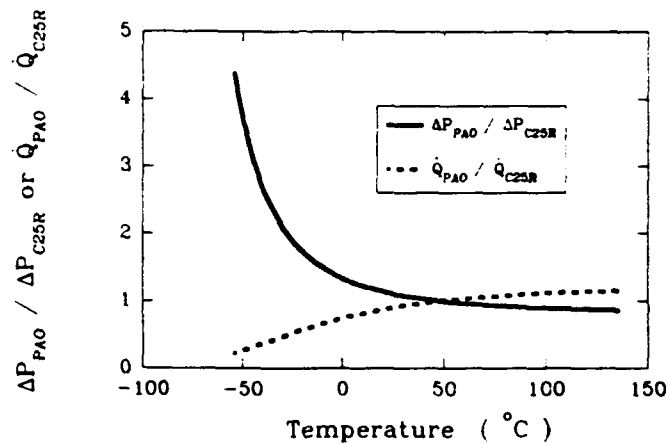


Fig. 8 Variation of PAO-to-C25R pressure drop or volume flow rate ratios with temperature (fully laminar case).

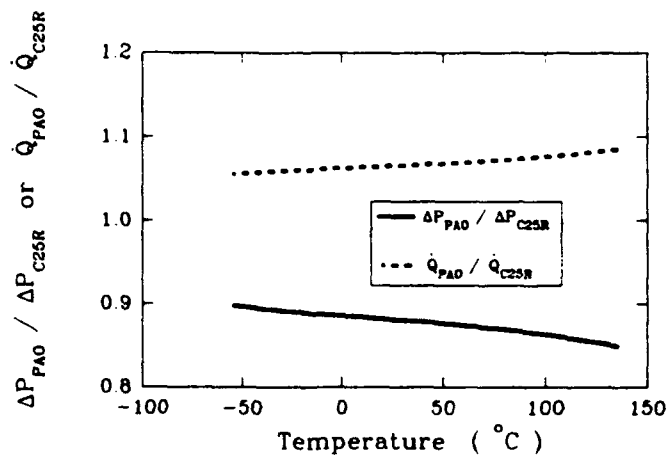


Fig. 9 Variation of PAO-to-C25R pressure drop or volume flow rate ratios with temperature (fully turbulent case).

where \dot{q} is the power dissipation, h is the forced convection heat transfer coefficient, and A is the component surface area.

The influence of different coolants (PAO and Coolanol 25R) and flow regimes (laminar and turbulent) on the temperature rises obtained from Eqs. (18) and (19) will be discussed next.

Liquid Coolant Temperature Rise: Apply Eq. (18) to the two fluids under consideration, assuming two identical systems at identical power dissipations and coolant flow rates. Divide the resulting equations to obtain

$$\frac{\Delta T_{C_{PAO}}}{\Delta T_{C_{C25R}}} = \frac{(\rho C_p)_{C25R}}{(\rho C_p)_{PAO}} \quad (20)$$

An equation identical to Eq. (20) can be developed for volume flow rate ratio of the two fluids, assuming identical systems at identical power dissipation and coolant temperature rises. The resulting equation is

$$\frac{\dot{Q}_{PAO}}{\dot{Q}_{C25R}} = \frac{(\rho C_p)_{C25R}}{(\rho C_p)_{PAO}} \quad (21)$$

Comparison of Eqs. (20) and (21) shows that the PAO-to-C25R coolant temperature rise and volume flow rate ratios are directly proportional to the C25R-to-PAO heat capacity ratio. The variation of ratios given in Eqs. (20) and (21) with coolant temperature are shown in Figure 10. The results of this figure can be better understood by examining Figure 11 which shows the variation of heat capacities with temperature for the two fluids. The figures indicate that due to the higher heat capacity of PAO at temperatures below 61°C, the coolant temperature rise is lower than that of Coolanol 25R at the same coolant flow rate. The maximum difference is about 12% at the lowest temperature of -54°C. Therefore, for temperatures below 61°C, the contribution from coolant temperature rise to the component surface temperature would be smaller using PAO as opposed to Coolanol 25R, assuming the same coolant flow rates. For coolant temperatures above 61°C, the reverse is true. The Coolanol 25R temperature rise is lower than that of PAO. The difference reaches a maximum of about 7% at 135°C.

The results presented in Figure 10 can also be interpreted as the variation of PAO-to-C25R volume flow rate ratio with temperature for the same coolant temperature rise. As indicated, at the lowest temperature of -54°C, in order to have the same coolant temperature rise for the two fluids, the volume flow rate of PAO should be about 1.12 times greater than that of Coolanol 25R. This is in sharp contrast with the hydraulic analysis results at the same temperature (see Fig. 8). At -54°C, for comparable pressure drop

in the system for the two fluids, the volume flow rate of PAO has to be about 4.4 times larger than that of Coolanol 25R. Further comparison of Figures 10 and 8 indicates that at low temperatures (<0°C), the compatibility between the hydraulic performance of the two fluids should be of greater concern than the thermal performance.

Convection-Film Temperature Rise: Apply Eq. (19) to the two fluids under consideration, assuming two identical systems at identical power dissipations and volume flow rates. Divide the resulting equations to obtain

$$\frac{\Delta T_{F_{PAO}}}{\Delta T_{F_{C25R}}} = \frac{h_{C25R}}{h_{PAO}} \quad (22)$$

It was shown earlier that, the heat transfer coefficient can be represented in terms of a dimensional grouping of fluid heat transfer properties called heat transfer parameter (HTP), see Eqs. (5) and (6). Introducing Eq. (6) into Eq. (22) results in

$$\frac{\Delta T_{F_{PAO}}}{\Delta T_{F_{C25R}}} = \frac{HTP_{C25R}}{HTP_{PAO}} \quad (23)$$

where the specific expressions for laminar and turbulent forced convection is given by Eqs. (7) and (8), respectively.

The variation of PAO-to-C25R convection-film temperature rise ratio with temperature is shown in Figure 12. The results indicate that at low temperatures in turbulent flow regime, there is a substantial variation in the convection-film temperature rise ratio. As shown, the convection-film temperature rise at low temperatures for both flow regimes, is smaller when Coolanol 25R is used in comparison to PAO. This is due to the better heat transfer properties of Coolanol 25R, see Figure 6. The convection-film temperature rise for PAO at -54°C is about 11% for laminar flow and increases to about 78% for turbulent flow. The differences between the two fluids diminishes at about -14°C for laminar flow and around 56°C for turbulent flow. Therefore, for the systems operating with PAO in the turbulent flow regime and at low temperatures (-54 to 6°C), the contribution of the temperature rise across the liquid coolant convection-film to the component surface temperature could be substantially higher than the systems using Coolanol 25R for the same identical conditions. Based on these observations, for comparable forced convection-film temperature rise between the two fluids in the low temperature regions, flow should be in the laminar regime.

Combined Temperature Rises: In order to determine the collective contributions of the liquid coolant to the component surface temperature,

temperature rises expressed by Eqs. (18) and (19) should be added together. However, this approach requires information on the specifics of the system under consideration. In an attempt to keep the analysis simple, general, and the results dimensionless, the next best approach was to consider the product of the two temperature rises. Taking the product of Eqs. (20) and (23) results in

$$\frac{(\Delta TC \cdot \Delta TF)_{PAO}}{(\Delta TC \cdot \Delta TF)_{C25R}} = \frac{(\rho C_p)_{C25R} (HTP_{C25R})}{(\rho C_p)_{PAO} (HTP_{PAO})} \quad (24)$$

The variation of Eq. (24) with temperature is shown in Figure 13 for both flow regimes. In the laminar flow regime, the net effect of temperature rises on the component surface temperature for the two fluids is about the same. In the temperature range from -54 to 61°C the component surface temperature for the system with PAO would be slightly lower (at the most by 6%), than the system with Coolanol 25R. This is due primarily to the fact that in this region, the higher heat capacity of PAO (see Fig. 11), slightly exceeds its lower heat transfer properties (see Fig. 6). For temperatures greater than 61°C, the reverse is true. Therefore, in the low temperature regions with laminar flow regime, use of PAO in comparison to Coolanol 25R is preferred.

In the turbulent flow regime, the net effect of the two temperature rises on the component surface temperature for the two fluids is substantially different in the low temperature region. In the temperature range from -54 to 61°C, the lower coolant temperature rises with PAO (due to the higher heat capacity of PAO), can not offset the much larger temperature rises across the convection-film (due to the much lower heat transfer properties of PAO). For example, at the lowest temperature of -54°C, the component surface temperature with PAO as the cooling fluid could be by as much as 60% higher than the system with Coolanol 25R as the coolant at comparable conditions. This difference drops to about 13% at -14°C and to less than 6% for temperatures above 1°C. Therefore, in the low temperature regions with turbulent flow regime, from a thermal performance view point, use of PAO over Coolanol 25R for the same operating conditions is not advisable.

Thermal Time Constant: In the thermal performance analysis presented so far, steady state operation was assumed. In order to find out how long it would take for the coolant to reach a specified steady state temperature, introduce the concept of thermal time constant (τ), which is the product of the thermal resistance and the thermal capacitance, as shown in Eq. (25)

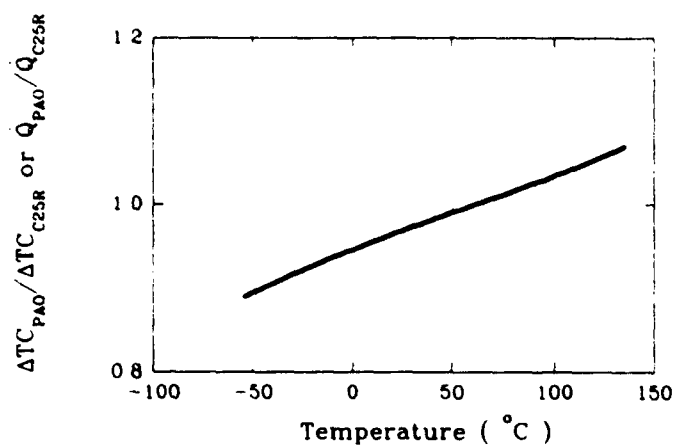


Fig. 10 Variation of PAO-to-C25R coolant temperature rise or volume flow rate ratios with temperature.

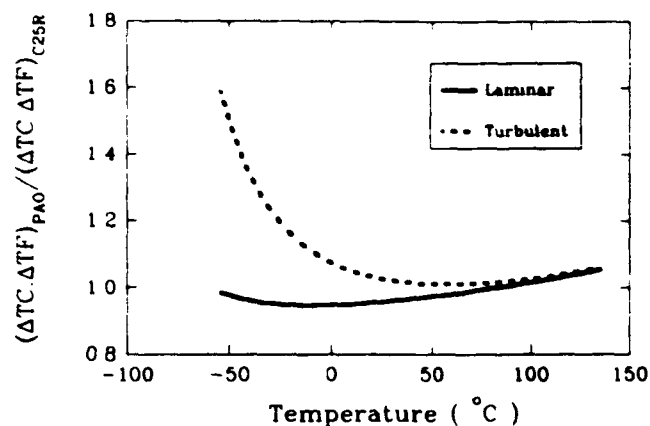


Fig. 13 Variation of PAO-to-C25R combined temperature rises ratio with temperature (laminar and turbulent flows).

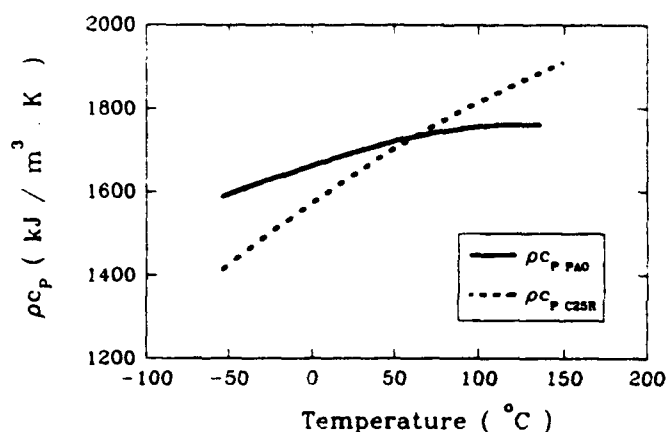


Fig. 11 Variation of heat capacity with temperature for PAO and Coolanol 25R.

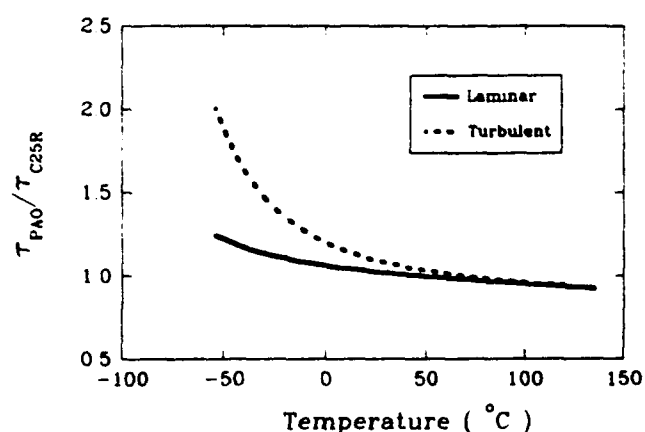


Fig. 14 Variation of PAO-to-C25R thermal time constant ratio with temperature (laminar and turbulent flows).

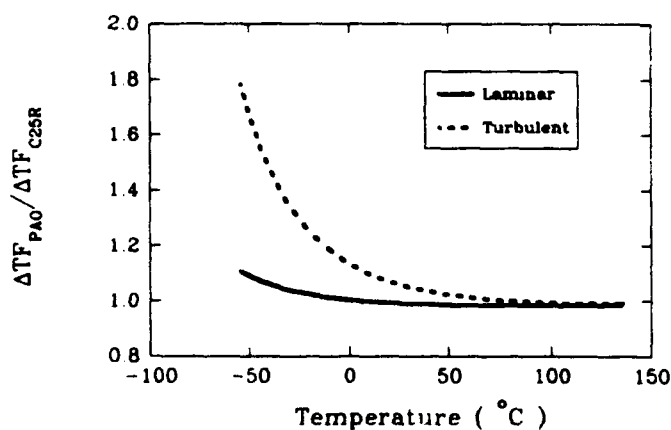


Fig. 12 Variation of PAO-to-C25R convection-film temperature rise ratio with temperature (laminar and turbulent flows).

$$\tau = \left(\frac{1}{hA} \right) (\rho C_p V) = \left(\frac{\rho C_p}{h} \right) L_c \quad (25)$$

where the volume-to-area ratio is the characteristic length (L_c) for the system. Determination of the actual value of the thermal time constant requires specific information on a given system. However, a comparison between the relative magnitudes of the time constants for the two fluids under consideration can be made.

Apply Eq. (25) to PAO and Coolanol 25R, assuming the two fluids are running through two identical systems with identical velocities and characteristic lengths. Divide the resulting equations to obtain

$$\frac{\tau_{PAO}}{\tau_{C25R}} = \frac{(\rho C_p)_{PAO} (HTP_{C25R})}{(\rho C_p)_{C25R} (HTP_{PAO})} \quad (26)$$

where, as before, the heat transfer coefficient (h) has been replaced with the heat transfer parameter (HTP).

The variation of PAO-to-C25R thermal time constant ratio with temperature is shown in Figure 14 for both flow regimes. In the laminar flow regime, due to larger resistance in the heat flow path for PAO, its time constant is longer than that of Coolanol 25R by as much as 25% at -54°C. This difference quickly reduces with an increase in the coolant temperature. In the turbulent flow regime, the differences between the time constants of the two fluids in the low temperature region is even more pronounced. At -54°C, the PAO time constant is by a factor of two longer than that of Coolanol 25R. This difference slowly reduces with an increase in the coolant temperature. Therefore, to minimize the thermal time constant differences between the two fluids in the low temperature regions, it is recommended that the system with PAO to operate in the laminar flow regime.

CONCLUSIONS

The simple methodology and the general expressions offered in this study, provide the means by which the hydraulic and thermal performance of different liquid coolants, running through identical systems, can be compared against one another. The results for the hydraulic performance of PAO versus Coolanol 25R indicate that at low temperatures (below 0°C) and laminar flow regime (low flow rate), PAO due to its large pressure drop and low volume flow rate is not at all compatible with Coolanol 25R. However, for temperatures above 26°C the performance of PAO is as good or better than Coolanol 25R. In

the turbulent region, the hydraulic performance of PAO is better than Coolanol 25R over the entire reported temperature range (-54 to 135°C).

The comparison between the thermal performance of the two coolants in the laminar region showed much closer agreement. The thermal performance of PAO for temperatures below 61°C would be slightly better than Coolanol 25R. However, in the turbulent region for temperatures below 61°C, Coolanol 25R outperforms PAO. The difference is substantial at temperatures below -14°C.

Overall, for comparable hydraulic and thermal performance between the two coolants, at low temperatures (below 0°C) when using PAO, the flow must be laminar. In addition, to overcome the large pressure losses associated with PAO, the liquid cooling system pump must be larger in comparison to the Coolanol 25R system. For temperatures above 0°C, the overall performance of the two coolants are reasonably close and fairly independent of the flow regime.

REFERENCES

1. Gschwender, L.J., Snyder, C.E., and Conte, A.A., "Polyalphaolefins as Candidate Replacements for Silicate Ester Dielectric Coolants in Military Applications," Lubrication Engineering Journal, Vol. 41, No. 4, pp. 221-228, April 1985.
2. Zoppoth, R.C., and Dillard, J., "PAO Report: Extended Testing of Polyalphaolefin as a Dielectric/Coolant Fluid," Texas Instruments, Defense Systems and Electronics Group, Dallas, TX, July 1988.
3. Hughes Aircraft Company Report No. 2001-D, "F-15 R & M PAO Coolant Study," Radar Systems Group, El Segundo, CA, March 1988.
4. MIL-C-87252A, "Military Specification - Coolant Fluid, Hydrolytically Stable, Dielectric," 2 March 1992.
5. Coolanol 25R, Technical Data Sheets, Chevron International Oil Company, San Francisco, CA, May 1993.
6. Brayco Micronic 889, Technical Data Sheets, Castrol, Irvine, CA, May 1993.
7. ASTM Standard D341-74, "Viscosity - Temperature Charts for Liquid Petroleum Products," American National Standards Institute, pp. 205-208, 1974.
8. Moody, L.F., "Friction Factors for Pipe Flow," ASME Trans., Vol. 66, pp. 671-684, 1944.
9. Steinberg, D.S., Cooling Techniques for Electronic Equipment, Wiley, New York, 1980.
10. Kraus, A.D., and Bar-Cohen, A., Thermal Analysis and Control of Electronic Equipment, McGraw-Hill, New York, 1983.

**DESIGN AND VALIDATION OF ORTHOGONAL
THREE-COMPONENT LDV SYSTEM**

Dr. Richard D. Gould

**Mechanical and Aerospace Engineering
North Carolina State University
Raleigh, NC 27695**

**Final Report for:
Summer Research Program
Wright Laboratory**

**Sponsored by:
Air Force Office of Scientific Research
Bolling Air Force Base, Washington, D.C.**

September 1993

DESIGN AND VALIDATION OF ORTHOGONAL THREE-COMPONENT LDV SYSTEM

Dr. Richard D. Gould
Mechanical and Aerospace Engineering
North Carolina State University
Raleigh, NC 27695

ABSTRACT

The work accomplished at Wright Laboratory this past summer can be subdivided into four major tasks. They included: 1.) the design, fabrication and validation of an orthogonal three-component laser Doppler velocimeter (LDV) system, 2.) the modification of an existing low speed flow facility by adding radial fan blower to provide air flow instead of using compressed air (this allowed for day time running of experiments), 3.) the modification to the fuel injection test section to allow for optical access on all four sides and, 4.) the use and testing of new LDV data acquisition and analysis software. In addition, a Wright Laboratory senior engineer was trained to use this three-component LDV system as part of this effort.

Once the LDV system was built and tested, and modifications were made to the test facility, simultaneous two-component and three-component velocity measurements were made in the flow field surrounding an integrated fuel injector (IFI). The two-component velocity measurements are presented here.

DESIGN AND VALIDATION OF ORTHOGONAL THREE-COMPONENT LDV SYSTEM

Dr. Richard D. Gould

INTRODUCTION

Fuel injection from the sides of a rectangular cross-section strut has been proposed as an effective way to inject, mix and burn fuel in a combustion chamber or after-burner. Fundamental mixing studies, both with and without combustion, must be performed to assess the effectiveness of this geometry. Direct measurements of the fuel concentration allows one to quantify the mixing effectiveness of this device. However, measurement of the turbulent velocities is required if one is interested in understanding the turbulent transport processes. With this in mind, a three-component laser Doppler velocimeter (LDV) was fabricated so that simultaneous measurements of the three instantaneous, orthogonal velocities could be made. This instrument is ideal for making these kinds measurements because it is non-intrusive and has high temporal and spatial resolution. The only requirements for use of this instrument are: optical access to the flow (*i.e.* test section windows) and the flow must be seeded with small particles.

EXPERIMENTAL APPARATUS

Optical access to the flow field surrounding the integrated fuel injector (IFI) was accomplished by mounting four quartz windows in a 76.2 mm \times 127 mm (3 in. \times 5 in.) cross-section test section as shown in Figure 1. The top and bottom quartz windows were 101.6 mm wide by 381 mm long by 3.18 mm thick while the side quartz windows were 76.2 mm wide by 381 mm long by 19.05 mm thick. The integrated fuel injector was 12.7 mm thick and had a cord and span of 25.4 mm and 127 mm, respectively. The leading edge had a 6.35 mm radius. Air was provided by a radial fan blower driven by a 7.5 hp motor.

A TSI Model 9862 two-component ($\lambda = 514.5$ and 488 nm) fiber optic probe and a TSI Model 9831 single component ($\lambda = 476.5$ nm) fiber optic probe were mounted on an 4 \times 6 ft optical table as shown in Figure 2. The two-component probe had a focal length of 450 mm and was rotated so that the 514.5 nm wavelength (green) beams were used to make direct measurements of the axial (x-direction) velocity component and the 488 nm wavelength (blue) beams were used to make direct measurements of the transverse (y-direction) velocity component. This system employed $\times 3.75$ beam expansion optics and gave probe volumes approximately 60 μ m in diameter and 450 μ m in length. The single component probe had a focal length of 350 mm and was mounted orthogonal to the two-component system such that a direct measurement of the spanwise (z-direction) velocity component could be made. This system gave a probe volume approximately 90 μ m in diameter and 1.6 mm in length. All three components used 40 MHz frequency shifting and forward scatter signal collection. The measured fringe spacings for the green, blue and violet probe volumes were 1.8274, 1.7385, and 1.7304 μ m, respectively. Measurements were made at 15 axial planes, two of which were located upstream of the strut. Seventeen transverse measurements were made at each downstream axial position, while 31 transverse measurements were made at

the two upstream axial positions. All the LDV transmitting(fiber optic heads) and receiving optics were mounted on a precision xyz positioning table with resolution of $\pm 2.5\mu\text{m}$ in each axis. Narrow bandpass filters were placed in front of each photomultiplier tube to eliminate cross-talk between the three channels.

A TSI Model IFA750, three-channel, correlation based signal processor interfaced to an IBM compatible, Intel 486 based personal computer was used to collect and process the data. The TSI FIND software (Version 4.0) was used. High and low pass filters were set to 10 MHz and 100 MHz, respectively, for all channels. The processor was set to make a single measurement per burst and the time between data word and particle residence time word were stored along with the velocity information. A hardware coincident window was set to $20\mu\text{s}$ for all of the tests.

The flow field was seeded using titanium dioxide (TiO_2) particles generated by reacting dry titanium tetrachloride (TiCl_4) with the moist room air. Craig et al. (1984) measured the particle sizes generated by this device and found that they were fairly uniform and in the $0.2 - 1\mu\text{m}$ diameter range. Data validation rates varied between 10000 and 20000 per second on each channel(random mode) and depended mainly on how clean the quartz windows were and on the location in the flow field. Low data validation rates occurred in the recirculation zone behind the strut. Coincident data validation rates ranged from 1000 to 5000 measurements per second for three-component measurements and ranged from 3000 to 10000 measurements per second for two-component measurements. The resident time velocity bias correction scheme was employed in study.

EXPERIMENTAL PROCEDURE

All flow conditions were maintained at near constant values throughout the testing procedure. A reference velocity, U_{ref} , was defined as the maximum velocity measured at the first downstream axial station. This velocity was used as it was the largest value found in the flow field. The velocity was larger here than the upstream centerline value due to the blockage introduced by the strut. The reference velocity was maintained at 31 m/s (102 ft/s). Turbulent velocity statistics and histograms were formed by using either 10000 or 50000 individual realizations for each velocity channel at each measurement point. The larger samples were acquired so that conditional averaging techniques could be tested at a later date. The raw velocity data was filtered to remove data which deviated more than 3 standard deviations from the mean. Revised statistics were calculated once these outliers were discarded. Turbulent velocity statistics were calculated both with and without residence time velocity bias correction.

EXPERIMENTAL RESULTS

Two-component velocity measurements were made at 17 transverse positions and at 13 axial planes downstream of the integrated fuel injector. In addition, inlet conditions were determined by measuring the velocities at 31 transverse locations at two upstream axial positions. The origin of the experimental coordinate system is located at the downstream edge of the fuel injector strut and centered about the strut thickness as shown in Figure 1. Figures

3 through 12 show the measured profiles of the mean and rms axial and transverse velocities and the $\overline{u'v'}$ turbulent shear stress at 15 axial locations. All measurements were normalized by the reference velocity and the half-height of the test section ($H = 38.1$ mm). The circle symbols represent the turbulence statistics calculated without velocity bias correction while the square symbols represent the turbulence statistics calculated with residence time velocity bias correction. The first downstream axial position, $x = 12.7$ mm (0.5 in.), was located as close to the strut face as possible with the beam angles and beam orientation (*i.e.* 0° and 90°) used in this study. Measurements were made at axial stations every 12.7 mm (0.5 in.) downstream of the strut to $x = 76.2$ mm (3 in.) in order to capture the detailed velocity field just downstream of the strut. The larger (50000 sample) data sets were acquired at these measurement stations. Another axial station at $x = 19.05$ mm (0.75 in.) was added so that the structure of the recirculation zone downstream of the strut could be better defined. Measurements were made at six additional downstream axial locations, in one inch intervals, to complete the description of the flow field.

The mean axial velocity profiles (Figures 3 and 4) show that the inlet flow was reasonably symmetric. They also indicate that the flow accelerates around the strut producing flow separation. A shear layer and recirculation zone exist behind the strut. At downstream locations the wake deficit almost vanishes. A comparison between the uncorrected and the bias corrected mean axial velocities indicate that the corrected results give lower mean values as would be expected for a properly working correction scheme. In addition, this comparison shows that the largest difference occurs where the turbulence levels are high. Again this behavior is expected. Further analysis needs to be performed to determine if the residence time correction scheme is the proper one to use.

Figures 5 and 6 show the mean transverse velocity profiles. Positive values indicate that the flow is in the plus y -direction (up) as given in Figure 1. The measurements at $x = -1.5$ in. show an "S" shape behavior, as expected, due to the top-bottom symmetry of this flow field. The positive values for $y > 0$, at this axial location, suggest that the streamlines are displaced away from the centerline and around the strut. Negative values at $x = 0.5$ in. are a result of the recirculation zone behind the strut.

The maximum values of turbulence intensity were found to occur in the shear layer downstream of the strut. Peak values coincide with the locations of high mean axial velocity gradient. The transverse turbulence intensity profiles (Figures 9 and 10) look similar in shape to the axial turbulence intensity profiles (Figures 7 and 8), but have higher peak values. It is believed that this is due to the flapping of the shear layer downstream of the bluff body. Bimodal probability density functions (*i.e.* velocity histograms) of the transverse velocity component result in the shear layer and thus reinforce the flapping hypothesis. A spectral analysis and conditional averaging will be performed at a later date in an effort to separate the unsteady flapping phenomena from the turbulence. It is believed, that once the unsteady component is removed from the data, that the transverse turbulence intensity level will decrease and perhaps end up being less than the axial turbulence intensity.

Figures 11 and 12 show the turbulent shear stress, $\overline{u'v'}$, profiles in this flow field. Similar to the turbulence intensity profiles, peak values of turbulent shear stress occur at locations

where the mean axial velocity gradient is large. This indicates that simple gradient transport turbulence model may do a good job in predicting the turbulent shear stress. value was found

CONCLUSIONS

A three component LDV system, with orthogonal beam orientation, was designed, built and used to make velocity measurements. Successful two-component laser Doppler velocimetry (LDV) measurements were made in the flow field surrounding a bluff body strut. The measurements define the two-dimensional mean velocity flow field, the turbulence levels in the flow field and the shear stress distribution in the flow field. Further analysis will be performed on the raw LDV data sets in an effort to better understand the unsteady phenomena.

ACKNOWLEDGMENTS

The author would like to thank Dr. A. S. Nejad for use of his laboratory and equipment and for all the help he provided. Thanks are also due to Mr. C. Raffoul for helping in operating the LDV data acquisition system and to Mr. K. Kirkendall for all his technical support in the laboratory. This investigation was performed at Aeropropulsion and Power Directorate, Wright Laboratory (WL/POPT) under the Summer Faculty Research Program supported by AFOSR.

REFERENCES

1. Craig, R. R., Nejad, A. S., Hahn, E. Y. and Schwartzkopf, K. G. 1984 "A General Approach for Obtaining Unbiased LDV Data in Highly Turbulent Non-Reacting and Reacting Flows," AIAA Paper. No. 84-0366.

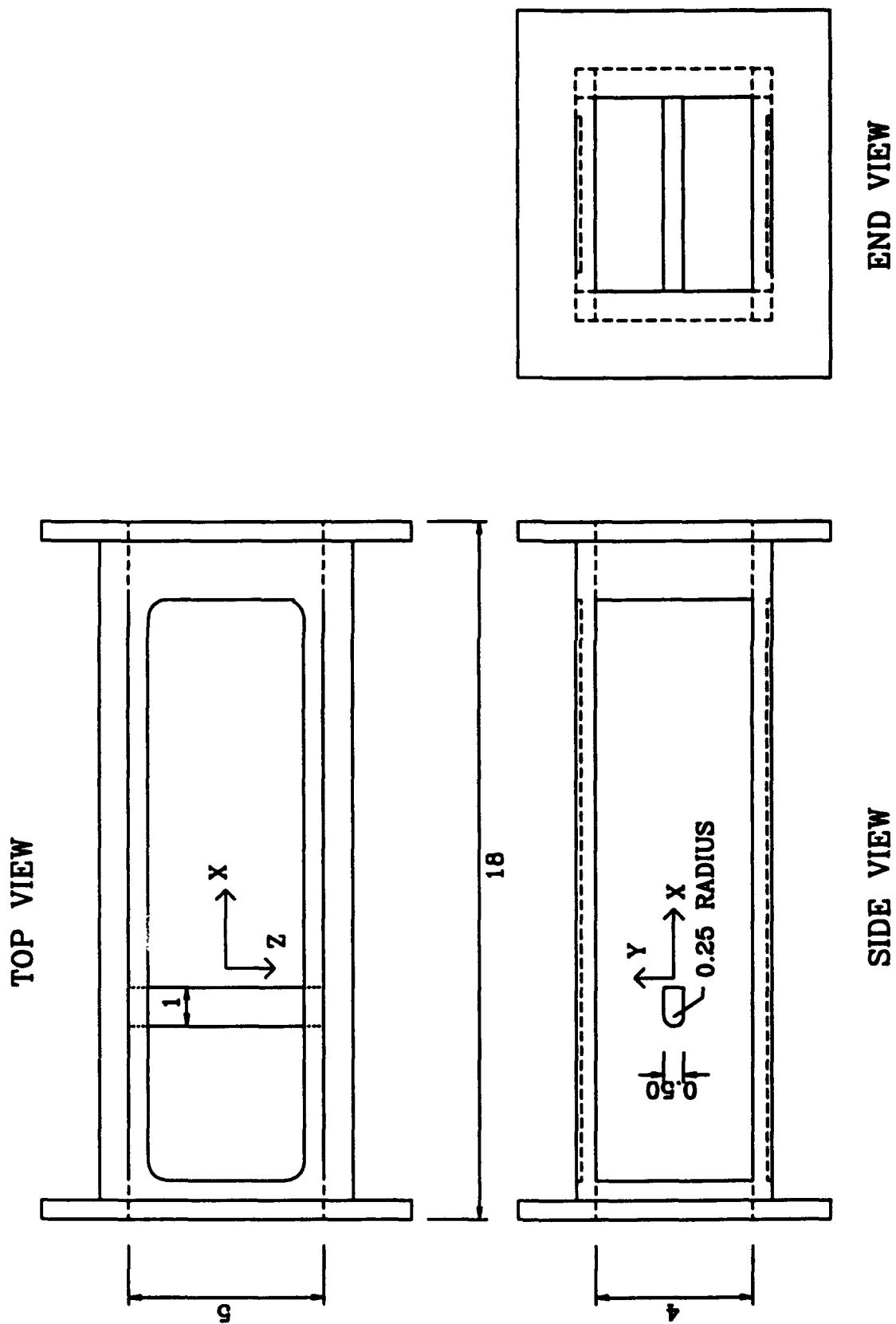


Figure 1. Test section geometry.

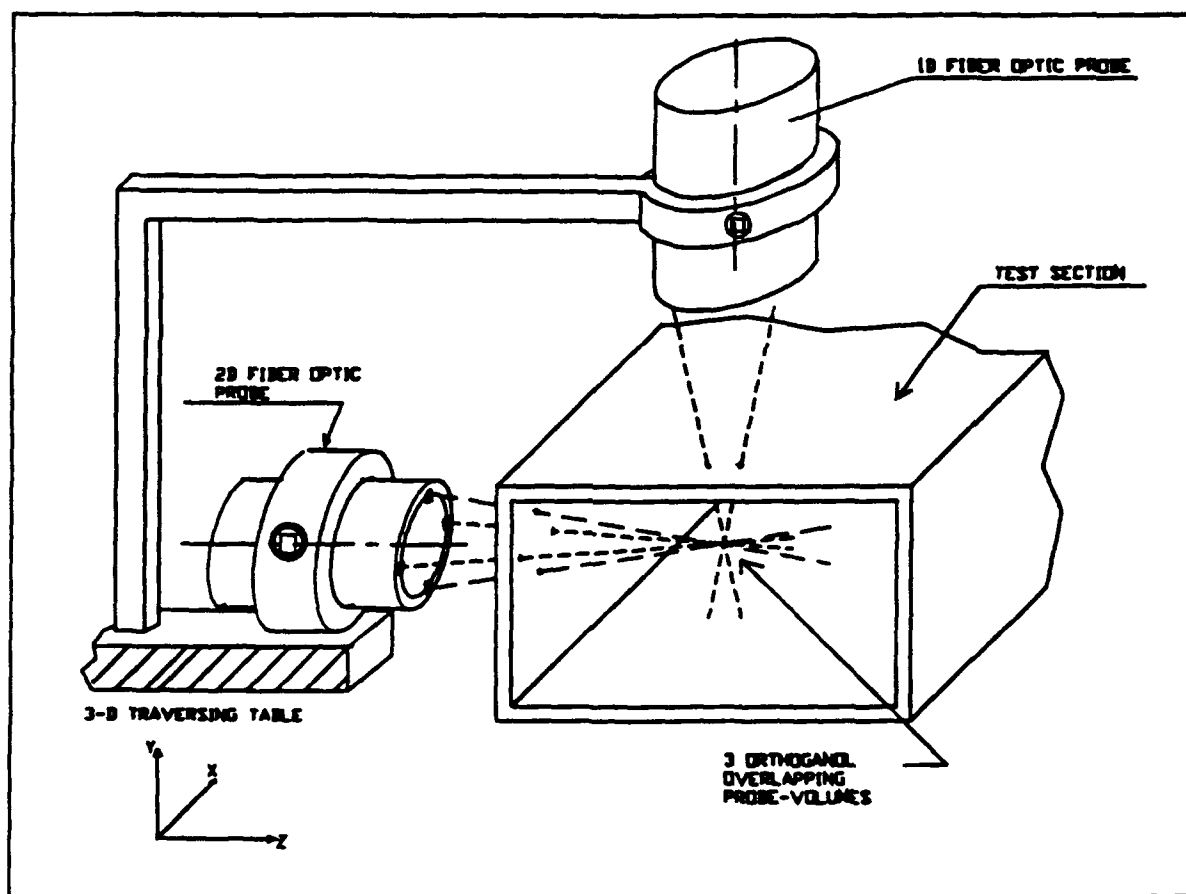


Figure 2. Three-component LDV orientation.

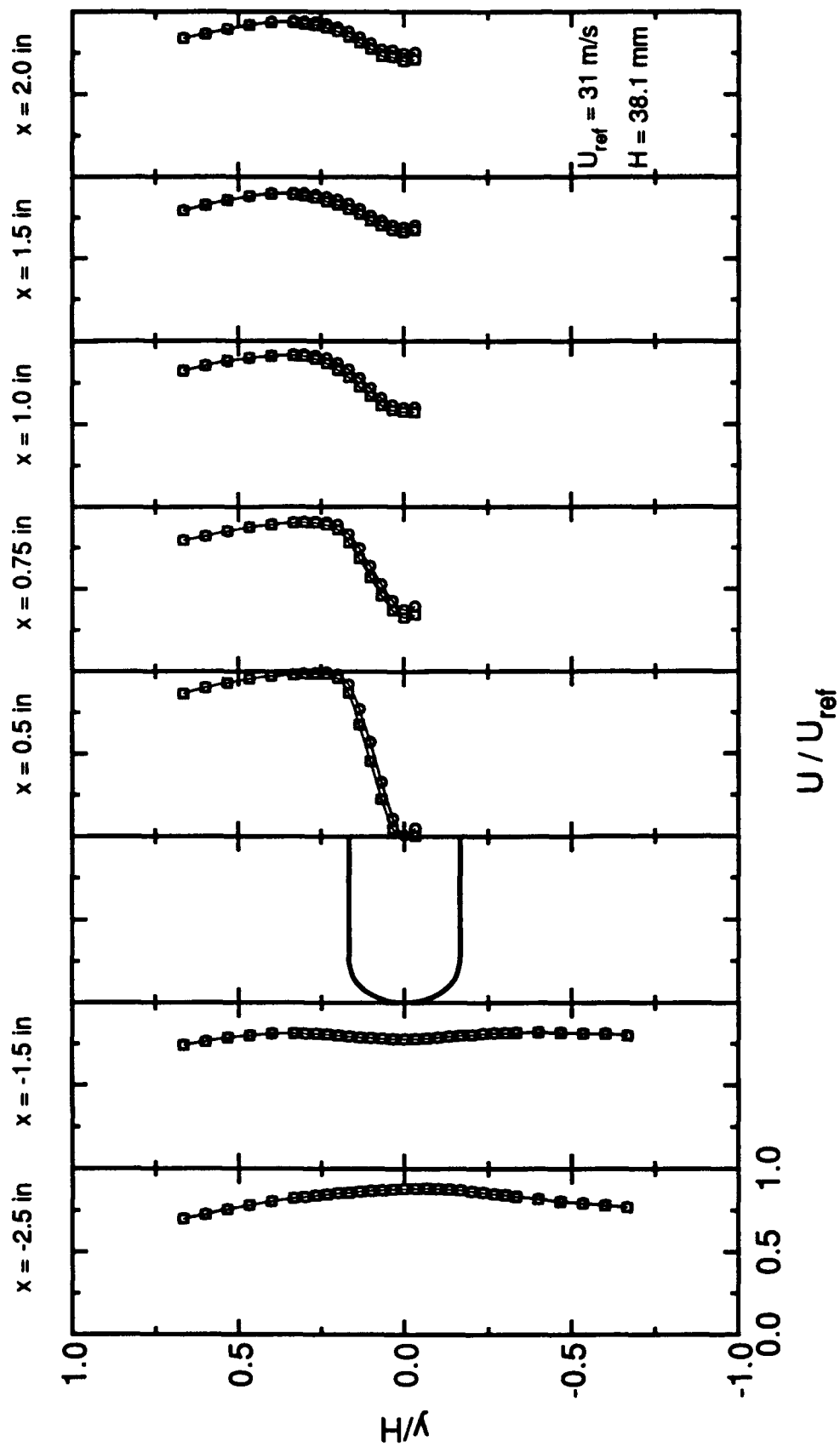


Figure 3. Normalized mean axial velocity profiles.

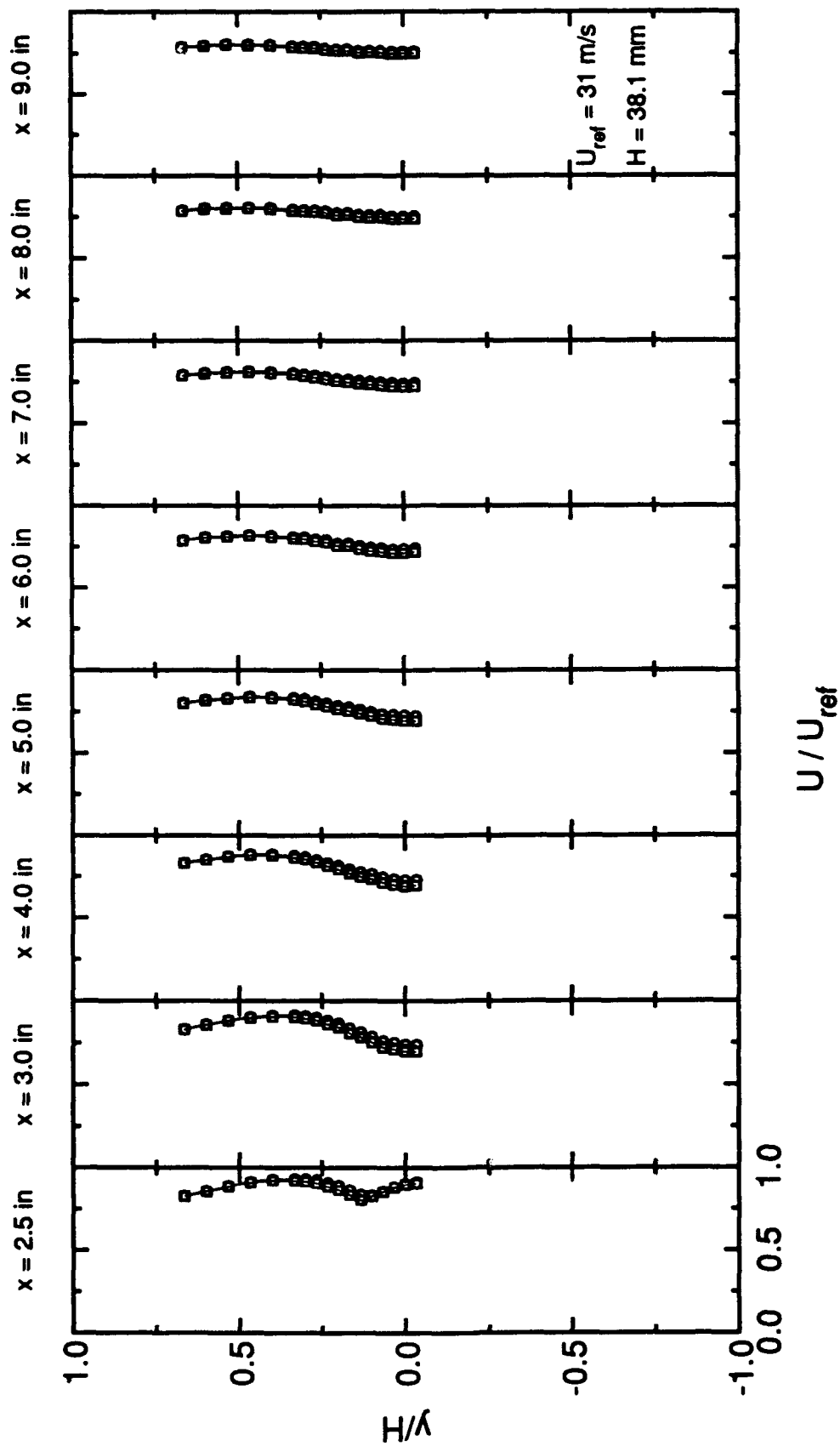


Figure 4. Normalized mean axial velocity profiles(continued).

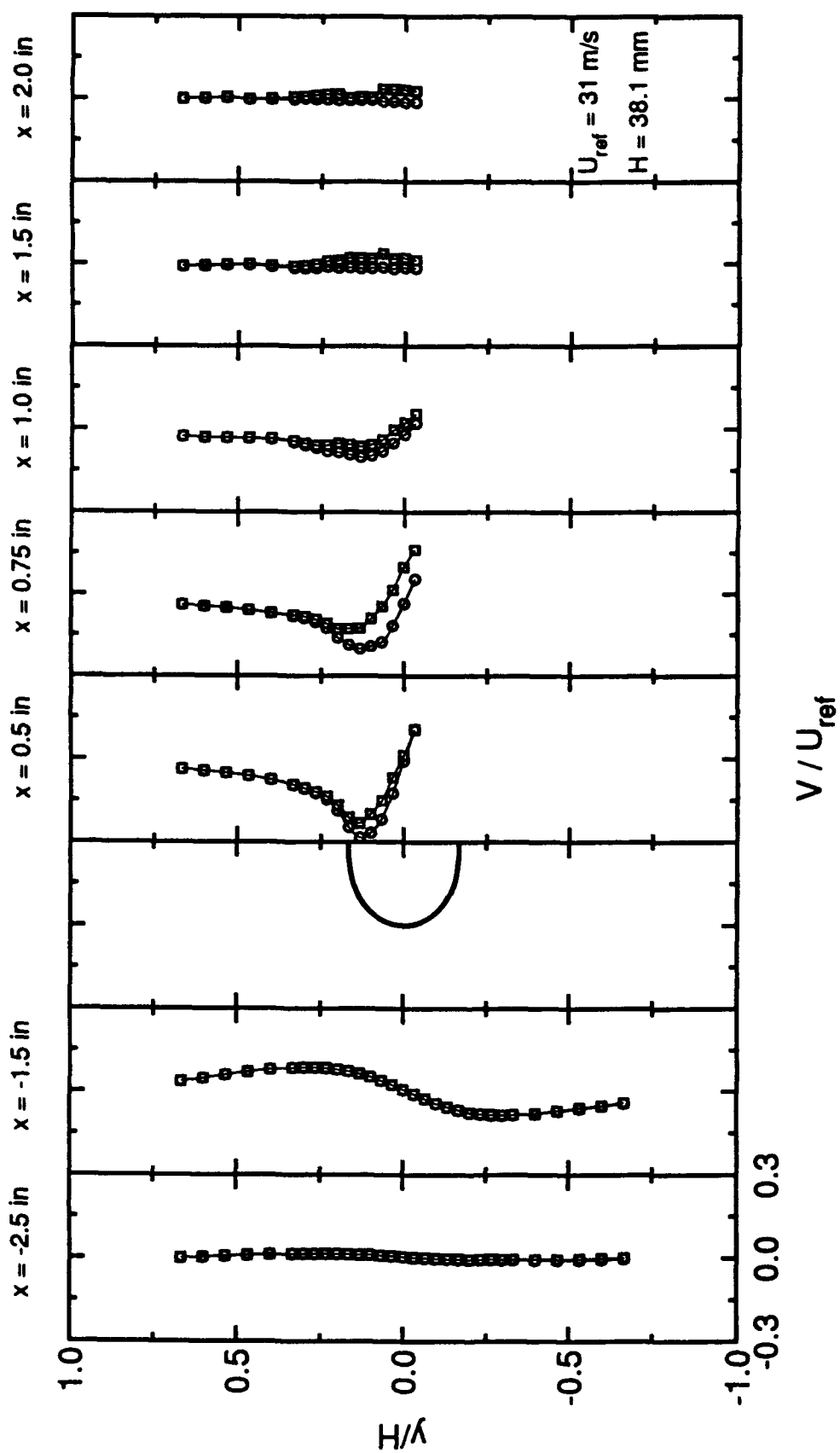


Figure 5. Normalized mean transverse velocity profiles.

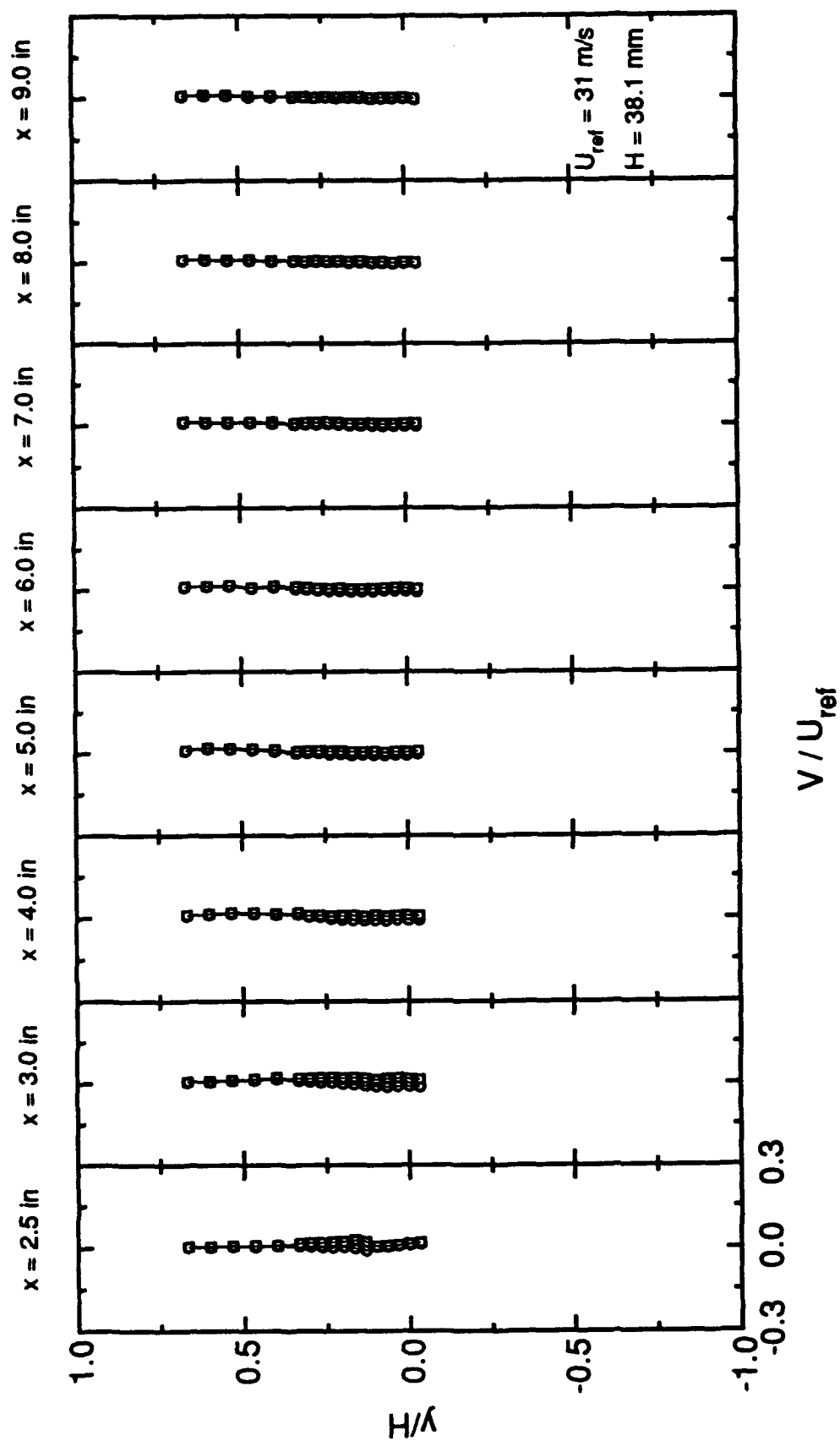


Figure 6. Normalized mean transverse velocity profiles(continued).

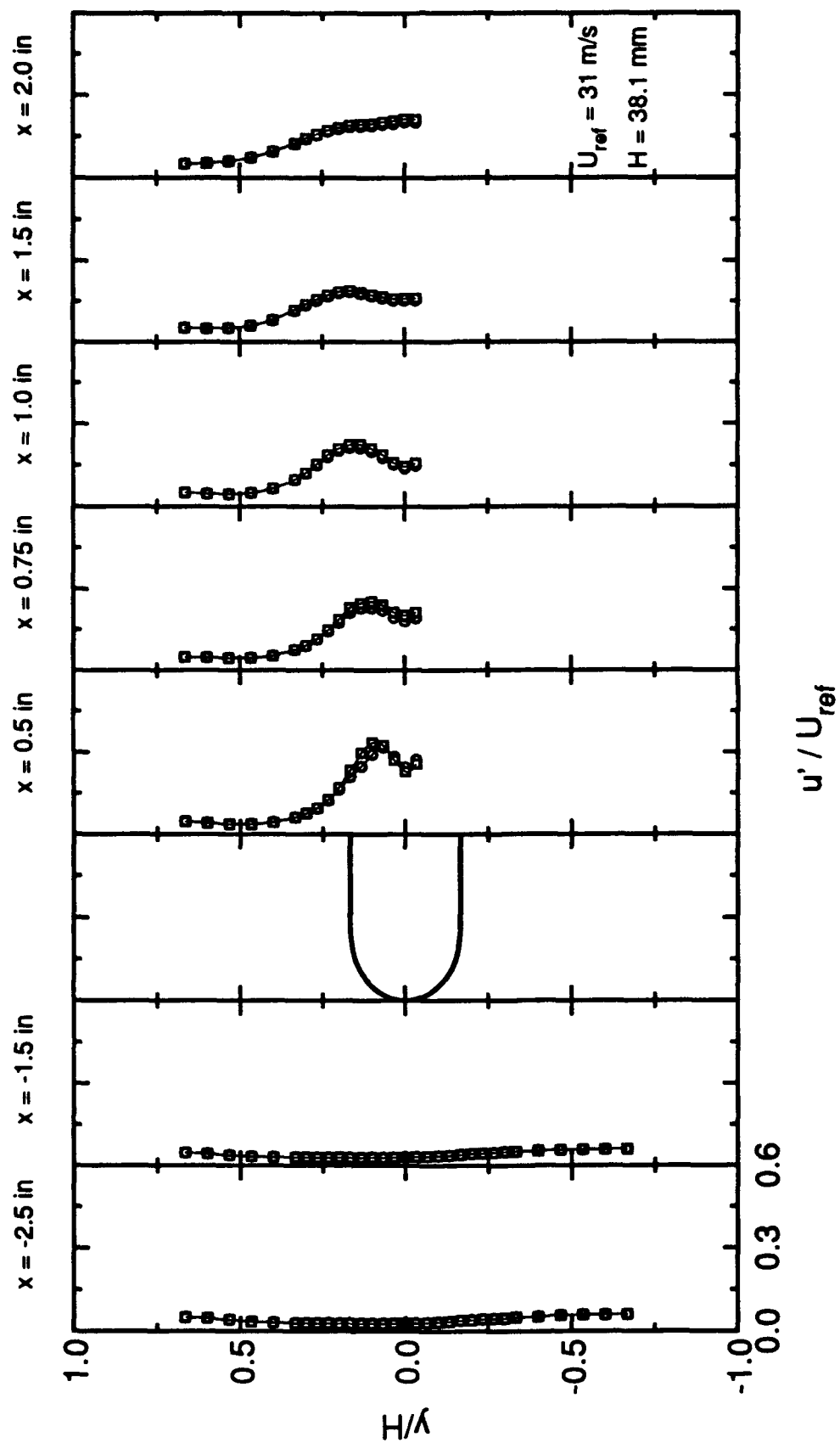


Figure 7. Normalized axial turbulence intensity profiles.

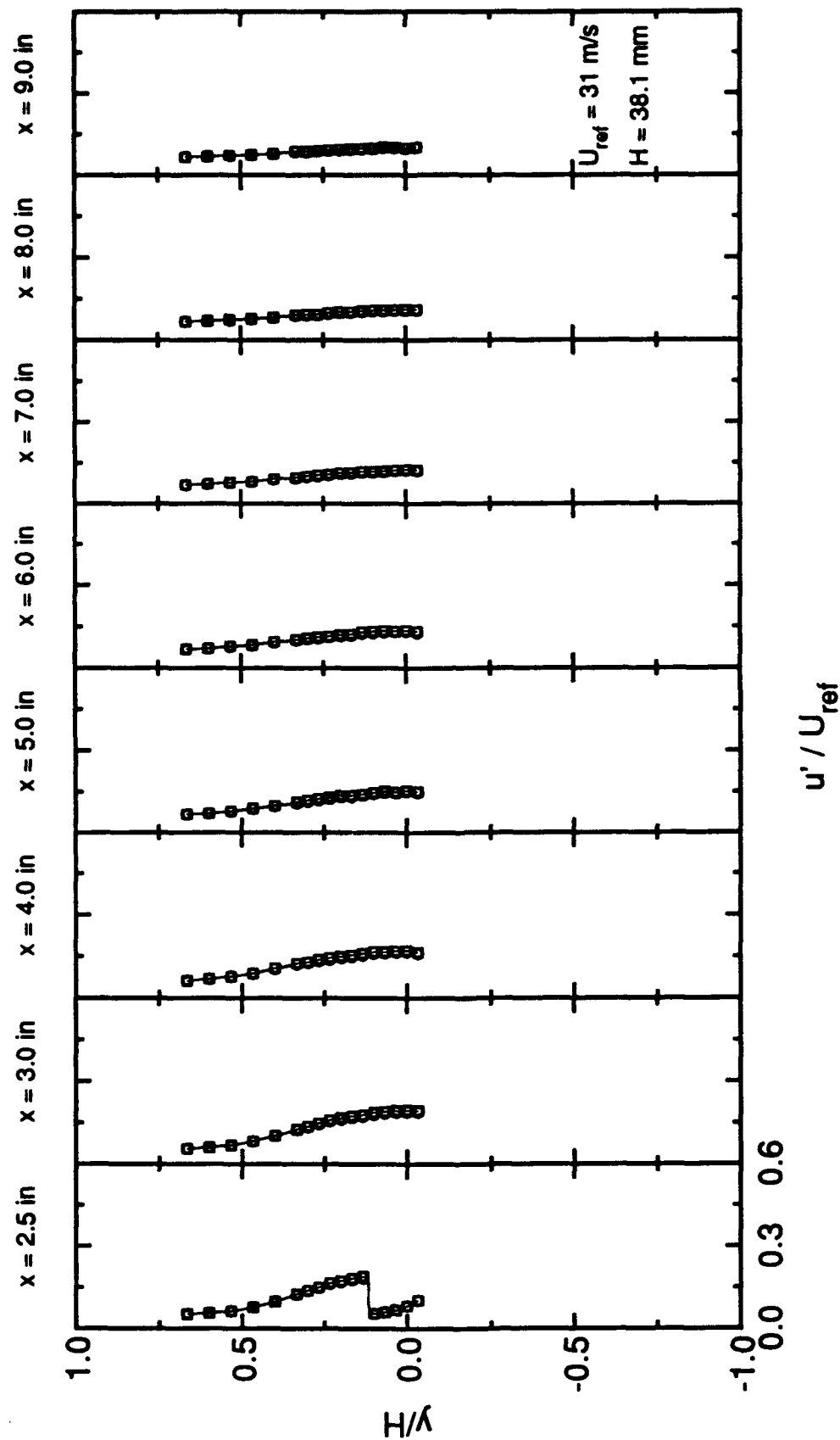


Figure 8. Normalized axial turbulence intensity profiles(continued).

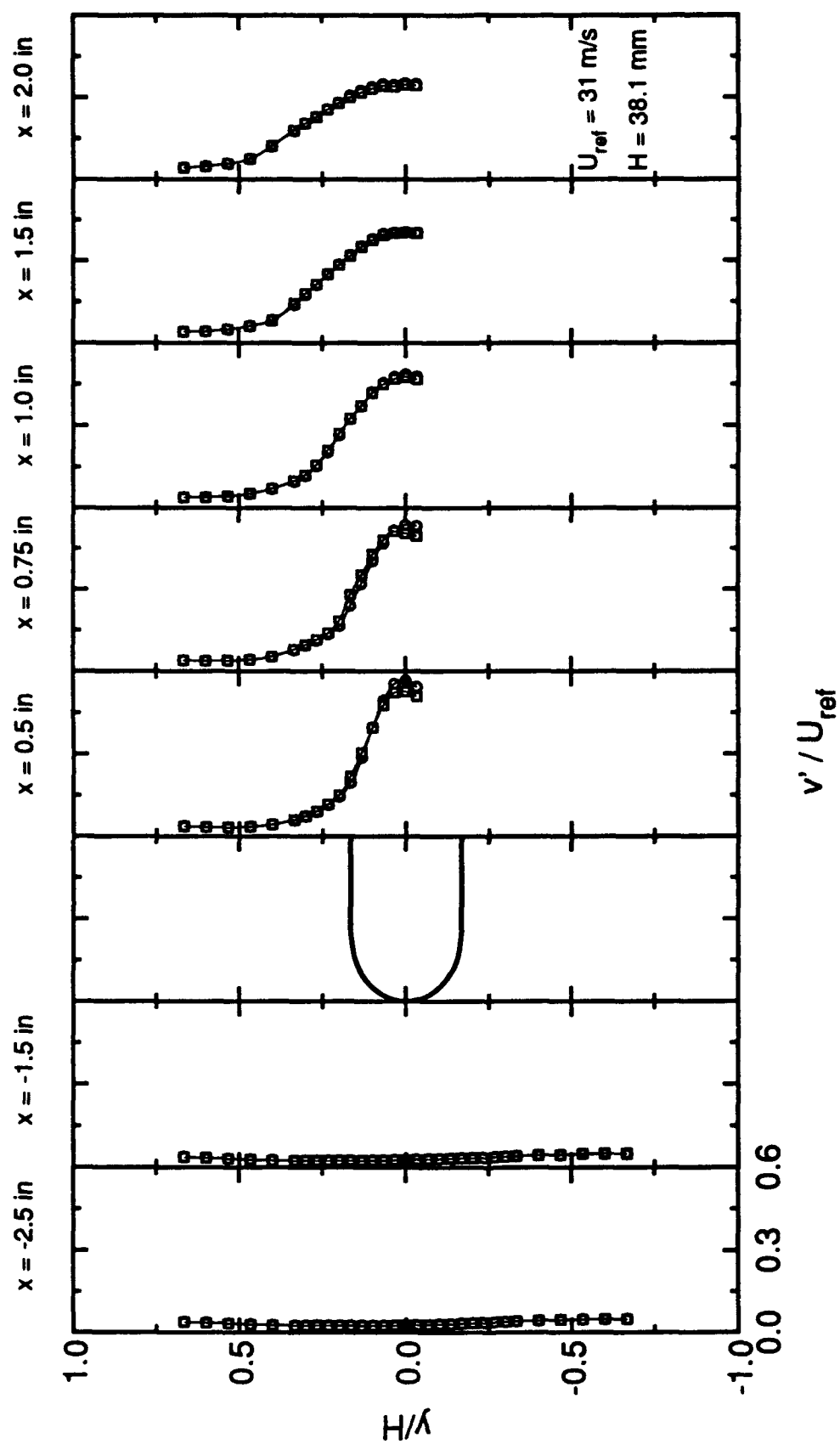


Figure 9. Normalized transverse turbulence intensity profiles.

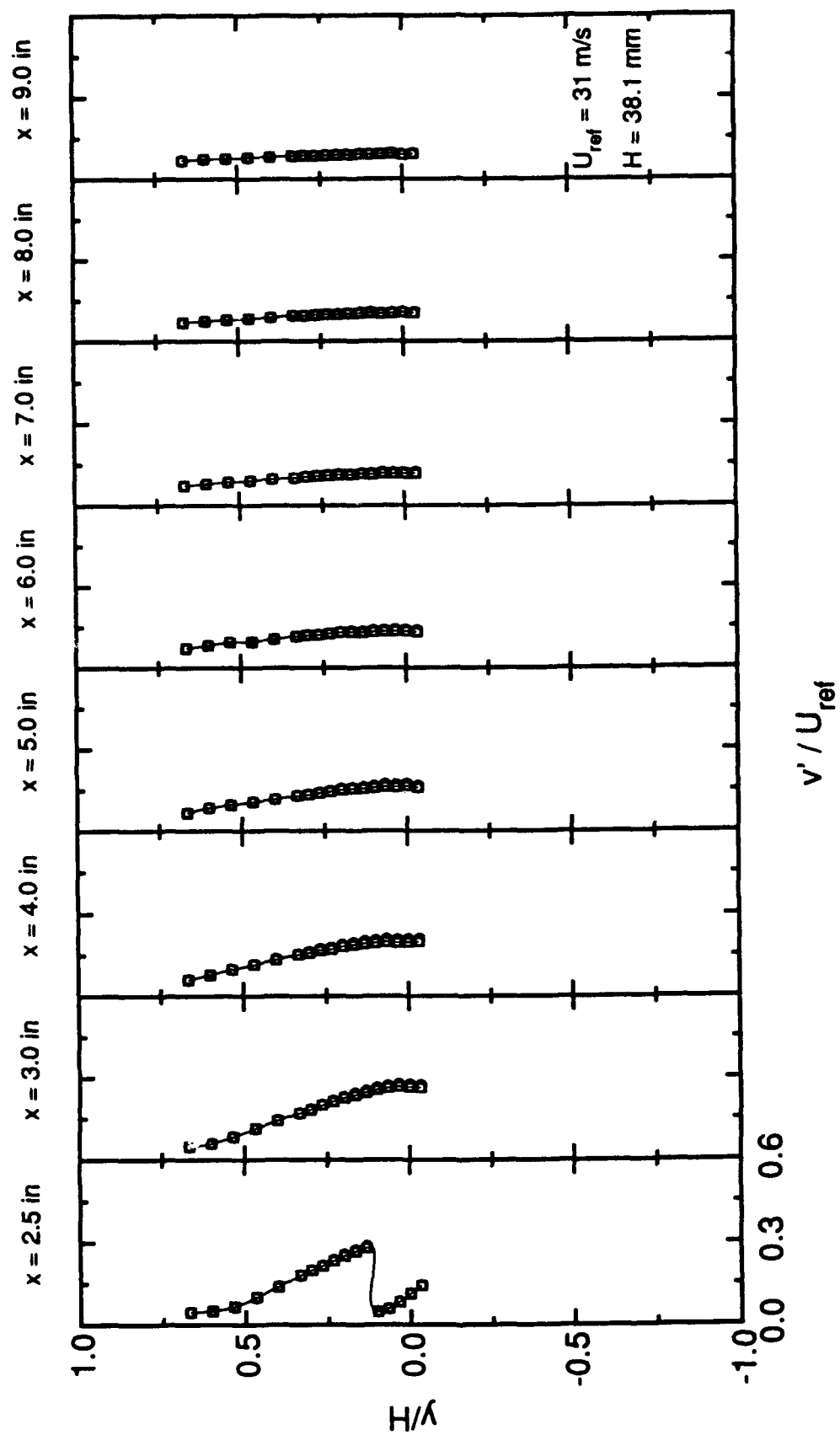


Figure 10. Normalized transverse turbulence intensity profiles(continued).

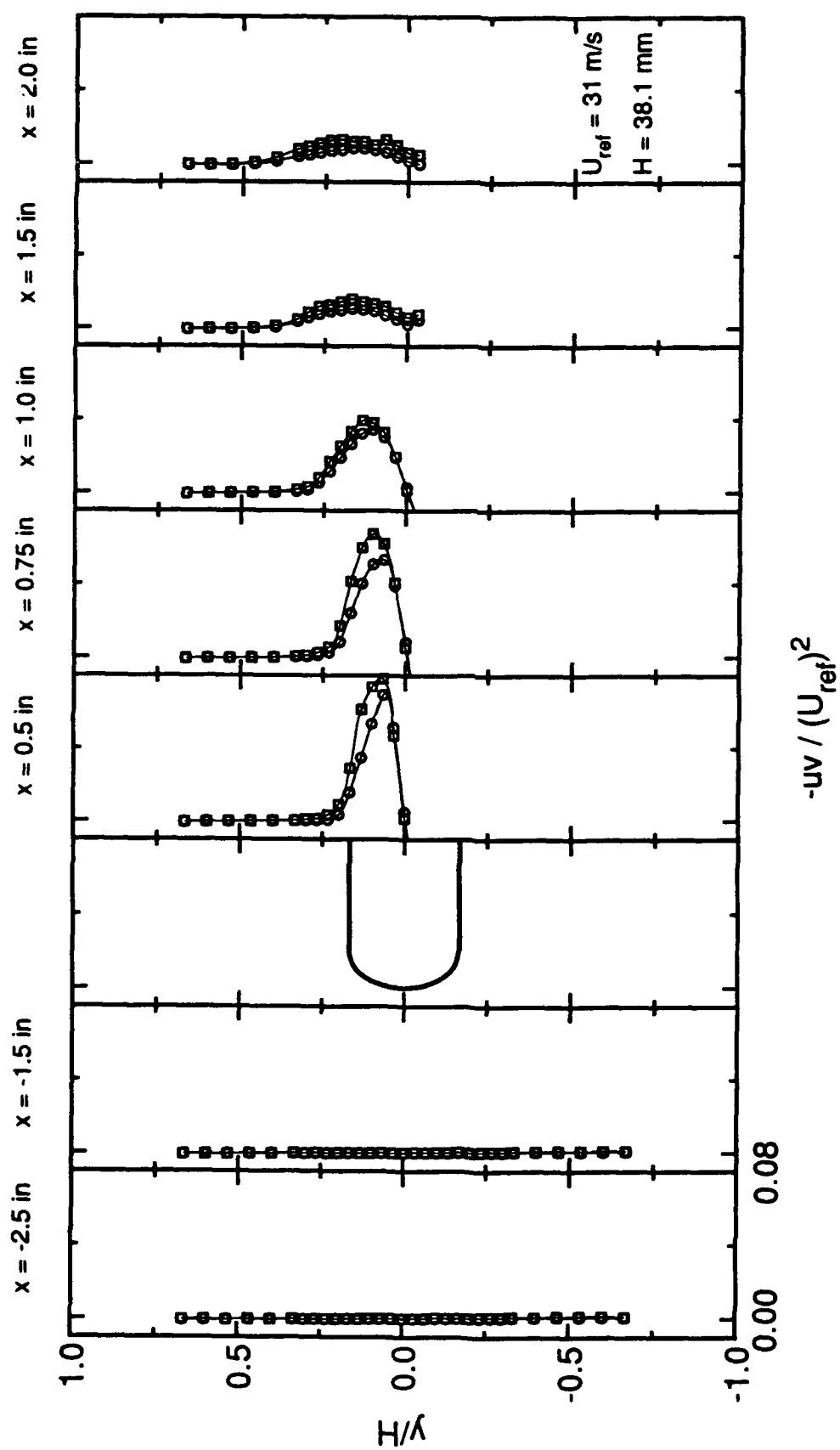


Figure 11. Normalized shear stress profiles.

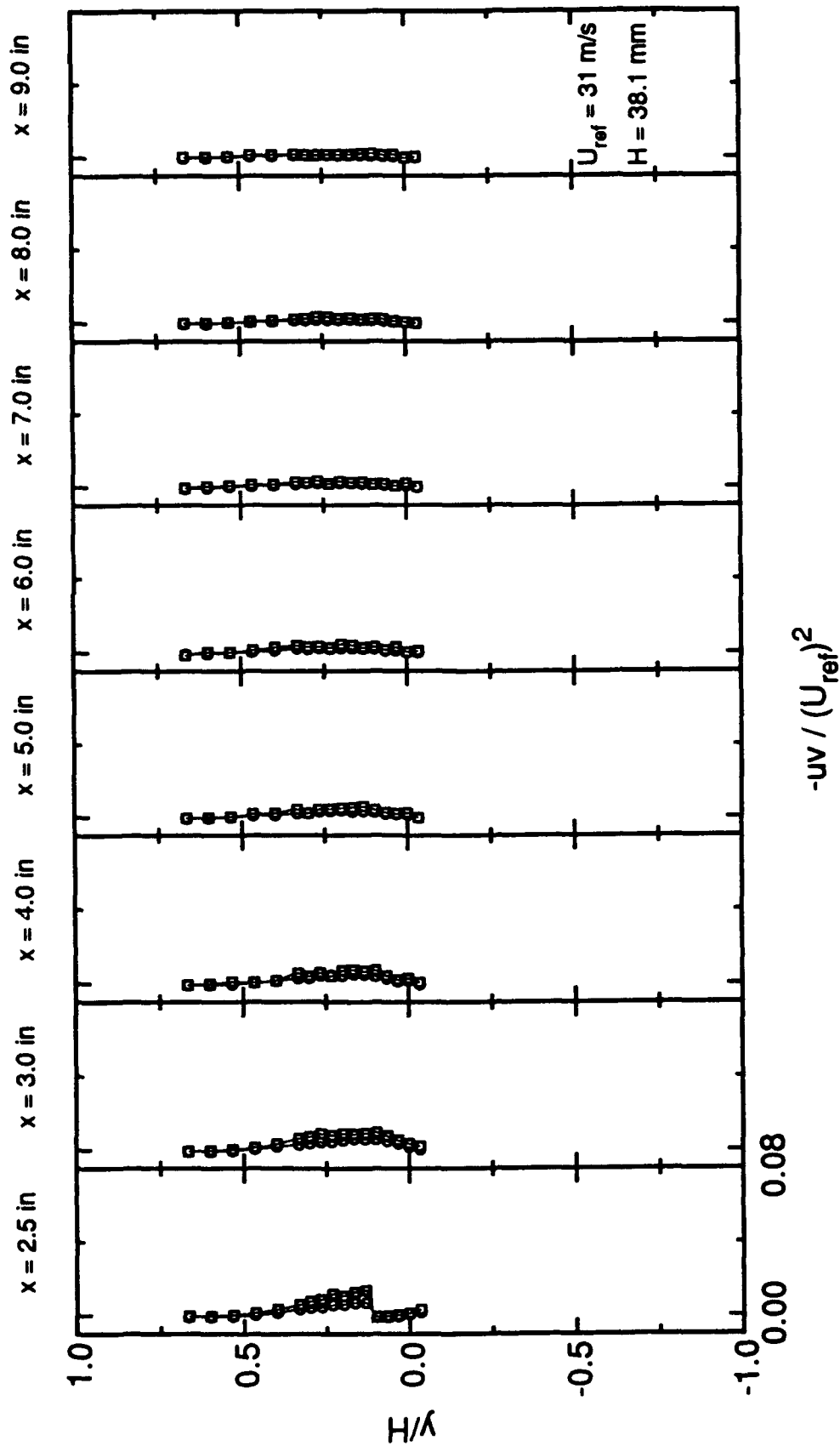


Figure 12. Normalized shear stress profiles(continued).

**VAPORIZATION AND DECOMPOSITION OF
TRICRESYL PHOSPHATE(TCP)**

Christopher C. Lu *Christopher C. Lu* 8/14/93
Associate Professor
Department of Chemical and Materials
Engineering

University of Dayton
300 College Park Avenue
Dayton, OH 45469

Final Report for:
Summer Research Program
Research & Development Laboratories

Sponsored by:
Air Force Office of Scientific Research
Wright Patterson Air Force Base, Dayton, OH

August 1993

Laboratory Focal Point: *RLW*, 13 AUG 93
Robert L. Wright Jr.
Senior Project Engineer, WL/POSL
WPAFB, OH 45433-6563

**VAPORIZATION AND DECOMPOSITION OF
TRICRESYL PHOSPHATE(TCP)**

**Christopher C. Lu
Associate Professor
Department of Chemical and Materials
Engineering
University of Dayton**

ABSTRACT

The boiling point of tricresyl phosphate (TCP) was estimated to be 440°C at atmospheric pressure using the Clausius-Clapeyron equation, and was observed to be between 420°C and 435°C by distilling a commercial grade TCP at atmospheric pressure. Experiments were conducted to study the rheological changes, viscosity and molecular weight by heating a commercial grade TCP in open and sealed tubes between 250°C and 480°C in both dry air and nitrogen environments. It was found that below 380°C, both the viscosity and the molecular weight increased significantly with temperature in dry air, while the changes were very minor in nitrogen. Above 450°C, the TCP solution decomposed in both air and nitrogen with decreases in molecular weight and viscosity. Between 390°C and 410°C, the molecular weight began to decrease while the viscosity continued to increase. We suggest that this is a transition region where TCP molecular chains begin to break and evaporation begins to occur.

VAPORIZATION AND DECOMPOSITION OF TRICRESYL PHOSPHATE(TCP)

INTRODUCTION

Tricresyl phosphate has long been used as an anti-wear additive for turbine engine lubricants. Recently, Wedeven (Ref.1) conducted a traction study using a rotating ball and disc tribometer and found that by using TCP vapor as a lubricant with dry air or nitrogen as a delivery gases, the traction coefficient can be maintained at a range of 0.04 to 0.08 over a temperature range of 500 to 670°C. Klaus, et al. (Ref.2) reported that the deposition rate of TCP vapor condensates on iron and stainless steel surfaces increased when temperature increased from 500 to 700°C.

The potential application of vapor lubricants in advanced, high temperature engines appears promising, and further understanding of the physical and chemical behaviors of TCP in the liquid and vapor phases is needed. Lu (Ref.3) used thermogravimetric analysis(TGA), differential scanning calorimetry (DSC), and gel permeation chromatography (GPC) to conduct thermal analysis and molecular weight distribution studies for the TCP solution, and found that the molecular weight of the solution increased with temperature at a range of 175 to 304°C in an oxygen environment. These results agree with the results of this study that both molecular weight and viscosity increased significantly below 380°C with temperature under dry air. The purpose of this study is mainly twofold: (1) to determine temperature ranges where the TCP solution begins to evaporate and to decompose, and (2) to observe the rheological changes of TCP, such as molecular weight distribution and viscosity, for these temperature ranges. To accomplish these goals, a theoretical approach was taken to calculate the vapor pressure of TCP, and several experiments were conducted to observe the physical and rheological changes of the TCP solution at elevated temperatures.

PROCEDURES AND RESULTS

1. VAPOR PRESSURE AND TEMPERATURE

The Clausius-Clapeyron equation was used to calculate the vapor pressure of TCP between one and two atmospheres,

$$\ln p_v = -\frac{\Delta H_v^*}{RT} + B ,$$

where p_v is a vapor pressure with units of mmHg, ΔH^* is the heat of vaporization in units of cal/gm, R is the gas constant equal to 1.987 cal/(mole.K), and B is a constant calculated as a value of 18.186 for the units used. The physical properties of TCP are given as: boiling point = 265°C at 10 mm Hg, and heat of vaporization = 44.5 cal/g (Ref. 4), while the boiling point of p-tricresyl phosphate is 410°C at atmospheric pressure (Ref. 5). Table 1 compares our results with the literature values.

Table 1. Vapor Pressure Temperature Relationship for TCP

P_v (mmHg)	T (°C)	
10	265	(90% mixture of isomers, Ref. 4)
760	441	(this study)
760	410	(p- TCP, Ref. 5)
1520	487	(this study)

The above values are plotted on a semi-log scale for p_v vs $1/T(^{\circ}K)$ and the result is shown as a straight line in Figure 1.

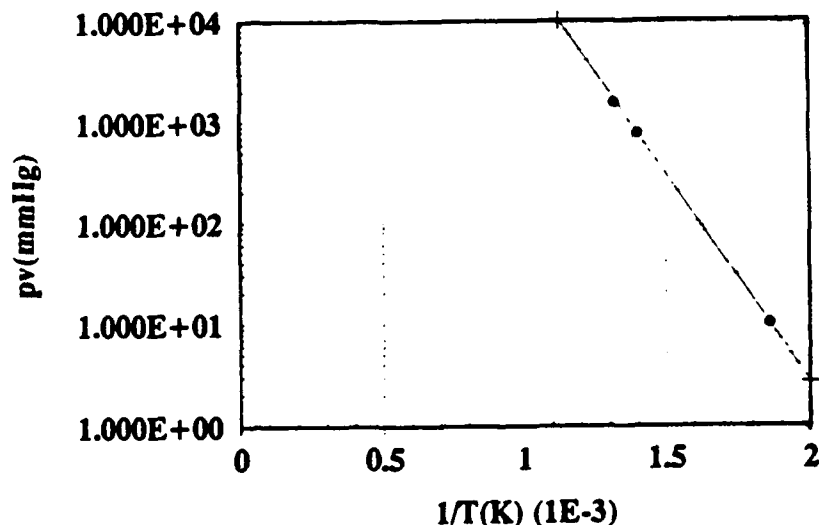


Fig.1: Vapor Pressure for TCP

The same equation was also used to calculate for p_v vs $T(^{\circ}\text{C})$ and the result is shown as a curve in Figure 2.

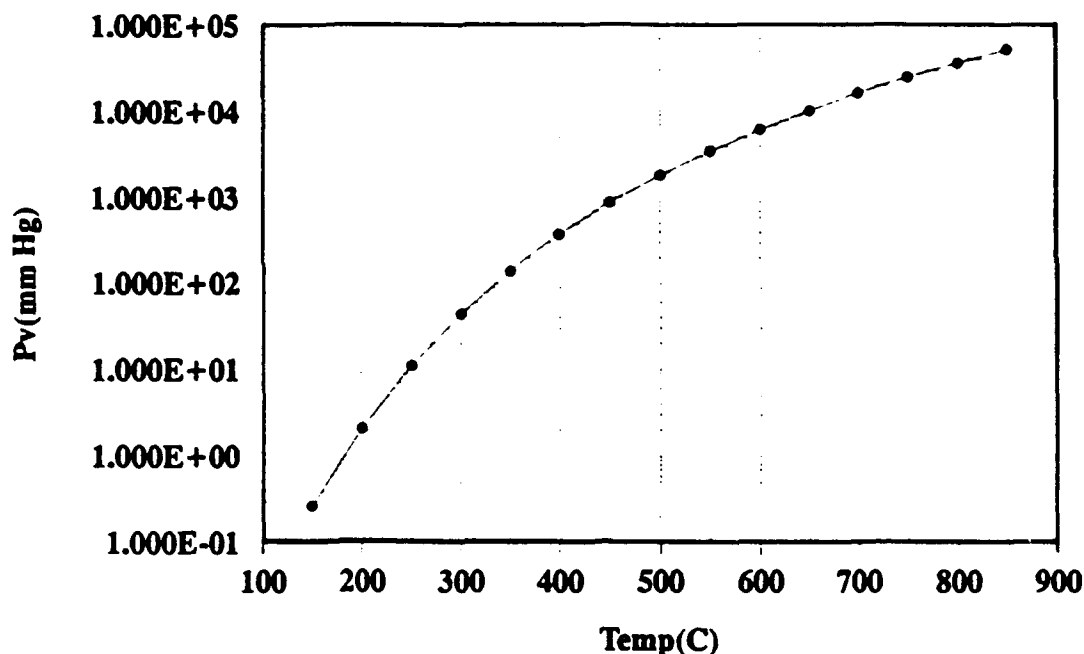


Fig. 2: Vapor Pressure for TCP

Blake et al. (Ref.6) found the decomposition temperature of triphenyl phosphate to be 423°C . For tricresyl phosphate, the decomposition temperature will be different from 423°C because of the methyl group attached to the phenyl as shown in Figure 3. It

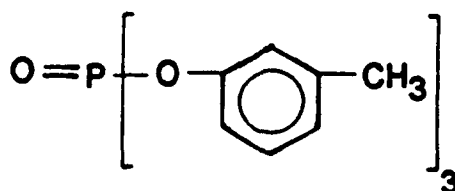


Fig.3 *m*-tricresyl phosphate

is believed that TCP begins to boil and decompose at 410°C to 440°C. To verify this result we studied the oxidation of TCP in both open and sealed tubes. The detail is described in the following section.

2. Oxidation and Thermal Decomposition

A commercial TCP solution was evaluated the change of viscosity and molecular weight at high temperatures under both air and nitrogen atmospheres. The tests were conducted by: (a) open tube: 100 ml of TCP solution was added to a glass tube of about 5 cm in diameter and 50 cm in length. The tube was placed in a thermo-bath, and air or nitrogen was allowed to bubble through the solution at a flow rate of 10 liter/hr. The tube was equipped with a condenser to allow refluxing of TCP so that condensate returns for reheating. (b) sealed tube: A quantity of 0.25 ml or 5 ml of TCP solution was added to a pyrex tube of about 3 cm in diameter and 15 cm in length. The solution was purged with dry air or nitrogen and the tube was sealed. The tube was heated in a muffle furnace between 250°C and 480°C. As discussed in the previous section the TCP solution starts to boil and decomposes between 410°C and 440°C. Therefore, the test results between 250°C and 380°C correspond to a liquid phase, and those between 390°C and 410°C correspond to a transition phase from liquid to vapor. The thermally oxidized TCP solution was collected to measure the viscosity and the molecular weight distribution. A semi-micro viscometer was used to measure the kinematic viscosity at 40°C and 100°C. For the molecular weight distribution, a gel permeation liquid chromatography (GPC) was used. The apparatus consists of μ -styragel columns with 5 μ m bead particle sizes and two 100 angstrom and one 500 angstrom pore size openings. The TCP solution was diluted with tetrahydrofuran (THF), and the effluent exited from the GPC column was detected by a 254 nm UV-detector. The molecular weight was calculated from the retention time using the following formula:

$$\log(M_w) = -0.1195 * \text{Time}(\text{minute}) + 5.2035.$$

This formula was based on the calibration using polyphenyl ether of molecular weights 4P3E, 5P4E, and 6P5E as 354, 446, and 538 respectively.

The size equivalent number-average molecular weight M_n is calculated as:

$$M_n = \frac{\sum N_i \times M_i}{\sum N_i} ,$$

and, the size equivalent weight-average molecular weight M_w is defined as:

$$M_w = \frac{\sum N_i \times M_i^2}{\sum N_i \times M_i} ,$$

where N_i and M_i indicate the number of mole and the molecular weight respectively.

The ratio of M_w to M_n , M_w/M_n is called the polydispersity index and is used to measure the broadness of the molecular weight distribution. The larger the index the broader is the molecular weight distribution. When the index equals 1, the polymer solution is a mono-dispersion. The experimental results are shown in Table 2.

Table 2. Viscosity and Size Equivalent Molecular Weight of TCP

Condition	Viscosity (cSt)		M_n	M_w	M_w/M_n
	40°C	100°C			
Fresh TCP	24.89	4.02	360.91	394.84	1.09
Air Bubble					
280°C, 1hr.	41.65	6.02	374.09	425.08	1.14
2hr.	63.53	6.63	386.41	471.73	1.22
3hr.	88.63	8.84	388.64	487.94	1.26
330°C, 1hr.	60.24	7.16	392.18	491.71	1.25
2hr.	111.93	11.02	426.53	587.50	1.38
3hr.	185.00	15.66	433.18	627.93	1.45
380°C, 1hr.	65.92	7.24	410.43	514.92	1.25
2hr.	120.19	10.33	436.35	576.77	1.32
3hr.	217.29	14.73	465.98	669.60	1.43
N₂ Bubble					
280°C, 1hr.	25.33	4.04	-	-	-
2hr.	25.30	4.06	-	-	-
3hr.	25.46	4.08	-	-	-
330°C, 1hr.	25.55	4.08	-	-	-
2hr.	25.65	4.08	-	-	-
3hr.	26.02	4.12	364.88	408.32	1.11
380°C, 1hr.	25.68	4.10	-	-	-
2hr.	26.78	4.18	-	-	-
3hr.	27.62	4.28	-	-	-

406°C, 1hr.	26.04	-	360.03	418.49	1.16
2hr.	27.42	-	374.85	424.23	1.13
3hr.	28.88	-	375.68	425.92	1.13
8hr.	38.19	-	384.70	431.84	1.12

Air Bomb

250°C, 1hr.	24.71	4.02	366.68	406.25	1.11
2hr.	29.07	16.79	364.67	401.32	1.10

345°C, 1hr.	35.35	5.24	359.24	417.69	1.16
2hr.	40.70	5.71	363.24	425.78	1.17
3hr.	43.55	6.30	374.24	451.91	1.21

390°C .5hr.	58.82	-	367.03	484.84	1.32
1hr.	75.32	-	362.84	479.65	1.32
2hr.	98.63	-	314.55	435.70	1.38

410°C, .5hr.	62.34	-	340.80	465.74	1.37
1hr.	111.35	-	319.57	458.50	1.43
2hr.	-	-	257.60	381.53	1.48

450°C (0.25 ml TCP)					
* 1hr.	-	-	261.61	396.15	1.51
* 2hr.	-	-	224.89	410.87	1.83
460°C (5 ml TCP)					
* 2hr.	-	-	241.27	487.97	2.02

N₂ Bomb

450°C (0.25 ml TCP)					
* 1hr.	-	-	343.86	433.04	1.26
* 2hr.	-	-	238.85	408.03	1.71
460°C (5 ml TCP)					
* 1hr.	-	-	220.37	395.2	1.79
* 2hr.	-	-	217.68	395.8	1.82
** 5hr.	1.11	-	245.65	526.65	2.14
480°C					
** 6hr.	1.01	-	250.45	531.37	2.12

* Sample was too thick and quantity was too small to test.

** Sample was heated slowly.

DISCUSSIONS

The above results show : (1) at 280°C, 330°C, and 380°C, both viscosity and molecular weight of TCP solution substantially increase with both the temperature and heating time in the air environment. The molecular weight distribution also becomes broader. In the nitrogen environment, however, these increases are relatively minor. This suggests that the polymerization reaction takes place in the presence of oxygen. It was also discussed by Lu (Ref.3) that the oxidation reaction enhanced the polymerization of TCP solution at a temperature range of 175°C to 304°C; (2) at 250°C, and 345°C "air bomb" condition, both molecular weight and viscosity increase, but only slightly. It is evident that the amount of oxygen inside the sealed tube was not enough to continue the oxidation reaction; (3) at 450°C, 460°, and 480°C, we observed that the TCP solution quickly decomposed and formed a dark residue inside the sealed tube under both dry air and nitrogen conditions. The viscosity test was not run because of an insufficient amount of TCP solution was left inside the tube. However, the GPC test shows that during the first two hours, the number average molecular weight, M_n , significantly decreases, the weight average molecular weight, M_w , only slightly increases, and the molecular weight distribution becomes slightly broader. This suggests that at the beginning of thermal decomposition, the binding chains of TCP molecules break and form smaller molecular weight species. However, when the temperature is slowly increased to 460°C and 480°C in 5 and 6 hours, these small molecules begin to combine to form larger molecules. The results are shown at 460°C and 480°C for 5 and 6 hours runs, where the weight average molecular weight, M_w , increases to around 530 and the molecular weight distribution further widens to 2.1; (4) at 406°C with nitrogen bubbling, both viscosity and molecular weight gradually increase without suffering thermal decomposition, which suggests that 406°C is still below the decomposition temperature; (5) at 390°C and 410°C "air bomb" conditions, viscosity increased by increasing the heating time from 1/2 hour to 2 hours. However, both M_n and M_w decreased with the heating time. The decrease of molecular weight was rather minor at 390°C, especially up to one hour of heating time, but it was rather severe at 410°C. These suggest that the range between 390°C and 410°C is the transition temperature range where some molecules chains may begin to break and some degree of polymerization may still take place. The above experimental data were plotted based on viscosity/ M_n and viscosity/ M_w and are shown in Figures 4 and 5.

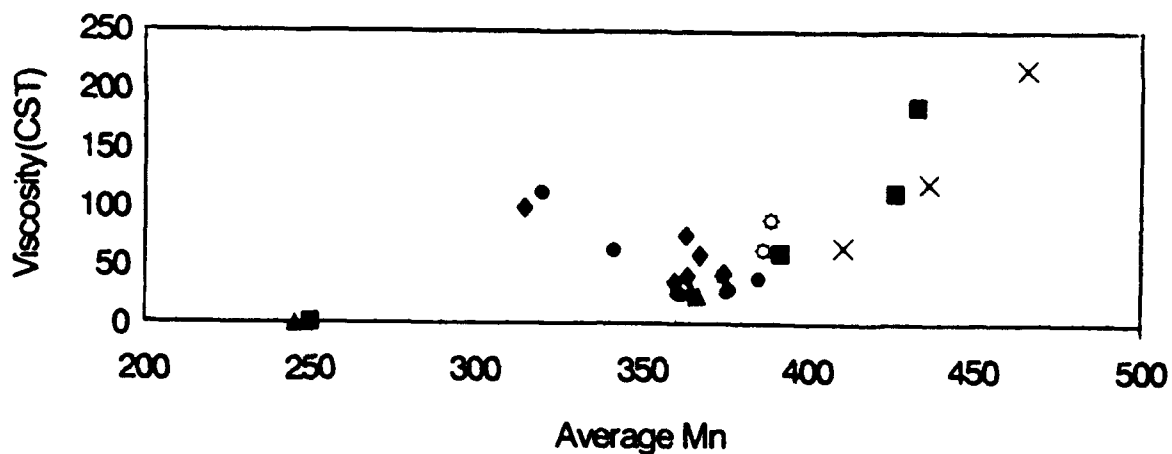
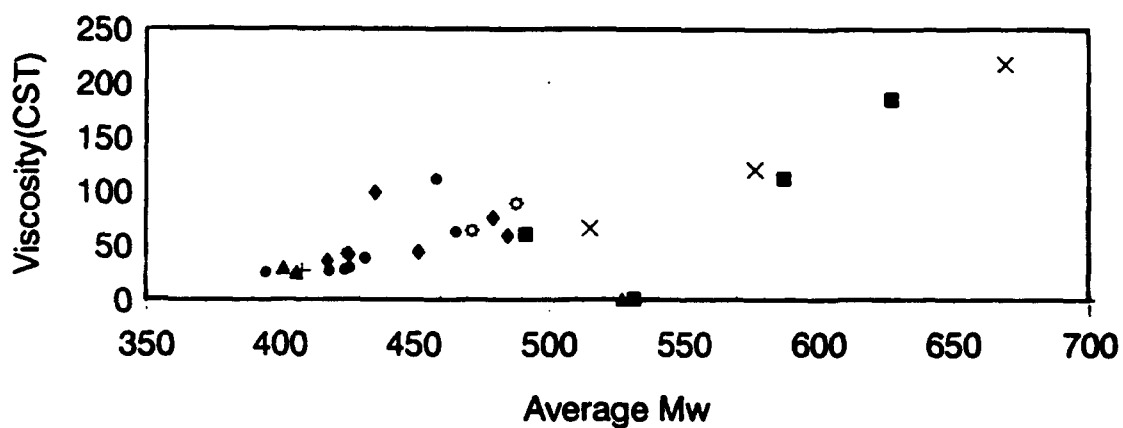


Fig. 4: Viscosity (40C) vs Mn



CONCLUSIONS

Commercial tricresyl phosphate (TCP) solution boils at a temperature of about 420°C to 435°C, and thermally decomposes at about 450°C. At a temperature between 390°C and 410°C, some molecular chains may break and some polymer molecules may still form. The viscosity increases with the heating time and the molecular weight begins to decrease. Below 380°C, the molecular weight and the viscosity of the TCP solution increase significantly with both temperature and heating time in the air environment, and the molecular weight distribution also widens. In the nitrogen environment, these changes are minimal. The results suggest that the oxidation reaction enhances the TCP polymerization below the boiling temperature. Above 450°C, the TCP will decompose thermally under both oxygen and nitrogen environments.

ACKNOWLEDGEMENTS

The author thanks the Air Force Office of Scientific Research (AFSOR) 1993 Summer Research Program and the Lubrication Branch of Wright Patterson Air Force Base for fund and facilities available for this project. Thanks also go to Michael A. Keller and Mary Borchers from the University of Dayton Research Institute for generating the molecular weight distribution and viscosity data for this study.

REFERENCES

1. Wedeven, L.D., "Extended Temperature Range Lubrication with Vaporized Liquids," Wedeven Associates, Inc. Technical Report, WL-TR-91-2034, March 6, 1991.
2. Klaus, E.E., Dada, J.L., and Naidu, S.K., "Formation of Lubricating Films at Elevated Temperature From the Gas Phase," NIST Special Publication 774, Sept. 1988.
3. Lu, C. "Thermal Analysis and Molecular Weight Distribution of Triaryl Phosphates," Final Report for Summer Research Program, Lubrication Branch, Aero Propulsion and Power Directorate, Wright Laboratory (AFMC), Sept. 1992.
4. Aldrich, Catalog Handbook of Fine Chemicals, 1992-1993.
5. CRC Handbook of Chemistry and Physics, 60th edition, CRC Press, Inc.
6. Blake, E.S., Hammann, W.C., Edwards, J.W., Reichard, T.E. and Ort, M.R., "Thermal Stability as a Function of Chemical Structure," Journal of Chemical and Engineering Data, Vol. 6, No. 1, Jan. 1961.

DESIGN OF A STABILIZED CENTER-BODY COMBUSTOR

S. RAGHU
Assistant Professor
Department of Mechanical Engineering

State University of New York
Stony Brook, New York 11794-2300

Final Report for:

Summer Faculty Research Program
Wright Research and Development Laboratory
Wright Patterson Air Force Base, Ohio 45433

Sponsored by:

Air Force Office of Scientific Research
Bolling Air Force Base, Washington, D.C.

September 1993

DESIGN OF A STABILIZED CENTER-BODY COMBUSTOR

S. RAGHU

Assistant Professor

Department of Mechanical Engineering

State University of New York

Stony Brook, New York 11794-2300

ABSTRACT

The objective of the present work was to design a stable, low NO_x , high performance center-body combustor. Five different center-body configurations were studied experimentally to determine their performance characteristics under various operating conditions. The lean blow out limit in all the cases was found to be around 0.03 which is an order of magnitude lower than the present combustors in use. A multiple air-fuel jet configuration with independent control of the primary air showed a promising over-all performance and further tests are in progress to determine their emissions characteristics. Increased and controlled mixing was found to be the key factor in extending the operating range of the combustor.

DESIGN OF A STABILIZED CENTER-BODY COMBUSTOR

S. RAGHU

I. INTRODUCTION

A good stability and performance of the combustion system under a wide range of operating conditions is necessary to meet the demands of both military and commercial gas turbines. In military applications, the maneuverability of the aircraft is increased if large changes in the thrust can be brought about without flame-out conditions of the engines. In commercial aircrafts efficient, low NO_x engines are necessary to meet the increasing demands of environmental regulations. There has recently been a surge of activity on the design of new combustors whose main goal is to achieve the above two objectives by increased mixing as well as staged combustion [1],[2],[3] & [4]. Increased mixing reduces locally hot spots that are conducive to NO_x formations. Staged combustion [1] allows non-stoichiometric combustion, i.e., an initial stage of rich burning and a second stage of lean burning and in both these combustion processes the NO_x formation is considerably less than the stoichiometric burning.

Some important requirements of a gas turbine combustor are:

1. Flame stabilization
2. A low lean blow out limit (stable operation at low loading)
3. A high rich blow out limit (stable operation at high loading)
4. Low NO_x emissions
5. Desirable temperature profiles at the end of the combustion chamber
6. Low pressure drop across the combustor

All these requirements, except for the pressure drop, depend on the efficiency of mixing in one way or another. Mixing of air and fuel is necessary in the primary combustion zone, while mixing of the high temperature

combustion products with the dilution air is necessary downstream of the combustion zone. Control of the mixing process is therefore essential in order to control the stability limits of combustion as well as the emissions of undesirable NOx and THCs.

This work is aimed at developing new concepts for combustor design keeping in mind the above requirements and constraints of a practical combustor. In particular, the present objectives are to increase the range of stable operation of a combustor and the reduction of the NOx and THC emissions through proper control of the mixing processes in the combustor. Studies of some new configurations for the center body designed for this purpose are described in this report.

II. METHODOLOGY

Several configurations of the center-body designed to achieve the fore-mentioned goals were experimented with for comparison of their performance. Figure 1 shows the new center-body combustor configurations used in the present experiments. Important features of each of these are described in the following paragraphs.

Configuration 1

It consists of a circular disk with a central fuel tube of 89 mm length and 12.7 mm diameter extending into the recirculating zone. The blockage ratio between the primary air duct and the disk is 78%. The fuel is introduced into the recirculation zone through a circular array of eight holes of size 2 mm diameter drilled in the extension tube and located 38 mm downstream from the disk. The fuel jets are directed at an angle of 45 degrees inclined back towards the circular disk. The objective of these directed fuel jets is to distribute the fuel into the recirculation zone.

Configuration 2

Fuel in this case is introduced through 8 radial holes of size 1 mm located at the base of the extension piece of the same length as configuration 1 (89 mm). Fuel from these jets flow outward on the disk so that they are

entrained into the annular flow and transported back into the recirculation zone.

Configuration 3

In this configuration an additional disk of 57 mm diameter was placed at a height of 64 mm from the base of the central tube in order to increase the recirculation by directing some of the annular flow into the recirculation zone. Fuel is introduced in the same way as configuration 3.

Configuration 4

This is similar to (1) except that the fuel is introduced at two locations --- one at the base of the disk through eight 1.5 mm diameter holes and the other at a height of 38 mm and directed 45 degrees upstream with the aim of obtaining a more uniform distribution of the fuel in the recirculation zone.

Configuration 5

This was designed after preliminary tests were run on the previous designs. Additional air into the recirculation zone is provided by a separate source than the primary entrained air. It consists of a central manifold with 8 fuel holes of 1.75 mm diameter and concentric holes for air, with a row on the inner side and a row on the outer side of the fuel tubes. The 8 inner air holes have a diameter of 2.2 mm and the outer holes are 2.3 mm diameter and sixteen in number. All these are directed into the recirculating zone. Thus, each fuel jet is surrounded by 4 air jets in order to enhance the mixing of the fuel and the air. The air to these jets are supplied from a source separate from the primary air so that the local mixing can be monitored. With the same exit velocities for the fuel and the air jets, the air fuel ratio based on the volumetric flow rates is about 5. This amount of air in addition to the recirculation air should aid in the stoichiometric combustion for all fuel flow rates. Also, this configuration can sustain combustion with the complete cut-off of primary air thus acting like a pilot flame.

III. EXPERIMENTS

The experiments were conducted in the combustion facility at the WRDC. The details of the facility are described in [5]. Briefly, it consists of a chamber with annular air flow with provision for holding any center-body configuration. The lean blow out limit, the onset of the blue flame and the flame height was measured for all the above configurations for different primary air flow rates. The flame height was directly measured and the equivalence ratios were calculated based on the total amount of air and the fuel, both of which were monitored by flow meters. The center line temperature was measured at a downstream distance of 20 cm (8") from the disk. The pressure drop across the disk was measured by a water manometer.

IV. RESULTS AND DISCUSSION

Figure 2 shows the lean blow out limit for the various configurations. The equivalence ratio corresponding to LBO for all the configurations lie within 0.02 -- 0.04, the configuration 1 having the higher LBO limit while the configuration 2 has the lower LBO limit. This entire range of equivalence ratios are of an order of magnitude lower than those of the current center body combustors (see for eg., [1]-[4]).

Another aspect of performance is the stoichiometric burning of the fuel in the combustor. Figure 3 shows the onset of blue flame for two configurations. For both cases, the blue flame occurs at a very low equivalence ratio indicating limited supply of oxygen in the recirculation at higher fuel flow rates. The other configurations also showed similar trends but the data was not recorded.

The occurrence of sooty flames even at low equivalence ratios indicates that there is not sufficient flow of the primary air into the recirculation zone and also limited entrainment of the combustion products back into the primary flow. The former depends on the strength of the recirculation while the latter depends on the mixing characteristics of the separated shear layer from the disk. Since for a given geometry both these quantities are fixed, higher fuel flow rates result in *locally* rich burning of the fuel. In order to promote larger entrainment, a disk with 8 azimuthal lobes was also fabricated. Although this yielded a slightly better performance, it was

not significant enough to warrant further studies.

Figure 4 shows the center line temperature measured at a downstream location of 8" from the disk for the different configurations. The centerline temperature increases with increasing equivalence ratio as can be expected. However, the temperature appears to be independent of the air flow rates and this can be particularly seen for the cases (1) and (2). This is possibly due to the limited amount of entrainment in the recirculation zone and the limited amount of mixing along the axis of the disk.

Configuration 5:

A more detailed study of this configuration was undertaken since it was designed to overcome the shortcomings of the previous configurations. The present discussion is based on the results available so far. Four parameters were varied: the annular air, the primary air (air from the jet-nozzles, the fuel flow rate and the height of the center-body.

1. Visual observations of the flame

The flame exhibits excellent stability over most of the run conditions. At times an azimuthal rotation of the flame was observed but this did not lead to flame blow out. Several factors that could trigger this azimuthal rotation need to be examined in detail such as the flip-flopping of the air/fuel jets, asymmetry in the annular flow, helical instability of the disk wake or the center-body wake, non-uniformity in the air/fuel injection, etc.

2. Lean Blow Out limits for different air flow rates

2a. Varying the annular air flow rate

Figure 5 shows the lean blow out limit expressed in terms of the overall equivalence ratio plotted as a function of the annular air flow. The overall equivalence ratio is calculated using the total amount of air (annular air + primary air) supplied to the combustor. In all the experiments the primary air was fixed at 99 slpm and the

fuel and the annular air flow rates were varied. The values of the equivalence ratio for lean blow out are around 0.03 and hence an order of magnitude lower than that of the present combustors. A local equivalence ratio in the primary combustion zone (primary equivalence ratio) based on the primary air injected and the fraction of the air entrained into the primary zone from the annular air flow was also calculated. The entrained air was assumed to be a fraction of the annular air. Based on the previous experience of lean blow out values of bluff-body combustors, entrainment ratios of 5 % and 7 % were assumed for calculations and the results are plotted in

figure 6. The equivalence ratio appears to asymptote towards a value of about 0.4 based on 5% entrainment and is slightly lower for a 7% entrainment. Since the flammability limit for propane in a well-stirred reactor is 0.5, the results appear to be consistent to the extent that the equivalence ratio is below the flammability limit.

2b. Effect of varying the primary air

In this set of experiments, the annular air was fixed at 2000 slpm and the lean blow out limit was determined for varying amount of primary air and is shown in figure 7. The primary equivalence ratio is again in the flammability limits for propane and is consistent with the previous set of data.

3. Performance at high loading

The fuel velocity at 20 slpm (maximum flow rate tested with the other configurations) is approximately 17 m/s and the stoichiometric air necessary for combustion is about 320 slpm. If all the combustion air is supplied by the manifold, the velocity of air is 55 m/s and this is approximately half the primary air velocity. This velocity is also of the same order as the reverse flow velocity in the recirculation zone. Thus even at high loadings, there is local stoichiometric burning and hence a high combustion efficiency is maintained in the burner. Visual observation of the flame indicated this trend, i.e., by increasing the amount of primary air injection, a blue flame was obtained even for the highest fuel loading.

4. Performance at low loading

At very low thermal loading, the requirement of the combustor is to sustain a stable flame without blow out or in other words, we would like to extend the lean blow out limit of the combustor. This is easily achieved by cutting off the manifold air supply and this configuration is then similar to the other configurations discussed before in which we saw that the lean blow out was extended by an order of magnitude compared to the conventional burners.

5. Effect of varying the height of the center-body from the disk

The variation of the overall equivalence ratio and the primary equivalence ratio for LBO for different heights of the center-body are shown in figures 8 and 9 respectively. The lean blow limit rapidly increases with the height in both the figures. Visual observation indicated a detached and unstable flame for the higher center-body locations. It is possible that the mixing in the primary zone is inefficient due to a weaker recirculation zone.

6. Rich-lean combustion to reduce NO_x

By controlling the amount of primary air it was possible to obtain a rich (yellow colored flame) in the vortex core and a blue flame both in the disk shear layer as well as in the rest of the primary zone. Since the fuel and the combustion products in the rich burning region (vortex core) are later entrained into the separating shear layer of the disk, a lean combustion occurs in the shear layer zone. Thus it is possible to reduce the NO_x formation which is maximum at the stoichiometric combustion regime. Emissions tests will be conducted in the near future to examine this conjecture.

7. Thermal loading of the combustor/center-body

Another problem encountered with the previous configurations was the excessive heating of the center-body extension tube due to the flame. At higher fuel flow rates the center body was red hot thus, reducing the life time of the tube. The present design has both air and fuel flowing continuously through the center-body in

order to keep it at lower temperatures. Except for the cases of either no primary air injection or very low air flows, the center-body appeared to be sufficiently cooled by the air/fuel flow.

8. Emission tests

It is planned to evaluate the combustion efficiency and the NO_x emissions in the near future.

V. CONCLUSIONS

The objective of the present work was to design a stable, low NO_x, high performance center-body combustor. Five different center-body configurations were studied experimentally to determine their performance characteristics under various operating conditions. The lean blow out limit was found to be around 0.03 which is an order of magnitude lower than the present combustors in use. A configuration with independent control of the primary air and hence primary mixing (configuration 5) also had excellent performance at higher fuel loading and further tests are in progress to determine their emissions characteristics. Increased and controlled mixing was found to be the key factor that governs the performance of a combustor.

VI. ACKNOWLEDGEMENTS

The author would like to acknowledge the help of Dr. K-Y. Hsu (Systems Research Laboratories) in conducting the experiments. This project was initiated by Dr. W.M. Roquemore and his continued interest and suggestions at all stages of this work is gratefully acknowledged.

VII. REFERENCES

1. Micklow, G.J., Roychoudhury, S., Nguyen, H.L. and Cline, M.C. (1993), Emissions reduction by varying the swirler airflow split in advanced gas turbine combustors, J. Engrg for Gas Turb. and Power, Trans. ASME, vol. 115, pp. 563-569.
2. McVey, J.B., Padget, F.C., Rosfjord, T.J., Hu, A.S., Peracchio, A.A., Schlein, B and Tegel, D.R., (1993). Evaluation of low-NO_x combustor concepts for aeroderivative gas turbine engines, J. Engrg for Gas Turb. and

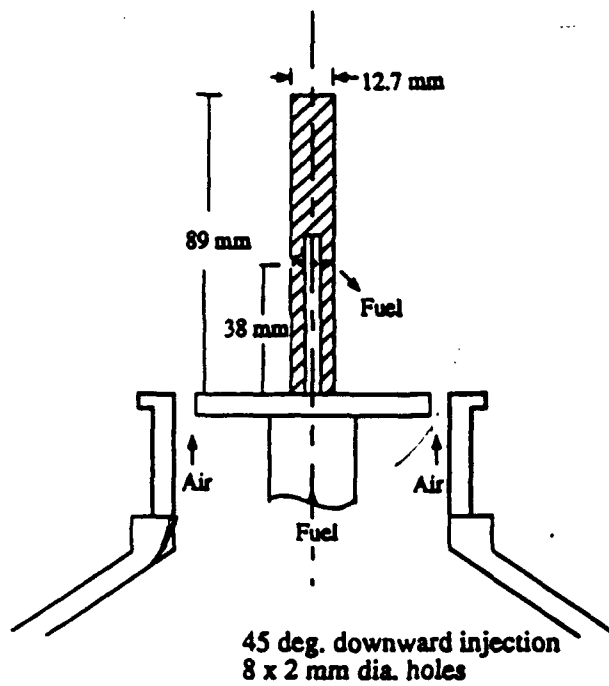
Power, Trans. ASME, vol. 115, pp. 581-587.

3. Cowell, L.H. and Smith, K.O. (1993), Development of a liquid-fueled, lean-premixed gas turbine combustor,

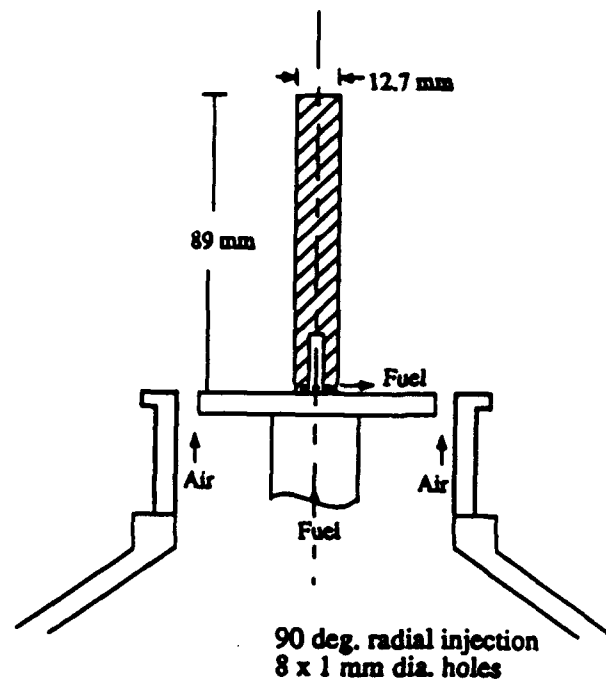
J. Engrg for Gas Turb. and Power, Trans. ASME, vol. 115, pp. 554-562.

4. Aigner, M. and Muller, G. (1993), Second-generation low-emission combustors for ABB gas turbines: Field measurements with GT11N-EV, J. Engrg for Gas Turb. and Power, Trans. ASME, vol. 115, pp. 533-536.

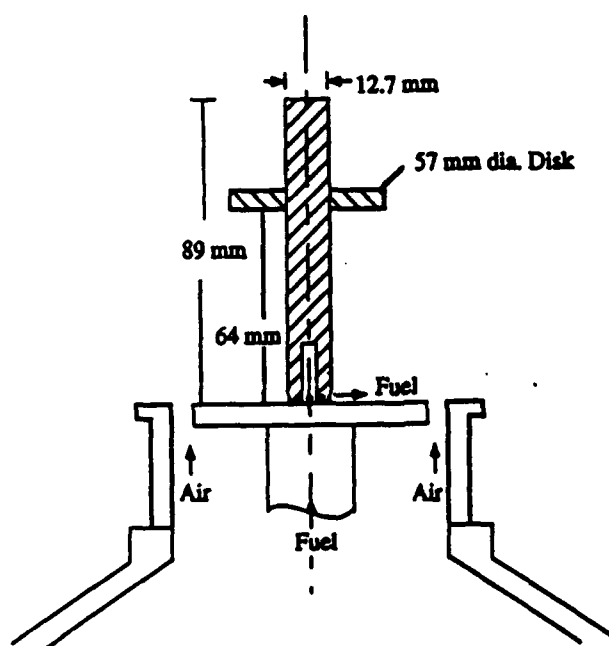
5. Roquemore, W.M., Tankin, R.S., Chiu, H.H. and Lottes, S.A. (1986), A study of bluff-body combustor using laser sheet lighting, Exp. Fluids, vol. 4, pp. 205-213.



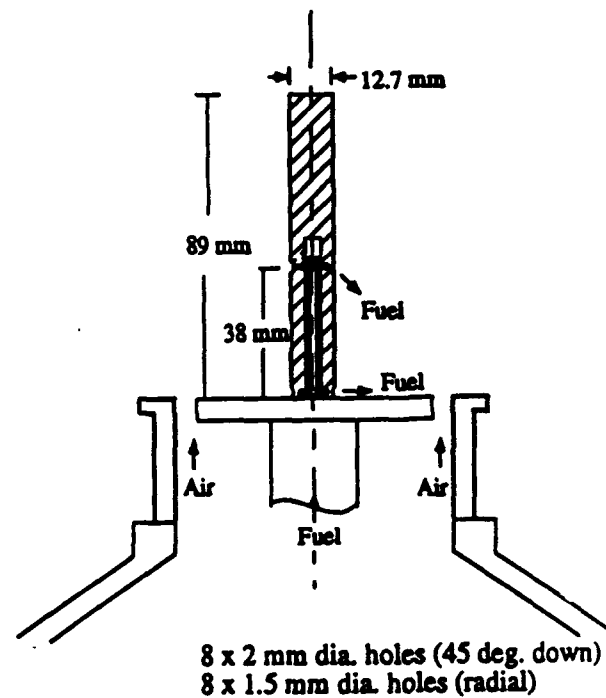
1a. Configuration 1



1b. Configuration 2



1c. Configuration 3



1d. Configuration 4

Figure 1. Bluff-body configurations. Blockage ratio: 76 %

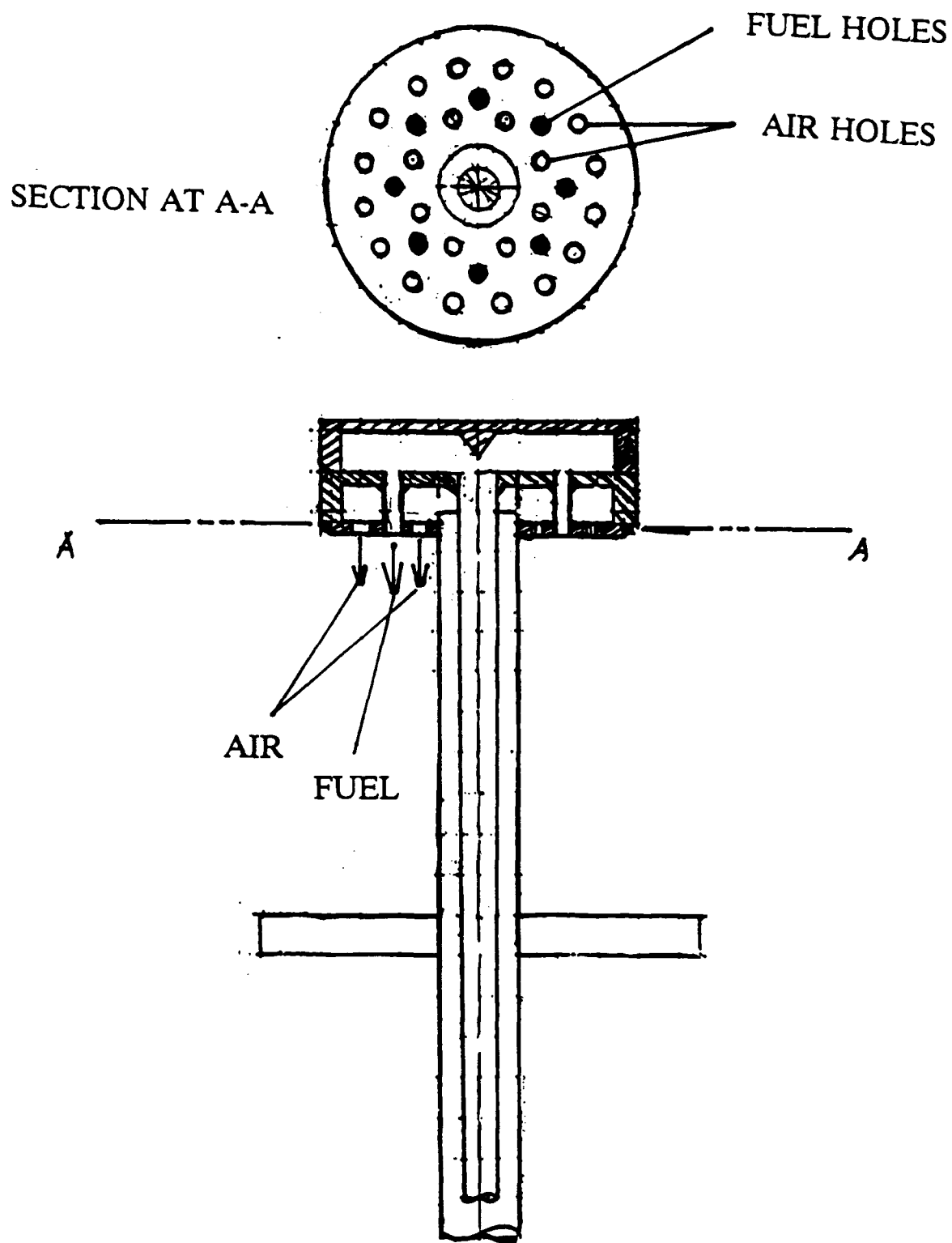


Figure 1e. Configuration 5
62-13

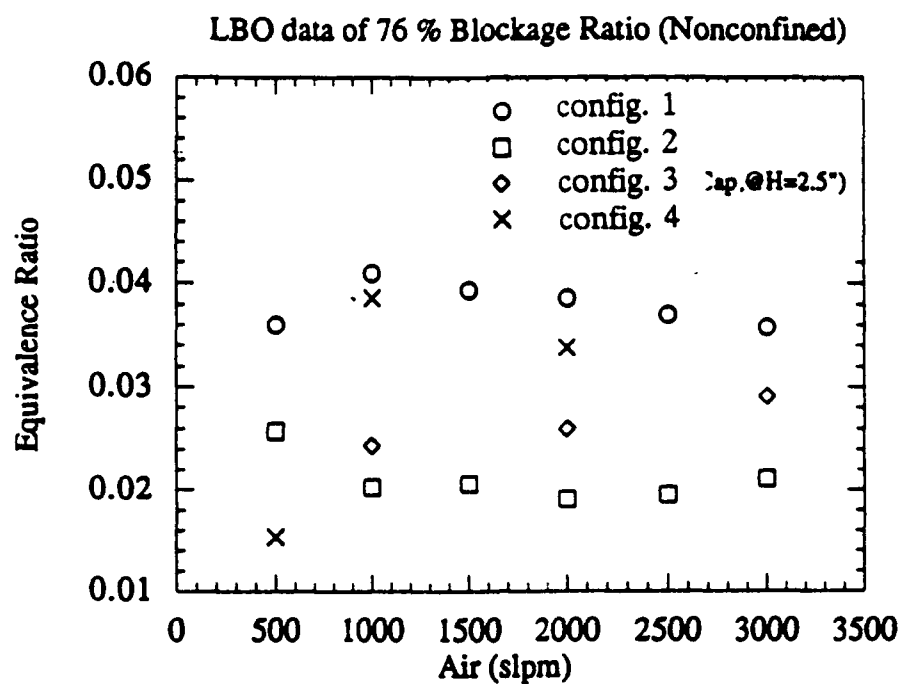


Figure 2. Lean blow-out limit for various configurations

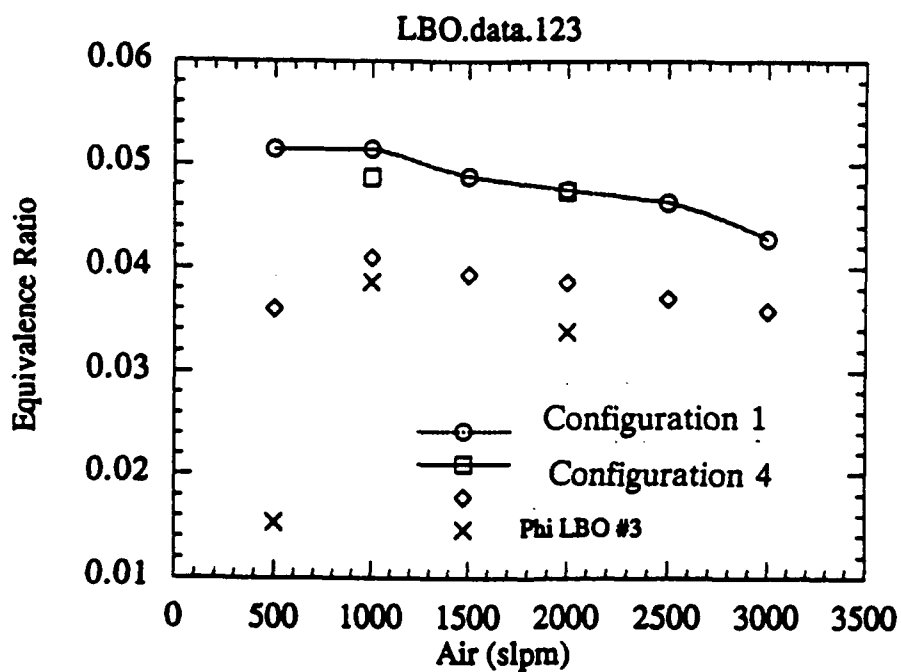
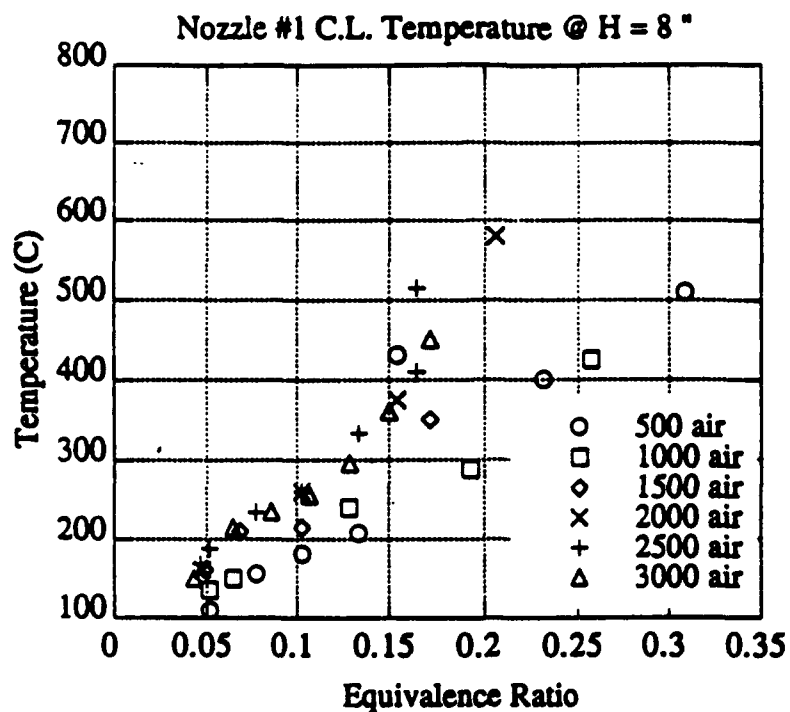
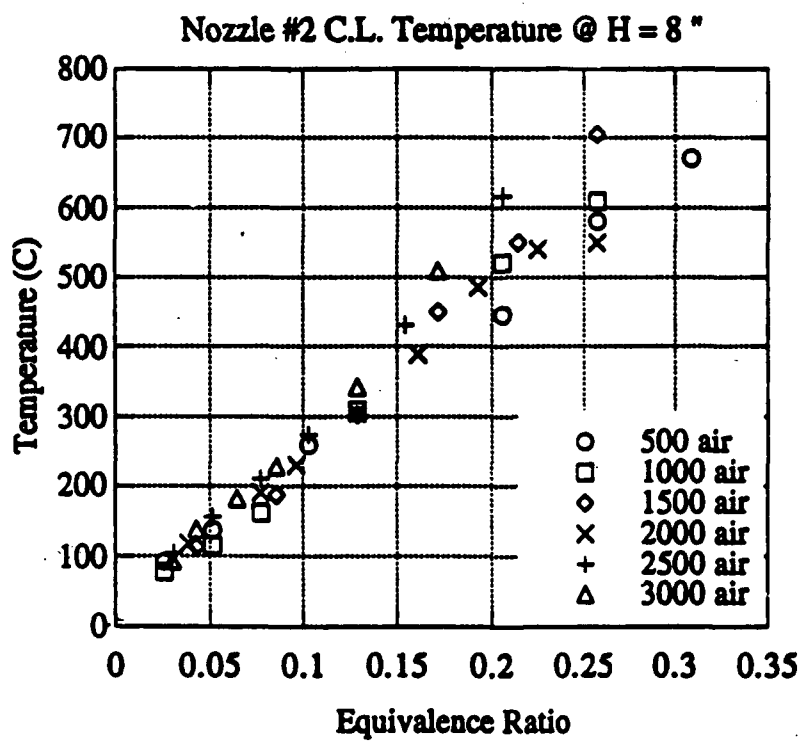


Figure 3. Onset of blue-flame for different configurations.

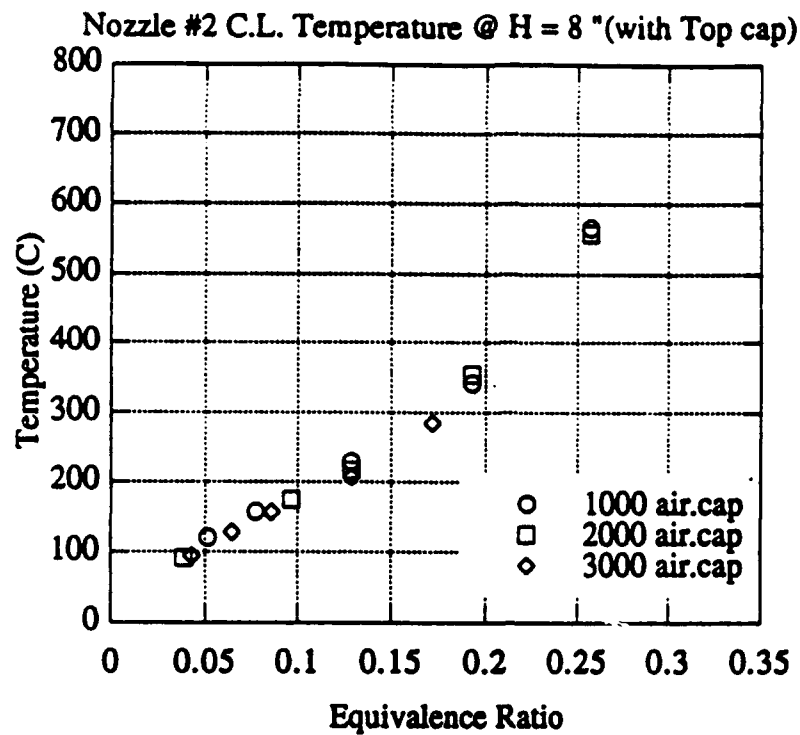


Configuration 1

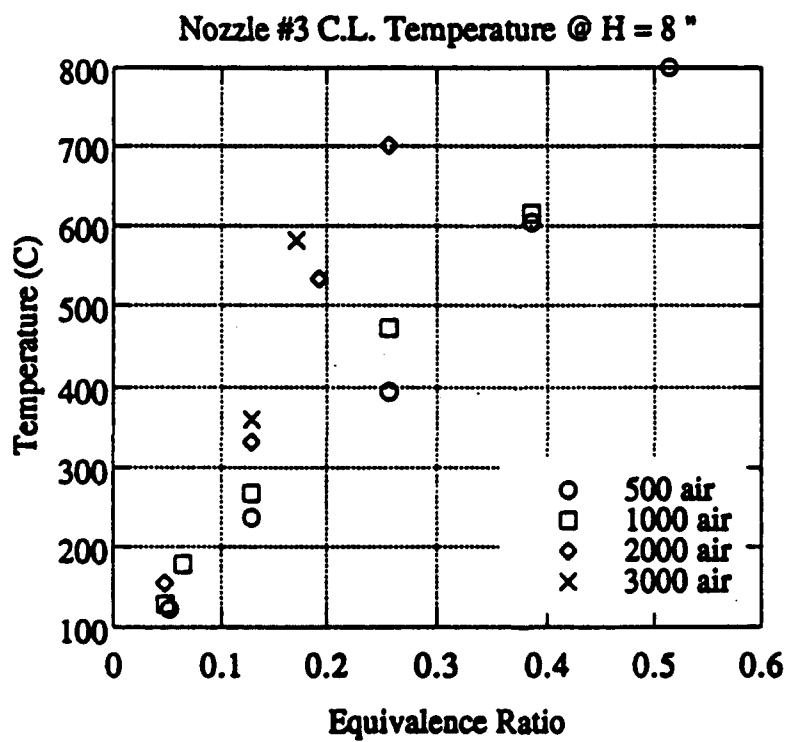


Configuration 2

Figure 4. Center-line temperature at 20 cm downstream distance



Configuration 3



Configuration 4

Figure 4 (contd). Center-line temperature at 20 cm downstream distance

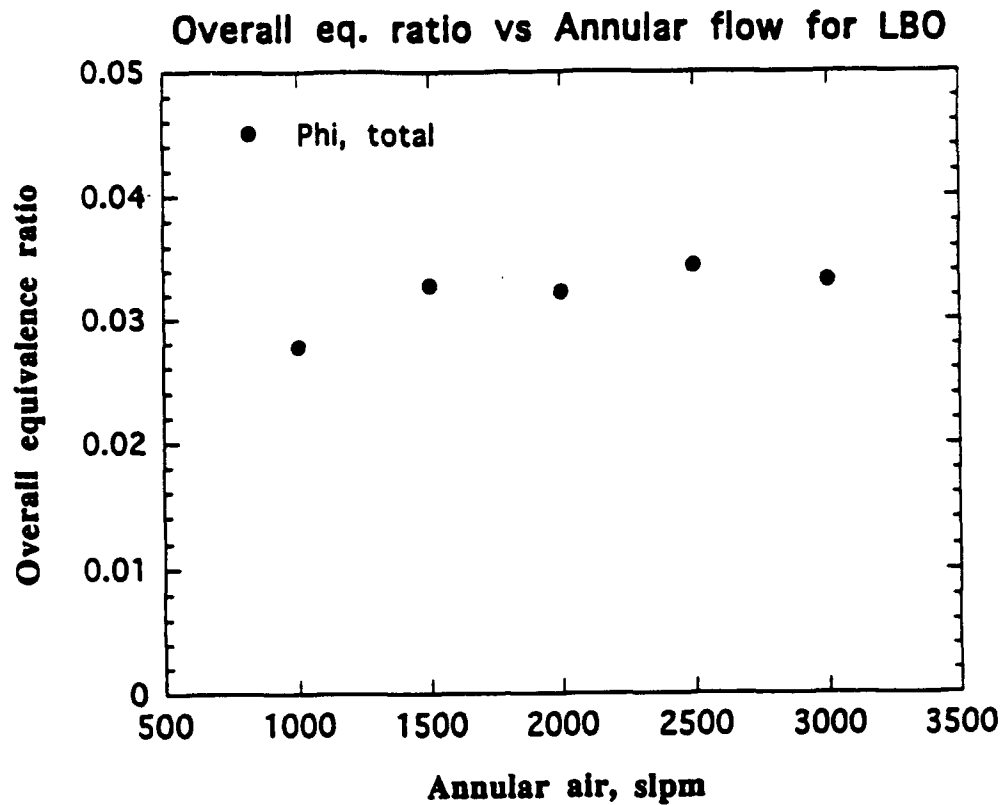


Figure 5. Overall equivalence ratio for lean blow-out vs annular air flow (Configuration 5)

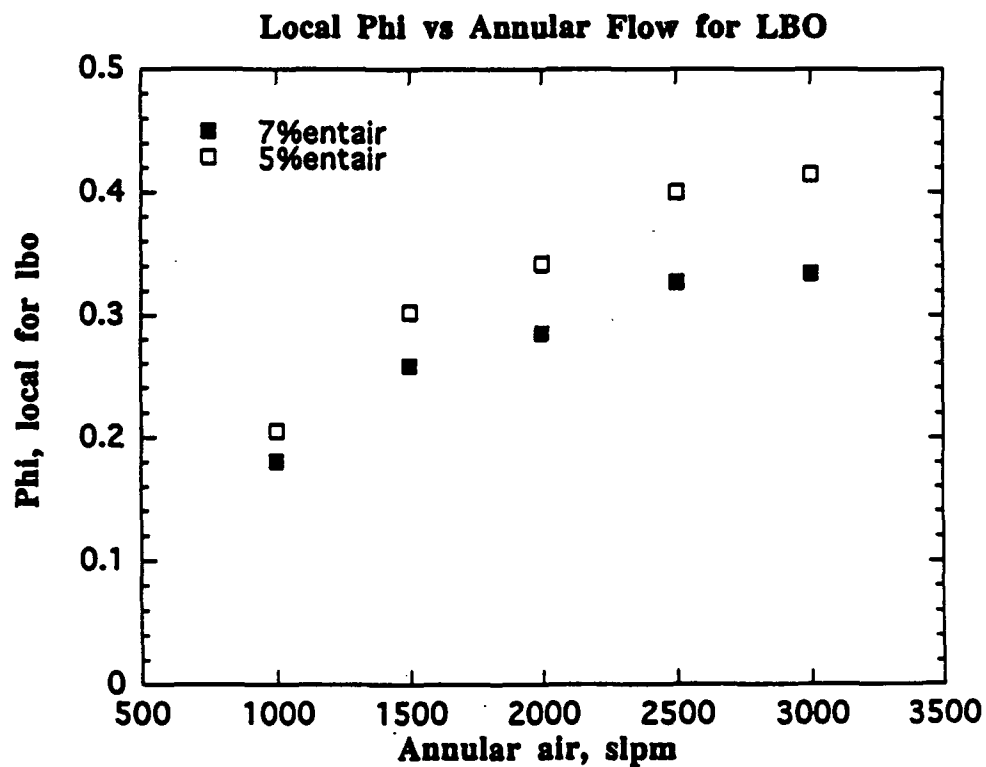


Figure 6. Primary equivalence ratio for lean blow-out vs annular air flow (Configuration 5)

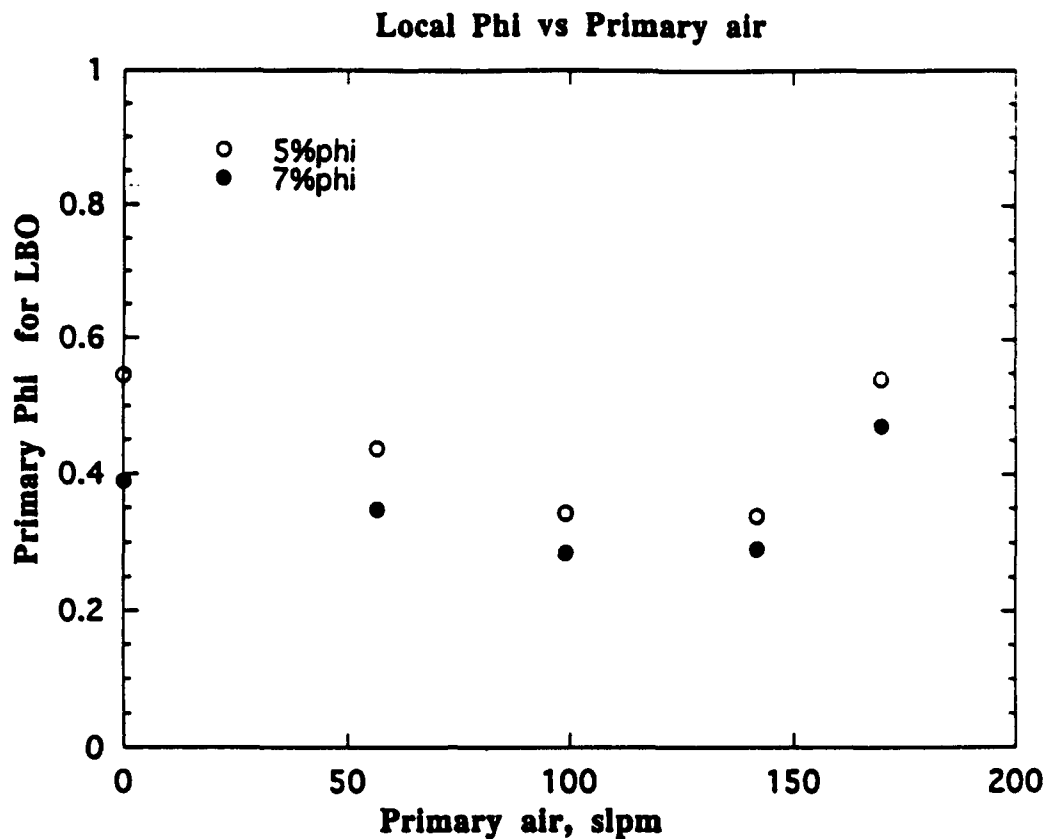


Figure 7. Primary equivalence ratio for LBO vs primary air flow rate. (Configuration 5)

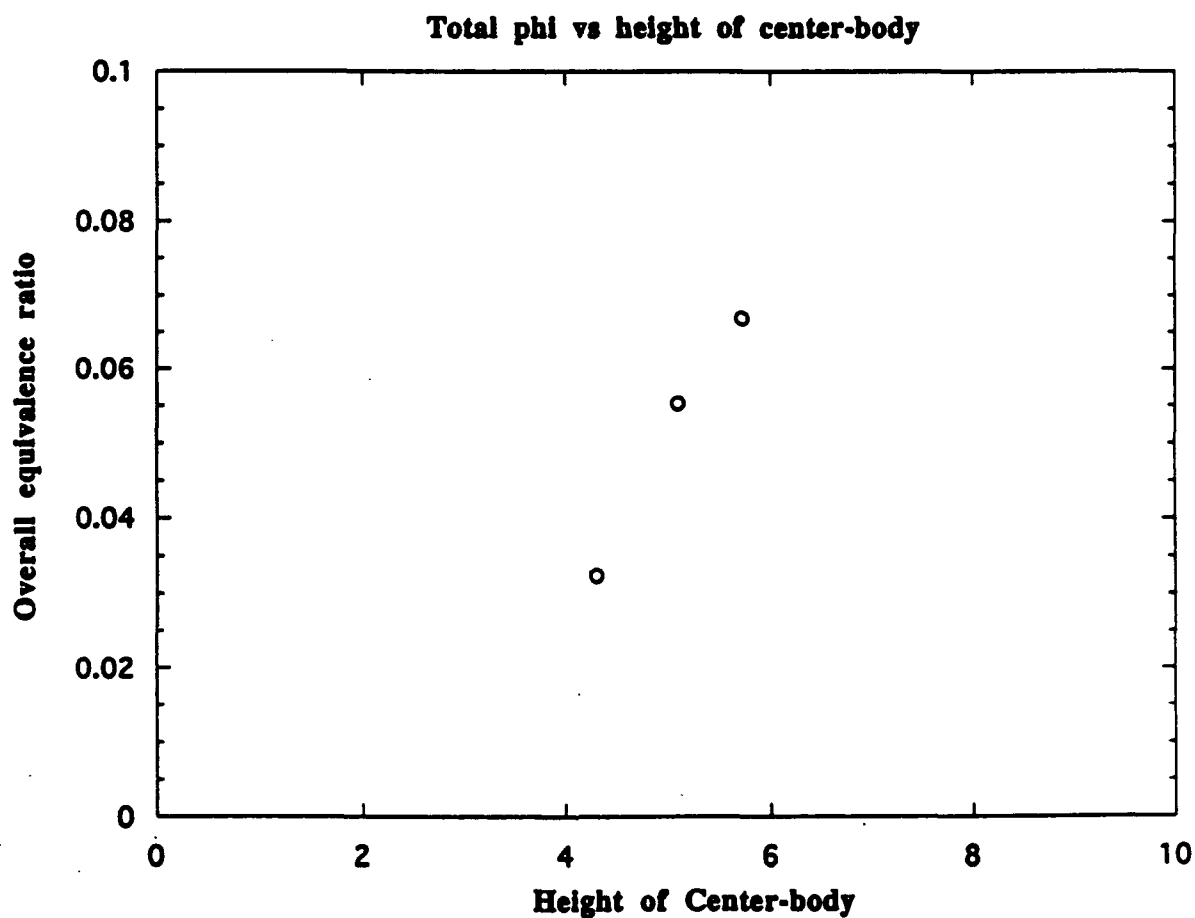


Figure 8. Overall equivalence ratio for LBO for different center-body heights.

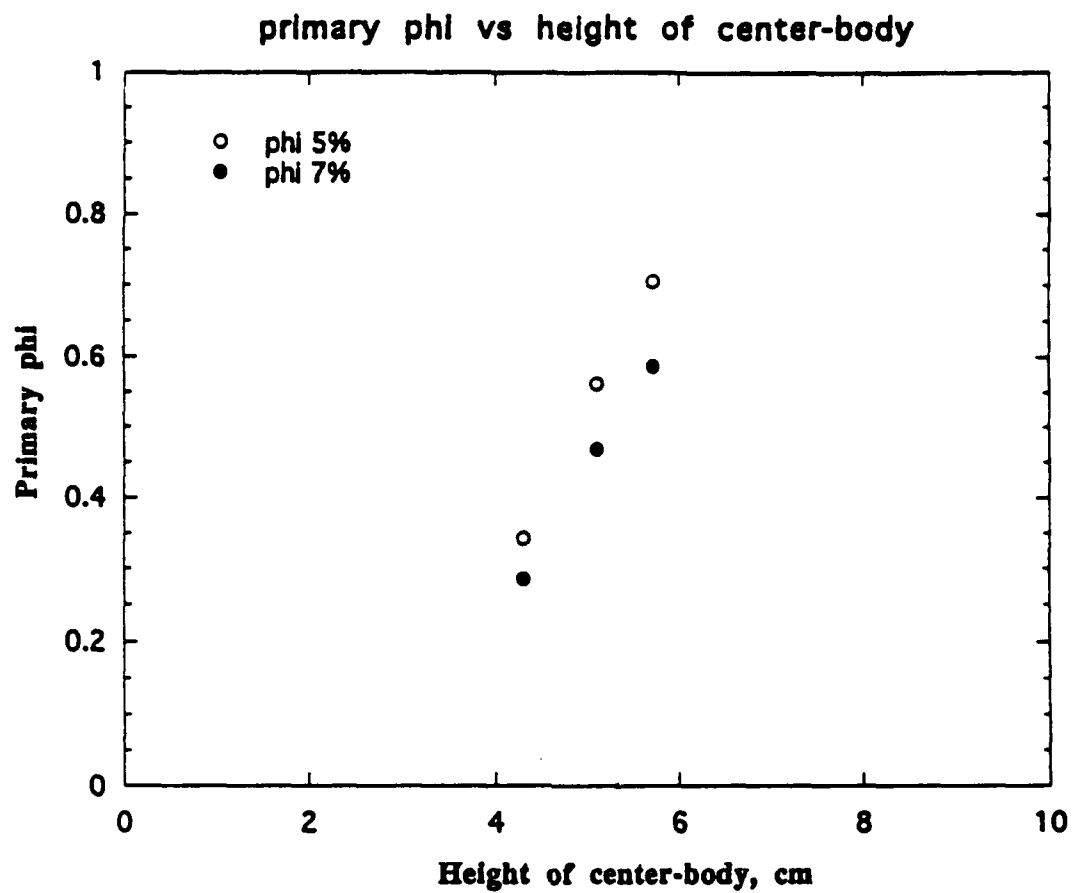


Figure 9. Primary equivalence ratio for LBO for different center-body heights.

Comprehensive Analysis of Switched Reluctance Machine by The Coupled Field and Circuit Modeling Method

Longya Xu
Assistant Professor
Department of Electrical Engineering

The Ohio State University
2015 Neil Avenue
Columbus, Ohio 43210

Final Report for:
Summer Research Program
Wright Laboratory

Sponsored by:
Air Force Office of Scientific Research
5800 Uplander Way
Culver City, CA 90230-6608
August, 1993

COMPREHENSIVE ANALYSIS OF SWITCHED RELUCTANCE MACHINE BY THE COUPLED FIELD AND CIRCUIT MODELING METHOD

Longya Xu
Assistant Professor
Department of Electrical Engineering
The Ohio State University

Abstract

One of the very important research topics in a switched reluctance machine (SRM) system is its complicated dynamics under various transient or fault conditions. These transients or faults impact not only the SRM magnetic field internally but also the associated power control circuit externally. In this research project, a computer model including the power electronic converter, control circuits and the nonlinear magnetic field of the SRM is established. Finite element method is used to model the nonlinear magnetic field of the SRM. The SRM field model is further tightly coupled to the circuit model of the overall system. With simultaneous computation over the entire system including the SRM magnetic field and power converter circuit, the proposed computer model provides a powerful computer tool to investigate the SRM system extensively. Initial experimental results are presented to validate the computer model.

Table of Contents

1. Introduction	4
2. Principle of Switched Reluctance Machine	5
3. Field and Circuit Combined Modeling Method	7
4. Results of Theoretical Analysis	11
5. Results of Experimental Testing	17
6. Conclusions and Future Work	18
References	20

1. Introduction

Although induction machine drives are still the workhorse of industry, the switched reluctance machine (SRM) drive has been actively researched for more than a decade with very promising results [1-3]. The SRM has a simple and rugged construction as well as very good overall performance over a wide torque-speed range [2]. Recently, doubly-salient switched reluctance machines have been found to be an attractive alternative to more conventional PM synchronous and induction machines in converter fed variable-speed drives and generating systems.

The SRM, in effect, is an advanced type of stepping motor in which the current waveform of the machine must be carefully programmed to extract the maximum torque/ampere[4]. The fundamental feature of this type of motor system is that the SRM requires only unidirectional current and thus the converter topology and corresponding switching algorithm of the power converter is greatly simplified. In addition, unidirectional current of the SRM enables that the power circuit configuration is immuned from shooting-through fault, which is a particularly attractive feature for high reliability in aerospace applications.

While the recent work on SRMs are encouraging, the unresolved issues of system transient performance and failure riding-through capability remain. These issues need to be addressed and solved for applications requiring high reliability, such as aerospace propulsion and generating systems. In this project, a new approach of modeling a SRM is proposed and studied. In particular, the field analysis of the SRM by finite element analysis is combined with the circuit analysis of the entire system. As a result, this coupled field-circuit modeling method on the SRM will not only reveal the internal magnetic stress of the SRM during the transient but also provide sufficient information regarding the terminal dynamics of the system.

An experimental SRM has been chosen and the corresponding power converter circuit has been set up to verify the proposed modeling method. The results from the experimental SRM system are very close to those from the model prediction, indicating the accuracy of the field-circuit model.

2. Principle of Switched Reluctance Machine

Electromechanical energy conversion in a SRM, ideally shown in Fig. 1(a), is accomplished by means of a time varying inductance due to the variation of the rotor position. The physics of the model can also be represented by the simple circuit shown in Fig. 1(b).

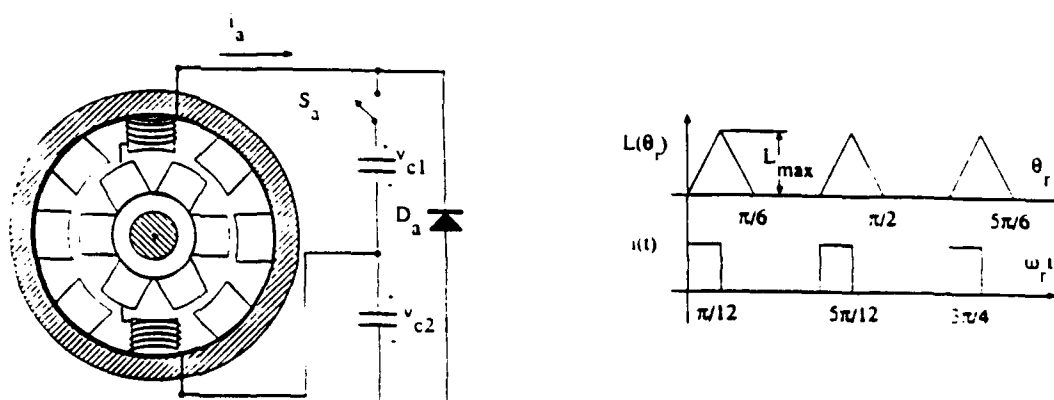


Figure 1.(a) Configuration and Idealized Inductance and Current of SRM

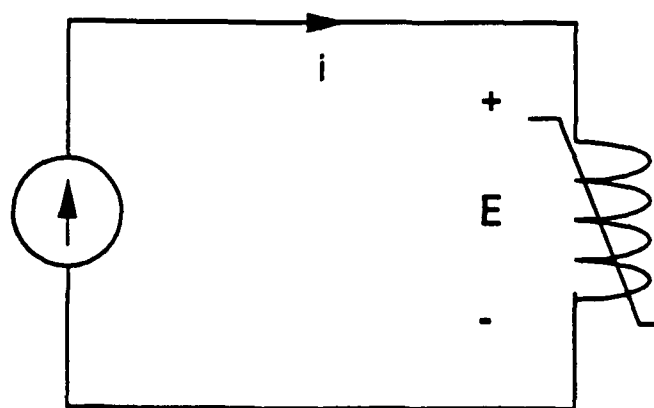


Figure 1.(b) Equivalent Circuit of the Idealized SRM

For simplicity of analysis, all the losses are neglected for the time being, and therefore no resistance is involved in the circuit. The circuit is assumed to be fed with a prescribed current as shown in Fig. 1(a) from the source and the inductance is time-varying due to the rotor rotation. The flux linkage associated with the inductance L is λ and if saturation of the magnetic material is neglected, the flux linkage can be expressed as

$$\lambda = L(\theta_r) i$$

where $L(\theta_r)$ is only a function of rotor angle displacement (saturation neglected). The induced voltage by the inductance is

$$\begin{aligned} E &= \frac{d\lambda}{dt} \\ &= L \frac{di}{dt} + i \frac{dL}{d\theta_r} \frac{d\theta_r}{dt} \end{aligned} \quad (1)$$

The instantaneous power entering the circuit is

$$\begin{aligned} P &= Ei \\ &= Li \frac{di}{dt} + \omega_r i^2 \frac{dL}{d\theta_r} \end{aligned} \quad (2)$$

where the rotor angular speed $d\theta_r/dt$ is assumed to be a constant, ω_r . Replacing the first term by $\frac{1}{2} L \frac{di^2}{dt}$ and splitting the second term into two parts, $\omega_r \frac{1}{2} i^2 \frac{dL}{d\theta_r}$ and $\frac{1}{2} i^2 \frac{dL}{dt}$.

Equation (2) can be further written in the form of

$$\begin{aligned} P &= \frac{1}{2} L \frac{di^2}{dt} + \frac{1}{2} i^2 \frac{dL}{dt} + \omega_r \frac{1}{2} i^2 \frac{dL}{d\theta_r} \\ &= \frac{d}{dt} \left(\frac{1}{2} Li^2 \right) + \omega_r \frac{1}{2} i^2 \frac{dL}{d\theta_r} \end{aligned} \quad (3)$$

Equation (3) yields the well known result that the input electrical power is equal to the derivative of the stored field energy and the mechanical output power. The second term in the right hand side of (3) indicates that the electromagnetic torque can be expressed as:

$$T_e = \frac{1}{2} i^2 \frac{dL}{d\theta_r} \quad (4)$$

By examining (4), the following conclusions can be reached immediately:

- 1) Motoring torque is produced if the SRM machine is excited during the interval in which the inductance of the winding is increasing, that is, when $\frac{dL}{d\theta_r}$ is positive.
- 2) Generating torque is produced if SRM machine is excited during the interval in which the inductance of the winding is decreasing, that is, when $\frac{dL}{d\theta_r}$ is negative.
- 3) Torque production is proportional to the square of the current and therefore independent of current polarity if mutual inductance is not involved. That is, when only one winding at a time is excited.
- 4) For a given current, to maximize the torque, $\frac{dL}{d\theta_r}$, should be maximized. From a motor design point of view, 4) implies that within a certain angle of rotor rotation, the variation in the stator winding inductance should be as large as possible.

Although simple, the circuit model presented in the Fig 1(b) gives little information to the SRM designer and control engineer. In particular, the internal magnetic field of the SRM is totally neglected. The local saturation, magnetic stress and electromagnetic forces under various transients, and the interaction to the power converter can not be predicted. For the above reason, a much more detailed and versatile model accounting for both the SRM internally and the associated external power circuit is necessary.

3. Coupled Field and Circuit Modeling Method

In order to analyze the complicated airgap flux pattern of the SRM and its terminal characteristics simultaneously, the coupled finite element method can be used to solve the terminal equations and the flux equations at the same time. The magnetic field of the SRM is governed by the Poisson equation:

$$\frac{\partial}{\partial x} \left(v \frac{\partial A_z}{\partial x} \right) + \frac{\partial}{\partial y} \left(v \frac{\partial A_z}{\partial y} \right) = -J_0 \quad (5)$$

By solving this magnetostatic equation, the internal distribution of the magnetic field can be obtained. However, the excitation currents which determine the current density, J_0 , must be known for computation.

The terminal voltage equations of the SRM can be easily written according to the circuit configuration of the system, assuming four-phase stator windings

$$\underline{v}_{abcd} = r_l \underline{i}_{abcd} + \frac{d\lambda_{abcd}}{dt} \quad (6)$$

where $\underline{v}_{abcd} = (v_a, v_b, v_c, v_d)^T$ are the terminal voltages across the stator windings; $\underline{i}_{abcd} = (i_a, i_b, i_c, i_d)^T$ are the phase currents of the stator winding; $\lambda_{abcd} = (\lambda_a, \lambda_b, \lambda_c, \lambda_d)^T$ are the flux linkages of the stator windings; and r_l is the windings resistance of the stator. "T" indicates a transposed matrix. To find terminal current, the flux linkage variation as a function of time must be known.

By inspecting Equations (5) and (6), it is seen that the current vector, \underline{i}_{abcd} in (6) is related to the current density J_0 in (5) and the flux linkage vector, λ_{abcd} , is related to the vector potential A_z . In the proposed coupled modeling method, the basic Equations (5) and (6) are to be solved simultaneously by numerical method. A matrix of equations contained in Equation (5) are discretized into elemental form over the entire SRM cross-section as usual. To discretize Equations (6), one critical problem is to discretize the time derivatives, $\frac{d\lambda_{abcd}}{dt}$. The time derivative is replaced by the backward differences. That is,

$$\frac{d\lambda_{abcd}}{dt} = \frac{\Delta\theta}{\Delta t} \frac{\Delta\lambda_{abcd}}{\Delta\theta} = \omega \frac{\lambda_{abcd}(\theta, i_\theta) - \lambda_{abcd}(\theta - \Delta\theta, i_\theta - \Delta i_\theta)}{\Delta\theta} \quad (7)$$

where $\omega = \frac{\Delta\theta}{\Delta t}$. As indicated clearly by Equation (7), the time derivative terms are properly discretized. Then, the global equation set containing Equations (5) and (7) can be obtained and solved simultaneously, provided that the terminal voltages \underline{v}_{abcd} are given.

Two important aspects need more explanations for discretizing Eq. (6) into Eq. (7). First, in Eq. (6), the flux linkage is a function of both the current levels and the rotor positions. Equivalently, the flux linkage changes from one level to another not only because of rotor position variation but also because of current variation. The flux linkage change due to either variation should be included in the discretized equation. Indeed, in Eq. (7) both current and rotor position variations are considered. Physically, it can be interpreted that the backward difference term in Eq. (7) represents not only the induced speed voltage but also the induced transformer voltage. However, it is the induced speed voltage that makes contribution to the electromechanical energy conversion.

Second, The flux linkages in Eq. (6) contain the self and mutual flux linkage components which should be included properly in the discretized equation. Recall that in flux linkage evaluation, the magnetic field and the flux linkages are computed from the vector potential equation. In evaluating magnetic field, all possible currents are included and specified to the coil locations. Therefore, the resultant vector potential solutions automatically contain the components representing self and mutual flux linkages. The flux linkage derived from the vector potential is, therefore, a complete flux linkage. By computing the overall magnetic field and the consequent winding flux linkages, we can avoid unnecessary complexity to split flux linkages into various components.

In summary, the current density in Equations (5) and the currents in (6) are treated as equivalent variables of the global system and so are the vector potential and the flux linkages in the same set of equations. In computing equations of the coupled field and current model, the field equations constantly communicate with the circuit equations to continue the computation till both the field and circuit equations are satisfied simultaneously. Attentions are needed in formulating the incremental current to accelerate numerical convergency process.

Figure 2 shows the computation flow chart used for the proposed modeling method of the SRM. Two major loops are designed in the algorithm, the inner current loop and the outer rotor position loop.

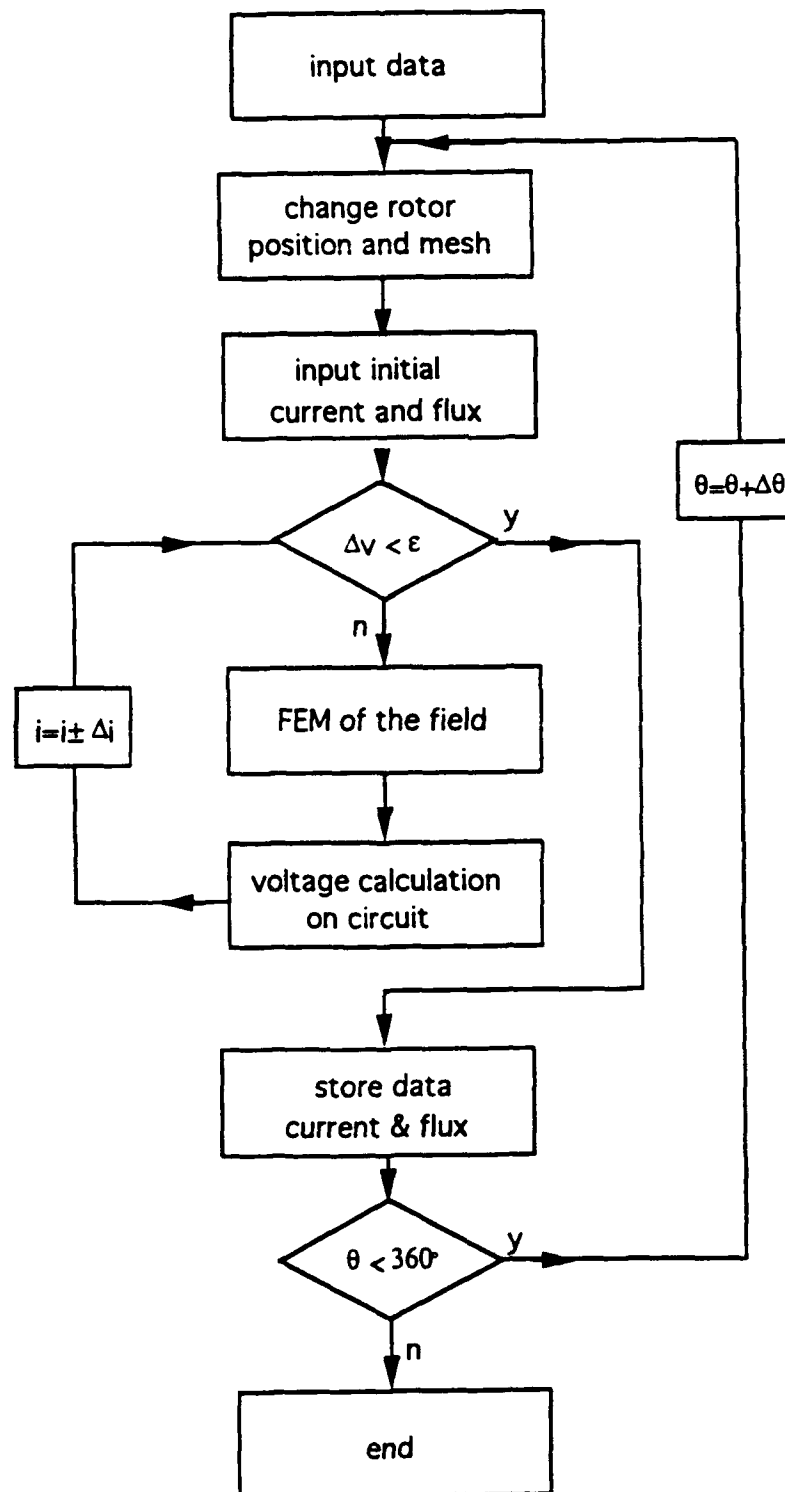


Figure 2. Flow Chart of the Coupled Field and Circuit Modeling Method

4. Results of Theoretical Analysis

The computation procedures outlined in the Flow Chart is implemented and the finite element package, MAGNET, developed by INFOLYTICA Co is used as the major subroutine. Several analysis has been conducted on an existing SRM, SR-90, manufactured by MAGNET PHYSICS Co.. The major specifications of SR-90 are listed in Table 1.

TABLE 1

Power rating	200 watts;	Base Speed	5000 rpm;	Torque	3.67 lb-in;
Voltage	160 volts;	Current (rms)	1.2 amps;	Efficiency	81.66%;
Stator OD	3.286 inch	Rotor OD	1.784 inch;	Core Length	1.96 inch;
Poles number	(stator/rotor) 8/6;			Turns/pole	150.

4.1 Flux Distribution

The 2-dimensional geometry of the SR-90 machine is shown in Fig. 3 and the meshes for FEM over the across-section of the machine is generated in such a way that the meshes of the rotor are separable from those of the stator. When the movement of rotor is assumed, the whole meshes of the rotor advance an incremental angle and are re-stitched to those of the stator. The separable meshes of the rotor from those of the stator greatly simplify the mesh generation process for different rotor positions.

Two typical flux distributions of the SR-90 machine are shown in Figs. 4(a) and (b), where the rotor axis is completely aligned and unaligned with the stator poles, respectively. Since the flux distribution plots display the details of the magnetic field over the entire cross-section, locating local saturation and magnetic force distribution by inspection of flux plots becomes straight forward. SRM geometry optimization can be made based on the information gathered from the flux distribution plots.

The limitation of using the flux distribution plot alone is the lack of information regarding the SRM terminal characteristics. Because the current in the computation is prescribed and movement of the rotor is not included, the back EMF can not be simulated. It may be said that flux plot under the assumed excitation current contributes little to the understanding of the system operation of a SRM.

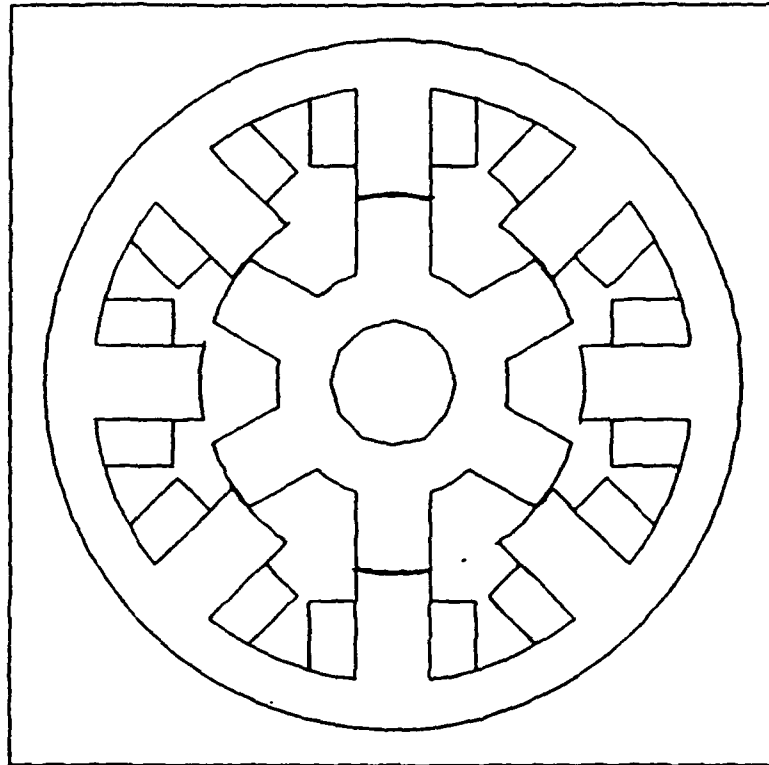
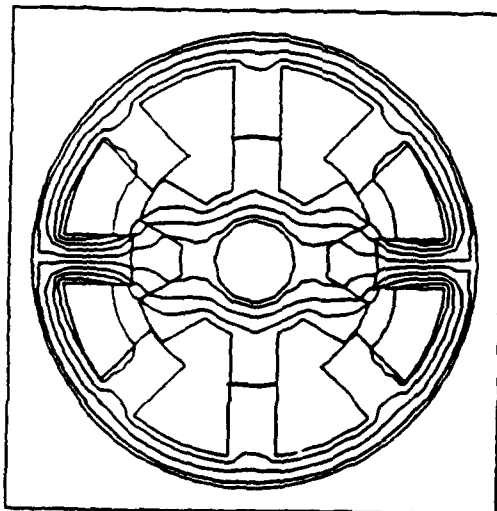
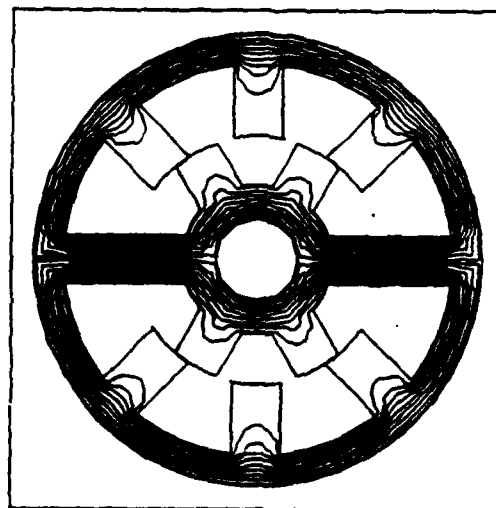


Figure 3. Geometry of SR-90 Switched Reluctance Machine



(a) Rotor is unaligned with the Stator Poles



(b) Rotor is Aligned with the Stator Poles

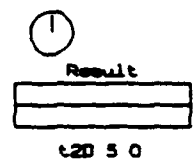


Figure 4. Flux Distribution of SR-90 SRM

4.2 Winding Flux Linkages

As far as the terminal characteristics of an electric machine is concerned, computation of winding flux linkages provides a solution. Flux linkages are calculated because variations of flux linkages due to the mechanical movement determines the induced speed EMF, the kernel of electromechanical energy conversion. In equivalent circuit analysis, flux linkages are modeled by the product of inductance and current. However, many researchers have noted that inductance representation does not adequately account for local saturation or the non-linearity of magnetic field in the machine. If the flux linkages were modeled directly, and highly accurate model would result. This direct modeling of flux linkage could be done using finite element analysis.

Winding flux linkages have been computed for the SR-90 machine in this research project at many current levels for many rotor positions. The results are shown in Fig. 5. As clearly indicated by the computer results, the flux linkages are functions of both rotor positions and current levels. In particular, the relations between the current and flux are highly nonlinear and the non-linearity is further complicated by different rotor positions. When the rotor is near the unaligned position with respect to the stator pole, flux linkage is almost a linear function of current and insensitive to the rotor positions. As soon as the rotor pole reaches positions close to the stator pole, magnetic field saturates and the influence of the rotor position becomes obvious, indicated by the distance between the flux linkage lines in the same figure.

The flux linkage profile described by the figure can be used to explain the inadequacy of SRM equivalent circuit where the complicated SRM is simply represented by lumped resistance or inductance parameters. Compared with the equivalent circuit, the computed flux linkages by FEM give much better results for SRM modeling. For a given SRM the flux linkages can be computed or measured comprehensively to encompass all the possible operating points and then the data can be stored in a look-up table. During system simulation, the look-up table is repetitively accessed to search for the actual operating point.

Nevertheless, in certain situations, computing and storing a large number of data for winding flux linkages have difficulties which, to a certain extent, restrict the use of the method. For example to model multiphase excitation with winding mutual coupling, two or more phases of winding currents are considered. The possible combinations of the

current levels from different phases are vast. To evaluate every possible current combination under many rotor positions, the computation time and storage memories may not be practical, if not impossible. Other limitations of the method include the lack of description of the internal magnetic field and the accuracy problems caused by interpolation of an actual operating point based on finite computed or measured operation points.

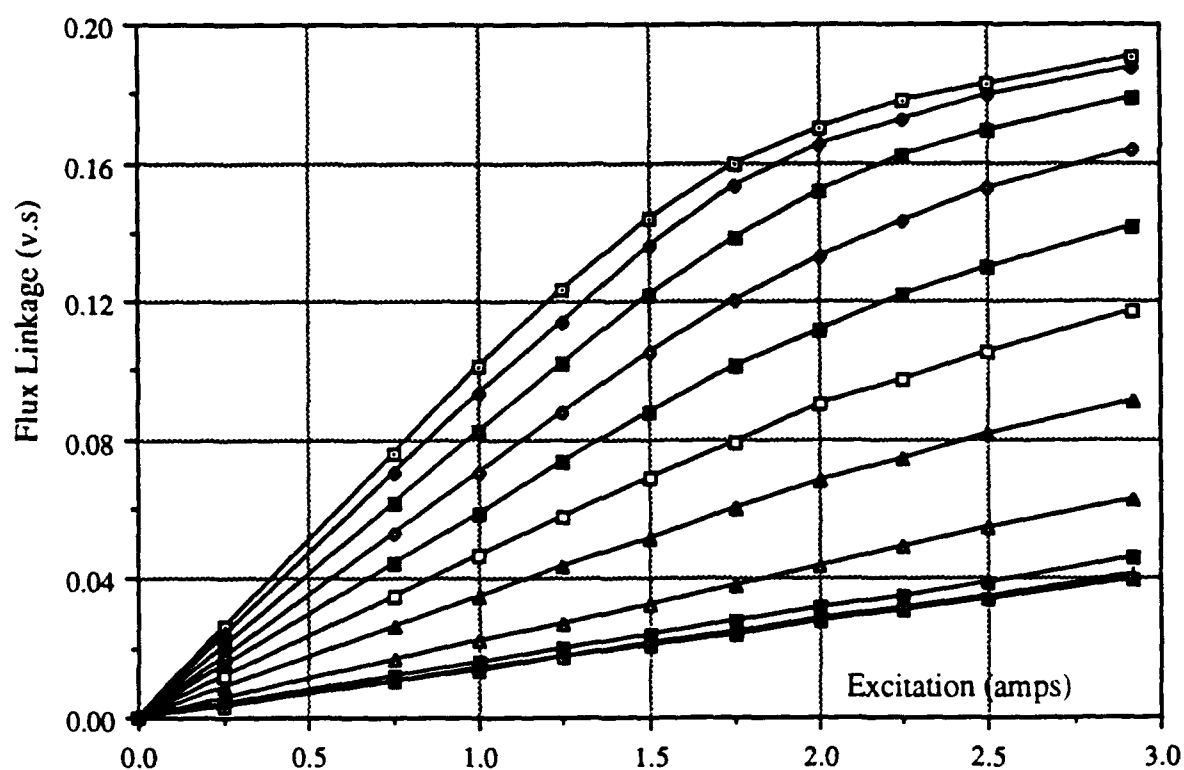


Figure 5. Plot of Flux Linkages of the SR-90 SRM

4.3 Simultaneous Field and Circuit Analysis

From the results and discussions presented above, it is made evident that simultaneous computation on the magnetic field and system circuit is attractive and, in some cases, necessary. The method is especially suitable for investigating dynamic behavior of the SRM in which both the terminal characteristics and corresponding internal magnetic field are concerned. The SR-90 machine is analyzed by the coupled field and circuit modeling method with the operating conditions summarized in Table 2.

TABLE 2

rotor speed	5000 rpm	transistor turn-on angle	30°
DC bus voltage	160 volts	transistor turn-off angle	45°

Fig. 6 shows the internal flux distribution of SR-90 covering 30° rotation of the rotor in 3° steps. It is interesting to notice that the flux density in general increases over the entire cross-section of the SRM in time. However, the corner tips of both rotor and stator poles saturate more quickly when the rotor moves towards the alignment with the stator. This local saturation reduces later when the rotor moves further towards the stator poles. The SRM magnetic field is fully charged in 15° of rotor rotation and gradually discharged to zero at approximately another 15° rotor rotation. From the dynamic plot of the SRM flux distribution, other important variables, such as the torque, radial forces can be conveniently evaluated in the post process.

As stated previously, the coupled field and circuit modeling method not only reveals the internal magnetic field variation, but also gives the description of terminal characteristics on the SRM for the same instants. Fig. 7 shows the current and imposed voltage at the terminal of the winding while the SRM experiences a series of flux changes plotted in Fig. 6. Note that although the input voltage maintained constant, the phase current fluctuates around 1.65 amps after the current reached its peak value at about 8° rotor rotation. Furthermore, the peak current is not corresponding to the instant when the maximum flux linkage occurs.

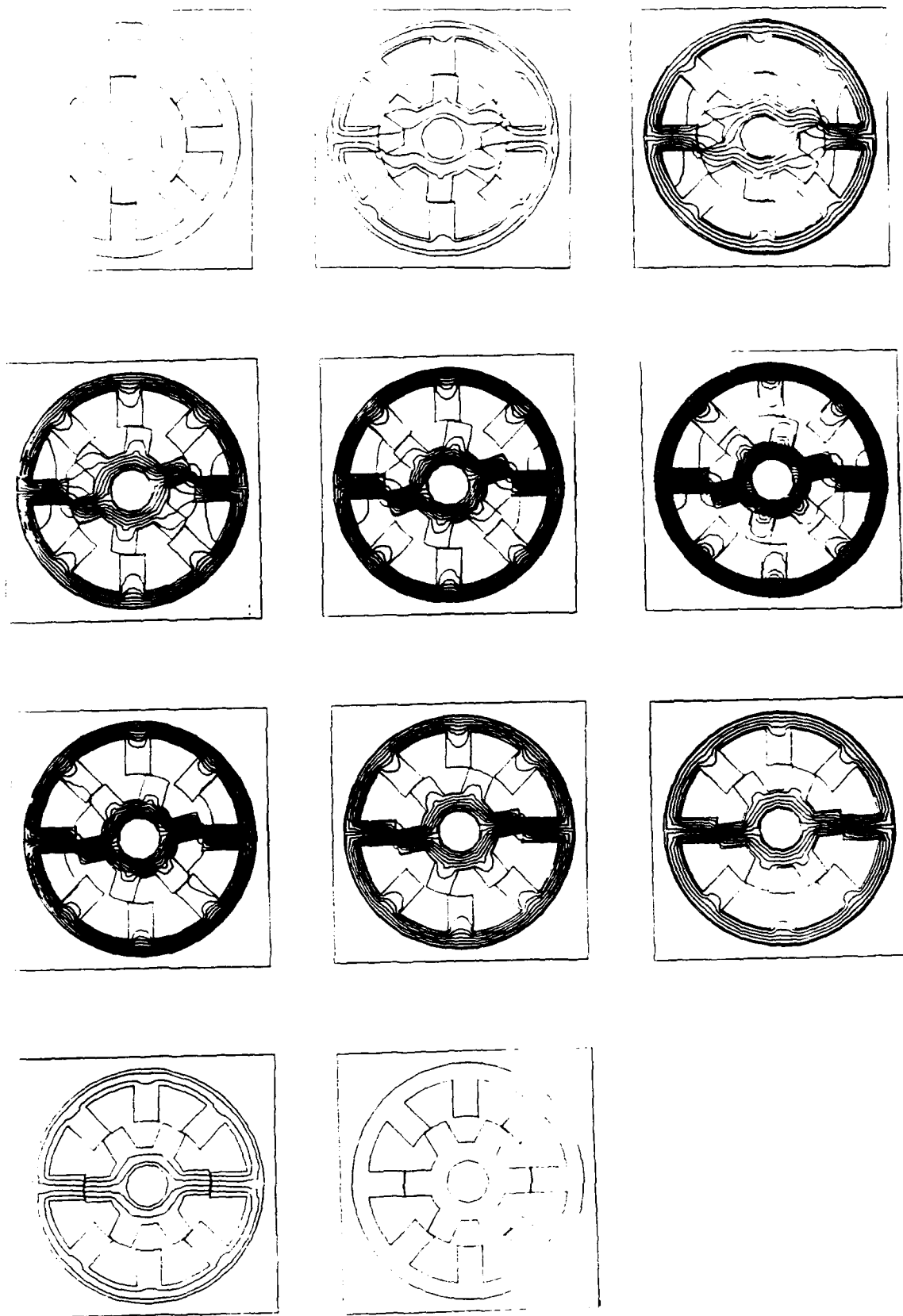


Figure 6. Flux Distribution Covering 30° Rotor Rotation with Voltage Source Control

5. Results of Experimental Testing

For the same operational conditions as simulated in the last section, the SR-90 machine is tested in the laboratory. The SR-90 is mechanically coupled to a dynamometer as the load. During testing, the tested machine delivers 30 oz-in torque. Fig. 8 shows the oscillogram traces of the phase current. Compared to the tested results, the current waveform predicted by the coupled field and circuit modeling method is in very good agreement with that from the testing. The accuracy of the modeling method is verified.

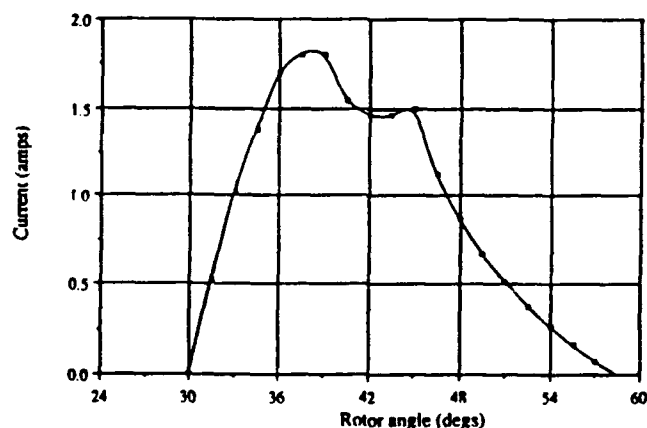


Figure 7. Predicted Current Waveform from Modeling

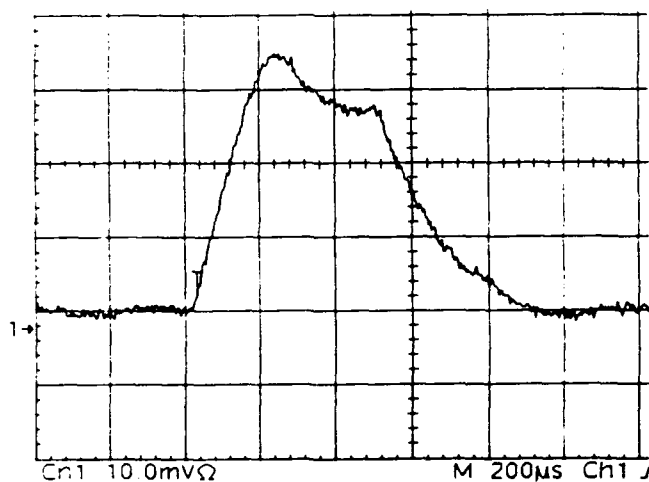


Figure 8. Measured Current Waveform from Testing

6. Conclusions and Future Work

Modeling of the SRM system is very complicated. The complicity stems from the highly nonlinear nature of the magnetic field and its interaction with the unconventional, electronic control of the SRM system. To fully account for the complexity, a simultaneous modeling of the SRM internal magnetic field and external power electronics circuitry is necessary. The coupled field and circuit modeling technique presented and implemented in this research work provides a powerful tool for the situation. Through principle discussion, modeling development, computer implementation, and experimental validation, the following conclusions have been reached.

- 1). The conventional magnetostatic finite element analysis can be extended to include circuit analysis to investigate complicated transient behavior of SRM systems. Formulation of the problem is simple and conveys very understandable physics of the modeled system. The implementation of the modeling can be realized conveniently by using commercially available and technically matured finite element packages used for static field analysis. The programming time and cost for modeling is minimum, and the accuracy is high.
- 2). The outputs from the combined field-circuit modeling method are comprehensive. In the field-circuit coupled approach, investigation is conducted in time domain. Therefore, the solutions to the field equations naturally presents the results of the field variation both in space and in time, as opposed to the those obtained from conventional static field analysis. Furthermore, the modeling method enables the circuit current to interact with the field flux intensively under the constrains imposed simultaneously by the voltage and field equations. The results, therefore, contains all information regarding the effects of interaction between the external circuit and internal magnetic field.
- 3). The coupled field-circuit modeling is versatile and flexible. In the field-circuit modeling of the SRM, the inputs to the system are the terminal voltages to the windings, rather than current, and the geometry and material specifications of the SRM. Both the input functions and the geometry specifications of the SRM can be changed flexibly according to the modeling purpose. By changing the input voltages, various electrical fault conditions can be simulated. In other situations, we can change the geometry or material of the SRM to model mechanical or material errors. Regardless of the origins of the fault or error (electrical or mechanical, internal or external), the results from the modeling will be

EFFECT OF FREE STREAM TURBULENCE ON THE BURST
PHENOMENA AT THE WALL IN A WALL-JET

SAVAS YAVUZKURT

Associate Professor

Department of Mechanical Engineering

The Pennsylvania State University

University Park, PA 16802

Final Report for:

Summer Faculty Research Program 1993

WL/PO Wright Patterson AFB, Ohio

Sponsored by

Air Force Office of Scientific Research

Bolling AFB, Washington, DC

and

WL/POTC Aero Propulsion & Power Directorate

September 1993

EFFECT OF FREE STREAM TURBULENCE ON THE BURST
PHENOMENA AT THE WALL IN A WALL-JET

SAVAS YAVUZKURT
Associate Professor
Department of Mechanical Engineering
The Pennsylvania State University
University Park, PA 16802

Abstract

Effects of free stream turbulence (FST) on the burst phenomena at the wall was studied in a wall-jet flow. It was found that the number of bursts and/or ejections associated with a burst event per unit time increases with increasing intensity of FST. This fact can be used as an explanation of why FST results in an increase in the heat transfer at the wall. For this purpose a wall-jet test rig was designed and built. The initial height and velocity of the jet were 4" and 73.5 ft./s respectively. The ejection processes associated with a burst event were identified from the output of a surface flush hot-film probe positioned at 4" intervals on the surface along the flow direction. The profiles of mean velocity, axial component of the turbulent stress were measured with a horizontal hot-wire probe. Autocorrelations were used to calculate the length scales in the flow direction. Two horizontal hot-wire probes were used for the measurement of length scales in the spanwise and vertical directions. Large amounts of data were collected. Apart from the important result of increase in the rate of ejections with increasing FST intensity, further analysis of data is expected to reveal some of the fundamental mechanisms through which FST affects the rate of heat transfer.

EFFECT OF FREE STREAM TURBULENCE ON THE BURST PHENOMENA AT THE WALL IN A WALL-JET

SAVAS YAVUZKURT

Introduction

Free-stream turbulence (FST) is the turbulence in the approach stream. It is experienced in many applications. For example, nozzle guide vanes and rotor blades in a gas turbine are exposed to high levels of FST.

The FST has an important influence on the heat transfer. Under high levels of turbulence (10-20%) there is an appreciable increase in the heat transfer rate regardless of the character of the boundary layer.

Some representative results in this area can be found in the studies by Kestin (1966), Kearney et al. (1970), Brown and Burton (1978), Bradshaw and Simonich (1978), and Blair (1983). A detailed review of this literature is given by Moffat and Maciejewski (1984). They conclude that the free stream turbulence levels up to 10% cause a proportional increase in heat transfer for constant velocity and accelerating turbulent boundary layers. It is indicated that large effects on the average values may result if the turbulence affects the location of the transition and if the heat transfer data are compared at constant x -Reynolds numbers.

One of the important observations from the literature in this area is that, under the same levels of turbulence, different researchers have found different enhancement of heat transfer rates. This leads to the speculation that not only the velocity scale but also the length scale of the turbulence is important. In fact, Moffat and Maciejewski (1984) relate to this fact and suggest that the effect of the length scale should be investigated.

Most of the studies that were discussed used, one way or another, grid generated turbulence in their experiments where the length and velocity scales are usually small. More recently, the flow fields of jets and wall jets have been used in order to simulate high free stream turbulence encountered in turbomachinery. Moffat and Maciejewski (1985) used a circular wall jet in order to obtain free stream turbulence intensities up to 48%. They measured Stanton numbers which are as much as 350% above the standard zero free stream velocity gradient turbulence correlations. Ames and Moffat (1990) have investigated the effects of free stream turbulence created by 2.5 inch diameter jet injection into a main flow in a plenum chamber followed by a wind tunnel test section on the heat transfer to a flat plate boundary layer. This study used autocorrelations to measure the length scales. In another recent study, MacMullin et al. (1989) investigated the effects of free stream turbulence from a circular wall jet on a flat plate boundary layer heat and momentum transfer with turbulence

intensities 7-18%. They also observed increased Stanton numbers and skin friction coefficient with increasing turbulence intensities. They used autocorrelations for the determination of length scales. The influence of length scale on the Stanton numbers was not conclusive. Rivir et al. (1992) studied the heat transfer in a 2D planar wall jet up to FST intensities of 20% and observed up to 100% increases in heat transfer compared to standard correlations. However, no general correlation could be found that would represent the data from all these studies.

The present belief of the author is that the length scales in the vertical direction to the wall and in the transverse direction to the flow are more important in determining the scales within the boundary layer which affect the heat transfer. Yavuzkurt (1990, 1993) has carried out experiments on the experimental set up used by Ames and Moffat (1990). In these experiments length scales of all the turbulent stresses were measured in all three coordinate directions both in the free stream and within the boundary layer using two triple hot wire probes. A quantity FST number was defined using all the velocity and length scales of the normal stresses in the free stream normalized by the boundary layer thickness and free stream velocity. This quantity correlated the heat transfer data very well.

A detailed discussion on the free stream turbulence distortion for flows approaching stagnation and its effects on heat transfer can be found in Yavuzkurt and Tafti (1987) and Tafti (1989). It was seen from these investigations that there is a need to understand the fundamental mechanisms through which FST effects heat transfer. A fundamental study of near wall layers of the flow under the effects of FST might be helpful in clarifying these issues.

Research on structure of turbulent flows have shown that they contain considerable structure. The presence of near wall "streaks" and "bursts" are well documented. These are the structures that are found in the viscous sublayer and that differentiates turbulent flows from laminar flows. One means of investigating the flow structures is called "quadrant analysis" (Wallace et al. 1972, Willmarth and Lu, 1972). The technique involves partitioning the flow signal into four quadrants based on the instantaneous signs of the fluctuating velocity components u' and v' . As explained in Volino and Simon (1993), in a boundary layer type flow when the wall is heated, a turbulent parcel of fluid moving away from the wall ($v' > 0$) would most likely to be of relatively low velocity ($u' < 0$) and high temperature ($t' > 0$). Such a motion would be classified as a "hot ejection". The present author's opinion is that this hot ejection is related to the burst phenomena and will increase the heat transfer at the wall. Therefore, there is a strong correlation between the instantaneous increase in heat transfer and ejections. It is postulated that FST leads to increases in burst events at the wall thereby increasing the heat transfer. The main objective of this research is to test this hypothesis.

Experimental Procedures

The experiments were carried out in a wall-jet flow as shown in Figure 1. The rationale in using wall-jet flows for simulating high FST is explained in Moffat and Maciejewski (1989), MacMullin et al. (1989) and River et al. (1992). A centrifugal blower with a flow rate 2000 scfm is connected to a transition section containing a honeycomb. Honeycomb was used to even out the disturbances in the blower flow. A sheet metal nozzle was built with an exit which was 4" high and 1 ft wide giving it an aspect ratio of 3. The initial jet velocity at the centerline was about 80 ft./s. To the nozzle exit a test section made of plexiglas was attached. The test surface was 6 ft. long and 1 ft. wide. The side walls were 1 ft. in height in order to prevent external disturbances. The top of the test section was open to facilitate a wall-jet flow. However, a top wall was also built to be used later for boundary layer type flows.

The velocity data was taken with two TSI 1210-T1.5 horizontal hot wire probes. A universal traverse mechanism was built which allowed the probes to be moved in "y" (vertical) and "z" (transverse) directions with respect to each other for space correlation measurements. The probes can also be moved in "x" (axial) direction with a slider mechanism riding on the side wall of the test section. A TSI 1237 surface flush hot film probe was used to measure instantaneous heat transfer thereby to identify the ejections of turbulent fluid from the wall. Test surface had 1/2" holes located at 4" centers for the positioning of the plug that held the hot film probe. The hot wire and hot film probes were connected to a TSI IFA 100 flow analyzer operating in constant temperature anemometry mode. The hot-wire probes were calibrated using a 486 computer and a calibration program utilizing modified King's Law. The same computer was also used for data acquisition and partial data reduction. A DT2829, 8 channel simultaneous A/D board with 30 kHz response for each channel is used as an interface between the analog signals and the computer. The 486 computer produced instantaneous values of streamwise velocity u' for both hot-wire probes and also a value proportional to q' (instantaneous heat transfer) for the hot film probe. These quantities were stored in magnetic disks and later were analyzed in a main frame computer to produce, mean velocities, rms values of u' , autocorrelations of u' and q' , space correlations of u'_1 and u'_2 (subscripts 1 and 2 refer to the two hot wire probes) in y and z directions, and space correlations of u'_1 and q' in the y direction. The correlations were defined as follows:

Autocorrelation of u'

$$R_{uu} = \frac{\overline{u'(x, y, z, t)u'(x, y, z, t + \Delta t)}}{\overline{u'(x, y, z, t)u'(x, y, z, t)}}$$

Space correlation of u_1' and u_2'
in the y direction

$$R_{uu} = \frac{\overline{u_2'(x, y, z, t)u_1'(x, y, +\Delta y, z, t)}}{\overline{u_2'(x, y, z, t)u_2'(x, y, z, t)}}$$

Space correlation of u_1' and u_2'
in the z direction

$$R_{uu} = \frac{\overline{u_2'(x, y, z, t)u_1'(x, y, z + \Delta z, t)}}{\overline{u_2'(x, y, z, t)u_2'(x, y, z, t)}}$$

Space correlation of u' and q'
in the y direction

$$R_{uq} = \frac{\overline{u'(x, \Delta y, 0, t)q'(x, 0, 0, t)}}{\sqrt{\overline{u'^2} \overline{q'^2}}}$$

The data was taken at 4000 Hz with a sample size of 40960 points resulting in 10.2 seconds of real time data for all quantities measured at every measurement location. The measurements were made under isothermal conditions.

Results and Discussion

As stated in the objectives at the end of the introduction section, the main goal was to show that the number of bursts, or ejections related to a burst event increases as the FST increases. This goal was partly achieved. Figure 2 shows the axial Reynolds stress normalized by maximum value of the mean velocity at the y location at which the maximum mean velocity occurs as a function of number of peaks per unit time in the instantaneous heat transfer traces obtained from the hot film probe. The peaks in the instantaneous q traces will be discussed later. This figure shows that as hypothesized there is a definite increase in the number of peaks with increasing FST level.

Figures 3 and 4 show important mean parameters of the wall jet. As expected, the maximum mean velocity decreases linearly and the y_{\max} (location at which the maximum mean velocity occurs) increases linearly in the axial direction. The axial distance was measured from the end of the nozzle or the start of the test section. These figures indicate the presence of a well-behaved wall jet.

Figure 5 shows instantaneous traces of q' at the wall ($y = 0$) indicated by the hot-film probe as a function of time. The values of q' were normalized with the mean value of the heat transfer Q . The traces are shown at two axial stations of 4" and 56" along the centerline ($z = 0$)

of the test surface. As can be seen, there are definite peaks in heat transfer traces. These peaks were identified as ejections that are associated with a burst event following Clark et al. (1992) and Volina and Simon (1993). In calculating number of peaks per unit time the signals were conditioned in order to reduce the uncertainty such that values of $q'/Q < 0.02$ were discarded. Then number of peaks per second were calculated for time intervals of 1s, 2s, 3s, up to 10s. It was seen that in all axial locations number of peaks per unit time reached a steady level within a 10s time interval. Similar results are obtained if the signal is conditioned such that values of $q'/Q < 0.01$ are rejected but number of peaks considered increases accordingly.

Figure 6 shows the normalized mean velocity profiles at six axial stations along the centerline. After some initial nonuniformities the profiles take a well known shape for a wall jet and the maximum in the mean velocity near the wall starts becoming noticeable at $x = 32''$.

Figure 7 shows the normalized turbulence intensity profiles at six axial stations along the centerline. The turbulence intensity far away from the wall at about $y = 100$ mm is high due to very low levels of mean velocity in these regions. However, the intensity which is defined as the intensity of FST at $y = y_{\max}$ increases from 5% to 18% from $x = 16''$ to $x = 64''$. This is the intensity which is used in calculations for Figure 2. In fact at the last axial station of $x = 64''$ intensity is almost constant in the y direction.

Figure 8 shows the autocorrelations of u' at different axial locations and at $y = y_{\max}$. There is a definite increase in the integral timescale after the shear layer of the wall jet is established. These time scales when multiplied with the mean velocity at $y = y_{\max}$ results in the length scales in the axial direction.

Figure 9 gives the space correlation of u' and q' at several axial locations. As can be seen from this figure the values of R_{uq} near $y = 0$ are quite high, they are in the order of 0.6 in the developed wall jet. Considering in the definition of R_{uq} the denominator is $\sqrt{u'^2 \cdot q'^2}$, this high value indicates a very strong correlation between u' and q' as expected. It is also apparent from this figure that the effects of fluctuations far from the wall ($y \approx 60$ mm for a 100 mm initial wall jet height) is felt at the wall, indicating high levels of FST strongly influences the events near the wall.

Figure 10 shows the autocorrelations of q' at several axial locations. Again, the time scales of q' fluctuations increase in the axial direction. Considering that the eddies containing this energy traveling with the speed of the flow near the wall, a length scale for q' eddies or a size for the region of effect can be defined.

A video containing quadrant plots of u'_1 , u'_2 and q' has also been made and it is available from the author.

The space correlation coefficients between u'_1 and u'_2 in the y direction at $y = y_{\max}$ is shown in Figure 11 at several x locations. As can be seen all the length scales in the vertical

direction in the developed wall jet (after $x = 32''$) are about 80 mm long (if extrapolated). This indicates a strong interaction between the outer and inner layers of the flow. In fact, at $x = 16''$ there seems to be a dual length scale. One for the free shear layer and the other for the injected wall jet.

The space correlation coefficients in the z direction for u'_1 and u'_2 can be seen in Figure 12 at several locations along the centerline. It looks like length scales in z direction are also quite long especially in the near jet up to $x = 32''$. However, at stations $x = 48''$ and $64''$ they are very similar to y scales and are about 80 mm long. Again the dual length scale structure can be seen at $x = 4''$ and $16''$.

Figure 13 shows the length scales (L_{ux} , L_{uy} , L_{uz}) of u' in x , y , and z directions. These length scales were obtained at a location where the value of the correlation coefficient is $R_{uu} = 0.5$ due to the limits of the data. There seems to be a decrease in the length scales in the y and z direction for the near jet up to about $48''$. This is the region in which dual length scale structures are obtained. Whereas the length scale in the x direction stays pretty much constant. For the established wall jet however, the length scales in the x and y direction increases in the axial direction and the length scale in the z direction stays pretty much constant. Effect of these length scales on the burst phenomena will be analyzed later.

Conclusions

- Experiments were carried out in a wall jet to explore the effects of high FST on the burst phenomena at the wall.
- It was found that number of ejections identified by the number of peaks in the instantaneous q' traces increases as the FST intensity increases as postulated.
- Length scales of u' were measured in all three coordinate directions using auto and space correlations. These length scales are quite long (~ 80 mm) when compared to initial thickness of the jet and indicates strong interaction between outer and inner layers of the flow. Effect of these scales on burst phenomena will be analyzed later.
- Space correlations between u' and q' in the vertical direction show that the effects of fluctuations as far as 60 mm from the wall are felt at the wall suggesting mechanisms through which FST affects heat transfer.

Future Work

The work here is by no means complete. The large amount of data stored in disks will be analyzed further in order to explore the relationship between the length scales of FST and the burst phenomena. The same experiments will be repeated using two triple wire probes for the measurement of length scales of u' , v' and w' components in all three coordinate directions. It is possible that v' and w' components of FST have more important effects on the events near the wall. VITA techniques such as explained in Bogard and Tiederman (1986) will also be used to identify the burst events. Results of this technique will be compared with the results obtained from the peak counting technique used here. A proposal to carry out this work will be submitted to AFOSR Summer Research Extension Program.

Acknowledgments

Author expresses his deep appreciation to AFOSR Summer Faculty Research Program for supplying this opportunity to carry out this research at WPAFB. His sincere thanks goes to Dr. Richard Rivir of WL/POTC, WPAFB for his help and guidance during this research. The last but not least, the cooperation of Greg Cala, David Pestian and John Schmoll are greatly appreciated; their help made it possible to get so many results in a two month period.

References

- Ames, F. & Moffat, R. J. 1990. Heat Transfer with High Intensity, Large Scale Turbulence: The Flat Plate Turbulent Boundary Layer and the Cylindrical Stagnation Point. Rep. No.: HMT-44 Thermosciences Div. Mech. Engr. Dept., Stanford University.
- Blair, M. F. 1983. Influence of Free Stream Turbulence on Turbulent Boundary Layer Heat Transfer-Part I and II. *ASME J. of Heat Transfer*, February.
- Bogard, D. G. & Tiederman, W. G. 1986. Burst Detection with Single-Point Velocity Measurements. *J. Fluid Mech.*, Vol. 169, pp. 389-413.
- Bradshaw, P., & Simonich, P. 1978. Effect of Free Stream Turbulence on Heat Transfer Through a Turbulent Boundary Layer. *ASME J. of Heat Transfer*, 100-4.
- Brown, A., & Burton, R. C. 1978. The Effects of Free Stream Turbulence Intensity and Velocity Distribution on Heat Transfer to Curved Surfaces. *J. of Engr. for Power*, 100, 159-168.

- Clark, J. P., LaGraff, J. E., Magari, P. J. & Jones, T. V. 1992. Measurement of Turbulent Spots and Intermittency Modelling at Gas Turbine Conditions. *Proc. of the 80th Symp. of NATO/AGARD, Propulsion and Energetics Panel. Heat Transfer and Cooling in Gas Turbines.* Antalya, Turkey, 12-16 Oct. 1992.
- Kearney, D. W., Kays, W. M., & Moffat, R. J. 1970. The Effect of Free Stream Turbulence on Heat Transfer to a Strongly Accelerated Turbulent Boundary Layer. *Proc. of 1970 Heat Transfer and Fluid Mechanics Institute*, edited by T. Sarpkaya.
- Kestin, J. 1966. The Effect of Free Stream Turbulence on Heat Transfer Rates. *Advances in Heat Transfer*.
- MacMullin, R., Elrod, W., & Rivir, R. 1989. Free Stream Turbulence from a Circular Wall Jet on a Flat Plate Heat Transfer and Boundary Layer flow. *Trans. ASME J. of Turbomachinery*, iii, 78-86.
- Moffat, R. J., & Maciejewski, P. K. 1984. Effects of Very High Turbulence on Convective Heat Transfer. *Proc. of HOST Conference*, NASA Conference Publication 2339, NASA Lerc, 381-388.
- Moffat, R. J., & Maciejewski, P. K. 1985. Heat Transfer with Very High Free Stream Turbulence. *Proc. of HOST Conference*, NASA Conference Publication 2405, NASA Lerc, 203-215.
- Rivir, R. B., Troha, W. T., Eckele, W. A., & Schmoll, W. J. 1992. Heat Transfer in High Turbulence Flows-A 2D Planar Wall Jet. *Proc. NATO/AGARD 80th Symposium of the Propulsion and Energetics Panel*, Antalya, Turkey, 12-16 October 1992.
- Tafti, D., 1989. Prediction of Heat Transfer Characteristics for Discrete Hole Film Cooling on Flat Plate and Turbine Blades. Ph.D. Dissertation, Penn State Univ., Dept. of Mechanical Engr.
- Volino, R. J. & Simon, T. W. 1993. An Application of Octant Analysis to Turbulent and Transitional Flow Data. ASME Paper #93-GT-72. Presented at the Intl. Gas Turbine and Aeroengine Congress and Exposition, Cincinnati, OH, May 24-27, 1993.
- Wallace, J. M., Eckelmann, H. & Brodkey, R. S., 1972. The Wall Region in Turbulent Shear Flow. *J. Fluid Mech.*, Vol. 54, Part 1, pp. 39-48.

Willmarth, W. W. & Lu, S. S. 1972. Structure of the Reynolds Stress Near the Wall. *J. Fluid Mech.*, Vol. 55, Part 1, pp. 65-92.

Yavuzkurt, S., & Tafti, D. 1987. Turbulence Modeling for Flat Plate and Turbine Airfoil with Discrete Film Cooling. Contractors Report RFQ:PC693359, Textron Lycoming Corp., Stratford, Conn.

Yavuzkurt, S. 1990. Characterization of Length and Velocity Scales of Free Stream Turbulence and Investigation of their Effects on Surface Heat Transfer. Center for Turbulence Research, Stanford University, Annual Research Briefs 1990, pp. 253-262.

Yavuzkurt, S. & Batchelder 1993. A Correlation for Heat Transfer under High Free Stream Turbulence Conditions. *Proc. of 9th Symposium on Turbulent Shear Flows*, Kyoto, Japan, Aug. 10-18, 1993.

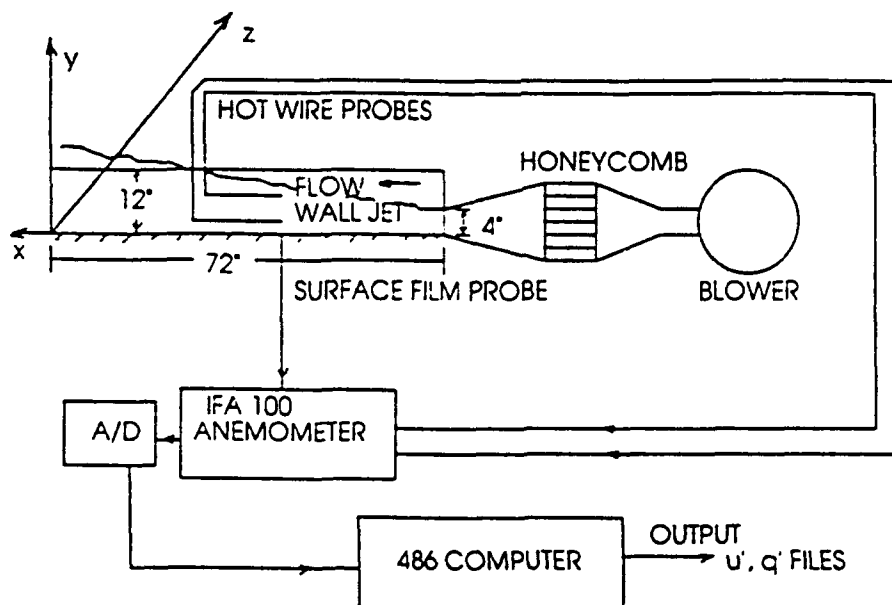


FIGURE 1. WALL JET TEST RIG AND DATA ACQUISITION SYSTEM

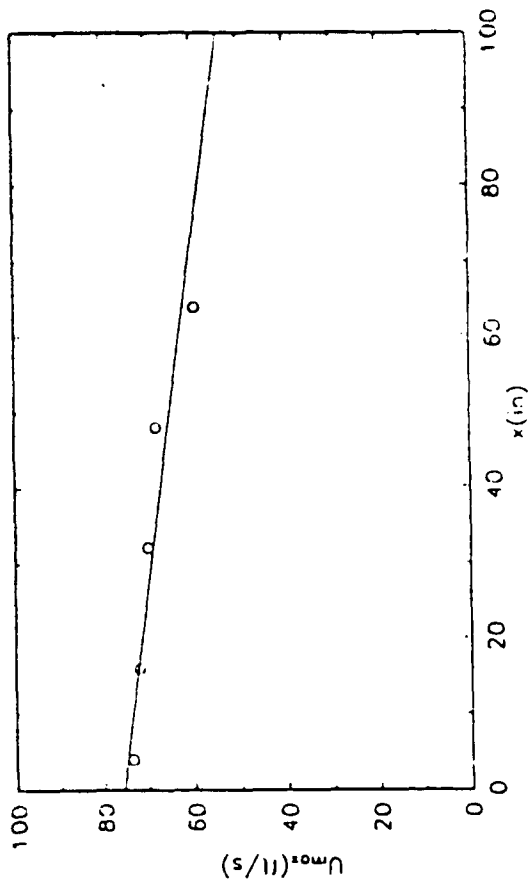


FIGURE 3. U_{max} vs. x IN THE WALL JET RIG

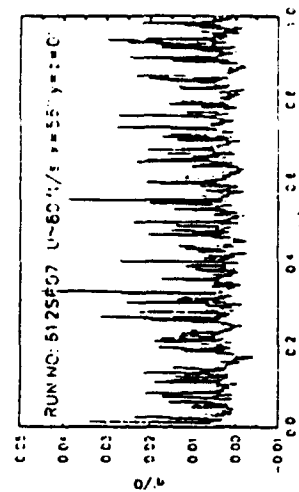
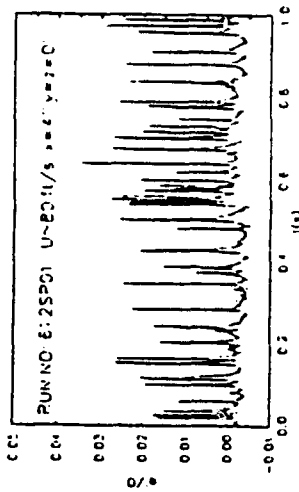


FIGURE 4. q' vs. t IN THE WALL JET RIG

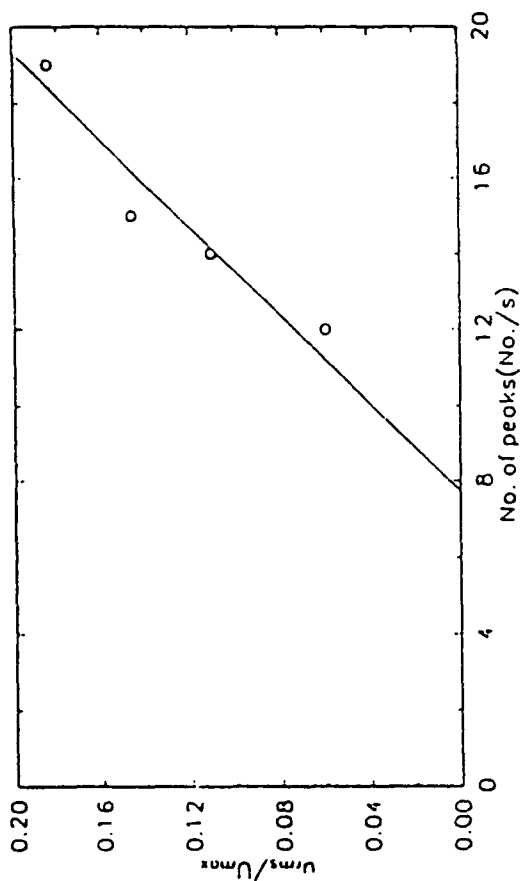


FIGURE 2. U_{rms}/U_{max} vs. NUMBER OF PEAKS IN q' PER UNIT TIME WALL JET RIG $q'/Q < 0.02$ ARE FILTERED OUT

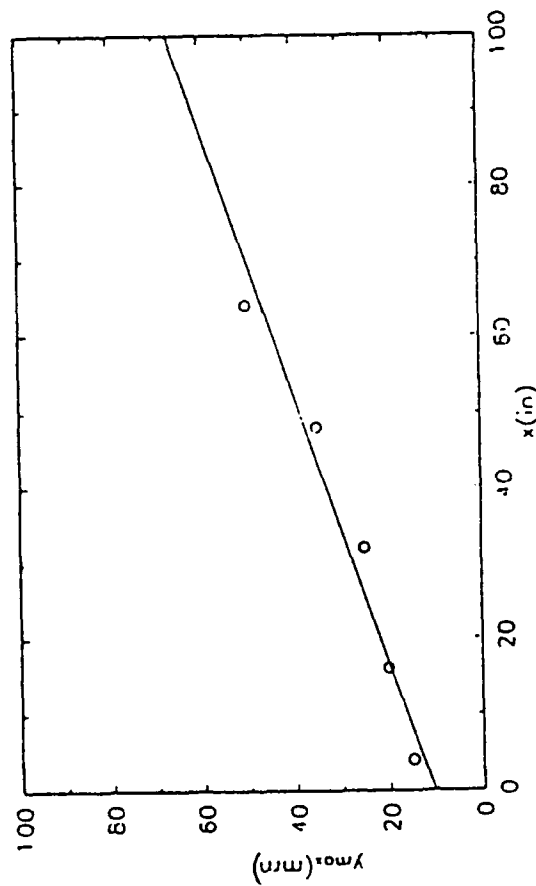


FIGURE 4. y_{max} vs. x IN THE WALL JET RIG

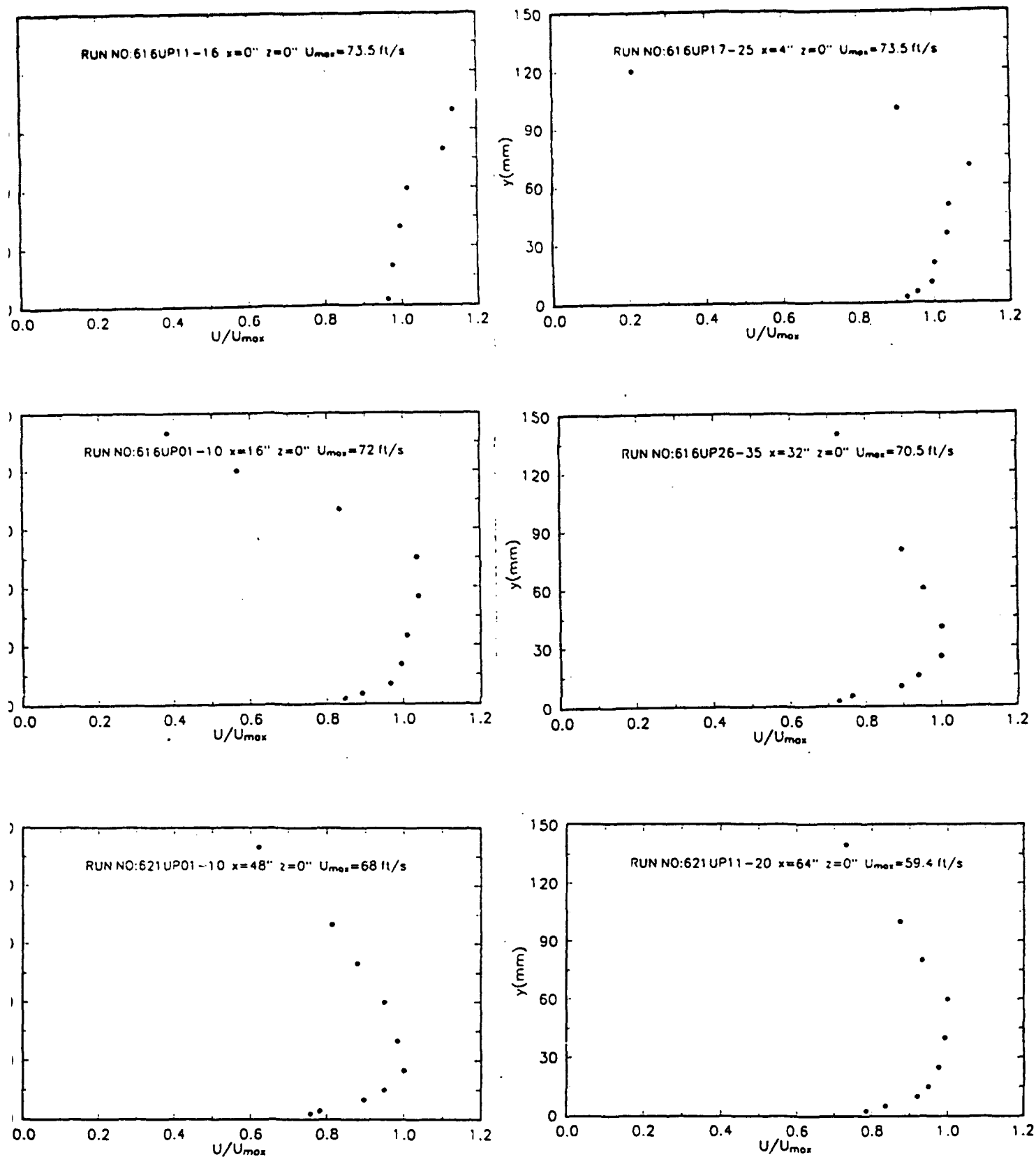


FIGURE 6. MEAN VELOCITY PROFILES IN THE WALL JET RIG

COPY AVAILABLE TO DTIC FROM NATIONAL AERONAUTICS AND SPACE ADMINISTRATION

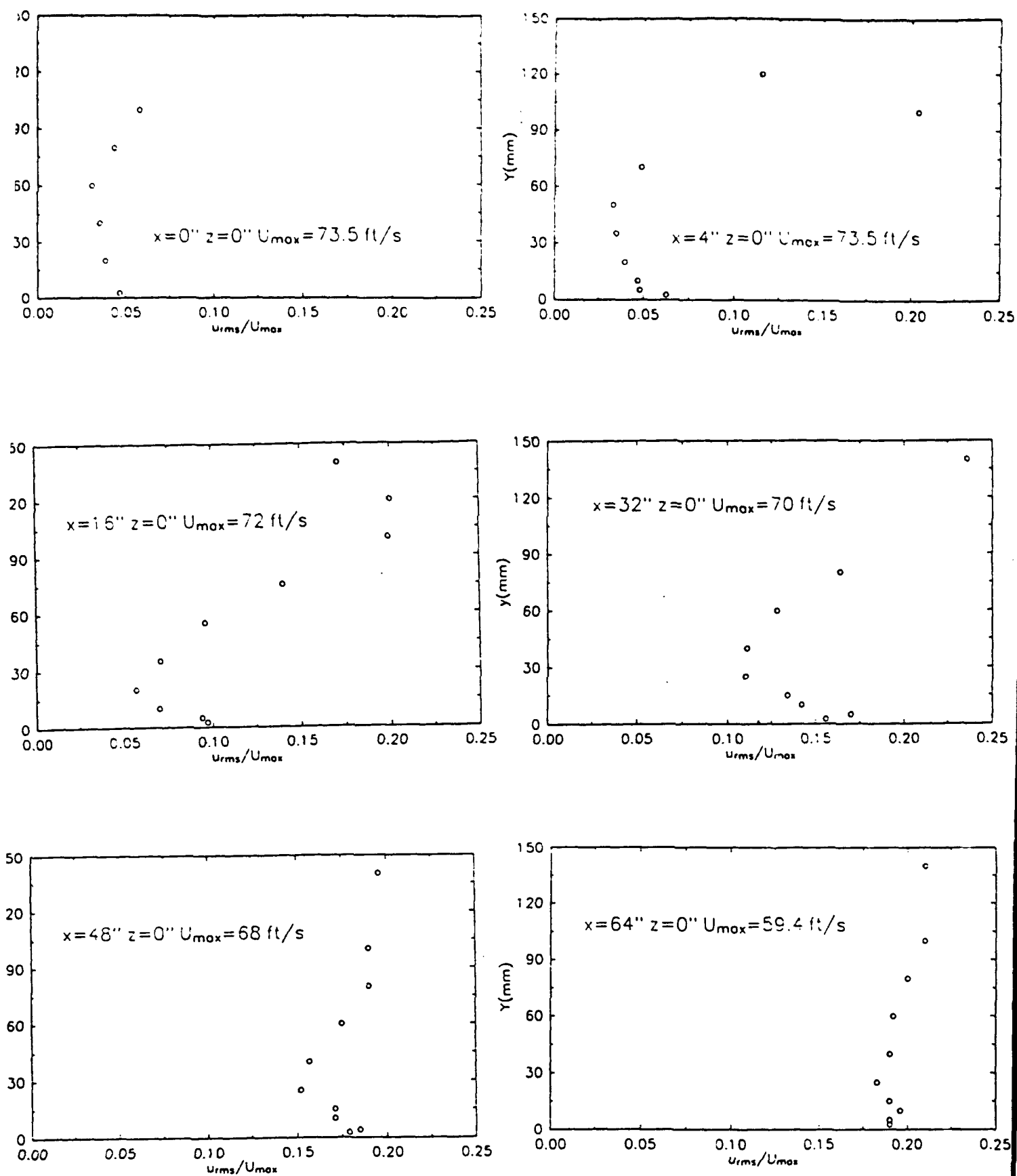


FIGURE 7. TURBULENCE INTENSITY IN THE WALL JET RIG

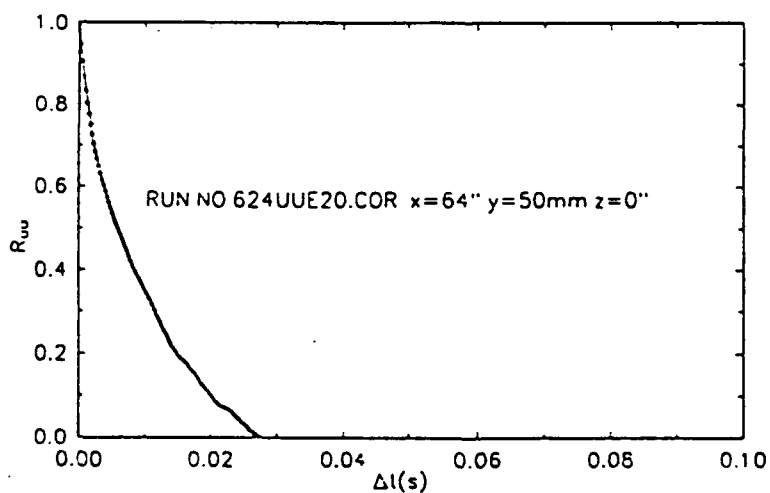
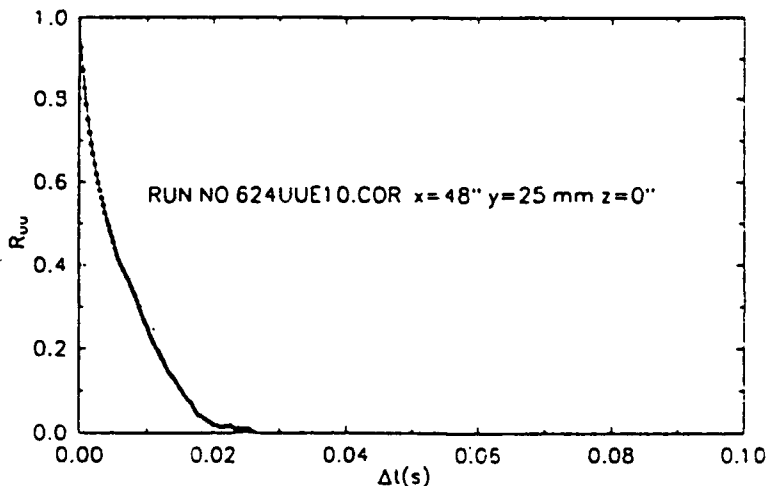
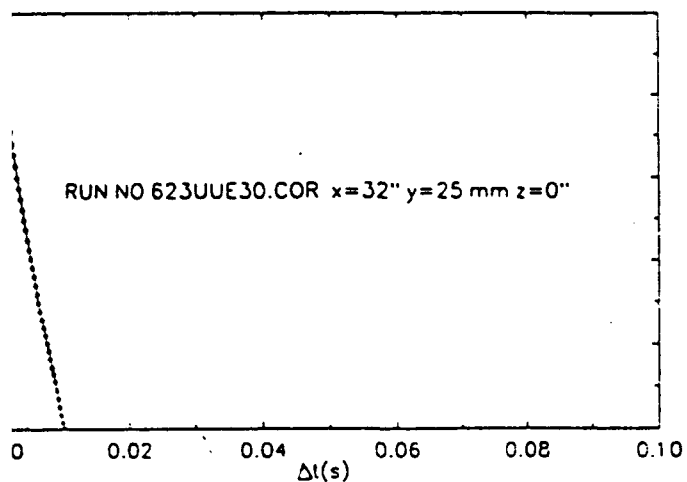
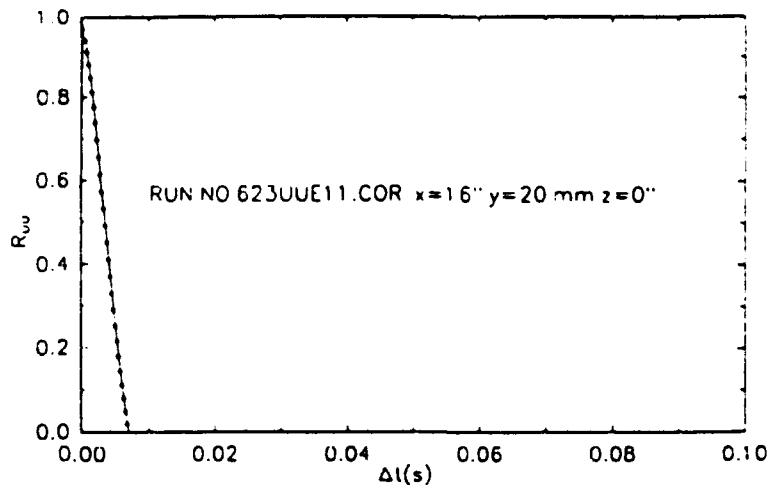
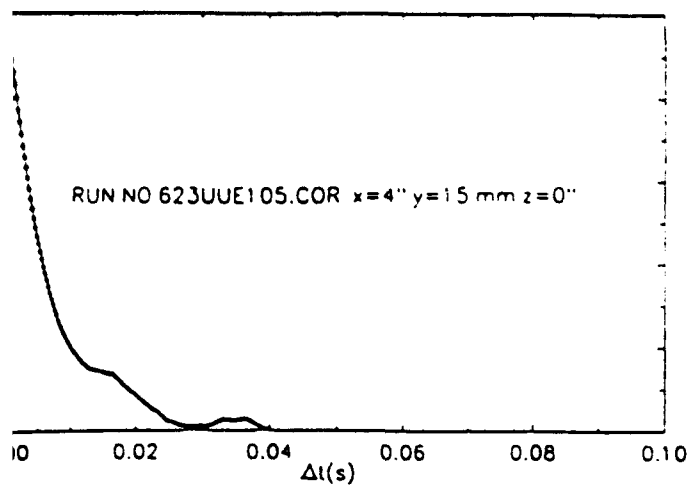


FIGURE 8. AUTOCORRELATION OF u' IN THE WALL JET RIG

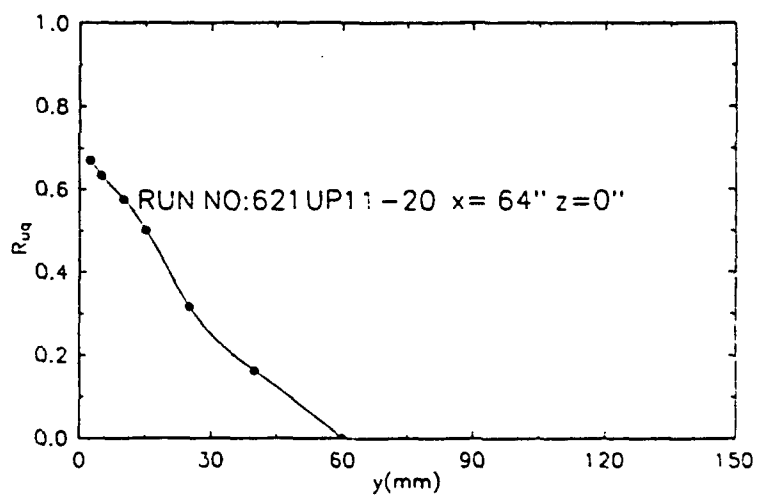
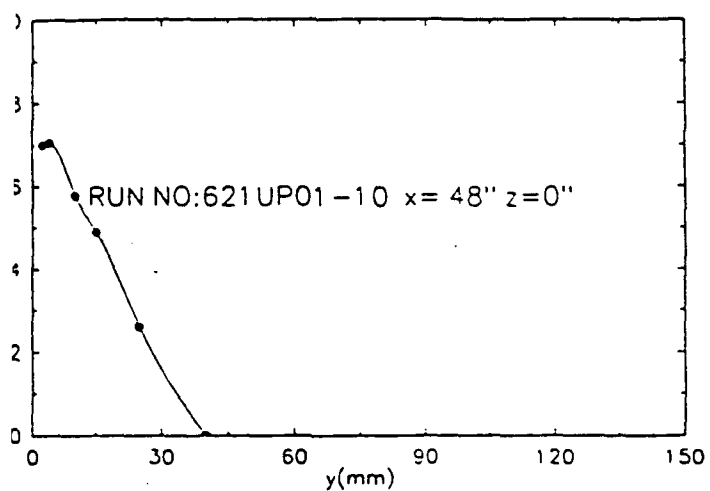
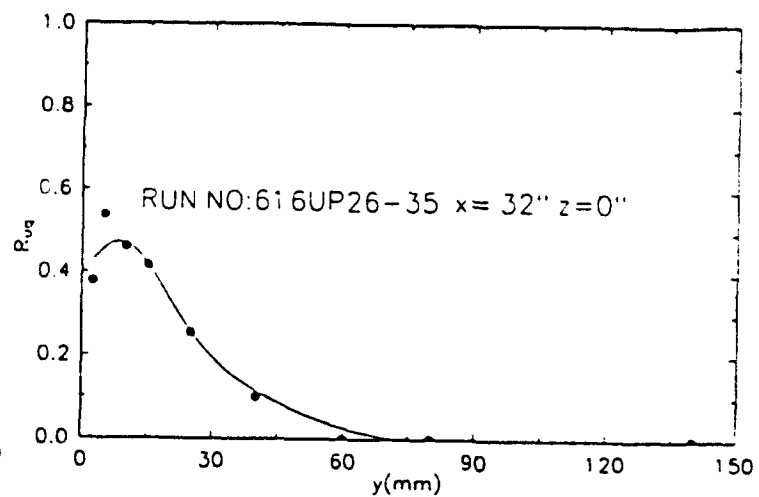
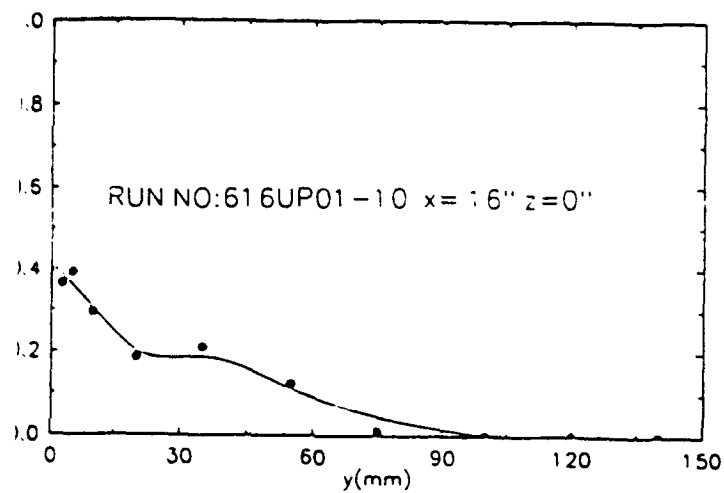


FIGURE 9. SPACE CORRELATION OF u' AND q' IN THE WALL JET RIG

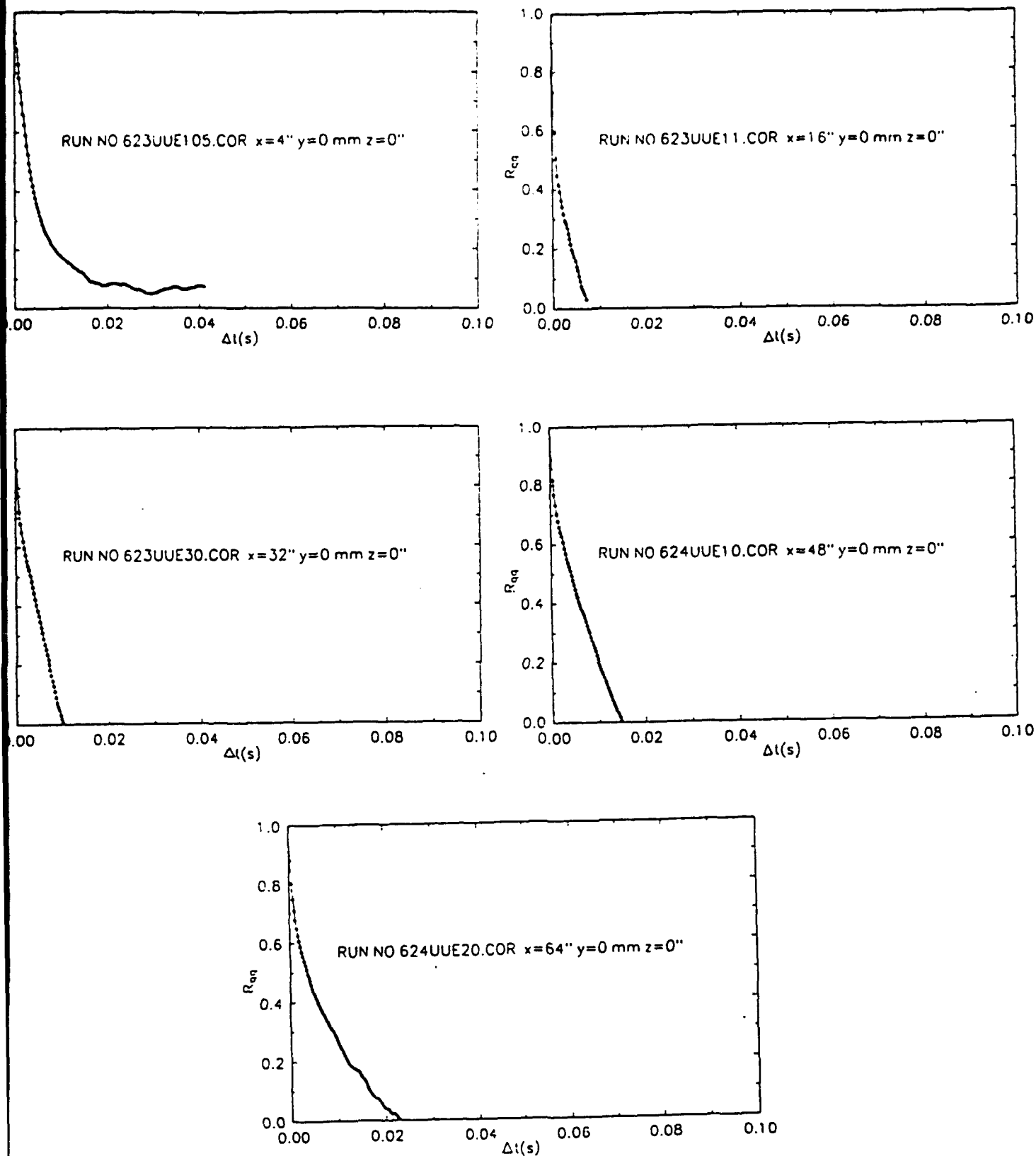


FIGURE 10. AUTOCORRELATION OF q' IN THE WALL JET RIG

COPY AVAILABLE TO DRIC DOES NOT INCLUDE ILLUSTRATIONS OF THE TEST SECTION

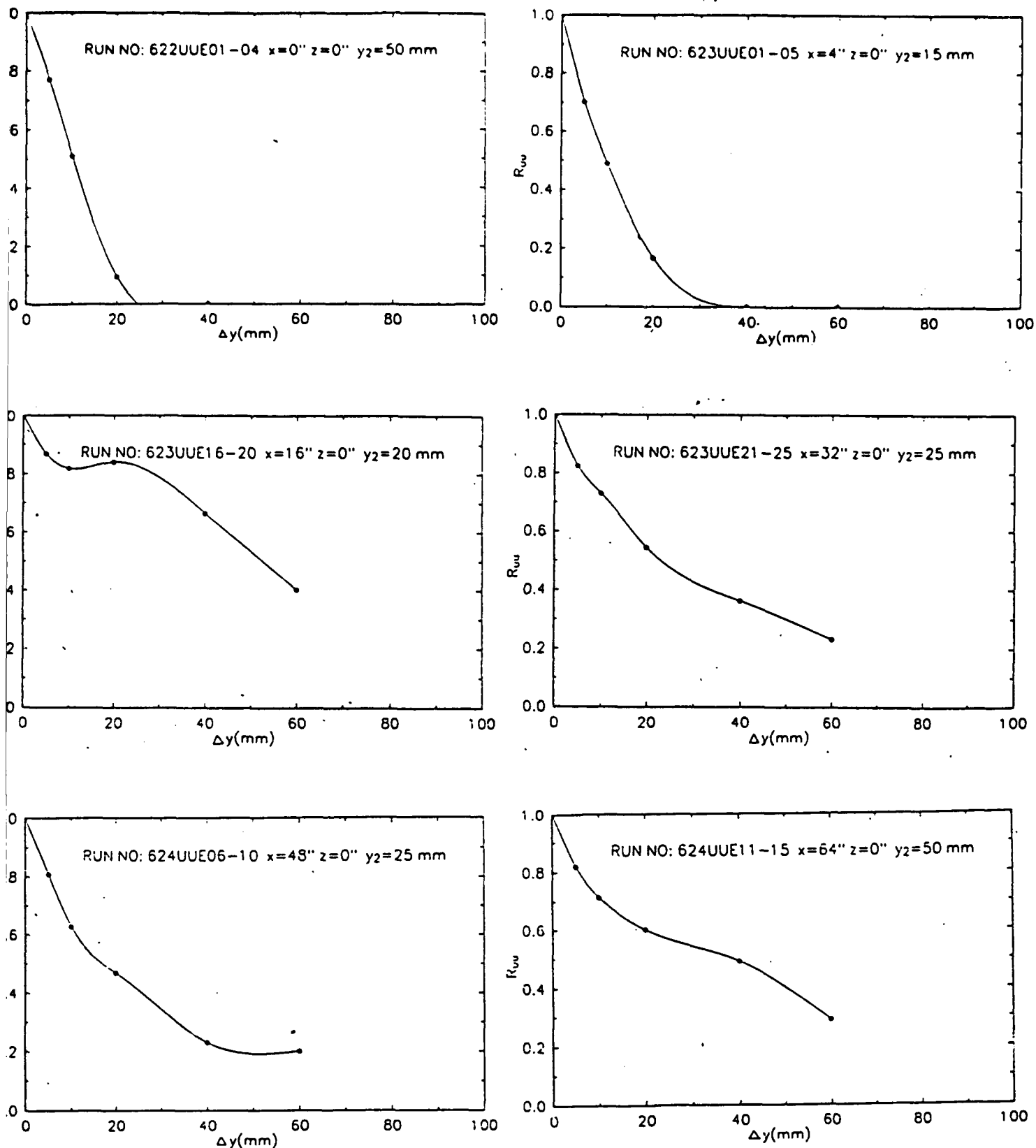


FIGURE 11. SPACE CORRELATION OF u'_1 AND u'_2
 LENGTH SCALE MEASUREMENT AT U_{max} LOCATION
 COPY AVAILABLE TO DTIC DOES NOT PERMIT FURTHER REPRODUCTION

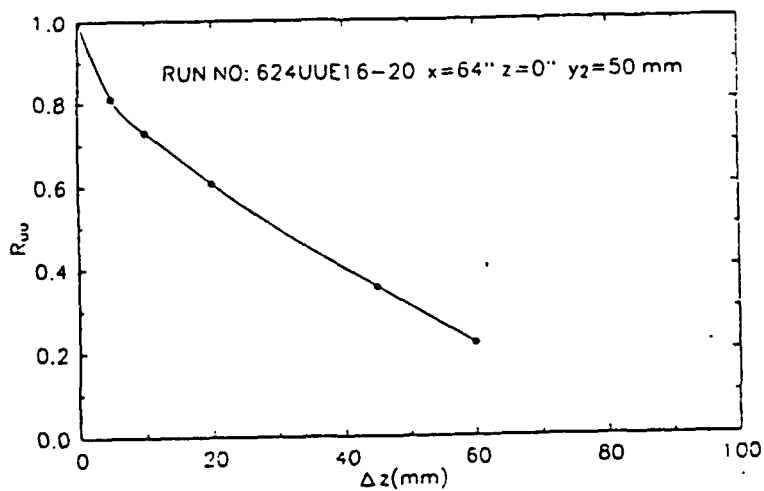
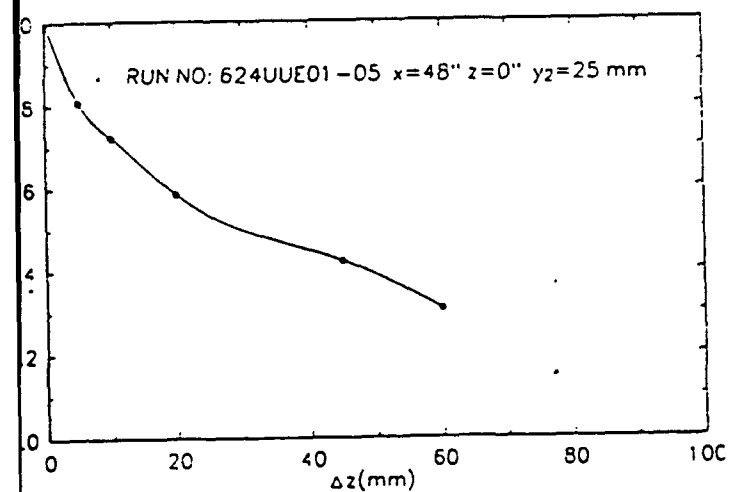
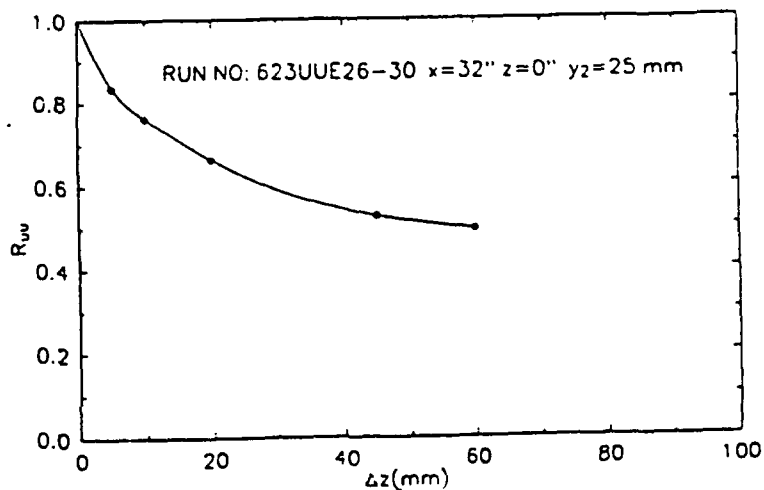
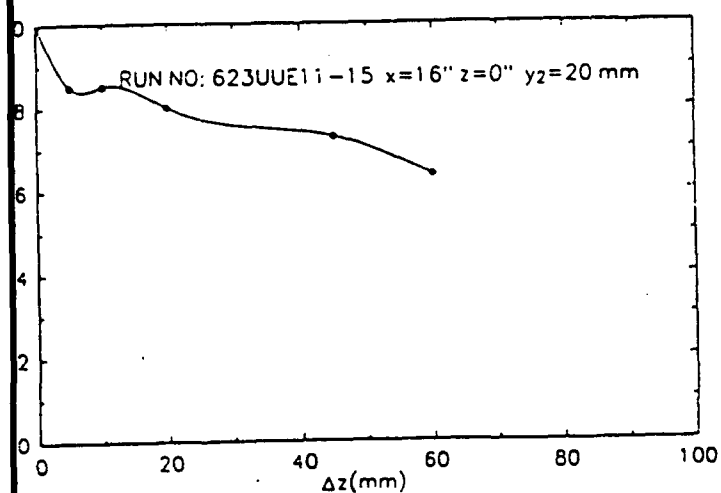
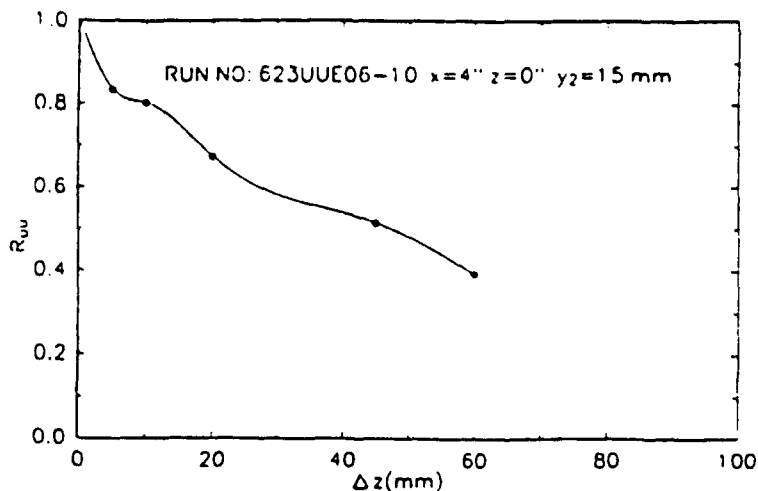
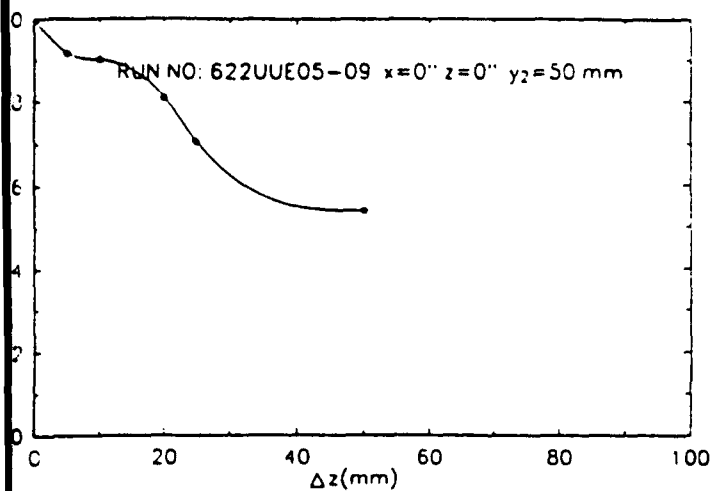


FIGURE 12. SPACE CORRELATION OF u'_1 AND u'_2
LENGTH SCALE MEASUREMENT AT U_{max} LOCATION

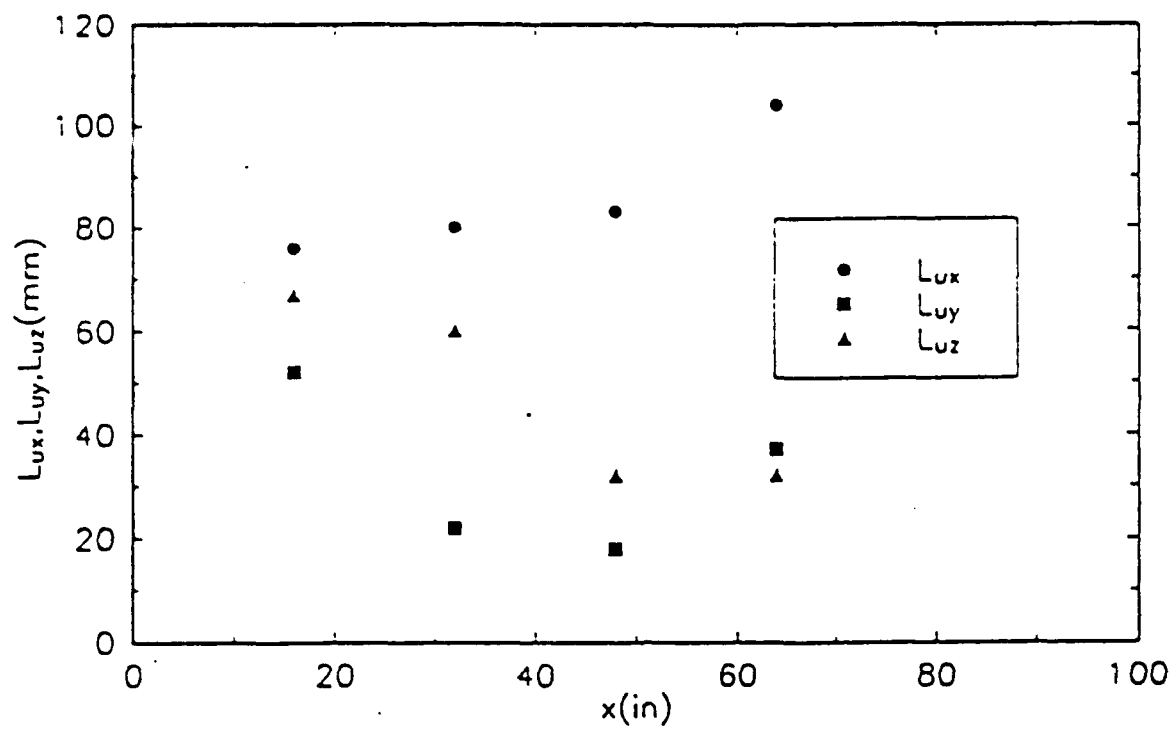


FIGURE 13. LENGTH SCALES OF u' OBTAINED FROM THE R_{uu} AT A LOCATION WHERE $R_{uu} = 0.5$